TESIS DE LA UNIVERSIDAD DE ZARAGOZA
2024
71

Javier Bonet Aletá

Nanoparticle-driven Novel Cancer Therapeutics: Catalysis for Homeostasis Disruption

Director/es
Santamaría Ramiro, Jesús Marcos
Hueso Martos, José Luis

ISSN 2254-7606

Prensas de la Universidad
Universidad Zaragoza

Universidad de Zaragoza
Servicio de Publicaciones

ISSN 2254-7606

Universidad Zaragoza
1542

Tesis Doctoral

NANOPARTICLE-DRIVEN NOVEL CANCER THERAPEUTICS: CATALYSIS FOR HOMEOSTASIS DISRUPTION

Autor

Javier Bonet Aletá

Director/es

Santamaría Ramiro, Jesús Marcos
Hueso Martos, José Luis

UNIVERSIDAD DE ZARAGOZA
Escuela de Doctorado

Programa de Doctorado en Ingeniería Química y del Medio Ambiente

2023

Nanoparticle-driven Novel Cancer Therapeutics:

Catalysis for Homeostasis Disruption

Javier Bonet-Aleta

University of Zaragoza, 2023

Departamento de Ingeniería Química y Tecnologías del Medio Ambiente
Universidad Zaragoza

INMA
INSTITUTO DE NANOCIENCIA Y MATERIALES DE ARAGÓN

El Prof. **Jesús Santamaría Ramiro**, Catedrático de Universidad, y el Doctor **José Luis Hueso Martos**, ambos pertenecientes al Departamento de Ingeniería Química y Tecnologías del Medio Ambiente de la **Universidad de Zaragoza**

CERTIFICAN:

Que la memoria de Tesis Doctoral titulada: "**Nanoparticle-driven Novel Cancer Therapeutics: Catalysis & Homeostasis Disruption**", ha sido realizado por D. Javier Bonet Aletá bajo su supervisión en el Instituto de Nanociencia y Materiales de Aragón (INMA), y en el Departamento de Ingeniería Química y Tecnologías del Medio Ambiente de la Universidad de Zaragoza. En consecuencia, autorizan la presentación de la misma.

Y para que conste, firmamos la presente Certificación en Zaragoza a 21 de junio del 2023.

Prof. Jesús Santamaría Ramiro

Dr. José Luis Hueso Martos

A **Jesús***, por enseñarme la pasión por descubrir. Por hacer de mi un científico y enseñarme lo que significa la palabra exigencia. Por darme la libertad para explorar pero ponerme en mi sitio cuando era necesario. Siempre a hombros de gigantes.*

A **JL***, por no ponerme nunca ningún límite. Por estar a mi lado en todo momento apoyándome y hacerme crecer durante estos años. Hubiera sido imposible sacar todo este trabajo delante de no ser por tu implicación constante. Gracias por confiar en mi siempre.*

A mis compañeros del proyecto CADENCE, la historia alrededor de la cual gira esta tesis. A mi compañero de trinchera **Miguel***, tú trabajo nos da algunas de las conclusiones más importantes de esta tesis y sin el cual ésta se quedaría a medias. Por implicarte al máximo desde el minuto 0. A* **Nacho***, mi camarada desde el inicio y junto al que he peleado en infinitas ocasiones contra la ciencia (y contra lo que no es la ciencia). A las demás personas que pertenecen o han pertenecido al equipo, especialmente con las que he trabajado directamente,* **Ángeles***,* **Pilar** *y* **Ana***.*

A todas las personas que forman o han formado parte del grupo NFP, acogiéndome de la mejor manera posible cuando comencé esta aventura en 2019. Agradezco especialmente a **Víctor, Silvia, Gema, Ainhoa** *y* **Ramiro** *su trabajo, parte del cual está integrado directamente en esta tesis doctoral o en otros trabajos.*

Completamente imposible no agradecer toda la ayuda, paciencia, organización, gestión, profesionalidad, y un sinfín de calificativos más a **Nuria***, la piedra angular sobre la cual se sustenta el grupo. Sólo espero poder trabajar allá donde vaya con gente como tú.*

A todos mis compañeros de la sala que forman o han formado parte del mejor ambiente que uno puede tener en el día a día. Podría llenar doscientas páginas con innumerables anécdotas e historias, pero simplemente lo resumiré en: **dogs**.

To all the people from Chang lab. at UC Berkeley, specially to my closer collaborators **Aidan** *and* **Miku** *for the lessons I have been fortunate enough to learn alongside them. Thanks* **Chris** *for welcoming me into your group and supporting me throughout my stay at UC Berkeley and beyond. I am truly privileged to have had the opportunity to work with all of you. It was an unbeatable experience that will accompany me during all my scientific career.*

A mis **padres**, *por enseñarme lo que significa realmente esforzarse y creer en mi ciegamente en todo momento. Para vosotros rendirse nunca ha sido una opción.*

Simplemente sois el mejor ejemplo que una persona puede tener.

A **Ana**, *por apoyarme incondicionalmente en todo momento desde cualquier parte del planeta. Por hacerme sentir la persona mas afortunada que existe.*

Eres la mejor persona con la que alguien puede recorrer la vida. Eres única.

A mi **gente**, *por haber intentado, y en muchas ocasiones conseguido, que no se trabaje. Por estar cerca para celebrar las victorias, pero también para olvidar las derrotas. Por estar a mi lado cuando me iba lejos. Por estar siempre presentes en todas las etapas de mi vida. Sois mis p**** padres.*

Me lo habéis dado todo.

Summary

Catalytic cancer therapy aims to induce tumor cell death by triggering harmful chemical reactions, exploiting the distinct chemical differences between cancer and healthy cells as a targeted treatment approach. The primary strategy employed in this approach involves the introduction of nanoparticles based on transition metals, which can interact with various features of the tumor microenvironment and ultimately disrupt tumor homeostasis through catalytic processes.

The central idea of this Ph.D. thesis revolves around the utilization of a copper-iron oxide nanocatalyst, referred to as CuFe, as a promising nanomedicine for anticancer purposes. Various catalytic reactions with therapeutic potential have been investigated, including the depletion of Glutathione, one of the major antioxidant systems in cancer cells, the removal of glucose, the primary energy source for cells, through the combination of CuFe with a gold catalyst, and the modification of the amino acid and peptide pool in cells via transamination reactions. Furthermore, the fate of the catalyst after internalization in cancer cells has been extensively studied using fluorescent probes to decipher the cellular response to these therapeutic nanoparticles.

Additionally, the thesis explores not only the introduction of transition metals into cells for therapeutic purposes but also the removal of existing metals in cancer cells as a therapeutic strategy to block key chemical reactions by inhibiting metal-dependent enzymes.

The manuscript comprises six distinct chapters, with chapters 1 to 5 focusing on the introduction of metals and chapter 6 dedicated to their depletion. Lastly, a conclusion section summarizes the main findings and conclusions derived from this research.

Resumen

La terapia catalítica contra el cáncer tiene como objetivo inducir la muerte de las células tumorales mediante el uso de reacciones químicas perjudiciales, aprovechando las diferencias químicas existentes entre las células cancerosas y las células. La estrategia principal empleada en este enfoque implica la introducción de nanopartículas basadas en metales de transición, que pueden interactuar con diversas características del microentorno tumoral y, en última instancia, perturbar la homeostasis tumoral mediante procesos catalíticos.

La idea central de esta tesis doctoral gira en torno al uso de un nanocatalizador de óxido de cobre-hierro, denominado CuFe, como una nanomedicina prometedora en terapia. Se han investigado diversas reacciones catalíticas con potencial terapéutico, incluida la eliminación de glutatión, uno de los principales sistemas antioxidantes en las células cancerosas, la eliminación de glucosa, la principal fuente de energía para las células, mediante la combinación de CuFe con un catalizador de oro, y la modificación de los diferentes aminoácidos y péptidos en las células mediante reacciones de transaminación. Además, se ha estudiado exhaustivamente el destino del catalizador después de su internalización en las células cancerosas utilizando sondas fluorescentes para estudiar la respuesta celular a estas nanopartículas terapéuticas.

Además, esta tesis explora no solo la introducción de metales de transición en las células con fines terapéuticos, sino también la eliminación de los metales existentes en las células cancerosas como estrategia para bloquear las reacciones químicas clave mediante la inhibición de enzimas dependientes de metales.

El manuscrito consta de seis capítulos distintos, con los capítulos del 1 al 5 centrados en la introducción de metales y el capítulo 6 dedicado a su eliminación. Por último, una sección de conclusiones resume los principales hallazgos y conclusiones derivados de esta investigación.

Introduction

Among all the diseases affecting human health, cancer represents one the major challenges of XXI century. Despite the huge economic and human efforts spent on the development of therapies, results are yet far from being satisfactory. Indeed, no disease has more different treatments than cancer, but in spit of this cancer still causes around 10 M deaths per year. Part of the problem is caused by the intrinsic complexities of cancer metabolism and growth. Understanding this complexity and overcoming the challenges involved requires not only major research funding, but also the creation of novel strategies to exploit therapeutic opportunities..

Our approach aims to combine two fields of knowledge that are rarely integrated: catalysis and cancer therapy. The industry uses catalysts to drive chemical reactions towards valuable products. In this thesis, we envision the tumor environment as a reactor, where a catalyst can be introduced to induce selective reactions with a therapeutic outcome. However, cancer cells possess different chemistry and operate under different rules than healthy cells. Leveraging this understanding, catalysis can be used to develop more efficient and selective therapies.

Typically, we chemists use reaction vessels to run chemical reactions where every single parameter is controlled. Herein, we face the most complex of chemical reactors: living systems. This thesis covers all the stages involved in the development and use of the catalysts, from the basics of synthesis and catalysis to animal models. As author, I hope this work will provide a new approach towards understanding the vulnerabilities of cancer cells and guide the development of new more effective nanocatalytic therapies.

1.1 Cancer Nanomedicine basics

Going down to the nanoscale endows materials with special properties. Some can be exploited for medical purposes, giving rise to the field of Nanomedicine. Vaccines, artificial implants, new diagnosis tools or antibacterial devices are some specific examples where Nanotechnology is being applied [1]. Current Nanomedicine aspires to overcome some of the challenges cancer treatment currently faces such as severe side-effects, poor drug solubility or low drug accumulation in tumor [2, 3], mainly through the encapsulation of chemotherapeutics [4].

The complex journey of drugs into tumors. Try to imagine yourself as a drug that has just been injected into a human body. Your primary goal consists in reaching the tumor site, and then getting into the cellular compartment where the drugs is supposed to act. For example, if you are a cisplatin molecule you will aim for the cell nuclei to bind DNA, but not for a mitochondria or a lysosome. Before reaching the tumor site, the drug must navigate the circulatory system and somehow transport across vessel walls and surrounding tumor tissue. All of this while avoiding the penetration into healthy tissues, causing an undesired damage. This is highly challenging, considering how drug molecules move inside our body. Basic mechanisms of biological mass transport consist on convection (i.e. molecule is carried by a moving fluid) and diffusion (i.e. random molecular movements following a thermodynamic gradient, mostly ruled by concentration differences). While diffusion predominates over short distances, convection does so over long distances, which is why, in general, it is responsible for taking the drug to the tumor [5].

The next step consists in penetrating the blood vessel walls towards the tumor. One minute is enough for blood to traverse all the circulatory system [5], so the drug will necessarily be in contact with different several healthy parts of the body. Vessel walls present barriers that allow for a exchange of substances depending both on the structural features of the vessel and the type of solute to exchange [6, 7]. For example, small non-polar molecules as O_2 or lipophilic species can diffuse through these barriers because of their high solubility in cell membranes, mostly consisting of lipids. Other hydrophilic or large solutes must go through apertures in the endothelial barrier. Once in the tissue, the drug can enter the cells through passive diffusion across cell membrane or by active mechanisms mediated by pores or proteins [8].

Several physicochemical factors of the drug will affect to its complex journey including the molecular mass, charge, solubility or acid-base behavior, among others [5]. The randomness of the mass transport throughout the human body and the uptake by healthy tissue contributed to the final percentage of drug able to reach targeted areas being quite limited. In addition drugs are not immune to transformation in the human body. For example, Zeng and coworkers [9] reported in 2021 how after administration of cisplatin, some components of blood could promote its *in situ* transformation into platinum nanoparticles. Another example consists on the antibodies employed in immunotherapy, which can be glycated after their injection by reacting with sugars present in blood stream [10].

Helping drugs to accomplish their goal. Nanomedicine provides a solid alternative to overcome these limitations. Administration of a drug-nanoparticle hybrid delays drug biodegradation after injection [11], enables drug release under concrete tumor-specific conditions, like acidic pH [12] or elevated temperatures [13] and improves drug delivery by functionalizing the nanocarrier to bind tumor specific-receptor [13, 14], among others. A representative example consist on the use of polyethyleneglycol (PEG) nanoparticles to transport therapeutics and increase their systemic circulation time without reducing their activity [15]. By PEGylation of drugs it is possible to increase the blood circulation half-time from <30 minutes to 5 hours [16]. In terms of clinical translation, encapsulation of the drug doxorubicin (DOX) within PEGylated liposomes was approved by FDA in 1995. This formulation increased DOX bioavailability by a 90-fold after 1 week of administration in comparison to the free drug [17, 18]. Other polymeric formulations include imine [19] or acetal [20] bonds that are sensitive to lower pHs found in tumors [21] to release more selectively the drug and reduce damage to healthy tissue.

By using nanoparticles, we are now injecting a completely different agent than a molecular-based drug, with other characteristics that must be considered for the nanoparticle journey along the body, summarized in **Figure 1**. **Size**, **shape**, **charge**, **surface functionalization** or **composition** are important parameters that will affect the interaction with several components of human body (**Figure 1**) [22]. Nanoparticles with a **size** below 10 nm are rapidly cleared by the kidneys whereas nanoparticles larger than 200 nm can activate complement systems, a part of the immune system

based on plasma proteins that recognize external substances [23]. The **shape** is also a important factor specially in relation to localization to blood vessels [22]. Flow dynamics of blood facilitate the isolation, vessel wall adhesion and extravasation of nanoparticles with shapes presenting a high aspect-ratio relationship, as discoid and rod-shaped nanoparticles, more than spheres [24, 25]. Regarding **charge** influence, cell membrane is negatively charged and will be exposed to repulsive forces against anionic nanoparticles, whereas an excess of positive charge in nanoparticles may cause cytotoxicity to healthy tissues by damaging cell membrane [26, 27] or cause a rapid clearance by macrophages [22]. Besides the already mentioned increase of the blood circulation time of drugs, modification of nanoparticle **surfaces** has been used to target cancer cells actively (**Figure 1**). Widespread strategies are based on decorating nanoparticle surface with molecules which can interact with tumor receptors. For example, different cancers overexpress the folate receptor, employed by cells to internalize folic acid, on their membrane [28]. Encapsulation of anticancer drugs in folate-based formulations showed increased cytotoxicity to cancer cells [29-31] in contrast to their non-functionalized counterpart. A systematic obstacle faced by nanoparticles is the recognition and clearance by the immune system [32]. A strategy to face this problem consists in the isolation of cell membranes and their use to wrap nanoparticles to elude immune system. Different cell types have been employed, including blood-derived cells as erythrocytes or platelets, immune system cells as neutrophils, macrophages or T-cells and the same cancer cells [32].

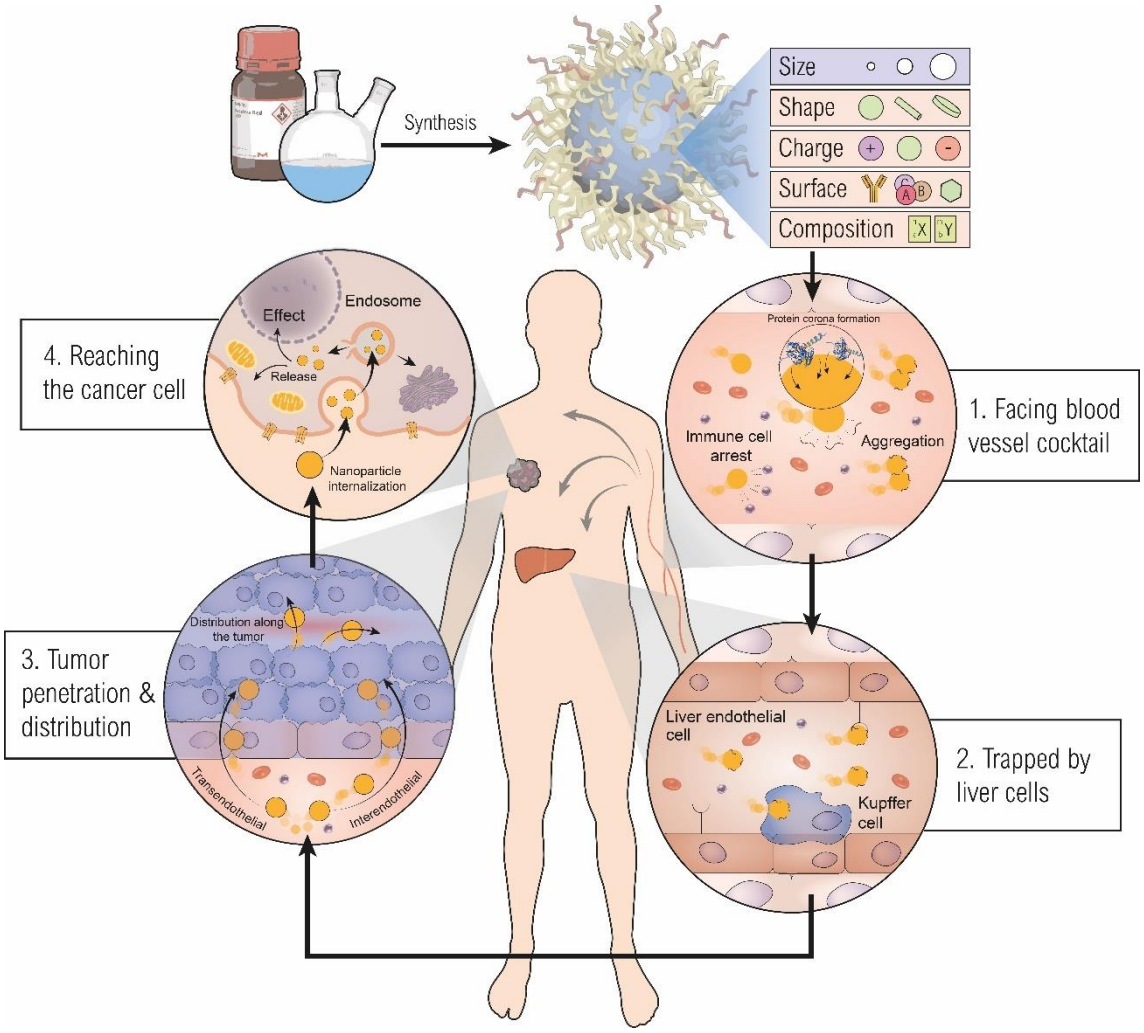

Figure 1. From the laboratory to the human body. *By chemical synthesis it is possible to build up a wide variety of nanostructures with multiple functionalities in cancer therapy. In order to achieve an efficient therapy consideration of its size, shape, charge, surface and composition is important as they affect their interaction with components of human body [22]. Once injected, the nanomedicine vector will face many obstacles before reaching the tumor site. These include potential interactions with (1) components of circulatory system that may lead to aggregation, capture by macrophages or (2) by liver cells [4]. Some of the material administered will penetrate into (3) the vessel walls surrounding the tumor through transendothelial or interendothelial pathways depending on its physicochemical properties to be then distributed throughout the tumor microenvironment. Finally, (4) nanoparticle will be internalized in tumor cells mainly through the endosomal pathway to be lately released in the cytosol.*

1.2 Combining Nanomedicine with Catalysis

At this point, the potential of Nanotechnology for cancer therapy seems clear. However, despite the large number of evaluated nanomedicines in the literature only 14 anticancer nanomedicines have currently reached the clinical use status worldwide (summarized in **Table 1**) as pointed out by de Lázaro et al. in a recent perspective [4]. In addition, although the therapeutic outcome of the nanomedicine systems is generally better than that of the free administered drug, differences are not as large as could be expected. The nanostructure function in 85% of approved nanomedicines is as mere chemotherapeutic carrier (**Figure 2**), while in the remaining 15% therapies apply their physical properties (i.e. magnetic hyperthermia or radiotherapy). Therefore, it becomes clear that the chemical properties of nanostructures are not being sufficiently exploited by cancer nanomedicine.

Table 1. Nanomedicines approved in clinical use [4].

Therapy	Drug	Nanostructure	Cancer type	Comparison vs. free drug
Chemotherapy	Neocarzinostatin	Polymer conjugate	Liver and renal cancer	N/A
	Doxorubicin	PEGylated liposomes	Kaposi sarcoma	OS[33] Nano: 320 Free drug: 246 Improved toxicological profile
			Multiple myeloma	Improved toxicological profile[34]
			Ovarian cancer	N/A
			Metastatic breast cancer	Higher ORR, significant reduced cardiotoxicity[35]
	Daunorubicin	Liposomes	Kaposi sarcoma	N/A
	Doxorubicin	Liposomes	Metastatic breast cancer	PFS Nano: 5.1 Free: 5.5 ORR Nano: 43 Free: 43 Cardiotoxicity is significantly reduced
	Paclitaxel	Liposomes	Metastatic gastric cancer	ORR[36]

			Nano: 47 Free: 46
Paclitaxel	Albumin-bound paclitaxel nanoparticles	Advanced non-small-cell lung cancer	ORR Nano: 33 Free: 25
		Metastatic breast cancer	TLRR Nano: 21.5 Free: 11.1
		Metastatic pancreatic cancer	N/A
Paclitaxel	Polymeric micelles	Breast cancer	N/A
		Non-small-cell lung cancer	N/A
Mifamurtide	Liposomes	Osteosarcoma	N/A
Vincristine	Liposomes	Philadelphia chromosome-negative acute lymphoblastic leukaemia	N/A
		Non-small-cell lung cancer	N/A
Paclitaxel	Polymer/lipid nanoparticles	Metastatic breast cancer	N/A
Irinotecan	PEGylated liposomes	Metastatic pancreatic cancer	PFS Nano: 4.1 Free: 3.1 OS[35] Nano: 7.1 Free: 6.7
Cytarabine /daunorubicin (5:1)	Liposomes	Acute myeloid leukaemia	OS (P=0.005) Nano: 9.6 Free: 5.9 ORR (P=0.036) Nano: 38 Free: 26
Paclitaxel	Polymeric micelles	Ovarian, peritoneal and fallopian tube cancer	PFS Nano: 10.3 Free: 10.1 OS Nano: 25.7 Free: 24.8
L-asparaginase	PEGylated conjugate	Acute lymphoblastic leukaemia	Hypersensitivity to asparaginase is statistically reduced
Paclitaxel	Lipid nanoparticles	Advanced gastric cancer	PFS Nano: 3.0 Free: 2.6 OS Nano: 9.7 Free: 8.9 ORR[37] Nano: 17.8 Free: 25.4
Hyperthermia	N/A	Iron oxide nanoparticles	Recurrent glioblastoma	N/A
Radiotherapy enhancer	N/A	HfO_2 nanoparticles	Locally advanced soft tissue sarcoma	N/A

OS: Overall survival, PFS: Progression-free survival, ORR: Overall response rate, TLRR: reconciled target lesion response rate

Inducing chemical reactions within cells. Catalysis; derived from the Greek "καταλύω" (*loosen)*, is the process of increasing the reaction rate of a chemical process after the addition of a substance called catalyst that does not get consumed in the process and acts by *loosening* the kinetic limits of at least one reaction. Ideally, as the catalyst remain unchanged after the reaction it can be reused indefinitely (**Figure 2**). On the other hand, classic chemotherapeutics, as cisplatin or doxorubicin, only perform one event per molecule (i.e. *one* molecule of cisplatin binds to *one* DNA nucleobase, **Figure 3**) which is a problem, considering their low tumor accumulation. Thus, by designing a nanoparticle capable of catalyzing selectively a harmful reaction for cancer cells it would be possible to increase the number of detrimental events and maximize the effectiveness of therapy. This encompasses a wide range of scenarios, from the production of a toxic substances to the depletion of essential nutrients (**Figure 3**). Traditional catalyst design is based on the consideration of the physical and chemical properties of the reaction environment. In this situation, the reaction environment will be the tumor microenvironment (TME).

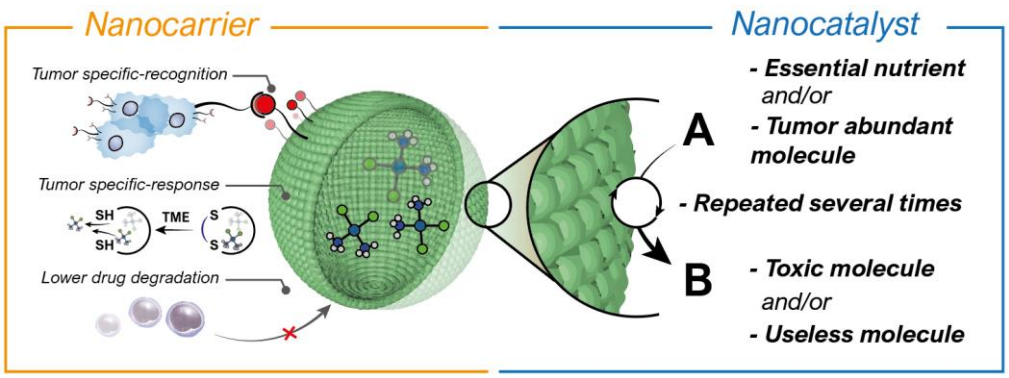

Figure 2. Active nanoparticles with roles beyond cargo carriers. *Nanoparticles can be engineered with different features to gain specificity and selectivity towards cancer cells, in addition to prevent drug degradation. Tuning the nanoparticle to be a catalyst can add a valuable functionality to trigger repeatedly harmful events to cancer cells. These include the conversion of non-toxic prodrugs or essential nutrients into toxics or useless molecules.*

The tumor microenvironment. For the successful development of this approach, the first question shall be: *what reaction is needed to occur for targeting cancer cells?*. The fundamental answer is found in the TME chemical properties, which are defined by the tumor metabolic

requirements and the availability of nutrients. Ideally, once the catalyst is already internalized within the cell (typically through the endosomal pathway [38], **Figure 3**), it will chemically interact with the TME elements to produce detrimental reactions in the cancer cell. Five main differential elements in tumor cells are exploited by catalysis: (i) the high glucose uptake shown by cancer cells (**Figure 3a**), (ii) a lower pH as a consequence of the lactate production during glycolysis (**Figure 3b**), (iii) larger hydrogen peroxide concentration (H_2O_2) (**Figure 3c**), (iv) high glutathione (GSH) levels (**Figure 3d**) compared to healthy cells and (v) the scarcity of oxygen (**Figure 3e**). The origin of these chemical differences and how nanostructured catalysts can leverage these features is discussed in the next section. All of them have been explored throughout the present thesis in different degrees.

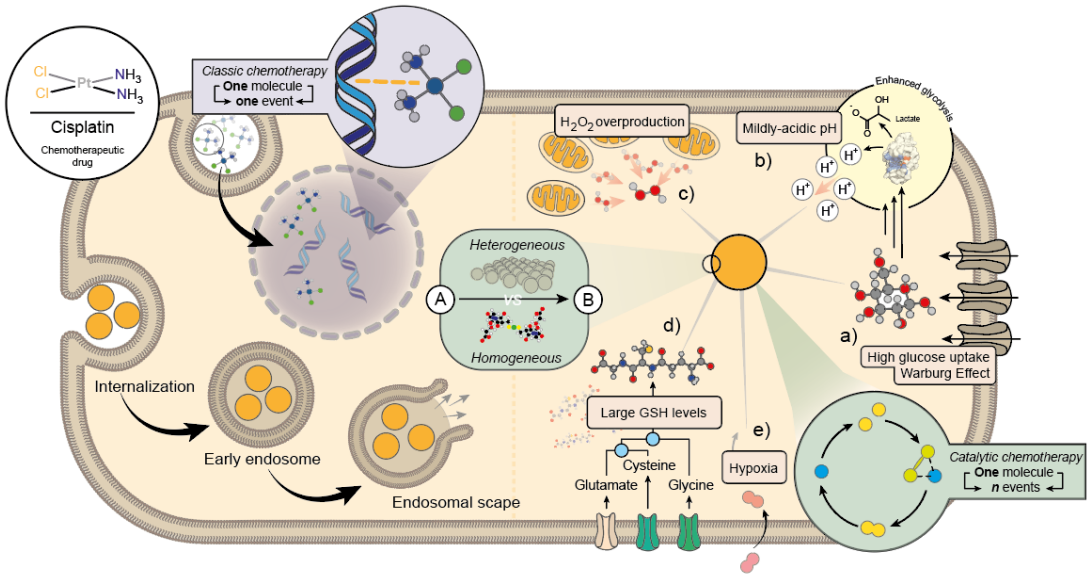

Figure 3. Comparison between traditional chemotherapy and catalytic chemotherapy. *Chemotherapeutics such as cisplatin are capable of damaging DNA by binding to its electrophilic sites. However, only one union per molecule of cisplatin can occur. The concept of catalytic chemotherapy, uses a nanostructured catalyst that can be internalized within cells. Once in the cytosol, the unique chemical conditions of cancer cells can be leveraged by the catalyst (through heterogeneous or homogeneous processes) to cause damage to cancer cells repeatedly until the reagents are consumed or the catalyst is poisoned/damaged. The main elements targeted by nanostructured catalysts are: (a) high glucose consumption, (b) mildly-acidic conditions, larger (c) H_2O_2 and (d) GSH levels and (e) low O_2 concentration.*

1.3 Translating the classic Fenton reaction into the tumor microenvironment

One of the key features of cancer is the disruption of the cell cycle: an uncontrolled expansion needs changes in their metabolism to sustain the large energetic demands of cancer growth [39-41]. In this section, the consequences of tumor metabolism on its chemical features will be discussed and analyzed as opportunities for catalytic therapy.

In 1942, Otto H. Warburg observed a significant trend of cancer cells to consume glucose independently of the O_2 availability, yielding an accumulation of lactic acid in tumor [40] (**Figure 4a**). Intuitively, one can find this reasonable as glucose is one of the major sources of ATP in cells, which is required to sustain energetically multiple metabolic processes. However, ATP is not the only factor required by cells to growth. Replication also requires the production of other biomolecules: lipids, proteins and nucleotides to ensure the viability of the nascent cells. Indeed, the synthesis of amino acids or nucleotides consume more equivalents of carbon atoms and NADPH than ATP [42]. Palmitate, a major component of the cell membrane, represents a good example of this: 7 molecules of ATP, 8 molecules of acetyl-Coenzyme A (CoA) and 14 molecules of NADPH are required for the synthesis of one molecule of palmitate [42]. In terms of glucose consumption, a total of 11 glucose molecules are necessary to build one palmitate molecule. However, only 1 molecule of glucose is necessary to generate the required ATP, while 7 and 3 molecules are employed in the biosynthesis of the NADPH equivalents and the acyl groups for acetyl-CoA, respectively [42]. Therefore, it becomes clear that converting all the glucose into CO_2 via oxidative phosphorylation is not the best option for a fast cell proliferation. In fact, 85% of the pyruvate, the main product of glycolysis, produced by tumor is fermented into lactate rather than directing it to the oxidative phosphorylation route in cancer cells [40] (**Figure 4a**). Although is still on debate, some authors point out this can be the cause of the decrease in the local pH typically found in tumors [21, 43, 44]. Some nanomedicines based on pH-responsive polymers or inorganic materials [45, 46] exploit this condition to achieve a selective and controlled drug release when they encounter a lower pH scenario. Increased H^+ concentration can induce changes in polymer solubility [47] or the breakage of imine [19] or acetal [20] groups to release chemotherapeutics with less effect on healthy tissue.

The Fenton reaction in cancer nanobiomedicine. This mildly-acidic condition is also a favorable scenario for the Fenton reaction to produce harmful Reactive Oxygen Species (ROS) to induce cell apoptosis. The Fenton reaction consists in the decomposition of intracellular H_2O_2 into hydroxyl radicals (•OH) (***Figure 4b-1***) and the subsequent regeneration of the active Fe species (***Figure 4b-2***) [48] This process is favored by acidic conditions due to the potential chelation of OH^- towards the dissolved metallic ions or the heterogeneous surfaces where reaction occurs [48, 49]. Another advantage of this strategy is that the kinetics are much slower in healthy tissue with a physiological pH around 7.4 avoiding undesired damage. The first example of introducing exogenous nanostructured Fe to induce oxidative stress in cancer cells was published by Zhang et al. [50]. Other transition metal nanomedicines mainly composed of Fe [51-53] (also in form of Single Atom Catalysts [54] or formed *in* situ complexes [52]), Cu [55-57], Mn [58, 59] but also noble metals such as Pt [60] or Pd [61] have been successfully employed for catalytic cancer therapy through an overproduction of ROS (***Figure 4c***).

The Fenton reaction was one of the first processes studied in this thesis because of its relevance in the field of Catalytic chemotherapy [62]. The first chapter describes how Fenton reaction can be catalytically turned on at mildly-acidic pH whereas it becomes deactivated at neutral pHs. It points out how TME abundant molecules can trigger this chemical reaction if the appropriate nanostructured catalyst enters the cell and maintains its activity by a cyclic regeneration.

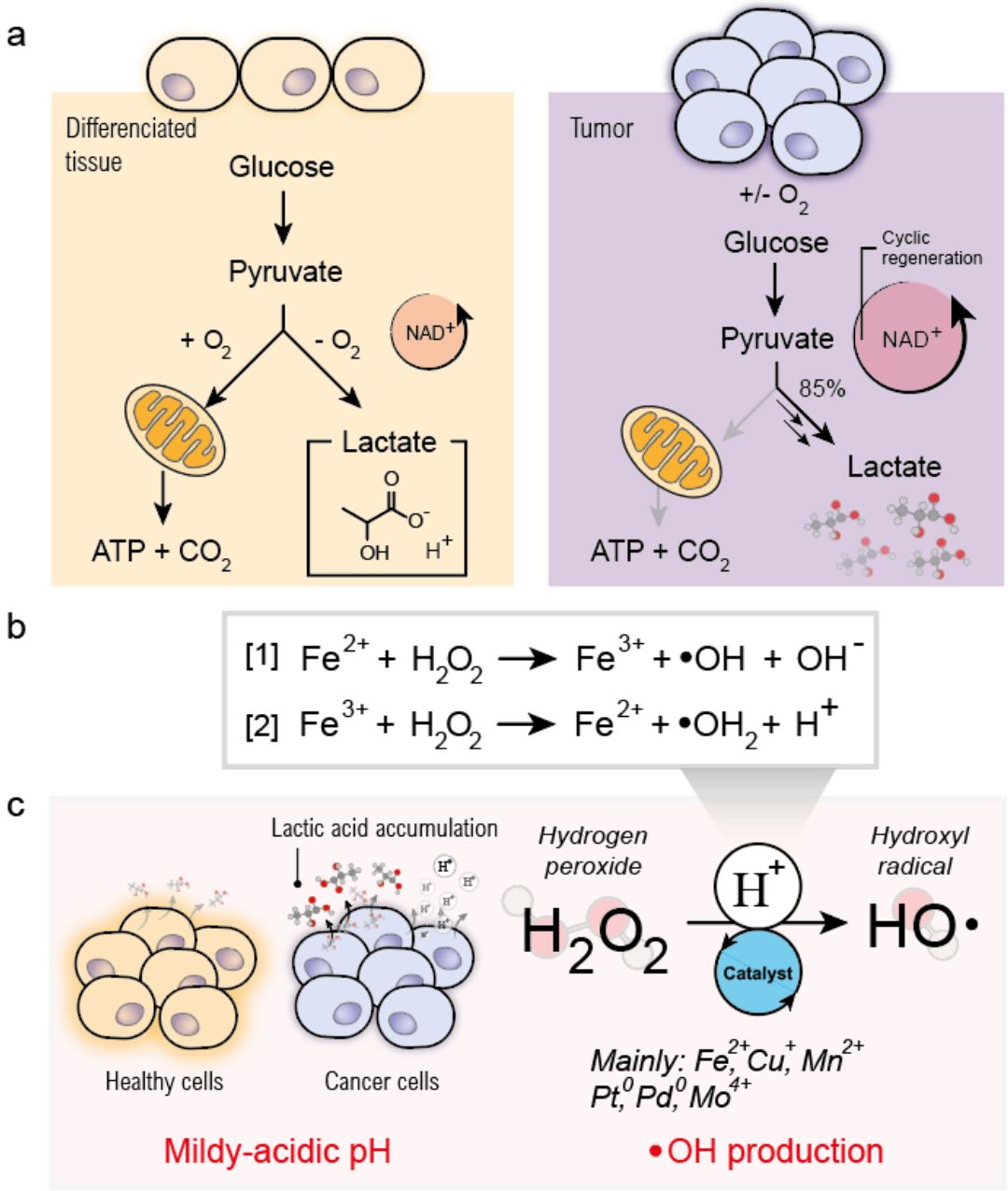

Figure 4. Acidic pH and overexpressed H_2O_2 in tumor favor •OH production through Fenton processes. *(a) Lactic acid accumulation in tumors causes mildly-acidic conditions in the tumoral extracellular space. (b) Fenton reaction catalyzed by transition metal ions has two stages: (1) Low-valence Fe^{2+} ions can form highly toxic •OH radicals by donating one electron to H_2O_2. (2) Regeneration of the active species can be achieved by the reverse process where another molecule of H_2O_2 donates one electron to Fe^{3+} [48]. (c) Transition-metal based nanocatalysts as Fe, Cu or Mn, among others, can use this process to decompose endogenous H_2O_2 into toxic HO• species to induce cancer cell death by disrupting ROS homeostasis.*

1.4. Modifying redox environment in cancer cells for therapy: the case of Glutathione

Cancerous or not, all cells are subject to a delicate equilibrium of species. Achieving redox homeostasis in cells involves maintaining a suitable equilibrium between oxidation and reduction processes in levels that not affect their viability [63]. While it has been demonstrated that ROS are pro-tumorigenic, excessive ROS become cytotoxic [64]. Besides the altered metabolism presented in the previous section, a high proliferation rate in cancer cells is also associated with a high ROS production [65]. To face this situation and maintain a proper redox balance, cancer cells overexpress an antioxidant species: glutathione (GSH), a tripeptide composed of glutamic acid, cysteine and glycine synthesized by the enzyme γ-glutamylcysteine ligase (GLC) (**Figure 5a**). Its main role consists on reacting with ROS (including H_2O_2, $\bullet O_2^-$ or •OH) through Glutathione Peroxidase (GPX4) to reduce them, eventually converting to H_2O and avoiding further potential toxicity [42] (**Figure 5a**). GPX4 possess a Selenium active center which can easily react with H_2O_2 to yield an oxidized selenium atom. This can be regenerated later by its consecutive reaction with two GSH molecules [42]. Thus, GSH stands as one of the key molecules in cancer due to its importance in counteracting oxidative stress in cancer cells [65] and its relation to tumorigenesis [66]. Therefore, GSH has been targeted as one of the key cancer biomolecules and widely studied in this thesis.

Tackling cell antioxidants to improve chemotherapy. Besides being an antioxidant agent, it has been reported that GSH also participates in processes that counter the effectivity of chemotherapeutics such as cisplatin [67] or doxorubicin [68]. In the case of cisplatin ($Pt(NH_3)_2(Cl)_2$), the nucleophilic thiol group of GSH can easily bind to Pt^{2+} centers of cisplatin yielding $Pt(SG)_2$ complexes and deactivating the capability of cisplatin to bind DNA [69]. Although still on debate, part of doxorubicin cytotoxicity is attributed to ROS formation after the electron transfer from its quinone group to oxygen [68] which can be easily quenched by GSH (**Figure 5b**). In addition, even though not so directly related as in the previous examples, some Multidrug Resistant Proteins (MRP) use GSH as cofactor to remove different chemotherapeutics from the cell [70] resulting in a higher drug efflux towards extracellular space (**Figure 5b**) [71]. Therefore,

one of the routes explored to decrease GSH-mediated resistance involves the inhibition of GLC using Buthionine sulfoximine (BSO) (**Figure 5a**) biosynthesis to block the production of antioxidant molecules of diverse cancer cell lines [72], increasing cisplatin effects [73]. However, the development of nanostructured materials based on transition metals with potential catalytic activity towards GSH oxidation is now replacing this strategy.

Oxidation of biological thiols using transition-metal catalysis. Sulphur possess $[Ne]3s^2 3p^4$ electronic configuration, resulting in large 3p orbitals (**Figure 5b*)*** with high nucleophilicity in comparison to 2p orbitals from oxygen or nitrogen, other abundant elements in biomolecules. Then, GSH can easily form metal-thiolate complexes through the binding of metal centers to the thiol group from its cysteine group, which is a natural pathway of cells to detoxify metals [74]. After the formation of the complex, the presence of electron acceptor molecules such as O_2 can enhance the oxidation of GSH into GSSG catalyzed by transition metals leading to the generation of ROS such as H_2O_2 or $\bullet O_2^-$ [75]. Given this reactivity, nanomedicines containing oxidized transition metals have been employed to disrupt the redox homeostasis in cancer cells by decreasing antioxidants and generating ROS simultaneously (**Figure 5c**) [76]. The larger GSH concentration found in cancer cells (up to mM levels) can be leveraged to improve the selectivity and effectiveness of the catalytic chemotherapy *[77-79].* Another advantage of targeting GSH through oxidative catalysis is the lower GSH levels outside cancer cells (**Figure 5c**)*[80]* that help to reduce the effects of therapy in healthy tissues. Copper deposited onto g-C_3N_4 was one of the first examples of successful catalysts in cancer therapy with the capability of depleting GSH [81] as the labile redox potential displayed by Cu^{2+}/Cu^+ pair (E^0 = 0.15 V) makes it an efficient catalyst. Interestingly, also organic-based nanoparticles such as carbon dots [82] or polymers [83] can oxidize GSH similarly to transition metal nanoparticles, but more studies are required to clarify their efficacy and the different mechanisms of organic and inorganic materials.

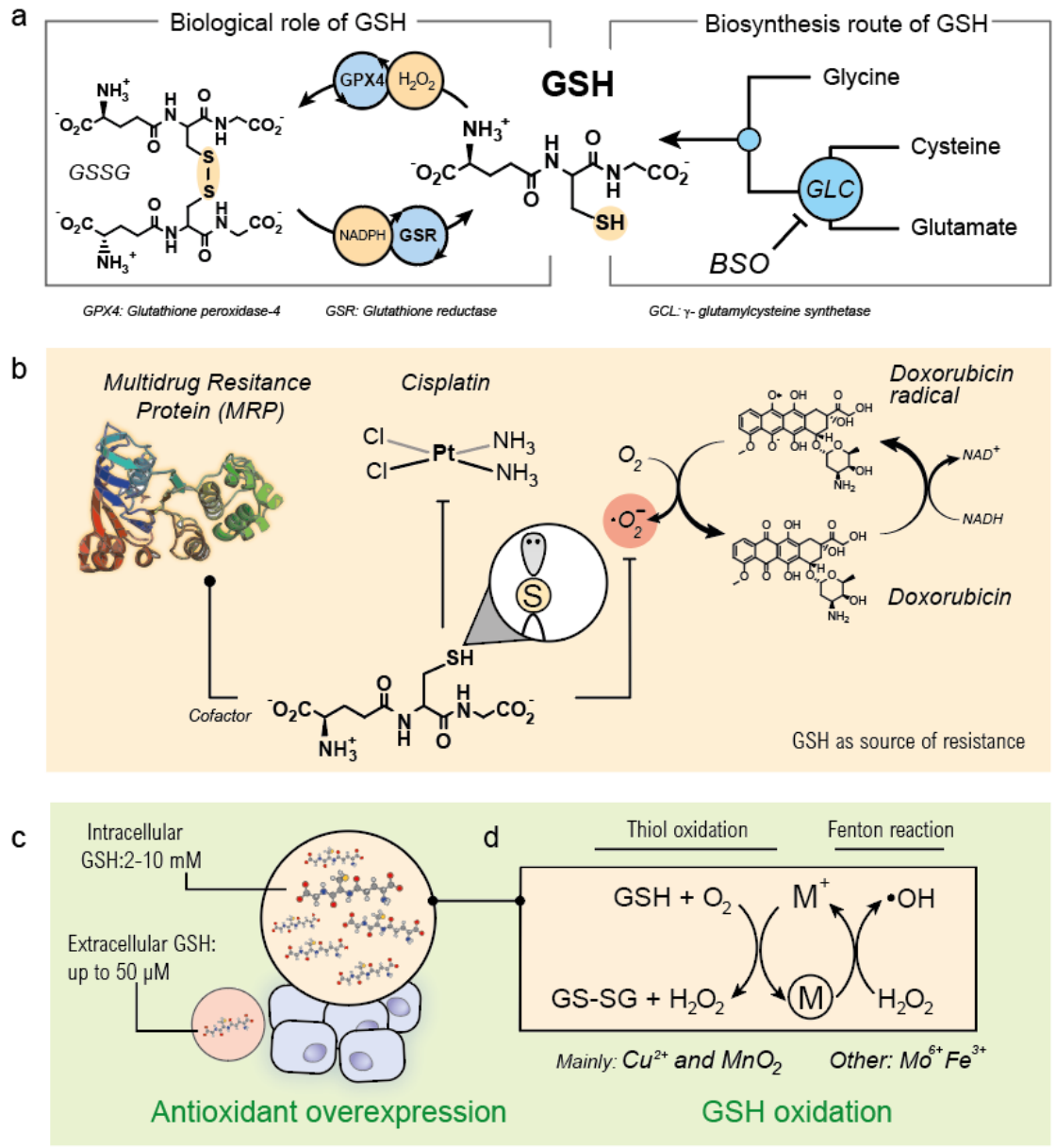

Figure 5. GSH is a key molecule in tumor redox homeostasis. *(a) Biological role of GSH involves downregulation of harmful oxidative species such as H_2O_2 through GPX4 route. This reaction yield its analogous oxidized molecule, GSSG, which can be converted back into GSH by the aid of GSR. Cells can biosynthesize GSH using Glycine, Cysteine and Glutamate as building blocks. These are later combined by GLC, which can be inhibited by BSO as an adjuvant for cancer therapy. (b) Role of GSH conferring cancer cells of resistance against chemotherapeutics. GSH can act as MRP cofactor promoting drug detoxification, as chelating agent to cisplatin or scavenging ROS generated by doxorubicin. BSO has been studied to block GSH biosynthesis by inhibition of GCL enzyme. (c) Larger GSH pools can be found in cancer cell cytosol in contrast to*

healthy cells [76]. (d) Transition metal-based nanostructures can catalyze the oxidation of the -SH group of cysteine to form GSSG and disrupt the redox homeostasis in cancer cells. The transition metal is typically reduced in the process. This reduced species fosters Fenton-like reactions to yield toxic •OH species and regenerate the oxidized metal to start again GSH depletion.

***Glutathione-triggered ROS production through reaction cascade*.** GSH can also participate in the Fenton reaction, presented in section 1.3, by fostering the regeneration the active species (**Figure 5d**). This concept was first presented by Lin et al. in 2018. They demonstrated how GSH can also react directly with Mn^{4+} from MnO_2 nanostructures (E^0 MnO_2/Mn^{2+} = 1.22 V) to yield Mn^{2+}. This latter can further undergo Fenton reaction to produce ROS through decomposition of endogenous H_2O_2 [58]. In fact, nanostructures based on oxidized transition metals can be designed to leverage GSH reaction and yield active Fenton species, coupling GSH oxidation with Fenton chemistry to overcome one of the limitations of Fenton reaction: the regeneration of the active species. For example, in the case of Fenton reaction catalyzed by Fe (**Figure 4b-1**), decomposition of H_2O_2 into •OH by Fe^{2+} is a fast process with a kinetic constant in the range of 40-80 $L{\cdot}mol^{-1}{\cdot}s^{-1}$ (**Figure 4b-1**) in contrast to the poor kinetics of the Fe^{2+} regeneration from Fe^{3+} and H_2O_2 (k = $9{\cdot}10^{-7}$ $L{\cdot}mol^{-1}{\cdot}s^{-1}$, **Figure 4b-2**) [49]. The presence in the reaction medium of reductive molecules as GSH can accelerate the regeneration of the active Fenton species [77]. Several examples of this cascade reaction with Cu [56, 77], Fe [59, 77, 84] (also in form of FeS_2 [53]) or Mo [85] based nanostructures can be found in literature in recent years and has been successfully applied to increase ROS generation within tumors (**Figure 5d**).

In summary, GSH is overexpressed in cancer cells to manage their delicate redox balance. Its chemical structure and biochemistry decreases the therapeutic efficacy in some chemotherapeutics. By using oxidized transition-metal based nanomedicines, it is possible to catalyze GSH conversion into GSSG thus reducing this natural source of resistance for cancer cells.

GSH is the central molecule of this thesis. We have studied the fundamental aspects of its catalytic oxidation using transition metals (Chapter 1), how to avoid GSH-mediated deactivation of catalysts (Chapter 2), the transformations of metal nanoparticles induced by GSH (Chapter 3), together with other possible reactions different from oxidation (Chapter 4). Also, in collaboration with Prof. Christopher Chang from UC Berkeley, we were able to track these transformations inside cells and decipher what intracellular mechanisms regulate them by using Activity-based sensing, which will be described in Chapter 5.

1.5 Impairing the balance of key nutrients in cancer cells.

Cells require nutrients to sustain their metabolic processes and proliferate. Depending on the availability of nutrients, cells adapt to new environments and in consequence, modify their metabolism [86]. Cancer cells have to survive and proliferate in scenarios where both nutrients and O_2 are scarce not only because of their larger consumption due to tumor fast growth, but also due to the aberrant vasculature surrounding tumors that difficult a proper influx of nutrients [87, 88]. From the nutrient perspective, this unfavorable scenario force cancer cells to rewire their metabolism and use alternative nutrients [89, 90]. Thus, cancer cells suffer from mutations and protein expression modifications in order to reprogram metabolic pathways and use nutrients not essential for healthy cells, creating new dependencies and vulnerabilities which can be leveraged by catalytic therapy.

Cutting-off the glucose efflux in cancer cells. Given its high importance for proliferation, using catalysis to target glucose and reduce nutrient influx to cancer cells has been a topic of interest in the recent years giving rise to the so-called “starvation therapy”. Indeed, ketogenic diets with very low content in carbohydrates have been studied as an adjuvant cancer therapy both in animal models [91] (malignant glioma [92, 93], prostate [94] or gastric cancer [95]) and even in clinical trials with humans [96]. In contrast, the catalytic approach consists in using catalyst to oxidize glucose into gluconic acid, which cannot be metabolized by cells so easily, to decrease glucose

availability. The first example of catalytic glucose starvation was reported by the Shi group in 2018, using the natural enzyme glucose oxidase (GOx) [51] to oxidize glucose within tumors [97] (***Figure 6***). Although less active, inorganic-based nanomaterials which include Au nanoparticles [98-100] or MnO_2 nanoflakes [101] have also been successfully evaluated for this purpose given their higher stability in comparison to natural enzymes to resist harsher tumor conditions (***Figure 6***). Another advantage widely explored using GOx is its capacity to generate H_2O_2 as a secondary reaction by-product [51, 97, 102]. Then, H_2O_2 can be used in cascade reactions in combination with a Fenton catalyst, as previously explained (**Figure 4**) to enhance the production of •OH and induce oxidative stress in the cancer.

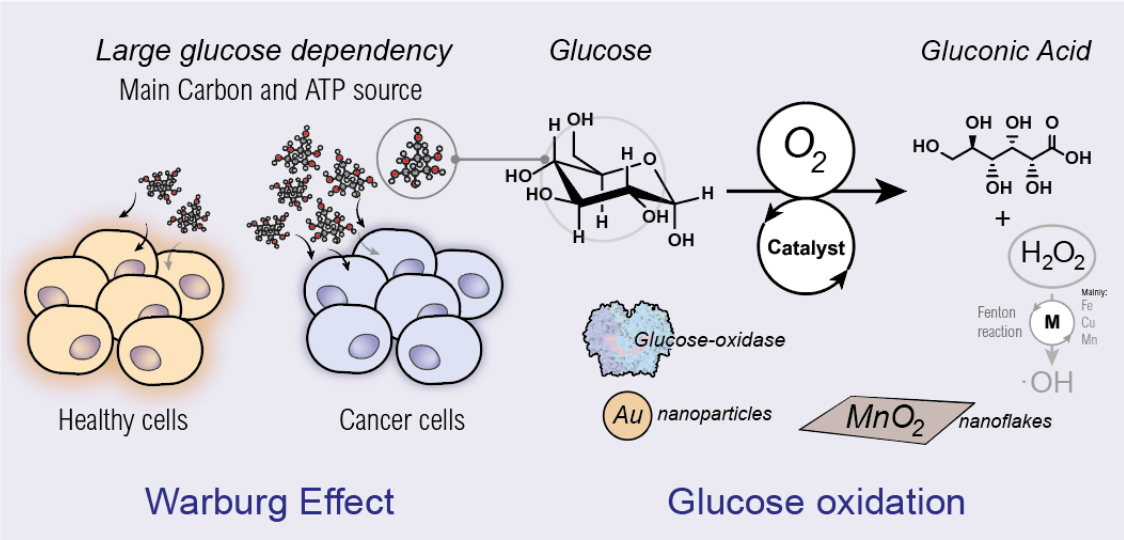

Figure 6. **Cancer cells need glucose to growth**. Uncontrolled tumor proliferation modifies its metabolism and increases their dependency on glucose as carbon, NADH and ATP source. Glucose-oxidase or enzyme-mimicking nanostructured catalysts such as Au nanoparticles or MnO_2 nanoflakes have been successfully employed to oxidize intratumoral glucose and stop the cancer nutrient influx. Additionally, the H_2O_2 generated in the process can be transformed into harmful •OH species if a Fenton promoting catalyst as Fe, Cu or Mn is combined with the glucose oxidation reaction.

Designing nanoparticles able to avoid the deactivation undergone by other catalysts such as Au nanoparticles with thiols (-SH) present in living systems [103] is of critical importance to achieve an efficient glucose oxidation. Chapter 2 faces this challenge. By combining Au with nanoparticles capable of oxidizing thiol groups, we achieved oxidation of glucose in the presence of Glutathione, one of the most common thiol-containing molecules in cells.

Increasing oxygen availability in tumors to enhance oxidative therapies. Another relevant feature is the mentioned aberrant tumour vasculature [104], which is a consequence of the fast rate of growth in tumors, with a leaky architecture presenting abundant tortuosity different from normal or inflamed tissue [105]. To realize the magnitude of this event it should be considered that the turnover of lining in normal vasculature is approximately 1000 days while in tumors the endothelium can double approximately every 10 days [106]. The structural abnormalities resulting from this phenomena results in a limitation in the O_2 diffusion towards tumor sites, with differences of 30 mmHg of O_2 in normal tissues to almost zero mmHg in solid tumors creating *hypoxic* areas [105]. (***Figure 7***). Indeed, current therapies which rely on O_2 concentration to create ROS under the application of external stimuli (X-rays, radiotherapy (RT) [107]; Light, photodynamic therapy (PDT) [108, 109]) to cause localized cell apoptosis are often severely limited by this hypoxic condition. RT uses X-rays to cause DNA damage which can be repaired easier in the absence of O_2 [110]. In the case of PDT, a photosensitizer (PS, generally an organic molecule) is administered and excited using laser irradiation to activate surrounding O_2 molecules and generate ROS [111]. Thus, hypoxic state of tumors directly limits the efficacy of both of therapies. Catalytic nanoparticles offer unique opportunities to relief tumor hypoxia for enhancing effectivity of RT and PDT based on their capability of transforming endogenous H_2O_2 into O_2 (**Figure 7**) [112].

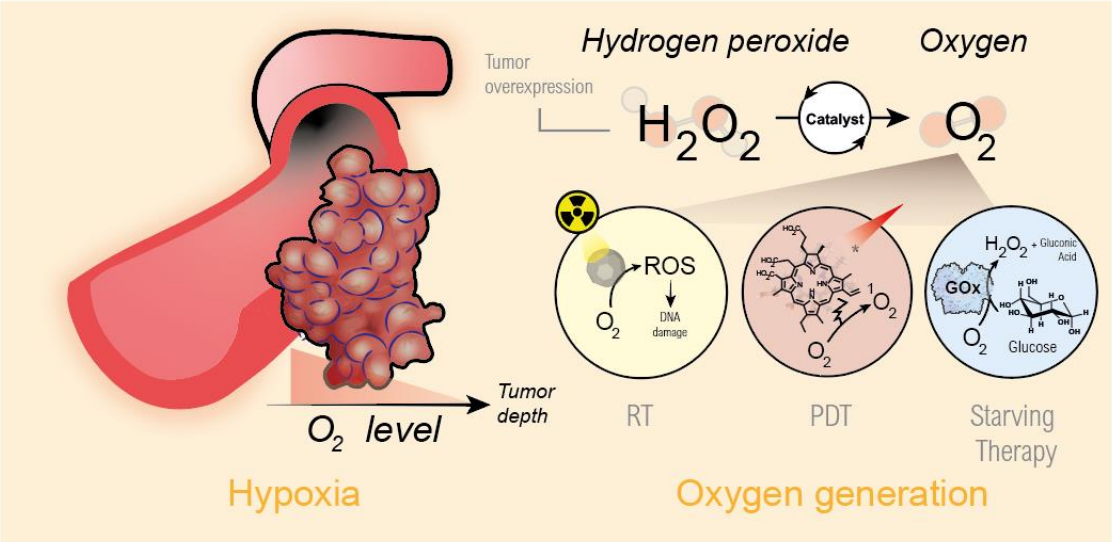

Figure 7. Low oxygen levels are detrimental for ROS-related therapies. *Tumor aberrant vasculature causes difficulties to O_2 to diffuse within the tumor and this combined with the fast O_2 consumption due to enhanced metabolism, leads to low O_2 for deep tumor areas. This limits some O_2-based therapies as RT, PDT or starvation therapies based on nutrient oxidation. Nanostructured catalysts as MnO_2 or Pt nanoparticles can decompose H_2O_2 into O_2 to relief tumor hypoxia and enhance the outcome of these therapies.*

The first example of tumor oxygenation using nanoparticles was conducted by Prasad et al. in 2014 [113]. By treating mice with MnO_2 nanoparticles embedded in Bovine Serum Albumin (BSA), O_2 concentration in tumor sites was increased together with downregulation of the Hypoxia Induced Factor (HIF-1α) and Vascular Endothelial Growth Factor (VAGF), two widely known hallmarks of cancer cells [113]. Hypoxia is tightly related to VAGF as low O_2 concentration increases tumor vascularization as mentioned before [114]. After this publication, a plethora of PS have been synergistically combined with MnO_2 [115]. In this manner, the O_2 generated can be consumed by the excited-PS generating a larger amount of ROS. (***Figure 7***). Besides MnO_2, Pt nanoparticles may also catalyze this reaction [60]. One major advantage that Pt possess over Mn is its higher atomic number (Z_{Pt} = 78 and Z_{Mn} = 25) for RT. The larger metal electron density of Pt promotes an increment in radiation dose accumulation around Pt nanoparticles, along with extra-radiation effects related to a higher energy release in form of Auger electrons which enhances localized damage to cancer cells [60]. In contrast, an advantage of MnO_2 is that it can be deposited

very easily on a wide variety of nanoplatforms [115]. Finally, starving therapy typically uses the enzyme GOx to oxidize glucose and prevents its further use by cancer cells (**Figure 6**). This reaction requires of O_2 and the hypoxic state of solid tumors described before limits the efficacy of the catalysis, in a similar way as RT or PDT. Therefore, combination of Pt and MnO_2 nanostructures, to generate *O_2 in situ,* with GOx has also been proven to enhance the efficacy of starving therapy (**Figure 7**).

Not only RT or PDT need O_2. Some catalytic reactions, such as glucose [116] or GSH [53] oxidation require molecular O_2 as final electron acceptor. In Chapter 3 we studied how using bimetallic nanoparticles is it possible to couple O_2-consuming (GSH oxidation) and O_2-generating (H_2O_2 decomposition) catalytic reactions. This can extend the active lifespan activity of a catalyst within hypoxic tumors.

The unexplored horizon of modifying the aminoacid pool using transition metal catalysis.

Amino acids are the essential building blocks of proteins, the cornerstone to maintain cellular functions [42]. They are especially relevant in a scenario of fast proliferation. Targeting amino acids can therefore be critical in certain types of cancer. Most reported examples involve the asparagine [117]. Leukemia cells can not synthesize asparagine from aspartate through asparagine synthetase route, in contrast to other cell types [118]. Given this metabolic vulnerability, the use of the enzyme L-asparaginase to deplete asparagine was one of the first strategies which targeted amino acid for cancer therapy [119, 120], and is currently employed in clinically to treat acute lymphoblastic leukemia or Non-Hodgkin lymphoma [117]. Arginine is another targeted amino acid in cancer cells by using the enzyme arginase [121]. Similarly to the case of asparagine, some cancer types are not able to synthesize arginine becoming dependent on their uptake [88]. Although different enzymes have been employed, no examples of inorganic catalysts to modify the amino acid pool are found in literature.

Chapter 4 tackles this new scenario. For the first time, we have studied how copper ions released from nanoparticles can act as catalysts to drive amino acid and short-peptide transamination with an α-ketoacid omnipresent in cells: pyruvate. This adds a new kind of reaction to the classical set employed in catalytic cancer therapy may pave the way to discover new cancer vulnerabilities.

1.6 Beyond targeting organic molecules: disruption of the ionic metal pool in cancer cells

In previous sections we discussed many advantages of introducing catalysts in cancer cells. However, it's important to be aware that catalysts are already present within cells to help drive fundamental reactions catalyzed by enzymes. This section is not focused on the triggering of a chemical reaction, but on preventing cells from doing it. Some enzymes possess intrinsic activity, but multitude of enzymes require cofactors to become functional [42]. Cofactors can be both organic molecules (ATP, NADH or NADPH, among others) and inorganic metal ions [42].

The most extended approach consist in the use of organic molecules (**Figure 8a**) with chelating capabilities to sequester metal ions in order to block the activity of key enzymes for cancer cells. Ribonucleotide reductase (RNR) catalyze the transformation of ribonucleotides in deoxyribonucleotides employed in DNA biosynthesis [122]. This reaction is fundamental in cell division and employs iron as cofactor. Triapines, a class of thiosemicarbazoles can efficiently bind iron via its sulfur and nitrogen atoms, acting as a potent inhibitor of RNR [123]. This has been explored in Phase II clinical trials for treating different tumors as pancreatic adenocarcinoma [124] or advanced renal cell adenocarcinoma [125].

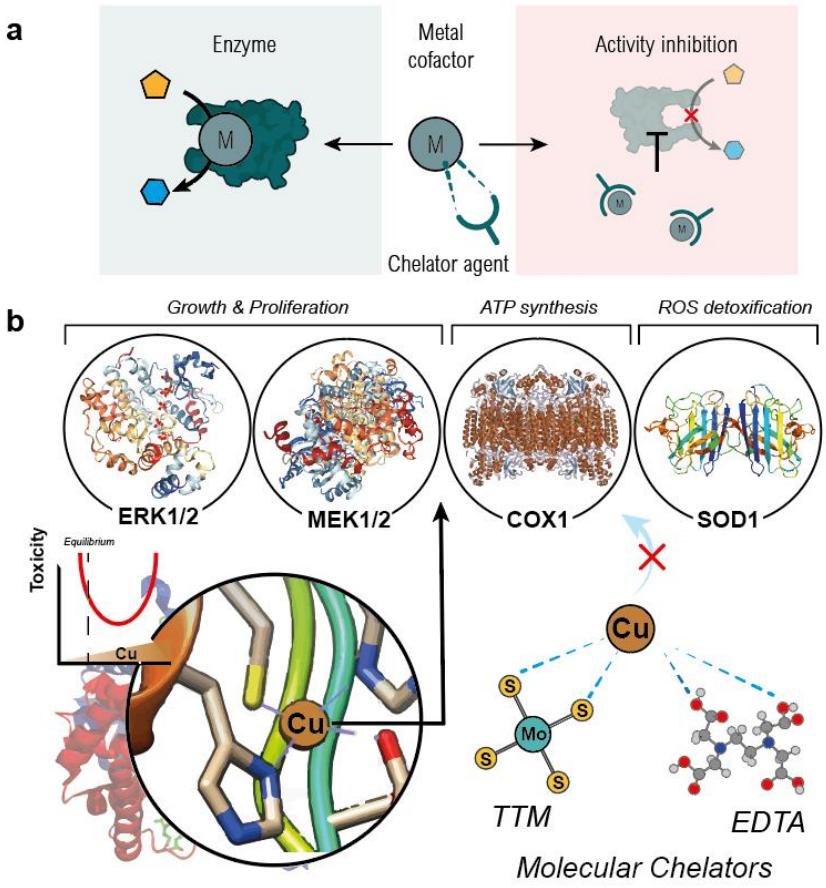

Figure 8. Nature ensure metals are in the right place at the right time. *(a) Several enzymes require of a metallic cofactor to catalyze a reaction. Adding metal chelators to reduce metal availability can inhibit enzymatic activity. Finding key and necessary metal-dependent enzymes in tumor cells can result in the discovery of new therapies based on metal sequestration. (b) Copper is a metal cofactor for several fundamental enzymes involved cells involved in cell growth and proliferation (ERK1/2, MEK1/2), ATP synthesis (COX1) or ROS detoxification (SOD1). Several studies demonstrate that copper deprivation through using molecular chelators is specifically detrimental for TNBC cells given their high reliance on copper-related enzymes [126, 127].*

Copper seems particularly appropriate as a target given the large dependency shown by Triple Negative Breast Cancer (TNBC) cells by this metal [126, 127], which will be described below. Nature has designed a very efficient system to regulate intracellular metal levels. While a copper excess is related with oxidative damage [128, 129], a copper defect is associated with Menkes disease [130]. Also, copper dysregulation is linked to cancer growth through changes in glycolysis [131, 132], metastatic expansion [133] or blood vessel formation [134]. All these features are

grouped in a new term coined *cuproplasia,* as a new copper-dependent cancer growth and proliferation *[135] (**Figure 8b**)*. TNBC are characterized by the lack of expression in three receptors: estrogen (ER-), progesterone (PR-) and epidermal growth factor (HER2-) [136]. This cell line possess a marked upregulation of copper chaperone proteins COX17 and SCO2 (i.e. proteins that delivery copper to other proteins) [137, 138] pointing out to an increasing demand on copper. In 2021, the therapeutic efficacy of Tetrathiomolybdate (TTM) [127] or pyridine-based [126] chelators was validated with TNBC with *in vivo* models. Moreover, TTM has even reached phase II in clinical trials [139]. (***Figure 8b**).*

In Chapter 6, we approached cancer cell killing by removing metals instead of adding it. In collaboration with Prof. Christopher Chang from UC Berkeley, we explored how the treatment with polydopamine (PDA) organic nanoparticles, that present high affinity towards transition metals, could affect not only the viability, but also the metabolism, protein activity or redox homeostasis of MDA-MB-231, a TNBC line.

References – Introduction

1. Pelaz, B.; Alexiou, C.; Alvarez-Puebla, R. A.; Alves, F.; Andrews, A. M.; Ashraf, S.; Balogh, L. P.; Ballerini, L.; Bestetti, A.; Brendel, C.; Bosi, S.; Carril, M.; Chan, W. C. W.; Chen, C.; Chen, X.; Chen, X.; Cheng, Z.; Cui, D.; Du, J.; Dullin, C.; Escudero, A.; Feliu, N.; Gao, M.; George, M.; Gogotsi, Y.; Grünweller, A.; Gu, Z.; Halas, N. J.; Hampp, N.; Hartmann, R. K.; Hersam, M. C.; Hunziker, P.; Jian, J.; Jiang, X.; Jungebluth, P.; Kadhiresan, P.; Kataoka, K.; Khademhosseini, A.; Kopeček, J.; Kotov, N. A.; Krug, H. F.; Lee, D. S.; Lehr, C.-M.; Leong, K. W.; Liang, X.-J.; Ling Lim, M.; Liz-Marzán, L. M.; Ma, X.; Macchiarini, P.; Meng, H.; Möhwald, H.; Mulvaney, P.; Nel, A. E.; Nie, S.; Nordlander, P.; Okano, T.; Oliveira, J.; Park, T. H.; Penner, R. M.; Prato, M.; Puntes, V.; Rotello, V. M.; Samarakoon, A.; Schaak, R. E.; Shen, Y.; Sjöqvist, S.; Skirtach, A. G.; Soliman, M. G.; Stevens, M. M.; Sung, H.-W.; Tang, B. Z.; Tietze, R.; Udugama, B. N.; VanEpps, J. S.; Weil, T.; Weiss, P. S.; Willner, I.; Wu, Y.; Yang, L.; Yue, Z.; Zhang, Q.; Zhang, Q.; Zhang, X.-E.; Zhao, Y.; Zhou, X.; Parak, W. J., Diverse Applications of Nanomedicine. *ACS Nano* **2017,** *11* (3), 2313-2381.

2. Liz-Marzán, L. M.; Nel, A. E.; Brinker, C. J.; Chan, W. C. W.; Chen, C.; Chen, X.; Ho, D.; Hu, T.; Kataoka, K.; Kotov, N. A.; Parak, W. J.; Stevens, M. M., What Do We Mean When We Say Nanomedicine? *ACS Nano* **2022,** *16* (9), 13257-13259.

3. Chabner, B. A.; Roberts, T. G., Chemotherapy and the war on cancer. *Nature Reviews Cancer* **2005,** *5* (1), 65-72.

4. de Lázaro, I.; Mooney, D. J., Obstacles and opportunities in a forward vision for cancer nanomedicine. *Nature Materials* **2021,** *20* (11), 1469-1479.

5. Dewhirst, M. W.; Secomb, T. W., Transport of drugs from blood vessels to tumour tissue. *Nature reviews. Cancer* **2017,** *17* (12), 738-750.

6. Levick, J. R., *An introduction to cardiovascular physiology*. Butterworth-Heinemann: 2013.

7. Jain, R. K., Transport of molecules across tumor vasculature. *Cancer metastasis reviews* **1987,** *6* (4), 559-93.

8. Dobson, P. D.; Kell, D. B., Carrier-mediated cellular uptake of pharmaceutical drugs: an exception or the rule? *Nature Reviews Drug Discovery* **2008,** *7* (3), 205-220.

9. Zeng, X.; Sun, J.; Li, S.; Shi, J.; Gao, H.; Sun Leong, W.; Wu, Y.; Li, M.; Liu, C.; Li, P.; Kong, J.; Wu, Y.-Z.; Nie, G.; Fu, Y.; Zhang, G., Blood-triggered generation of platinum nanoparticle functions as an anti-cancer agent. *Nature Communications* **2020,** *11* (1), 567.

10. Goetze, A. M.; Liu, Y. D.; Arroll, T.; Chu, L.; Flynn, G. C., Rates and impact of human antibody glycation in vivo. *Glycobiology* **2012,** *22* (2), 221-34.

11. Davis, M. E.; Zuckerman, J. E.; Choi, C. H. J.; Seligson, D.; Tolcher, A.; Alabi, C. A.; Yen, Y.; Heidel, J. D.; Ribas, A., Evidence of RNAi in humans from systemically administered siRNA via targeted nanoparticles. *Nature* **2010,** *464* (7291), 1067-1070.

12. Chen, C.; Ma, T.; Tang, W.; Wang, X.; Wang, Y.; Zhuang, J.; Zhu, Y.; Wang, P., Reversibly-regulated drug release using poly(tannic acid) fabricated nanocarriers for reduced secondary side effects in tumor therapy. *Nanoscale Horizons* **2020,** *5* (6), 986-998.

13. Al-Ahmady, Z. S.; Chaloin, O.; Kostarelos, K., Monoclonal antibody-targeted, temperature-sensitive liposomes: in vivo tumor chemotherapeutics in combination with mild hyperthermia. *Journal of controlled release : official journal of the Controlled Release Society* **2014,** *196*, 332-43.

14. Landgraf, M.; Lahr, C. A.; Kaur, I.; Shafiee, A.; Sanchez-Herrero, A.; Janowicz, P. W.; Ravichandran, A.; Howard, C. B.; Cifuentes-Rius, A.; McGovern, J. A.; Voelcker, N. H.; Hutmacher, D. W., Targeted camptothecin delivery via silicon nanoparticles reduces breast cancer metastasis. *Biomaterials* **2020,** *240*, 119791.

15. Suk, J. S.; Xu, Q.; Kim, N.; Hanes, J.; Ensign, L. M., PEGylation as a strategy for improving nanoparticle-based drug and gene delivery. *Advanced Drug Delivery Reviews* **2016,** *99*, 28-51.

16. Klibanov, A. L.; Maruyama, K.; Torchilin, V. P.; Huang, L., Amphipathic polyethyleneglycols effectively prolong the circulation time of liposomes. *FEBS Lett* **1990,** *268* (1), 235-7.

17. Ahmed, M.; Lukyanov, A. N.; Torchilin, V.; Tournier, H.; Schneider, A. N.; Goldberg, S. N., Combined Radiofrequency Ablation and Adjuvant Liposomal Chemotherapy: Effect of Chemotherapeutic Agent, Nanoparticle Size, and Circulation Time. *Journal of Vascular and Interventional Radiology* **2005,** *16* (10), 1365-1371.

18. Laginha, K. M.; Verwoert, S.; Charrois, G. J.; Allen, T. M., Determination of doxorubicin levels in whole tumor and tumor nuclei in murine breast cancer tumors. *Clinical cancer research : an official journal of the American Association for Cancer Research* **2005,** *11* (19 Pt 1), 6944-9.

19. Tao, Y.; Cai, K.; Liu, S.; Zhang, Y.; Chi, Z.; Xu, J., Pseudo target release behavior of simvastatin through pH-responsive polymer based on dynamic imine bonds: Promotes rapid proliferation of osteoblasts. *Materials science & engineering. C, Materials for biological applications* **2020,** *113*, 110979.

20. Wu, W.; Luo, L.; Wang, Y.; Wu, Q.; Dai, H.-B.; Li, J.-S.; Durkan, C.; Wang, N.; Wang, G.-X., Endogenous pH-responsive nanoparticles with programmable size changes for targeted tumor therapy and imaging applications. *Theranostics* **2018,** *8* (11), 3038-3058.

21. Zhang, X.; Lin, Y.; Gillies, R. J., Tumor pH and its measurement. *Journal of nuclear medicine : official publication, Society of Nuclear Medicine* **2010,** *51* (8), 1167-70.

22. Mitchell, M. J.; Billingsley, M. M.; Haley, R. M.; Wechsler, M. E.; Peppas, N. A.; Langer, R., Engineering precision nanoparticles for drug delivery. *Nature Reviews Drug Discovery* **2021,** *20* (2), 101-124.

23. Hoshyar, N.; Gray, S.; Han, H.; Bao, G., The effect of nanoparticle size on in vivo pharmacokinetics and cellular interaction. *Nanomedicine (London, England)* **2016,** *11* (6), 673-92.

24. Cooley, M.; Sarode, A.; Hoore, M.; Fedosov, D. A.; Mitragotri, S.; Sen Gupta, A., Influence of particle size and shape on their margination and wall-adhesion: implications in drug delivery vehicle design across nano-to-micro scale. *Nanoscale* **2018,** *10* (32), 15350-15364.

25. Da Silva-Candal, A.; Brown, T.; Krishnan, V.; Lopez-Loureiro, I.; Ávila-Gómez, P.; Pusuluri, A.; Pérez-Díaz, A.; Correa-Paz, C.; Hervella, P.; Castillo, J.; Mitragotri, S.; Campos, F., Shape effect in active targeting of nanoparticles to inflamed cerebral endothelium under static and flow conditions. *Journal of Controlled Release* **2019,** *309*, 94-105.

26. Ho, L. W. C.; Liu, Y.; Han, R.; Bai, Q.; Choi, C. H. J., Nano–Cell Interactions of Non-Cationic Bionanomaterials. *Accounts of Chemical Research* **2019,** *52* (6), 1519-1530.

27. Foroozandeh, P.; Aziz, A. A., Insight into Cellular Uptake and Intracellular Trafficking of Nanoparticles. *Nanoscale research letters* **2018,** *13* (1), 339.

28. Ebrahimnejad, P.; Sodagar Taleghani, A.; Asare-Addo, K.; Nokhodchi, A., An updated review of folate-functionalized nanocarriers: A promising ligand in cancer. *Drug Discovery Today* **2022,** *27* (2), 471-489.

29. Ebrahimnejad, P.; Dinarvand, R.; Sajadi, A.; Jaafari, M. R.; Nomani, A. R.; Azizi, E.; Rad-Malekshahi, M.; Atyabi, F., Preparation and in vitro evaluation of actively targetable nanoparticles for SN-38 delivery against HT-29 cell lines. *Nanomedicine: Nanotechnology, Biology and Medicine* **2010,** *6* (3), 478-485.

30. Alsaab, H.; Alzhrani, R. M.; Kesharwani, P.; Sau, S.; Boddu, S. H.; Iyer, A. K., Folate Decorated Nanomicelles Loaded with a Potent Curcumin Analogue for Targeting Retinoblastoma. *Pharmaceutics* **2017,** *9* (2).

31. Koirala, N.; Das, D.; Fayazzadeh, E.; Sen, S.; McClain, A.; Puskas, J. E.; Drazba, J. A.; McLennan, G., Folic acid conjugated polymeric drug delivery vehicle for targeted cancer detection in hepatocellular carcinoma. *Journal of biomedical materials research. Part A* **2019,** *107* (11), 2522-2535.

32. Liu, W.; Huang, Y., Cell membrane-engineered nanoparticles for cancer therapy. *Journal of Materials Chemistry B* **2022,** *10* (37), 7161-7172.

33. Judson, I.; Radford, J. A.; Harris, M.; Blay, J. Y.; van Hoesel, Q.; le Cesne, A.; van Oosterom, A. T.; Clemons, M. J.; Kamby, C.; Hermans, C.; Whittaker, J.; di Paola, E. D.; Verweij, J.; Nielsen, S., Randomised phase II trial of pegylated liposomal doxorubicin (DOXIL (R)/CAELYX (R)) versus doxorubicin in the treatment of advanced or metastatic soft tissue sarcoma: a study by the EORTC Soft Tissue and Bone Sarcoma Group. *Eur J Cancer* **2001,** *37* (7), 870-877.

34. Rifkin, R. M.; Gregory, S. A.; Mohrbacher, A.; Hussein, M. A., Pegylated liposomal doxorubicin, vincristine, and dexamethasone provide significant reduction in toxicity compared with doxorubicin, vincristine, and dexamethasone in patients with newly diagnosed multiple myeloma: a Phase III multicenter randomized trial. *Cancer* **2006,** *106* (4), 848-58.

35. Xing, M.; Yan, F.; Yu, S.; Shen, P., Efficacy and Cardiotoxicity of Liposomal Doxorubicin-Based Chemotherapy in Advanced Breast Cancer: A Meta-Analysis of Ten Randomized Controlled Trials. *PLoS One* **2015,** *10* (7), e0133569.

36. Xu, X.; Wang, L.; Xu, H. Q.; Huang, X. E.; Qian, Y. D.; Xiang, J., Clinical Comparison between Paclitaxel Liposome (Lipusu (R)) and Paclitaxel for Treatment of Patients with Metastatic Gastric Cancer. *Asian Pac J Cancer P* **2013,** *14* (4), 2591-2594.

37. Kang, Y.-K.; Ryu, M.-H.; Park, S.; Kim, J.; Kim, J.; Cho, S.-H.; Park, Y.-I.; Park, S.; Rha, S.; Kang, M. J. A. o. O., Efficacy and safety findings from DREAM: a phase III study of DHP107 (oral paclitaxel) versus iv paclitaxel in patients with advanced gastric cancer after failure of first-line chemotherapy. **2018,** *29* (5), 1220-1226.

38. Mazumdar, S.; Chitkara, D.; Mittal, A., Exploration and insights into the cellular internalization and intracellular fate of amphiphilic polymeric

nanocarriers. *Acta Pharmaceutica Sinica B* **2021,** *11* (4), 903-924.

39. Hanahan, D.; Weinberg, R. A., Hallmarks of cancer: the next generation. *Cell* **2011,** *144* (5), 646-74.

40. Vander Heiden, M. G.; Cantley, L. C.; Thompson, C. B., Understanding the Warburg effect: the metabolic requirements of cell proliferation. *Science (New York, N.Y.)* **2009,** *324* (5930), 1029-33.

41. DeBerardinis, R. J.; Chandel, N. S., We need to talk about the Warburg effect. *Nature Metabolism* **2020,** *2* (2), 127-129.

42. Nelson, D. L.; Lehninger, A. L.; Cox, M. M., *Lehninger Principles of Biochemistry*. W. H. Freeman: 2008.

43. Tannock, I. F.; Rotin, D., Acid pH in tumors and its potential for therapeutic exploitation. *Cancer Res* **1989,** *49* (16), 4373-84.

44. Gerweck, L. E., Tumor pH: Implications for treatment and novel drug design. *Seminars in Radiation Oncology* **1998,** *8* (3), 176-182.

45. Lee, C. H.; Cheng, S. H.; Huang, I. P.; Souris, J. S.; Yang, C. S.; Mou, C. Y.; Lo, L. W., Intracellular pH-responsive mesoporous silica nanoparticles for the controlled release of anticancer chemotherapeutics. *Angewandte Chemie (International ed. in English)* **2010,** *49* (44), 8214-9.

46. Tang, H.; Guo, J.; Sun, Y.; Chang, B.; Ren, Q.; Yang, W., Facile synthesis of pH sensitive polymer-coated mesoporous silica nanoparticles and their application in drug delivery. *International Journal of Pharmaceutics* **2011,** *421* (2), 388-396.

47. Wu, X. L.; Kim, J. H.; Koo, H.; Bae, S. M.; Shin, H.; Kim, M. S.; Lee, B.-H.; Park, R.-W.; Kim, I.-S.; Choi, K.; Kwon, I. C.; Kim, K.; Lee, D. S., Tumor-Targeting Peptide Conjugated pH-Responsive Micelles as a Potential Drug Carrier for Cancer Therapy. *Bioconjugate Chemistry* **2010,** *21* (2), 208-213.

48. Pignatello, J. J.; Oliveros, E.; MacKay, A., Advanced Oxidation Processes for Organic Contaminant Destruction Based on the Fenton Reaction and Related Chemistry. *Critical Reviews in Environmental Science and Technology* **2006,** *36* (1), 1-84.

49. Bonet-Aleta, J.; Calzada-Funes, J.; Hueso, J. L., Chapter 9 - Recent developments of iron-based nanosystems as enzyme-mimicking surrogates of interest in tumor microenvironment treatment. In *Nanomaterials for Biocatalysis*, Castro, G. R.; Nadda, A. K.; Nguyen, T. A.; Qi, X.; Yasin, G., Eds. Elsevier: 2022; pp 237-265.

50. Zhang, C.; Bu, W.; Ni, D.; Zhang, S.; Li, Q.; Yao, Z.; Zhang, J.; Yao, H.; Wang, Z.; Shi, J., Synthesis of Iron Nanometallic Glasses and Their Application in Cancer Therapy by a Localized Fenton Reaction. *Angewandte Chemie (International ed. in English)* **2016,** *55* (6), 2101-6.

51. Huo, M.; Wang, L.; Chen, Y.; Shi, J., Tumor-selective catalytic nanomedicine by nanocatalyst delivery. *Nature Communications* **2017,** *8* (1), 357.

52. Yang, B.; Yao, H.; Tian, H.; Yu, Z.; Guo, Y.; Wang, Y.; Yang, J.; Chen, C.; Shi, J., Intratumoral synthesis of nano-metalchelate for tumor catalytic therapy by ligand field-enhanced coordination. *Nature Communications* **2021,** *12* (1), 3393.

53. Meng, X.; Li, D.; Chen, L.; He, H.; Wang, Q.; Hong, C.; He, J.; Gao, X.; Yang, Y.; Jiang, B.; Nie, G.; Yan, X.; Gao, L.; Fan, K., High-Performance Self-Cascade Pyrite Nanozymes for Apoptosis–Ferroptosis Synergistic Tumor Therapy. *ACS Nano* **2021,** *15* (3), 5735-5751.

54. Huo, M.; Wang, L.; Wang, Y.; Chen, Y.; Shi, J., Nanocatalytic Tumor Therapy by Single-Atom Catalysts. *ACS Nano* **2019,** *13* (2), 2643-2653.

55. Lin, L.-S.; Huang, T.; Song, J.; Ou, X.-Y.; Wang, Z.; Deng, H.; Tian, R.; Liu, Y.; Wang, J.-F.; Liu, Y.; Yu, G.; Zhou, Z.; Wang, S.; Niu, G.; Yang, H.-H.; Chen, X., Synthesis of Copper Peroxide Nanodots for H_2O_2 Self-Supplying Chemodynamic Therapy. *Journal of the American Chemical Society* **2019,** *141* (25), 9937-9945.

56. Ma, B.; Wang, S.; Liu, F.; Zhang, S.; Duan, J.; Li, Z.; Kong, Y.; Sang, Y.; Liu, H.; Bu, W.; Li, L., Self-Assembled Copper–Amino Acid Nanoparticles for in Situ Glutathione "AND" H_2O_2 Sequentially Triggered Chemodynamic Therapy. *Journal of the American Chemical Society* **2019,** *141* (2), 849-857.

57. Lu, X.; Gao, S.; Lin, H.; Yu, L.; Han, Y.; Zhu, P.; Bao, W.; Yao, H.; Chen, Y.; Shi, J., Bioinspired Copper Single-Atom Catalysts for Tumor Parallel Catalytic Therapy. *Advanced Materials* **2020,** *32* (36), 2002246.

58. Lin, L.-S.; Song, J.; Song, L.; Ke, K.; Liu, Y.; Zhou, Z.; Shen, Z.; Li, J.; Yang, Z.; Tang, W.; Niu, G.; Yang, H.-H.; Chen, X., Simultaneous Fenton-like Ion Delivery and Glutathione Depletion by MnO2-Based Nanoagent to Enhance Chemodynamic Therapy. *Angewandte Chemie International Edition* **2018,** *57* (18), 4902-4906.

59. Wu, F.; Du, Y.; Yang, J.; Shao, B.; Mi, Z.; Yao, Y.; Cui, Y.; He, F.; Zhang, Y.; Yang, P., Peroxidase-like Active Nanomedicine with Dual Glutathione Depletion Property to Restore Oxaliplatin Chemosensitivity and Promote Programmed Cell Death. *ACS Nano* **2022,** *16* (3), 3647-3663.

60. Garcia-Peiro, J. I.; Bonet-Aleta, J.; Santamaria, J.; Hueso, J. L., Platinum nanoplatforms: classic catalysts claiming a prominent role in cancer therapy. *Chemical Society Reviews* **2022,** *51* (17), 7662-7681.

61. Chen, X.; Jia, Z.; Wen, Y.; Huang, Y.; Yuan, X.; Chen, Y.; Liu, Y.; Liu, J., Bidirectional anisotropic palladium nanozymes reprogram macrophages to enhance collaborative chemodynamic therapy of colorectal cancer. *Acta biomaterialia* **2022,** *151*, 537-548.

62. Tang, Z.; Zhao, P.; Wang, H.; Liu, Y.; Bu, W., Biomedicine Meets Fenton Chemistry. *Chemical Reviews* **2021,** *121* (4), 1981-2019.

63. Le Gal, K.; Schmidt, E. E.; Sayin, V. I., Cellular Redox Homeostasis. *Antioxidants (Basel, Switzerland)* **2021,** *10* (9).

64. Reczek, C. R.; Birsoy, K.; Kong, H.; Martínez-Reyes, I.; Wang, T.; Gao, P.; Sabatini, D. M.; Chandel, N. S., A CRISPR screen identifies a pathway required for paraquat-induced cell death. *Nature chemical biology* **2017,** *13* (12), 1274-1279.

65. Hayes, J. D.; Dinkova-Kostova, A. T.; Tew, K. D., Oxidative Stress in Cancer. *Cancer cell* **2020,** *38* (2), 167-197.

66. Lu, S. C.; Ge, J. L., Loss of suppression of GSH synthesis at low cell density in primary cultures of rat hepatocytes. **1992,** *263* (6), C1181-C1189.

67. Traverso, N.; Ricciarelli, R.; Nitti, M.; Marengo, B.; Furfaro, A. L.; Pronzato, M. A.; Marinari, U. M.; Domenicotti, C., Role of glutathione in cancer progression and chemoresistance. *Oxidative medicine and cellular longevity* **2013,** *2013*, 972913.

68. McLellan, L. I.; Wolf, C. R., Glutathione and glutathione-dependent enzymes in cancer drug resistance. *Drug Resistance Updates* **1999,** *2* (3), 153-164.

69. Ishikawa, T.; Ali-Osman, F., Glutathione-associated cis-diamminedichloroplatinum(II) metabolism and ATP-dependent efflux from leukemia cells. Molecular characterization of glutathione-platinum complex and its biological significance. *Journal of Biological Chemistry* **1993,** *268* (27), 20116-20125.

70. Kuo, M. T., Redox regulation of multidrug resistance in cancer chemotherapy: molecular mechanisms and therapeutic opportunities. *Antioxidants & redox signaling* **2009,** *11* (1), 99-133.

71. Fletcher, J. I.; Haber, M.; Henderson, M. J.; Norris, M. D., ABC transporters in cancer: more than just drug efflux pumps. *Nature Reviews Cancer* **2010,** *10* (2), 147-156.

72. Lewis-Wambi, J. S.; Kim, H. R.; Wambi, C.; Patel, R.; Pyle, J. R.; Klein-Szanto, A. J.; Jordan, V. C., Buthionine sulfoximine sensitizes antihormone-resistant human breast cancer cells to estrogen-induced apoptosis. *Breast Cancer Research* **2008,** *10* (6), R104.

73. Saikawa, Y.; Kubota, T.; Kuo, T.-H.; Furukawa, T.; Tanino, H.; Watanabe, M.; Ishibiki, K.; Kitajima, M., Enhancement of Antitumor Activity of Cisplatin on Human Gastric Cancer Cells in vitro and in vivo by Buthionine Sulfoximine. *Japanese Journal of Cancer Research* **1993,** *84* (7), 787-793.

74. Jozefczak, M.; Remans, T.; Vangronsveld, J.; Cuypers, A., Glutathione is a key player in metal-induced oxidative stress defenses. *International journal of molecular sciences* **2012,** *13* (3), 3145-3175.

75. Ngamchuea, K.; Batchelor-McAuley, C.; Compton, R. G., The Copper(II)-Catalyzed Oxidation of Glutathione. *Chemistry – A European Journal* **2016,** *22* (44), 15937-15944.

76. Ding, Y.; Dai, Y.; Wu, M.; Li, L., Glutathione-mediated nanomedicines for cancer diagnosis and therapy. *Chemical Engineering Journal* **2021,** *426*, 128880.

77. Bonet-Aleta, J.; Sancho-Albero, M.; Calzada-Funes, J.; Irusta, S.; Martin-Duque, P.; Hueso, J. L.; Santamaria, J., Glutathione-Triggered catalytic response of Copper-Iron mixed oxide Nanoparticles. Leveraging tumor microenvironment conditions for chemodynamic therapy. *Journal of colloid and interface science* **2022,** *617*, 704-717.

78. Gamcsik, M. P.; Kasibhatla, M. S.; Teeter, S. D.; Colvin, O. M., Glutathione levels in human tumors. *Biomarkers : biochemical indicators of exposure, response, and susceptibility to chemicals* **2012,** *17* (8), 671-91.

79. Niu, B.; Liao, K.; Zhou, Y.; Wen, T.; Quan, G.; Pan, X.; Wu, C., Application of glutathione depletion in cancer therapy: Enhanced ROS-based therapy, ferroptosis, and chemotherapy. *Biomaterials* **2021,** *277*, 121110.

80. Wu, G.; Fang, Y.-Z.; Yang, S.; Lupton, J. R.; Turner, N. D., Glutathione Metabolism and Its Implications for Health. *The Journal of Nutrition* **2004,** *134* (3), 489-492.

81. Ju, E.; Dong, K.; Chen, Z.; Liu, Z.; Liu, C.; Huang, Y.; Wang, Z.; Pu, F.; Ren, J.; Qu, X., Copper(II)–Graphitic Carbon Nitride Triggered Synergy: Improved ROS Generation and Reduced Glutathione Levels for Enhanced Photodynamic Therapy. **2016,** *55* (38), 11467-11471.

82. Yao, L.; Zhao, M.-M.; Luo, Q.-W.; Zhang, Y.-C.; Liu, T.-T.; Yang, Z.; Liao, M.; Tu, P.; Zeng, K.-W., Carbon Quantum Dots-Based Nanozyme from Coffee

Induces Cancer Cell Ferroptosis to Activate Antitumor Immunity. *ACS Nano* **2022,** *16* (6), 9228-9239.

83. Zhou, Z.; Wu, H.; Yang, R.; Xu, A.; Zhang, Q.; Dong, J.; Qian, C.; Sun, M., GSH depletion liposome adjuvant for augmenting the photothermal immunotherapy of breast cancer. *Sci Adv* **2020,** *6* (36), eabc4373.

84. Liu, J.; Wu, M.; Pan, Y.; Duan, Y.; Dong, Z.; Chao, Y.; Liu, Z.; Liu, B., Biodegradable Nanoscale Coordination Polymers for Targeted Tumor Combination Therapy with Oxidative Stress Amplification. *Advanced Functional Materials* **2020,** *30* (13), 1908865.

85. Chang, M.; Wang, M.; Wang, M.; Shu, M.; Ding, B.; Li, C.; Pang, M.; Cui, S.; Hou, Z.; Lin, J., A Multifunctional Cascade Bioreactor Based on Hollow-Structured Cu_2MoS_4 for Synergetic Cancer Chemo-Dynamic Therapy/Starvation Therapy/ Phototherapy /Immunotherapy with Remarkably Enhanced Efficacy. **2019,** *31* (51), 1905271.

86. Palm, W., Metabolic plasticity allows cancer cells to thrive under nutrient starvation. *Proceedings of the National Academy of Sciences of the United States of America* **2021,** *118* (14).

87. DeBerardinis, R. J.; Chandel, N. S., Fundamentals of cancer metabolism. *Sci Adv* **2016,** *2* (5), e1600200.

88. Garcia-Bermudez, J.; Williams, R. T.; Guarecuco, R.; Birsoy, K., Targeting extracellular nutrient dependencies of cancer cells. *Molecular Metabolism* **2020,** *33*, 67-82.

89. Lyssiotis, C. A.; Kimmelman, A. C., Metabolic Interactions in the Tumor Microenvironment. *Trends in Cell Biology* **2017,** *27* (11), 863-875.

90. DeBerardinis, R. J.; Lum, J. J.; Hatzivassiliou, G.; Thompson, C. B., The Biology of Cancer: Metabolic Reprogramming Fuels Cell Growth and Proliferation. *Cell Metabolism* **2008,** *7* (1), 11-20.

91. Allen, B. G.; Bhatia, S. K.; Anderson, C. M.; Eichenberger-Gilmore, J. M.; Sibenaller, Z. A.; Mapuskar, K. A.; Schoenfeld, J. D.; Buatti, J. M.; Spitz, D. R.; Fath, M. A., Ketogenic diets as an adjuvant cancer therapy: History and potential mechanism. *Redox Biology* **2014,** *2*, 963-970.

92. Seyfried, T. N.; Sanderson, T. M.; El-Abbadi, M. M.; McGowan, R.; Mukherjee, P., Role of glucose and ketone bodies in the metabolic control of experimental brain cancer. *British journal of cancer* **2003,** *89* (7), 1375-82.

93. Maurer, G. D.; Brucker, D. P.; Bähr, O.; Harter, P. N.; Hattingen, E.; Walenta, S.; Mueller-Klieser, W.; Steinbach, J. P.; Rieger, J., Differential utilization of ketone bodies by neurons and glioma cell lines: a rationale for ketogenic diet as experimental glioma therapy. *BMC cancer* **2011,** *11*, 315.

94. Beck, S. A.; Tisdale, M. J., Nitrogen excretion in cancer cachexia and its modification by a high fat diet in mice. *Cancer Res* **1989,** *49* (14), 3800-4.

95. Otto, C.; Kaemmerer, U.; Illert, B.; Muehling, B.; Pfetzer, N.; Wittig, R.; Voelker, H. U.; Thiede, A.; Coy, J. F., Growth of human gastric cancer cells in nude mice is delayed by a ketogenic diet supplemented with omega-3 fatty acids and medium-chain triglycerides. *BMC cancer* **2008,** *8* (1), 122.

96. Schmidt, M.; Pfetzer, N.; Schwab, M.; Strauss, I.; Kämmerer, U., Effects of a ketogenic diet on the quality of life in 16 patients with advanced cancer: A pilot trial. *Nutrition & metabolism* **2011,** *8* (1), 54.

97. Wang, M.; Wang, D.; Chen, Q.; Li, C.; Li, Z.; Lin, J., Recent Advances in Glucose-Oxidase-Based Nanocomposites for Tumor Therapy. *Small (Weinheim an der Bergstrasse, Germany)* **2019,** *15* (51), e1903895.

98. Gao, S.; Lin, H.; Zhang, H.; Yao, H.; Chen, Y.; Shi, J., Nanocatalytic Tumor Therapy by Biomimetic Dual Inorganic Nanozyme-Catalyzed Cascade Reaction. *Advanced Science* **2019,** *6* (3), 1801733.

99. Bonet-Aleta, J.; Hueso, J. L.; Sanchez-Uriel, L.; Encinas-Gimenez, M.; Irusta, S.; Martin-Duque, P.; Martinez, G.; Santamaria, J., Synergistic assembly of gold and copper-iron oxide nanocatalysts to promote the simultaneous depletion of glucose and glutathione. *Materials Today Chemistry* **2023,** *29*, 101404.

100. Liu, X.; Pan, Y.; Yang, J.; Gao, Y.; Huang, T.; Luan, X.; Wang, Y.; Song, Y., Gold nanoparticles doped metal-organic frameworks as near-infrared light-enhanced cascade nanozyme against hypoxic tumors. *Nano Research* **2020,** *13* (3), 653-660.

101. Tang, W.; Fan, W.; Zhang, W.; Yang, Z.; Li, L.; Wang, Z.; Chiang, Y.-L.; Liu, Y.; Deng, L.; He, L.; Shen, Z.; Jacobson, O.; Aronova, M. A.; Jin, A.; Xie, J.; Chen, X., Wet/Sono-Chemical Synthesis of Enzymatic Two-Dimensional MnO_2 Nanosheets for Synergistic Catalysis-Enhanced Phototheranostics. *Advanced Materials* **2019,** *31* (19), 1900401.

102. Feng, W.; Han, X.; Wang, R.; Gao, X.; Hu, P.; Yue, W.; Chen, Y.; Shi, J., Nanocatalysts-Augmented and Photothermal-Enhanced Tumor-Specific Sequential Nanocatalytic Therapy in Both NIR-I and NIR-II Biowindows. *Advanced materials (Deerfield Beach, Fla.)* **2019,** *31* (5), e1805919.

103. Pérez-López, A. M.; Rubio-Ruiz, B.; Sebastián, V.; Hamilton, L.; Adam, C.; Bray, T. L.; Irusta, S.; Brennan, P. M.; Lloyd-Jones, G. C.; Sieger, D.; Santamaría, J.; Unciti-Broceta, A., Gold-Triggered Uncaging Chemistry in Living Systems. *Angewandte*

Chemie International Edition **2017,** *56* (41), 12548-12552.

104. Shi, J.; Kantoff, P. W.; Wooster, R.; Farokhzad, O. C., Cancer nanomedicine: progress, challenges and opportunities. *Nature Reviews Cancer* **2017,** *17* (1), 20-37.

105. McKeown, S. R., Defining normoxia, physoxia and hypoxia in tumours-implications for treatment response. *The British journal of radiology* **2014,** *87* (1035), 20130676.

106. Hobson, B.; Denekamp, J., Endothelial proliferation in tumours and normal tissues: Continuous labelling studies. *British journal of cancer* **1984,** *49* (4), 405-413.

107. Horsman, M. R.; Mortensen, L. S.; Petersen, J. B.; Busk, M.; Overgaard, J., Imaging hypoxia to improve radiotherapy outcome. *Nature Reviews Clinical Oncology* **2012,** *9* (12), 674-687.

108. Shen, Z.; Ma, Q.; Zhou, X.; Zhang, G.; Hao, G.; Sun, Y.; Cao, J., Strategies to improve photodynamic therapy efficacy by relieving the tumor hypoxia environment. *NPG Asia Materials* **2021,** *13* (1), 39.

109. Jung, H. S.; Han, J.; Shi, H.; Koo, S.; Singh, H.; Kim, H.-J.; Sessler, J. L.; Lee, J. Y.; Kim, J.-H.; Kim, J. S., Overcoming the Limits of Hypoxia in Photodynamic Therapy: A Carbonic Anhydrase IX-Targeted Approach. *Journal of the American Chemical Society* **2017,** *139* (22), 7595-7602.

110. Schaue, D.; McBride, W. H., Opportunities and challenges of radiotherapy for treating cancer. *Nature reviews. Clinical oncology* **2015,** *12* (9), 527-40.

111. Kwiatkowski, S.; Knap, B.; Przystupski, D.; Saczko, J.; Kędzierska, E.; Knap-Czop, K.; Kotlińska, J.; Michel, O.; Kotowski, K.; Kulbacka, J., Photodynamic therapy – mechanisms, photosensitizers and combinations. *Biomedicine & Pharmacotherapy* **2018,** *106*, 1098-1107.

112. Najafi, A.; Keykhaee, M.; Khorramdelazad, H.; Karimi, M. Y.; Nejatbakhsh Samimi, L.; Aghamohamadi, N.; Karimi, M.; Falak, R.; Khoobi, M., Catalase application in cancer therapy: Simultaneous focusing on hypoxia attenuation and macrophage reprogramming. *Biomedicine & Pharmacotherapy* **2022,** *153*, 113483.

113. Prasad, P.; Gordijo, C. R.; Abbasi, A. Z.; Maeda, A.; Ip, A.; Rauth, A. M.; DaCosta, R. S.; Wu, X. Y., Multifunctional Albumin–MnO_2 Nanoparticles Modulate Solid Tumor Microenvironment by Attenuating Hypoxia, Acidosis, Vascular Endothelial Growth Factor and Enhance Radiation Response. *ACS Nano* **2014,** *8* (4), 3202-3212.

114. Steinbrech, D. S.; Mehrara, B. J.; Saadeh, P. B.; Chin, G.; Dudziak, M. E.; Gerrets, R. P.; Gittes, G. K.; Longaker, M. T., Hypoxia regulates VEGF expression and cellular proliferation by osteoblasts in vitro. *Plastic and reconstructive surgery* **1999,** *104* (3), 738-47.

115. Bonet-Aleta, J.; Calzada-Funes, J.; Hueso, J. L., Manganese oxide nano-platforms in cancer therapy: Recent advances on the development of synergistic strategies targeting the tumor microenvironment. *Applied Materials Today* **2022,** *29*, 101628.

116. Zhang, Y.-H.; Qiu, W.-X.; Zhang, M.; Zhang, L.; Zhang, X.-Z., MnO_2 Motor: A Prospective Cancer-Starving Therapy Promoter. *ACS Applied Materials & Interfaces* **2018,** *10* (17), 15030-15039.

117. Butler, M.; van der Meer, L. T.; van Leeuwen, F. N., Amino Acid Depletion Therapies: Starving Cancer Cells to Death. *Trends in endocrinology and metabolism: TEM* **2021,** *32* (6), 367-381.

118. Lomelino, C. L.; Andring, J. T.; McKenna, R.; Kilberg, M. S., Asparagine synthetase: Function, structure, and role in disease. *Journal of Biological Chemistry* **2017,** *292* (49), 19952-19958.

119. Broome, J. D., Evidence that the L-asparaginase of guinea pig serum is responsible for its antilymphoma effects. I. Properties of the L-asparaginase of guinea pig serum in relation to those of the antilymphoma substance. *The Journal of experimental medicine* **1963,** *118*, 99-120.

120. Kidd , J. G., Regression of transplanted lymphomas induced in vivo by means of normal guinea pig serum : i. course of transplanted cancers of various kinds in mice and rats given guinea pig serum, horse serum, or rabbit serum. *Journal of Experimental Medicine* **1953,** *98* (6), 565-582.

121. Bach, S. J.; Swaine, D., The Effect of Arginase on the Retardation of Tumour Growth. *British journal of cancer* **1965,** *19* (2), 379-386.

122. Elledge, S. J.; Zhou, Z.; Allen, J. B., Ribonucleotide reductase: regulation, regulation, regulation. *Trends in Biochemical Sciences* **1992,** *17* (3), 119-123.

123. Chaston, T. B.; Lovejoy, D. B.; Watts, R. N.; Richardson, D. R., Examination of the antiproliferative activity of iron chelators: multiple cellular targets and the different mechanism of action of triapine compared with desferrioxamine and the potent pyridoxal isonicotinoyl hydrazone analogue 311. *Clinical cancer research : an official journal of the American Association for Cancer Research* **2003,** *9* (1), 402-14.

124. Attia, S.; Kolesar, J.; Mahoney, M. R.; Pitot, H. C.; Laheru, D.; Heun, J.; Huang, W.; Eickhoff, J.; Erlichman, C.; Holen, K. D., A phase 2 consortium (P2C) trial of 3-aminopyridine-2-carboxaldehyde thiosemi-

carbazone (3-AP) for advanced adenocarcinoma of the pancreas. *Investigational New Drugs* **2008,** *26* (4), 369-379.

125. Knox, J. J.; Hotte, S. J.; Kollmannsberger, C.; Winquist, E.; Fisher, B.; Eisenhauer, E. A., Phase II study of Triapine® in patients with metastatic renal cell carcinoma: a trial of the National Cancer Institute of Canada Clinical Trials Group (NCIC IND.161). *Investigational New Drugs* **2007,** *25* (5), 471-477.

126. Cui, L.; Gouw, A. M.; LaGory, E. L.; Guo, S.; Attarwala, N.; Tang, Y.; Qi, J.; Chen, Y.-S.; Gao, Z.; Casey, K. M.; Bazhin, A. A.; Chen, M.; Hu, L.; Xie, J.; Fang, M.; Zhang, C.; Zhu, Q.; Wang, Z.; Giaccia, A. J.; Gambhir, S. S.; Zhu, W.; Felsher, D. W.; Pegram, M. D.; Goun, E. A.; Le, A.; Rao, J., Mitochondrial copper depletion suppresses triple-negative breast cancer in mice. *Nature Biotechnology* **2021,** *39* (3), 357-367.

127. Ramchandani, D.; Berisa, M.; Tavarez, D. A.; Li, Z.; Miele, M.; Bai, Y.; Lee, S. B.; Ban, Y.; Dephoure, N.; Hendrickson, R. C.; Cloonan, S. M.; Gao, D.; Cross, J. R.; Vahdat, L. T.; Mittal, V., Copper depletion modulates mitochondrial oxidative phosphorylation to impair triple negative breast cancer metastasis. *Nature Communications* **2021,** *12* (1), 7311.

128. Solomon, E. I.; Sundaram, U. M.; Machonkin, T. E., Multicopper Oxidases and Oxygenases. *Chemical Reviews* **1996,** *96* (7), 2563-2606.

129. Que, E. L.; Domaille, D. W.; Chang, C. J., Metals in Neurobiology: Probing Their Chemistry and Biology with Molecular Imaging. *Chemical Reviews* **2008,** *108* (5), 1517-1549.

130. Pham, V. N.; Chang, C. J., Metalloallostery and Transition Metal Signaling: Bioinorganic Copper Chemistry Beyond Active Sites. *Angewandte Chemie International Edition* **2023,** *62* (11), e202213644.

131. Ishida, S.; Andreux, P.; Poitry-Yamate, C.; Auwerx, J.; Hanahan, D., Bioavailable copper modulates oxidative phosphorylation and growth of tumors. **2013,** *110* (48), 19507-19512.

132. Viale, A.; Corti, D.; Draetta, G. F. J. C. r., Tumors and Mitochondrial Respiration: A Neglected ConnectionMitochondrial Role in Tumor Progression. **2015,** *75* (18), 3687-3691.

133. Erler, J. T.; Bennewith, K. L.; Nicolau, M.; Dornhöfer, N.; Kong, C.; Le, Q.-T.; Chi, J.-T. A.; Jeffrey, S. S.; Giaccia, A. J. J. N., Lysyl oxidase is essential for hypoxia-induced metastasis. **2006,** *440* (7088), 1222-1226.

134. Habeck, M., Copper and angiogenesis: a new piece to the puzzle. *The Lancet Oncology* **2002,** *3* (11), 650.

135. Ge, E. J.; Bush, A. I.; Casini, A.; Cobine, P. A.; Cross, J. R.; DeNicola, G. M.; Dou, Q. P.; Franz, K. J.; Gohil, V. M.; Gupta, S.; Kaler, S. G.; Lutsenko, S.; Mittal, V.; Petris, M. J.; Polishchuk, R.; Ralle, M.; Schilsky, M. L.; Tonks, N. K.; Vahdat, L. T.; Van Aelst, L.; Xi, D.; Yuan, P.; Brady, D. C.; Chang, C. J., Connecting copper and cancer: from transition metal signalling to metalloplasia. *Nature Reviews Cancer* **2022,** *22* (2), 102-113.

136. Chavez, K. J.; Garimella, S. V.; Lipkowitz, S., Triple negative breast cancer cell lines: one tool in the search for better treatment of triple negative breast cancer. *Breast disease* **2010,** *32* (1-2), 35-48.

137. Nagaraja, G. M.; Othman, M.; Fox, B. P.; Alsaber, R.; Pellegrino, C. M.; Zeng, Y.; Khanna, R.; Tamburini, P.; Swaroop, A.; Kandpal, R. P., Gene expression signatures and biomarkers of noninvasive and invasive breast cancer cells: comprehensive profiles by representational difference analysis, microarrays and proteomics. *Oncogene* **2006,** *25* (16), 2328-38.

138. Blockhuys, S.; Celauro, E.; Hildesjö, C.; Feizi, A.; Stål, O.; Fierro-González, J. C.; Wittung-Stafshede, P., Defining the human copper proteome and analysis of its expression variation in cancers. *Metallomics* **2017,** *9* (2), 112-123.

139. Chan, N.; Willis, A.; Kornhauser, N.; Ward, M. M.; Lee, S. B.; Nackos, E.; Seo, B. R.; Chuang, E.; Cigler, T.; Moore, A.; Donovan, D.; Vallee Cobham, M.; Fitzpatrick, V.; Schneider, S.; Wiener, A.; Guillaume-Abraham, J.; Aljom, E.; Zelkowitz, R.; Warren, J. D.; Lane, M. E.; Fischbach, C.; Mittal, V.; Vahdat, L., Influencing the Tumor Microenvironment: A Phase II Study of Copper Depletion Using Tetrathiomolybdate in Patients with Breast Cancer at High Risk for Recurrence and in Preclinical Models of Lung Metastases. *Clinical Cancer Research* **2017,** *23* (3), 666-676.

Objectives & Thesis structure

In the introduction of this thesis, we thoroughly examined the groundbreaking works that have set significant milestone in nanocatalytic therapy. These works, which are chronologically summarized in Figure 1a, have paved the way for further exploration of the field. Subsequently, numerous nanocatalysts with diverse compositions and structures have been studied in vivo[1-3], providing a wealth of insight to define candidate materials and therapeutic strategies. This abundance of research outcomes serves to reinforce the central idea presented at the beginning of section 1.2: nanomedicines should exploit on their chemical reactivity to enhance cancer therapeutics. In our analysis, we identified key questions that require further investigation and were fixed as objectives of Ph.D. thesis.

#1. Achieving catalysis under the challenging conditions of the tumour microenvironment (TME) through effective catalyst design. Exploiting the unique features of the TME lays the foundation of this therapeutic approach. However, catalyzing chemical reactions within a living organism poses significant challenges. For instance, the Fenton reaction requires an acidic pH to proceed. Although tumors exhibit a mildly acidic pH, this acidity primarily exists outside the cell rather than inside. Therefore, it is highly desirable to discover catalysts capable of extending their activity to higher pH levels, thus inducing oxidative stress within cells. Another example is the oxidation of glucose using noble-metal nanoparticles, which are prone to deactivation in the presence of thiol-containing molecules found in biological media. Overcoming these catalytic limitations holds immense potential for enhancing therapy.

In Chapter 1, our investigation focused on the reactivity of a copper-iron nanocatalyst towards depleting glutathione (GSH) and generating hydroxyl radicals (•OH). We discovered that the process leading to the depletion of GSH also triggers the production of Fenton-active species, allowing for the generation of •OH under physiological conditions (pH = 7). In Chapter 2, we capitalized on the GSH depletion capabilities of CuFe nanoparticles and combined them with ultrasmall Au nanoparticles. The hybrid was effective in reducing the deactivation of Au nanoparticles during glucose oxidation in the presence of GSH.

#2. Understanding reaction mechanisms from a fundamental chemistry viewpoint. Without a clear comprehension of reaction mechanisms it will not be possible to design efficient catalytic processes. An illustrative example is the oxidation of glutathione (GSH). Seminal papers by Ju et al. [4] and Ma et al. [5] described GSH depletion using Cu-based catalysts, but they failed to identify oxygen (O_2) as a crucial molecule for catalysis. Considering the hypoxic state of tumors, as described in section 1.2.1, this results in a significant limitation of therapeutic outcomes.

In Chapter 3, our research focused on studying in-depth the catalytic oxidation of GSH using CuFe nanoparticles. We observed that GSH selectively leaches copper from the nanoparticles. Once in solution, Cu^{2+} ions catalyze the oxidation of GSH into GSSG by utilizing oxygen (O_2), which is typically scarce within tumors. The Fe-enriched particles that result from preferential copper leaching are not inert agents; on the contrary they have the ability to regenerate O_2 by utilizing the byproducts of GSH oxidation, namely $\bullet O_2^-$ and H_2O_2, thus completing the catalytic cycle.

#3. Extending the range of reactions for cancer therapy beyond those described in literature. Cells present an most intricate chemical environments. Despite this complexity, catalytic chemotherapy has so far focused on only four processes described in Chapter 4. However, it seems reasonable to assume that the array of possible reaction with therapeutic purposes does not end here and in particular transition metal-based nanoparticles have the potential to interact with a broader range of molecules beyond glucose, GSH, or H_2O_2.

In 2021, Mayer et al.[6] published a study demonstrating how aqueous transition metal ions can catalyze transamination reactions between amino acids and pyruvate, a central molecule in the Krebs cycle[7]. This work, addressed mainly the realm of prebiotic chemistry, exploring the formation of complex molecules such as amino acids from simpler components, inspired us to explore the activity of CuFe nanoparticles in this reaction. In Chapter 4, we show that copper released from CuFe nanoparticles can catalyze the transamination between crucial amino acids for cell metabolism, such as glutamine or aspartic acid, and pyruvate, an α-keto acid present in most living systems. To the best of our knowledge, this type of in cellulo reactivity has not yet been explored with nanoparticles. We discovered that not only single amino acids but also dipeptides or tripeptides, such as GSH, are susceptible to undergo transamination.

#4. Unravel the fate of metal ions within cells. One of the main findings of Chapter 3 is that copper-based particles have the ability to release copper inside the cell and the catalyst itself is transformed in this process. However, the fate of metals within cells is often overlooked in the literature. While catalyst transformation upon cell internalization may not necessarily be detrimental as long as the activity is preserved, it is crucial to understand the various scenarios and processes encountered by the catalyst during its intracellular journey. In particular, once in solution, copper cations face the pathways designed by nature to regulate its concentration, thereby influencing its availability.

Chapter 5 departs significantly from the tours of earlier chapters in this thesis, as it delves into the challenges of studying metals within cells. First, metals are subject to exchange between different oxidation states. Conventional metal analysis techniques such as atomic spectroscopy fail to differentiate between these oxidation states, leading to a significant loss of information. Furthermore, metals can be tightly or loosely bound to proteins. The latter category, known as labile metals, plays a vital role in regulating and signaling processes within living systems, making their quantification crucial. In this regard, activity-based sensing offers a unique methodology exploiting the reactivity between the probe and the analyte, surpassing mere molecular recognition and providing high selectivity to detect and quantify labile metals within cells. In Chapter 5, we combine therapeutic nanoparticles with activity-based probes to investigate the fate of copper ions in cancer cells.

#5. Study the therapeutic potential of metal sequestration. While a significant portion of the literature concentrates on introducing transition metal-based nanoparticles for cancer therapy metal, metal homeostasis can be disrupted not only by addition, but also by removal of metals. Thus, recent studies have highlighted the therapeutic potential of depleting metals using molecular chelators. The objective is generally to hinder key reactions catalyzed by enzymes that rely on these metals as a cofactors.

In Chapter 6, we explore this approach by employing polydopamine (PDA) nanoparticles with chelating-binding properties, as done by other groups (e.g. del Valle et al.[8]). In this case we here paid special attention to the fate of sequestered copper. By incorporating chelating functionalities into nanoparticles, we seek to enhance the effectiveness of metal depletion as a therapeutic strategy.

This novel approach holds promise for expanding the repertoire of therapeutic interventions aimed at targeting specific metal ions within cells.

Manuscript structure. This thesis represents the compilation of six separate publications dealing with nanoparticles active as therapeutic agents in cancer. Three of which have already been published and three that are currently undergoing the review process for publication. The shared thread is of course the application of active nanoparticles in cancer therapy both in the role of in-releasing and as in-sequestering nanoparticles. The structure of each chapter in this thesis adheres to a specific format, encompassing (1) a concise two-page introduction that contextualizes the research and outlines the objectives, (2) the research paper itself, (3) supplementary information and (4) references cited. Each chapter is self-contained, featuring its own introduction, results and discussion, experimental methodology and specific conclusions. This structure aims to provide clarity and consistency throughout the thesis, enabling readers to navigate and comprehend the research findings effectively. Finally, we have added one section containing the main conclusions of each chapter and general conclusions of the thesis.

The arrangement of the chapters in this thesis follows the development of the research conducted. The initial studies (*Chapters 1 and 2*) were designed as proofs of concept, showcasing the potential of nanocatalysis in the field of cancer therapy (***Figure 1a***). However, the primary objective of this thesis is to address the emerging questions and current gaps in the field of catalytic cancer therapy (***Figure 1b***) (*Chapters 3-6*). The thread linking these questions also serves as the underlying principle organizing the chapters. This organization can be visualized as an iceberg, where the visible part corresponds to the successful catalyst examples, while ongoing efforts to deepen our understanding of the interactions between nanoparticles and living systems constitute the larger, submerged part (***Figure 1c***). In the case of Chapter 6, our work represents one of the initial examples of the metal-depletion strategy. Therefore, we conceive this chapter as yet another iceberg, where our research encompasses not only the application of this methodology but also an in-depth exploration of its underlying mechanisms and functionality (***Figure 1d***).

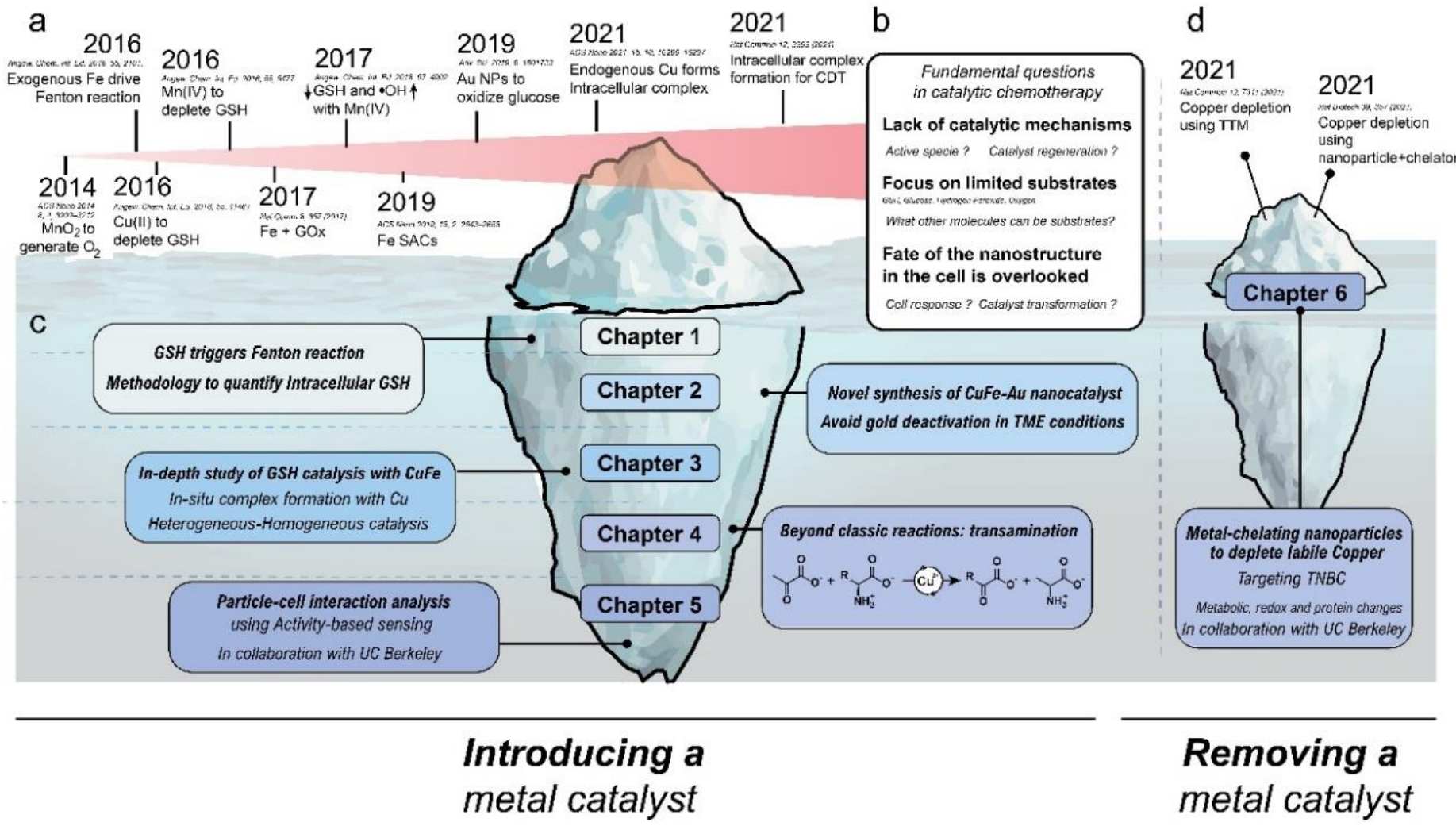

Figure 1. The thesis iceberg. *(a) Timeline of key publications in the field of catalytic chemotherapy from 2014, where different nanomaterials have been applied in different catalytic. Although the number of publications and materials is numerous, (b) fundamental questions needed to advance the field remain unanswered. (c) The present thesis has sought some answers from a chemical perspective, organized in chapters. This goes from the synthesis and characterization of Cu-Fe particles to the in-depth study of its catalytic mechanisms, transformations in the TME, and some non-explored reactions or particle-cell interactions. (d) Another, less explored and opposite strategy consists in removing a metal catalyst instead of introducing it. For instance this strategy can exploit metal requirements displayed by TNBC cells to achieve an efficient therapy.*

References – Objectives & Thesis structure

1. Li, S.-L.; Jiang, P.; Jiang, F.-L.; Liu, Y., Recent Advances in Nanomaterial-Based Nanoplatforms for Chemodynamic Cancer Therapy. *Advanced Functional Materials* **2021,** *31* (22), 2100243.

2. Lu, J.; Yang, Y.; Xu, Q.; Lin, Y.; Feng, S.; Mao, Y.; Wang, D.; Wang, S.; Zhao, Q., Recent advances in multi-configurable nanomaterials for improved chemodynamic therapy. *Coordination Chemistry Reviews* **2023,** *474*, 214861.

3. Wang, X.; Zhong, X.; Liu, Z.; Cheng, L., Recent progress of chemodynamic therapy-induced combination cancer therapy. *Nano Today* **2020,** *35*, 100946.

4. Ju, E.; Dong, K.; Chen, Z.; Liu, Z.; Liu, C.; Huang, Y.; Wang, Z.; Pu, F.; Ren, J.; Qu, X., Copper(II)–Graphitic Carbon Nitride Triggered Synergy: Improved ROS Generation and Reduced Glutathione Levels for Enhanced Photodynamic Therapy. **2016,** *55* (38), 11467-11471.

5. Ma, B.; Wang, S.; Liu, F.; Zhang, S.; Duan, J.; Li, Z.; Kong, Y.; Sang, Y.; Liu, H.; Bu, W.; Li, L., Self-Assembled Copper–Amino Acid Nanoparticles for in Situ Glutathione "AND" H2O2 Sequentially Triggered Chemodynamic Therapy. *Journal of the American Chemical Society* **2019,** *141* (2), 849-857.

6. Mayer, R. J.; Kaur, H.; Rauscher, S. A.; Moran, J., Mechanistic Insight into Metal Ion-Catalyzed Transamination. *Journal of the American Chemical Society* **2021,** *143* (45), 19099-19111.

7. Nelson, D. L.; Lehninger, A. L.; Cox, M. M., *Lehninger Principles of Biochemistry*. W. H. Freeman: 2008.

8. Nieto, C.; Marcelo, G.; Vega, M.; Martín del Valle, E. M., Antineoplastic behavior of polydopamine nanoparticles prepared in different water/alcohol media. *Colloids and Surfaces B: Biointerfaces* **2021,** *199*, 111506.

Chapter 1 |

From catalysis to cells

Summary – Chapter 1

Chemotherapeutics aim to affect a key processes of cancer cells. For example, several drugs target cell division. Paclitaxel specifically binds to the subunit-β of tubulin, hindering the disassembly of microtubules required for cell division. Similarly, 5-fluorouracil (5-FU) blocks DNA replication by inhibiting thymidylate synthase (**Figure 1a**). The efficacy of these drugs stems from the fact that rapidly dividing cells, such as cancer cells, are more sensitive to processes that disrupt cell division. Therefore, the primary objective of a nanocatalyst is also to alter a crucial process in cancer cells.

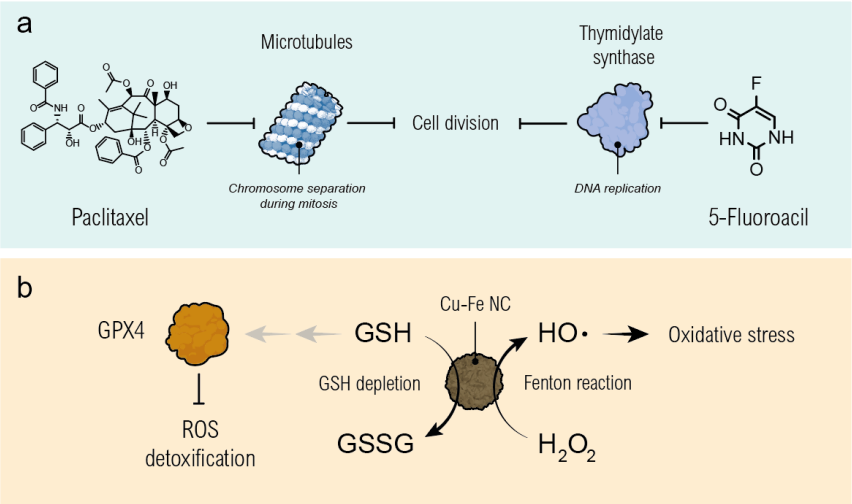

Figure Intro-1. *(a) Examples of drugs targeting key processes of cancer cells include those that interfere with microtubules separation and thymidylate synthase, which are essential for DNA replication and cell division. (b) The proposed mechanism of action of the CuFe nanocatalyst involves a cascade reaction that depletes intracellular GSH while increasing oxidative species, ultimately leading to a significant impairment of redox homeostasis.*

In our case, we chose to target GSH due to its high concentration in cancer cells and its central role in maintaining redox homeostasis. We employed copper-iron oxide nanoparticles for this purpose (**Figure 1b**). GSH functions as a cofactor for the enzyme glutathione peroxidase-4 (GPX4), enabling it to react with ROS generated during various metabolic processes and to

prevent potential oxidative damage. Additionally, by using transition-metal-based nanoparticles, our second aim was to exploit the Fenton reaction to generate ROS. As mentioned in the introduction, the Fenton reaction is enhanced in acidic environments, which are commonly found in the tumor microenvironment. The objective of this strategy is to obtain a strong synergic effect by simultaneously provoking the depletion of the main cell antioxidant reservoir and an intense generation of ROS, leading to a disruptive redox imbalance through catalysis.

The choice of these two metals was motivated by the well-known capability of Cu for oxidizing GSH and of Fe and also Cu as Fenton-like catalyst. Our first step was to validate the catalytic activity of Cu-Fe nanoparticles towards GSH. Additionally, these nanoparticles were found to be active in the Fenton reaction (i.e., converting H_2O_2 into •OH) at acidic pH, as expected. However, their activity was nearly negligible when the pH was shifted towards physiological values. Interestingly, when we evaluated the entire reaction (i.e., GSH + H_2O_2 + Cu-Fe) together, we observed that the Fenton reaction occurred at unusually high pH levels. One advantage of working at the interface between catalysis and biology is the ability to apply concepts traditionally associated with catalysis to explain certain experimental observations in biology. We discovered that GSH was actually reducing the copper and iron present on the nanoparticle surface and at the same time enhancing their leaching from the solid phase (which was further studied in Chapter 3). This reduction of the metal species, which is difficult to achieve at physiological pH levels, enabled them to catalyze the Fenton reaction through a cascade of reactions. The explanation behind this phenomenon lies in the higher kinetic constants for H_2O_2 decomposition exhibited by the reduced metals (i.e., Cu^{+} and Fe^{2+}) compared to their oxidized counterparts (i.e., Cu^{2+} and Fe^{3+}). Therefore, the presence of GSH could trigger a cascade reaction that allows for the occurrence of the Fenton reaction in scenarios that were not previously considered. The other reaction is of course the oxidation of GSH to GSSG, a highly desirable outcome.

Our hypothesis was that higher levels of GSH, found in cancer cells, could enhance the cascade reaction, thereby increasing the selectivity and toxicity of Cu-Fe nanoparticles for cancer cells. To validate this hypothesis, we developed a methodology in the laboratory to measure intracellular GSH levels in cancer glioblastoma (U251MG) and healthy (hpMSC) cells using UPLC. Our findings

revealed an intracellular GSH concentration in U251MG cells that was approximately four times higher than that in hpMSC cells. This correlation supports the notion of higher cytotoxicity of Cu-Fe nanoparticles for U251MG cells. Finally, we demonstrated that GSH levels in U251MG cells decreased after treatment with Cu-Fe nanoparticles for 6 and 24 hours, while no significant alterations were observed in hpMSC cells.

The results from this chapter were published in *Journal of Colloid and Interface Science 617 (2022) 704–717.*

Adapted from:

Glutathione-Triggered catalytic response of Copper-Iron mixed oxide Nanoparticles. Leveraging tumor microenvironment conditions for chemodynamic therapy

Javier Bonet-Aleta [a,b,c,1], Maria Sancho-Albero [a,b,c,d,1], Javier Calzada-Funes [a,b,c], Silvia Irusta [a,b,c], Pilar Martin-Duque [b,e,f,g], Jose L. Hueso [a,b,c,e], Jesus Santamaria [a,b,c,e,]

[a] *Instituto de Nanociencia y Materiales de Aragon (INMA) CSIC-Universidad de Zaragoza Campus Rio Ebro, Edificio I+D, C/ Poeta Mariano Esquillor, s/n, 50018 Zaragoza, Spain*

[b] *Networking Res. Center in Biomaterials, Bioengineering and Nanomedicine (CIBER-BBN), Madrid, Spain. Instituto de Salud Carlos III, 28029 Madrid, Spain*

[c] *Department of Chemical and Environmental Engineering, University of Zaragoza, Campus Rio Ebro, C/María de Luna, 3, 50018 Zaragoza, Spain*

[d] *Department of Molecular Biochemistry and Pharmacology, Istituto di Ricerche Farmacologiche Mario Negri IRCCS, 20156 Milan, Italy*

[e] *Instituto Aragonés de Ciencias de la Salud (IACS)/IIS Aragón, Avenida San Juan Bosco, 13, 50009 Zaragoza, Spain*

[f] *Fundación Araid. Av. de Ranillas 1-D, planta 2ª, oficina B, 50018 Zaragoza, Spain*

[g] *Present Address: Department of Surgery, University of Zaragoza Medical School; University of Zaragoza, Zaragoza, Spain*

Graphical abstract

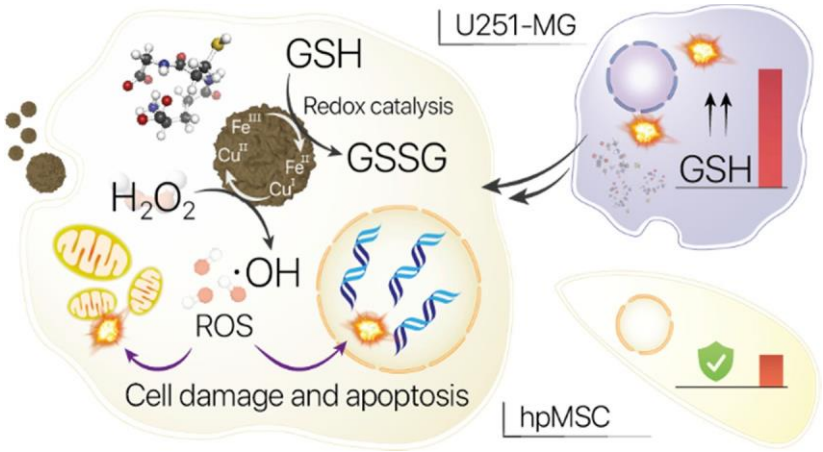

Abstract

Heterogeneous catalysis has emerged as a promising alternative for the development of new cancer therapies. In addition, regarding the tumor microenvironment as a reactor with very specific chemical features has provided a new perspective in the search for catalytic nanoarchitectures with specific action against chemical species playing a key role in tumor metabolism. One of these species is glutathione (GSH), whose depletion is the cornerstone of emerging strategies in oncology, since this metabolite plays a pivotal regulatory role as antioxidant agent, dampening the harmful effects of intracellular reactive oxidative species (ROS). Herein, we present copper-iron oxide spinel nanoparticles that exhibit a versatile and selective catalytic response to reduce GSH levels while generating ROS in a cascade reaction. We demonstrate a clear correlation between GSH depletion and apoptotic cell death in tumor cells in the presence of the copper-iron nanocatalyst. Furthermore, we also provide a novel analytical protocol, alternative to state-of-the-art commercial kits, to accurately monitoring the concentration of GSH intracellular levels in both tumor and healthy cells. We observe a selective action of the nanoparticles, with lower toxicity in healthy cell lines, whose intrinsic GSH levels are lower, and intense apoptosis in tumor cells accompanied by a fast reduction of GSH levels.

Introduction – Chapter 1

Despite intense research efforts in almost every branch of the natural sciences, cancer continues to be one of the leading causes of death worldwide [1]. Given the extensive panoply of oncologic treatments available, it is noteworthy that the use of heterogeneous catalysts has scarcely been explored until recent years. However, heterogeneous catalysts could in principle play two fundamental roles in cancer treatment: i) transform or destroy molecules that are essential for tumor growth and/or ii) generate toxic products in situ. Both effects, the depletion of useful metabolites and the generation of toxic species such as reactive oxidative species (ROS) have been the subject of a recent number of studies with different heterogeneous nanocatalysts delivered and activated in tumor microenvironments (TME) [2–5]. The metabolic differences between tumoral and healthy cells offer interesting opportunities for cancer therapy that can be

leveraged with catalytic nanoparticles [6]. Notably, cancer cells possess a high dependence on ATP production to sustain their rapid proliferation [7] and exhibit an enhanced mitochondrial overproduction of ROS such as hydrogen peroxide (H_2O_2) or oxygen superanions ($\bullet O_2^-$) [8–10] that are present in higher concentrations compared to normal cells [10]. In addition, H_2O_2 can be decomposed into highly reactive hydroxyl radicals. All of these species (H_2O_2, $\bullet O_2^-$, •OH) may induce significant transformations in key biomolecules such as lipids, proteins or nucleic acids and lead to cell apoptosis [6,11]. In this regard, ChemoDynamic Therapy (CDT) exploits the decomposition of overproduced H_2O_2 through Fenton-like reaction catalyzed by transition metal based nanoparticles (Fe, Co, Mn, Cu, Ni) to selectively induce apoptosis in cancer cells due to

hydroxyl radical (•OH) generation [12–16]. However, the effectiveness of this strategy is often low, due to multiple challenges. In the first place, the concentration of intracellular H_2O_2 remains relatively low (i.e. 0.1–1.0 mM) [17,18] even for cancer cells, and therefore the capability of Fenton processes to yield •OH is necessarily limited [6]. On top of that, the production of antioxidant molecules such as Glutathione (GSH) is upregulated in cancer cells [19] and this interferes with the products resulting from Fenton reactions, further preventing the effectiveness of ROS-triggered cancer treatments [13,20,21]. GSH is a natural tripeptide with ROS scavenging capacity and is mainly localized in the cyto- sol. Usual concentrations are in the range of 1–2 mM [22]. How ever, in some cell lines such as hepatocytes or malignant cancer cells this value can reach 10 mM [21,23,24]. The major role of GSH in cancer metabolism has been recognized for some time and has been linked to regulation of carcinogenic mechanisms as well as to cell proliferation and apoptotic processes[13,25–27]. However, understanding the intracellular mechanisms involving GSH remains elusive. This is likely hindering the development of new therapies, since the interplay between antioxidant molecules and ROS in the regulation of oxidative stress in cancer cells is central in the design of more effective CDT treatments [6,28]. Thus, while the modification of GSH metabolism has been proposed as a tool to enhance cell response to antitumoral drugs, this strategy is strongly limited due to its lack of specificity towards cancer cells, with potential side effects on healthy cells and tissues [21]. It is therefore not surprising that developing new ways to regulate GSH levels in tumor cells is being intensely investigated in recent years [27–29]. The

main biochemical detoxification pathway of GSH is directly related with H_2O_2 [30] through the seleno-enzyme Glutathione Peroxidase (GPX4) [31]. H_2O_2 is able to oxidize the Se active center of the enzyme into Se-OH, which can react with GSH through its nucleophile thiol (-SH) group [32], forming a Se-SG intermediate (see Figure 1). Then, another GSH molecule is able to establish a disulfide bridge with Se-SG, releasing GSSG, and regenerating the Se center. The process removes H_2O_2 and in doing so avoids the responding cell damage [32] (see Figure 1). Because of this, reducing GSH levels has a direct impact on the capacity of cells to damp oxidative stress, and this has been exploited in CDT. Thus, recent investigations show how nanoparticles containing high-valence transition metals (Fe [28,33,34], Cu [35–37], Mn [29,34,38], Mo [36,39]) that are able to oxidize GSH can create a synergy that enhances the effect of CDT by promoting a scenario of lower GSH concentrations. Fenton processes and GSH-depleting nanocatalysts can be connected through an oxidation–reduction catalytic cycle. Fenton-like reactions are typically catalyzed more efficiently by Fe(II) [40,41], Cu(I) [42,43] or Mn(II) [44] species, i.e. reduced transition metal elements, in comparison with their oxidized counterparts. A smart design of catalytic nanoparticles can successfully target the GSH/ H_2O_2 system within the

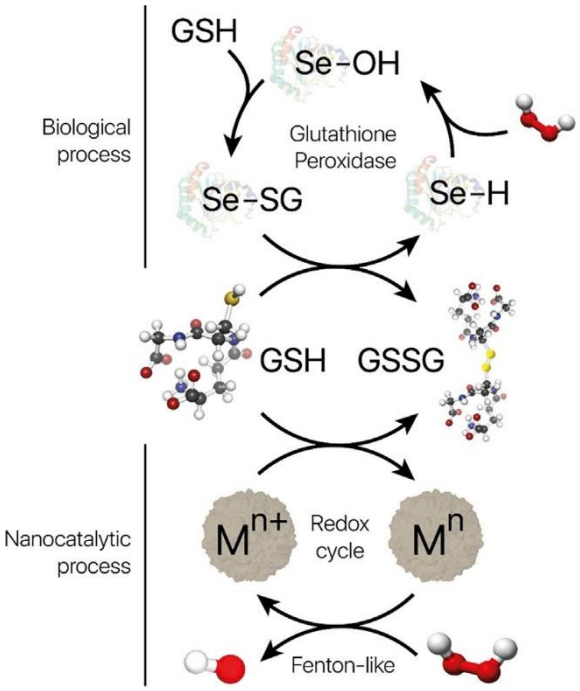

Figure 1. *Scheme depicting some key processes involving GSH: (Top) GPX4-catalyzed H_2O_2 removal through GSH oxidation into GSSG- H_2O_2 is able to oxidize Se-H active group from GPX4 yielding Se-OH. One GSH molecule is able to bind to Se-OH, forming Se-SG intermediate. Finally, another GSH molecule reacts with Se-SG releasing the final GSSG product. (Bottom) Catalytic redox process mediated by transition metal oxide nanoparticles. Electrons from -SH group of GSH are able to reduce the oxidized metal specie (M^{n+}) to form active species in Fenton-like reaction (M^{n}). Once formed, Mn can decompose H_2O_2 into toxic •OH radicals.*

TME using cascade redox processes [17,29,35]. First, high-valence metal species are internalized inside cells reacting with GSH to yield oxidized GSH species (GSSG) and reduced-valence metal species (Figure 1, bottom). Considering the faster Fenton kinetics [43,45,46] of reduced species, H_2O_2 molecules in the vicinity of the newly reduced metal will rapidly decompose yielding •OH while regenerating M^{n+} species, thus providing positive feedback to the catalytic cycle. This strategy leverages the comparatively high GSH [24,30,47] and H_2O_2 [17,18] levels inside tumor cells to couple GSH depletion and H_2O_2 decomposition processes. Nevertheless, a study that not only correlates GSH levels in tumor and healthy cells but also relates these GSH concentrations to the performance of nanocatalysts has not been carried out. Encouraged by the possibilities arising from the above-described scenario, herein we have synthesized a copper-iron mixed oxide (CuFe) nanoparticle and evaluated its catalytic response in the presence of GSH, H_2O_2 and glucose. Furthermore, we have been able to develop an analytical protocol to accurately estimate GSH concentrations inside cells, demonstrating the high GSH concentrations levels in U251MG tumor cells in comparison with non- tumoral cell lines (i.e. human placental mesenchymal stem cells - hpMSC). This enabled us to establish for the first time a clear correlation between GSH levels and the catalytic capability to generate ROS while depleting GSH. Interestingly, our CuFe nanocatalyst is also able to trigger a parallel process of glucose oxidation, leading to a significant reduction of glucose levels, thus allowing the combination of CDT and starvation therapy, given the high glucose dependence of tumor metabolism. The results of the study shed light on the role played by GSH in the tumor environment and explain the enhanced response observed in the tumor cells after their exposure to CuFe NPs, in terms of their higher GSH content, suggesting the potential use of this catalyst nanoparticle to selectively induce tumoral cell death.

Results and discussion – Chapter 1

Synthesis and characterization of the CuFe nanocatalyst. The synthesis of the Cu-Fe nanocatalyst uses Bovine Serum Albumin (BSA) as template (***Figure 2***). BSA favors the nucleation and growth of the CuFe nanoparticles thanks to the high density of carboxy, amino and thiol groups which can coordinate to Cu^{2+} and Fe^{3+} precursor ions to provide nucleation sites [48]. In

addition, ethylene glycol (EG) was used as co-solvent, hindering the agglomeration between particles formed at nearby nucleation points, this and the large number of nucleation points contribute to the final distribution of small, well dispersed nanoparticles [49]. TEM and HAADF-STEM images show pseudo-spherical morphologies with a uniform diameter distribution (mean size of 7.8 ± 2.2 nm) (***Figure 2b-g***) and the random presence of some bigger nanoparticles in the 20–35 nm range (**Figure *2d-i***). NTA sizes were close to the 70 to 370 nm range (see Fig. S1a) indicating a limited degree of agglomeration in H_2O, while an even narrower dispersion in DMEM (Fig. S1b) was obtained. XRD analysis revealed the existence of a $CuFe_2O_4$ cubic spinel phase with the identification of (220), (311), (400), (511), (440) and (533) planes and a minor Cu cubic phase contribution (***Figure 2c***). HRTEM images and FFT analysis of localized areas revealed lattice spacing of 0.148, 0.210 and 0.251 nm matching of the $CuFe_2O_4$ spinel with cubic phase, respectively [50,51] (***Figure 2h***). EDS mappings further revealed a homogeneous distribution of Cu and Fe in the smaller nanoparticles (***Figure 2e***) and the preferential presence of Cu surrounded by a sulfur-enriched outer layer in the bigger nanoparticles (***Figure 2j***). Fourier Transform Infrared Spectroscopy (FTIR) reveals some characteristic features attributable to BSA in the purified catalyst, presenting bands at 2950, 1655 and 1395 cm^{-1} which can be attributed to Csp_3-H stretching, amide C=O stretching and -C-N- stretching, respectively [52,53] (***Figure 2k***). XPS analysis corroborated the existence of the carbon surface species as shown in Fig. S2 where C-C/C-C, C-O and O-C=O contributions with Binding Energies (BEs) centered at 284.5, 286 and 288.8 eV were identified [54]. XPS also confirmed the presence of highest valence states for Fe(III) and Cu(II) catalytic species (***Figure 2l-m***). X-ray photoemission peaks of the Cu2p revealed the major presence of Cu^{2+} species with binding energies of 933.7 eV and well defined satellite shakeups at 940–945 eV [55,56]. It is also worth mentioning the presence of a minor fraction (12 %) of either monovalent or metallic Cu, attributable to the lower binding energy a second contribution at ca. 932 eV [55,56]. Likewise, the analysis of the Fe2p region revealed a combination of Fe^{2+}/Fe^{3+} valence states with peaks centered at 710.5 eV and 712.4 eV attributable to Fe 2p3/2 orbitals of Fe^{3+} and Fe^{2+}, respectively [57,58]. The presence of satellite peaks at 715 and 719.8 eV corroborated the existence of both oxidation states [57,58] (see Tables S1-S2).

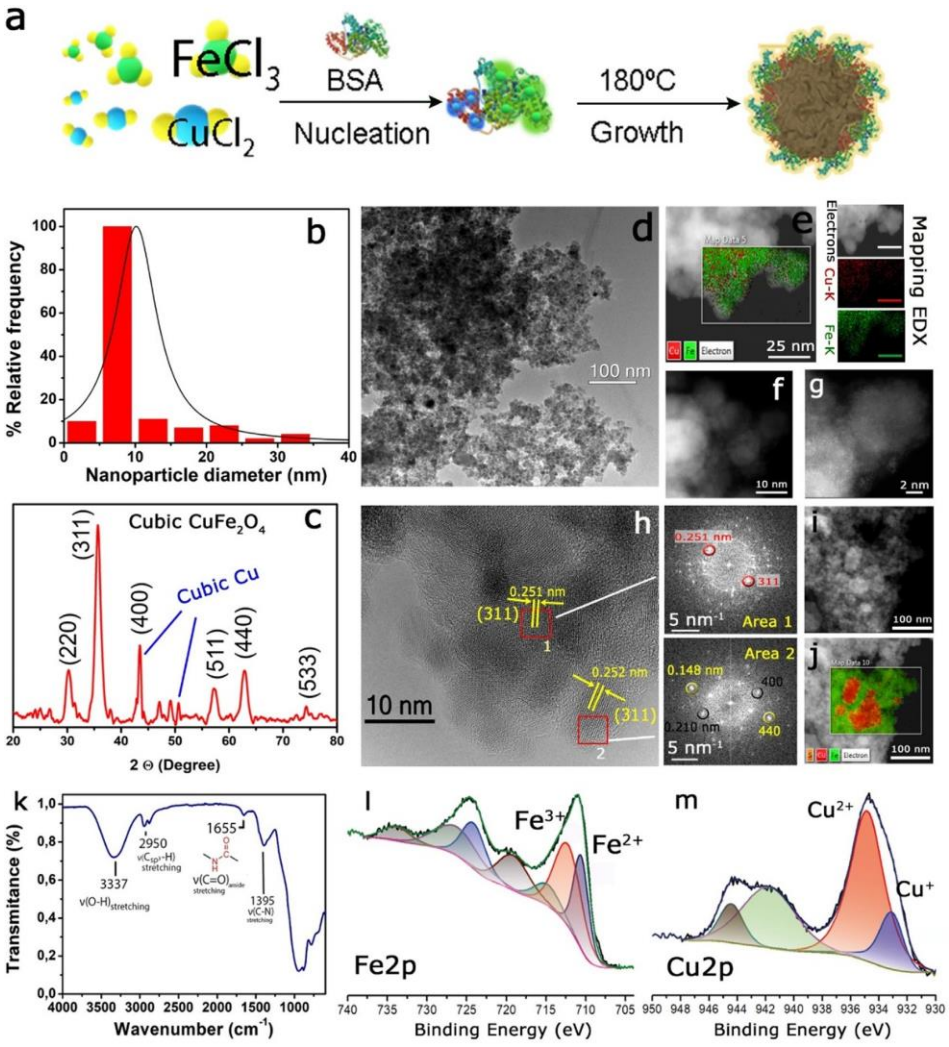

Figure 2. *Morpho-chemical characterization of the Cu-Fe nanoparticles: (a) Synthesis scheme of CuFe nanocatalyst using BSA as template The coordination of Cu^{2+} and Fe^{3+} cations to BSA functional groups generates a host of polymer-bound nucleation sites which provide a controlled and homogeneous growth of the particle; (b) Particle size distribution based on TEM image analysis with imageJ software (n = 150); (c) XRD pattern of CuFe nanoparticles attributable to a predominant cubic spinel phase of $CuFe_2O_4$ and a secondary phase of Cu; (d) Low magnification TEM image of the CuFe nanoparticles; (e) HAADF-STEM image and EDS elemental mappings corresponding to the Fe-K and Cu-K intensities and distributions; (f)-(g): High resolution HAADF-STEM images accounting for the crystallinity of the nanoparticles; (h) High resolution TEM images of the CuFe nanoparticles and corresponding FFT in selected areas (marked with red squares with the identification of lattice spacings matching to (311), (400) or (440) planes of $CuFe_2O_4$; (i) STEM image accounting for the presence of 20–35 nm nanoparticles; (j) EDS elemental mapping of (i) accounting for the preferential*

presence of Cu and an outer layer of S in the bigger nanoparticles; (k) FT-IR spectrum exhibiting characteristic BSA bands; (l) X-ray photoemission spectra (XPS) corresponding to Fe2p region; (m) X-ray photoemission spectra (XPS) corresponding to Cu2p region; Binding Energies and fitting assignations can be found in the Supplementary Information.

CuFe catalytic activity towards GSH depletion and GSH quantification. The presence of high-valent oxidation states in the surface (Fe^{III} and Cu^{II}) confers the possibility of promoting the oxidation of reducing molecules such as GSH. This would be highly interesting as it would deplete GSH levels inside the cell while at the same time yielding Fe(II) and Cu(I), species that are active in Fenton reaction, reacting with H_2O_2 to yield hydroxyl radicals (•OH), as depicted in ***Figure 1***. Thus, the first step in the proposed cascade- reaction consisted in the catalytic oxidation of GSH by CuFe. The capabilities of CuFe regarding GSH depletion were evaluated using a benchmarking assay with 5,5'-Dithiobis(2-nitrobenzoic acid (DNTB). DNTB represents a dimer of TNB linked by a SAS bond. In the presence of GSH (in a pH range between 7 and 8), this SAS bond is broken yielding TNB as product, which is easily detectable thanks to its absorption at 412 nm (Fig. S3). In fact, catalytic GSH oxidation experiments described in the literature typically use spectroscopic analysis (via UV–vis) to follow the reaction indirectly through analysis of TNB^{2-} [28,36,59–61]. However, while this kind of analysis is valid to establish a proof of concept, it remains insufficient to quantify GSH concentration with time due to: (1) Difficulties to obtain an accurate calibration curve that allows precise determination of intracellular GSH and (2) Overlapping between DTNB and TNB^{2-} signals. To overcome these drawbacks, in this work we have established a quantification protocol using UPLC-PDA (see Experimental Section for details). We observed that our CuFe nanoparticles were able to convert a large proportion (up to 70% under the conditions tested) of the GSH at room temperature, even in the absence of H_2O_2 (see ***Figure 3a***). The addition of H_2O_2 increased the GSH conversion levels to up to 85% only in the presence of the CuFe catalyst (***Figure 3a***). XPS analysis after reaction (Fig. S4 and Table S3) confirmed the generation of reduced Fe(II) and Cu(I) species on the catalyst as previously claimed by Liu et al.[28] and Hu et al. [61] with Cu-Fe based nanocatalysts. For Cu-based nanoparticles, literature reports show a clear reduction of Cu(II) to Cu(I) after GSH reaction [35,61]. Interestingly, in contrast with the strong reduction detected in the Cu(II) species, Fe(III) species are still present

after 1 h of GSH reaction, although a clear decrease of the Fe^{3+}/Fe^{2+} ratio can be observed. It is reasonable to assume that GSH-oxidation is preferentially occurring via interaction with Cu(II) sites than with Fe(III), in agreement with the lower redox potential of Cu^{2+}/Cu^{+} (0.16 V) in comparison with Fe^{3+}/Fe^{2+} potential (0.77 V). The newly reduced species are prone to undergo Fenton reaction with H_2O_2 to produce •OH radicals and regenerate Fe(III) and Cu(II) species, thereby enhancing its catalytic response (see also **Figure *4*** below). Furthermore, Fenton-like response is more favored at higher pH values for Cu than for Fe catalysts [62,63]. In this study, in addition to GSH depletion, we have also studied the formation of the main reaction product (GSSG) using ^{1}H NMR analysis of the reaction medium (***Figure 3b-c***). It can be seen that GSH characteristic chemical shifts (4.45 ppm, Cys-CH; 2.83 ppm, Cys-CH_2) disappeared after 24 h of incubation with CuFe. The newly formed peaks (3.17 ppm, Cys-CH_2; 2.86 ppm, Cys-CH_2) matched with GSSG signals [64,65].

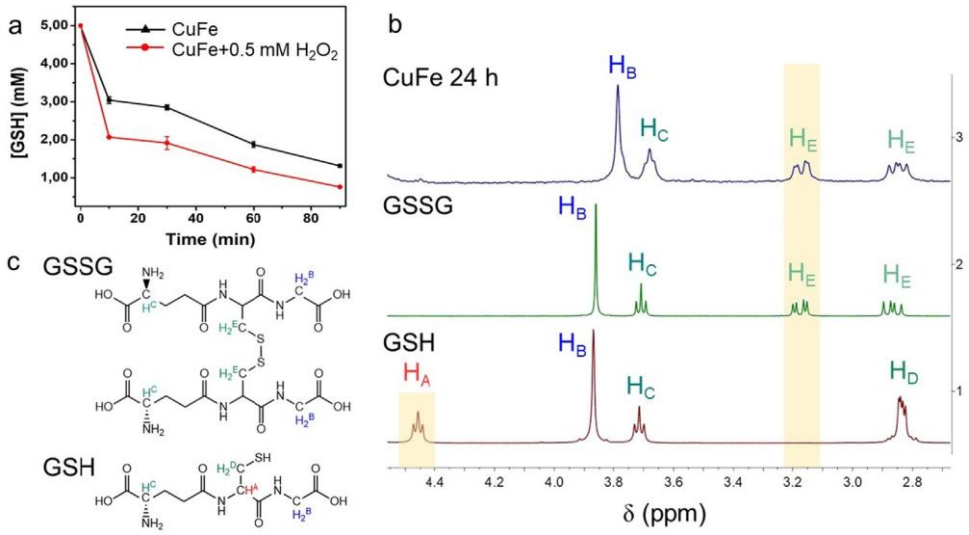

Figure 3. *GSH-depletion capabilities of CuFe nanoparticles and detection of GSH and GSSG by NMR spectroscopy: (a) Evolution of GSH in the presence of CuFe in the absence and in the presence of H_2O_2; No GSH conversion was detected in the absence of the CuFe catalyst (n = 3), Reaction conditions: [Catalyst] = 0.1 mg-mL^{-1}, $[GSH]_0$ = 5 mM, $[H_2O_2]_0$ = 0.5 mM, total volume of reaction = 2.5 mL;; (b) ^{1}H NMR spectra of GSH, GSSG and GSH + CuFe after 24 h; Reaction conditions: [Catalyst] = 0.1 mg-mL^{-1}, $[GSH]_0$ = 5 mM, total volume of reaction = 2.5 mL; (c) Molecular structures of GSH and GSSG with the corresponding signal assignment.*

Wang et al. [61] found this analogous reaction product (GSSG) with Cu-hexacyanoferrate nanoparticles. However, no further studies of reaction product have been performed with Fe(III) species. Taking into account that no additional signals are found in the ^{1}H NRM spectra, it can therefore be concluded that Fe(III)-assisted GSH catalysis yields GSSG as product (***Figure 3c***).

Evaluation of catalytic ·OH generation. To confirm the generation of reactive species derived from Fenton-like reactions, a systematic evaluation was carried out via MB assay [29,66]. At lower pH values (pH = 4.5, AcONa/AcOH buffer), CuFe NPs can promote methylene blue oxidation through Fenton processes (**Figure *4a***, scenarios 1–3) in comparison with neutral pH (7.0, PBS) (**Figure *4a***, scenarios 4–6), where the reaction is negligible in the absence of GSH. The main representative reactions are presented in **Figure *4e-f***. In the absence of GSH (**Figure *4e***), H_2O_2 must act as reducing agent of Fe(III) and Cu(II) (Reactions 1–2 and 4, respectively). Fe^{2+} is the active iron specie in Fenton reaction responsible of producing •OH (Reaction 3), yielding Fe^{3+} as product [40,41]. However, the generation of Fe^{2+} is hampered by slow kinetics and this retards the continuous production of •OH [41]. In the case of Cu, a similar trend is also found with the pair Cu^{+}/ Cu^{2+} [42,43]. Nevertheless, the characteristic tumoral environment offers a large GSH concentration [24,47] and this enables an alter- native mechanism to take place. This antioxidant molecule with $E_0 < 0$ mV [67] can act as an accelerator for the generation of Cu^{+} [35] and Fe^{2+} [34] species. These Fe(II) and Cu(II) species formed in reactions 2 and 4 readily react with intracellular H_2O_2 (reactions 3 and 5) yielding •OH radicals that quickly react with MB, dramatically enhancing the reaction rate compared to the process in the absence of GSH (**Figure *4a-b***). An alternative OH detection method with sodium terephthalate (NaTA) was also employed to validate the generation of ROS via a Fenton-like mechanism (Fig. S5) [60]. Interestingly, the concentration of GSH outside cancer cells is much lower, down to mM levels [68] and this is low enough to avoid triggering this cascade reaction outside the cell (Fig. S6). In general, GSH concentration in cell cytosol have been found to be heterogeneous being present in millimolar concentrations (varying from 1 to 10 mM) [69]. However, in normal and healthy cells, GSH levels range from 1 to 2 mM. For instance, in red blood cells, GSH concentrations vary from 0.4 to 3 mM [70]. In the case of the brain, GSH concentrations have been described to be approximately 1.5–3 mM) [71]. Nevertheless, some cell types such as hepatocytes (whose role is to export GSH) the

concentration of intracellular GSH can even reach 10 mM, a concentration comparable to the GSH levels in cancer cells [22]. Also, discrepancies in GSH levels have also been observed in tumoral areas, depending on the tissue under study. GSH has been shown to be elevated in breast, ovarian, head and neck and lung cancer, but lower in brain and liver tumors, in com- parison to normal tissue [20]. Therefore, the analysis of the GSH levels should performed in every organ and tissue comparing to their disease-free controls, as it has been discussed whether the tumor might induce changes in glutathione in nearby disease-free peritumoral tissue.

Ma et al. [35] also reported cascade reaction with Cu-cysteine nanoparticles employing 0.5 mM GSH to in situ generate Cu(I) active species that could then react with H_2O_2. It is noteworthy that, even though the studied H_2O_2 concentration in their case was high (10 mM), their •OH generation rate was still slow in comparison with the results presented in this work. This again points out to the critical role of the GSH initial concentration: the presence of GSH is directly related with the generation rate of Fenton-active species. Wang et al. [61], found a higher peroxidase-like activity when Cu-hexacyanoferrate nanoparticles were pretreated with GSH. Also pH has a critical influence on Fen-ton reaction, since hydroxide ions (OH^-) can complex Fe and Cu centers of the catalyst [72]. Heterogeneous Fenton reaction starts after the interaction of H_2O_2 with the surface of the metal [41], being in several cases the Rate Determining Step (RDS) [73]. The higher the pH, the more complexed the CuFe surface by OH^- ions will be, thereby hindering the coordination of H_2O_2 and the subsequent formation of •OH. A similar trend has been observed in homogeneous Fenton catalysis [40]. This may explain the result obtained for CuFe catalyst towards •OH production. At pH = 4.5, the large $[H^+]$ is enough to drive the reaction following the mechanism presented in **Figure *4e*** where the H_2O_2 can act also as reducing agent, so the influence of GSH in the metal reduction is negligible. However, given the slower kinetics of Fenton reactions at pH = 7.4, the reduction power of GSH is critical to generate the active Fenton species following **Figure *4f***. We also analyzed the influence of GSH on metal leaching (Fig. S7): the presence of GSH quickly releases Cu from the crystalline structure.

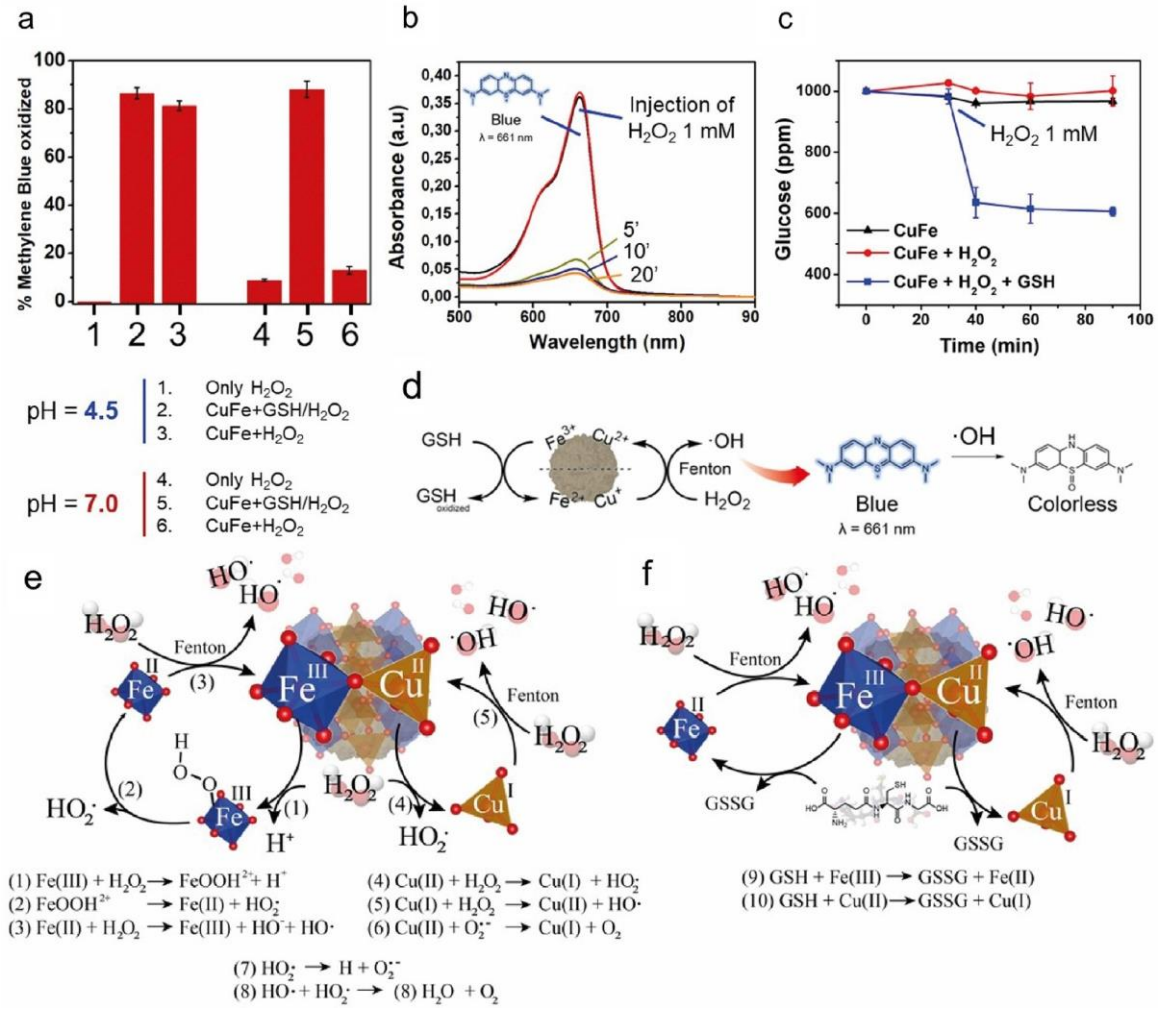

Figure 4. *CuFe assisted •OH generation experiments. (a) Percentage of methylene blue oxidized after 20 min of reaction at pH = 4.5 (scenarios 1–3) and at pH = 7.0 (scenarios 4– 6); (b) Evolution of MB over time under scenario 5 (CuFe + GSH/H_2O_2) at pH = 7.0, $[GSH]_0$ = 5 mM; (c) Glucose conversion under different reaction scenarios at pH = 7.0; d) Schematic representation of CuFe mechanism: after reaction with GSH, the generated Fe(II) and Cu(I) species can decompose H_2O_2 into •OH which can be detected via MB reaction; Reaction conditions: [CuFe] = 0.1 mg-mL^{-1}, $[GSH]_0$ = 5 mM, $[H_2O_2]_0$ = 1 mM, $[MB]_0 = 5.78 \cdot 10^{-5}$ M. In 4c H_2O_2 was added to the system after 40 min of reaction. (e-f) Interaction between GSH and CuFe nanoparticles towards •OH generation. (e) The generation of Fe(II) and Cu(I) active Fenton species through reactions (1,2) and (4), respectively, represents the bottleneck of the catalytic process. (f) The presence of GSH acts as an accelerator, providing the required reduction power to generate these active Fenton species through reactions (9) and (10).*

This is in contrast with the behaviour observed for iron, which only starts to be leached significantly once the preferential release of Cu has occurred to a large extent. An enhanced Cu leaching in the presence of GSH was also reported by Xu et al. with Cu-Mn based biodegradable nanoparticles [66] although in this case, Mn release also took place at the same time. They attributed the Cu-leaching to the high lability of Mn-O bond under tumor-microenvironment conditions (i.e. large GSH concentrations and mildly-acidic pH). The breakage of the Mn-O induced the formation of lattice defects [74] which led to the cleavage of Cu-O bonds. The capacity of the same GSH-activated mechanism to target glucose, was also evaluated as this is a key molecule for cancer cell metabolism. The results are shown in **Figure *4c***. It can be seen that, while there is little or no effect of the catalyst alone or with H_2O_2 added, when GSH is present a similar trend to that observed for MB follows, with a fast decrease of glucose concentration (up to 70% from 5.5 mM a value that could be considered representative of physiological concentrations) as soon as H_2O_2 (1 mM) was added when GSH was present in the system. From the above discussion we attribute this behavior to the generation of Fe(II) and Cu(I) active species on the catalyst mediated by GSH (reactions 9 and 10, **Figure *4f***). Glucose is especially important in tumors and is being proposed as a central target of the so-called starvation therapy, focusing on glucose metabolism to hinder tumor growth [75]. Tumor cells consume an abnormally high amount of glucose in comparison with healthy ones to satisfy their energy needs and the anabolic demands for growth [10]. This glucose dependency has been known for a century and is generally known as the Warburg effect [76]. The strong depletion of glucose shown in **Figure *4c*** validates the potential of CuFe nanoparticles to generate ROS able to convert glucose as an attractive alternative to other catalysts exhibiting glucose oxidase-like activity [77].

Cellular uptake and CuFe biocompatibility. The tolerability of exposure to CuFe NPs of cancer (U251-MG) and mesenchymal stem cells (hpMSCs) was determined by incubating increasing quantities of the catalyst with the respective cells during 6 and 24 h, respectively. According to the ISO 10993–5 (Biological evaluation of medical devices. Part 5: test for *in vitro* cytotoxicity) a reduction in cell viability higher than 30 % compared to the control is considered as cytotoxic effect. **Figure *5a*** and **Figure *5b*** show that a clear decrease on cell viability could be observed above a certain concentration of CuFe NPs. Interestingly, the vulnerability of U251-MG cancer

cells to these nanoparticles was significantly higher compared to hpMSCs after incubation. Thus, after 6 h of incubation, 1.5 mg mL^{-1} and 0.4 mg mL^{-1} of CuFe were the doses that significantly reduced cell viability in hpMSCs and U251-MG cells (compared with untreated cells), respectively (i.e. hpMSCs can tolerate concentrations of CuFe NPs that are nearly four times the corresponding levels for U251-MG cells). Similar results were obtained also after a 24 h incubation period, with cell viability significantly affected at 0.4 and 0.1 mg mL^{-1} for hpMSCs and U251- MG cells respectively, compared to untreated cells, again a factor of four. These data suggest that the viability of cancer glioma cells is more strongly affected upon the exposure to CuFe NPs compared with healthy hpMSC cells. To further study the interaction of these nanoparticles with both types of cells, a CuFe concentration of 0.1 mg mL^{-1} was selected as subcytotoxic dose lines in the subsequent experiments. The internalization of CuFe into U251-MG cells and hpMSCs was assessed by confocal microscopy. **Figure *5c*** and **Figure *5d*** (and Fig. S8) include representative images from hpMSCs and U251-MG cells, respectively, after treatment with CuFe for 4, 6, 10, 24 and 48 h. After 6 h a significant accumulation of CuFe inside both cell lines was observed, higher than at other time points studied. The internalization route was studied by marking lysosomes and CD63 positive endosomes and investigating their co-localization with CuFe NPs under confocal microscopy. The results (see the Z-stack sections of the images in **Figure *5*** as well as in Figures S8 and S9) confirmed the localization of the CuFe NPs within an endosomal pathway, with preference to the lysosomal route. This is a favorable result, as a faster CuFe degradation would take place in the lysosomal acidic compartments within the cells.

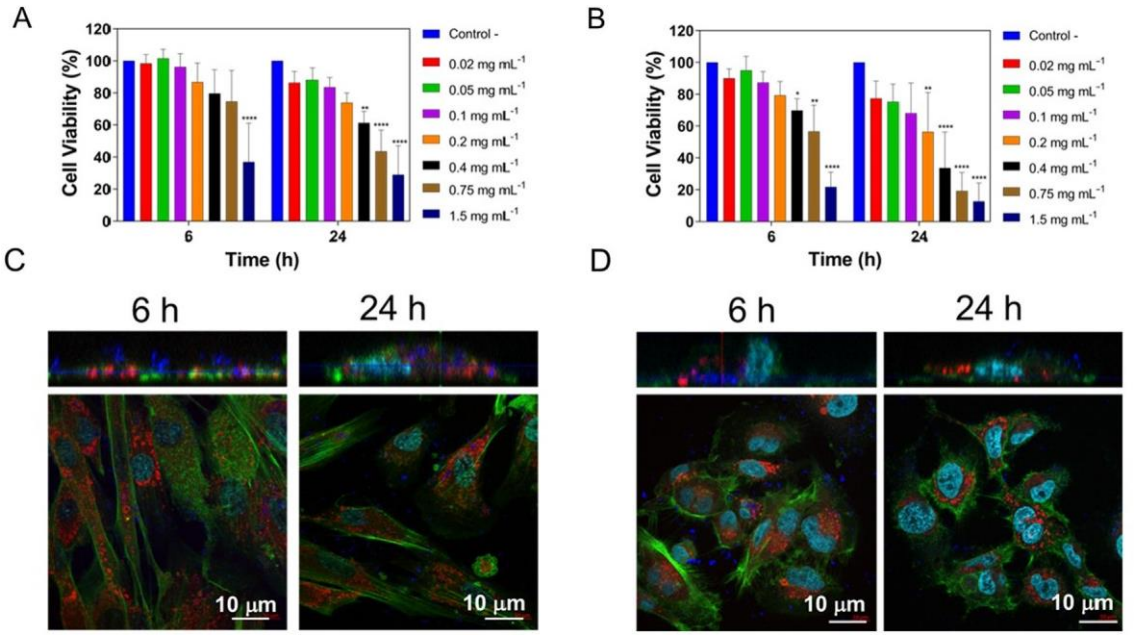

Figure 5. *(a) Tolerability study of CuFe incubated with hpMSCs cells after 6 h and 24 h. (b) Tolerability study of CuFe incubated with cancer U251-MG cells after 6 and 24 h (n = 4). (c) Confocal trafficking study of CuFe in hpMSCs showing endosomal pathway. (d) Confocal trafficking study of CuFe in U251-MG cells showing endosomal pathway (actin is shown in green, nuclei in cyan, CuFe in blue and CD63 positive vesicles in red).*

Estimation of intracellular GSH concentration. Encouraged by the above findings on the role played by GSH in enhancing the catalytic effects of CuFe NPs, we decided to investigate whether the higher sensitivity exhibited by U251-MG cells could be related to their GSH content. Although it is generally known that cancer cells tend to increase the production of GSH compared with healthy cells, (a feature that is thought to be related to the role of GSH as antioxidant molecule) [19], to date there are no systematic studies correlating catalytic effects to GSH levels which is likely due to the lack of an accurate method to determine intracellular GSH levels. Here, we estimated the cytoplasmic GSH concentration in U251-MG and hpMSCs by: i) measuring GSH levels in cells after their trypsinization, lysate and derivatization with DTNB for a subsequent

quantification using UPLC-PDA (***Figure 6a*** and Experimental section) and ii) relating the amount of GSH determined to the number of cells present in the sample and to the cell volume (to estimate GSH concentrations inside each individual cell) (***Figure 6a***). Cell volumes were estimated from optical images obtained from cells in suspension with an inverted optical microscope (Olympus IX81) (***Figure 6a*** and Fig. S10b). As expected, the suspended cells had an approximately spherical morphology and their average radius were calculated as 14.4 ± 4.6 mm and 9.2 ± 1.8 mm for hpMSCs and U251-MG cells, respectively (Fig. S10a). According to these mean values, hpMSCs and U251-MG cells presented a total volume of $1.2 \cdot 10^{-11}$ L and $3.3 \cdot 10^{-12}$ L per cell, respectively. Then, the total amount of GSH determined by UPLC on the cell culture could be related to the total cell volume, taking into account the volumes of each cell and the number of cells in the respective cultures. ***Figure 6b*** shows intracellular GSH levels estimated for both types of cells and it can be seen that in the case of U251-MG cancer cells GSH concentrations were significantly higher 7.3 ± 1.2 mM compared to 1.9 ± 0.2 mM for hpMSCs cells.

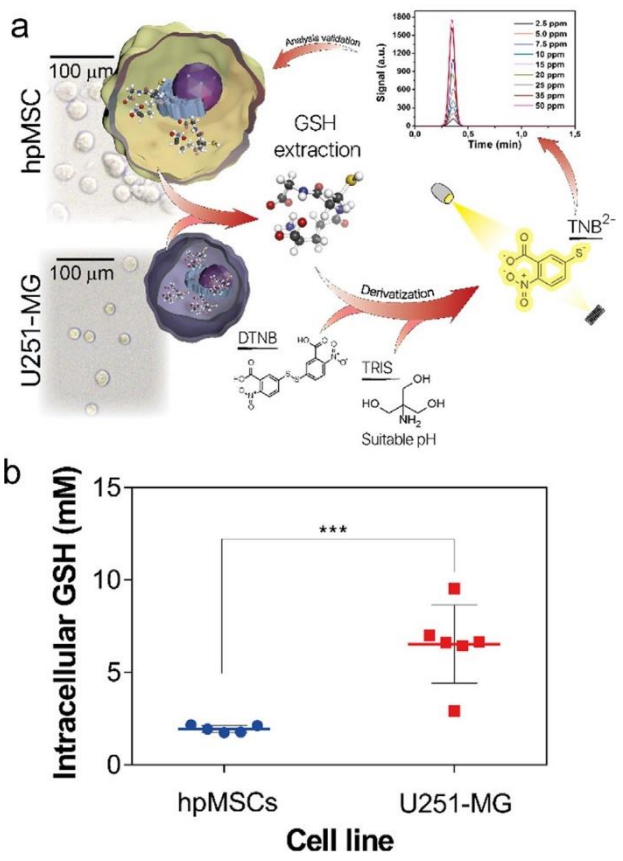

Figure 6. *Scheme summarizing the intracellular GSH quantification method developed in this work: (a) GSH extraction from cells after trypsinization, lysate and derivatization with DTNB for final quantification by UPLC-PDA analysis. GSH intracellular concentrations were expressed on a cell volumetric basis taking into account number of cells in the culture and their volume, obtained from optical inverted microscopy images; (b) Intracellular GSH concentration for hpMSCs and U251-MG lines, evidencing the larger amount of GSH in the latter (n = 6).*

Cell death mediated by CuFe nanoparticles. The ability of CuFe nanocatalyst to induce cell death through by Fenton-type reactions was evaluated in both cancer and stem cells. Specifically, the cell cycle distribution and death mechanisms were studied by flow cytometry. **Figure *7*** shows that, when exposed to CuFe NPs (0.2 mg mL^{-1}) both cell lines undergo changes in the distribution of cells in each cycle phase, but a clearly more acute effect was observed on U251-MG cells leading to cell death (**Figure *7a***).

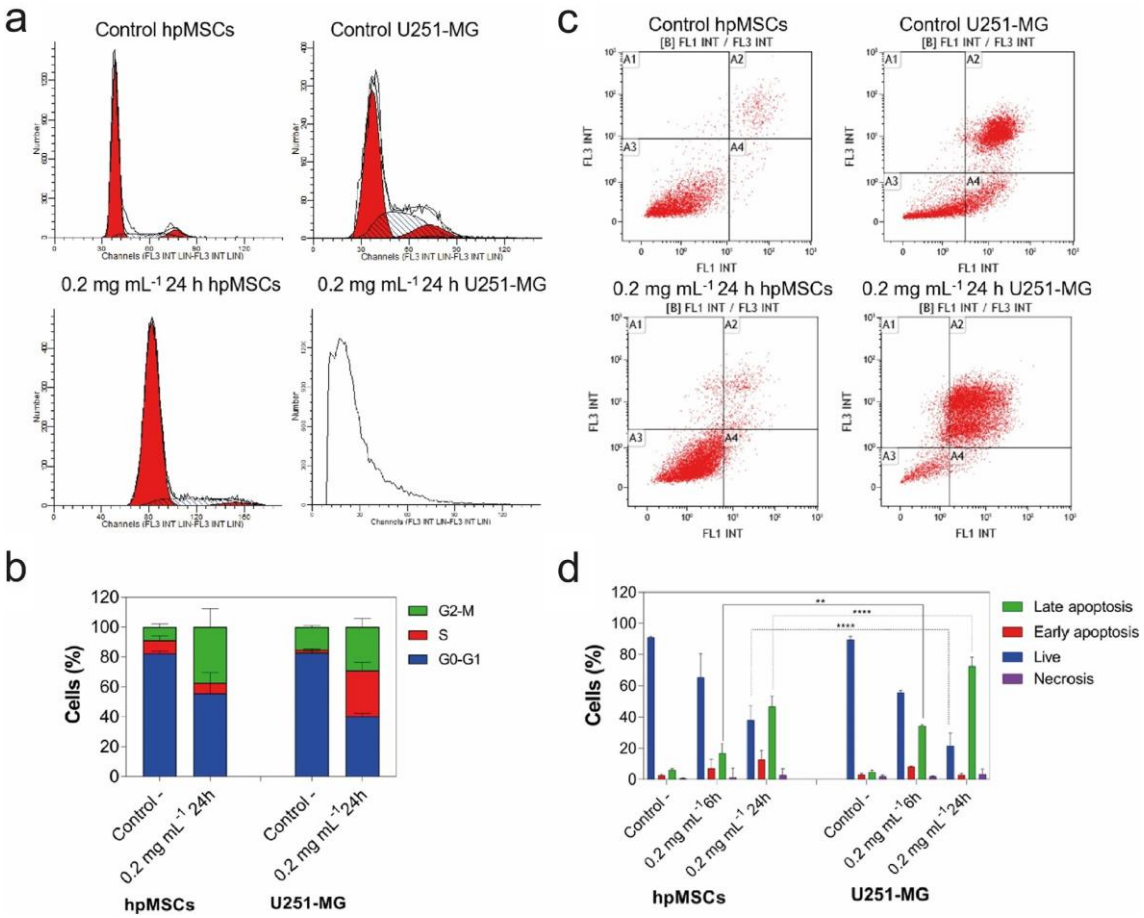

Figure 7. *Flow cytometry analyses: (a) Cell cycle histograms obtained by flow cytometry; (b) Percentage of cells in cell cycle after the treatment with CuFe during 24 h at 0.2 mg mL^{-1} compared to untreated cells (control); (c) Apoptosis and necrosis results obtained by flow cytometry; (d) Percentage of cells in early or late apoptosis and necrosis after the treatment with CuFe during 24 h at 0.2 mg mL^{-1} compared to untreated cells (control).*

In fact, in some cases it was not even possible to evaluate the distribution of cells in each phase of the cell cycle because tumoral cells were strongly affected by CuFe particles (**Figure *7a***). A

significant increase in S phase (from 1.8 to 30.6 %) as well as in G2-M phase (<10%) and a decrease on G0-G1 phases (almost a 40 % decrease) was observed after cancer cell treatment compared to control samples (**Figure *7b*** and Table S4). Flow cytometry also elucidated the mechanism of cell death caused by CuFe (**Figure *7c***). The incubation of the two cell lines (hpMSCs and U251-MG cells) with 0.2 mg mL^{-1} of CuFe during 6 and 24 h did not exhibit remarkable changes compared to control (untreated) samples regarding the percentage of cells death by necrosis. However, after CuFe NPs treatment, apoptosis was induced for both cell lines, again much more intensely for U251-MG cells (see **Figure *7d***). Thus, for hpMSCs, 16.7 and 46.5% of cells were in a late apoptotic phase after 6 and 24 h of incubation with CuFe, respectively while in the case of cancer U251-MG cells the corresponding percentages were 34.3 % and 72.6 % respectively when they were incubated with the same concentration of CuFe nanoparticles at 6 and 24 h, respectively. Especially in late apoptosis, very significant increases were observed for U251-MG cells. Finally, the evolution of cell morphology by confocal microscopy also corroborates the results of flow cytometry regarding the effect of CuFe nanoparticles. **Figure *8a*** shows how U251-MG morphology was strongly affected upon CuFe treatment (particularly after 24 h of incubation). The presence of the nanocatalyst caused the features typical of apoptosis including spherical rounded shape, cytoplasmatic aggregation, membrane irregularity and the formation of multiple apoptotic bodies compared with untreated cells. Interestingly, apoptosis features are not yet evident the microscopy images of hpMSCs incubated with CuFe NPs under the same conditions, even though CuFe NPs are clearly present inside MSC cells. These data again confirm the enhanced effect of CuFe nanocatalyst in the cancer cells studied compared to the stem cell counterparts.

GSH levels inside both hpMSCs and U251-MG cells after their treatment with CuFe were measured. U251-MG cells exhibited a very significant decrease on GSH intracellular levels when treated with CuFe compared to control cells (untreated) (see **Figure *8b***). Specifically, the presence of the nanocatalyst led to an abrupt decrease of cytoplasmatic GSH from 7.3 mM to 5.2 mM (6 h) and to 2.5 mM (24 h) in the cancer cells. These results demonstrate an enhanced totoxic response towards the U251-MG tumor cell line, being much more susceptible to GSH depletion compared to stem cells after their interaction to CuFe NPs.

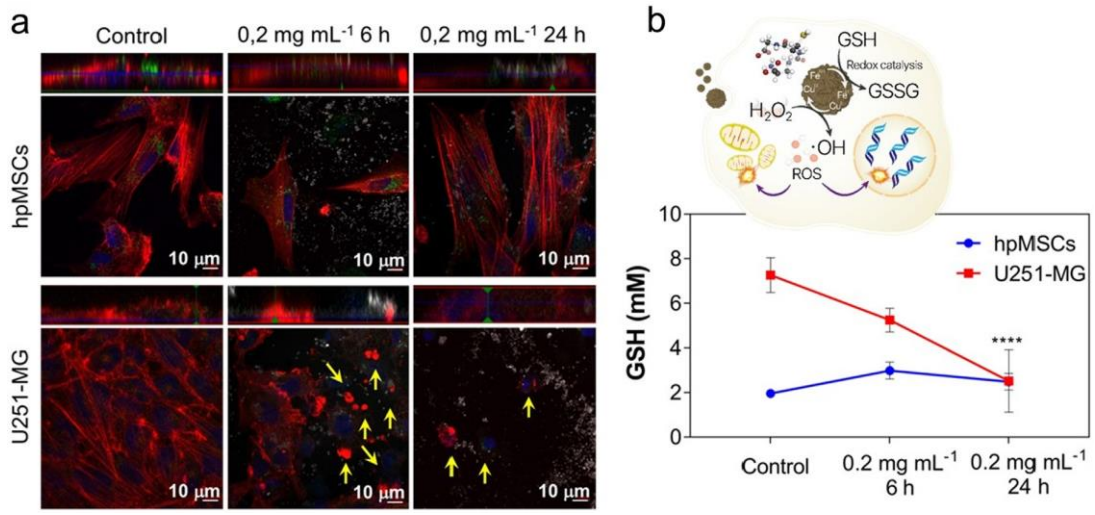

Figure 8. *(a) Morphological changes of cells incubated with CuFe during 6 and 24 h (0.2 mg mL^{-1}). Actin is visualized in red, CD63 positive vesicles in green, nuclei in blue and CuFe in white; (b). Evolution of intracellular GSH levels of hpMSCs and U251-MG after their incubation with the nanocatalyst or under control (non-treated) conditions. Inset illustrates the GSH depletion-ROS generation cycle (n = 3).*

Taking together, the results of flow cytometry and confocal microscopy indicate that: i) after CuFe exposure, U251-MG cancer undergo intense apoptosis compared with hpMSCs, a catalytic action that is triggered by the high GSH levels inside U-251-MG cells; and ii) U251-MG GSH levels significantly decrease when incubated with CuFe compared to hpMSCs (**Figure *7b***) as a result of the above-described cascade processes.

Conclusions – Chapter 1

The CuFe nanoparticles synthesized in this work can enable a GSH-triggered cascade reaction that gives rise to the depletion of intracellular GSH in a process that produces reduced species on the surface of the nanoparticles. These reduced species in turn promote Fenton processes in the presence of H_2O_2 and the subsequent generation of ROS species that induce cell death by apoptosis. Especially at close to neutral pH, the catalytic action needs the presence of both GSH and H_2O_2 as a trigger, and is strongly enhanced by higher GSH concentrations. Our comparative study with hpMSCs and U251-MG cells as examples of healthy and cancer cells support this

conclusion: CuFe nanoparticles were much more toxic towards U251-MG cells leading to an enhancement of apoptosis, as confirmed by flow cytometry and confocal microscopy observations. The effect was damped on hpMSCs, with considerably lower GSH basal levels. Both intra- and extracellular GSH levels were accurately measured in this work, and the concentrations correlated well with the catalytic action observed. Interestingly, the presence of GSH not only pulled the catalytic action regarding the reduction of GSH levels and the concomitant generation of ROS, but also the depletion of other molecules. Glucose in particular was tested in this work, undergoing a strong reduction in the presence of GSH, H_2O_2 and CuFe nanoparticles. In summary, the higher concentration of GSH in cancer cells enables a combined therapeutic action (ROS generation and starvation therapy through glucose depletion), leading to enhanced apoptosis. This could open up new opportunities that leverage GSH upregulation in the tumor environment, adding a new element to the growing chemodynamic therapy toolbox.

Experimental section – Chapter 1

Chemicals and materials. Iron (III) chloride hexahydrate ($FeCl_3$-$6H_2O$, 97%), copper (II) chloride dihydrate ($CuCl_2{\cdot}2H_2O$, 2: 99.0%), sodium acetate anhydrous (CH_3COONa), Bovine Serum Albumin (BSA), ethylene glycol (EG) (99.8%), Glutathione (98, HPLC), Glutathione oxidized (98, HPLC), 5,5' -Dithiobis(2-nitrobenzoic acid) (DNTB), lactose (Standard Quality), methylene blue (MB), hydrogen peroxide (H_2O_2, 33% v/v), sodium bicarbonate ($NaHCO_3$, 99%) were purchased from Sigma Aldrich. D-glucose was purchased from MP Biomedicals. Acetonitrile (ACN) (HPLC Quality) was purchased from WVR (Avantor) . UPLC grade water was obtained from a Milli-Q Advantage A10 System with resistivity of 18.2 mΩ (Merk Millipore, Germany).

Synthesis of CuFe nanoparticles. $CuFe_2O_4$ nanoparticles were synthetized following a templated- growth method. In a typical synthesis, 250 mg of BSA were dis- solved in 2.5 mL of deionized water. After that, 12.5 mL of EG were added to the mixture, followed by 270.5 mg of $FeCl_3{\cdot}6H_2O$, 121.0 mg $CuCl_2{\cdot}2H_2O$ and 375 mg of CH_3COONa. Reagents were thoroughly stirred for 2 h at room temperature. The reaction was then transferred to a Teflon autoclave and the temperature was kept at 180 ºC for 24 h. Finally, the product was centrifuged at 12 000 rpm for

20 min and washed twice in the same conditions with distilled water. The catalyst was stored at 4 ºC until further use. The synthesis of these materials has been performed at the Platform of Production of Biomaterials and Nanoparticles of the NANBIOSIS ICTS, more specifically by the Nanoparticle Synthesis Unit of the CIBER in BioEngineering, Biomaterials & Nanomedicine (CIBER-BBN).

***Characterization techniques*.** Transmission electron microscopy (TEM) was performed using a FEI TECNAI T20 microscope operated at 200 keV. Samples were prepared by drop casting 5 mL of the nanoparticle suspension on a holey carbon TEM grid. High-resolution transmission electron microscopy (HRTEM) was performed using a FEI Titan (80– 300 kV) microscope at an acceleration voltage of 300 kV. Sample was prepared by depositing 5 mL of the nanoparticle suspension on a holey carbon TEM grid. UV–vis spectra were obtained on a UV–vis double beam spectrophotometer Jasco V67. Fourier trans- form infrared spectroscopy (FTIR) was performed on a Bruker Vertex 70. X-ray photoelectron spectroscopy (XPS) was performed with an Axis Supra spectrometer (Kratos Tech). The samples were mounted on a sample rod placed in the pretreatment chamber of the spectrometer and then evacuated at room temperature. The spectra were excited by a monochromatized Al Ka source at 1486.6 eV and subsequently run at 8 kV and 15 mA. A survey spectrum was measured at 160 eV of pass energy, and for the individual peak regions, spectra were recorded with a pass energy of 20 eV. Analysis of the peaks was performed with the CasaXPS software using a weighted sum of Lorentzian and Gaussian component curves after Shirley background subtraction. The binding energies were referenced to the internal C 1 s standard at 284.5 eV. X-ray diffraction patterns were obtained in a PANalytical Empyrean equipment in Bragg-Brentano configuration using Cu-Kα radiation and equipped with a PIXcel1D detector. ^{1}H spectra (D_2O) were recorded at 25 ºC using a Bruker Avance 400 MHz NMR spectrometer with TMS as the internal standard and deuterated water as solvent in a 5 mm QNP probe. Nanoparticle Tracking Analysis was measured on Malvern Nanosight 300.

Catalytic oxidation of GSH. The catalytic activity of $CuFe_2O_4$ nanoparticles oxidizing GSH was evaluated according to the following protocol: in a total volume of 2.5 mL, 5 mM of GSH were

mixed with 0.1 mg-mL^{-1} of CuFe at 37 ºC. In the experiments adding H_2O_2, the final concentration in the reaction was fixed at 0.5 mM. GSH concentration was quantified by UPLC (*vide infra*).

Generation of hydroxyl radicals. The capability of CuFe nanoparticles to generate •OH was evaluated via MB assay [29,66]. In a total volume of 2.5 mL, a final con- centration of $5.78 \cdot 10^{-5}$ M of MB and 0.1 mg mL^{-1} of CuFe were mixed. For experiments containing GSH, a concentration of 5 mM was selected. The pH of the reactions was set to 4.5 and 7.0 using CH_3COO/CH_3COOH and PBS buffer, respectively. H_2O_2 was added after 40 min with a final concentration of 1 mM. Alternatively, •OH formation was detected via the terephtalic acid assay [60,78,79]. In a total volume of 2.5 mL, 5 mM of disodium terephthalate, 0.1 mg mL^{-1} CuFe and 5 mM of GSH were mixed. The pH was maintained at 4.5 using a CH_3COO^-/CH_3COOH buffer. H_2O_2 was added after 25 min of reaction, with a final concentration of 1 mM. The generation of 2-hydroxy disodium terephthalate was evaluated by measuring the fluorescence with an excitation wavelength of 315 nm.

Cell culture conditions. hpMSCs were obtained from Cellular Engineering Technologies (CET) (Coralville, IA, USA) and U251-MG glioblastoma cells were kindly obtained from Cancer Research UK Cell services. hpMSCs were cultured in Dulbecco's modified Eagle's medium (DMEM; Biowest, France) supplemented with 5 g mL^{-1} of FGF-2 growth fac- tor (PeproTech, USA), with 10 % of fetal bovine serum (FBS, GIBCO, USA), 1% penicillin/streptomycin and 1% amphotericin (Biowest, France) and maintained at 37 ºC in a 5% CO_2-humidified atmosphere under hypoxic conditions (3 %). For culturing U251-MG cells DMEM with 10 % of FBS supplemented with 1% penicillin/ streptomycin and 1% amphotericin was used.

Study of CuFe nanoparticles biocompatibility. hpMSCs and U251-MG cells were seeded in a 96-well plate for- mat (at 5000 and 4000 U251-MG cells and hpMSCs per well, respectively) and incubated for 24 h before treatment. Each well was then replaced with a suspension of CuFe in culture media at a concentration ranged from 0.025 to 1.5 mg mL^{-1} After 6 and 24 h cells were washed with PBS buffer. Blue Cell viability reagent (10% v/v) was used to determine cell viability under the effect of CuFe [80]. Experiments were performed in triplicates.

Cellular uptake and trafficking of CuFe nanoparticles. Confocal microscopy was employed to follow the internalization of CuFe in both hpMSCs and U251-MG cells. hpMSCs and U251-MG cells were seeded at a density of 30,000 and 20,000 U251-MG cells and hpMSCs per well, respectively onto 20 mm cover slips (deposited onto a 24-well plate) and incubated under standard culture conditions for 24 h. Then, CuFe at the subcytotoxic dose (0.1 $mg \cdot mL^{-1}$) were added to each well and incubated for 4, 6, 10, 24 and 48 h. Cells were finally fixed with 4 % paraformaldehyde. In order to label the cytoplasmic actin, cells were stained with phalloidin-Alexa546 (Invitrogen, USA), the endosomal pathway was labelled using an anti-CD63-Alexa-488 (ThermoFisher Scientific) and Draq-5 was used to observe the nuclei. Reflection of the incident light at 488/490 nm was used to directly visualize CuFe aggregates. Lysosomes were also labelled using a Lysotracker Green DND-26 (molecular probes) without previously fixing the cells and following manufacturer instructions. The cellular uptake was observed under a confocal micro-scope (SEISS LSM880 Confocal Laser Scanning Microscope) with a 63x oil immersed N.A. 1.40 objective. Z-stack orthogonal projec- tions were developed to determine the presence of NPs inside the cytosol.

Intracellular GSH quantification. In order to determine the intracellular GSH concentration, U251-MG and hpMSCs were seeded onto P100 culture dishes upon they reach 80 % of confluence. Cells were finally trypsinized, washed twice with PBS (500 g, 5 min) and collected. Before GSH quantification, cells were centrifuged twice at 13300 rpm for 5 min. Supernatant was discarded and a certain volume of 12% CCl_3COOH solution was added to lysate the cells and precipitate proteins avoiding its interference in the analysis (500 mL for GSH determination and 400 mL for GSH-consumption experiments). Samples were sonicated and left 15 min at 4C. The suspension was centrifuged at 13 300 rpm for 5 min. The supernatant was isolated for derivatization process (see details below) and labelled as *in vitro.* In order to express the result in terms of GSH cell concentration, an estimation of total cell volume in the samples was established. After quantifying the number of cells in each sample, and assuming 3-dimensional spherical shapes, average cell volumetric distribution was estimated after measuring the radius of 250 individual cells from inverted conventional microscopy images (see Fig. S10b). Average radii of 14.4 ± 4.6 mm and 9.2 ± 1.8 mm were determined for hpMSCs and U251-MG cells, respectively),

Likewise, hpMSCs presented a calculated volume of $1.2 \cdot 10^{-11}$ L whereas U251-MG volumes were $3.3 \cdot 10^{-12}$ L.

GSH derivatization protocols for UPLC analysis. The derivatization of GSH using DTNB yields a quantifiable yellow-colored product, 5-thiobis-(2-nitrobenzoic acid) (TNB^{2-}) which absorbs at 412 nm following reaction shown in Fig. S3. Depending on the experiment (ex vitro GSH oxidation or *in vitro* GSH quantification), analysis conditions are different due to matrix differences. In the case of catalytic oxidation of GSH, a calibration curve was prepared following the amounts specified in Table S2. For the sample preparation, 20 mL of the reaction were mixed with 100 mL of 1 mM DTNB, 50 mL of 0.2 M $NaHCO_3$ and 880 mL of ACN: H_2O (1:1) solutions. For *in vitro* GSH quantification, calibration curve was prepared following the amounts specified in Table S3. Due to the acidic nature of TCA employed for GSH extraction, during the sample preparation, 50 mL of *in vitro* GSH solution were mixed with 20 mL DNTB (2.5 mM), 6.5 mL NaOH (3 M) and 930 mL TRIS (0.01 M) solution. Final pH both of standards and samples was 7.8–7.9. Both samples and standards were filtered with 0.22 mm Nylon filters before injecting in UPLC system.

UPLC-PDA-MS equipment for GSH and glucose analysis. GSH and glucose analysis were performed on Waters ACQUITY system H-Class which consisted of a binary pump, an autosampler, a column thermostat and a photodiode array (PDA) detector. This system is coupled to a single quadrupole mass spectrometer with an electrospray ionization (ESI) ACQUITY QDa mass detector. Data acquisition and processing were performed by using MASSLYNX software (Waters Corporation USA). On the one hand, in order to analyze GSH from derivatized samples as describe below, chromatographic separation was performed using an ACQUITY UPLC BEH C18 column (130 Å, 1.7 mm 2.1 x 50 mm, from WATERS) at 40 ºC under an isocratic flow of 0.3 mL/min containing 50% acetonitrile, 50% milli Q water. PDA detector was employed to monitor absorbance from derivatized GSH at 412 nm during analysis time. On the other hand, glucose was monitored after the chromato- graphic separation was performed using an ACQUITY UPLC BEH Amide column (130 Å, 1.7 mm, 2.1 mm X 100 mm, WATERS). In this case, mobile phase consisted of an initial mixture of acetonitrile/ water (90:10), containing 0.1% 10 mM ammonium chloride in ammonium, as a mobile phase modifier, at a 0.5 mL/min initial flow rate. Thereon a gradient in the

mobile phase was employed to separate the different metabolites present in the samples. Water composition increased for 3 min until a 65% acetonitrile is reached and then the system can recover initial conditions. ACQUITY QDa mass detector was employed to quantify sugar concentrations according to the most abundant ions generated as described below. Calibrations were performed using commercial standards of glucose and lactose.

Cell viability and intracellular GSH levels depletion. To determine how CuFe presence within cell cytoplasm leads to cell death mediated by GSH decrease, firstly the distribution of the cell cycle phases after CuFe treatment was assessed by flow cytometry. Cells were seeded onto 6-well plates at a density of 200,000 and 300,000 hpMSCs and U251-MG cells per well, respectively. After 24 h, CuFe (0.2 mg mL^{-1}) were added into the treated wells. After 24 h, cells were trypsinized and washed twice with PBS (500 g, 5 min). Then, cells were collected in PBS and fixed with 70 % ice-cold ethanol and maintained at 4 ºC in this solution almost for 24 h. DNA staining was performed by adding RNase A and propidium iodide (PI) to the cell suspension. Finally, samples were analyzed in a FACSARRAY BD equipment with the MODIFIT 3.0 Verity software. Control samples (not treated cells) were also evaluated to estimate the standard distribution of cell cycles in the cell lines assayed. Moreover, cell morphology was evaluated upon their exposure to CuFe 0.2 mg mL^{-1} during 6 and 24 h by confocal microscopy as previously mentioned.

In order to study cell mechanisms induced by the presence of CuFe, cells were again seeded onto 6-well plates and CuFe was added at previously mentioned (0.2 mg mL^{-1} during 6 and 24 h). After these time points, cells were collected and washed twice with PBS. Cell pellet was finally suspended in 200 mL of PBS containing ethylenediaminetetraacetic acid (EDTA) before cell labeling with 5 mL of Anexin V-FITC and 5 mL of PI during 15 min. Cancer cell mechanism (necrosis or apoptosis) was determined by flow cytometry (FACSAria BD cytometer, BD Bioscience). Flow cytometry experiments were performed in triplicates. Finally, GSH intracellular levels of CuFe treated hpMSCs or U251-MG cells (0.2 mg mL^{-1} during 6 and 24 h) were quantified as described above in order to corroborate that CuFe lead cytotoxicity effect is mediated by GSH depletion inside cell cytoplasm. Experiments were performed in triplicates.

GSH triggered conversion of glucose. GSH-assisted peroxidation of glucose was carried out as follows: 1000 ppm of glucose (5.55 mM) were mixed with 0.05 mg mL^{-1} of CuFe at 37 ºC in a total volume of 2.5 mL. For experiments containing GSH, a concentration of 5 mM was established. 100 mL H_2O_2 (125 mM) were added after 30 min of reaction to reach a final concentration of 1 mM. The pH was adjusted to 7.0 with $NaHCO_3$ solution. Glucose concentration from samples collected at different times were analyzed by UPLC-MS. After ESI, glucose most abundant ion is the chloride adduct [M-Cl^-] at *m/z* formed due to the presence of NH_4Cl in the mobile phase [81]. Calibration curve was prepared following the amounts specified in Table S6. Lactose was used as internal standard, being 377.45 the m/s corresponding to its most abundant chloride adduct. For the sample preparation, 20 mL of reaction was mixed with 25 mL of 1000 ppm Lactose solution and 955 mL of a mixture ACN:H_2O (1:1). Both samples and standards were filtered with 0.22 mm Nylon filters before injecting in UPLC system.

Statistical analysis. All the results are expressed as mean ± SD. Statistical analysis of the biological experiments and the significant differences among the means were evaluated by two-way analysis of variance (ANOVA) for multiple comparisons by Dunnett's multiple comparisons test using GraphPad Software). Statistically significant differences were express as follows: *$p < 0.05$, **$p < 0.005$, ***$p < 0.0005$ and ****$p < 0.00005$.

References – Chapter 1

1. WHO, World Health Organization: Global Health Estimates 2020: Deaths by Cause, Age, Sex, by Country and by Region, 2000-2019, World Health Organization: Global Health Estimates 2020: Deaths by Cause, Age, Sex, by Country and by Region, 2000-2019, (2020).

2. Z. Tang, P. Zhao, H. Wang, Y. Liu, W. Bu, Biomedicine Meets Fenton Chemistry, Chem. Rev. 121 (4) (2021) 1981–2019.

3. I.S. Harris, G.M. DeNicola, The Complex Interplay between Antioxidants and ROS in Cancer, Trends Cell Biol. 30 (6) (2020) 440–451.

4. Y. Liu, H. Liu, L.i. Wang, Y. Wang, C. Zhang, C. Wang, Y. Yan, J. Fan, G. Xu, Q. Zhang, Amplification of oxidative stress via intracellular ROS production and antioxidant consumption by two natural drug-encapsulated nanoagents for efficient anticancer therapy, Nanoscale Adv. 2 (9) (2020) 3872–3881.

5. B. Yang, Y.u. Chen, J. Shi, Nanocatalytic Medicine, Adv. Mater. 31 (39) (2019) 1901778.

6. X. Wang, X. Zhong, Z. Liu, L. Cheng, Recent progress of chemodynamic therapy- induced combination cancer therapy, Nano Today 35 (2020) 100946.

7. L. Wang, M. Huo, Y.u. Chen, J. Shi, Tumor Microenvironment-Enabled Nanotherapy, Adv. Healthcare Mater. 7 (8) (2018) 1701156, https://doi.org/10.1002/adhm.v7.810.1002/adhm.201701156.

8. R.H. Burdon, Superoxide and hydrogen peroxide in relation to mammalian cell proliferation, Free Radical Biol. Med. 18 (1995) 775–794.

9. M. López-Lázaro, Dual role of hydrogen peroxide in cancer: possible relevance to cancer chemoprevention and therapy, Cancer Lett. 252 (2007) 1–8.

10. R.J. DeBerardinis, N.S. Chandel, Fundamentals of cancer metabolism, Sci. Adv. 2 (5) (2016), https://doi.org/10.1126/sciadv.1600200.

11. B. Yang, Y.u. Chen, J. Shi, Reactive Oxygen Species (ROS)-Based Nanomedicine, Chem. Rev. 119 (8) (2019) 4881–4985.

12. S.-L. Li, P. Jiang, F.-L. Jiang, Y.i. Liu, Recent Advances in Nanomaterial-Based Nanoplatforms for Chemodynamic Cancer Therapy, Adv. Funct. Mater. 31 (22) (2021) 2100243.

13. Y. Xiong, C. Xiao, Z. Li, X. Yang, Engineering nanomedicine for glutathione depletion-augmented cancer therapy, Chem. Soc. Rev. 50 (10) (2021) 6013–6041.

14. C. Maksoudian, N. Saffarzadeh, E. Hesemans, N. Dekoning, K. Buttiens, S.J. Soenen, Role of inorganic nanoparticle degradation in cancer therapy, Nanoscale Adv. 2 (9) (2020) 3734–3763.

15. X. Lu, S. Gao, H. Lin, L. Yu, Y. Han, P. Zhu, W. Bao, H. Yao, Y. Chen, J. Shi, Bioinspired Copper Single-Atom Catalysts for Tumor Parallel Catalytic Therapy, Adv. Mater. 32 (2020) 2002246.

16. C. Zhang, W. Bu, D. Ni, S. Zhang, Q. Li, Z. Yao, J. Zhang, H. Yao, Z. Wang, J. Shi, Synthesis of Iron Nanometallic Glasses and Their Application in Cancer Therapy by a Localized Fenton Reaction, Angewandte Chemie (International ed. in English), 55 (2016) 2101–2106.

17. C. Liu, D. Wang, S. Zhang, Y. Cheng, F. Yang, Y. Xing, T. Xu, H. Dong, X. Zhang, Biodegradable Biomimic Copper/Manganese Silicate Nanospheres forChemodynamic/Photodynamic Synergistic Therapy with Simultaneous Glutathione Depletion and Hypoxia Relief, ACS Nano 13 (2019) 4267–4277.

18. T.P. Szatrowski, C.F. Nathan, Production of Large Amounts of Hydrogen Peroxide by Human Tumor Cells, Cancer Res. 51 (1991) 794.

19. A. Bansal, M.C. Simon, Glutathione metabolism in cancer progression and treatment resistance, J. Cell Biol. 217 (2018) 2291–2298.

20. M.P. Gamcsik, M.S. Kasibhatla, S.D. Teeter, O.M. Colvin, Glutathione levels in human tumors, Biomarkers 17 (2012) 671–691.

21. A.L. Ortega, S. Mena, J.M. Estrela, Glutathione in Cancer Cell Death, Cancers 3 (1) (2011) 1285–1310.

22. H.J. Forman, H. Zhang, A. Rinna, Glutathione: overview of its protective roles, measurement, and biosynthesis, Mol. Aspects Med. 30 (2009) 1–12.

23. S.C. Lu, Regulation of glutathione synthesis, Mol. Aspects Med. 30 (2009) 42– 59.

24. N.S. Kosower, E.M. Kosower, The glutathione status of cells, Int. Rev. Cytol. 54 (1978) 109–160.

25. J.M. Estrela, A. Ortega, E. Obrador, Glutathione in Cancer Biology and Therapy, Crit. Rev. Clin. Lab. Sci. 43 (2006) 143–181.

26. L. Kennedy, J.K. Sandhu, M.E. Harper, M. Cuperlovic-Culf, Role of Glutathione in Cancer: From Mechanisms to Therapies, Biomolecules 10 (2020).

27. Y. Ding, Y. Dai, M. Wu, L. Li, Glutathione-Mediated Nanomedicines for Cancer Diagnosis and Therapy, Chem. Eng. J. 426 (2021) 128880, https://doi.org/ 10.1016/j.cej.2021.128880.

28. Y. Liu, W. Zhen, L. Jin, S. Zhang, G. Sun, T. Zhang, X. Xu, S. Song, Y. Wang, J. Liu, H. Zhang, All-in-One Theranostic Nanoagent with Enhanced Reactive Oxygen Species Generation and Modulating Tumor Microenvironment Ability for Effective Tumor Eradication, ACS Nano 12 (2018) 4886–4893.

29. L.-S. Lin, J. Song, L. Song, K. Ke, Y. Liu, Z. Zhou, Z. Shen, J. Li, Z. Yang, W. Tang, G. Niu, H.-H. Yang, X. Chen, Simultaneous Fenton-like Ion Delivery and Glutathione Depletion by MnO2-Based Nanoagent to Enhance Chemodynamic Therapy, Angew. Chem. Int. Ed. 57 (2018) 4902–4906.

30. R. Franco, J.A. Cidlowski, Apoptosis and glutathione: beyond an antioxidant, Cell Death Differ. 16 (10) (2009) 1303–1314.

31. M. Cox, D. Nelson, Lehninger Principles of Biochemistry, 2000.

32. K.P. Bhabak, G. Mugesh, Functional Mimics of Glutathione Peroxidase: Bioinspired Synthetic Antioxidants, Acc. Chem. Res. 43 (11) (2010) 1408–1419.

33. J. Liu, M. Wu, Y. Pan, Y. Duan, Z. Dong, Y. Chao, Z. Liu, B. Liu, Biodegradable Nanoscale Coordination Polymers for Targeted Tumor Combination Therapy with Oxidative Stress Amplification, Adv. Funct. Mater. 30 (2020) 1908865.

34. S.-Y. Yin, G. Song, Y. Yang, Y. Zhao, P. Wang, L.-M. Zhu, X. Yin, X.-B. Zhang, Persistent Regulation of Tumor Microenvironment via Circulating Catalysis of MnFe2O4@Metal–Organic Frameworks for Enhanced Photodynamic Therapy, Adv. Funct. Mater. 29 (2019) 1901417.

35. B. Ma, S. Wang, F. Liu, S. Zhang, J. Duan, Z. Li, Y. Kong, Y. Sang, H. Liu, W. Bu, L. Li, Self-Assembled Copper-Amino Acid Nanoparticles for in Situ Glutathione "AND" H2O2 Sequentially Triggered Chemodynamic Therapy, J. Am. Chem. Soc. 141 (2019) 849–857.

36. M. Chang, M. Wang, M. Wang, M. Shu, B. Ding, C. Li, M. Pang, S. Cui, Z. Hou, J. Lin, A Multifunctional Cascade Bioreactor Based on Hollow-Structured Cu2MoS4 for Synergetic Cancer Chemo-Dynamic Therapy/Starvation Therapy/Phototherapy/Immunotherapy with Remarkably Enhanced Efficacy, Adv. Mater. 31 (2019) 1905271.

37. E. Ju, K. Dong, Z. Chen, Z. Liu, C. Liu, Y. Huang, Z. Wang, F. Pu, J. Ren, X. Qu, Copper(II)–Graphitic Carbon Nitride Triggered Synergy: Improved ROS Generation and Reduced Glutathione Levels for Enhanced Photodynamic Therapy, Angew. Chem. Int. Ed. 55 (2016) 11467–11471.

38. B. Ding, P. Zheng, P.a. Ma, J. Lin, Manganese Oxide Nanomaterials: Synthesis, Properties, and Theranostic Applications, Advanced Materials, 32 (2020) 1905823.

39. G. Liu, J. Zhu, H. Guo, A. Sun, P. Chen, L. Xi, W. Huang, X. Song, X. Dong, Mo2C- Derived Polyoxometalate for NIR-II Photoacoustic Imaging-Guided Chemodynamic/Photothermal Synergistic, Therapy 58 (2019) 18641–18646.

40. J.J. Pignatello, E. Oliveros, A. MacKay, Advanced Oxidation Processes for Organic Contaminant Destruction Based on the Fenton Reaction and Related Chemistry, Critical Rev. Environm. Sci. Technol. 36 (2006) 1–84.

41. J. He, X. Yang, B. Men, D. Wang, Interfacial mechanisms of heterogeneous Fenton reactions catalyzed by iron-based materials: A review, J. Environ. Sci. 39 (2016) 97–109.

42. Å. Björkbacka, M. Yang, C. Gasparrini, C. Leygraf, M. Jonsson, Kinetics and mechanisms of reactions between H2O2 and copper and copper oxides, Dalton Trans. 44 (2015) 16045–16051.

43. H. Wang, Z. Zhang, H. Yin, Y. Wu, Synthesis of Cu2(OH)3Cl as facile and effective Fenton catalysts for mineralizing aromatic contaminants: Combination of r-Cu-ligand and self-redox property, Appl. Catal. A 614 (2021) 118055.

44. E. Ember, S. Rothbart, R. Puchta, R. van Eldik, Metal ion-catalyzed oxidative degradation of Orange II by H2O2 High catalytic activity of simple manganese salts, New J. Chem. 33 (2009) 34–49.

45. Y. Sun, P. Tian, D. Ding, Z. Yang, W. Wang, H. Xin, J. Xu, Y.-F. Han, Revealing the active species of Cu-based catalysts for heterogeneous Fenton reaction, Appl. Catal. B 258 (2019) 117985.

46. C.M. Lousada, A.J. Johansson, T. Brinck, M. Jonsson, Mechanism of H2O2 Decomposition on Transition Metal Oxide Surfaces, J. Phys. Chem. C 116 (17) (2012) 9533–9543.

47. J.A. Cook, D. Gius, D.A. Wink, M.C. Krishna, A. Russo, J.B. Mitchell, Oxidative stress, redox, and the tumor microenvironment, Seminars Rad. Oncol. 14 (3) (2004) 259–266.

48. D. Li, M. Hua, K. Fang, R. Liang, BSA directed-synthesis of biocompatible Fe3O4 nanoparticles for dual-modal T1 and T2 MR imaging in vivo, Anal. Methods 9 (21) (2017) 3099–3104.

49. C. Hai, S. Li, Y. Zhou, J. Zeng, X. Ren, X. Li, Roles of ethylene glycol solvent and polymers in preparing uniformly distributed MgO nanoparticles, J. Asian Ceram. Soc. 5 (2) (2017) 176–182.

50. Y. Fu, Q. Chen, M. He, Y. Wan, X. Sun, H. Xia, X. Wang, Copper Ferrite-Graphene Hybrid: A Multifunctional Heteroarchitecture for Photocatalysis and Energy Storage, Ind. Eng. Chem. Res. 51 (36) (2012) 11700–11709.

51. M. Zhu, D. Meng, C. Wang, G. Diao, Facile Fabrication of Hierarchically Porous CuFe2O4 Nanospheres with Enhanced Capacitance Property, ACS Appl. Mater. Interfaces 5 (13) (2013) 6030–6037.

52. I.-M. Tang, N. Krishnamra, N. Charoenphandhu, R. Hoonsawat, W.J.N.R.L. Pon- On, Biomagnetic of apatite-coated cobalt ferrite: a core–shell particle for protein adsorption and pH-controlled release, 6 (2011) 19.

53. S.-H. Rhee, J.D. Lee, J. Tanaka, Nucleation of Hydroxyapatite Crystal through Chemical Interaction with Collagen, 83 (2000) 2890–2892.

54. J. Hueso, J. Espinós, A. Caballero, J. Cotrino, A.J.C. González-Elipe, XPS investigation of the reaction of carbon with NO, O2, N2 and H2O plasmas, 45 (2007) 89–96.

55. S.S. Maluf, P.A.P. Nascente, E.M. Assaf, CuO and CuO–ZnO catalysts supported on CeO2 and CeO2–LaO3 for low temperature water–gas shift reaction, Fuel Process. Technol. 91 (11) (2010) 1438–1445.

56. E. Cano, C.L. Torres, J.M. Bastidas, An XPS study of copper corrosion originated by formic acid vapour at 40% and 80% relative humidity, Mater. Corros. 52 (2001) 667–676.

57. K. Yuan, D. Lützenkirchen-Hecht, L. Li, L. Shuai, Y. Li, R. Cao, M. Qiu, X. Zhuang, M.K.H. Leung, Y. Chen, U. Scherf, Boosting Oxygen Reduction of Single Iron Active Sites via Geometric and Electronic Engineering: Nitrogen and Phosphorus Dual Coordination, J. Am. Chem. Soc. 142 (2020) 2404–2412.

58. J. Yang, X. Wang, B. Li, L. Ma, L. Shi, Y. Xiong, H. Xu, Novel Iron/Cobalt- Containing Polypyrrole Hydrogel-Derived Trifunctional Electrocatalyst for Self-Powered Overall Water Splitting, Adv. Funct. Mater. 27 (2017) 1606497.

59. X. Meng, D. Li, L. Chen, H. He, Q. Wang, C. Hong, J. He, X. Gao, Y. Yang, B. Jiang, G. Nie, X. Yan, L. Gao, K. Fan, High-Performance Self-Cascade Pyrite Nanozymes for Apoptosis-Ferroptosis Synergistic Tumor Therapy, ACS Nano 15 (3) (2021) 5735–5751.

60. J. Shan, K. Yang, W. Xiu, Q. Qiu, S. Dai, L. Yuwen, L. Weng, Z. Teng, L. Wang, Cu2MoS4 Nanozyme with NIR-II Light Enhanced Catalytic Activity for Efficient Eradication of Multidrug-Resistant Bacteria, Small 16 (2020) 2001099.

61. D. Wang, H. Wu, C. Wang, L. Gu, H. Chen, D. Jana, L. Feng, J. Liu, X. Wang, P. Xu,

62. Z. Guo, Q. Chen, Y. Zhao, Self-Assembled Single-Site Nanozyme for Tumor- Specific Amplified Cascade Enzymatic Therapy, Angew. Chem. Int. Ed. 60 (2021) 3001–3007.

63. E. Brillas, M.A. Baños, S. Camps, C. Arias, P.-L. Cabot, J.A. Garrido, R.M. Rodríguez, Catalytic effect of Fe2+, Cu2+ and UVA light on the electrochemical degradation of nitrobenzene using an oxygen-diffusion cathode, New J. Chem. 28 (2004) 314–322.

64. T. Soltani, B.-K. Lee, Enhanced formation of sulfate radicals by metal-doped BiFeO3 under visible light for improving photo-Fenton catalytic degradation of 2-chlorophenol, Chem. Eng. J. 313 (2017) 1258–1268.

65. H. Speisky, M. Gómez, F. Burgos-Bravo, C. López-Alarcón, C. Jullian, C. Olea- Azar, M.E. Aliaga, Generation of superoxide radicals by copper–glutathione complexes: Redox-consequences associated with their interaction with reduced glutathione, Bioorg. Med. Chem. 17 (2009) 1803–1810.

66. M.R. Ciriolo, A. Desideri, M. Paci, G. Rotilio, Reconstitution of Cu, Zn-superoxide dismutase by the Cu(I).glutathione complex, J. Biol. Chem. 265 (1990) 11030– 11034.

67. J. Xu, R. Shi, G. Chen, S. Dong, P. Yang, Z. Zhang, N. Niu, S. Gai, F. He, Y. Fu, J. Lin, All-in-One Theranostic Nanomedicine with Ultrabright Second Near-Infrared Emission for Tumor-Modulated Bioimaging and Chemodynamic/ Photodynamic Therapy, ACS Nano 14 (2020) 9613–9625.

68. L. Flohé, The fairytale of the GSSG/GSH redox potential, Biochimica et Biophysica Acta (BBA), - General Subjects 1830 (2013) 3139–3142.

69. M. Smeyne, R.J. Smeyne, Glutathione metabolism and Parkinson's disease, Free Radical Biol. Med. 62 (2013) 13–25.

70. A. Meister, Glutathione metabolism and its selective modification, J. Biol. Chem. 263 (1988) 17205–17208.

71. T.J. van 't Erve, B.A. Wagner, K.K. Ryckman, T.J. Raife, G.R. Buettner, The concentration of glutathione in human erythrocytes is a heritable trait, Free Radical Biol. Med. 65 (2013) 742–749.

72. F. Bottino, M. Lucignani, A. Napolitano, F. Dellepiane, E. Visconti, M.C. Rossi Espagnet, L. Pasquini, In Vivo Brain GSH MRS Methods and Clinical Applications, Antioxidants 10 (2021).

73. C.F. Wells, M.A. Salam, Hydrolysis of Ferrous Ions : a Kinetic Method for the Determination of the Fe(II) Species, Nature 205 (1965) 690–692.

74. X. Shen, Z. Wang, X. Gao, Y. Zhao, Density Functional Theory-Based Method to Predict the Activities of Nanomaterials as Peroxidase Mimics, ACS Catal. 10 (2020) 12657–12665.

75. L. Yu, Y. Chen, M. Wu, X. Cai, H. Yao, L. Zhang, H. Chen, J. Shi, Manganese Extraction Strategy Enables Tumor-Sensitive Biodegradability and Theranostics of Nanoparticles, J. Am. Chem. Soc. 138 (2016) 9881–9894. B. Yang, L. Ding, Y. Chen, J. Shi,

Augmenting Tumor-Starvation Therapy by Cancer Cell Autophagy Inhibition, Advanced science (Weinheim, Baden- Wurttemberg, Germany), 7 (2020) 1902847.

76. M.G. Vander Heiden, L.C. Cantley, C.B. Thompson, Understanding the Warburg Effect: The Metabolic Requirements of Cell Proliferation, Science 324 (5930) (2009) 1029–1033.

77. L.-H. Fu, C. Qi, J. Lin, P. Huang, Catalytic chemistry of glucose oxidase in cancer diagnosis and treatment, Chem. Soc. Rev. 47 (17) (2018) 6454–6472.

78. M.C. Ortega-Liebana, J.L. Hueso, R. Arenal, J. Santamaria, Titania-coated gold nanorods with expanded photocatalytic response Enzyme-like glucose oxidation under near-infrared illumination, Nanoscale 9 (5) (2017) 1787– 1792.

79. Nitrogen-doped luminescent carbon nanodots for optimal photo-generation of hydroxyl radicals and visible-light expanded photo-catalysis, Diam. Relat. Mater. 65 (2016) 176–182.

80. M. Sancho-Albero, N. Navascués, G. Mendoza, V. Sebastián, M. Arruebo, P. Martín-Duque, J. Santamaría, Exosome origin determines cell targeting and the transfer of therapeutic nanoparticles towards target cells, J. Nanobiotechnol. 17 (2019) 16.

81. E. Rogatsky, H. Jayatillake, G. Goswami, V. Tomuta, D. Stein, Sensitive LC MS quantitative analysis of carbohydrates by Cs+ attachment, J. Am. Soc. Mass Spectrom. 16 (2005) 1805–1811.

Supplementary information – Chapter 1

Adapted from:

Glutathione-Triggered catalytic response of Copper-Iron mixed oxide Nanoparticles. Leveraging tumor microenvironment conditions for chemodynamic therapy

Javier Bonet-Aleta [a,b,c,1], Maria Sancho-Albero [a,b,c,d,1], Javier Calzada-Funes [a,b,c], Silvia Irusta [a,b,c], Pilar Martin-Duque [b,e,f,g], Jose L. Hueso [a,b,c,e,⇑], Jesus Santamaria [a,b,c,e,⇑]

[a] *Instituto de Nanociencia y Materiales de Aragon (INMA) CSIC-Universidad de Zaragoza Campus Rio Ebro, Edificio I+D, C/ Poeta Mariano Esquillor, s/n, 50018 Zaragoza, Spain*

[b] *Networking Res. Center in Biomaterials, Bioengineering and Nanomedicine (CIBER-BBN), Madrid, Spain. Instituto de Salud Carlos III, 28029 Madrid, Spain*

[c] *Department of Chemical and Environmental Engineering, University of Zaragoza, Campus Rio Ebro, C/María de Luna, 3, 50018 Zaragoza, Spain*

[d] *Department of Molecular Biochemistry and Pharmacology, Istituto di Ricerche Farmacologiche Mario Negri IRCCS, 20156 Milan, Italy*

[e] *Instituto Aragonés de Ciencias de la Salud (IACS)/IIS Aragón, Avenida San Juan Bosco, 13, 50009 Zaragoza, Spain*

[f] *Fundación Araid. Av. de Ranillas 1-D, planta 2ª, oficina B, 50018 Zaragoza, Spain*

[g] *Present Address: Department of Surgery, University of Zaragoza Medical School; University of Zaragoza, Zaragoza, Spain*

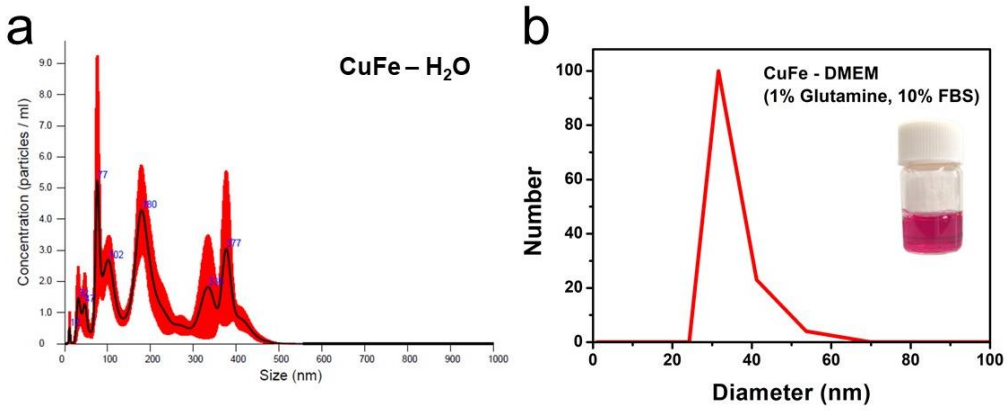

Figure S1. *CuFe size distribution in (a) H_2O and (b) DMEM (1% Glutamine, 10% FBS).*

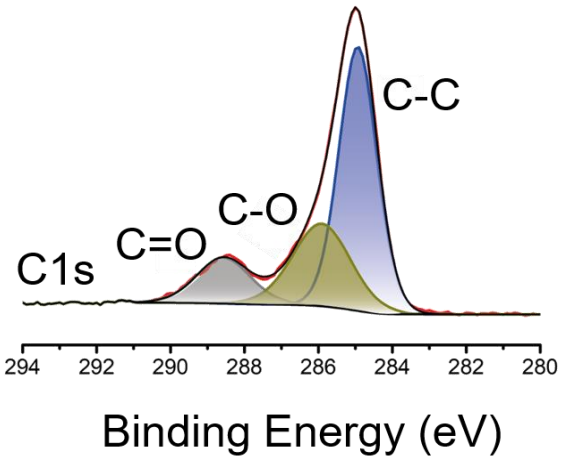

Figure S2. *CuFe XPS spectra at C1s region.*

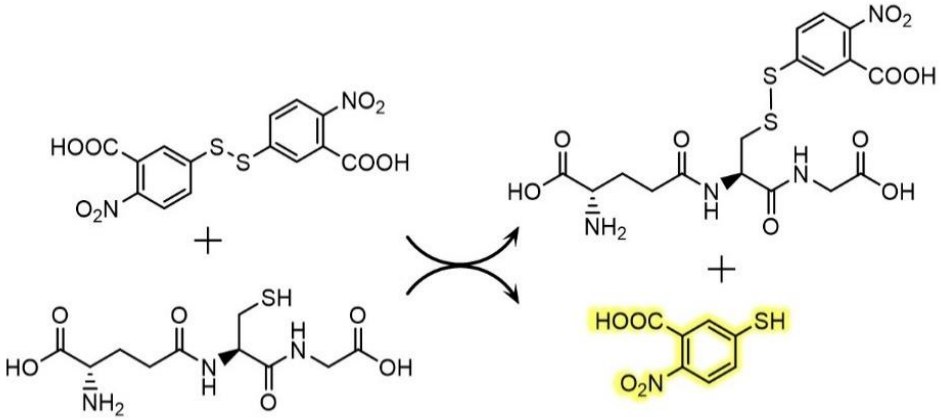

Figure S3. *Reaction of GSH with DTNB to generate quantifiable TNB^{2-} product, highlighted in yellow color.*

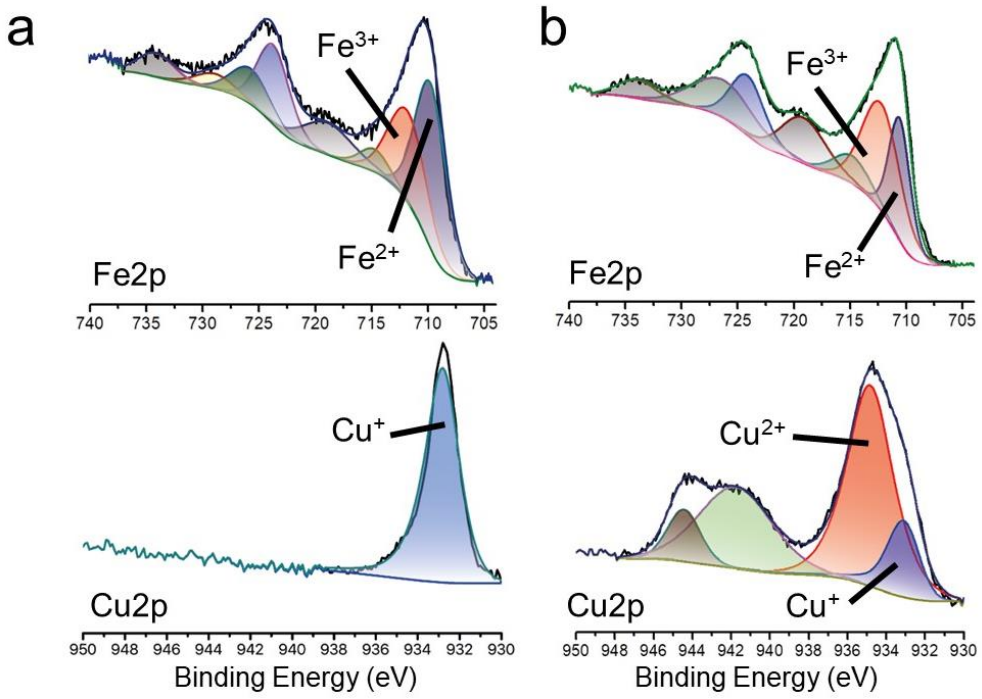

Figure S4. *X-ray Photoemission spectra corresponding to the Fe2p and Cu 2p regions of the CuFe catalyst: (a) after and (b) before reaction with GSH.*

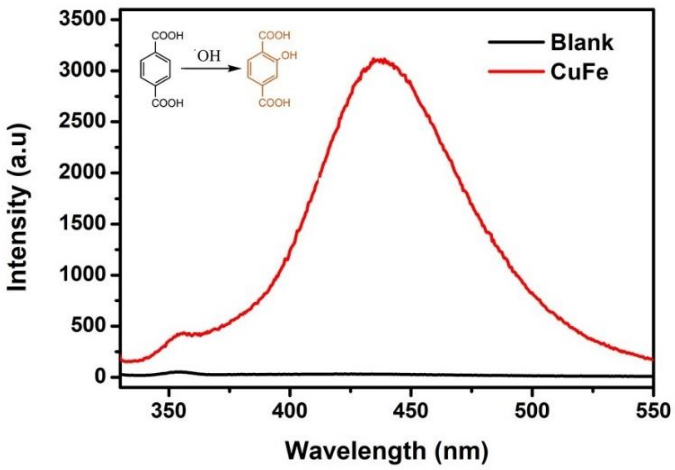

Figure S5. *Detection of hydroxyl radicals using disodium terephthalate (NaTA). Fluorescence spectra of the reaction product (2-hydroxy disodium terephthalate) validating the generation of •OH radicals. Reaction conditions: [CuFe] = 0.1 mg·mL^{-1}, [NaTA]$_0$ = 5 mM, [GSH]$_0$ = 5 mM, [H_2O_2] = 1 mM. pH was fixed at 4.5 using AcONa/AcOH buffer. H_2O_2 was added into the system after 25 minutes of CuFe+GSH reaction. The reaction was quenched after 40 minutes.*

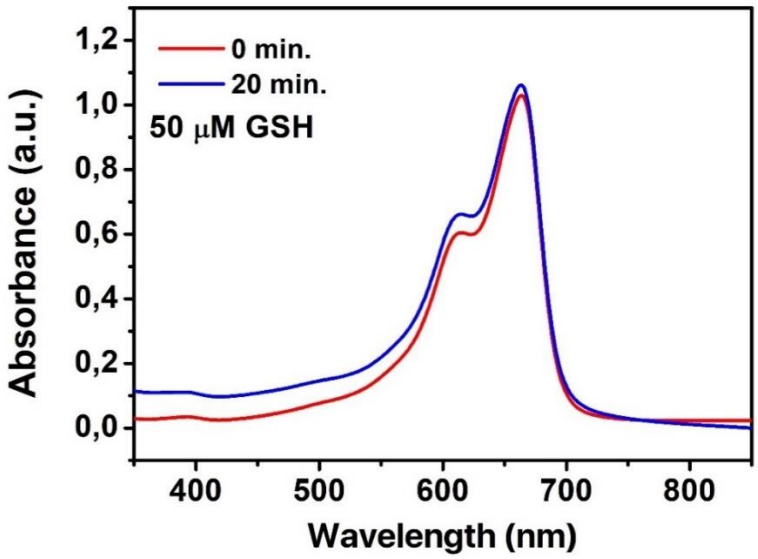

Figure S6. *UV-vis spectra of Methylene Blue with after 1 mM H_2O_2 addition in presence of CuFe and 50 μM GSH.*

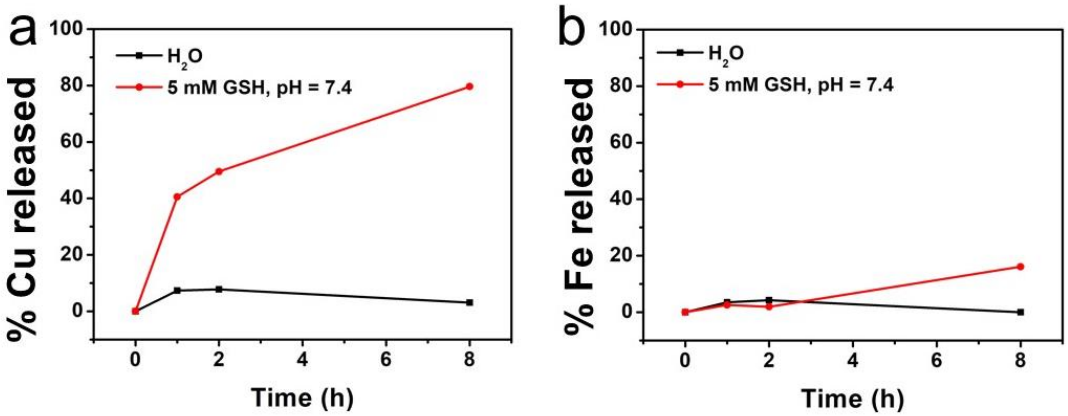

Figure S7. *Metal release percentages in the CuFe NPs either in the absence (black squares) or in the presence of GSH (red circles): (a) Cu % and (b) Fe %.*

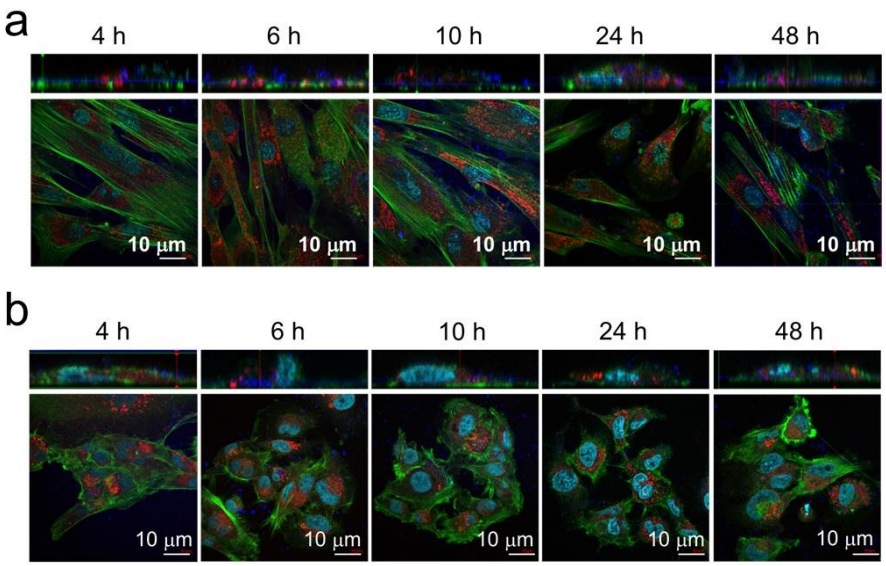

Figure S8. *Validation of the internalization strategy of the CuFe NPs by in vitro confocal trafficking study of CuFe via the endosomal pathway. Cross and top view images of (a) hpMSC incubated with CuFe during 4, 6, 10, 24 and 48 h; (b) U251-MG incubated with CuFe during 4, 6, 10, 24 and 48 h. Actin is shown in green, nuclei in cyan, CuFe in blue and CD63 positive vesicles in red).*

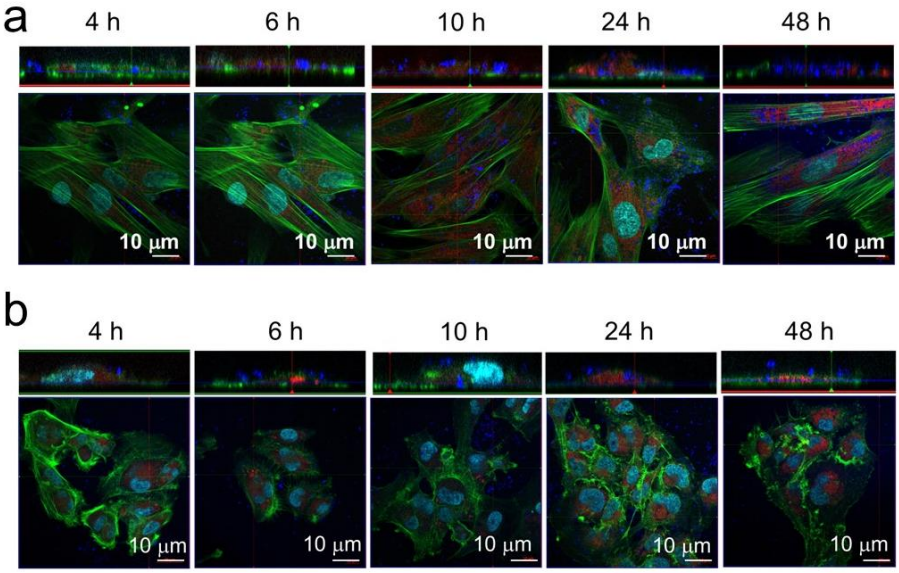

Figure S9. *Cross and top-view confocal microscopy selected images to illustrate the localization of the CuFe nanoparticles in lysosomes at different interval times: (a) hpMSC cells; (b) U251-MG cells (actin is shown in green, nuclei in cyan, CuFe in blue and lysosomes in red).*

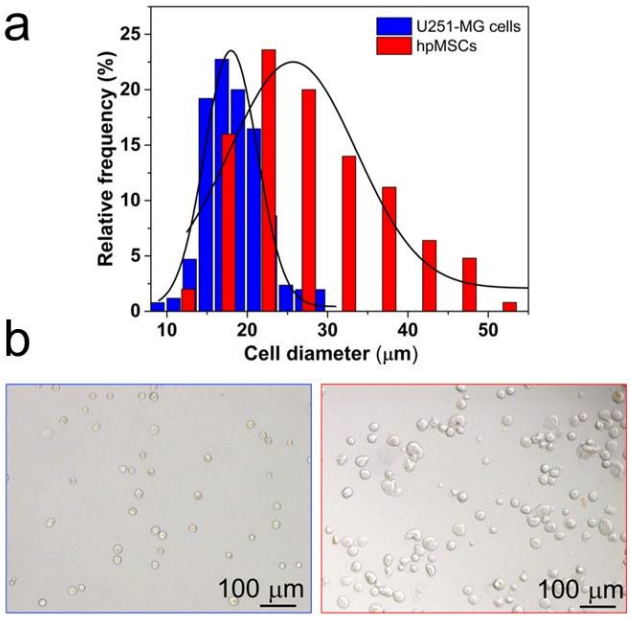

Figure S10. *Determination of cell diameter distribution of U251-MG and hpMSC cells: (a) Diameter distribution histogram of U251-MG (blue) and hpMSCs (red) retrieved from optical microscopy images; (b) Optical microscopy image corresponding to U251-MG cells (left) and hpMSCs (right) evidencing the larger mean diameters of stem cells. Assuming 3-dimensional spherical shapes for both cells, these diameters were used to establish the average volume corresponding to each cell type. (14.4 ± 4.6 mm and 9.2 ± 1.8 mm for hpMSCs and U251-MG cells, respectively), hpMSCs presented a volume of $1.2 \cdot 10^{-11}$ L whereas U251-MG of $3.3 \cdot 10^{-12}$ L. Number of visualization events by optical microscopy (n= 250 cells).*

Table S1. *Elemental composition of catalyst surface analysed by XPS.*

Binding energy (eV)				
Cu 2p	Fe 2p	O 1s	N 1s	C 1S
934.7	710.9	530.5	400.0	285.0
9.05%	11.16%	35.99%	2.54%	41.26%

Table S2. *XPS quantification of the different Fe and Cu species present on the catalyst surface.*

Fe 2+		Fe 3+	
2p3/2	S.O	2p3/2	S.O
710.6	714.0	712.3	719.2
37%	-	63%	-
Cu $^{0/+}$		Cu $^{2+}$	
2p3/2	2p3/2	S.O.1	S.O.2
933.1	934.8	941.7	944.4
12%	88%	-	-

Table S3. *XPS quantification of the different Fe and Cu species present on the catalyst surface after reaction with GSH (37°C, reaction time: 1 hour, [GSH]0 = 5 mM)*

Fe 2+		Fe 3+	
2p3/2	S.O	2p3/2	S.O
708.74	714.8	711.06	719.2
49.61%	-	50.39%	-
Cu 0/+		Cu 2+	
2p3/2	2p3/2	S.O.1	S.O.2
932.8	-	-	-
100%	-	-	-

Table S4. *Cell cycle distribution of control (untreated) and treated (CuFe NPs at 0.2 mg mL^{-1} during 24 h) hpMSCs and U251-MG*

		Cell %			
		hpMSCs		U251-MG	
		Control	0.2 mg mL-1 24 h	Control	0.2 mg mL-1 24 h
Cell cycle phase	G0-G1	82.3	55.5	82.9	40.2
	S	8.7	7.2	1.8	30.6
	G2-M	8.9	37.2	15.2	29.1

Table S5. *Percentage of cells in early or late apoptosis and necrosis after the treatment with CuFe during 24 h at 0.2 mg·mL^{-1} compared to untreated cells (control).*

	Cell %					
	hpMSCs			U251-MG		
	Control	0.2 mg mL^{-1} 6 h	0.2 mg mL^{-1} 24 h	Control	0.2 mg mL^{-1} 6 h	0.2 mg mL^{-1} 24 h
Live	91.1	65.5	38.1	89.8	55.7	21.5
Early apoptosis	2.4	7.04	12.8	2.8	8.2	2.6
Late apoptosis	5.9	16.7	46.5	4.5	34.3	72.6
Necrosis	0.6	1.3	2.7	1.9	1.9	3.2

Table S6. *Glucose standards composition employed to analyze glucose consumption with time.*

[Glucose] (ppm)	V Glucose, 100 ppm (µL)	VLactose, 1000ppm (µL)	V ACN:H_2O (1:1) (µL)
2.5	25	25	950
5.0	50	25	925
10	100	25	875
15	150	25	825
20	200	25	775
35	350	25	625

Table S7. *GSH standards composition employed to analyze GSH-catalytic experiments.*

[GSH] (ppm)	VGSH 100 ppm (µL)	VDTNB 1 mM (µL)	VHCO_3^- 0.2M (µL)	VACN:H_2O (1:1) (µL)
2.5	25	100	75	800
5.0	50	100	75	775
7.5	75	100	75	750
10	100	100	75	725
15	150	100	75	675
20	200	100	75	625
25	250	100	75	575
35	350	100	75	475
50	500	100	75	325

Table S8. *GSH standards composition employed to analyze in vitro GSH levels and catalytic consumption.*

[GSH] (ppm)	VGSH, TCA (µL)	[GSH]TCA (ppm)	VDTNB, 2.5 mM (µL)	VTRIS 0.01M (µL)
0.25	50	5	20	930
0.50	50	10	20	930
0.75	50	15	20	930
1.00	50	20	20	930
2.00	50	40	20	930
5,00	50	100	20	930

Chapter 2 |

Avoiding catalyst deactivation

Summary – Chapter 2

Starving therapy generally involves the use of a catalyst to deplete intracellular glucose levels, aiming to disrupt ATP generation. This strategy draws inspiration from the principles of the Warburg effect, a metabolic alteration observed in cancer cells characterized by increased glucose uptake and utilization. Ultrasmall Au nanoparticles have been explored as a catalyst for this purpose due to their glucose oxidase-like behavior (**Figure Summary-1a**). However, biological environments present challenging conditions for noble metal catalysts. Numerous biomolecules can interact with the nanoparticles to varying extents. Among these biomolecules, GSH is one of the most abundant molecules in the cytosol and can bind to the surface of Au nanoparticles through its thiol group, inhibiting their glucose-oxidase activity.

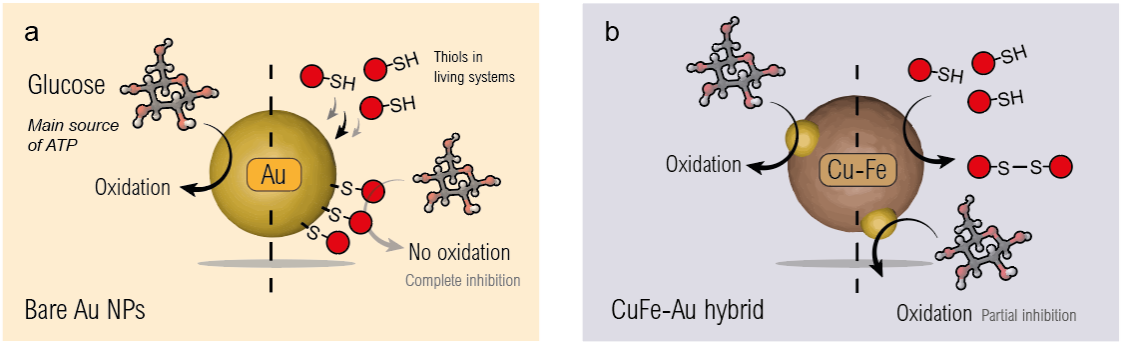

Figure Summary-1. *Different scenarios encountered by Au-based nanocatalysts in the absence/presence of GSH. (a) Naked Au NPs exhibit a well-known glucose oxidase-like activity but undergo deactivation in the presence of thiolated molecules, which strongly bind to their surface. (b) Combining ultrasmall Au NPs with GSH-depleting nanoparticles, may help to prevent catalyst deactivation by inducing the oxidation of GSH facilitated by the catalytic action of the Cu-Fe support.*

In this chapter, we developed a novel platform by assembling ultrasmall Au NPs onto Cu-Fe nanoparticles. The synthesis of Au NPs followed a methodology based on the use of the reductive ligand THPC, previously developed by our research group. Our strategy involved functionalizing Cu-Fe nanoparticles with dimercaptosuccinic acid (DMSA) to enable the deposition and binding

of gold through a covalent bond with DMSA. This innovative platform demonstrated the ability to effectively reduce glucose levels under physiologically relevant conditions, such as a saline buffer with pH 7.4, even in the presence of 5 mM GSH, without experiencing complete deactivation (**Figure Summary-1b**).

To highlight the influence of the support, we also assembled the same Au NPs onto SiO_2 nanoparticles, which lack catalytic activity towards GSH oxidation. Notably, a concentration of 5 mM GSH in the reaction completely inhibited the catalytic activity of gold in this system. On the other hand, the presence of gold did not affect the catalytic activity of Cu-Fe towards GSH. We propose that the affinity of GSH for the Cu-Fe nanoparticle retarded the contamination of gold thereby allowing the catalytic oxidation of glucose to proceed.

Subsequently, we conducted toxicity evaluations of the particles using A549 cells. We selected A549 cells due to their previously reported reliance on glycolysis and GSH. The CuFe-Au nanohybrid exhibited toxicity towards A549 cells within the range of 0.0125-0.1 mg $Cu{\cdot}mL^{-1}$, while human fibroblasts CCD-32Sk appeared to remain viable. Understanding the inherent limitations of a catalyst is crucial for overcoming them. In this specific case, the combination of CuFe and Au enabled catalysis to occur in an unfavorable scenario.

This results obtained from this chapter were published in *Materials Today Chemistry 29 (2023) 101404.*

Adapted from:

Synergistic assembly of gold and copper-iron oxide nanocatalysts to promote the simultaneous depletion of glucose and glutathione

J. Bonet-Aleta [a, b, c], J.L. Hueso [a, b, c, *], L. Sanchez-Uriel [a, b, c], M. Encinas-Gimenez [a, b, c], S. Irusta [a, b, c], P. Martin-Duque [b, d, e, f], G. Martinez [a, b, c], J. Santamaria [a, b, c, **]

[a] *Instituto de Nanociencia y Materiales de Aragon (INMA) CSIC-Universidad de Zaragoza, Campus Rio Ebro, Edificio I+D, C/ Poeta Mariano Esquillor, S/n, 50018, Zaragoza, Spain*

[b] *Networking Res. Center in Biomaterials, Bioengineering and Nanomedicine (CIBER-BBN), Instituto de Salud Carlos III, Madrid, 28029, Spain*

[c] *Department of Chemical and Environmental Engineering, Campus Rio Ebro, University of Zaragoza, Campus Rio Ebro, C/Mariano Esquillor, s/n, Zaragoza, 50018, Spain*

[d] *Instituto de Investigacion Sanitaria (IIS) de Aragon, Avenida San Juan Bosco, 13, 50009, Zaragoza, Spain*

[e] *Fundacion Araid. Av. de Ranillas 1-D, 50018 Zaragoza, Spain*

[f] *Departamento de Cirugía, Facultad de Medicina, Universidad de Zaragoza, 50009 Zaragoza, Spain*

Graphical abstract

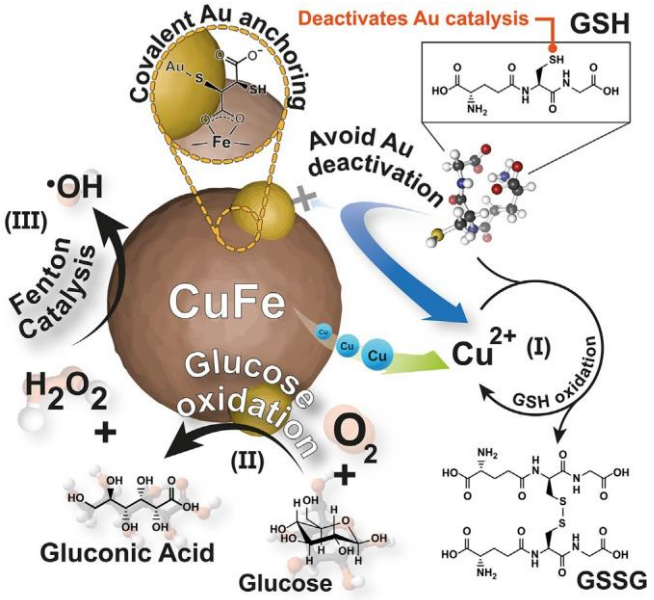

Abstract

Glucose and glutathione (GSH) are key biomolecules for the regulation and growth of tumor cells. The use of inorganic nanocatalysts in biomedicine to target and deplete such specific molecules represents a novel and promising strategy against cancer. In this work, we present a ternary assembled nanohybrid based on Au and CuFe2O4 with the capability to simultaneously deplete glucose and GSH and generate reactive oxidative species (ROS) in a cascade process. We describe an example of a synergistic heterogeneous nanoarchitecture able to maintain the glucose oxidase-like activity of Au while preventing its deactivation in the presence of GSH. Au sites remain active due to the rapid response of the CuFe co-catalyst to deplete GSH levels. This example of hybrid heterostructure represents an appealing alternative with dual-activity within the tumor microenvironment (TME) for potential anticancer therapy.

Introduction – Chapter 2

The development of inorganic nanocatalysts in biomedicine has irrupted as a promising alternative for multiple therapies such as antibacterial, anti-inflammatory, Alzheimer or brain disease and even tissue engineering or diagnostic imaging [1]. Cancer still represents the most challenging systemic disease faced by human mankind and the number of catalytic materials devoted to this endeavour has increased exponentially in the past few years [2]. In this context, the unique chemistry featuring the tumor microenvironment (TME) offer a powerful opportunity for engineered nanocatalysts to selectively induce cancer cell death by targeting key metabolites and biomolecules [3]. Moreover, the erratic and accelerated metabolism of tumor cells require an enormous and continuous energy supply, mainly in the form of glucose via aerobic glycolysis [4]. This is also known as Warburg effect and the principal consequence is a large glucose uptake by cancer cells. Thus, one of the most employed catalytic strategies consists in reducing glucose levels through its catalytic oxidation to cut off the ATP production-flux of the cancer cell [4,6]. Among the inorganic catalysts reported for glucose starvation therapy, freestanding and supported Au nanoparticles (Au NPs) represent the most active alternative to natural enzymes

with a glucose oxidase mimicking response [7-10]. While this catalytic activity is well established, the potential influence of sulphur-containing biomolecules present in the TME such as glutathione (GSH) [11,12] is typically overlooked. Sulphur strongly binds to the Au surface hence blocking and "poisoning" the active sites for glucose oxidation [13,14]. As a result, the potential use of Au NPs for starvation therapy becomes less effective.

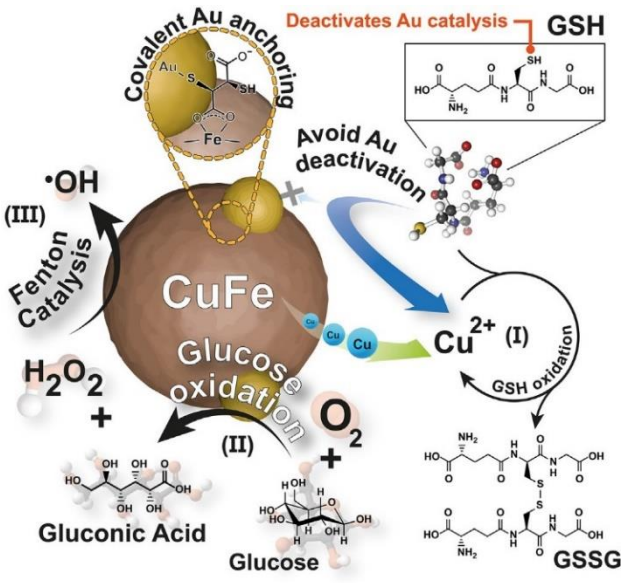

Figure 1. *Summary of the proposed catalytic reactions and mechanisms involved in the simultaneous depletion of glucose and GSH and the generation of hydroxyl radicals in the presence of the CuFe-Au nanohybrid linked via DMSA: SH group from GSH is responsible of deactivate Au nanoparticles and thus inhibiting their glucose oxidase-like activity. However, after deposition of Au on CuFe, the large affinity of GSH by Cu provokes their catalytic oxidation (step I) to avoid Au poisoning, which is then able to catalyze glucose oxidation (step II); Since H_2O_2 in one of the glucose oxidation by- products, CuFe nanoparticle can transform it into •OH in a reaction cascade (step III).*

Another interesting feature of the glucose oxidation process catalyzed by Au NPs is related with the generation of hydrogen (H_2O_2) as reaction by-product [10]. Most of the literature reports exploiting glucose depletion typically combine Au nanoparticles with transition metals to decompose the generated H_2O_2 into hydroxyl radicals (•OH) via Fenton-like catalysis in a cascade reaction process [7-9]. The generated •OH are highly-reactive species that can irreversibly modify key biomolecules such as lipids, proteins or nucleic acids leading to cell apoptosis [15]. Nevertheless, considering the previously mentioned issue regarding Au deactivation with GSH, this molecule represents a severe obstacle to achieve an effective starvation therapy. On the other hand, the catalytic targeting of GSH with the aid of transition metal catalysts is becoming a potential anticancer strategy itself [16]. GSH is a key antioxidant molecule

strongly involved in the regulation and damage prevention from Reactive Oxygen Species (ROS) generated in cancer cells [17]. Thus, the potential development of co-catalysts that can transform GSH into its dimeric GSSG form (Figure *1*) may represent an advantageous "two birds-one stone" scenario to prevent Au deactivation while enhancing oxidative stress due to the depletion of GSH levels. If terminal thiol groups from GSH evolve into -S-S- groups, the blockage of Au sites might be minimized. The aim of this work has been the design and development of a nanocatalytic hybrid platform combining Au NPs and copper-iron oxide (CuFe) NPs with specific response towards glucose and GSH, respectively. We intended to prevent the deactivation of Au under GSH levels typically found in the TME and provide a synergistic response towards the simultaneous depletion of both key biomolecules.

Results and discussion – Chapter 2

Synthesis, assembly and characterization of the CuFe-Au nanocatalyst. We have fabricated a CuFe oxide spinel with reported activity and selectivity towards GSH oxidation [19] and modified its surface with dimercaptosuccinic acid (DMSA) as linker to subsequently attach ultrasmall Au NPs through covalent bonding (

Figure **2**). We analyzed in previous works how GSH interacted with CuFe in a first step (*Figure 1*-i), and promoted the release of Cu^{2+} ions from the spinel network. These cations subsequently oxidized GSH into GSSG through homogeneous catalysis (*Figure 1*-ii). At this point, we hypothesized that this strong affinity between Cu and GSH [20] might prevent the excessive inactivation of Au sites induced by thiol groups from GSH during the glucose oxidation process (*Figure 1*-ii). In addition, we also demonstrated that the H_2O_2 generated as by-product during the glucose oxidation could be further trans- formed into •OH through a cascade reaction (***Figure 1***-iii). The synthesis of the ternary CuFe-Au nanocatalyst took place following a two-stage process (

***Figure* 2**). The first part consisted on the hydro- thermal preparation of the CuFe spinel oxide NPS using BSA as stabilizing agent [19] (

Figure* 2a-i*). Then, CuFe-BSA NPs were functionalized with DMSA [21] in a basic solution (Experimental section and Fig. S4).

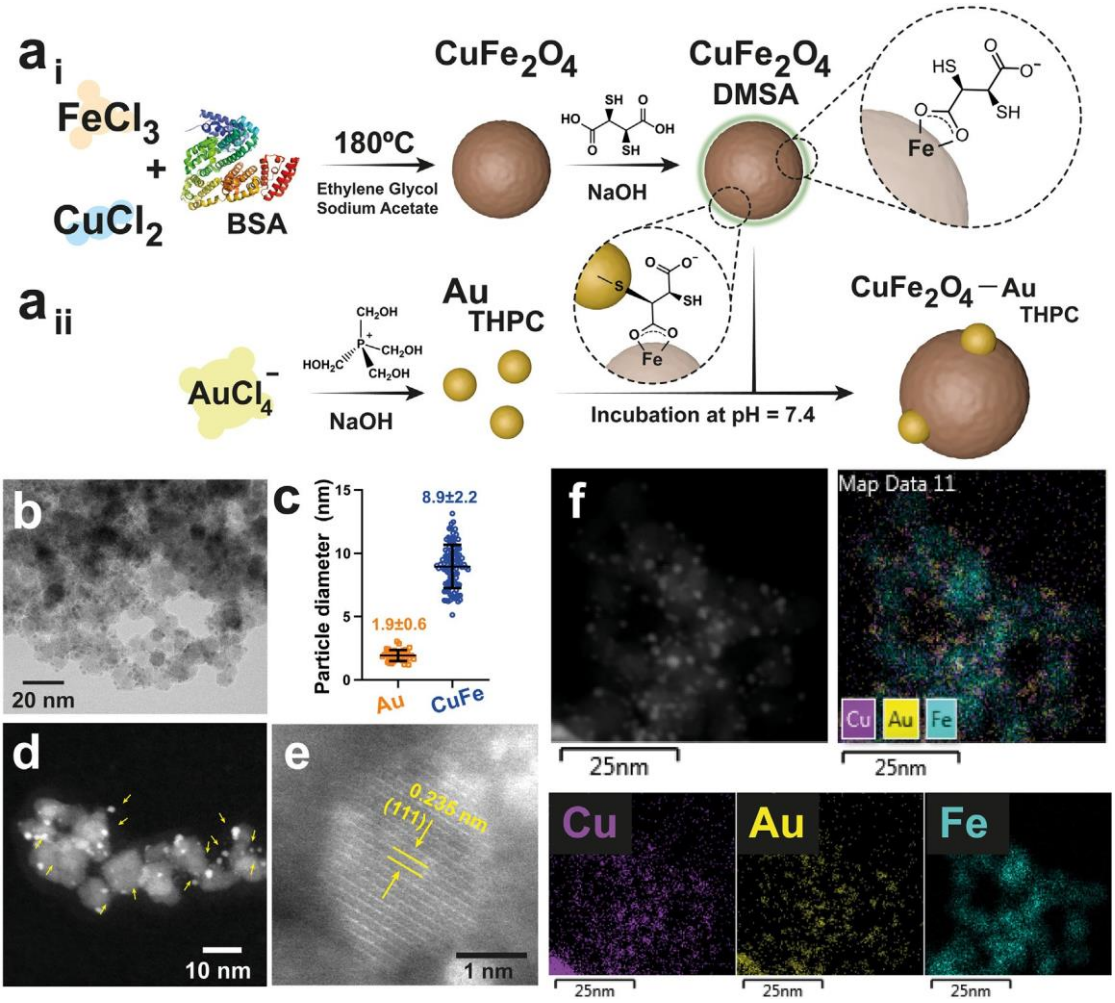

Figure 2. *Synthesis and electronic microscopy analysis of the CuFe-Au catalyst: (a) Scheme of the two-stage synthesis of the CuFe-Au nanohybrids: (a-i) Synthesis of the DMSA coated CuFe NPs using a hydrothermal assisted protocol in the presence of BSA, acting as template to induce particle growth at 180 ºC and subsequent ligand exchange with DMSA in basic; (a-ii) Generation of Au NPs using THPC as simultaneous reducing and stabilizing agent in the presence of NaOH and final assembly of CuFe and Au NPs via Au-S covalent bonding. (b) TEM image of the CuFe-Au NPs; (c) Particle size distribution histograms corresponding to the individual diameters of AuNPs and CuFe NPs after attachment (n = 50); (d-e) HAADF- STEM of CuFe-Au nanocatalyst where ultrasmall Au NPs are pin-pointed with yellow arrows and (e) HR-STEM image of a single Au nanoparticle deposited on CuFe, where an interplanar distance of 0.235 nm can be attributed to the (111) plane of cubic structure of metallic Au; (f) STEM-EDS mapping analysis of CuFe-Au nanoparticles: Top row: HAADF- STEM*

image and EDS mapping distribution of Cu, Au and Fe (merged); Bottom row: specific mapping distribution for Cu, Au and Fe respectively.

The ligand exchange and coating of CuFe-BSA NPs with DMSA took place through bonding between the carboxylic end groups and the Fe^{III} sites [21] of the spinel network (

Figure 2*a-i*). The second stage consisted in the synthesis of ultrasmall AuNPs using tetrakis-(hydroxymethyl)-phosphonium chloride (THPC) as reduction/stabilizing agent [10,18] (

Figure 2*a-ii*). Finally, both CuFe and Au NPs were assembled via covalent linking between the Se-H terminal groups from DMSA and the Au NPs (

Figure 2 and SI for further details). Transmission electron microscopy (TEM) and High Angle Annular Dark Field Scanning Transmission Electron Microscopy (HAADF-STEM) analysis of the CuFe-Au nanohybrids confirmed the successful assembly (

Figure 2*b* and d-f) with an average diameter of 8.9 ± 2.2 nm and 1.9 ± 0.6 nm, respectively (

Figure 2*c*). HR-STEM analysis of individual Au NPs confirmed the (111) crystalline plane of cubic Au (

Figure 2*e*). The presence of Au was also confirmed by STEM-Electron Dispersive X-ray Spectroscopy (EDS) (

Figure 2*f*). STEM-EDS analysis of the nanohybrid (Fig. S5) also revealed a Cu:Fe:Au ratio of 1.0:1.6:0.3, respectively. In the same analysis performed by MP-AES, we obtained a Cu:Fe:Au ratio of 1.0:1.5:0.1, respectively. The XRD analysis also confirmed that the crystalline structure of the $CuFe_2O_4$ spinel was preserved after Au deposition. No clear signal from the Au NPs could be discerned given their reduced size (Fig. S6). X-ray photoelectron spectroscopy (XPS) analysis of the CuFe-DMSA NPs before and after the assembly of Au NPs corroborated the increase of Au atomic percent on the surface of the hybrid (see Tables S1-S2). Furthermore, the binding energies (BEs) centered at 84.4 and 87.9 eV confirmed the metallic nature of the Au species associated to the $Au4f_{7/2}$ and $Au4f_{5/2}$ regions, respectively [22] (***Figure 3a***).

Two photoemission contributions at 85.2 and 88.6 eV were attributed to Audþ species probably in closer contact with the CuFe spinel [22] (***Figure 3a***). XPS analysis of the Fe2p region revealed the coexistence of both divalent and trivalent oxidation states (***Figure 3b***) with main contributions at 710.9 and 712.9 eV for Fe(II)$2p_{3/2}$ and Fe(III)$2p_{3/2}$, respectively [23]. Cu XPS spectra (***Figure 3c***) showed a clear contribution of Cu(II)$2p_{3/2}$ and Cu(I)$2p_{3/2}$ at BEs of 934.9 and 933.5 eV [24]. Moreover, the assembly of Au nanoparticles did not alter the oxidation state of Fe and Cu (see Tables S3-S4). The S2p region (***Figure 3d*** and Tables S3-S4) disclosed three main doublet at 161.0 and 161.6 eV, attributed to S binding to Fe and Cu [25], 162.3 and 163.1 eV attributable to Au-S binding [26,27] and unbounded thiol groups at 163.8 ($S2p_{3/2}$) and 164.9 eV ($S2p_{1/2}$), respectively [28]. Finally, a contribution from oxidized species could be identified at higher BEs [28]. FTIR analysis mostly revealed different contributions from DMSA and THPC present in the nanohybrids (see ***Figure 3e***). Two main contributions from DMSA (asymmetric/ symmetric contributions of C=O bond at 1560 and 1390 cm^{-1}) [29,30] and THPC (O-H stretching/bending/deformation at 3250, 1630 and 1360 cm^{-1}, respectively) [31] confirmed the presence of the organic linker and the stabilizing ligand of AuNPs. Raman spectroscopy of the $CuFe_2O_4$ NPs revealed the presence of contributions at low Raman shifts in the region between 200 and 400 cm^{1} that could be attributed to Fe and Cu oxides [32] (Fig. S7). The hybrid CuFe-Au also revealed additional contributions in the 594- 680 cm^{-1} region corresponding to Cu and Fe oxides with higher valence states. Additional Raman features appearing at 132 cm^{-1} can be attributed to a small presence of gold oxide (Au-O stretching/ bending), chloride (Au-Cl stretching) and/or sulfide (Au-S stretching) [33].

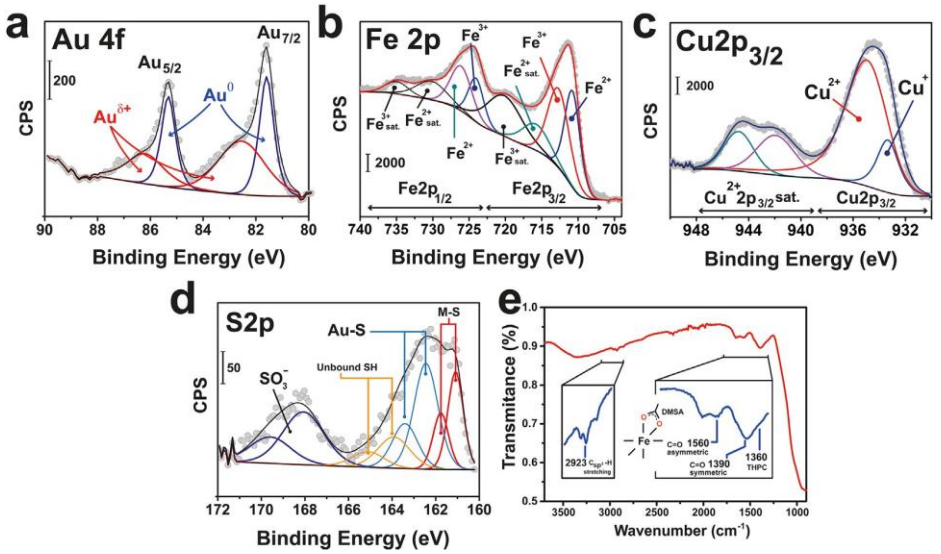

Figure 3. *Spectroscopic characterization of the CuFe-Au catalyst: (a) X-ray photoemission spectrum corresponding to the Au 4f region of CuFe-Au catalyst; (b) X-ray photoemission spectrum of the Fe2p region of the CuFe-Au catalyst accounting for the presence of divalent and trivalent Fe species; (c) X-ray photoemission spectrum of the Cu2p3/2 region accounting for the presence of Cu(II) and Cu(I) species in the CuFe-Au catalyst; (d) X-ray photoemission spectrum of the S2p region where the peaks detected at higher binding energies (i.e. 162.5 and 163.6 eV) are attributed to Au-S bond formation [26,27]; (e) Fourier Transformed Infrared spectroscopy (FT-IR) analysis of the CuFe-Au nanohybrid.*

Simultaneous conversion of GSH and glucose: synergistic influence of the CuFe NPs and comparison with inert SiO_2. Figure 4a shows the glucose conversion levels achieved by the Au NPs either in the presence or in absence of CuFe NPs and/or GSH with analogous reaction kinetics (Fig. S8). The glucose-oxidase mimicking activity of the Au NPs in the absence of GSH rendered glucose conversions close to 25% when deposited on inert SiO_2 NPs (see ***Figure 4a*** and Fig. S9-S10). This conversion rose up to ca. 50% glucose conversion after 90 min of reaction at pH 7.4 in saline buffer (Phosphate Buffer Saline, PBS) at physiological temperature (i.e. 37 ºC) with the CuFe-Au nanohybrid. These values are in agreement with those reported in the literature [7-10]. Interestingly, the enhanced catalytic conversion of the CuFe-Au NPs can be probably attributed to the capacity of Cu and Fe to trigger a cascade reaction to transform H_2O_2, generated as secondary by-product of the glucose oxidation, into $^{\bullet}OH$. This latter process (see ***Figure 1-iii***) would be favored via Fenton-like reaction [34] and would be contributing to the additional

oxidation of glucose observed in ***Figure 4a***. In order to demonstrate this cascade reaction, we performed a series of experiments using the colorimetric probe 3,3',5,5'- tetramethyl--benzidine (TMB) whose reaction with oxidizing species (i.e. OH) yields a colored probe that can be monitored by UV-vis spectroscopy (Fig. S11). A control experiment in the presence of 2 mM of H_2O_2 yielded an increase of the absorbance at 652 nm, due to the formation of the oxidized TMB species [10,12]. In the absence of H_2O_2, the enhancement of the signal could be only attributed to the oxidase-like capacity of the Au NPs, which can also transform TMB by themselves in the presence of dissolved O_2 [35]. However, in the presence of 5.5 mM of glucose, the absorbance at 652 nm was higher due to the progressive generation of H_2O_2 after catalyzing the glucose oxidation (Fig. S11).

Previous studies have demonstrated that GSH and other biomolecules containing -SH moieties [11] can induce the progressive deactivation of noble metals and the loss of their oxidase mimicking response [12-14]. In our case, the addition of GSH reduced the overall glucose conversion levels, regardless of the catalysts tested (***Figure 4a***). Nevertheless, while the activity of the Au-SiO_2 NPs decreased in the presence of GSH (only 3% conversion was achieved after 90 min, a 9-fold decrease, see ***Figure 4a***), the CuFe-Au NPs were still able to achieve 35% glucose conversion (i.e. 70% of its original conversion) despite the strong deactivation scenario induced by GSH. Moreover, these NPs were able to maintain the GSH depletion activity in comparison with the DMSA coated CuFe analogous NPs [19] (***Figure 4b***). Furthermore, ^{1}H NMR analysis of the catalytic GSH oxidation showed an increasing contribution at 3.2 ppm due to the generation of $Cu(SG)_2$ and GSSG species, both present in the homogeneous GSH oxidation [20] (***Figure 4c***). In summary, using CuFe NPs as co-catalyst of Au NPs delays their deactivation by GSH following the process illustrated in ***Figure 4d***. We hypothesize that both Au and CuFe NPs possess available active sites with strong affinity towards GSH. The preference of GSH to bind and with Cu sites [20] favors a delayed deactivation and poisoning of Au active sites that can continue the glucose conversion reaction in the presence of GSH and generate H_2O_2 for subsequent Fenton chemistry able to induce ROS generation. Likewise, the strong affinity of -SH group by Cu sites in the $CuFe_2O_4$ structure promotes its leaching following the reported mechanism in our previous work [20]. Once in solution, Cu^{2+} starts to catalyze oxidation of GSH to yield GSSG. We suggest that the

decrease of free -SH groups from GSH after its oxidation can prevent the complete deactivation of the Au NPs towards the glucose oxidation.

Finally, the interaction of CuFe-Au catalyst in a biological media was evaluated studying their cytotoxicity in A549 (lung cancer) and CCD-32Sk (human fibroblasts). A549 was the selected cancer cell line due to their known dependence on glycolysis [36] and GSH [37] metabolism. The viability of A549 cells decayed in the presence of CuFe-Au catalyst while fibroblast remained healthy at all the evaluated concentrations of catalysts (***Figure 4e***). We assume that the simultaneous depletion of both glucose and GSH have a direct impact on their survival and the high specificity towards the cancer cells corroborates the efficiency of the combined strategy targeting two key biomolecules for these cancer cells, simultaneously. Moreover, representative fluorescence confocal microscopy (***Figure 4f***, Fig. S12) images of A549 incubated with CuFe-Au NPs after 48 h demonstrated the presence of the catalyst within the cells to trigger the described catalytic reactions and also the presence of some non-internalized aggregates. All these data suggest CuFe-Au as a promising and selective catalyst for Chemodynamic-starvation therapy.

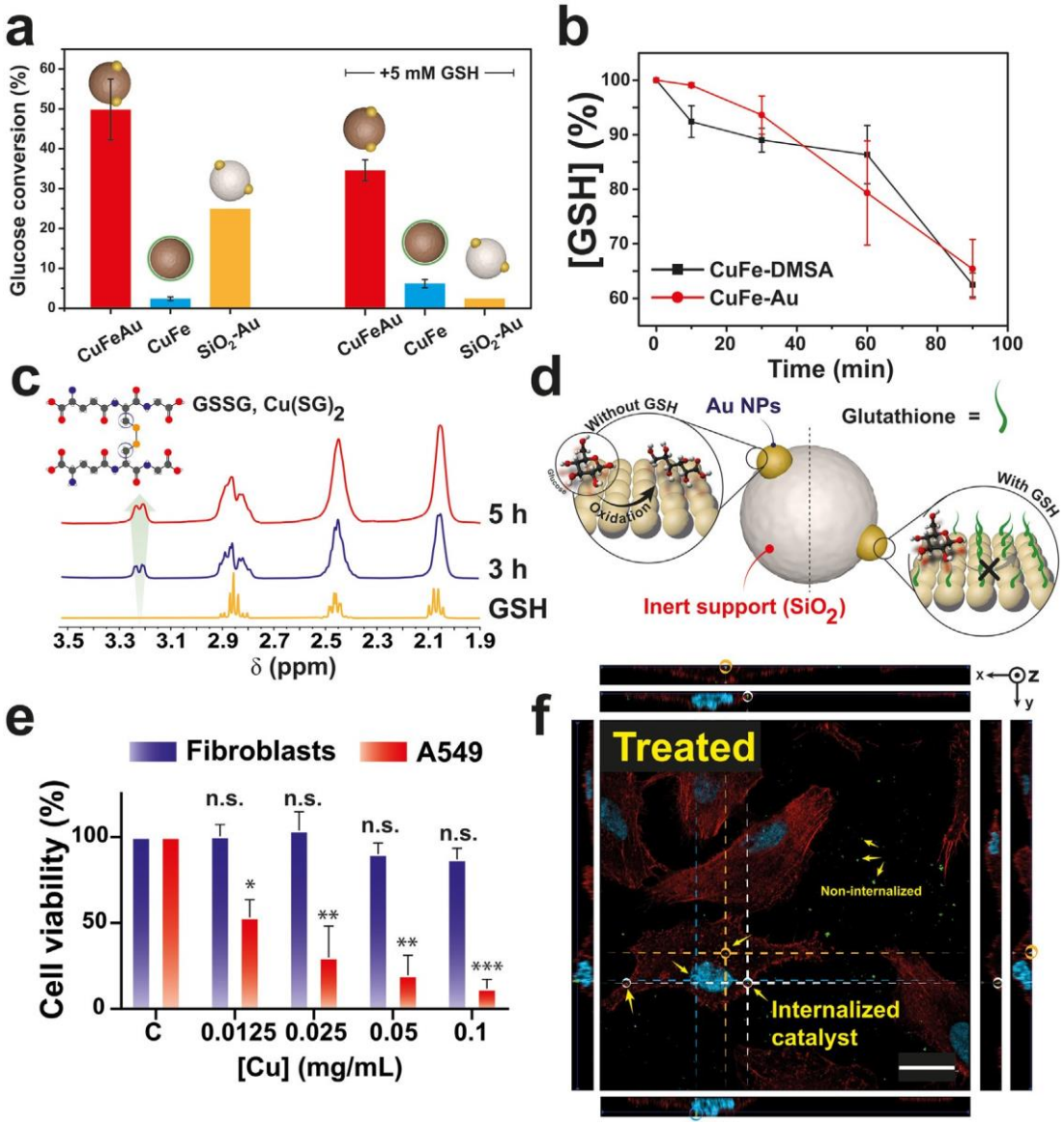

Figure 4. *Catalytic activity displayed by the DMSA-coated CuFe, CuFe-Au and SiO_2-Au nanocatalysts: (a) Glucose conversion in the presence and in the absence of GSH (5 mM) after 90 min; Reaction conditions: pH = 7.4, buffered PBS; $[Glucose]_0$ = 5.5 mM; $[GSH]_0$ = 5 mM; [Au] = 0.02 mg·mL^{-1}; (b) GSH conversion levels before and after the assembly of Au NPs; (c) ^{1}H-NMR analysis of GSH catalytic oxidation reaction at different reaction times. Signal at 3.20 ppm identifies as oxidized GSH (i.e. GSSG) or $Cu(SG)_2$ complex [20]; (d) Schematic illustration of the influence of GSH towards the deactivation of Au sites due to the competing poisoning induced by the GSH molecules that prevent the catalytic conversion of glucose; (e) Cell viability at different catalyst concentrations (expressed in [Cu]) after 48 h of incubation in A-549 (lung cancer cells, blue bar) and CCD-32Sk (human fibroblasts, red bar); (f) Confocal microscopy images obtained from treated*

A-549 cells with 6.25 mg Cu·mL^{-1} cells after 48 h. Actin fibers are shown in red after staining with phalloidin-Alexa 488, nuclei are displayed in light blue and stained with DAPI. CuFe-Au aggregates appear in green color and correspond to the reflected light. Top and right bar shows the profile of X and Y planes, respectively. Selected nanoparticles appear as non-internalized or exhibit co-location with red-actin fibers in the X, Y and Z plane. Scale bar: 20 μm.

Conclusions – Chapter 2

We have demonstrated the versatility of a CuFe-Au nanoplatform able to simultaneously prevent the deactivation of Au sites during the catalytic oxidation of glucose and the oxidation of GSH. GSH is rapidly consumed due to the synergistic action of the CuFe mixed oxide NPs assembled to the Au NPs. To the best of our knowledge, this is the first example in literature where this glucose conversion is successfully carried out in the presence of GSH [19,20]. The synergistic action of these heterostructures may pave the way to develop more efficient and selective nanocatalysts while preventing side effects or undesired deactivation events.

Experimental section – Chapter 2

Chemicals and materials. Iron (III) chloride hexahydrate ($FeCl_3 \cdot 6H_2O$, 97%), copper (II) chloride dihydrate ($CuCl_2 \cdot 2H_2O$, 99.0%), sodium acetate anhydrous (CH_3COONa, 99.0%), Bovine Serum Albumin (BSA), ethylene glycol (EG), Dimercaptosuccinic Acid (DMSA, 99.0%), Gold (III) chloride hydrate (50% Au basis), Tetrakis (hydroxymethyl) phosphonium chloride solution (THPC, 80 wt%, Germany), Tetraethyl orthosilicate (TEOS, 99.0%, GC), (3-aminopropyl)triethoxysilane (APTES, 99%), 3,3',5,5'-tetramethylbenzidine (TMB, 95%), Glutathione (GSH), 5,5'-Dithiobis (2-nitrobenzoic acid) (DNTB), hydrogen peroxide (H_2O_2, 33% v/v), sodium bicarbonate ($NaHCO_3$, 99%), Tetraethyl orthosilicate (TEOS, 99.5% GC), were purchased from Sigma Aldrich. D-glucose was purchased from MP- biomedicals. Acetonitrile (ACN) was purchased from VWR (Avan- tor). Sodium phosphate monobasic (NaH_2PO_4, 99.0) and Potassium phosphate dibasic (K_2HPO_4, 99.0) were purchased from Fisher Chemical. Deuterium Oxide (D_2O, 99.9% in D) was purchased from

Cambridge Isotope Laboratories. UPLC grade water was obtained from a Milli-Q Advantage A10 System with resistivity of 18.2 mU (Merk Millipore, Germany).

***Characterization techniques*.** Transmission electron microscopy (TEM) was performed using a FEI TECNAI T20 microscope (Tecnai, Eindhoven, The Netherlands) operated at 200 keV. Aberration-corrected scanning transmission electron microscopy (Cs-corrected STEM) images were acquired using a high angle annular dark field detector (HAADF) in a FEI XFEG TITAN electron microscope (FEI, Eindhoven, The Netherlands) operated at 200e300 kV. Elemental analysis was carried out with an EDAX detector in scanning mode. Samples were prepared by drop casting 3e5 mL of the NPs suspension onto a holey carbon TEM grid. UV-vis spectra were obtained on a V67 UV-vis double beam spectrophotometer (JASCO, Madrid, Spain). Individual particle size was measured using ImageJ software. X-ray photoelectron spectroscopy (XPS) to analyze the surface of the nanohybrid was carried out with the aid of an AXIS Supra (Kratos Tech., Manchester, UK) using a monochromatic Al-Ka source (1486.6 eV) run at 8 kV and 10 mA. For the individual peak regions, a pass energy of 20 eV was used. Peaks analysis was performed with the CasaXPS soft- ware, using a weighted sum of Lorentzian and Gaussian components curves after Shirley background subtraction. The binding energies were referenced to the internal C1s (284.5 eV) standard. Cu, Fe and Au contents were measured on a 4100 MPAES instrument (Agilent, Madrid, Spain) after dissolving the sample in a mixture 5:1 of H_2O:aqua regia. Empyrean equipment in Bragg-Brentano configuration using CuKα radiation and equipped with a PIXcel1D detector. Raman spectroscopy was performed using alpha300 R, Raman Imaging Microscope, (WITec, Germany). Experimental conditions for CuFe-Au, Au and Si were 785 nm laser source, 2 mW power, 3 s exposure time and 5 accumulations. For $CuFe_2O_4$, conditions were 532 nm laser wavelength, 5 mW, 10 s exposure time and 3 accumulations. ^{1}H-NMR spectra were acquired using a Bruker AV-500 MHz NMR spectrometer.

Synthesis of CuFe-DMSA nanoparticles. 250 mg of BSA were dissolved in 2.5 mL of miliQ water for 10 min and mixed with 12.5 mL of Ethylene glycol. Then, 270.0 mg of $FeCl_3{\cdot}6H_2O$, 85.0 mg of $CuCl_2$ and 375.0 mg of CH_3COONa were added into the reaction flask. The reaction was stirred for 2 h at room temperature. Then, the reaction was transferred to a Teflon autoclave where the

temperature was set to 180 C for 24 h. Finally, the product was centrifuged at 12 000 rpm for 20 min. DMSA ligand (20 mL, 25 mM) and 5 mL of 0.7 M NaOH solution were added to the obtained suspension using ultrasonication for 5 min. The final product was purified by two centrifugation cycles at 12 000 rpm for 20 min. The resulting solid was stored at 4 ^{o}C until further use.

Synthesis of ultrasmall Au nanoparticles. The preparation of ultrasmall Au nanoparticles was performed following previous group work protocols [10,18]. Briefly, to a total volume of 14 mL of distilled water, 165 mL of a 1 M NaOH solution, 333 mL of a 65 mM THPC solution and 1 mL of a $HAuCl_4 \cdot H_2O$ (3 mg/mL) solution were sequentially added. Time between the addition of THPC and Au precursor was fixed to 2 min. The reaction mixture was stirred overnight at room temperature and directly used to fabricate CuFe-Au nanostructures.

Assembly of CuFe-Au nanohybrids. In a total volume of 2 mL, 750 mL of Au-THPC nanoparticles solution was mixed with 250 mL of CuFe-DMSA. The pH was adjusted to 7.4 using a 0.1 M HCl solution. Final solution stirred overnight at room temperature. CuFe-Au nanoparticles were purified by centrifugation (13 300 rpm, 10 min, twice) and were resuspended in 2 mL of miliQ H_2O.

Catalytic glucose oxidation. Elimination of glucose by CuFe-Au catalyst was analyzed according to the following method. 5.5 mM of glucose were mixed with 0.1 mg/mL of CuFe-Au in a total volume of 2.5 mL at 37 ^{o}C, using Phosphate Buffer Saline as medium (pH 7.4). Glucose concentration at different reaction times was measured by UPLC-QDa detector. 20 mL of reaction were sampled and mixed with 955 mL of a mixture 1:1 Acetonitrile:H_2O and with 25 mL of a lactose 1000 ppm solution as internal standard.

Catalytic GSH depletion. Catalytic activity towards GSH oxidation of CuFe-Au nano- particles was evaluated according to the following protocol: 5 mM of GSH were mixed with 0.1 mg·mL^{-1} of CuFe-Au in a total volume of 2.5 mL at 37 ^{o}C. GSH concentration at different reaction times was measured by UPLC-PDA detector. 20 mL of reaction were mixed with 100 mL of Disulfanediylbis-(2-nitrobenzoic acid) (DTNB) and 880 mL of 0.01 M 2-amino-2-hydroxymethyl propane 1,3 diol (TRIS).

UPLC-PDA-MS equipment for glucose and GSH analysis. Glucose and GSH analysis were performed on Waters ACQUITY system H-Class that consisted of a binary pump, an autosampler, a column thermostat and a photodiode array (PDA) detector. This system is coupled to a single quadrupole mass spectrometer with an electrospray ionization (ESI) ACQUITY QDa mass detector. Glucose was monitored through its adduct $[M\ Cl]^-$ at m/z 215.15 (see Fig. S1). Data acquisition and processing were performed by using MASSLYNX software (Waters Corporation USA). On the one hand, in order to analyze GSH from derivatized samples (*vide infra*), chromatographic separation was performed using an ACQUITY UPLC BEH C18 column (130 Å, 1.7 mm 2.1 x 50 mm, from WATERS) at 40 °C under an isocratic flow of 0.3 mL/min containing 50% acetonitrile, 50% milli Q water. PDA detector was employed to monitor the absorbance from derivatized GSH at 412 nm during analysis time (see Fig. S2). On the other hand, glucose was monitored after chromatographic separation using an ACQUITY UPLC BEH Amide column (130 Å, 1.7 mm, 2.1 mm 100 mm, WATERS). In this case, the mobile phase consisted of an initial mixture of acetonitrile/water (90:10), containing 0.1% 10 mM ammonium chloride as a mobile phase modifier, at a 0.5 mL/min initial flow rate. A gradient in the mobile phase was employed to separate the different metabolites present in the samples. Water composition increased for 3 min until a 65% acetonitrile was reached and then the system recovered initial conditions. ACQUITY QDa mass detector was employed to quantify sugar concentrations according to the most abundant ions generated as described below. Calibrations were performed using commercial standards of glucose and lactose.

GSH derivatization protocols for UPLC analysis. The derivatization of GSH using DTNB yields a quantifiable yellow-colored product, 5-thiobis-(2-nitrobenzoic acid) (TNB^{2-}) which absorbs at 412 nm (see Fig. S3). 20 mL of reaction were mixed with 100 mL of 5,50-Disulfanediylbis (2-nitrobenzoic acid) (DTNB) and 880 mL of 0.01 M 2-Amino-2-hydroxymethyl-propane-1,3-diol (TRIS). Both samples and standards were filtered with 0.22 mm Nylon filters before injecting in UPLC system.

^{1}H-NMR analysis of catalytic GSH oxidation. A 50 mM K_2HPO_4, 50 mM NaH_2PO_4 and 20 mM GSH solution was prepared in D_2O. Then, the CuFe catalyst was added until reaching a [Cu] 2.0

$mg \cdot mL^{-1}$. Samples were collected at reaction times of 5 and 7 h and then centrifuged for 10 min at 13 000 rpm). Supernatant was filtered using 0.22 mm Nylon filters and incubated with 400 mg of Chelex resin for 30 min prior to the NMR analysis.

TMB oxidation assays. A freshly prepared TMB (5 mg dissolved in 1 mL of DMSO) solution was used before each assay. 2.3 mL of CH_3COONa (0.05 M) solution at pH ¼ 5.80 were mixed with 200 mL of CuFe-Au solution (final Au concentration 0.01 mg/mL) and 15 mL of TMB solution to reach a final concentration of 0.10 mM. Absorbance at 652 nm was monitored for 500 s to check the generation of oxidized TMB.

Cell viability experiments. Cells were maintained by the UC Berkeley Tissue Culture Facility. A-549 and CCD-32Sk cells were seeded in 75% and 85% confluence, respectively using Dulbecco's modified Eagle medium (DMEM supplemented with Glutamax) in a 96-well cell plate. CuFe-Au NPs stock solution was centrifuged and the solid was dissolved in DMEM at different concentrations, ranging from 0.1 to 0.0125 mg/ mL of Cu. After 48 h, the wells were washed with PBS. Then, 100 mL of solution containing CCK-8 in DMEM (10% v/v) was added to the well. The cell plate was incubated at 37 C in a 5% CO_2 for 2.5 h (for A-549 cells) and 3.5 h (for CCD-32Sk cells). Finally, the absorbance at 450 nm was measured using a plate reader.

Internalization capacity of A549 cells and confocal imaging. Briefly, 20,000 A-549 cells were seeded onto Ø 12 mm cover- slips, which were deposited on a 24-well plate. Cells were allowed to attach to the coverslip at 37 C and 5% CO_2 and, 48 h after the seeding, cells were treated with a suspension of CuFe-Au NPs in DMEM at 6.25 mg/ml of Cu for 48 h (for control cells, media renewal was carried out). After this time, cells were washed thrice with PBS, fixed with 4% paraformaldehyde for 30 min, and washed again thrice with DPBS. Preparation of the samples for confocal microscopy assay included an initial permeabilization of the samples in a solution of DPBS/1% BSA/0.1% saponine, followed by a 1 h incubation with phalloidin-Alexa 488 (dilution 1:200) for actin fibers staining. After the incubation, coverslips were gently deposited onto a drop of mounting media (Fluoromount-G) which also contained DAPI for nuclei staining. Regarding the CuFe-Au NPs, aggregates could be detected due to the reflection of the incident light. In order to ensure the internalization of the NPs in the cells, a Z-Stack of the whole cell was performed. Images

were analyzed, and the maximum orthogonal projection was obtained for each image. The NPs could be observed due to the contrast detected with the photomultiplier for transmitted light (T-PMT). This experiment was performed in a confocal microscope (ZEISS LSM 880 Confocal Microscope), using a 63/1.4 Oil DIC M27 objective.

References – Chapter 2

1. B. Yang, Y. Chen, J. Shi, Nanocatalytic Medicine, Adv. Mater. 31 (2019), 1901778.

2. J. Chen, Y. Zhu, C. Wu, J. Shi, Nanoplatform-based cascade engineering for cancer therapy, Chem. Soc. Rev. 49 (2020) 9057e9094.

3. H. Lin, Y. Chen, J. Shi, Nanoparticle-triggered in situ catalytic chemical re- actions for tumour-specific therapy, Chem. Soc. Rev. 47 (2018) 1938e1958.

4. R.J. DeBerardinis, N.S. Chandel, We need to talk about the Warburg effect, Nature Metabol. 2 (2020) 127e129.

5. M.G. Vander Heiden, L.C. Cantley, C.B. Thompson, Understanding the Warburg effect: The metabolic requirements of cell proliferation, Science 324 (2009) 1029e1033.

6. X. Wang, T. Xiong, M. Cui, X. Guan, J. Yuan, Z. Wang, R. Li, H. Zhang, S. Duan,

7. F. Wei, Targeted self-activating Au-Fe3O4 composite nanocatalyst for enhanced precise hepatocellular carcinoma therapy via dual nanozyme-catalyzed cascade reactions, Appl. Mater. Today 21 (2020), 100827.

8. S. Gao, H. Lin, H. Zhang, H. Yao, Y. Chen, J. Shi, Nanocatalytic tumor therapy by biomimetic dual inorganic nanozyme-catalyzed cascade reaction, Adv. Sci. 6 (2019), 1801733.

9. X. Liu, Y. Pan, J. Yang, Y. Gao, T. Huang, X. Luan, Y. Wang, Y. Song, Gold nanoparticles doped metal-organic frameworks as near-infrared light-enhanced cascade nanozyme against hypoxic tumors, Nano Res. 13 (2020) 653e660.

10. M.C. Ortega-Liebana, J. Bonet-Aleta, J.L. Hueso, J. Santamaria, Gold-based nanoparticles on amino-functionalized mesoporous silica supports as nanozymes for glucose oxidation, Catalysts 10 (2020).

11. M.P. Gamcsik, M.S. Kasibhatla, S.D. Teeter, O.M. Colvin, Glutathione levels in human tumors, Biomarkers 17 (2012) 671e691.

12. J. Bonet-Aleta, J.I. Garcia-Peiro, S. Irusta, J.L. Hueso, Gold-Platinum nano- particles with core-shell configuration as efficient oxidase-like nanosensors for glutathione detection, Nanomaterials 12 (2022).

13. Y. Zhao, Y. Huang, H. Zhu, Q. Zhu, Y. Xia, Three-in-One: sensing, self-assembly, and cascade catalysis of cyclodextrin modified gold nanoparticles, J. Am. Chem. Soc. 138 (2016) 16645e16654.

14. Y. Lin, Z. Li, Z. Chen, J. Ren, X. Qu, Mesoporous silica-encapsulated gold nanoparticles as artificial enzymes for self-activated cascade catalysis, Bio- materials 34 (2013) 2600e2610.

15. X. Wang, X. Zhong, Z. Liu, L. Cheng, Recent progress of chemodynamic therapy-induced combination cancer therapy, Nano Today 35 (2020), 100946.

16. Y. Ding, Y. Dai, M. Wu, L. Li, Glutathione-mediated nanomedicines for cancer diagnosis and therapy, Chem. Eng. J. 426 (2021), 128880.

17. J. Garcia-Bermudez, R.T. Williams, R. Guarecuco, K. Birsoy, Targeting extra- cellular nutrient dependencies of cancer cells, Mol. Metabol. 33 (2020) 67e82.

18. J.L. Hueso, V. Sebastia'n, A'. Mayoral, L. Uso'n, M. Arruebo, J. Santamaría, Beyond gold: rediscovering tetrakis-(hydroxymethyl)-phosphonium chloride (THPC) as an effective agent for the synthesis of ultra-small noble metal nanoparticles and Pt-containing nanoalloys, RSC Adv. 3 (2013) 10427e10433.

19. J. Bonet-Aleta, M. Sancho-Albero, J. Calzada-Funes, S. Irusta, P. Martin-Duque, J.L. Hueso, J. Santamaria, Glutathione-Triggered catalytic response of Copper- Iron mixed oxide Nanoparticles. Leveraging tumor microenvironment con- ditions for chemodynamic therapy, J. Colloid Interface Sci. 617 (2022) 704e717.

20. J. Bonet-Aleta, M. Encinas-Gimenez, E. Urriolabeitia, P. Martin-Duque, J.L. Hueso, J. Santamaria, Unveiling the interplay between homogeneous and heterogeneous catalytic mechanisms in coppereiron nanoparticles working under chemically relevant tumour conditions, Chem. Sci. (2022).

21. N. Miguel-Sancho, O. Bomatí-Miguel, G. Colom, J.P. Salvador, M.P. Marco, J. Santamaría, Development of stable, water-dispersible, and bio-functionalizable superparamagnetic iron oxide nanoparticles, Chem. Mater. 23 (2011) 2795e2802.

22. I. Moreno, N. Navascues, S. Irusta, J. Santamaria, Electrospun Au/CeO2 nano- fibers: a highly accessible low-pressure drop catalyst for preferential CO oxidation, J. Catal. 329 (2015) 479e489.

23. K. Yuan, D. Lützenkirchen-Hecht, L. Li, L. Shuai, Y. Li, R. Cao, M. Qiu, X. Zhuang, M.K.H. Leung, Y. Chen, U. Scherf, Boosting oxygen reduction of single iron active sites via geometric and electronic engineering: nitrogen and phos- phorus dual coordination, J. Am. Chem. Soc. 142 (2020) 2404e2412.

24. M.C. Biesinger, Advanced analysis of copper X-ray photoelectron spectra, Surf. Interface Anal. 49 (2017) 1325e1334.

25. R.S.C. Smart, W.M. Skinner, A.R. Gerson, XPS of sulphide mineral surfaces: metal-deficient,

polysulphides, defects and elemental sulphur, Surf. Interface Anal. 28 (1999) 101e105.

26. P. Gobbo, S. Novoa, M.C. Biesinger, M.S. Workentin, Interfacial strain- promoted alkyneeazide cycloaddition (I-SPAAC) for the synthesis of nano-material hybrids, Chem. Commun. 49 (2013) 3982e3984.

27. P. Gobbo, Z. Mossman, A. Nazemi, A. Niaux, M.C. Biesinger, E.R. Gillies, M.S. Workentin, Versatile strained alkyne modified water-soluble AuNPs for interfacial strain promoted azideealkyne cycloaddition (I-SPAAC), J. Mater. Chem. B 2 (2014) 1764e1769.

28. L. Carlini, C. Fasolato, P. Postorino, I. Fratoddi, I. Venditti, G. Testa, C. Battocchio, Comparison between silver and gold nanoparticles stabilizedwith negatively charged hydrophilic thiols: SR-XPS and SERS as probes for structural differences and similarities, Colloids Surf. A Physicochem. Eng. Asp. 532 (2017) 183e188.

29. L.N. Song, N. Gu, Y. Zhang, A moderate method for preparation DMSA coated Fe_3O_4 nanoparticles, IOP Conf. Ser. Mater. Sci. Eng. 164 (2017), 012026.

30. S. Aryal, K.C.R. B, N. Dharmaraj, N. Bhattarai, C.H. Kim, H.Y. Kim, Spectroscopic identification of S-Au interaction in cysteine capped gold nanoparticles, Spectrochim. Acta Mol. Biomol. Spectrosc. 63 (2006) 160e163.

31. W.W. Bryan, A.C. Jamison, P. Chinwangso, S. Rittikulsittichai, T.-C. Lee, T.R. Lee, Preparation of THPC-generated silver, platinum, and palladium nanoparticles and their use in the synthesis of Ag, Pt, Pd, and Pt/Ag nanoshells, RSC Adv. 6 (2016) 68150e68159.

32. S. Rackauskas, A.G. Nasibulin, H. Jiang, Y. Tian, V.I. Kleshch, J. Sainio, E.D. Obraztsova, S.N. Bokova, A.N. Obraztsov, E.I. Kauppinen, A novel method for metal oxide nanowire synthesis, Nanotechnology 20 (2009), 165603.

33. T.M. Devine, F. Adar, Raman Spectroscopy of Solids, Character. Mater. (2012) 1e38.

34. Z. Tang, P. Zhao, H. Wang, Y. Liu, W. Bu, Biomedicine meets Fenton chemistry, Chem. Rev. 121 (2021) 1981e2019.

35. X. Shen, W. Liu, X. Gao, Z. Lu, X. Wu, X. Gao, Mechanisms of oxidase and superoxide dismutation-like activities of gold, silver, platinum, and palladium, and their alloys: a general way to the activation of molecular oxygen, J. Am. Chem. Soc. 137 (2015) 15882e15891.

36. M. Wu, A. Neilson, A.L. Swift, R. Moran, J. Tamagnine, D. Parslow, S. Armistead, K. Lemire, J. Orrell, J. Teich, S. Chomicz, D.A. Ferrick, Multipa-rameter metabolic analysis reveals a close link between attenuated mito- chondrial bioenergetic function and enhanced glycolysis dependency in human tumor cells, American journal of physiology, Cell physiology 292 (2007) C125eC136.

37. H.-x. Zhang, Y. Chen, R. Xu, Q.-y. He, Nrf2 mediates the resistance of human A549 and HepG2 cancer cells to boningmycin, a new antitumor antibiotic, in vitro through regulation of glutathione levels, Acta Pharmacol. Sin. 39 (2018) 1661e1669.

Supplementary information – Chapter 2

Adapted from:

Synergistic assembly of gold and copper-iron oxide nanocatalysts to promote the simultaneous depletion of glucose and glutathione

J. Bonet-Aleta [a, b, c], J.L. Hueso [a, b, c, *], L. Sanchez-Uriel [a, b, c], M. Encinas-Gimenez [a, b, c], S. Irusta [a, b, c], P. Martin-Duque [b, d, e, f], G. Martinez [a, b, c], J. Santamaria [a, b, c, **]

[a] *Instituto de Nanociencia y Materiales de Aragon (INMA) CSIC-Universidad de Zaragoza, Campus Rio Ebro, Edificio I+D, C/ Poeta Mariano Esquillor, S/n, 50018, Zaragoza, Spain*

[b] *Networking Res. Center in Biomaterials, Bioengineering and Nanomedicine (CIBER-BBN), Instituto de Salud Carlos III, Madrid, 28029, Spain*

[c] *Department of Chemical and Environmental Engineering, Campus Rio Ebro, University of Zaragoza, Campus Rio Ebro, C/Mariano Esquillor, s/n, Zaragoza, 50018, Spain*

[d] *Instituto de Investigacion Sanitaria (IIS) de Aragon, Avenida San Juan Bosco, 13, 50009, Zaragoza, Spain*

[e] *Fundacion Araid. Av. de Ranillas 1-D, 50018 Zaragoza, Spain*

[f] *Departamento de Cirugía, Facultad de Medicina, Universidad de Zaragoza, 50009 Zaragoza, Spain*

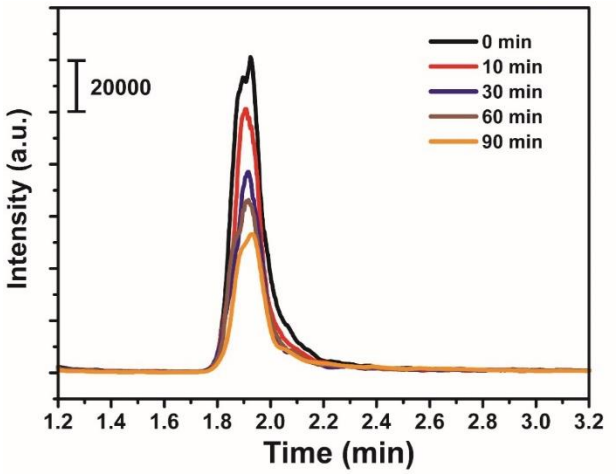

Figure S1. *Chromatograms of glucose at different reaction times in the presence of the CuFe-Au nanocatalyst; Reaction conditions: pH = 7.4 (adjusted with PBS 1X), Temperature = 37ºC, $[Glucose]_0$ = 5.5 mM, [Au] = 0.02 mg·mL^{-1}.*

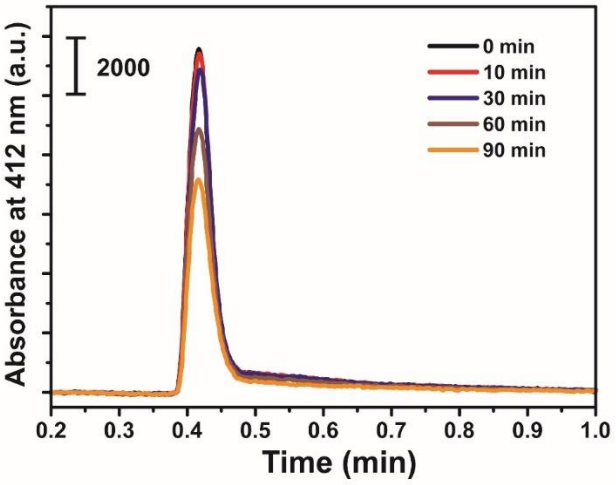

Figure S2. *Chromatograms of TNB^{2-} acquired with a PDA at different reactions times; Reaction conditions: pH = 7.4 (adjusted with PBS 1X), Temperature = 37ºC, $[GSH]_0$ = 5 mM, [CuFe] = 0.1 mg·mL^{-1}.*

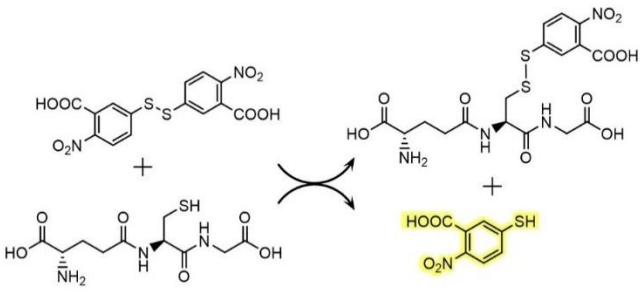

Figure S3. *Reaction of GSH with DTNB to generate quantifiable TNB^{2-} product.*

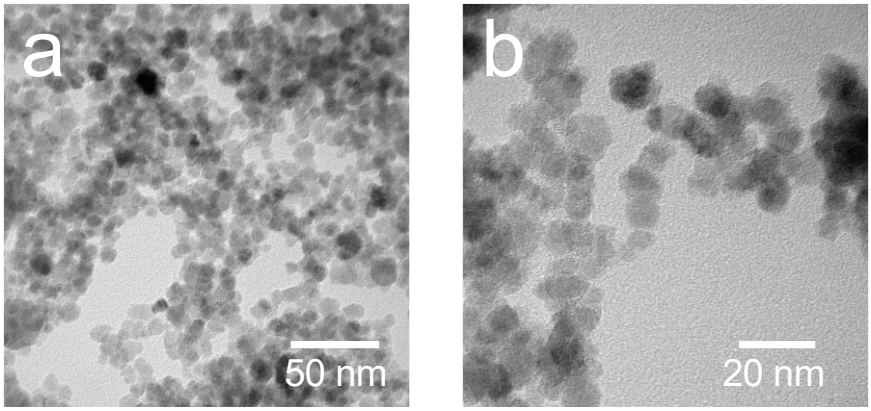

Figure S4.*TEM images of the DMSA coated CuFe nanoparticles prior to the Au assembly.*

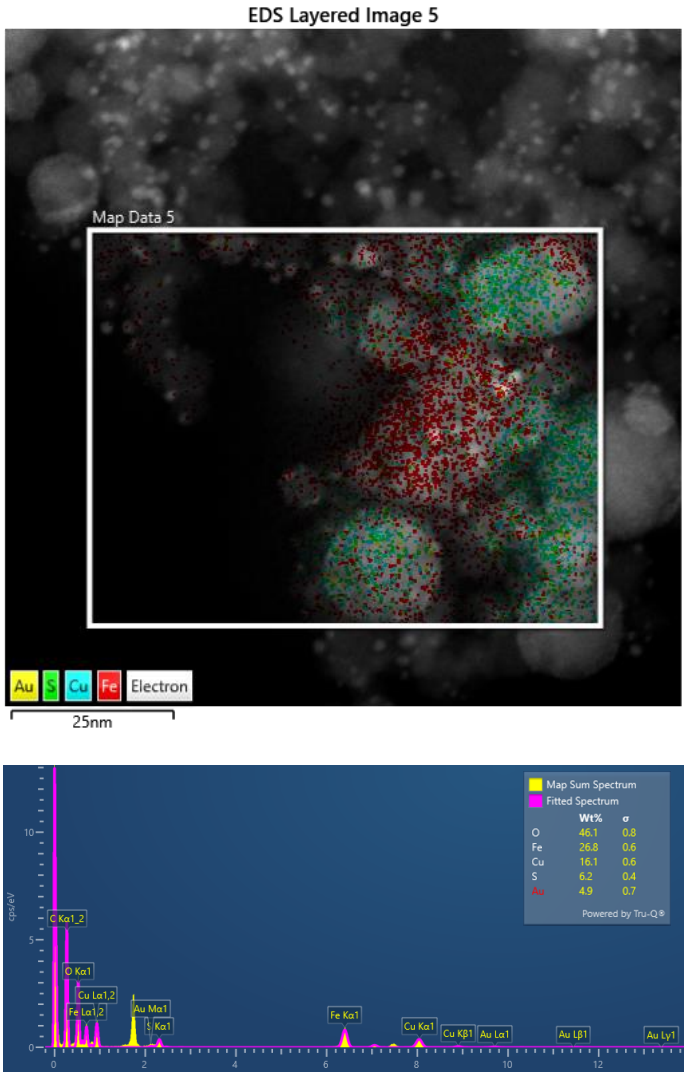

Figure S5. *STEM-EDS mapping analysis of the CuFe-Au nanohybrid revealing a Cu:Fe:Au ratio of 1:1.6:0.3, respectively.*

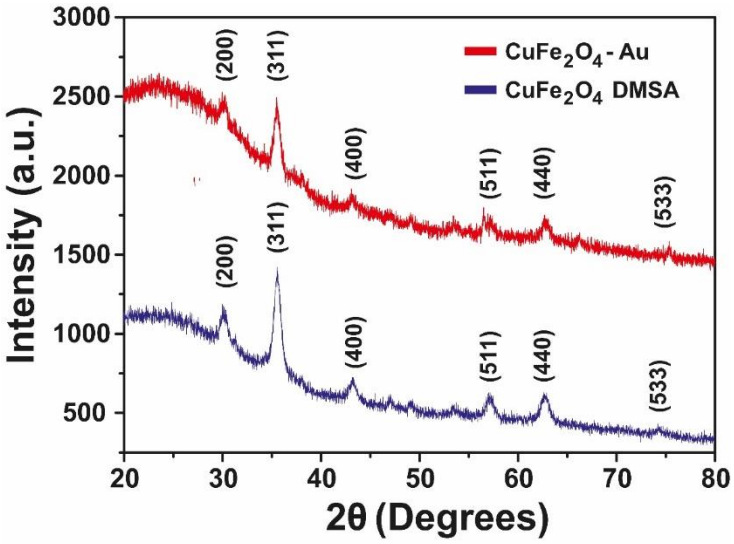

Figure S6. *XRD spectrum of $CuFe_2O_4$ nanoparticles after (red line) and before (blue line) Au nanoparticle deposition. The ultrasmall size of Au NPs deposited onto CuFe makes impossible their detection by XRD.*

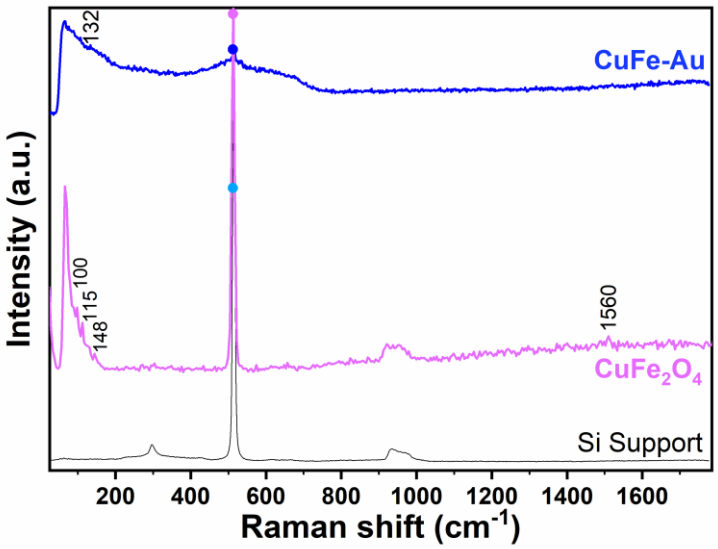

Figure S7. *Raman spectra for the CuFe-Au, bare $CuFe_2O_4$ particles and the Si wafer as reference.*

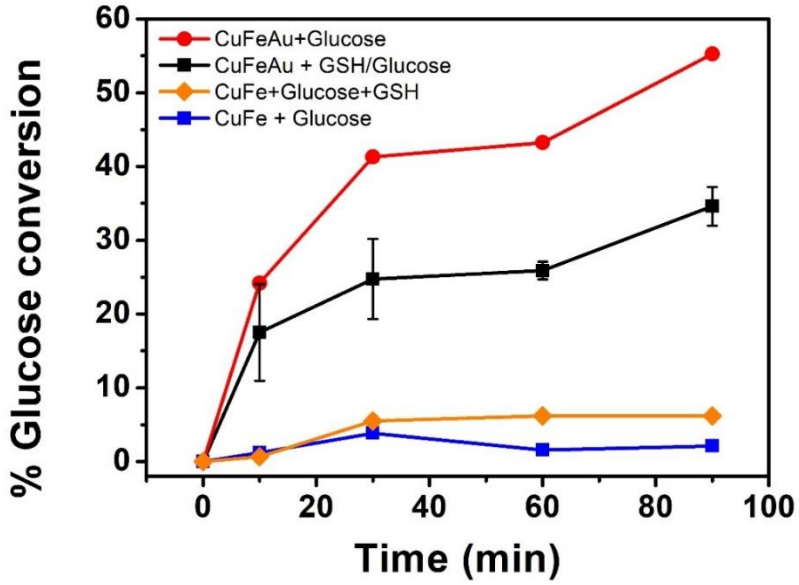

Figure S8. *Kinetics of glucose conversion under different reaction conditions: (red line + filled circle symbols) in the presence of CuFeAu; (black line + filled squares) CuFeAu+5 mM GSH; (orange line + filled diamonds) CuFe+5 mM GSH and (blue line + filled squares) CuFe. The Au nanoparticles deposited onto CuFe fastly oxidizes glucose. The presence of a GSH-consuming platform as support for the Au catalysts allows the glucose oxidation reaction to occur even in the presence of GSH with similar kinetics rates. Reaction conditions: pH = 7.4 (adjusted with PBS 1X), Temperature = 37ºC, $[Glucose]_0$ = 5.5 mM, [Au] = 0.02 mg·mL^{-1}.*

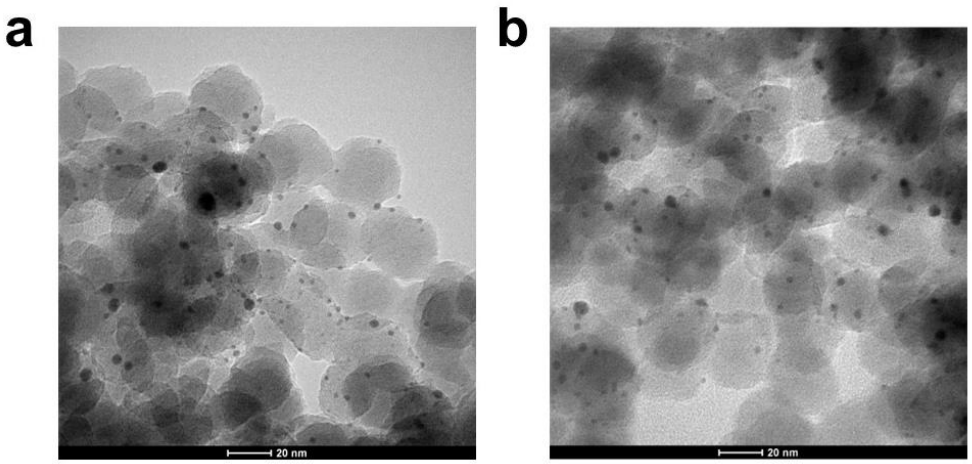

Figure S9. *TEM images of Au-SiO_2 nanoparticles used as control to demonstrate the poisoning of Au surface by GSH, as SiO_2 is inert support.*

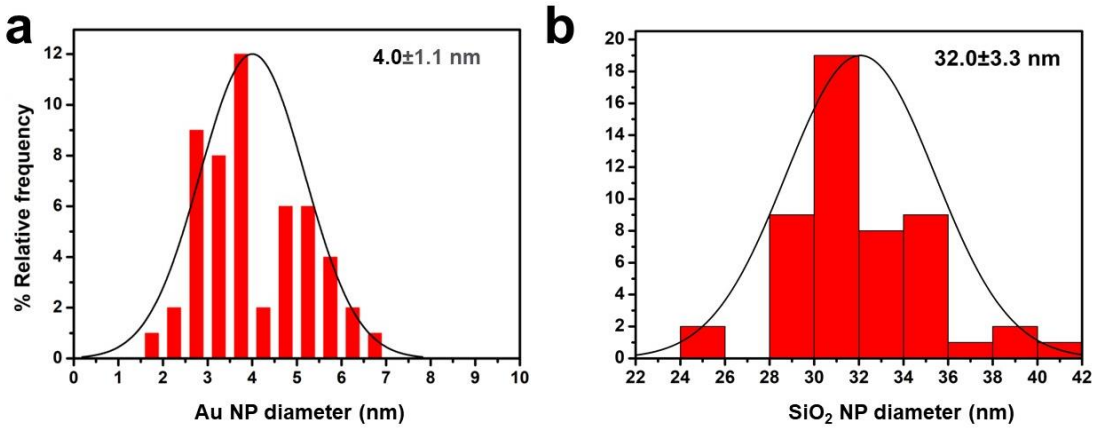

Figure S10. *Size histogram of (a) Au NPs deposited onto (b) SiO_2 support (n=50).*

.

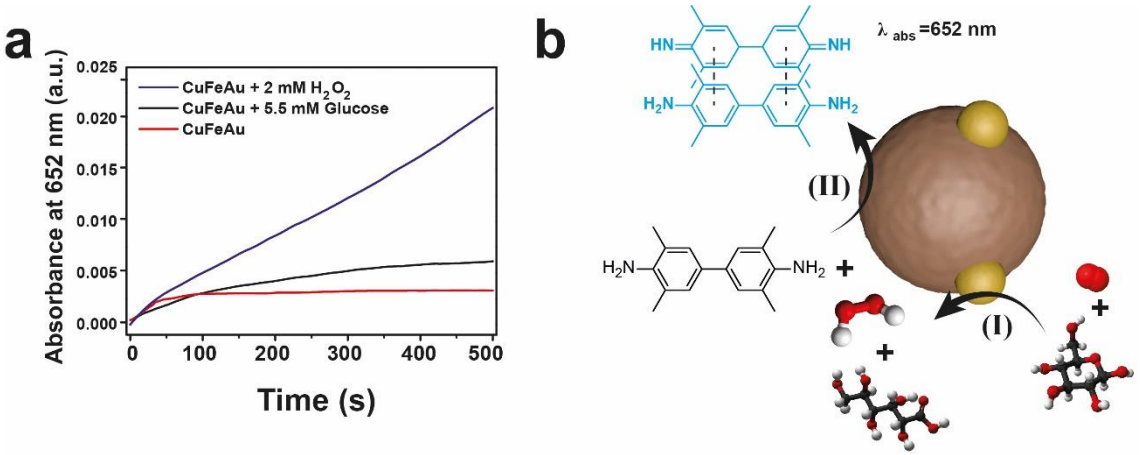

Figure S11. *(a) Monitorization of the absorbance at 652 nm which is directly related with the formation of a charge-transfer complex after TMB oxidation. Comparison between the addition of 2 mM H_2O_2 and 5.5 mM of Glucose. After glucose oxidation by Au nanoparticles, H_2O_2 is generated which can be transformed into •OH species by CuFe support; (b) Scheme of reactions occurring during the experiment: in a first step (I) Au catalyzes the glucose oxidation by O_2 into gluconic acid and H_2O_2, which can be used by the CuFe platform (II) to oxidize TMB into TMB_{ox}. Reaction conditions: pH = 5.8 (CH_3COONa, CH_3COOH buffer, 0.05 M), Temperature = 25ºC, [TMB] = 0.10 mM, [Au] = 0.01 mg·mL^{-1}, [H_2O_2] = 2 mM, [Glucose] = 5.5 mM.*

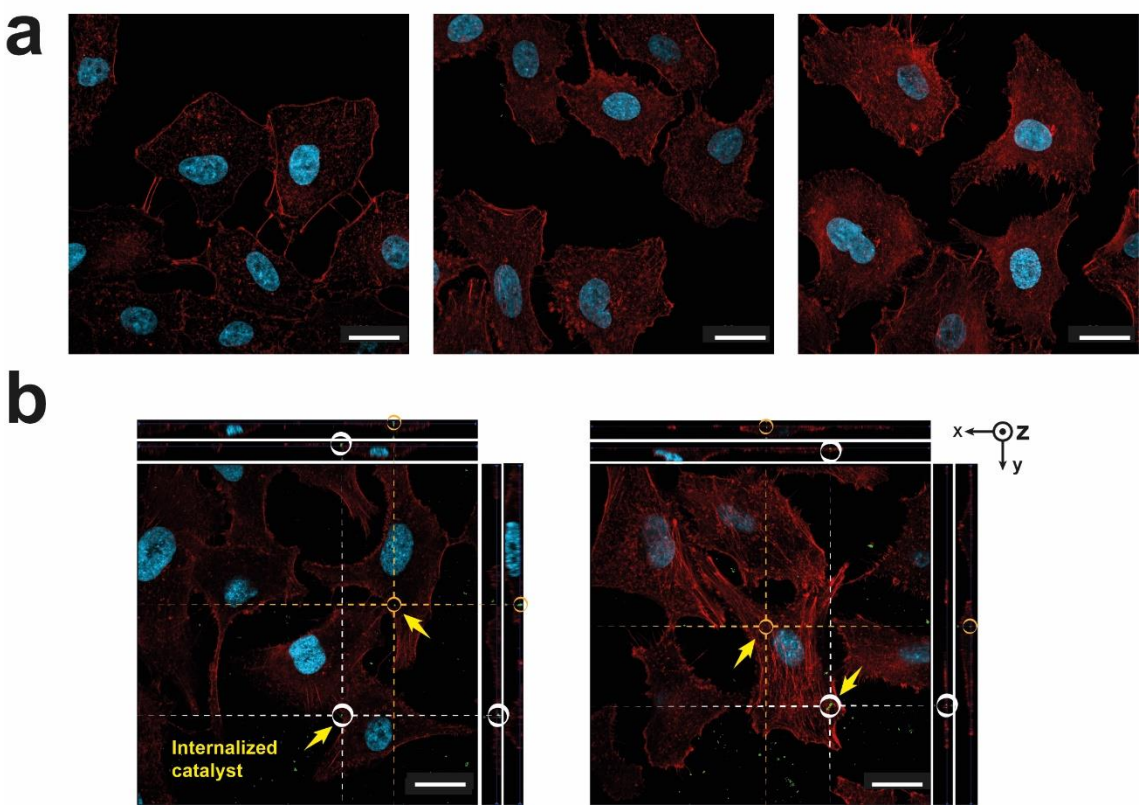

Figure S12. *Confocal microscopy images of A-549: (a) control experiment in the absence of CuFe-Au nanoparticles and (b) cells incubated with CuFe-Au nanoparticles for 48 hours. Selected CuFeAu nanoparticles exhibit internalization and are co-localized with the actin fibers in all the planes. Scale bar = 20 μm.*

Table S1. *Elemental composition of CuFe-Au surface measured by XPS*

B.E. (eV)						
Atomic %						
Cu 2p	Fe 2p	O 1s	C 1s	S 2p	P 2p	Au 4f
934.4	711.1	530.8	285.0	162.9	133.3	84.3
10.45	18.14	45.43	24.05	1.03	0.70	0.20

Table S2. *Elemental composition of CuFe-DMSA surface measured by XPS*

B.E. (eV)						
Atomic %						
Cu 2p	Fe 2p	O 1s	C 1s	S 2p	P 2p	Au 4f
932.6	710.8	530.4	285.0	161.6	n.d.	n.d.
7.79	18.71	40.07	32.41	1.00	-	-

Table S3. *XPS quantification of different Fe^{II}/Fe^{III} and Cu^{I}/Cu^{II} species present on the CuFe-Au nanocatalyst surface*

Fe^{2+}		**Fe^{3+}**	
2p3/2	S.O	2p3/2	S.O
710.8	715.6	712.7	720.1
41%	-	59%	-

$Cu^{0/+}$	**Cu^{2+}**		
2p3/2	2p3/2	S.O.1	S.O.2
933.3	934.9	941.9	944.7
14%	86%	-	-

Table S4. *XPS quantification of different Fe^{II}/Fe^{III} and Cu^{I}/Cu^{II} species present on the CuFe-DMSA nanocatalyst surface*

Fe^{2+}		**Fe^{3+}**	
2p3/2	S.O	2p3/2	S.O
710.6	714.0	712.1	718.4
40%	-	60%	-

$Cu^{0/+}$	**Cu^{2+}**		
2p3/2	2p3/2	S.O.1	S.O.2
932.6	934.3	941.2	944.2
17%	83%	-	-

Chapter 3 |

Combining Heterogeneous and Homogeneous catalysis

Summary – Chapter 3

From the previous results, it became evident that Cu-Fe nanoparticles exhibited remarkable efficacy in catalyzing GSH oxidation both in free, test tube conditions and also within living cells. Our research focused on determining the rate at which these nanoparticles were internalized, enabling us to precisely quantify the amount of Cu or Fe delivered to cancer cells. During this investigation, we observed a substantial change in the Cu:Fe ratio. Initially set at 1:2, we noticed a significant alteration in the ratio to approximately 1:10 after the particles were exposed to a GSH-enriched biological medium. This finding indicated an important loss of copper while the iron content remained largely constant, implying a transformation of the nanoparticles. In the existing literature, various transition-based nanoparticles utilized for catalytic cancer therapy were reported to catalyze GSH oxidation. However, this catalytic process was generally considered as solely heterogeneous, without considering significant modifications on the catalyst (see **Figure Summary-1, left**). In latest, the results of this work demonstrated that the species responsible for GSH oxidation were leached cations, therefore defining a homogeneous process. The clinical translation of therapies based on inorganic nanoparticles will never be achieved unless the underlying processes involved are understood and controlled. Considering the significance of these processes, we delved into investigating the GSH-induced release of copper and the catalytic interaction between GSH and the resulting copper ions. To gain a more comprehensive understanding, we employed precise analytical techniques such as ^{1}H-NMR and High-resolution mass spectroscopy. These analyses successfully demonstrated the formation of a copper complex in solution, termed $Cu(SG)_2$, where GSH is bonded to copper. Further experimentation revealed that the GSH bonded to copper was converted into GSSG in the presence of dissolved oxygen, leading to the generation of $\bullet O_2^-$ and H_2O_2 (**Figure Summary-1**). This prompted us to consider the potential significance of the remaining iron-enriched nanoparticles in the reaction. Remarkably, these nanoparticles exhibited the ability to recycle the generated $\bullet O_2^-/H_2O_2$ species back into oxygen (O_2). This unique attribute of the new iron-enriched nanoparticle becomes advantageous under the hypoxic conditions commonly found within tumors, enabling sustained homogeneous GSH oxidation.

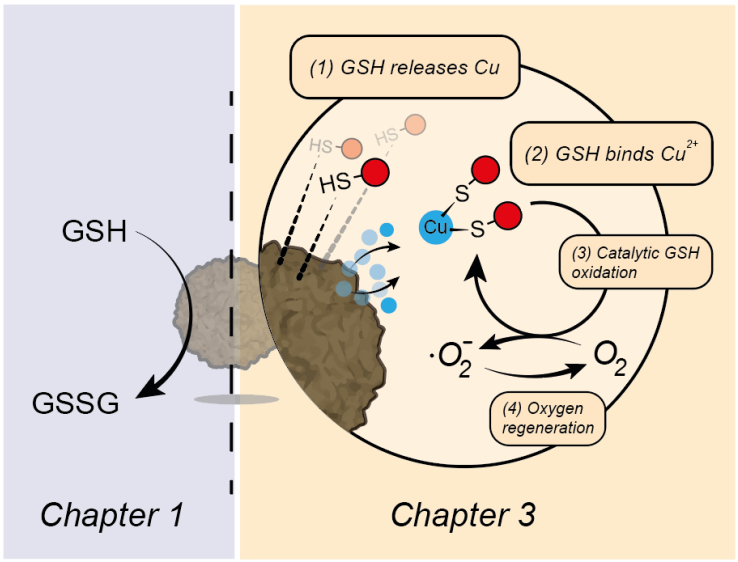

Figure Summary-1. *Same process, different degree of detail. In chapter 1, we studied the GSH oxidation reaction by quantifying how GSH and GSSG concentration were altered in the reaction media. Chapter 3 sheds light on the complexity of this apparently simple reaction.*

In order to illustrate the potential selectivity of the catalytic reaction towards cancer cells, we conducted a comprehensive toxicity screening of Cu-Fe nanoparticles against various cell lines. This screening encompassed four cancerous cell lines (SKOV3, HeLa, U251-MG, and U87) as well as two healthy cell lines (hpMSC and fibroblasts). Our findings revealed that this nanocatalyst exhibited a 4-10 times greater toxicity towards cancer cells compared to healthy cells. This was explained in terms of the higher GSH level in cancer cells and underscores the relevance and advantages of specifically targeting GSH as a means of combating cancer. Building upon the insights gained in Chapter 1, we further demonstrated the capability of Cu-Fe nanoparticles to effectively decrease GSH levels in HeLa, U251, and hpMSC cell lines following treatment.

To the best of our knowledge, the Cu-Fe oxidation of GSH represents the first instance where homogeneous and heterogeneous catalysis are synergistically coupled with the aim of depleting a vital molecule within tumors. These results also shed light on the often ignored dynamic properties of inorganic nanoparticles, beyond their conventional description as inert substances.

The results of our study have been published in *Chem. Sci., 2022, 13, 8307-8320*.

Adapted from:

Unveiling the interplay between homogeneous and heterogeneous catalytic mechanisms in copper–iron nanoparticles working under chemically relevant tumour conditions

Javier Bonet-Aleta,[a,b,c] Miguel Encinas-Gimenez,[a,b,c] Esteban Urriolabeitia,[d] Pilar Martin-Duque[b,e,f,g], Jose L. Hueso[a,b,c,f] and Jesus Santamaria[a,b,c,f]

[a]Institute of Nanoscience and Materials of Aragon (INMA), CSIC-Universidad de Zaragoza, Campus R´ıo Ebro, Edificio I+D, C/Poeta Mariano Esquillor, s/n, 50018, Zaragoza, Spain.

[b]Networking Research Center in Biomaterials, Bioengineering and Nanomedicine (CIBER-BBN), Instituto de Salud Carlos III, 28029, Madrid, Spain

[c]Department of Chemical and Environmental Engineering, University of Zaragoza, Campus Rio Ebro, C/Mar´ıa de Luna, 3, 50018 Zaragoza, Spain

[d]Instituto de Sintesis Quimica y Catalisis Homogenea, ISQCH (CSIC-Universidad de Zaragoza), 50009 Zaragoza, Spain

[e]Instituto Aragones de Ciencias de la Salud (IACS), Avenida San Juan Bosco, 13, 50009

Zaragoza, Spain

[f]Instituto de Investigacion Sanitaria (IIS) Aragon, Avenida San Juan Bosco, 13, 50009 Zaragoza, Spain

[g]Fundacion Araid, Av. de Ranillas 1-D, 50018 Zaragoza, Spain

Graphical abstract

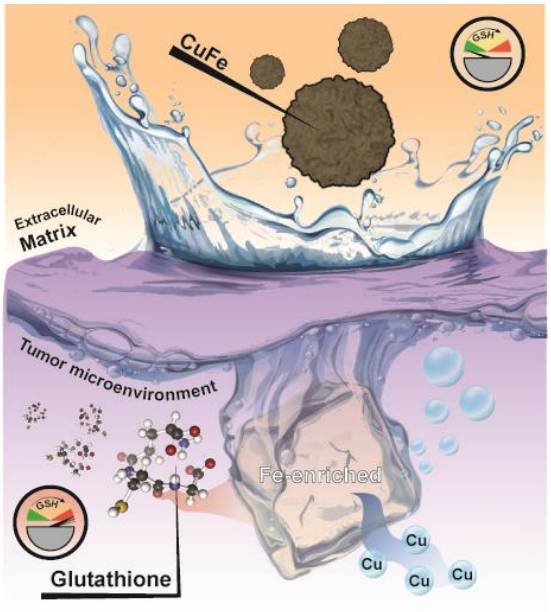

Abstract

The present work sheds light on a generally overlooked issue in the emerging field of bio-orthogonal catalysis within tumour microenvironments (TMEs): the interplay between homogeneous and heterogeneous catalytic processes. In most cases, previous works dealing with nanoparticle-based catalysis in the TME focus on the effects obtained (e.g. tumour cell death) and attribute the results to heterogeneous processes alone. The specific mechanisms are rarely substantiated and, furthermore, the possibility of a significant contribution of homogeneous processes by leached species – and the complexes that they may form with biomolecules – is neither contemplated nor pursued. Herein, we have designed a bimetallic catalyst nanoparticle containing Cu and Fe species and we have been able to describe the whole picture in a more complex scenario where both homogeneous and heterogeneous processes are coupled and fostered under TME relevant chemical conditions. We investigate the preferential leaching of Cu ions in the presence of a TME overexpressed biomolecule such as glutathione (GSH). We demonstrate that these homogeneous processes initiated by the released by Cu– GSH interactions are in fact responsible for the greater part of the cell death effects found (GSH, a scavenger of reactive oxygen species, is depleted and highly active superoxide anions are generated in the same catalytic cycle). The remaining solid CuFe nanoparticle becomes an active catalyst to supply oxygen from oxygen reduced species, such as superoxide anions (by-product from GSH oxidation) and hydrogen peroxide, another species that is enriched in the TME. This activity is essential to sustain the homogeneous catalytic cycle in the oxygen-deprived tumour microenvironment. The combined heterogeneous–homogeneous mechanisms revealed themselves as highly efficient in selectively killing cancer cells, due to their higher GSH levels compared to healthy cell lines.

Introduction – Chapter 3

Glutathione (GSH) is a key peptide in the regulation of intra- cellular reactive oxygen species (ROS) levels. Its role is of paramount importance in the tumour microenvironment (TME)[1], where GSH is overexpressed to counteract the overproduction of oxidizing species such as H_2O_2 that may disrupt redox homeostasis leading to apoptosis.[2] GSH counteracts the generation of ROS

via enzymatic reaction with the glutathione peroxidase (GPx) enzyme.[3] Consequently, GSH is quickly becoming the target of new cancer therapies.1 In addition, the high intratumoral GSH concentrations (up to mM levels [4,5]) may interfere with emerging cancer therapies (chemodynamic- (CDT), sonodynamic- (SDT), and photodynamic (PDT)) therapy that are ROS-dependent and become less effective in the presence of increased GSH levels.[6] Nanocatalytic cancer therapy is rapidly emerging as a novel alternative able to trigger selective catalytic reactions in cancer cells to induce their apoptosis.[7,8] Transition metal nanocatalysts in particular are able to promote GSH depletion *via* oxidation mechanisms thereby interfering in the survival and protection mechanisms of cancer cells.[7] The ideal scenario involves catalytic materials that can eliminate antioxidant molecules such as GSH, while simultaneously promoting the generation of ROS. It is obvious that a deeper understanding of the role of nano- catalysts in the TME is critical to enhance their efficient action. However, this still represents a formidable challenge: the catalytic mechanisms of the most promising nanoplatforms and their interplay with key biomolecules remains elusive due to the complexity of the interactions in the TME.

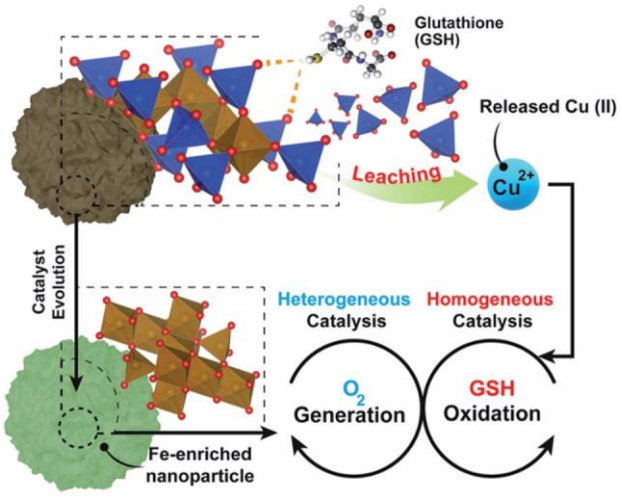

Figure 1. *Simplified overview of the homogeneous and heterogeneous processes fostered by the CuFe nanocatalyst in the presence of GSH. After a GSH-triggered Cu release from the nanocatalyst, Cu^{2+} catalyzes the homogeneous oxidation of GSH into GSSG. Simultaneously, Fe(III) species present on the nanoparticle surface catalyze the conversion of H_2O_2 and $\bullet O_2^-$ species, considered as by-products from GSH oxidation into O_2 necessary to sustain the GSH depletion homogeneous cycle.*

A fundamental aspect of the interaction between catalyst nanoparticles (NPs) and the TME that is often overlooked relates to the surface phenomena involved. In particular, leaching (*i.e.* metal ions lixiviated from the surface of the nanostructured catalysts into the surrounding fluid) is a

phenomenon likely to have a strong influence on the final therapy outcome. Previous investigations have aimed at designing nanoplatforms with pH-triggered metal ion lixiviation given the mildly-acidic TME.[9] The influence of acidity in metal lixiviation has been explored in several cancer related works for Fe,[10,11] Mn[12–14] or Cu.[15–20] It has also been shown that the complex chemical composition in biological environments includes molecular species such as amino acids, that may promote lixiviation especially in the case of Cu.[21–23] However, the role that these species may play as catalysts and the interactions with heterogeneous processes fostered by the solid phase have not been investigated.

Some valuable insights can be derived from conventional, aqueous phase catalysis. Eremin *et al.* [24] recently pictured an expanded vision of the nature of transition-metal-catalyzed reactions. These authors described the well-established scenarios of (i) molecular-based catalysis and (ii) nanoparticle-based catalysis (hetero- geneous catalysis) and presented three additional intermediate scenarios given by (iii) lixiviation-driven catalysis; (iv) "cocktail" of catalysts derived from the nanoparticle (clusters, atoms, lixiviated ions) and (v) dynamic catalytic systems. The action of the catalyst nanoparticles used in medical applications is generally interpreted on the premises of purely heterogeneous mechanisms. Only in a few cases, (*e.g.* MnO_2-based nanomaterials, where dissolution of the nano- oxide structure through reaction with GSH is followed by Fenton processes facilitated by the as-formed Mn^{2+} ions) an attempt has been made to describe processes closer to lixiviation-driven catalysis. It must be noticed that the nanoplatforms evaluated as catalysts for cancer therapy are usually composed by more than one metal, (*e.g.* Cu_2MoS_4,[25] $MnFe_2O_4$,[26] $CuFe_2O_4$,[27] copper/ manganese silicate,[17] $Cu_xFe_yS_z$ [28] or $SrCuSi_4O_{10}$ [20]) and these may be affected to a different extent by lixiviation phenomena under the mildly-acidic, hypoxic and GSH-enriched conditions prevalent in the TME. In any case, issues such as the extent of the lixiviation process, the possibility of a preferential leaching of a specific transition metal or the influence of specific chemical species present in the TME remain mostly unexplored. At present, is not possible to state whether the therapeutic action of nanocatalysts in the TME is attributable to lixiviated ions, a purely heterogeneous reaction, or a combination of both phenomena. Here, we have thoroughly evaluated the catalytic mechanisms behind the action of a copper–iron mixed oxide (CuFe) nanocatalyst under TME representative

conditions. This is a bimetallic system, complex enough to illustrate the main phenomena taking place. Our results shed light on the inter- play between heterogeneous and homogeneous processes occurring in the presence of GSH. We report for the first time how the presence of elevated levels of GSH induces a preferential lixiviation of Cu species, initiating a homogeneous catalytic cycle that efficiently oxidizes GSH into glutathione disulfide (GSSG), assisted by the *in situ* formation of Cu–GSH coordination complexes. Simultaneously, the progressively Fe-enriched NP gives rise to heterogeneous catalytic cycles using ROS generated in the homogeneous GSH oxidation cycle (***Figure 1***) or the overexpressed H_2O_2 present in the tumoral media.[29,30] The system chosen is of especial interest, considering the increasing relevance of Cu and its interaction with key processes in cancer development. [31] Overall, the results presented in this work provide new insight on the dynamics of the chemical reactions inside the TME and valuable clues for the design of more efficient catalysts to operate in this environment.

Results and discussion – Chapter 3

Cation leaching in the presence of GSH. The influence of GSH on the release of ionic Cu and Fe from the $CuFe_2O_4$ nanocatalyst was quantified by microwave plasma- atomic emission spectroscopy (see Experimental section for details). A concentration of GSH of 5 mM was selected for the experiments in order to mimic the average intracellular GSH levels reported in the literature for cancer cells.[32–35] The presence of GSH at a concentration of 5 mM changed considerably the leaching patterns. Thus, the release of Cu was strongly enhanced, with a cumulative release of *ca.* 70% of the initial Cu in the particle after 24 h (compared to about 20% in the absence of GSH). On the other hand, while Fe is not expected to be lixiviated significantly at this pH, we found that *ca.* 30% of the initial Fe content was released from the nanoparticle after 24 h (see ***Figure 2a***). We attribute this behaviour to the generation of high-energy vacancies after GSH-triggered Cu release that facilitates the transfer of Fe into the solution.[36] The fact that Cu release is favored in the presence of GSH is not totally unexpected, as previous works had reported Cu lixiviation from CuO nanoparticles in the presence of amino acids or peptides.[21,22] Interestingly, at lower pH values (pH of 5.80, close to the pH in a solid tumour medium) the extent of leaching for both Cu and Fe in the presence of GSH was reduced (***Figure 2b***), although the percentage of Cu

leached doubles that of iron. Considering the different ionic forms of GSH upon varying the pH [37] (***Figure 2c***), this behaviour can be linked to the stronger nucleophilic character of –SH group from GSH species as pH increases.[38] Compared to –SH, thiolate ($–S^-$) form exhibits much stronger nucleophile behaviour and the processes where $–S^-$ is involved may occur even at pH values far below thiol pK_a,[39] which may explain the promotion of Cu leaching at higher pH.

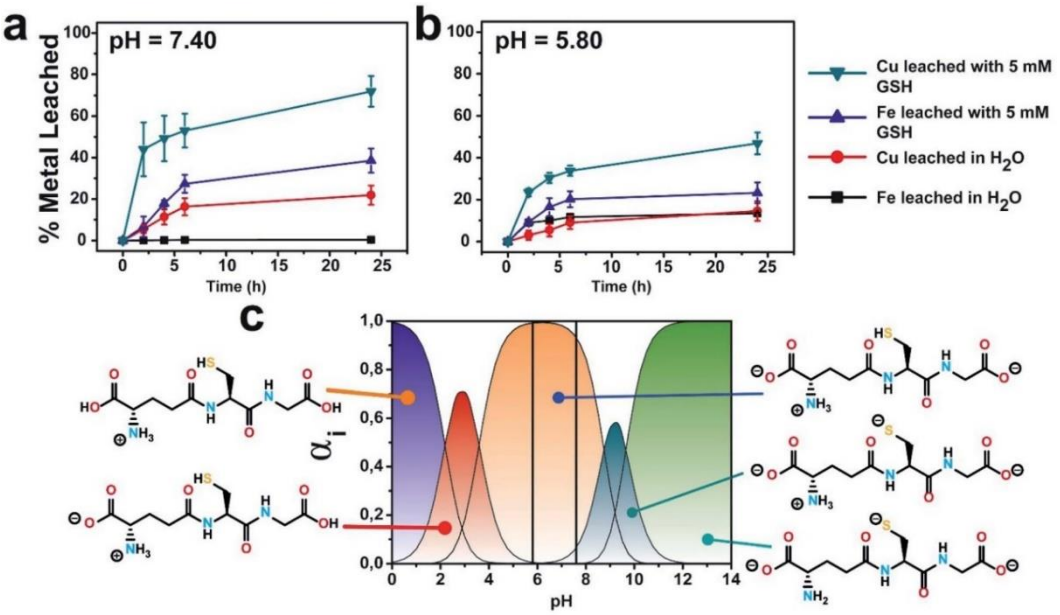

Figure 2. *GSH effect on the evolution of copper and iron cations lixiviated at different pH media: (a) pH 7.4; (b) pH 5.80; (c) different GSH ionic species as a function of different pH values; vertical lines represent the pH of selected experimental conditions for a better identification of expected GSH species; GSH concentration was set to 5 mM. Speciation diagram was generated using pKa values obtained from [40].*

Homogeneous GSH oxidation by cations leached from CuFe nanoparticles. After the abrupt cation release observed in the presence of GSH (***Figure 2a-b***) and its preferential action towards the lixiviation of Cu (roughly twice as much Cu is released, compared to Fe), it is reasonable to assume a catalytic scenario mainly composed by aqueous Cu^{2+} ions and GSH (5 mM).

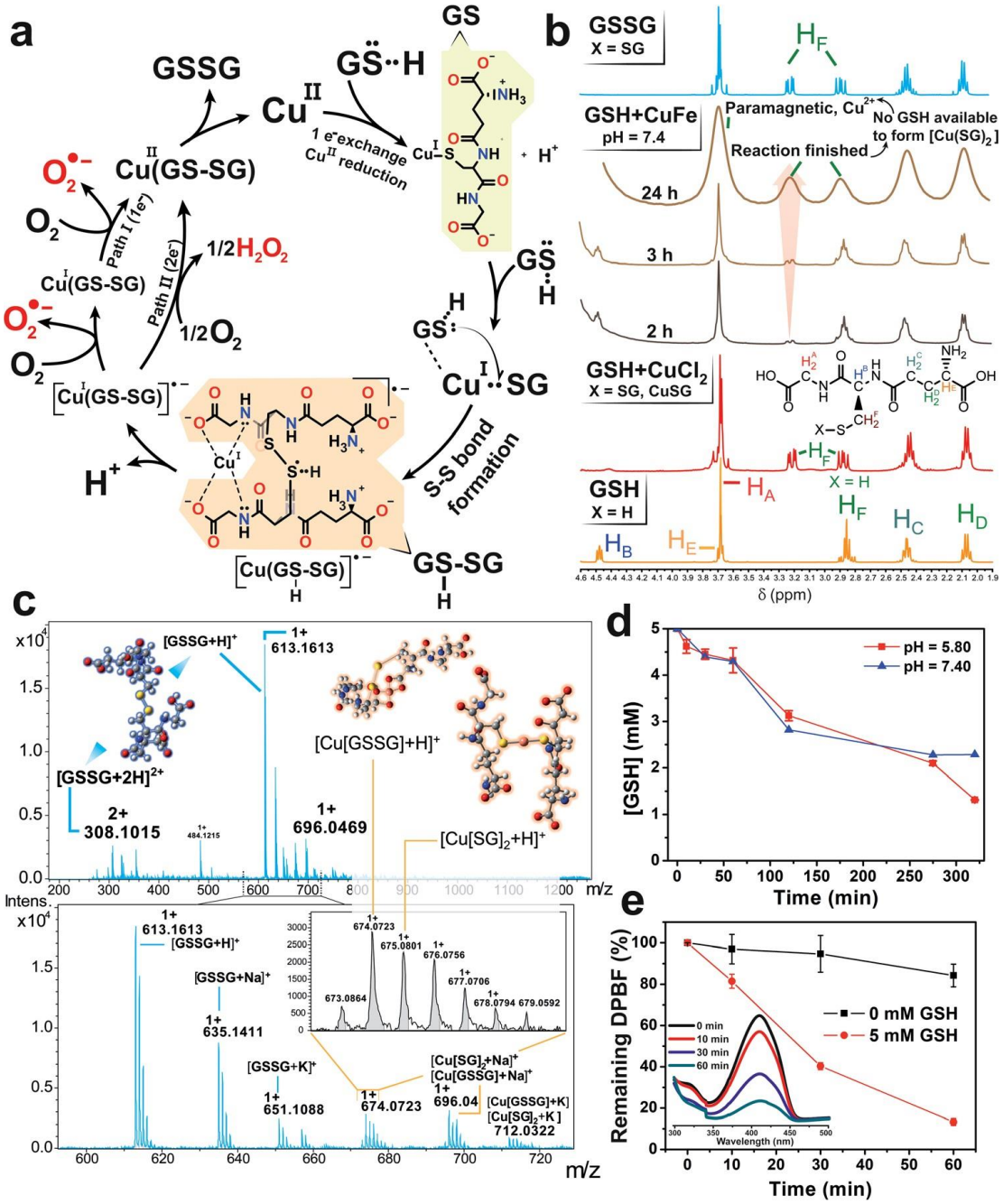

Figure 3. *Homogeneous catalysis of ionic Cu and GSH with O_2. (a) Proposed homogeneous catalytic cycle for the Cu-assisted GSH oxidation. The reoxidation of $Cu(SG)_2$ to Cu(GSSG) involves a reaction between the $Cu(GS–SG)^{\bullet-}$ complex and O_2, yielding superoxide radical species ($\bullet O_2^-$) as reaction by-product. The shaded areas correspond to the structure of GS and GS(H)SG, which are abbreviated for a better understanding; (b) ^{1}H NMR spectra of GSH, GSSG, GSH + $CuCl_2$ and GSH + CuFe at different reaction times (2, 3 and 24 h) with the corresponding proton assignments. ^{1}H NRM signal at 3.22 ppm implies a chemical modification near –SH group of the native GSH molecule, either $[Cu(SG)_2]^+$ or GSSG formation. ^{1}H NMR reaction spectra at 24 h is clearly altered due to*

paramagnetism induced by free Cu^{2+} in solution, since the reaction is complete and no GSH is available to coordinate Cu^{2+}; (c) HRMS-ESI from control experiments with $CuCl_2$ + GSH binary mixture in anaerobic conditions to quench the catalytic reaction. Two peaks at m/z = 613.16 and 635.14 corresponding to $[GSSG - H]^+$ and $[GSSG + Na]^+$ confirmed the generation of GSH oxidation product. The catalytic intermediate $Cu(SG)_2$ is detected at m/z = 674 and 675, respectively; (d) evolution of GSH concentration in the presence of the CuFe nanocatalyst at pH 7.40 or 5.80 (adjusted with HCO_3^-), 37 °C, $[GSH]_0$ 5 mM; [CuFe]=0.1 mg·mL^{-1}; (e) influence of GSH on the generation of anion superoxide species $\bullet O_2^-$ as side-product of the Cu-catalyzed GSH oxidation. The absorbance of DPBF at a wavelength of 411 nm was used as indirect probe; reaction conditions: pH=7.40 (adjusted with HCO_3^-), $[GSH]_0$= 5 mM, $[DPBF]_0$= 0.1 mM, [CuFe]=0.1 mg·mL^{-1}.

This is relevant because previous works have described a evolution of GSH into its oxidized form (GSSG) catalyzed by Cu^{2+}.[41] In this scenario, O_2 could act as electron acceptor yielding reduced reactive oxygen species ($\bullet O_2^-$ [42, 43] and H_2O_2 [41]) and GSSG as products, respectively (see ***Figure 3a***). Encouraged by these perspectives, we explored the possibility of fostering homogeneous oxidation processes using the cations released from our $CuFe_2O_4$ nanocatalyst, while retaining the heterogeneous catalytic activity of the nanoparticles themselves. In order to analyze the potential contribution of each lixiviated metal (Fe, Cu) in the homogeneous catalysis of GSH we performed a series of control experiments using chloride salt precursors ($CuCl_2$ and $FeCl_3$, respectively). We carried out ^{1}H-nuclear magnetic resonance (^{1}H-NMR) analysis of the mixture $CuCl_2$ + GSH (***Figure 3b***) to characterize the $Cu(SG)_2$ complex.[42–46] These assays were performed in the absence of O_2 to prevent the total evolution of the reaction to products. The resulting spectra revealed a splitting of the β-CH_2 protons of the Cys residue of GSH, appearing as an unresolved multiplet at 2.86 ppm into a well defined AB spin system at 3.22 and 2.88 ppm, due to the bonding of the S atom to the reduced Cu(I) center.[43,47] Other signals remained almost unchanged, suggesting that only the S atom is involved in bonding of GSH to Cu(I). This is in accordance with hard soft acid base theory (HSAB), soft-basic thiol (–SH) groups from GSH tend to bond soft-acidic Cu(I) centers.[48] Diffusion-ordered NMR spectroscopy (DOSY) experiments were also performed with GSH, GSSG and the $CuCl_2$ + GSH binary mixture to determine the molecular size of each molecule and complex intermediates present in the solution

based on their diffusion coefficients (D, $m^2 \cdot s^{-1}$). The diffusion coefficients from the control experiments with GSH and GSSG (Fig. S1a-b) were adjusted to $3.98 \cdot 10^{-10}$ and $2.75 \cdot 10^{-10}$ $m^2 \cdot s^{-1}$, respectively. Likewise, their corresponding hydrodynamic radii calculated through Stokes–Einstein equation were 0.6 and 0.9 nm. These values are in good agreement with intramolecular distances obtained in X-ray structures for GSH[49–51] and GSSG.[52,53] DOSY analysis of the $CuCl_2$ + GSH binary mixture yielded a product with a $D=2.75 \cdot 10^{-10}$ $m^2 \cdot s^{-1}$ (Fig. S2a). In the presence of Cu^{2+}, the species formed are larger than GSH (Fig. S1a) but of a similar size in comparison with GSSG (Fig. S1b). The complex $Cu(SG)_2$ is formed under these conditions,[42–46] which exhibit a rather analogous coefficient D with respect to GSSG. Also, we were able to confirm the formation of the Cu complex through the homogeneous catalytic cycle of ***Figure 3a*** using high resolution mass spectroscopy-electrospray ionization (HRMS-ESI) (***Figure 3c***), that allowed identification of peaks corresponding to $[GSSG + H]^+$ (m/z = 613.1613) and $[Cu(SG)_2 + H]^+$ (m/z = 675.0801). Ngamchuea et al.[41] studied the Cu(II)-mediated GSH catalytic oxidation and suggested a reaction pathway based on kinetic experiments where $Cu(SG)_2$, the same species detected in our control experiments (***Figure 3c***) also acted as reaction intermediate.

We also evaluated the potential contribution of Fe species to form complexes with GSH. In this case, control experiments with $FeCl_3$ were carried out at pH = 3.60 to minimize the formation of iron hydroxide species which interfere with NMR measurements and the introduction of species that are not normally present at physiological pH. ^{1}H-NMR and DOSY control experiments with $FeCl_3$ confirmed the formation of [Fe– $(SG)_x$] complexes (Fig. S3a-b), with proton chemical shifts at 3.04 and 2.76 ppm corresponding to assignments previously reported in the literature.54,55 In addition, HRMS-ESI analysis revealed the formation of $[Fe_2(SG)_2 + H]^+$ (m/z = 725.0352) and $[Fe(SG) + H]^+$ (m/z = 363.0173) complexes (Fig. S4).[54]

Once the formation of complexes with Cu and Fe cations were confirmed, analogous experiments with the CuFe nanocatalyst were subsequently carried out in the presence of GSH. The Cu lixiviated at pH 7.4 interacted with the excess of GSH like in the control experiments. ^{1}H-NMR and DOSY analysis of the solution (**Figure 3b** and Fig. S2b), revealed both the presence of unreacted GSH ($D = 4 \cdot 10^{-10}$ $m^2 \cdot s^{-1}$) and the formation of species with $D = 2.70 \cdot 10^{-10}$ $m^2 \cdot s^{-1}$. Taking into

account the control experiments with $CuCl_2$, the formation of the $Cu(SG)_2$ intermediates seemed also very likely in the presence of the CuFe catalyst. The widening on the spectra signals was attributed to different equilibria established between GSH and $Cu(SG)_2$.[45,56] The presence of very small amounts of para- magnetic [Fe–$(SG)_x$] complexes cannot be discarded, and could also contribute to the widened signal. MS-ESI analysis of the solution at different reaction times (3–24 h) yielded a mixture of Cu–SG-derived fragments (Fig. S5) supporting the hypothesis of Cu-SG as reaction intermediate in the catalytic cycle.

GSH levels were monitored via ultra performance liquid chromatography-photo diode array (UPLC-PDA) and revealed an important decrease at pH = 7.40 and 5.80 due to the catalytic activity of the Cu lixiviated by GSH (**Figure 3d**). Remarkably, the formation of H_2O_2 and $\bullet O_2^-$ were also detected in the presence of GSH (**Figure 3e**) using 1,3-diphenylisobenzofuran (DPBF) as analytical probe (see also Experimental section and scheme of the reactions in Fig. S6a)[57,58] The specific generation of $\bullet O_2^-$ was evaluated using dihydroethidium (DHE) (see Fig. S6a).[58–61] An enhancement of 20% of the fluorescence signal of oxidized DHE in the presence of 5 mM of GSH was found (Fig. S6b) in comparison to the control experiment in the absence of catalyst. Considering this set of experimental results we concluded that the simultaneous formation of H_2O_2 and $\bullet O_2^-$ was taking place during the catalytic GSH oxidation. These findings are also in agreement with other reports available in the literature[41,43,45,62] and allowed us to propose a homogeneous catalytic reaction taking place mainly between the Cu^{2+} cations released from the CuFe catalyst and GSH (reaction step displayed in **Figure 3a**): (i) GSH is able to bind and reduce aqueous Cu^{2+} species into Cu^+ through –SH group to form the $Cu^I(SG)$ intermediate; (ii) a second GSH molecule is able to cleave the Cu–S bond to promote S–S formation through a radical process.[39] This step is thermodynamically favoured since S–S bond energy is larger in comparison to Cu–S (429 vs. 285 $kJ{\cdot}mol^{-1}$, respectively[63]). Following reported thiol oxidation kinetics,[39] we propose the (iii) formation of the radical intermediate $[Cu^I(GSSG)]^{\bullet-}$. O_2 acting as electron acceptor withdraws one/two electron from this disulfide radical anion (Fig. S7) (iv) to yield the superoxide anion $\bullet O_2^-$ (path I, one electron) or H_2O_2 (path II, two electrons) that we have been able to detect together with $Cu^I(GSSG)$. After this fast electron transfer, (v) the Cu^I center rapidly oxidizes into Cu^{II} in the presence of O_2.[45] (vi) The catalytic cycle is restored after

GSSG is detached from the coordination sphere of Cu^{II} and replaced by a fresh GSH molecule. In the presence of a GSH excess, the Cu^{II}(GSSG) complex exchanges GSSG by GSH to restart the catalytic cycle.[45] This process is also thermodynamically favoured, since the formation constant (log K_0) of $Cu(SG)_2$ is significantly higher (26.6)[64] than Cu(GSSG) (3.63).[65] The appearance of the $Cu(SG)_2$ complex is also favored by pH values typically met in a tumour microenvironment (Fig. S8-9). Although the lixiviation of Cu triggered by GSH proceeds at a slower pace at pH = 5.80 (see ***Figure 2b***), the percentage of Cu leached after 2 h of reaction reached ~25%, enough to produce the oxidation of roughly half of the initial GSH at that time (***Figure 3d***). Furthermore, lower pH values may also increase the reaction rate of Fenton and Fenton-like processes related to the Cu and Fe[28,32,66] and enhance the GSH oxidation rates via ROS formation.

Similarly, to the control experiments carried out with $FeCl_3$, the experiments between CuFe and GSH excess were carried out under acidic conditions. After 3 hours of reaction, ^{1}H-NMR analysis (Fig. S3a) showed no meaningful fractions of GSSG/Fe(SG) complex formed. UPLC-PDA and MS-ESI analyses further corroborated the lower conversion of GSH in the presence of lixiviated Fe ions (Fig. S10 and Fig.S11, respectively). While an increase of the $[Fe(SG) + H]^+$ signal was found after 24 h of reaction (Fig. S8a) a significant concentration of GSH was still present (Fig. S8b) These GSH-oxidation results together with previous MP-AES results at neutral pH (***Figure 2a***) further suggest a limited influence of Fe in the homogeneous conversion of GSH. Two factors are key to justify these phenomena: (i) the much larger standard reduction potential of $Fe^{3+/2+}$ (E_0 = +0.77 V compared to +0.153 V for $Cu^{2+/+}$) implies a comparatively slower catalytic cycle since the regeneration of Fe^{3+} species to restart the cycle requires a higher energy demand, an energy penalty analogous to that observed in Fenton-like processes;[67] (ii) the scarcity of labile Fe^{3+} available, both due to its slower leaching rate compared to Cu (***Figure 2a***) and to the fact that at physiological pH released iron tend to rapidly form $Fe(OH)_3$ species.[68]

Heterogeneous O_2 generation of the Fe-enriched solid nanoparticles. Given the strong Cu release in comparison with the much less intense Fe lixiviation, we investigated the morphological and catalytic properties of the progressively Fe-enriched nanoparticles. After the interaction with GSH, most of Cu present in the NP is lixiviated into the aqueous media (see ***Figure 2a***).

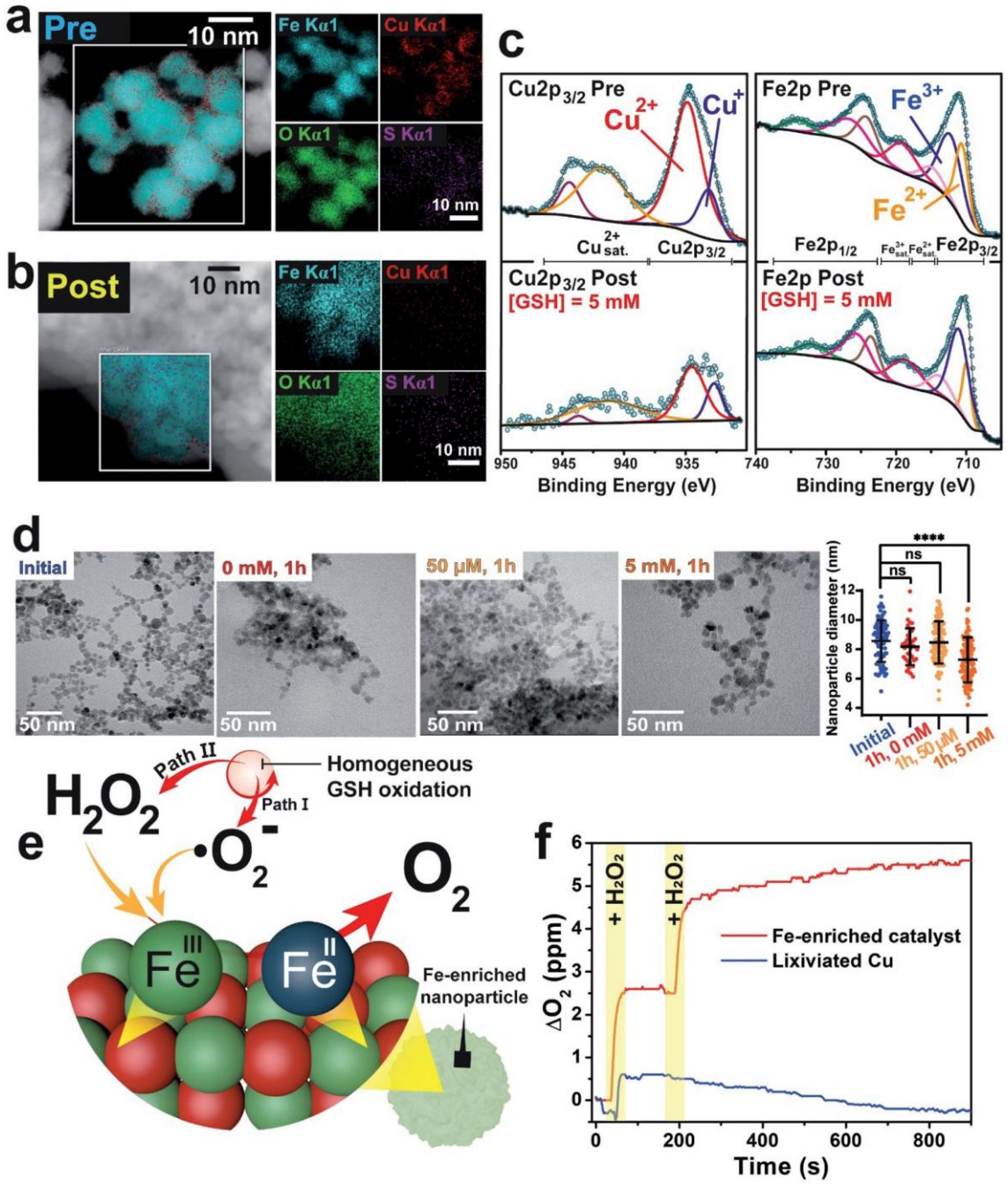

Figure 4. *Heterogeneous catalysis on the Fe-enriched nanoparticle surface: (a) and (b) STEM-EDX images before/after catalyst interaction with GSH. Prior to the GSH-triggered lixiviation of Cu, Fe and Cu co-localize within the crystalline network of the nanoparticle oxide. However, after GSH exposition, Cu starts to be released and its presence in the nanoparticle is strongly reduced; (c) X-ray photoemission spectra corresponding to the Cu 2p3/2 and Fe 2p regions before and after reaction of the CuFe nanocatalyst with GSH; as a consequence of leaching process, the intensity of Cu signal is close to noise; (d) TEM images of the CuFe nanocatalyst after 1 hour incubation with different GSH*

concentrations relevant at the intracellular and extracellular levels. Size analysis of individual nanoparticles reveals a certain reduction of size in the presence of larger GSH concentrations (5 mM); (e) scheme showing the transformation of the by-products generated via aerobic GSH oxidation into O_2 in the presence of the solid Fe-enriched catalyst that enables the regeneration of O_2 as electron acceptor to sustain the GSH oxidation cycle; (f) O_2 generation capabilities of the Fe-enriched nanoparticles and of the supernatant containing leached Cu cations after the addition of H_2O_2; experimental conditions: pH = 7.40; $[H_2O_2]_0$ = 1 mM, [CuFe] = 0.1 mg·mL^{-1}; addition of H_2O_2 is highlighted.

This was confirmed by high-angle annular dark field-scanning transmission electron microscopy (HAADF-STEM) and energy dispersive X-ray spectroscopy (EDX) mapping analysis of the NPs before (***Figure 4a***) and after (***Figure 4b***) reaction, revealing a very significant Fe enrichment following the preferential leaching of Cu after its interaction with GSH. X-ray photoelectron spectroscopy (XPS) analysis of the CuFe nanocatalyst further confirmed the strong reduction of the atomic percentage of Cu at the surface in comparison with the original sample (0.28 atomic% Cu after exposure, compared to 7.80 before, a 28-fold decrease, see Tables S1-S2). This was further sup- ported by the significant reduction of the Cu $2p_{3/2}$ photoemission contribution after incubation with GSH (***Figure 4c***).

In addition, the oxidation state of Cu was strongly affected by the process. The remaining Cu content was enriched in Cu^+ as shown by the ratios of the contributions at 932.6 and 934.3 eV due to the reduction capability of GSH,[69] compared to the original sample with a higher ratio of Cu(II) to Cu(I) states.[70] In contrast, the Fe surface atomic percentage slightly increased (see Tables S1-S2). TEM analysis of the CuFe nanocatalyst after one hour of incubation with different GSH concentrations revealed that some NP size reduction takes place in the presence of average intracellular GSH concentrations (*i.e.* 5 mM) as a consequence of metal leaching (***Figure 4d***). XRD analysis showed an important decrease of the intensity corresponding to the (400) diffraction peak[71] which accounts for the crystalline plane that includes four tetrahedral Cu sites (Fig. S12). This reduction is also consistent with the selective loss of copper sites upon the

incubation with GSH (***Figure 2***). In contrast, the Fe-enriched remaining solid nanoparticle matches well with the XRD patterns of Fe_3O_4 and $CuFe_2O_4$ (Fig. S12a).

Fe-based oxides have been reported as active catalysts to transform ROS species, such as $\bullet O_2^-$ [72,73] or H_2O_2 [7, 27, 74] into H_2O_2 and O_2, respectively. Specifically, both species ($\bullet O_2^-$ and H_2O_2) are interesting in our system. $\bullet O_2^-$ is a reaction side-product resulting from the homogeneous catalytic cycle (***Figure 3b***) and H_2O_2 is both an intratumoral overexpressed molecule[75,76] and a reported by-product of Cu-catalyzed GSH oxidation in the homogeneous phase.[41] Thus, the Fe-enriched fraction of the heterogeneous CuFe catalyst was not a mere spectator of the homogeneous catalytic cycle. On the contrary, it became an active agent in generating O_2 from H_2O_2 under hypoxic conditions (*i.e.* low O_2 concentration) that prevail in TME (***Figure 4e***). This is clearly shown in ***Figure 4f***. After each H_2O_2 injection a clear increase in the concentration of dissolved O_2 was observed in the presence of the Fe-enriched catalyst, acting as a catalase-mimicking surrogate. This experiment rendered the opposite result when carried out in the presence of the Cu leachate from the catalyst, where no O_2 generation could be observed (***Figure 4f***). The generated O_2 allowed to complete and sustain the homogeneous GSH-oxidation cycle, which needs O_2 as final electron acceptor.[77] We also evaluated the potential capability of this Fe-enriched catalyst to transform $\bullet O_2^-$ into O_2. KO_2 was selected as superoxide source. In spite of the rapid self-dismutation of $\bullet O_2^-$ itself in the control experiments,[78] the contribution of the catalyst could be clearly distinguished at longer reaction times (Fig. S13). Interestingly, while the Fe-enriched solid nanocatalyst was able to decompose H_2O_2 into O_2 (***Figure 4f***), it showed negligible activity towards •OH production *via* Fenton-like processes when tested with methylene blue (MB) (Fig. S14).

Interplay between homogeneous and heterogeneous catalysis in healthy and cancer cells with different GSH levels. To evaluate the biological action of the CuFe nanocatalyst, additional experiments were carried out against different cell lines. Different cancer cell lines were specifically selected for their intrinsic high GSH levels, while healthy cell lines (i.e. fibroblasts and mesenchymal cells) with lower GSH concentrations were used as control.[79,80] Specifically, four different tumour cell lines were chosen to assess the cytotoxic effect of this nanocatalyst: U251-

MG and U87-MG (both malignant glioblastoma cell lines), SKOV-3 (ovarian cancer cell line) and HeLa (cervical cancer cell line). The aim of the study was to compare the behaviour of cell lines against the action of our nanocatalyst, since we could expect variable effect depending on their specific GSH content (***Figure 5a***).

The results of the cytotoxicity studies after different incubation times with the CuFe nanocatalyst (***Figure 5b***) revealed a clear effect: the viability of the four tumour cell lines was reduced, even at the lower concentrations of the catalyst and shorter incubation times (see ***Figure 5b***). In contrast, the non- tumoral cell lines remained viable in the presence of much higher concentrations of the catalyst. The 50% cytotoxic concentration (CC50) determined for the CuFe nanocatalyst was significantly lower in the cancer cell lines than in the healthy ones (***Figure 5b*** and Table S6). In addition, the monitoring and quantification of intracellular GSH levels in U251-MG and HeLa cell (cancerous) and hpMSC (healthy) cell lines helped to correlate with their respective viabilities in the absence and presence of the CuFe nanocatalyst (***Figure 5b***). The corresponding GSH intracellular levels were quantified following a recently optimized protocol by Bonet-Aleta et al.[32] (see Experimental section). Both cancer cell lines (i.e. U251-MG and HeLa) showed a significant decrease in GSH levels (40.6 and 20.6%, respectively) while GSH levels of the evaluated healthy cell line remain unaltered. This behaviour may be attributed to the differences between the intracellular GSH concentration levels of cancer and healthy cell lines, respectively.[32,33] Catalytic conversion differences between U251-MG and HeLa may arise from distinct responses from different cells under a GSH-deprivation scenario. For instance, HeLa cell line treated with Cu salts at normal cysteine levels raise their intracellular GSH levels increasing its biosynthesis, which may be reflected as a reduced catalytic conversion.[81,82] Representative optical (Fig. S15) and confocal microscopy (***Figure 5c***) images of these cell lines treated with 25.0 $mg \cdot mL^{-1}$ at 24 h confirmed the internalization of the catalyst within all cell lines to trigger the above described catalytic cycle. Regarding the CuFe NPs internalization route, it has been widely reported that the internalization of both Cu or Fe-based nanomaterials mainly occurs through endocytosis[23] (*via* clathrin-mediated pathway[83]).

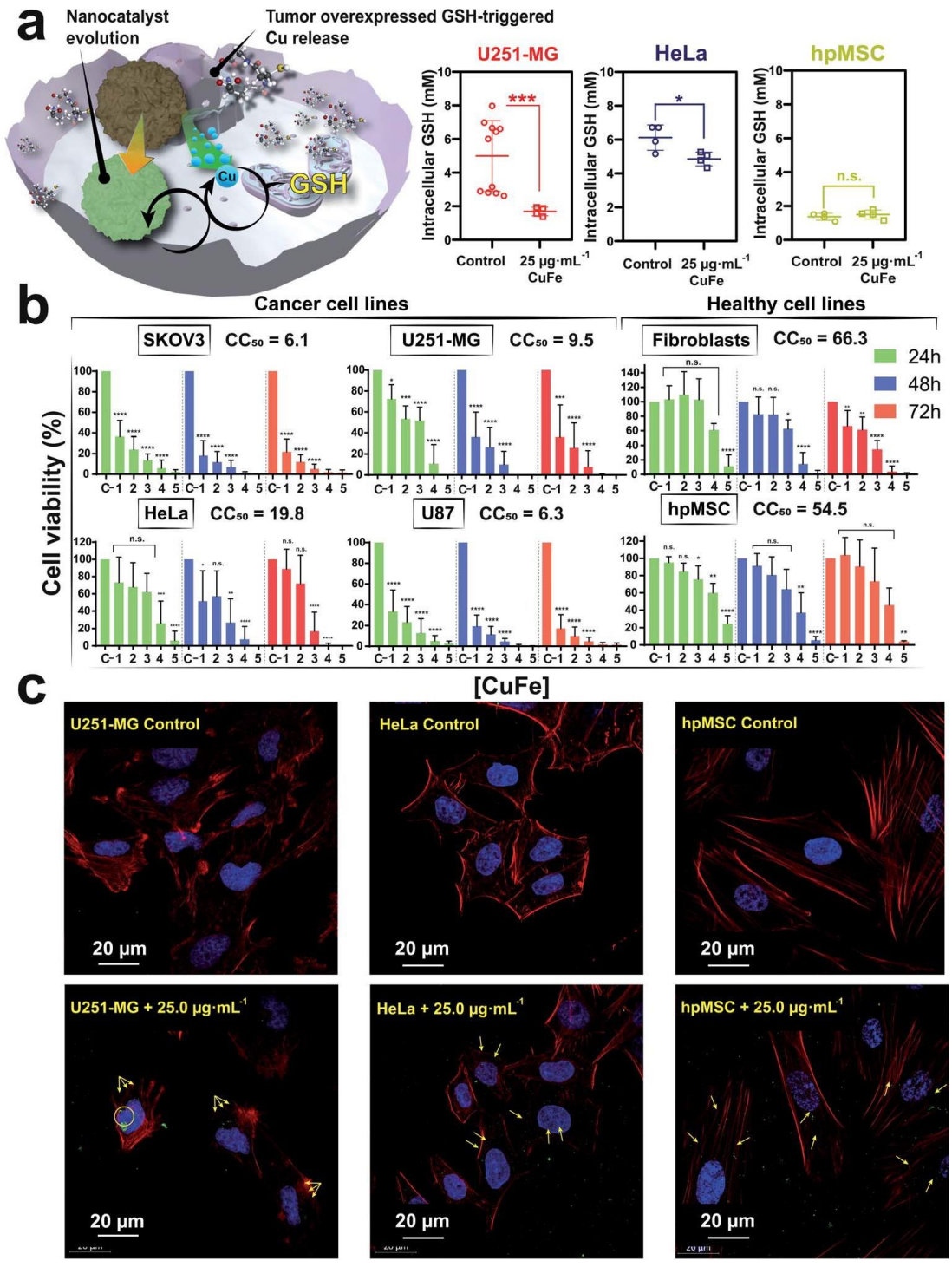

Figure 5. *Cancer cell lines with overexpressed GSH levels are intensely affected by CuFe-triggered catalysis. (a) Left: scheme of catalyst evolution inside the cell, highlighting the role played by GSH; Right: intracellular GSH concentration levels detected for U251-MG, HeLa and hpMSC cell lines before and after 24 h of incubation with 25.0 mg·mL^{-1} of CuFe nanocatalyst. Statistical analysis revealed significant differences for cancer cells with higher GSH levels (i.e. U251-MG and HeLa) in comparison to hpMSC, which likely enhance GSH-related pathways, affecting cell viability; (b) cell*

viability study of CuFe nanocatalyst with different cancer (SKOV-3, U251-MG, HeLa and U87) and non-tumoral (hpMSC and fibroblasts) cell lines. CC50 values stand for the cytotoxic concentration to kill 50% of cell populations after 48 h of incubation; [CuFe] concentration for each experiment was (1) 12.5 mg·mL^{-1}; (2) 25.0 mg·mL^{-1}; (3) 50.0 mg·mL^{-1}; (4) 100 mg·mL^{-1} and (5) 200 mg·mL^{-1}; (c) confocal microscopy images corresponding to the U251-MG, HeLa and hpMSC cell lines before and after the incubation with CuFe NPs for 24 h using 25.0 mg·mL^{-1} of nanocatalyst; (actin firers are displayed in red after staining with phalloidin-Alexa 488, nuclei are shown in blue and stained with DAPI and CuFe appear in green colour, pointed by yellow arrows and seen by reflection).

However surface coating also plays a key role, since for Fe_xO_y NPs coated with BSA and PEG, clathrin- or caveolin-mediated endocytosis were favoured, respectively.[84] Moreover, the use of DMSA as coating agent has been also reported as a way to boost the uptake efficiency for Fe_2O_3 NPs.[85] Up to now, the interaction between Cu and Fe based nanoparticles and GSH has been either interpreted from the perspective of a heterogeneous process taking place at the nanoparticle–liquid interface or directly neglected. We have detected both $\bullet O_2^-$ and H_2O_2 as the reaction by-products of Cu-catalyzed GSH oxidation, which is consistent with literature.[41,45,62,86] This reaction is taking place homogeneously with leached Cu species, *i.e.* while GSH interacts with the surface to produce the release of Cu(I) species, the GSH oxidation itself would be a homogeneous process taking place in the bulk of the solution and not on the catalyst particle. However, both reaction by-products $\bullet O_2^-$ and H_2O_2 can interact with the remaining Fe-enriched nanoparticle which acts as an heterogeneous catalyst yielding O_2, which in turn is necessary to sustain the homogeneous GSH oxidation.

Taking into account the above results, we propose the following reaction mechanism (see ***Figure 6***): (i) in a first step, nucleophilic thiol (–SH) groups from GSH promote the release of Cu species from the nanocatalyst crystalline network. GSH overexpressed in TME forms a coordination complex with released Cu, ($Cu(SG)_2$). The formation of this complex effectively removes free Cu(I) species from the environment, shifting liquid phase equilibria and increasing the rate of Cu leaching; (ii) the $Cu(SG)_2$ complex starts a homogeneous catalytic cycle where GSH is finally oxidized to GSSG by dissolved O_2. This latter process entails a one/two electron transfer

from $[Cu^{I}(GSSG)]^{\bullet-}$ to O_2, promoting the generation of H_2O_2 and $\bullet O_2^-$ species which readily (iii) react with the Fe^{III} sites remaining in the solid nanocatalyst through a Haber–Weiss reaction[87,88] to regenerate O_2 that feeds the homogeneously Cu-catalyzed reaction. Moreover, additional O_2 is produced by the Fe-enriched catalytic NP using the intracellular H_2O_2 (***Figure 4f***). Finally, (iv) GSSG is released from the coordination sphere of Cu^{2+}, which becomes available to be reduced by GSH and re-start the catalytic cycle. The proposed mechanism constitutes a perfect example of how two catalytic processes, namely the homogeneous Cu-catalyzed GSH oxidation and the heterogeneously catalyzed processes of H_2O_2 decomposition and $\bullet O_2$ reaction are synergistically coupled to produce the efficient oxidation of a key tumour metabolite (GSH) allowing to circumvent O_2-scarcity in the TME.

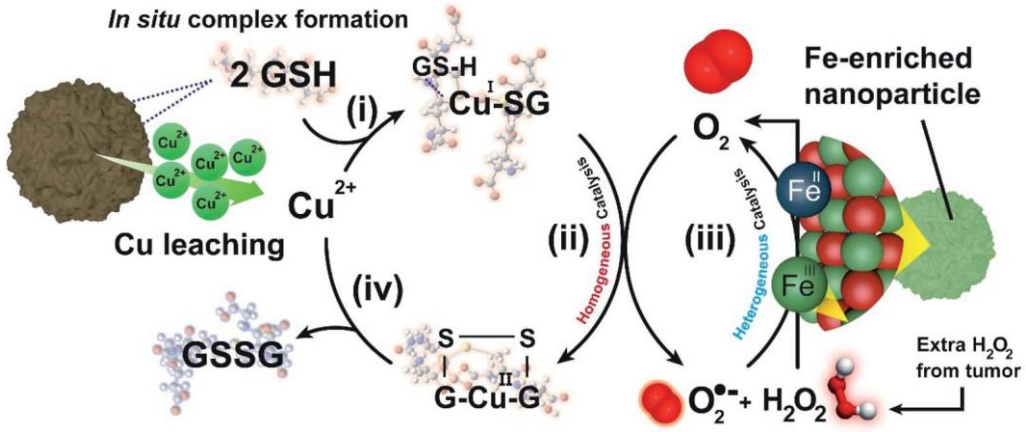

Figure 6. *Complete homogeneous-heterogeneous interplay for the CuFe nanoparticles in the presence of GSH and O_2: (i) in a first step, GSH triggers Cu-release from the spinel nanostructure (ii) excess GSH is able to form an coordination complex with Cu through thiol (–SH) groups to stabilize Cu^{I} (iii) molecular O_2 accepts electrons from $Cu(SG)_2$ complex to yield O_2 reduced species (H_2O_2 or $\bullet O_2^-$, depending on the number of electrons transferred) and Cu(GSSG); (iv) in a heterogeneously coupled process, as-generated H_2O_2 and $\bullet O_2^-$ donates electrons to the remaining Fe-enriched surface of the solid heterogeneous nanocatalyst in a process that generates oxygen needed for step (iii). Moreover, intratumoural H_2O_2 decomposes on the Fe-enriched catalyst, contributing additional oxygen generation.*

Conclusions – Chapter 3

Processes promoted by heterogeneous catalysts are not necessarily of a purely heterogeneous nature. Here we demonstrate that a combination of homogeneous and heterogeneous processes can originate from a copper–iron based nanocatalyst under conditions that are relevant in the tumour microenvironment. The main part of the contributing reactions take place in a homogeneous cycle catalyzed by released Cu species. The results shed light on the complexity of the processes taking place in developing fields such as nanocatalytic cancer therapy. As demonstrated in this work for a CuFe hybrid nanocatalyst, lixiviation mechanisms induced by specific biomolecules with a strong presence in the TME such as GSH may lead to new catalytic scenarios where homogeneous and heterogeneous processes are no longer unrelated events. This means that catalyst design becomes more complex, since it has to take into account the effect of environmental species on the stability of the catalyst, but also more powerful, since leaching processes can be engineered to yield synergistic catalytic actions. Under this scenario, the design of the catalyst will consider not only its ability to favour specific surface reactions, but also its role as a reservoir for the long-term release of active ions in response to stimuli from the chemical environment. This point of view will be key to develop novel nanoparticles capable of acting as successful bio-orthogonal catalysts.

Experimental section – Chapter 3

Chemicals and materials. Iron(III) chloride hexahydrate ($FeCl_3 \cdot 6H_2O$, 97%), copper(II) chloride dihydrate ($CuCl_2 \cdot 2H_2O$, 99.0%), sodium acetate anhydrous (CH_3COONa, 99.0%), bovine serum albumin (BSA), ethylene glycol (EG), dimercaptosuccinic acid (DMSA, 99.0%), glutathione, glutathione oxidized (GSSG, 98.0% HPLC), 5,5'-dithiobis(2-nitrobenzoic acid) (DNTB), hydrogen peroxide (H_2O_2, 33% v/v), sodium bicarbonate ($NaHCO_3$, 99%), methylene blue (MB, 95.0), dihydroethidium (DHE, 99%), potassium dioxide (KO_2, >99%), trichloroacetic acid (CCl_3COOH, >99%) and tris(hydroxymethyl)aminomethane (TRIS, >99%) were purchased from Sigma Aldrich. Acetonitrile (ACN) was purchased from WVR (Avantor). UPLC grade water was obtained from a Milli-Q Advantage A10 System with resistivity of 18.2 mΩ (Merk Millipore, Germany). Phalloidin-

Alexa 488 was acquired from Molecular Probes (A12379) and Fluoromount-G + DAPI from EMS (17984-24). Dulbecco's modified Eagle medium (DMEM) was purchased from Lonza (Ref. 12-614F). Dulbecco's phosphate buffered saline (DPBS 1x, Ref. 17-512F) and PBS (Ref. BE02-017F) were also purchased from Lonza.

***Characterization techniques*.** Transmission electron microscopy (TEM) was performed using a FEI TECNAI T20 microscope operated at 200 keV. High- resolution transmission electron microscopy (HRTEM) was performed using a FEI Titan (80–300 kV) microscope at an acceleration voltage of 300 kV. In both cases samples were prepared by drop casting 5 mL of the nanoparticle suspension on a holey carbon TEM grid. UV-vis spectra were obtained on a UV-vis double beam spectrophotometer Jasco V67. X-ray photoelectron spectroscopy (XPS) was performed with an Axis Supra spectrometer (Kratos Tech). The samples were mounted on a sample rod placed in the pretreatment chamber of the spectrometer and then evacuated at room temperature. The spectra were excited by a monochromatized Al Ka source at 1486.6 eV and subsequently run at 8 kV and 15 mA. A survey spectrum was acquired at 160 eV of pass energy, and for the individual peak regions, spectra were recorded with a pass energy of 20 eV. Analysis of the peaks was performed with the CasaXPS software using a weighted sum of Lorentzian and Gaussian component curves after Shirley background subtraction. The binding energies were referenced to the internal C 1s standard at 284.5 eV. X-ray diffraction (XRD) patterns were obtained in a PANalytical Empyrean equipment in Bragg–Brentano configuration using Cu Ka radiation and equipped with a PIXcel1D detector. ^{1}H spectra (D_2O) were recorded at 25 ^{o}C using a Bruker Avance 400 MHz NMR spectrometer with TMS as the internal standard and deuterated water as solvent in a 5 mm QNP probe. Nanoparticle tracking analysis was measured on Malvern Nanosight 300.

Synthesis of CuFe-DMSA nanoparticles. $CuFe_2O_4$ nanoparticles were synthesized *via* a templated-growth method.[32] Firstly, 250 mg of BSA were dissolved in 2.5 mL of Milli-Q water and consequently 12.5 mL of ethylene glycol were added. After that, 270.0 mg of $FeCl_3{\cdot}6H_2O$, 85.0 mg of $CuCl_2$ and 375.0 mg of CH_3COONa were added into the reaction vessel. Reaction was kept stirring for 2 h at room temperature to ensure a correct binding of BSA–nucleophile groups to the

metallic ions. Then, the reaction was transferred to a Teflon autoclave and the temperature was set to 180 °C for 24 h. Finally, the product was centrifuged at 12 000 rpm for 20 min. 20 mL of a 25 mM solution of DMSA were poured to the reaction pellet and the dispersion was assisted with ultrasonication. 5 mL of 0.7 M NaOH solution were added to ensure the correct DMSA dissolution to decorate the nanocatalyst surface. The final product was purified by two centrifugation cycles at 12 000 rpm for 20 min. The nanocatalyst was stored at 4 °C for further use. CuFe nanocatalysts were synthetized using bovine serum albumin (BSA) as template27,89 and ethylene glycol (EG) as a solvent to modulate particle size.90 The abundance of nucleophile functional groups in the BSA (–COO–, $–NH_2$) can chelate the metal ions (Cu^{2+}, Fe^{3+}) and serve as starting point to growth the nanostructure. Although the distribution size of the nanoparticles is homogeneous, these nanoparticles suffer from aggregation in aqueous media, which may hinders cell internalization.[91] As shown previously by Miguel-Sancho *et al.*,[92] DMSA functionalization enhanced the dispersion and stability of the nanoparticles in aqueous media (Fig. S16 and Fig. S17). The synthesis of these materials has been performed at the Platform of Production of Biomaterials and Nanoparticles of the NANBIOSIS ICTS, more specifically by the Nanoparticle Synthesis Unit of the CIBER in BioEngineering, Biomaterials & Nanomedicine (CIBER-BBN).

Metal leaching study by microwave plasma-atomic emission spectroscopy (MP-AES). Each solution was prepared in an Eppendorf tube with CuFe– DMSA nanoparticle at a concentration of 0.1 mg ·mL^{-1} (total volume = 1 mL). The different solutions were introduced in an Eppendorf thermoshaker at 37 °C and constant stirring of 400 rpm. At every time point (2 h, 4 h, 6 h, 24 h), samples were centrifuged at 13 300 rpm during 300, and the supernatants were collected for further analysis. The nanoparticle pellet was resuspended with the corresponding solution, until the next analysis cycle, where the procedure was repeated. At the experiment endpoint, the supernatant samples were analyzed together with final nanoparticle pellet, to close mass balances and elucidate how much metal moved to the solution. All the samples were digested with HCl:HNO_3 (3:1) mixture overnight. Cu and Fe concentrations were determined through the analysis with Agilent 4100 MP-AES.

^{1}H-NMR study of the CuFe-GSH interaction. The interaction study of leached metals (Cu, Fe) with GSH was performed by the ^{1}H-NMR and DOSY analysis of different reaction mixtures. For $CuCl_2$–GSH experiments, the pH was fixed to 7.4 (buffer Na_2HPO_4/KH_2PO_4) and the molar ratio $CuCl_2$:GSH was set to 1:4 ([GSH] = 20 mM, $[CuCl_2{\cdot}2H_2O]$ = 5 mM). For $FeCl_3$–GSH experiments, the pH was not fixed (pH = 3.60) and the molar ratio $FeCl_3$: GSH was set to 1:4 ([GSH] = 20 mM, $[FeCl_3{\cdot}6H_2O]$ = 4 mM). The reaction mixtures were analyzed after incubation for 5 minutes. For CuFe + GSH experiments, molar ratio CuFe : GSH was 1 : 44 ([GSH] = 20 mM, $[CuFe_2O_4]$ = 0.5 mM). Reaction were incubated at pH=7.4 (Na_2HPO_4/KH_2PO_4) and pH=3.70 (free pH) for 3 and 24 h. All samples were filtered before analysis.

Mass spectroscopy analysis of the reaction. ESI (ESI+) mass spectra were recorded using an Esquire 3000 ion-trap mass spectrometer (Bruker Daltonic GmbH) equipped with a standard ESI/APCI source. Samples were introduced by direct infusion with a syringe pump. Nitrogen served both as the nebulizer gas and the dry gas. The HRMS mass spectra were recorded using an MicroToF Q, API-Q-ToF ESI with a mass range from 20 to 3000 *m/z* and mass resolution 15 000 (FWHM). Samples prepared for ^{1}H-NMR/DOSY experiments were analyzed by using this methodology.

Catalytic GSH depletion. Catalytic activity towards GSH oxidation of CuFe–DMSA nanoparticles was evaluated according to the following protocol. 5 mM of GSH were mixed with 0.1 $mg{\cdot}mL^{-1}$ of CuFe–DMSA in a total volume of 2.5 mL. GSH concentration at different reaction times was measured by UPLC-PDA. 20 mL of reaction were mixed with 100 mL of 1 mM 5,5'-disulfanediylbis(2-nitrobenzoic acid) (DTNB) and 880 mL of 0.01 M 2-amino-2-hydroxymethyl-propane-1,3-diol (TRIS). Standards for the calibration curve were prepared following Table S5.

UPLC-PDA-MS equipment for GSH quantification. GSH analysis were performed on Waters ACQUITY system H-Class which consisted of a binary pump, an autosampler, a column thermostat and a photodiode array (PDA) detector. This system is coupled to a photo diode array (PDA) detector to monitor absorbance from derivatized GSH at 412 nm during analysis time. Data acquisition and processing were performed by using MASSLYNX software (Waters Corporation, USA). In order to analyze GSH from derivatized samples as describe below, chromatographic

separation was performed using an ACQUITY UPLC BEH C18 column (130 A, 1.7 mm 2.1 x 50 mm, from WATERS) at 40 °C under an isocratic flow of 0.3 mL·min^{-1} containing 50% acetonitrile, 50% Milli-Q water.

Generation of hydrogen peroxide H_2O_2 and superoxide radicals $\bullet O_2^-$. 1,3-Diphenylisobenzofuran (DPBF) was employed as a probe to measure the production of H_2O_2 and $\bullet O_2^-$ during homogeneous GSH oxidation. 20 mL of 10 mM DPBF solution (in ethanol) were added to 2.5 mL of a mixture ethanol: PBS(1x) 2:1. Catalyst and GSH concentration were 0.1 mg·mL^{-1} and 5 mM, respectively. UV-vis analysis of remaining DPBF was performed after centrifuging the sample (100 µL of reaction + 400 µL mixture ethanol : PBS 1x) at 13 000 rpm for 50. Selective $\bullet O_2^-$ detection was carried on using dihydroethidium (DHE) as a probe. [42,59–61] 15 µL of concentrated DHE solution was added to a Na_2HPO_4/ KH_2PO_4 buffer solution (pH 7.4) to reach a final concentration of 100 µM. Catalyst and GSH concentration were 0.01 mg·mL^{-1} and 5 µM, respectively. 500 µL were centrifuged, and 400 µL of the supernatant were mixed with 1000 µL PBS and measured on a LS 55 fluorescence spectrometer (PerkinElmer). I /I = 480 nm/500–700 nm, slit-widths of 10 nm for both excitation and emission wavelengths.

Analysis of O_2 consumption/generation. Molecular O_2 was measured with a NeoFox oximeter equipped with FOSPOR-R probe. In order to analyze the O_2-generation capabilities of the remaining nanoparticle, CuFe (0.1 mg·mL^{-1}) was incubated with 5 mM of GSH (pH = 7.40) for 3 h to induce selective Cu-release. The solution was centrifuged at 13 300 rpm for 100 to separate homogeneous and heterogeneous catalysts to analyze their individual catalytic activity towards O_2 production using $[H_2O_2]_0$ = 1 mM. To check O_2 production using KO_2, the heterogeneous catalyst was mixed with 100 µM KO_2 at pH = 7.40 (adjusted with Na_2HPO_4/KH_2PO_4 buffer).

Cell culture conditions and study of CuFe cytotoxicity. In order to assess the effect that these nanoparticles produced on the chosen cell lines, a viability assay on 96 well plates was carried out. Briefly, cells were seeded at different densities depending on their type (3000 cells per well for tumoral cell lines, *i.e.* U251-MG, SKOV-1, HeLa, U87-MG and 4000 cells per well for healthy cell lines, *i.e.* hpMSC and fibroblasts), using Dulbecco's modified Eagle medium (DMEM), supplemented with 1% L-glutamine, 1% PSA (penicillin, streptomycin, amphotericin), and 10%

fetal bovine serum (FBS); in the case of hpMSC, DMEM medium was also supplemented with fibroblast growth factor 2 (FGF-2) at 5 mg·mL^{-1} 24 h after the seeding, the wells were treated with CuFe nanoparticles, in such a way that the supernatant in each well was replaced with a suspension of CuFe nanoparticles in DMEM (DMEM + FGF-2 for hpMSC) at different concentrations, ranging from 200 to 12.5 mg·mL^{-1}. After 24, 48 and 72 h of incubation, the wells were washed with Dulbecco's phosphate buffered saline (DPBS), and then, a solution of blue cell viability reagent in DMEM (10% v/v) was used to assess the cytotoxic effect of these nanoparticles on the different cell lines. After 1 h of incubation with the blue cell viability reagent at 37 ºC, the signal was measured with a BioTek plate reader, exciting at 528 nm and measuring the emission at 590 nm.

Cellular analysis by confocal microscopy. Confocal microscopy assay was carried out to assess the capacity of internalization of CuFe NPs into 3 different cell lines: U251-MG, HeLa and hpMSC. Cells were seeded onto 12 mm Ø coverslips, which were deposited on a 24-well plate, at a density of 20 000 cells per well, and incubated at 37 C and 5% CO_2. After 24 h, cells were treated with CuFe NPs dispersed in DMEM at a concentration of 25 µg ·mL^{-1} during 24 h (for negative control C-wells, DMEM was replaced with fresh media). After this time, cells were washed 3 times with DPBS, fixed with 4% paraformaldehyde, and then washed 3 more times with DPBS. In order to prepare the samples for confocal microscopy, cells were permeabilized with 0.1% saponine. After that, cytoplasmic actin fibers were stained with phalloidin-Alexa of Fluoromount-G + DAPI for nuclei staining. Nanoparticle aggregates could be observed due to the reflection of the incident light. In order to confirm the presence of the nanoparticles inside the cell, a Z-Stack assay of the whole cell, and its ulterior maximum orthogonal projection were performed. This assay was carried out in a confocal microscope (ZEISS LSM 880 Confocal Microscope), using a 63x/1.4 Oil DIC M27 objective

Intracellular catalytic oxidation of GSH. In order to assess the catalytic effect of CuFe NPs and their correlation with intracellular GSH levels, U251-MG, HeLa and hpMSC cells were seeded in p100 dishes. Before they reached 90% of confluence, cells were treated with 25 µg·mL^{-1} for 24 h (for C-dishes, DMEM was replaced with fresh media). Then, cells were washed with PBS–EDTA

and trypsinized. Cells in suspension were counted with a Neubauer chamber and centrifuged at 500 g during 5 minutes, in order to obtain the cell pellet. Analysis of the intracellular GSH levels was performed as follows, based on a previously optimized protocol.[32] Briefly, cells were first trypsinized, washed twice with PBS (500 g for 5 minutes) and collected. Cells were again centrifuged at 13 300 rpm for 5 minutes. Supernatant was discarded and 400 µL of 12% CCl_3COOH solution was added to cell pellet to precipitate proteins and avoid their interference during the analysis. Samples were sonicated and left 15 minutes at 4 °C. The resulting suspension was centrifuged for 13 300 rpm for 5 minutes. The supernatant was isolated and subjected to a derivatization process: 50 µL of the sample were mixed with 930 mL of a 0.01 M TRIS solution and 20 mL of a 1 $mg \cdot mL^{-1}$ DTNB solution. pH of each individual sample was adjusted at a value of 8.0 using 4–6 mL of a 3 M NaOH solution. Standards for the calibration curve were prepared following Table ESI-7.† Samples were analyzed by UPLC-PDA equipment following the analysis conditions presented before. For the calculation of intracellular GSH, an average volume of $1.2 \cdot 10^{-11}$ L, $3.3 \cdot 10^{-12}$ L and $2.6 \cdot 10^{-12}$ L were selected for hpMSCs, U251-MG and HeLa cells, respectively.[32,93]

Statistical analysis. Results are expressed as mean ± standard deviation. Statistical analysis of biological experiments together with significance between means were evaluated by two-way analysis of variance (ANOVA) for multiple comparisons by Dunnett's multiple comparison test using GraphPad Software. Analysis of significance for intracellular catalytic oxidation of GSH was performed using *t* test. Statistically significant differences were expressed as follows: $*p < 0.05$, $**p < 0.005$, $***p < 0.0005$ and $****p < 0.00005$.

References – Chapter 3

1. Ding, Y.; Dai, Y.; Wu, M.; Li, L., Glutathione-mediated nanomedicines for cancer diagnosis and therapy. Chemical Engineering Journal 2021, 426, 128880.

2. Acharya, A.; Das, I.; Chandhok, D.; Saha, T., Redox regulation in cancer: a double-edged sword with therapeutic potential. Oxid Med Cell Longev 2010, 3 (1), 23-34.

3. Nelson, D. L.; Lehninger, A. L.; Cox, M. M., Lehninger Principles of Biochemistry. W. H. Freeman: 2008.

4. Balendiran, G. K.; Dabur, R.; Fraser, D., The role of glutathione in cancer. Cell Biochemistry and Function 2004, 22 (6), 343-352.

5. Traverso, N.; Ricciarelli, R.; Nitti, M.; Marengo, B.; Furfaro, A. L.; Pronzato, M. A.; Marinari, U. M.; Domenicotti, C., Role of glutathione in cancer progression and chemoresistance. Oxid Med Cell Longev 2013, 2013, 972913-972913.

6. Wang, L.; Huo, M.; Chen, Y.; Shi, J., Tumor Microenvironment-Enabled Nanotherapy. Advanced healthcare materials 2018, 7 (8), e1701156.

7. Li, S.; Shang, L.; Xu, B.; Wang, S.; Gu, K.; Wu, Q.; Sun, Y.; Zhang, Q.; Yang, H.; Zhang, F.; Gu, L.; Zhang, T.; Liu, H., A Nanozyme with Photo-Enhanced Dual Enzyme-Like Activities for Deep Pancreatic Cancer Therapy. Angewandte Chemie International Edition 2019, 58 (36), 12624-12631.

8. Sun, Q.; Wang, Z.; Liu, B.; He, F.; Gai, S.; Yang, P.; Yang, D.; Li, C.; Lin, J., Recent advances on endogenous/exogenous stimuli-triggered nanoplatforms for enhanced chemodynamic therapy. Coordination Chemistry Reviews 2022, 451, 214267.

9. Zhang, X.; Lin, Y.; Gillies, R. J., Tumor pH and Its Measurement. Journal of Nuclear Medicine 2010, 51 (8), 1167.

10. Yu, L.; Chen, Y.; Wu, M.; Cai, X.; Yao, H.; Zhang, L.; Chen, H.; Shi, J., "Manganese Extraction" Strategy Enables Tumor-Sensitive Biodegradability and Theranostics of Nanoparticles. Journal of the American Chemical Society 2016, 138 (31), 9881-9894.

11. Yue, L.; Wang, J.; Dai, Z.; Hu, Z.; Chen, X.; Qi, Y.; Zheng, X.; Yu, D., pH-Responsive, Self-Sacrificial Nanotheranostic Agent for Potential In Vivo and In Vitro Dual Modal MRI/CT Imaging, Real-Time, and In Situ Monitoring of Cancer Therapy. Bioconjugate Chemistry 2017, 28 (2), 400-409.

12. Jing, X.; Xu, Y.; Liu, D.; Wu, Y.; Zhou, N.; Wang, D.; Yan, K.; Meng, L., Intelligent nanoflowers: a full tumor microenvironment-responsive multimodal cancer theranostic nanoplatform. Nanoscale 2019, 11 (33), 15508-15518.

13. Wang, S.; Li, F.; Qiao, R.; Hu, X.; Liao, H.; Chen, L.; Wu, J.; Wu, H.; Zhao, M.; Liu, J.; Chen, R.; Ma, X.; Kim, D.; Sun, J.; Davis, T. P.; Chen, C.; Tian, J.; Hyeon, T.; Ling, D., Arginine-Rich Manganese Silicate Nanobubbles as a Ferroptosis-Inducing Agent for Tumor-Targeted Theranostics. ACS Nano 2018, 12 (12), 12380-12392.

14. Xu, J.; Han, W.; Yang, P.; Jia, T.; Dong, S.; Bi, H.; Gulzar, A.; Yang, D.; Gai, S.; He, F.; Lin, J.; Li, C., Tumor Microenvironment-Responsive Mesoporous MnO2-Coated Upconversion Nanoplatform for Self-Enhanced Tumor Theranostics. Advanced Functional Materials 2018, 28 (36), 1803804.

15. Jiang, F.; Ding, B.; Zhao, Y.; Liang, S.; Cheng, Z.; Xing, B.; Teng, B.; Ma, P. a.; Lin, J., Biocompatible CuO-decorated carbon nanoplatforms for multiplexed imaging and enhanced antitumor efficacy via combined photothermal therapy/chemodynamic therapy/chemotherapy. Science China Materials 2020, 63 (9), 1818-1830.

16. Guo, G.; Zhang, H.; Shen, H.; Zhu, C.; He, R.; Tang, J.; Wang, Y.; Jiang, X.; Wang, J.; Bu, W.; Zhang, X., Space-Selective Chemodynamic Therapy of CuFe5O8 Nanocubes for Implant-Related Infections. ACS Nano 2020, 14 (10), 13391-13405.

17. Xu, J.; Shi, R.; Chen, G.; Dong, S.; Yang, P.; Zhang, Z.; Niu, N.; Gai, S.; He, F.; Fu, Y.; Lin, J., All-in-One Theranostic Nanomedicine with Ultrabright Second Near-Infrared Emission for Tumor-Modulated Bioimaging and Chemodynamic/Photodynamic Therapy. ACS Nano 2020, 14 (8), 9613-9625.

18. Wu, H.; Chen, F.; You, C.; Zhang, Y.; Sun, B.; Zhu, Q., Smart Porous Core–Shell Cuprous Oxide Nanocatalyst with High Biocompatibility for Acid-Triggered Chemo/Chemodynamic Synergistic Therapy. Small 2020, 16 (45), 2001805.

19. Li, Y.; Gao, Z.; Chen, F.; You, C.; Wu, H.; Sun, K.; An, P.; Cheng, K.; Sun, C.; Zhu, X.; Sun, B., Decoration of Cisplatin on 2D Metal–Organic Frameworks for Enhanced Anticancer Effects through Highly Increased Reactive Oxygen Species Generation. ACS Applied Materials & Interfaces 2018, 10 (37), 30930-30935.

20. Yang, C.; Younis, M. R.; Zhang, J.; Qu, J.; Lin, J.; Huang, P., Programmable NIR-II Photothermal-Enhanced Starvation-Primed Chemodynamic Therapy

using Glucose Oxidase-Functionalized Ancient Pigment Nanosheets. Small 2020, 16 (25), 2001518.

21. Gunawan, C.; Teoh, W. Y.; Marquis, C. P.; Amal, R., Cytotoxic Origin of Copper(II) Oxide Nanoparticles: Comparative Studies with Micron-Sized Particles, Leachate, and Metal Salts. ACS Nano 2011, 5 (9), 7214-7225.

22. Wang, Z.; von dem Bussche, A.; Kabadi, P. K.; Kane, A. B.; Hurt, R. H., Biological and Environmental Transformations of Copper-Based Nanomaterials. ACS Nano 2013, 7 (10), 8715-8727.

23. Wang, Z.; Li, N.; Zhao, J.; White, J. C.; Qu, P.; Xing, B., CuO Nanoparticle Interaction with Human Epithelial Cells: Cellular Uptake, Location, Export, and Genotoxicity. Chemical Research in Toxicology 2012, 25 (7), 1512-1521.

24. Eremin, D. B.; Ananikov, V. P., Understanding active species in catalytic transformations: From molecular catalysis to nanoparticles, leaching, "Cocktails" of catalysts and dynamic systems. Coordination Chemistry Reviews 2017, 346, 2-19.

25. Chang, M.; Wang, M.; Wang, M.; Shu, M.; Ding, B.; Li, C.; Pang, M.; Cui, S.; Hou, Z.; Lin, J., A Multifunctional Cascade Bioreactor Based on Hollow-Structured Cu2MoS4 for Synergetic Cancer Chemo-Dynamic Therapy/Starvation Therapy/Phototherapy/Immunotherapy with Remarkably Enhanced Efficacy. Advanced Materials 2019, 31 (51), 1905271.

26. Yin, S.-Y.; Song, G.; Yang, Y.; Zhao, Y.; Wang, P.; Zhu, L.-M.; Yin, X.; Zhang, X.-B., Persistent Regulation of Tumor Microenvironment via Circulating Catalysis of MnFe2O4@Metal–Organic Frameworks for Enhanced Photodynamic Therapy. Advanced Functional Materials 2019, 29 (25), 1901417.

27. Liu, Y.; Zhen, W.; Jin, L.; Zhang, S.; Sun, G.; Zhang, T.; Xu, X.; Song, S.; Wang, Y.; Liu, J.; Zhang, H., All-in-One Theranostic Nanoagent with Enhanced Reactive Oxygen Species Generation and Modulating Tumor Microenvironment Ability for Effective Tumor Eradication. ACS Nano 2018, 12 (5), 4886-4893.

28. Wang, Z.; Wang, Y.; Guo, H.; Yu, N.; Ren, Q.; Jiang, Q.; Xia, J.; Peng, C.; Zhang, H.; Chen, Z., Synthesis of one-for-all type Cu5FeS4 nanocrystals with improved near infrared photothermal and Fenton effects for simultaneous imaging and therapy of tumor. Journal of Colloid and Interface Science 2021, 592, 116-126.

29. Wang, X.; Zhong, X.; Liu, Z.; Cheng, L., Recent progress of chemodynamic therapy-induced combination cancer therapy. Nano Today 2020, 35, 100946.

30. Szatrowski, T. P.; Nathan, C. F., Production of large amounts of hydrogen-peroxide by human tumor-cells. Cancer Research 1991, 51 (3), 794-798.

31. Ge, E. J.; Bush, A. I.; Casini, A.; Cobine, P. A.; Cross, J. R.; DeNicola, G. M.; Dou, Q. P.; Franz, K. J.; Gohil, V. M.; Gupta, S.; Kaler, S. G.; Lutsenko, S.; Mittal, V.; Petris, M. J.; Polishchuk, R.; Ralle, M.; Schilsky, M. L.; Tonks, N. K.; Vahdat, L. T.; Van Aelst, L.; Xi, D.; Yuan, P.; Brady, D. C.; Chang, C. J., Connecting copper and cancer: from transition metal signalling to metalloplasia. Nature Reviews Cancer 2021.

32. Bonet-Aleta, J.; Sancho-Albero, M.; Calzada-Funes, J.; Irusta, S.; Martin-Duque, P.; Hueso, J. L.; Santamaria, J., Glutathione-Triggered catalytic response of Copper-Iron mixed oxide Nanoparticles. Leveraging tumor microenvironment conditions for chemodynamic therapy. Journal of Colloid and Interface Science 2022, 617, 704-717.

33. Ortega, A. L.; Mena, S.; Estrela, J. M., Glutathione in cancer cell death. Cancers (Basel) 2011, 3 (1), 1285-1310.

34. Kosower, N. S.; Kosower, E. M., The glutathione status of cells. International review of cytology 1978, 54, 109-60.

35. Lu, S. C., Regulation of glutathione synthesis. Mol. Asp. Med. 2009, 30 (1-2), 42-59.

36. Hedberg, J.; Blomberg, E.; Odnevall Wallinder, I., In the Search for Nanospecific Effects of Dissolution of Metallic Nanoparticles at Freshwater-Like Conditions: A Critical Review. Environmental Science & Technology 2019, 53 (8), 4030-4044.

37. Tummanapelli, A. K.; Vasudevan, S., Ab Initio MD Simulations of the Brønsted Acidity of Glutathione in Aqueous Solutions: Predicting pKa Shifts of the Cysteine Residue. The Journal of Physical Chemistry B 2015, 119 (49), 15353-15358.

38. Wall, S.; Oh, J.-Y.; Diers, A.; Landar, A., Oxidative Modification of Proteins: An Emerging Mechanism of Cell Signaling. Front. Physiol. 2012, 3 (369).

39. Nagy, P., Kinetics and mechanisms of thiol-disulfide exchange covering direct substitution and thiol oxidation-mediated pathways. Antioxidants & redox signaling 2013, 18 (13), 1623-41.

40. Rabenstein, D. L., Nuclear magnetic resonance studies of the acid-base chemistry of amino acids and peptides. I. Microscopic ionization constants of glutathione and methylmercury-complexed glutathione. Journal of the American Chemical Society 1973, 95 (9), 2797-2803.

41. Ngamchuea, K.; Batchelor-McAuley, C.; Compton, R. G., The Copper(II)-Catalyzed Oxidation of Glutathione. Chemistry – A European Journal 2016, 22 (44), 15937-15944.

42. Speisky, H.; Gómez, M.; Carrasco-Pozo, C.; Pastene, E.; Lopez-Alarcón, C.; Olea-Azar, C., Cu(I)–Glutathione complex: A potential source of superoxide radicals generation. Bioorganic & Medicinal Chemistry 2008, 16 (13), 6568-6574.

43. Speisky, H.; Gómez, M.; Burgos-Bravo, F.; López-Alarcón, C.; Jullian, C.; Olea-Azar, C.; Aliaga, M. E., Generation of superoxide radicals by copper–glutathione complexes: Redox-consequences associated with their interaction with reduced glutathione. Bioorganic & Medicinal Chemistry 2009, 17 (5), 1803-1810.

44. Aliaga, M. E.; Carrasco-Pozo, C.; López-Alarcón, C.; Speisky, H., The Cu(I)–glutathione complex: factors affecting its formation and capacity to generate reactive oxygen species. Transition Metal Chemistry 2010, 35 (3), 321-329.

45. Aliaga, M. E.; López-Alarcón, C.; Bridi, R.; Speisky, H., Redox-implications associated with the formation of complexes between copper ions and reduced or oxidized glutathione. Journal of Inorganic Biochemistry 2016, 154, 78-88.

46. Morgan, M. T.; Nguyen, L. A. H.; Hancock, H. L.; Fahrni, C. J., Glutathione limits aquacopper(I) to sub-femtomolar concentrations through cooperative assembly of a tetranuclear cluster. Journal of Biological Chemistry 2017, 292 (52), 21558-21567.

47. Ciriolo, M. R.; Desideri, A.; Paci, M.; Rotilio, G., Reconstitution of Cu,Zn-superoxide dismutase by the Cu(I).glutathione complex. The Journal of biological chemistry 1990, 265 (19), 11030-4.

48. Pearson, R. G., Hard and Soft Acids and Bases. Journal of the American Chemical Society 1963, 85 (22), 3533-3539.

49. Moggach, S. A.; Lennie, A. R.; Morrison, C. A.; Richardson, P.; Stefanowicz, F. A.; Warren, J. E., Pressure induced phase transitions in the tripeptide glutathione to 5.24 GPa: the crystal structure of glutathione-II at 2.94 GPa and glutathione-III at 3.70 GPa. CrystEngComm 2010, 12 (9), 2587-2595.

50. Görbitz, C., A Redetermination of the Crystal and Molecular Structure of Glutathione (yL-Glutamyl-L-cysteinylglycine) at 120 K. Acta Chemica Scandinavica 1987, 41, 362-366.

51. Wright, W., The crystal structure of glutathione. Acta Crystallographica 1958, 11 (9), 632-642.

52. Jelsch, C.; Didierjean, C., The oxidized form of glutathione. Acta Crystallographica Section C: Crystal Structure Communications 1999, 55 (9), 1538-1540.

53. Kretzschmar, J.; Brendler, E.; Wagler, J.; Schmidt, A.-C., Kinetics and activation parameters of the reaction of organoarsenic (V) compounds with glutathione. Journal of Hazardous Materials 2014, 280, 734-740.

54. Gao, Z.; Carames-Mendez, P.; Xia, D.; Pask, C. M.; McGowan, P. C.; Bingham, P. A.; Scrimshire, A.; Tronci, G.; Thornton, P. D., The facile and additive-free synthesis of a cell-friendly iron (III)–glutathione complex. Dalton Transactions 2020, 49 (30), 10574-10579.

55. Qi, W.; Li, J.; Chain, C. Y.; Pasquevich, G. A.; Pasquevich, A. F.; Cowan, J. A., Glutathione Complexed Fe–S Centers. Journal of the American Chemical Society 2012, 134 (26), 10745-10748.

56. Corazza, A.; Harvey, I.; Sadler, P. J., 1H,13C-NMR and X-ray absorption studies of copper(I) glutathione complexes. European journal of biochemistry 1996, 236 (2), 697-705.

57. Jesse, K. A.; Anferov, S. W.; Collins, K. A.; Valdez-Moreira, J. A.; Czaikowski, M. E.; Filatov, A. S.; Anderson, J. S., Direct Aerobic Generation of a Ferric Hydroperoxo Intermediate Via a Preorganized Secondary Coordination Sphere. Journal of the American Chemical Society 2021, 143 (43), 18121-18130.

58. Żamojć, K.; Zdrowowicz, M.; Rudnicki-Velasquez, P. B.; Krzymiński, K.; Zaborowski, B.; Niedziałkowski, P.; Jacewicz, D.; Chmurzyński, L., The development of 1,3-diphenylisobenzofuran as a highly selective probe for the detection and quantitative determination of hydrogen peroxide. Free Radical Research 2017, 51 (1), 38-46.

59. Zielonka, J.; Srinivasan, S.; Hardy, M.; Ouari, O.; Lopez, M.; Vasquez-Vivar, J.; Avadhani, N. G.; Kalyanaraman, B., Cytochrome c-mediated oxidation of hydroethidine and mito-hydroethidine in mitochondria: Identification of homo- and heterodimers. Free Radical Biology and Medicine 2008, 44 (5), 835-846.

60. Gao, F.; Shao, T.; Yu, Y.; Xiong, Y.; Yang, L., Surface-bound reactive oxygen species generating nanozymes for selective antibacterial action. Nature Communications 2021, 12 (1), 745.

61. Ortega-Liebana, M. C.; Encabo-Berzosa, M. M.; Casanova, A.; Pereboom, M. D.; Alda, J. O.; Hueso, J. L.; Santamaria, J., Upconverting Carbon Nanodots from Ethylenediaminetetraacetic Acid (EDTA) as Near-Infrared Activated Phototheranostic Agents. Chemistry-A European Journal 2019, 25 (21), 5539-5546.

62. Meng, X.; Li, D.; Chen, L.; He, H.; Wang, Q.; Hong, C.; He, J.; Gao, X.; Yang, Y.; Jiang, B.; Nie, G.; Yan, X.; Gao, L.; Fan, K., High-Performance Self-Cascade Pyrite Nanozymes for Apoptosis–Ferroptosis Synergistic Tumor Therapy. ACS Nano 2021, 15 (3), 5735-5751.

63. Dean, J. A.; Lange, N. A., Lange's Handbook of Chemistry. McGraw-Hill: 1992.

64. Walsh, M. J.; Ahner, B. A., Determination of stability constants of Cu(I), Cd(II) & Zn(II) complexes with thiols using fluorescent probes. Journal of Inorganic Biochemistry 2013, 128, 112-123.

65. Shtyrlin, V. G.; Zyavkina, Y. I.; Ilakin, V. S.; Garipov, R. R.; Zakharov, A. V., Structure, stability, and ligand exchange of copper(II) complexes with oxidized glutathione. Journal of Inorganic Biochemistry 2005, 99 (6), 1335-1346.

66. Hu, T.; Yan, L.; Wang, Z.; Shen, W.; Liang, R.; Yan, D.; Wei, M., A pH-responsive ultrathin Cu-based nanoplatform for specific photothermal and chemodynamic synergistic therapy. Chemical Science 2021, 12 (7), 2594-2603.

67. Shen, X.; Wang, Z.; Gao, X.; Zhao, Y., Density Functional Theory-Based Method to Predict the Activities of Nanomaterials as Peroxidase Mimics. ACS Catalysis 2020, 10 (21), 12657-12665.

68. Crichton, R.; Crichton, R. R.; Boelaert, J. R., Inorganic Biochemistry of Iron Metabolism: From Molecular Mechanisms to Clinical Consequences. Wiley: 2001.

69. Ma, B.; Wang, S.; Liu, F.; Zhang, S.; Duan, J.; Li, Z.; Kong, Y.; Sang, Y.; Liu, H.; Bu, W.; Li, L., Self-Assembled Copper–Amino Acid Nanoparticles for in Situ Glutathione "AND" H2O2 Sequentially Triggered Chemodynamic Therapy. Journal of the American Chemical Society 2019, 141 (2), 849-857.

70. Biesinger, M. C., Advanced analysis of copper X-ray photoelectron spectra. Surface and Interface Analysis 2017, 49 (13), 1325-1334.

71. Liu, Y.; Guo, Z.; Li, F.; Xiao, Y.; Zhang, Y.; Bu, T.; Jia, P.; Zhe, T.; Wang, L., Multifunctional Magnetic Copper Ferrite Nanoparticles as Fenton-like Reaction and Near-Infrared Photothermal Agents for Synergetic Antibacterial Therapy. ACS Applied Materials & Interfaces 2019, 11 (35), 31649-31660.

72. Wang, W.; Jiang, X.; Chen, K., Iron phosphate microflowers as peroxidase mimic and superoxide dismutase mimic for biocatalysis and biosensing. Chemical Communications 2012, 48 (58), 7289-7291.

73. Guo, S.; Han, Y.; Guo, L., Mechanistic Study of Catalase- and Superoxide Dismutation-Mimic Activities of Cobalt Oxide Nanozyme from First-Principles Microkinetic Modeling. Catalysis Surveys from Asia 2020, 24 (1), 70-85.

74. Zhang, Y.; Xu, Y.; Sun, D.; Meng, Z.; Ying, W.; Gao, W.; Hou, R.; Zheng, Y.; Cai, X.; Hu, B.; Lin, X., Hollow magnetic nanosystem-boosting synergistic effect between magnetic hyperthermia and sonodynamic therapy via modulating reactive oxygen species and heat shock proteins. Chemical Engineering Journal 2020, 390, 124521.

75. Szatrowski, T. P.; Nathan, C. F., Production of Large Amounts of Hydrogen Peroxide by Human Tumor Cells. Cancer Research 1991, 51 (3), 794.

76. Liu, C.; Wang, D.; Zhang, S.; Cheng, Y.; Yang, F.; Xing, Y.; Xu, T.; Dong, H.; Zhang, X., Biodegradable Biomimic Copper/Manganese Silicate Nanospheres for Chemodynamic/Photodynamic Synergistic Therapy with Simultaneous Glutathione Depletion and Hypoxia Relief. ACS Nano 2019, 13 (4), 4267-4277.

77. Huo, M.; Wang, L.; Chen, Y.; Shi, J., Tumor-selective catalytic nanomedicine by nanocatalyst delivery. Nature Communications 2017, 8 (1), 357.

78. Wu, G.; Berka, V.; Derry, P. J.; Mendoza, K.; Kakadiaris, E.; Roy, T.; Kent, T. A.; Tour, J. M.; Tsai, A.-L., Critical Comparison of the Superoxide Dismutase-like Activity of Carbon Antioxidant Nanozymes by Direct Superoxide Consumption Kinetic Measurements. ACS Nano 2019, 13 (10), 11203-11213.

79. Zhao, Y.; Wang, D.; He, I. W.; Liu, J.; Jana, D.; Wu, Y.; Zhang, X.; Qian, C.; Guo, Y.; Chen, X.; Bindra, A. K., Missing-Linker-Assisted Artesunate Delivery by Metal-Organic Frameworks for Synergistic Cancer Treatment. Angewandte Chemie International Edition 2021, n/a (n/a).

80. Kuppusamy, P.; Li, H.; Ilangovan, G.; Cardounel, A. J.; Zweier, J. L.; Yamada, K.; Krishna, M. C.; Mitchell, J. B., Noninvasive Imaging of Tumor Redox Status and Its Modification by Tissue Glutathione Levels. Cancer Research 2002, 62 (1), 307.

81. Hultberg, M.; Isaksson, A.; Andersson, A.; Hultberg, B., Traces of copper ions deplete glutathione in human hepatoma cell cultures with low cysteine content. Chemico-Biological Interactions 2007, 167 (1), 56-62.

82. Hultberg, B.; Andersson, A.; Isaksson, A., Copper ions differ from other thiol reactive metal ions in their effects on the concentration and redox status of thiols in HeLa cell cultures. Toxicology 1997, 117 (2), 89-97.

83. Arsianti, M.; Lim, M.; Marquis, C. P.; Amal, R., Polyethylenimine Based Magnetic Iron-Oxide Vector: The Effect of Vector Component Assembly on Cellular Entry Mechanism, Intracellular Localization, and Cellular Viability. Biomacromolecules 2010, 11 (9), 2521-2531.

84. Svitkova, B.; Zavisova, V.; Nemethova, V.; Koneracka, M.; Kretova, M.; Razga, F.; Ursinyova, M.; Gabelova, A., Differences in surface chemistry of iron oxide nanoparticles result in different routes of internalization. Beilstein Journal of Nanotechnology 2021, 12, 270-281.

85. Xie, Y.; Jiang, J.; Tang, Q.; Zou, H.; Zhao, X.; Liu, H.; Ma, D.; Cai, C.; Zhou, Y.; Chen, X.; Pu, J.; Liu, P., Iron Oxide Nanoparticles as Autophagy Intervention Agents Suppress Hepatoma Growth by Enhancing Tumoricidal Autophagy. Advanced Science 2020, 7 (16), 1903323.

86. Speisky, H.; Gómez, M.; Burgos-Bravo, F.; López-Alarcón, C.; Jullian, C.; Olea-Azar, C.; Aliaga, M. E., Generation of superoxide radicals by copper-glutathione complexes: redox-consequences associated with their interaction with reduced glutathione. Bioorganic & medicinal chemistry 2009, 17 (5), 1803-10.

87. Weiss, J.; Humphrey, C. W., Reaction between Hydrogen Peroxide and Iron Salts. Nature 1949, 163 (4148), 691-691.

88. Hayyan, M.; Hashim, M. A.; AlNashef, I. M., Superoxide Ion: Generation and Chemical Implications. Chemical Reviews 2016, 116 (5), 3029-3085.

89. Zhang, J.; Gao, X.; Ma, D.; He, S.; Du, B.; Yang, W.; Xie, K.; Xie, L.; Deng, Y., Copper ferrite heterojunction coatings empower polyetheretherketone implant with multi-modal bactericidal functions and boosted osteogenicity through synergistic photo/Fenton-therapy. Chemical Engineering Journal 2021, 422, 130094.

90. Hai, C.; Li, S.; Zhou, Y.; Zeng, J.; Ren, X.; Li, X., Roles of ethylene glycol solvent and polymers in preparing uniformly distributed MgO nanoparticles. Journal of Asian Ceramic Societies 2017, 5 (2), 176-182.

91. Behzadi, S.; Serpooshan, V.; Tao, W.; Hamaly, M. A.; Alkawareek, M. Y.; Dreaden, E. C.; Brown, D.; Alkilany, A. M.; Farokhzad, O. C.; Mahmoudi, M., Cellular uptake of nanoparticles: journey inside the cell. Chemical Society Reviews 2017, 46 (14), 4218-4244.

92. Miguel-Sancho, N.; Bomatí-Miguel, O.; Colom, G.; Salvador, J. P.; Marco, M. P.; Santamaría, J., Development of Stable, Water-Dispersible, and Biofunctionalizable Superparamagnetic Iron Oxide Nanoparticles. Chemistry of Materials 2011, 23 (11), 2795-2802.

93. Zhao, L.; Kroenke, C. D.; Song, J.; Piwnica-Worms, D.; Ackerman, J. J. H.; Neil, J. J., Intracellular water-specific MR of microbead-adherent cells: the HeLa cell intracellular water exchange lifetime. NMR Biomed 2008, 21 (2), 159-164.

Supplementary information – Chapter 3

Adapted from:

Unveiling the interplay between homogeneous and heterogeneous catalytic mechanisms in copper– iron nanoparticles working under chemically relevant tumour conditions

Javier Bonet-Aleta,[abc] Miguel Encinas-Gimenez,[abc] Esteban Urriolabeitia,[d] Pilar Martin-Duque,[befg] Jose L. Hueso *[abcf] and Jesus Santamaria *[abcf]

[a]*Institute of Nanoscience and Materials of Aragon (INMA), CSIC-Universidad de Zaragoza, Campus R´ıo Ebro, Edificio I+D, C/Poeta Mariano Esquillor, s/n, 50018, Zaragoza, Spain.*

[b]*Networking Research Center in Biomaterials, Bioengineering and Nanomedicine (CIBER-BBN), Instituto de Salud Carlos III, 28029, Madrid, Spain*

[c]*Department of Chemical and Environmental Engineering, University of Zaragoza, Campus Rio Ebro, C/Mar´ıa de Luna, 3, 50018 Zaragoza, Spain*

[d]*Instituto de Sintesis Quimica y Catalisis Homogenea, ISQCH (CSIC-Universidad de Zaragoza), 50009 Zaragoza, Spain*

[e]*Instituto Aragones de Ciencias de la Salud (IACS), Avenida San Juan Bosco, 13, 50009*

Zaragoza, Spain

[f]*Instituto de Investigacion Sanitaria (IIS) Aragon, Avenida San Juan Bosco, 13, 50009 Zaragoza, Spain*

[g]*Fundacion Araid, Av. de Ranillas 1-D, 50018 Zaragoza, Spain*

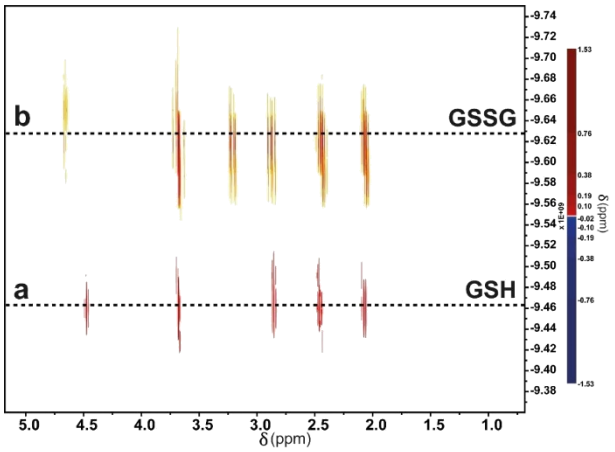

Figure S1. *DOSY spectra of (a) GSH and (b) GSSG standards. Molecular size differences between reduced (GSH) and oxidized GSH (GSSG) translate into different diffusion coefficients (D) of the molecule. Following this trend, determined D for GSH is larger in comparison to GSSG.*

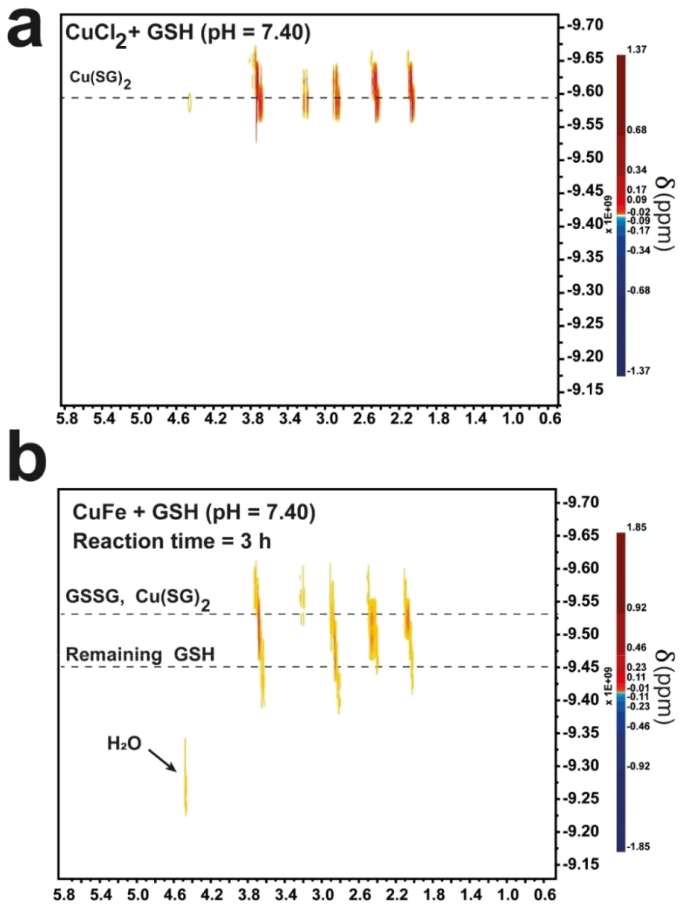

Figure S2. *Comparison of diffusion coefficients of (a), $CuCl_2$+GSH (red) and (b) CuFe+GSH (3h) (purple). Reaction conditions [GSH] = 20 mM, pH = 7.0 (HPO_4^{2-}/H_2PO_4), T = 25 ºC, reaction time = 3h. (a) DOSY spectra corresponding to the mixture $CuCl_2$ + GSH indicate the generation of $Cu(SG)_2$ complex and GSSG, which possess a similar molecular size and therefore a similar D is obtained. (b) DOSY spectra of CuFe+GSH reaction at pH = 7.40 at 3h. As reaction is not over at this time, some remaining GSH appears at low D values (highlighted in dashed line). Moreover, as GSH and GSSG/$Cu(SG)_2$ possess same signals for some H (**δ**=3.70 ppm, **δ**= 2.85 ppm, **δ**=2.45 ppm and **δ**=2.05 ppm), DOSY signals appear wider. A similar signal with a calculated D of $4.00 \cdot 10^{-10}$ $m^2 \cdot s^{-1}$ in comparison with $CuCl_2$+GSH mixture is obtained under conditions that favour leaching of Cu, suggesting the formation of $Cu(SG)_2$ complex in situ using the Cu released from the nanoparticle.*

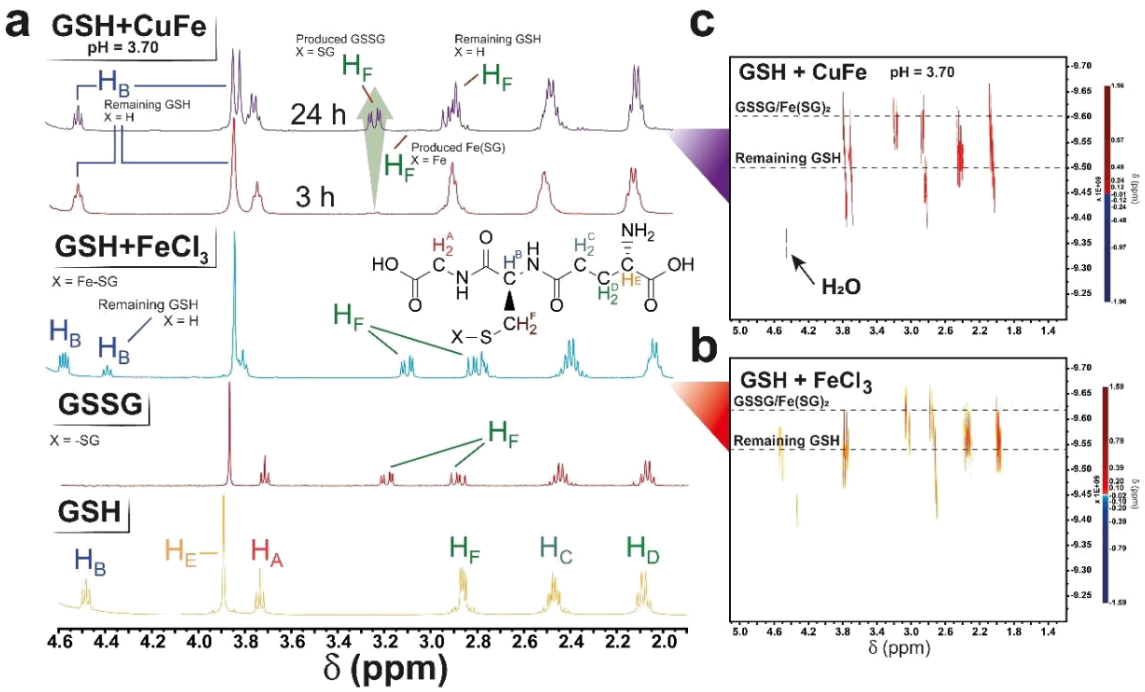

Figure S3. *(a) ^{1}H-NMR analysis from $FeCl_3$+GSH experiments. Generation of Fe-SG complex entails the splitting of H_F signals at 3.04 and 2.76 ppm. Analysis of reaction supernatant at 3 h reveals a small amount of GSSG produced in comparison with CuFe+GSH at pH = 7.40 consequence of slower reaction kinetics of Fe-homogeneous catalysis of GSH oxidation. However, after 24 h of reaction, a larger amount of Cu has been released and the reaction rate increases. (b) DOSY analysis of GSH+$FeCl_3$ mixture reveals the formation of a product with a D close to GSSG, while an important amount of GSH is still present in the solution (confirmed by ^{1}H-NMR in Fig. S3a). (c) DOSY spectra of CuFe+GSH at pH = 3.70.*

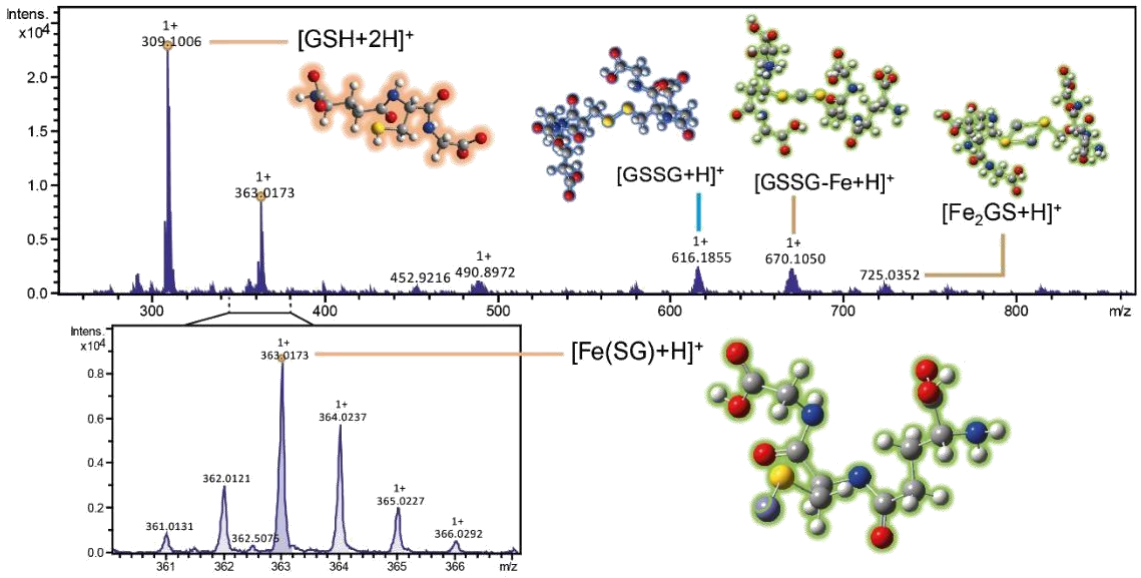

Figure S4. *HRMS-ESI analysis of different species found in $FeCl_3$+GSH mixture (pH = 3.60). Remaining GSH is found at m/z = 309.1006 ($[GSH+H]^+$), which is consistent with an important fraction of GSH still present in the solution detected by ^{1}H-NMR (Fig. S3). $[Fe(SG)_x]$ complexes are detected at m/z = 363.0173 ($[Fe(SG)+H]^+$) and m/z=670.1050 ($[Fe(GSSG)+H]^+$ Polynuclear species are also detected at 725.0352 ($[(Fe(SG))_2+H]^+$.*

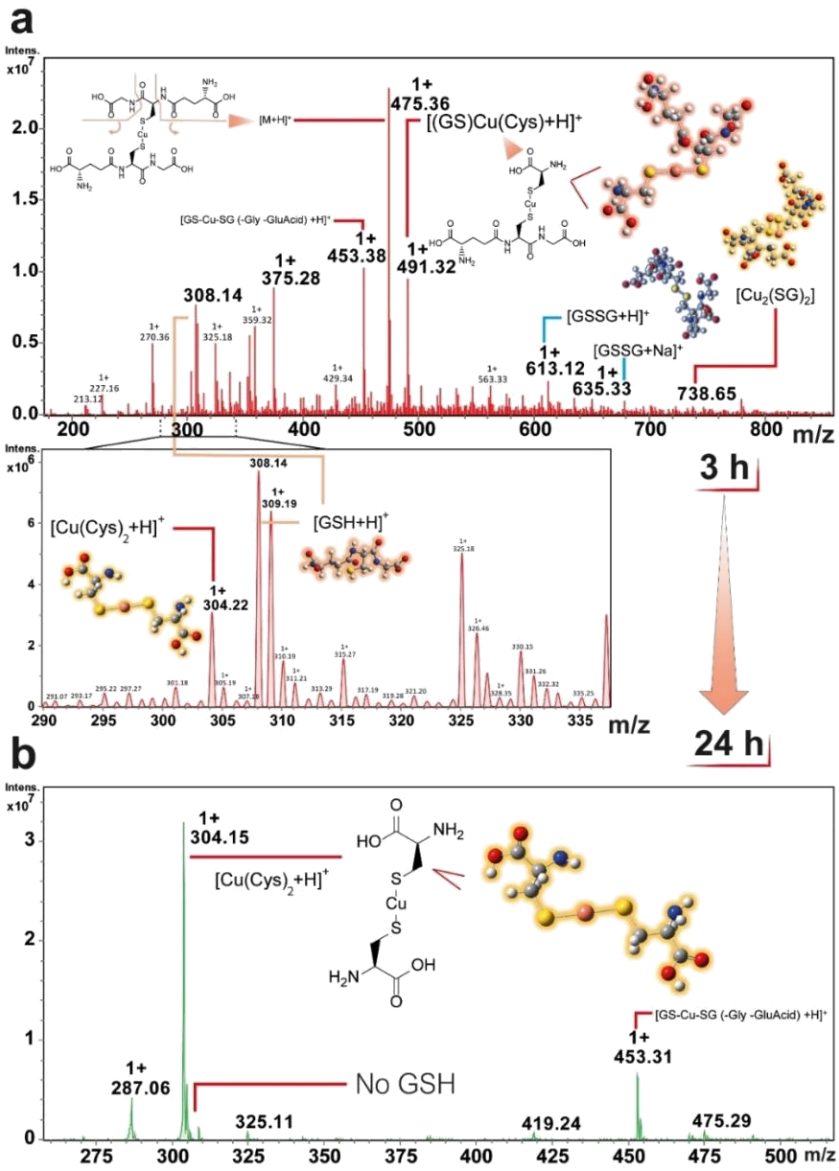

Figure S5. *MS-ESI analysis of CuFe+GSH (pH = 7.40) at different reaction times: (a) 3h and 24h. After 3 hours of reaction unreacted GSH and reaction product, GSSG signals at m/z = 308 and m/z = 613 are present in the spectra, in agreement with ^{1}H-NMR results. Different fragments from the $[Cu(SG)_2]$+ complex were found at m/z = 491.32 ($[Cu(SG)(Cys)]^+$), 453.38 ([Cu(SG)(SG)-Glutamic Acid-Glycine]$^+$) and 304.27 $[Cu(Cys)_2]^+$, with the Cu-S bond always present. Analysis of the reaction supernatant at reaction time 24 h revealed the total consumption of GSH, according to ^{1}H-NMR analysis and the prominence of the $[Cu(Cys)_2]^+$ fragment. We assume that the nanoparticle affects to the MS fragmentation pattern, as we were not able to detect those fragments by ^{1}H-NMR.*

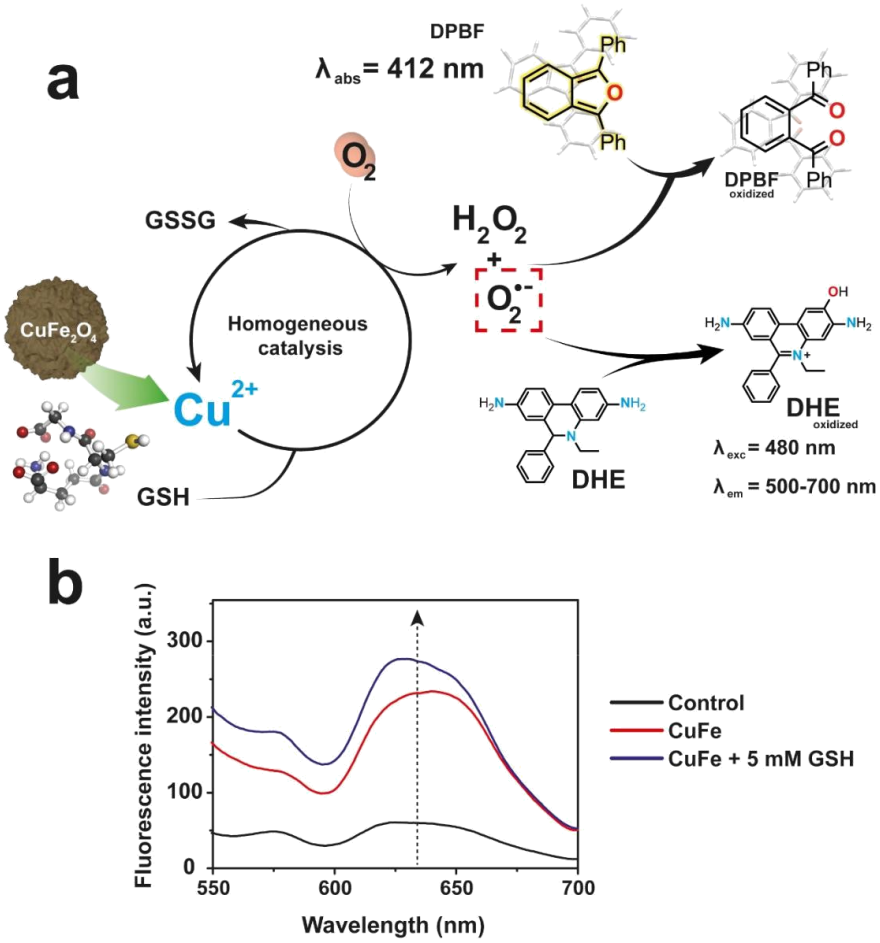

Figure S6. *(a) Scheme of the reaction mechanisms to detect ROS species formed when Cu2+ ions are released from the CuFe NPs upon interaction with GSH molecules: DPBF probe detects several ROS species (i.e. H_2O_2 and $•O_2^-$) while Dihydroethidine (DHE) selectively reacts with $•O_2^-$species to yield a fluorescent adduct (2-hydroxyethidium cation) in the range λ_{exc} = 480 nm/ λ_{em} = 500-700 nm; DPBF absorbs at 412 nm, is oxidized to 1,2-dibenzoylbenzene, a colorless molecule; Fluorescence spectra after 30 minutes of reaction which shows a 20% larger fluorescence signal of DHE oxidized in the presence of 5 mM of GSH due to the generation of $•O_2^-$. Reaction conditions: T = 25°C, pH = 7.4 (adjusted with Na_2HPO_4/KH_2PO_4 buffer), $[DHE]_0$ = 100 μM, [CuFe] = 0.1 mg·mL^{-1}, $[GSH]_0$=5 mM.*

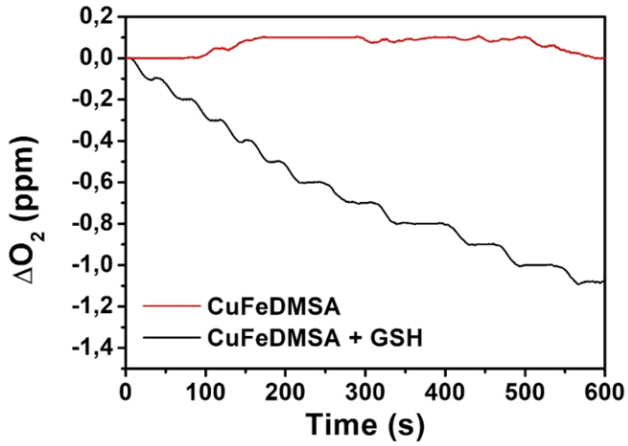

Figure S7. *O_2 consumption in the presence of CuFe with or without the addition of 5 mM GSH. [CuFe] = 0.1 mg·mL^{-1}, pH = 7.40 (adjusted with HPO_4^{2-}/$H_2PO_4^-$). The decrease of O_2 levels in solution once CuFe and GSH are mixed corresponds to its role as electron acceptor in the homogeneous GSH oxidation.*

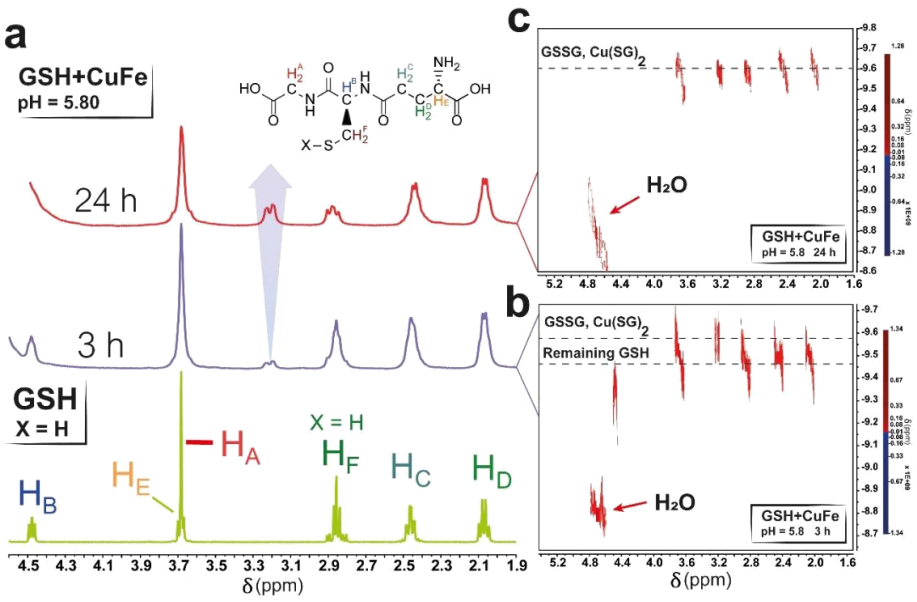

Figure S8.*(a) ^{1}H-NMR analysis from CuFe+GSH experiments at pH = 5.80. A similar behavior in comparison with CuFe+GSH at pH = 7.40 is found at tumor-characteristic pH. After 3h of reaction, a characteristic signal of GSSG/Cu(SG)$_2$ at 3.22 ppm appears as consequence of modification of -CH$_2$- close to -SH group. The reaction is complete after 24 h, as no signal of GSH is present at 4.5 ppm; (b) DOSY spectra of GSH+CuFe mixture at pH = 5.80 (HPO_4^{2-}/$H_2PO_4^-$), presenting both signals from GSH and GSSG/Cu(SG)$_2$; (c) DOSY spectra of GSH+CuFe (pH = 5.8) after 24 h of reaction, with the signal of GSH disappeared. Molecular species with a D similar to GSSG/Cu(SG)$_2$ are detected after 24 hours of reaction.*

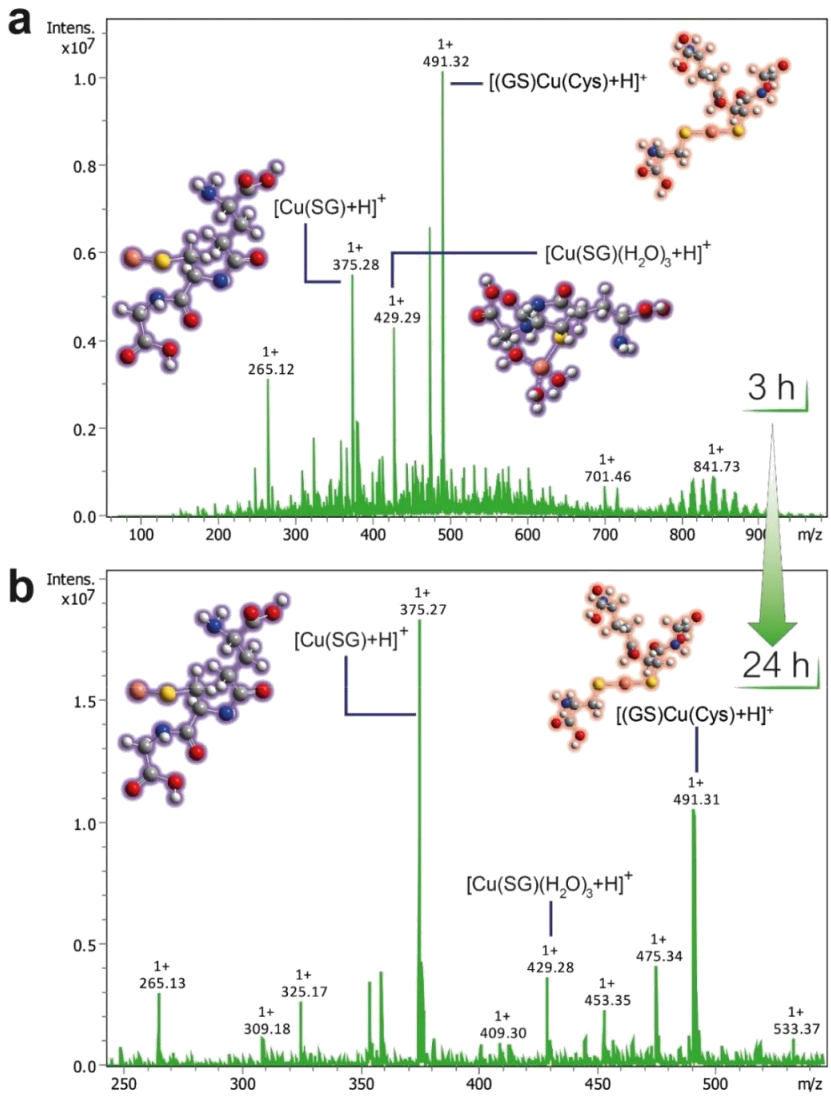

Figure S9. *MS-ESI analysis of CuFe+GSH (pH = 5.80) at reaction time (a) 3h and (b) 24h. $[Cu(SG)_2]^+$-derived fragments are present at m/z = 375.28 ($[Cu(SG)+H]^+$), 429.29 ($[Cu(SG)(H_2O)_3+H]^+$) and 491 ($[Cu(SG)(Cys)+H]^+$. Analysis of the reaction supernatant at reaction time 24 h revealed the total consumption of GSH, according to ^{1}H-NMR analysis and the prominence of a [Cu(SG)] fragment.*

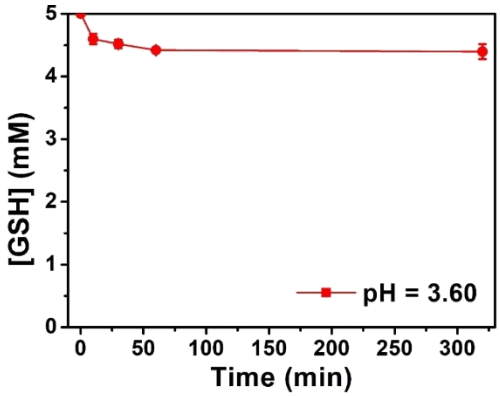

Figure S10. *Monitoring of GSH levels at pH = 3.60 in the presence of CuFe catalyst, showing a slight decrease in GSH concentration (in comparison with reaction at pH = 5.80 or 7.40) at early reaction time (320 minutes). Results are in agreement with ^{1}H-NMR/DOSY experiments (Figures S3a-c) indicating that GSH was present in the reaction after 3 h of reaction.*

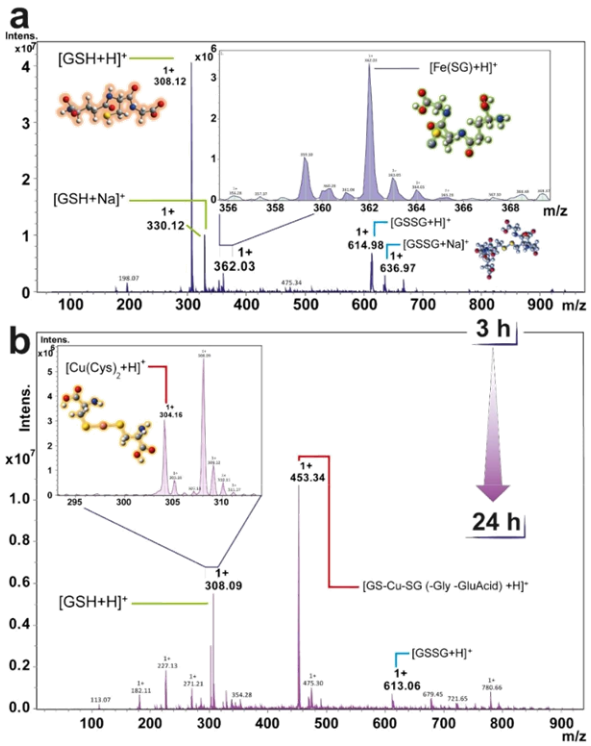

Figure S11. *MS-ESI analysis of CuFe+GSH reaction (pH = 3.60) at (a) 3 h and (b) 24 h. $[Fe(SG)+H]^+$ complex formed by Fe leached in the reaction at acidic pH is found at m/z = 362.03. Remaining GSH signal (m/z = 308.19, $[GSH+H]^+$ and m/z = 330.12 $[GSH+Na]^+$) is attributed to slow kinetics of Fe-catalytic oxidation of GSH. Analysis of the reaction at 24 h reveals the generation of $[Cu(SG)_2]^+$ as fragments of $[Cu(cys)_2]^+$ and [Cu(SG)-Gly-GluAcid] appears in the HRMS-ESI at m/z = 304 and 453, respectively.*

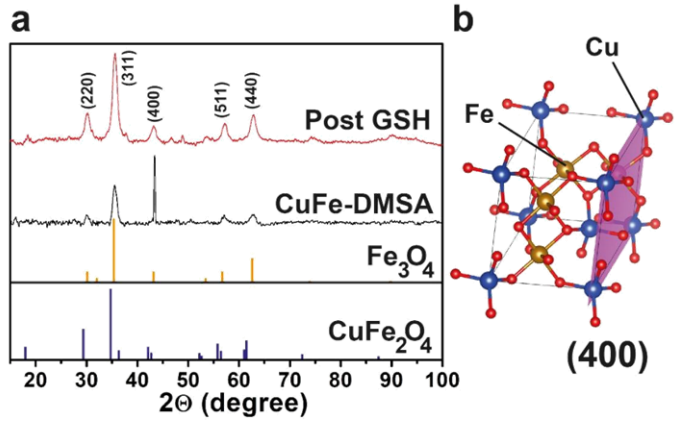

Figure S12. *(a) XRD pattern obtained from CuFe-BSA and CuFe-DMSA after reaction with 5 mM of GSH and (b) Cubic structure of $CuFe_2O_4$ where Fe and Cu occupy octahedral and tetrahedral sites, respectively.*

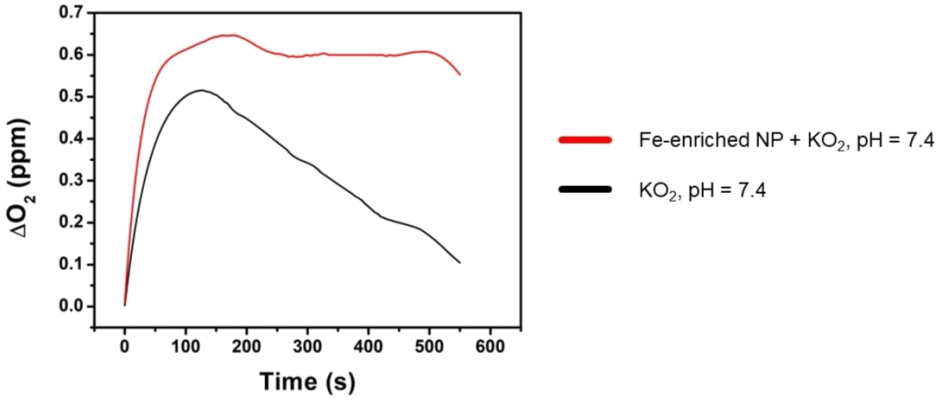

Figure S13. *O_2 evolution in the presence/absence of Fe-enriched nanoparticle (red and black line, respectively) using KO_2 as superoxide anion source. The role and influence of the catalyst becomes more evident at longer reaction times in spite of the the rapid self-dismutation of superoxide in reaction conditions (Temperature = 25 °C, pH = 7.4 (adjusted with Na_2HPO_4/KH_2PO_4 buffer), $[KO_2]_0$ = 100 μM, [Fe-enriched catalyst] = 0.08 mg·mL^{-1}.*

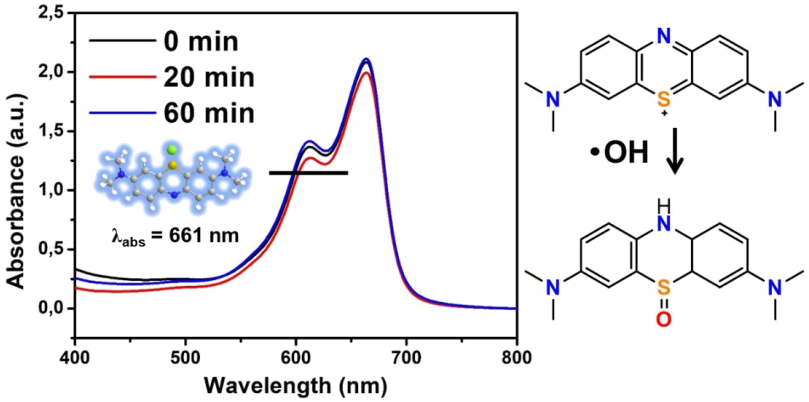

Figure S14. *Study of •OH generation from from reaction of Fe-enriched catalyst (0.1 mg·mL^{-1}). UV-vis spectra of Methylene Blue at different times (after CuFe incubation with 5 mM GSH to provoke Cu release) in the presence of H_2O_2 1 mM (T = 25 ºC, pH = 6.5 (adjusted with CH_3COO^- 0.05 M).*

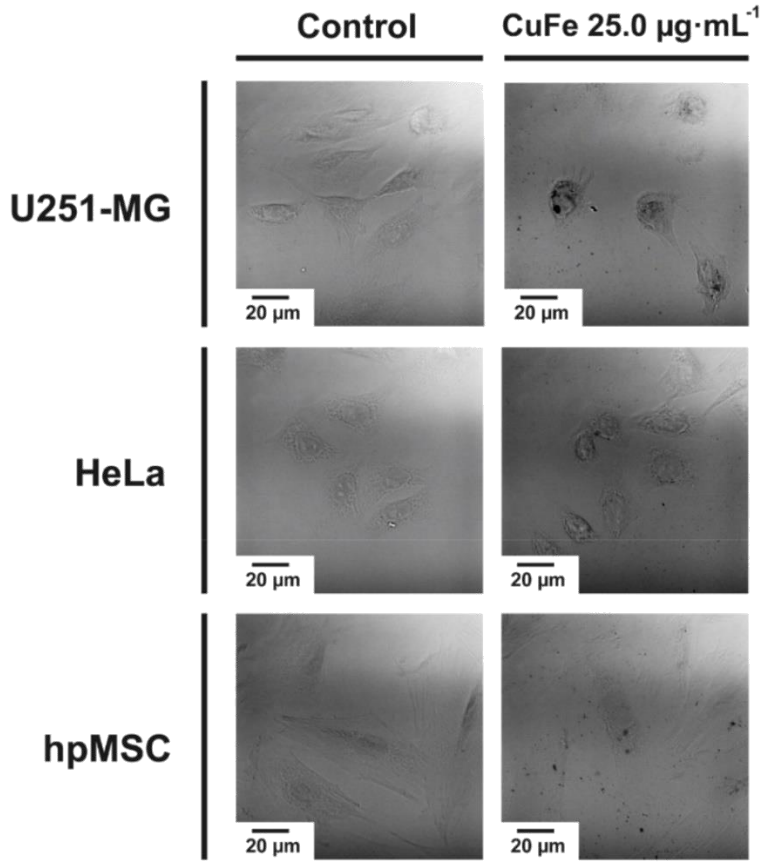

Figure S15. *Representative confocal microscopy images of U251-MG, HeLa and hpMSC cell lines treated with 25.0 µg·mL^{-1} after 24h of treatment analyzed through Transmitted Light Detector (T-PMT). The contrast provided by CuFe nanocatalyst aggregates possibilities its visualization within the cells.*

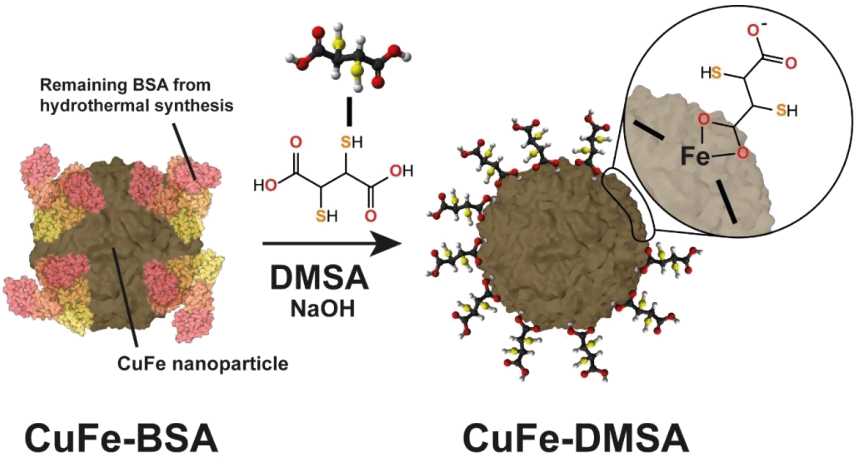

Figure S16. *CuFe-DMSA synthesis route. A ligand exchange process is applied to as-synthetized CuFe-BSA nanoparticles to promote the replacement of BSA remaining from the hydrothermal synthesis by DMSA. An alkaline medium is necessary to solubilize DMSA into the aqueous media. Once deprotonated, carboxyl groups from DMSA are able to bind to Fe^{III} sites in the nanoparticle to enhance the dispersion of the nanoparticles in aqueous media.*

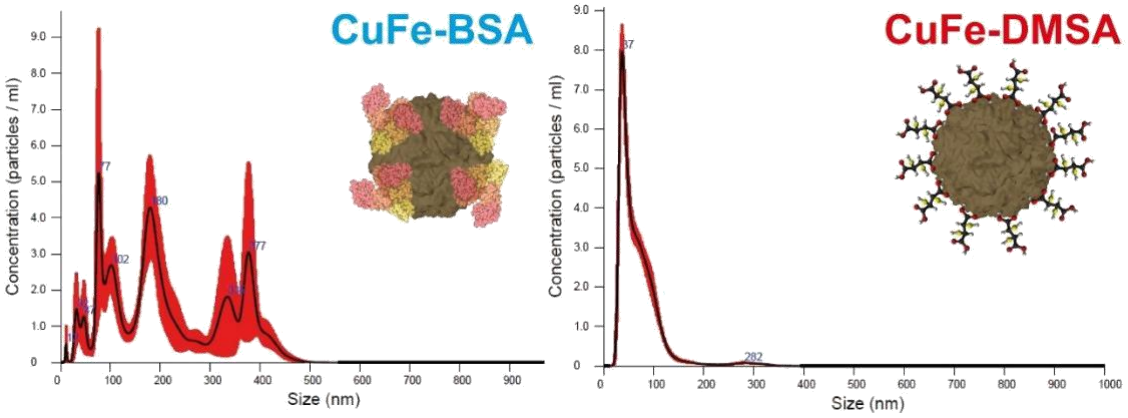

Figure S17. *Nanoparticle Tracking Analysis (NTA) of CuFe before (BSA) and after DMSA functionalization, showing the effectiveness of DMSA functionalization to disperse the nanoparticles in aqueous media.*

Table S1. *Elemental composition of CuFe surface measured by XPS before exposure to GSH.*

Binding Energy (eV)				
Cu 2p	**Fe 2p**	**O 1s**	**N 1s**	**C 1S**
932.6	710.8	530.4	400.2	285.0
7.80%	18.74%	40.15%	0.81%	32.47%

Table S2. *Elemental composition of CuFe surface measured by XPS after exposure to GSH.*

Binding Energy (eV)				
Cu 2p	**Fe 2p**	**O 1s**	**N 1s**	**C 1S**
932.2	711.2	530.3	400.1	285.0
0.28%	21.00%	44.24%	2.52%	31.96%

Table S3. *XPS quantification of the different Fe and Cu species present on the catalyst surface before exposure to GSH.*

Fe^{2+}		Fe^{3+}	
2p3/2	S.O	2p3/2	S.O
710.6	714.0	712.1	718.4
40%	-	60%	-

$Cu^{0/+}$	Cu^{2+}		
2p3/2	2p3/2	S.O.1	S.O.2
932.6	934.3	941.2	944.2
17%	83%	-	-

Table S4. *XPS quantification of the different Fe and Cu species present on the catalyst surface after exposure to GSH.*

Fe^{2+}		Fe^{3+}	
2p3/2	S.O	2p3/2	S.O
710.9	713.7	711.0	718.6
28.5%	-	71.5%	-

$Cu^{0/+}$	Cu^{2+}		
2p3/2	2p3/2	S.O.1	S.O.2
932.7	934.5	941.2	943.7
59%	41 %		

Table S5. *GSH standards composition employed to analyze GSH-catalytic experiments.*

[GSH] (ppm)	V_{GSH} 100 ppm (µL)	V_{DTNB} 1 mM (µL)	V_{TRIS} 0.01 M (µL)
2.5	25	100	875
5.0	50	100	850
10	100	100	800
20	200	100	700
40	400	100	500

Table S6. *CC50 values obtained for CuFe catalyst for different cell lines at different treatment times, expressed in µg·mL $^{-1}$.*

	Fibroblasts	hpMSC	U251-MG	U87	HeLa	SKOV3
24 h	110.7 ± 21.4	113.3 ± 24.6	31.7 ± 9.9	8.6 ± 3.0	47.9 ± 22.3	9.3 ± 2.4
48 h	66.3 ± 17.7	54.5 ± 13.4	9.5 ± 3.5	6.3 ± 1.5	19.8 ± 11.8	6.1 ± 2.0
72 h	83.4 ± 26.1	27.5 ± 7.4	9.5 ± 4.2	6.0 ± 2.0	32.0 ± 6.7	6.6 ± 1.6

Table S7. *GSH standards composition employed to analyze intracellular GSH-catalytic experiments.*

[GSH] (ppm)	$V_{GSH,\ TCA}$ (µL)	$[GSH]_{TCA}$ (ppm)	$V_{DTNB\ 1\ mg \cdot mL^{-1}}$	$V_{TRIS\ 0.01\ M}$
0.25	50	5	20	930
0.35	50	7	20	930
0.50	50	10	20	930
0.75	50	15	20	930
1.00	50	20	20	930
2.00	50	40	20	930
3.00	50	60	20	930
5.00	50	100	20	930

Chapter 4 |

Beyond classic catalytic therapy

Summary – Chapter 4

Throughout this Ph.D. research, a persistent question has revolved around the potential repertoire of reactions that a nanoparticle can catalyze within a living cell. Currently, and if we step outside the field of de-protection chemistry, the literature on catalytic cancer therapy exploits only four different reactions, which are succinctly summarized in **Figure Summary-1a**. These include GSH oxidation, extensively explored in chapters 1, 2, and 3, and the Fenton-like reactions elucidated in chapter 1. Additionally, glucose oxidation and oxygen generation have also been exploited and this thesis has dealt with these reaction in chapters 2 and 3, respectively. However, considering the vast array of diverse molecules that nanoparticles encounter within biological environments, it becomes hard to accept the notion that only four reactions can be leveraged in therapy. The inherent complexity of biological media suggests a much broader landscape of potential reactions.

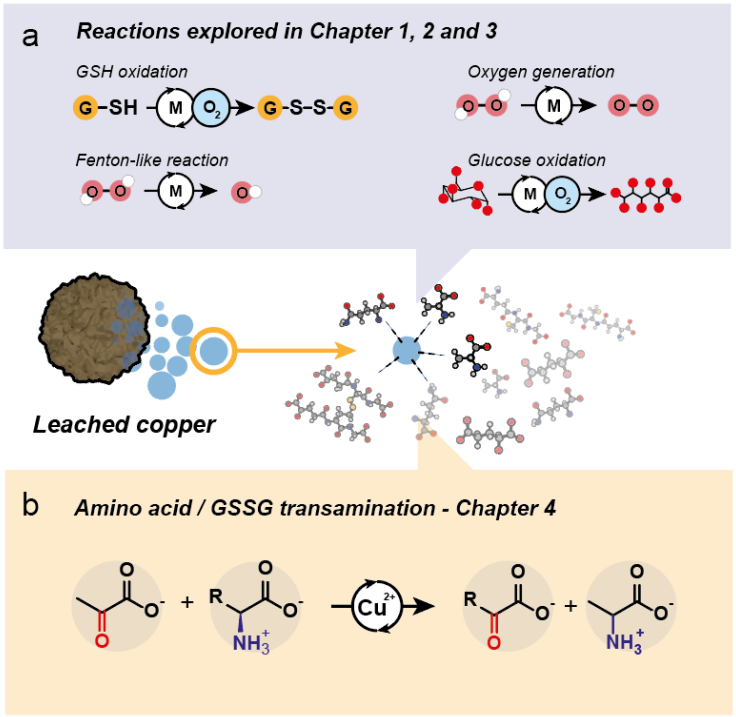

Figure Summary-1. *Expanding the toolkit of catalytic chemotherapy (a) beyond the four reactions considered in literature. Leached copper in biological environments catalyzes transamination using molecules such as amino acids and GSSG as amino-donors.*

In 2021, a research paper by Mayer et al. made a significant contribution to the field of prebiotic chemistry, which investigates various reactions involving biomolecules to shed light on the origins of life. This particular study focused on the transamination reaction, specifically exploring how the oxo group of pyruvate could be replaced by the amino group of an amino acid with the assistance of a transition metal cation, yielding the corresponding α-ketoacid and alanine as products. Inspired by the findings presented in chapter 3, where the release of copper from Cu-Fe nanoparticles was observed, we decided to investigate the transamination reaction as a potential therapeutic tool. Considering that intracellular GSH has the potential to yield free copper ions, it is plausible to hypothesize that these ions could serve as catalysts for this particular reaction. By bridging the insights from prebiotic chemistry and our own research on Cu-Fe nanoparticles, we aim to explore the possibility of harnessing the catalytic potential of these nanoparticles to facilitate the transamination reactions in a living cellular environment (**Figure Summary-1b**).

Our initial findings, obtained under tumor microenvironment-relevant conditions such as a higher presence of GSH and hypoxia, showcased the remarkable ability of CuFe nanoparticles to catalyze transamination reactions using glutamine as an amino acid donor. This choice of glutamine was particularly significant due to its close association with cancer cell metabolism. Encouragingly, we further validated this capability using other amino acids such as glutamic acid and aspartic acid.

We realized that the chemical structure required to serve as a suitable substrate for transamination was not restricted to amino acids. Instead, other molecules such as GSSG, the primary product of GSH oxidation, exhibited the same chemical structure necessary for transamination. This fact prompted us to demonstrate the potential susceptibility of other molecules, notably small peptides, including GSSG, to transamination reactions. In-depth DFT studies unveiled that the reaction mechanism for transamination with GSSG occurred in a similar manner to that observed with individual amino acids.

To investigate the transamination reaction, we conducted in vitro experiments wherein we monitored the intracellular levels of glutamine and alanine. Specifically, we focused on the U251-MG cell line, as our earlier investigations involving Cu-Fe nanoparticles (as described in Chapter

1 and 3) had demonstrated notable toxicity towards this particular cell line. We were intrigued to determine if this observed toxicity could be in part attributed to the disruption of amino acid and pyruvate species caused by the transamination reaction. Remarkably, our findings revealed a significant reduction in intracellular glutamine and a rise of alanine levels compared to the control experiment. These findings strongly suggested that Cu-Fe nanoparticles were actively catalyzing the transamination reaction within the cellular environment of U251 cells. The insights derived from this chapter contributes to the understanding of the interplay between inorganic nanoparticles and cellular processes, and suggest that catalyzed transamination could have potential uses in new cancer therapies.

Adapted from:

Cu-releasing nanoparticles induce the catalytic transamination of amino acids and GSSG under tumor microenvironment conditions

Javier Bonet-Aleta[1,2,3,4], Juan Vicente Alegre-Requena[5], Javier Martin-Martin[1,6], Miguel Encinas-Gimenez[1,2,3,4], Ana Martín-Pardillos[1,2,3,4], Jose L. Hueso[1,2,3,4,*], Jesus Santamaria[1,2,3,4,*]

[1] *Instituto de Nanociencia y Materiales de Aragon (INMA) CSIC-Universidad de Zaragoza, Campus Rio Ebro, Edificio I+D, C/ Poeta Mariano Esquillor, s/n, 50018, Zaragoza, (Spain).*

[2] *Department of Chemical and Environmental Engineering, University of Zaragoza, Campus Rio Ebro, C/María de Luna, 3, 50018 Zaragoza (Spain).*

[3] *Networking Res. Center in Biomaterials, Bioengineering and Nanomedicine (CIBER-BBN), Instituto de Salud Carlos III; 28029 Madrid (Spain)*

[4] *Instituto de Investigación Sanitaria (IIS) de Aragón, Avenida San Juan Bosco, 13, 50009 Zaragoza, Spain.*

[5] *Departamento de Química Inorgánica, Instituto de Síntesis Química y Catálisis Homogénea (ISQCH) CSIC-Universidad de Zaragoza, C/ Pedro Cerbuna 12, 50009 Zaragoza, Spain.*

[6] *Department of Organic Chemistry, University of Zaragoza, Zaragoza (Spain).*

Graphical abstract

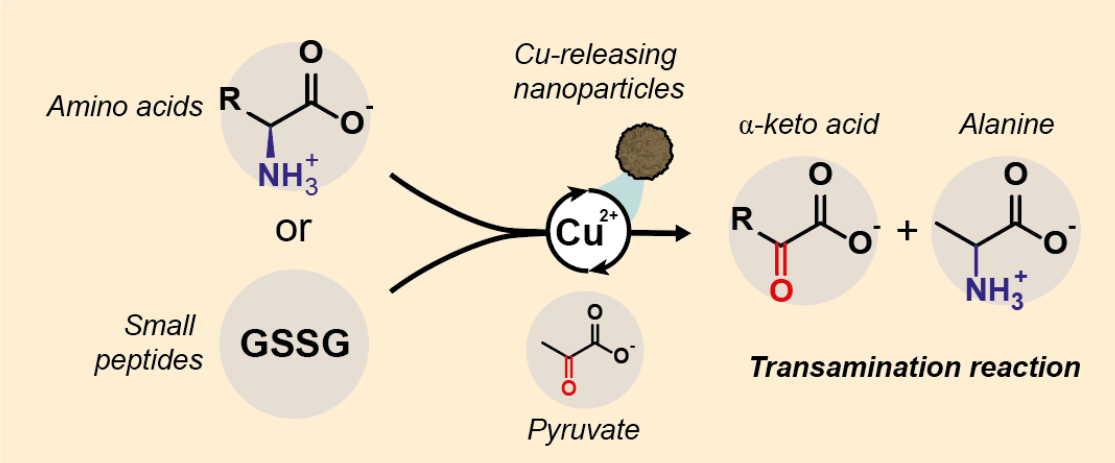

Abstract

Catalytic cancer therapy is emerging as a powerful tool to target cancer cells by exploiting specific characteristics of the tumor microenvironment (TME). To this end, the catalytic activity of nanoparticles, enzymes and homogeneous catalysts is recruited to induce reactions that are damaging to cancer cells. Thus, the pro-drug activation approach uses chemical constructs that become toxic species inside the tumor, typically following removal of a protecting group. In contrast, TME-based catalytic strategies do not rely on the introduction of foreign species and instead use molecules that are already present in the TME. So far, only four processes have been explored in relation to cancer therapy, two oxidation reactions (glucose and glutathione), generation of reactive oxygen species (ROS) and production of oxygen to alleviate tumor hypoxia. This is surprising, since the rich chemical environment in tumor cells could in principle provide many other therapeutic opportunities. In particular, amino groups seem a suitable target, given the abundance of proteins and peptides in biological environments. Here we show that catalytic CuFe nanoparticles are able to foster transamination reactions between different amino acids and pyruvate, another key molecule that abounds in the TME. Transamination would then reduce the available aminoacid pool, which is likely to affect cell homeostasis and to effectively hinder tumor proliferation. After internalization of Cu-containing nanoparticles in U251-MG cells, we observed a significant decrease in glutamine and alanine levels up to 48 hours after treatment. In addition, we have found that not only simple amino acids, but also di- and tri-peptides undergo catalytic transamination when exposed to the Cu cations released by our nanoparticles, thus extending the range of the effects to other molecules such as GSSG. Mechanistic calculations for GSSG transamination revealed the formation of an imine between the oxo-group of pyruvate and the free -NH_2 group of GSSG, followed by the coordination of the imine to Cu(II). Our results demonstrate that transamination reactions can be catalyzed in cellulo by Cu-releasing nanoparticles, adding a new reaction to the existing toolbox of catalytic therapies.

Introduction – Chapter 4

Catalytic nanoparticles have recently been enlisted as new warriors in the fight against cancer. In particular, it is expected that they will help to modify the chemistry of the tumor microenvironment (TME), fostering tumor cell death or at least a non-proliferative scenario. Catalytic actions have followed two main strategies. The first corresponds to the so-called "pro-drug activation" approach that involves *in situ* production of chemotherapy drugs from less toxic or inert molecules, usually by metal-catalyzed chemical reactions[1] such as dealkylation[2], azide-alkyne cycloaddition[3] or carbamate cleavage[4] (***Figure 1a***). This has given rise to a vast array of possibilities, especially with de-protection chemistry, as researchers devised creative ways of anchoring inactive functional groups that could later be cleaved on site by the action of a metal catalyst[1, 5]. The second strategy, often termed "Nanocatalytic Therapy", exploits essential features of the Tumor Microenvironment (TME)[6-8] and in contrast to the pro-drug activation route, rather than introducing foreign molecules, attempts to do chemistry with the chemical species already available. Researchers in this field have displayed remarkable creativity in the search for nanostructured vectors that are more selective or more efficient in nanocatalytic therapy and this trend continues to this day,[9-12]. However, some stagnation is visible regarding the reactions and biomolecules to be targeted. In fact, the set of reactions employed for catalytic therapy has not changed in years, including only four processes, namely: (**i**) Glutathione (GSH) oxidation[13]; (**ii**) Reactive Oxygen Species (ROS) production (H_2O_2, $\bullet O_2^-$ or •OH)[14, 15]; (**iii**) O_2 production using endogenous H_2O_2[16] and (**iv**) Glucose oxidation[17] (***Figure 1b***). These catalytic reactions are powerful tools to disrupt the tumor homeostasis by altering its redox balance (via processes **i**-**ii**), the typically hypoxic environment (via process **iii**), and nutrient supply (via process **iv**), respectively. Reactions **i**, **ii** and **iv** are oxygen-dependent and are therefore hampered under the hypoxic conditions of the TME. This is where reaction **iii** enters, aimed to alleviate hypoxia locally using available H_2O_2. These strategies interfere with cellular metabolism in general but are particularly harmful to cancer cells given their elevated oxidative stress[18] and dependency on glucose uptake[19]. *In vitro* and *in vivo* studies have analyzed potential effects on proteins, enzymes and genes involved in redox homeostasis whose functioning becomes altered by these catalytic

processes, such as, Glutathione Peroxidase (GPX4)[20], dihydroorotate dehydrogenase (DHODH)[21] or Hypoxia-Induced Factor (HIF-1)[22] among others.

As already mentioned, the existing nanoparticle catalysts for catalytic therapy work exclusively around the four processes described in ***Figure 1b***, and no new reaction pathways have been reported. This is surprising since the TME is teeming with key molecules and reactions that could be exploited, and it seems unlikely that these four processes could exhaust all the catalytic opportunities available to fight cancer growth. Recently, Moran and coworkers[23,24] demonstrated that transamination, a reaction of biological importance that is usually governed by enzymatic catalysis, could also be catalyzed in a test tube by Co^{2+}, Ni^{2+}, V^{5+} and especially Cu^{2+} cations. Inspired by this work, we hypothesized that the use of Cu-releasing nanoparticles that are easily internalized by endocytosis and display a rapid Cu^{2+} release kinetics[25] could effectively perform this type of catalysis within cancer cells thus adding a new reaction to the panoply pictured in ***Figure 1b***. Specifically, we propose that the catalytic action of transition metals on key molecules such as amino acids and α-ketoacids (***Figure 1c***) may open up unexplored therapeutic opportunities. Especially noteworthy, in view of its potential therapeutic value, is the oxygen-independent character of the transamination processes, enabling them to take place within the hypoxic TME without the need to resort to complex oxygen-generation schemes.

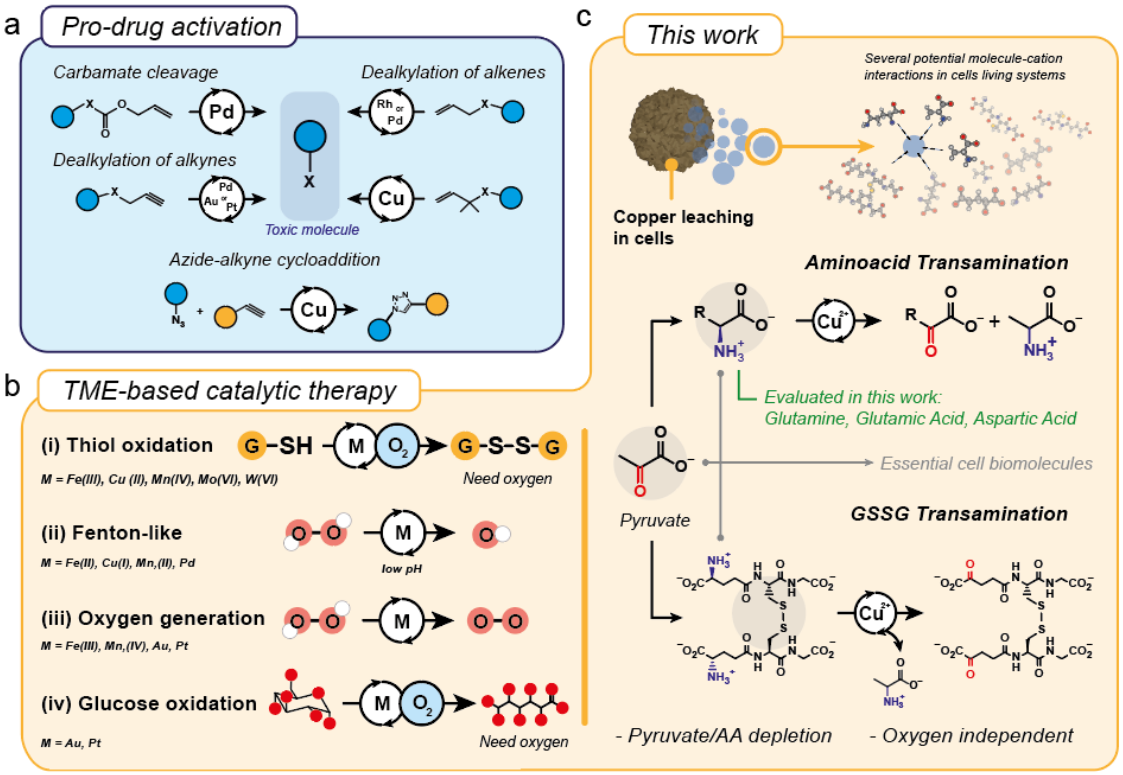

Figure 1. *Different catalytic strategies developed for cancer therapy. (**a**) Bioorthogonal catalysis based on pro-drug activation strategies typically require a transition-metal catalyst including Pd, Pt, Au, Rh or Cu to form a cytotoxic compound by either removing a chemical group from a pro-drug or binding two low-toxicity molecules; (**b**) Reactions employed in the context of nanocatalytic therapy in the TME: (i) GSH oxidation, (ii) •OH or (iii) O_2 generation using endogenous H_2O_2 and (iv) glucose oxidation; (**c**) New scenario potentially enabled by the internalization of transition-metal leaching nanoparticles. In particular, Cu^{2+} catalyzes the transamination reaction between the -NH_3^+ group attached to α-C of an aminoacid/peptide and the keto group of pyruvate to yield D/L-Alanine and the corresponding keto-acid derived from the aminoacid/peptide. Reactions target key biomolecules in the cell: Glutamine, glutamic acid, aspartic acid, GSSG.*

treat Acute lymphoblastic leukemia or Non-Hodgkin lymphoma by targeting Asparagine through the enzyme L-Asparaginase[27], while others like Glutamine, Arginine or Methionine are currently being explored in pre-clinical or clinical phases[28]. On the other hand, the role of pyruvate as a key molecule in cell metabolism does not need to be emphasized, as it provides energy through either through the Krebs cycle or lactic acid fermentation routes. Finally, as presented in ***Figure 1b***,

glutathione (GSH) is rapidly becoming another therapeutic target due to its central role in balancing intracellular redox stress in cancer cells. As such has been targeted through thiol oxidation and is one of the emerging areas of therapeutic potential using transition-metal catalysis[13] to yield GSSG[12, 25] as the main reaction product, although this can be easily converted back into GSH through the action Glutathione Reductase[29] by using FAD^+, somewhat reducing the therapeutic effect of the oxidation. In contrast, the transamination process of ***Figure 1c*** could provide another, non-oxidative way, to deplete both GSH and GSSG pools since they have an iso-peptidic bond between the $-COO^-$ group from the side chain of the glutamate residue and the amino group from cysteine that is expected to be chemically able to undergo transamination.

Using $CuCl_2$ as Cu(II) source requires a previous reduction step into Cu(I)[30] to be internalized through the high-affinity Cu(I)-selective copper ion channel (CTR1)[31], which restricts the total copper uptake by cell. Instead, here we have used $CuFe_2O_4$ nanoparticles as reservoirs to deliver much larger amounts of Cu upon internalization into U251-MG glioblastoma cells. Nanoparticle internalization typically occurs via an endocytosis[32-34] and this enables higher internalization rates. Specific Cu importers such as members of the Ctr1 family have evolved to maintain Cu homeostasis and therefore manage very low ion fluxes. In contrast, the primary particle size of the $CuFe_2O_4$ nanoparticles is around 8 nm and the specific Cu intake in each internalization event is likely to be much larger, as in the culture medium the particles form 37 nm agglomerates, according to NTA results[25]. This means that internalization of Cu-containing nanoparticles is highly efficient as a method to supply Cu to the cell, and in fact agglomerates of $CuFe_2O_4$ nanoparticles are easily visible in confocal microscopy images after a few hours of incubation[35] In this work, we investigate whether the Cu^{2+} cations leached from the nanoparticles, in addition to their known role of promoting GSH oxidation[25, 32], may also catalyze transamination reactions using pyruvate and different amino acids/peptides as targeted substrates. In addition, we have performed DFT calculations to provide a theoretical support to the catalytic outcomes observed and specifically to the variation of intracellular glutamine, as a key amino acid, together with alanine, as transamination reaction product. We also demonstrate a promising and non-previously reported specific transamination of GSH, thereby adding a new reaction that may target this antioxidant key for the regulation of redox homeostasis in cancer cells.

Results and discussion – Chapter 4

Catalytic transamination of single amino acids under TME conditions. Similar to the work of Mayer et al.[23] we first carried out kinetic studies of the removal of glutamine, glutamic acid and aspartic acid via transamination, although in this case we used Cu-releasing nanoparticles as catalysts (**Figure 2**). Also, the reactions in our case were carried out in the presence of 5 mM of GSH, an expected intracellular concentration in tumor cells[32]. This is important because the presence of GSH promotes Cu^{2+} leaching, in a much larger extent than any of the amino acids tested in this work (***Figure S1***). Concerning the transamination of glutamine, under the catalysis of the leached Cu^{2+} cations the primary amine of glutamine (highlighted in blue, ***Figure 2a***) undergoes exchange with the keto-group of pyruvate (highlighted in red, ***Figure 2a***) yielding the corresponding α-ketoacid derived from the amino acid and alanine (***Figure 2a***) a reaction catalyzed by the released Cu^{2+} from the Cu-Fe nanoparticles[25]. It is noteworthy that this reaction is non-stereospecific[23] and consequently, the D-alanine generated as by-product (half of the total produced) becomes useless for cells. Therefore, the transamination reaction depicted in ***Figure 2a*** is potentially very useful for a catalytic starvation therapy scenario since it simultaneously removes glutamine and pyruvate, two key molecules in different types of cancers[36, 37], and can do so in an oxygen-independent fashion, therefore not being hampered by the hypoxic conditions prevailing in the TME[38]. Next, we monitored the reaction of the $CuFe_2O_4$ nanoparticles with glutamine at different time intervals (***Figure 2b-d***). ^{1}H-NMR analysis at early reaction stages (5 h, ***Figure 2b***) revealed the characteristic signal of the generation of GSSG as by-product of the GSH oxidation[25, 39]. In contrast, we could not find the signal corresponding to alanine, suggesting that kinetics of Cu^{2+}-catalyzed GSH transformation into GSSG are faster in comparison to Cu^{2+}-catalyzed transamination reaction.

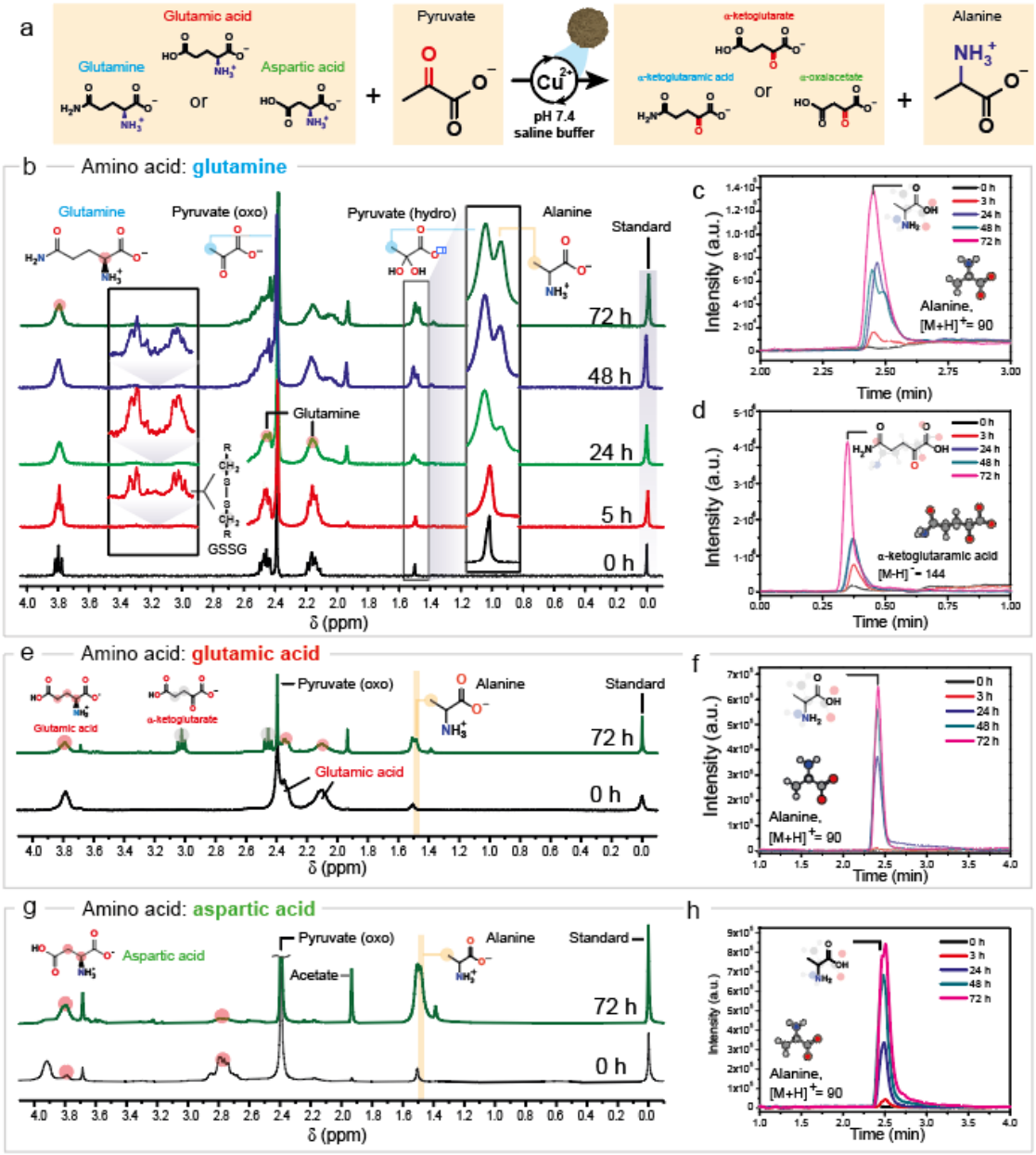

Figure 2. *^{1}H-NMR analysis of the transamination reaction in the presence of $CuFe_2O_4$ nanoparticles: (**a**) Schematic display of the transamination reaction between selected amino acids (glutamine, glutamic acid and aspartic acid acting as amino-donors) and pyruvate to yield α-ketoacid acid and alanine; (**b**) ^{1}H-NMR analysis of the glutamine-pyruvate transamination reaction at different times; (**c-d**) UPLC-MS spectra of the amino-acid by-products of the glutamine-pyruvate transamination corresponding to alanine (m/z = 90, $[M+H]^+$) and α-ketoglutaramic acid (m/z = 144, $[M-H]^-$ respectively; (**e**) ^{1}H-NMR spectra of the glutamic acid-pyruvate transamination at different reaction time intervals; (**f**) UPLC-MS analysis of the increasing formation of alanine as by product of the glutamic acid-pyruvate transamination reaction (additional ^{1}H-NMR spectra and UPLC-MS*

chromatograms can be found in ***Figure S3*** *and* ***Figure S4****); Alanine derived from aspartic acid-pyruvate transamination reaction was also found in (****g****)* ^{1}*H-NMR spectra corresponding to the aspartic acid-pyruvate transamination at different reaction time intervals; (****h****) UPLC-MS analysis of alanine derived from aspartic acid-pyruvate transamination; (Additional* ^{1}*H-NMR spectra/UPLC-MS chromatograms are depicted in* ***Figure S5*** *and* ***Figure S6****). Reaction conditions for all experiments: [Cu] = 6 mM, [Pyruvate] = 30 mM, [Amino acid] = 45 mM, [GSH] = 5 mM, pH = 7.4 (*Na_2HPO_4*/*NaH_2PO_4* 1M), T = 37 ºC.*

Longer reaction times resulted in an increase of the alanine signal (CH_3, 1.48 ppm, **Figure S2**), also detected by UPLC-MS (***Figure 2c***), and α-ketoglutaramic acid (***Figure 2d***), the α-ketoacid derived from glutamine. We also tested transamination with other important single amino acids, such as glutamic acid (***Figure 2e-f, Figure S3 and Figure S4***) and aspartic acid (***Figure 2g-h, Figure S5 and Figure S6***). The results were analogous to glutamine, ^{1}H-NMR and UPLC-MS analyses revealed a time-dependent increase of alanine and the corresponding α-ketoacid, (except for the case of the oxalacetate produced from aspartic acid which can be easily decarboxylated in the presence of transition metals such as Cu^{2+} (***Figure S5***)[40]), together with the depletion of pyruvate and the donor amino acid (***Figure S3-S6***). No alanine was found in the absence of the $CuFe_2O_4$ nanocatalyst (***Figure S7***). The efficiency of the reaction depended on the amino acid employed as substrate, with transamination yields in the order aspartic acid > glutamic acid > glutamine (***Figure S8***) in agreement with the results of Mayer et al.[23] using $CuCl_2$.

Beyond single amino acids: transamination of GSSG. We hypothesized that the same transamination investigated could extend beyond single amino acids to include peptides that possess free carboxyl ($–CO_2^-$) and amino ($–NH_3^+$) groups linked to the α-C atom of an amino acid residue. A very important example of this family of compounds would be GSH and its oxidized form GSSG. Both are peptides that exhibit this specific structural configuration (highlighted in orange in ***Figure 3a***). Given their central role in redox homeostasis in cancer cells, transamination of these molecules could have significant interest in cancer therapy because the resulting unnatural α-ketoGSSG product might be more challenging for cancer cells to metabolize compared to naturally-occurring antioxidants like GSH and GSSG[41].

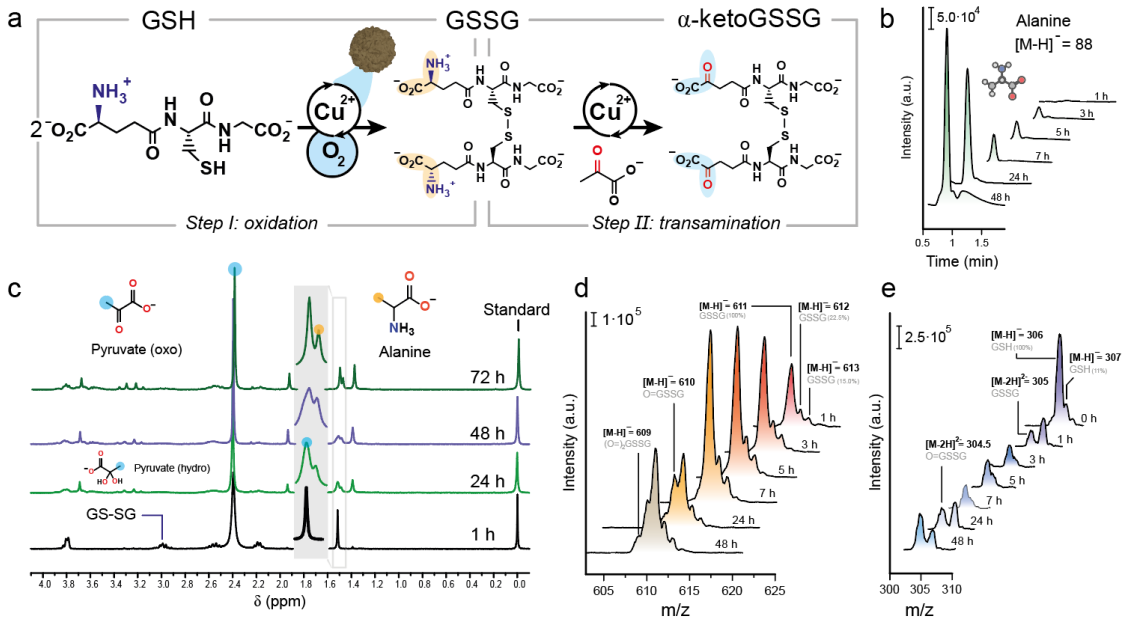

Figure 3. *Cu-catalyzed transamination of GSH-GSSG in the presence of $CuFe_2O_4$ nanoparticles: (**a**) Cu^{2+} released from $CuFe_2O_4$ nanoparticles first catalyzes GSH oxidation with dissolved O_2, giving GSSG; then it furthers catalyzes its transamination with pyruvate; (**b**) UPLC-MS and (**c**) ^{1}H-NMR analysis of the generation of alanine from transamination of GSSG at different reaction times; (**d**, **e**) MS analysis of the formation of α-ketoGSSG and the depletion of GSH at various reaction times. Reaction conditions: [Cu] = 6 mM, [pyruvate] = 30 mM, [GSH] = 5 mM, pH = 7.4 (Na_2HPO_4/NaH_2PO_4 1 M), T = 37 ºC.*

In the presence of O_2, the Cu^{2+}-catalyzed oxidation of GSH to GSSG exhibited faster kinetics than the competing transamination as can be seen at early reaction times (1 h), where UPLC-MS analysis revealed predominant generation of GSSG (***Figure 3d***) and depletion of GSH (***Figure 3e***), with minimal formation of alanine through transamination (***Figure 3b-c***). However, at longer reaction times (24 h and beyond), the UPLC-MS, ^{1}H-NMR, and MS analyses detected the formation of alanine and α-ketoGSSG, demonstrating successful transamination of GSSG (***Figures 3b-d***). Additional experiments confirmed the compatibility of other polypeptides such as γ-Glu-ε-Lys with this transformation (***Figure S10***). Moreover, it was determined that amino acids containing secondary amines like proline were not subjected to transamination (***Figure S9***).

The transamination mechanism was investigated using density functional theory (DFT). Consequently, we used a comprehensive modeling approach that encompassed all pertinent

reaction components, including GSSG/α-ketoGSSG, Cu^{2+}, pyruvate/alanine, and $HPO4^{2-}$, in the calculations illustrated in ***Figure 4***.

Initially, Cu^{2+} establishes strong interactions with the $–CO_2^-$ groups present in GSSG and pyruvate (**Int-I**, ***Figure 4d***). In the most stable conformation discovered, the cation predominantly coordinates with three $–CO_2^-$ groups, two of which stem from a folded branch of GSSG, and the other from pyruvate. Subsequently, one of the $–NH_3^+$ groups of GSSG reacts with the ketone of pyruvate, resulting in the formation of a protonated imine that needs/requires deprotonation before coordinating with Cu to generate **Int-II**. This sequence of steps exhibits slight endergonicity ($\Delta G = 4.1$ kcal·mol^{-1}) when one of the $–CO_2^-$ groups acts as the base for deprotonation to obviate the need for separate calculations. Consistent with previous Cu-catalyzed transaminations[23], the calculated rate-limiting step involves the presence of the activated imine···Cu group. Therefore, the pH employed could influence the reaction kinetics, as a more alkaline solution would render deprotonation and subsequent imine···Cu coordination more favorable. This theoretical approach is supported by the observed roughly doubling of the reaction rate upon raising the pH from 5 to 9 (***Figure 4c***). Furthermore, the computational findings indicate that the transamination equilibrium is essentially energetically balanced ($\Delta G = 1.1$ kcal·mol^{-1}, ***Figure 4d***), emphasizing the importance of an excess of pyruvate in the medium to drive the equilibrium towards the α-ketoGSSG product.

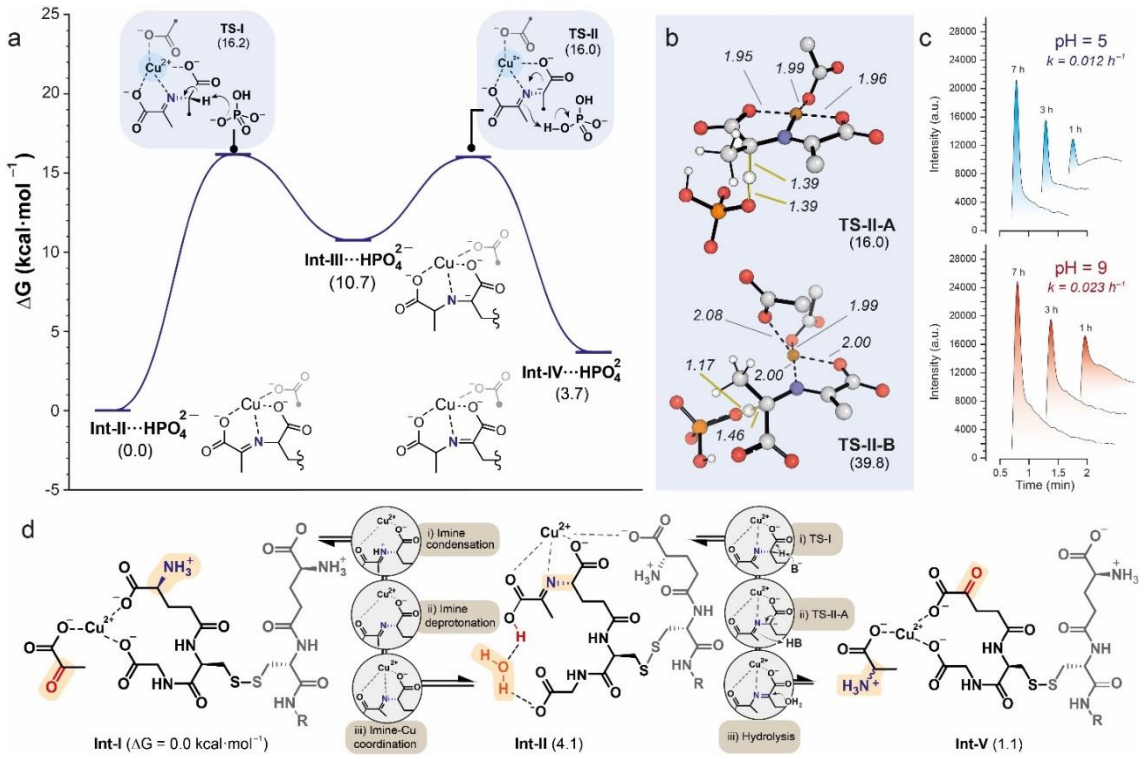

Figure 4. *(**a**) ΔG values for the 1,3-H shift with HPO_4^{2-} acting as the H-transferring agent; (**b**) Depiction of the most stable conformers of **TS-II A** and **TS-II B** (dotted black lines indicate Cu–ligand bonds, thin yellow lines represent TS bonds, and distances are displayed in Å); (**c**) Experimental reaction rates at different pH values after 7 h; (**d**) Thermodynamic aspects of the transamination process. Computational protocols: DFT calculations[42-44] were carried out with ωB97X-D/Def2-QZVPP//ωB97X-D/6-31+G(d,p) [45-53], SMD[54-59] (solvent = water) was included in all the calculations, standard state = 1 M, T = 37 ºC [60].*

Similar to previous mechanisms calculated for metal-catalyzed transaminations[23], the kinetics of the process are governed by a step-wise 1,3-H migration. In this mechanism, a HPO_4^{2-} basic molecule from the solution buffer triggers a H shift from the α-C atom to the iminic C atom (***Figure 4a***). As in the imine-Cu coordination process, this base-promoted 1,3-H migration should be favored by more basic pH environments, which aligns with the experimental kinetic trend (***Figure 4c***). Interestingly, this process not only involves C=N···Cu activation but also CO_2^-···Cu activation of the $-CO_2^-$ group located next to the carbanion resulting from H abstraction. The Cu atom coordinates with this $-CO_2^-$ group, enhancing its capability to stabilize neighboring carbanions

and thus reducing the energy barriers ($\Delta G^{\ddagger}$ from 39.8 to 16.0 kcal in **TS-II B** and **TS-II A**, respectively, ***Figure 4b***).

***Intracellular transamination in U251-MG catalyzed by $CuFe_2O_4$ nanoparticles*.** Encouraged by the activity of lixiviated Cu^{2+} as a transamination catalyst for a variety of biologically relevant substrates, we evaluated the capability of $CuFe_2O_4$ nanoparticles to disrupt the amino acid pool in U251-MG cancer cells. We selected this cell line on the account of the significant role played by glutamine in their metabolism[61]. Indeed, some studies point out the relevance of glutamine in NADPH production and anaplerotic reactions (i.e. to generate Kreb's cycle intermediates) beyond their role as a nitrogen source in glioblastoma cells.[61] We detected a significant decrease in the intracellular glutamine levels in U251-MG cells incubated with the $CuFe_2O_4$ nanoparticles after 72 h (**Figure 5a**). On the other hand, intracellular alanine levels clearly increased for the $CuFe_2O_4$-treated group up to 48 h. This is consistent with the results shown above, as there is a significant pool of intracellular pyruvate and using pyruvate as the ketoacid always yielded alanine in all transamination reactions evaluated throughout this work, regardless of the amino-precursor. Interestingly, alanine was consumed both in the control and in the treated U251-MG cells (**Figure 5b**) at 72 h. We interpret this result as a consequence of cellular metabolic responses. In the absence of other amino acids, alanine can be incorporated into the TCA cycle to support ATP biosynthesis through its enzymatic transamination to pyruvate[62]. In addition, alanine can also serve as nitrogen source in glutamine-starved glioblastoma cells[63]. Both of these facts may explain the strong decrease observed in both groups after 72 h. Finally, although only glutamine was monitored, our results show that the catalyst promotes transamination of a variety of amino-acids and peptides, causing a severe disruption of the cell metabolism. This helps to explain the abrupt interruption seen in the growth of cells for the treatment (**Figure 5c**) after 24 h.

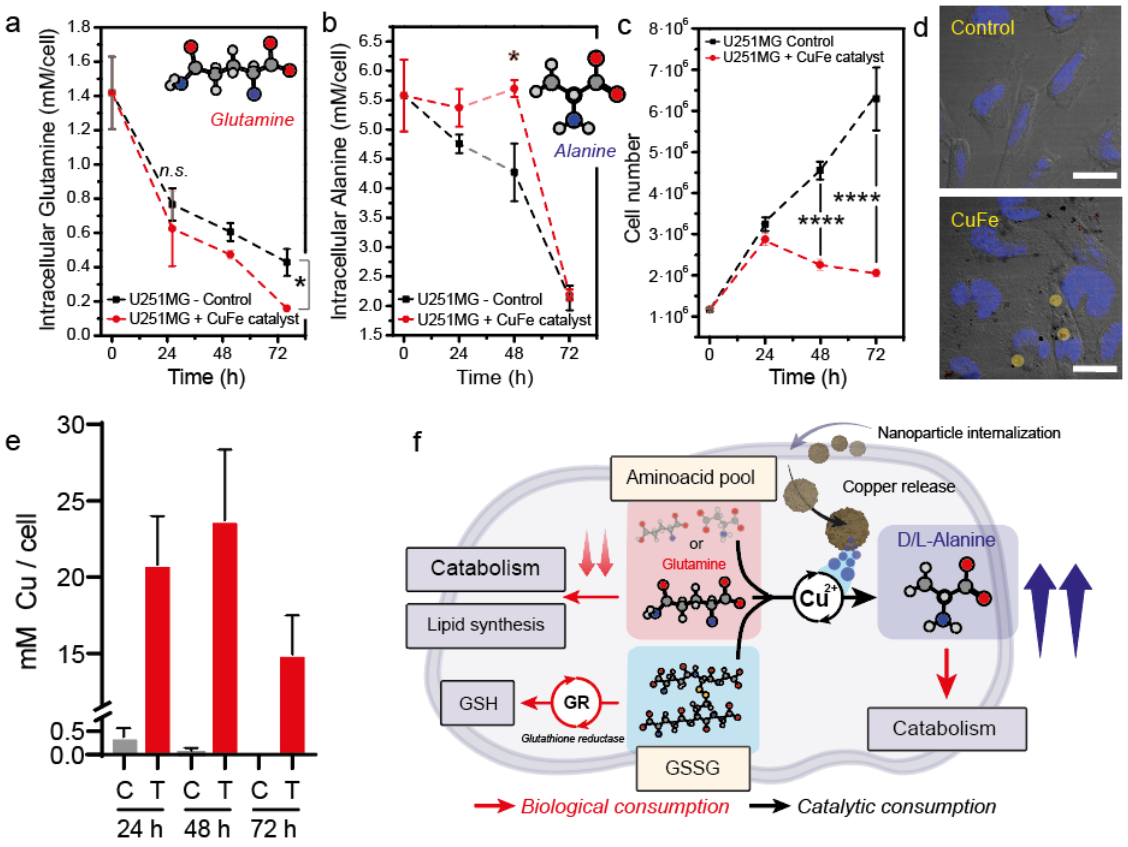

Figure 5. *Tracking the intracellular transamination induced by $CuFe_2O_4$ nanoparticles. (**a**) Intracellular glutamine concentrations decrease for both control and treated U251-MG cells. Glutamine is a key metabolite for cells as one of the major Nitrogen sources and its used both for TCA cycle or fatty acid/nucleotide biosynthesis[64]. Treatment with $CuFe_2O_4$ nanoparticles significantly decreased glutamine levels especially after 72 h; (**b**) Monitoring intracellular alanine concentration revealed different profiles in control/treated U251-MG cells. After 24 and 48 h, the alanine concentration was significantly larger for treated U251 suggesting that artificial transamination had been successfully induced; (**c**) Cell growth stopped in the presence of $CuFe_2O_4$ nanoparticles, while it increased linearly for the control sample; (**d**) Confocal microscopy analysis of U251-MG cells revealed the internalization of $CuFe_2O_4$ nanoparticles in the form of aggregates (highlighted in yellow); (**e**) Intracellular copper levels of U251-MG cells treated with 50 $\mu g \cdot mL^{-1}$ of $CuFe_2O_4$ showed a strong increase of copper concentration up to 48 h, followed by a decrease at 72h; (**f**) Schematic illustration of some possible catalytic pathways of intracellular aminoacid pool: glutamine (or other amino acids) can enter different metabolic routes to enable ATP or lipid biosynthesis. However, internalization of $CuFe_2O_4$ nanoparticles increases the intracellular concentration of Cu^{2+}, a catalyst that promotes*

*artificial amino acid / pyruvate transamination, as well as that of other species with suitable chemical structure such as GSH and GSSG. For GSSG this reaction competes with the reduction of GSSG to GSH by glutathione reductase. Statistically significant differences were express as follows: *p < 0.05, **p < 0.005, ***p < 0.0005 and ****p < 0.00005.*

The successful internalization of the $CuFe_2O_4$ nanocatalyst was confirmed by confocal microscopy (***Figure 5d***). Nanoparticle aggregates could be detected inside U251-MG cells due to their own reflection, close to the cellular nucleus stained in blue (***Figure 5d***). We also studied the evolution of total intracellular copper, the main homogeneous catalysts studied in this work, after the treatment with $CuFe_2O_4$ nanoparticles using microwave plasma atomic emission spectroscopy (MP-AES) (***Figure 5e***). The maximum intracellular copper value was reached at 48 h after the treatment with 50 $\mu g \cdot mL^{-1}$ of $CuFe_2O_4$, which is in agreement with the maximum concentration of intracellular alanine in treated U251-MG cells (***Figure 5b***). After 72 h, intracellular copper concentration decreased down to 14.5 mM, following cellular regulation mechanisms and excretion of nanoparticles via endosomes. However, 72 h gives ample time for Cu^{2+} to perform catalysis using the amino acid pool or the cytosolic GSSG as amino donors, and the pyruvate as α-ketoacid to catalyze the transamination reaction (***Figure 5f***).

Conclusions – Chapter 4

We have explored the catalytic activity of Cu derived from $CuFe_2O_4$ nanoparticles to catalyze reactions involving chemical species that are essential for cell metabolism and proliferation: amino acids, GSSG and pyruvate. Cu^{2+} cations released from Cu-Fe nanoparticles were able to catalyze transamination using glutamine, glutamic acid and aspartic acid as amino acid substrates under conditions relevant to TME (i.e. hypoxia and a 5 mM concentration of GSH). We have expanded the scope of transamination by demonstrating that tri- and dipeptides are also suitable substrates if a α-C with free $-COO^-$/$-NH_3^+$ group is present in their structure. The main candidate for this expanded transamination would be the GSH/GSSG tandem because of their central role to maintain homeostasis in the tumor microenvironment. We have shown experimentally that the reaction proceeds in GSSG and explained it through in-depth mechanistic studies as a result of

the formation of an imine between the oxo-group of pyruvate and the free -NH_2 group of GSSG, followed by the coordination of the imine to Cu(II). Finally, we have also shown that Cu-Fe nanoparticles could drive transamination reactions *in cellulo*. Internalization of Cu-Fe nanoparticles guarantees a high concentration of Cu within U251-MG cells for at least 48 h. As a result, glutamine consumption is accelerated while intracellular alanine levels rise and cell proliferation abruptly stops, a scenario in good agreement with transamination reactions catalyzed by Cu(II)-releasing nanoparticles. In summary, the results of this work establish copper-catalyzed transamination as a new valuable reaction to be added to the existing toolkit of TME-based nanocatalytic therapy.

Experimental section – Chapter 4

Chemicals. L-Glutamine (ReagentPlus®, ≥99% (HPLC)), L-Glutamic Acid (ReagentPlus®, ≥99% (HPLC)), L-Aspartic Acid (ReagentPlus®, ≥99% (HPLC)), L-Alanine (ReagentPlus®, ≥99% (HPLC)), L-Proline (ReagentPlus®, ≥99% (HPLC)), L_Glutathione reduced (≥98%), γ-Glu-ε-Lys (≥98.0% (TLC)), Sodium pyruvate (ReagentPlus®, ≥99%), Iron(III) chloride hexahydrate ($FeCl_3 \cdot 6H_2O$, 97%), copper(II) chloride dihydrate ($CuCl_2 \cdot 2H_2O$, 99.0%), sodium acetate anhydrous (CH_3COONa, 99.0%), bovine serum albumin (BSA), ethylene glycol (EG), dimercaptosuccinic acid (DMSA, 99.0%), Na_2HPO_4, NaH_2PO_4, $(CH_3)_3SiCD_2CD_2CO_2Na$ (98% atom D), Chelex resin were purchased from Sigma-Aldrich and were used without further purification. Acetonitrile (HPLC quality) was purchased from VWR chemicals. Dulbecco's modified Eagle's medium (DMEM, Biowest, France) cell culture medium was supplemented with 10% of Fetal Bovine Serum (FBS, GIBCO, USA) and 1% penicillin/streptomycin and 1% amphotericin (Biowest, France)

Synthesis of the copper-iron oxide nanocatalyst. $CuFe_2O_4$ nanoparticles were prepared following our previous methodologies[25].

^{1}H-NMR analysis of reaction. General procedure. Pyruvate, Aminoacid, Glutathione (GSH) and $CuFe_2O_4$ nanoparticles were added to a sealed vial up to reach a final concentration of 30 mM, 45 mM, 5 mM and 6 mM (expressed in [Cu]), respectively in 10 mL of 1 M Na_2HPO_4/NaH_2PO_4. Prior

to the addition of nanoparticles, O_2 was removed from solution using Ar. Finally, temperature was set up to 37 ºC.

For analysis, 1 mL of the sample was collected with a syringe and further filtered using a 0.22 µm Nylon filter. The resulting solution was incubated with 400 mg of Chelex resin for 30 minutes to remove metal ions to avoid paramagnetism in NMR. Then, 50 µL of D_2O containing 20.76 mM of $(CH_3)_3SiCD_2CD_2CO_2Na$ as internal standard, were mixed with 550 µL of the previous solution and were analyzed using a Bruker Avance III 300 spectrometer (Bruker, Billerica, MA, USA) operating at 300 MHz proton frequency. Quantification of produced alanine was carried out using MestRenova software by integrating -CH_3 peak of alanine and normalizing it to 1.76 mM of the internal standard ($(CH_3)_3SiCD_2CD_2CO_2Na$).

UPLC-MS analysis of reaction. General procedure for all AA except GSH and γ-Glu-ε-Lys. Pyruvate, Aminoacid, Glutathione (GSH) and Cu-Fe nanoparticles were added to a sealed vial up to reach a final concentration of 30 mM, 45 mM, 5 mM and 6 mM (expressed in [Cu]), respectively in 2 mL of 1 M Na_2HPO_4/NaH_2PO_4. Specifically, for γ-Glu-ε-Lys concentrations employed were x4 times lower (i.e. [γ-Glu-ε-Lys] = 11.25 mM, [Pyruvate] 7.5 mM, [GSH] = 1.25 mM and [Cu] = 1.5 mM) Prior to the addition of nanoparticles, O_2 was removed from solution using Ar. Finally, temperature was set up to 37 ºC.

For analysis, 50 µL of the sample were collected with a syringe and diluted in 50 µL of miliQ H_2O. 5 µL of the previous solution were diluted in 995 µL of H_2O:Acetonitrile mixture. Resulting solution was filtered and analyzed using a Waters ACQUITY system H-Class coupled to a single quadrupole mass spectrometer with an electrospray ionization (ESI) ACQUITY QDa mass detector. Data acquisition and processing were performed by using MASSLYNX software (Waters Corporation USA). Chromatographic separation was performed using an ACQUITY UPLC BEH Amide column (130 A, 1.7 u, 2.1 mm x 100 mm, Waters). Mobile phase consisted of an initial mixture of Acetonitrile:H_2O (90:10) at a flow rate 0.5 mL/min, 85 ºC. H_2O composition increased for 3 min until a 65% acetonitrile is reached and then system can recover initial conditions. For analysis of GSH and γ-Glu-ε-Lys reactions, a mobile phase employed was a constant Acetonitrile:H_2O (65:35) at a constant flow rate 0.5 mL/min, 85ºC.

Intracellular analysis of Glutamine and alanine. $8 \cdot 10^5$ U251 cells were seeded onto P100 dishes. After 24 h, cell media was replaced with DMEM (10% FBS, 1% penicillin/streptomycin and 1% amphotericin) supplemented with $CuFe_2O_4$ nanoparticles (0.05 $mg \cdot mL^{-1}$) for treated cells and left incubated for 24h, 48h or 72h, respectively. Then, cells were washed twice with PBS, trypsinized (5 minutes, 37ºC 5% CO_2), centrifuged (300g, 5') and washed again twice with ice-cold PBS (150 rpm , 5'). Finally, cell pellet was resuspended in 300 µL of mili-Q H_2O and ultrasonicated for 30' to ensure a correct cell lysis. Sample for UPLC-MS analysis was prepared by mixing 50 µL of the resulting solution with 950 µL of H_2O:ACN mixture (1:1). All samples were filtered with 0.22 mm w/w PFTE filters before injection in UPLC system. Chromatographic separation was performed using an ACQUITY UPLC BEH Amide column (130 A, 1.7 u, 2.1 mm x 100 mm, Waters). Mobile phase consisted of an initial mixture of Acetonitrile:H_2O (90:10) at a flow rate 0.5 mL/min, 85 ºC. H_2O composition increased for 3 min until a 65% acetonitrile is reached and then system can recover initial conditions.

Analysis of $CuFe_2O_4$ internalization by confocal microscopy. Confocal microscopy assay was carried out to assess the capacity of internalization of $CuFe_2O_4$ NPs into U251-MG. Cells were seeded onto 12 mm Ø coverslips, which were deposited on a 24-well plate, at a density of 20 000 cells per well, and incubated at 37 ºC and 5% CO_2. After 24 h, cells were treated with $CuFe_2O_4$ NPs dispersed in DMEM at a concentration of 25 $\mu g \cdot mL^{-1}$ during 24 h (for negative control wells, DMEM was replaced with fresh media). After this time, cells were washed 3 times with DPBS, fixed with 4% paraformaldehyde, and then washed 3 more times with DPBS. In order to prepare the samples for confocal microscopy, cells were permeabilized with 0.1% saponine. After that, samples were deposited onto a drop of Fluoromount-G + DAPI for nuclei staining. Nanoparticle aggregates could be observed due to the reflection of the incident light. To confirm the presence of the nanoparticles inside the cell, a Z-Stack assay of the whole cell, and its ulterior maximum orthogonal projection were performed. This assay was carried out in a confocal microscope (ZEISS LSM 880 Confocal Microscope), using a 63x/1.4 Oil DIC M27 objective.

Quantification of intracellular copper. In a 6 well-plate, $2 \cdot 10^5$ cells per well were seeded and incubated at 37ºC under an atmosphere of 5% CO_2 for 24 h. Then, the cell culture medium was

replaced by a dispersion of $CuFe_2O_4$ nanoparticles in DMEM with a final concentration of 50 $\mu g \cdot mL^{-1}$. To analyze the internalized copper, cells were detached using a 0.25% Trypsin (X0915-100, Biowest, France) solution in PBS, centrifuged at 6700 g for 5 minutes. The cell pellet was digested with Aqua Regia ($HCl \cdot HNO_3$ 3:1, v/v) overnight and analyzed with an Agilent 4100 MP-AES (Agilent, USA). All samples were filtered using a 0.22 µm nylon filter before their analysis.

Statistical analysis. All the results are expressed as mean ± S.E.M. Statistical analysis of the biological experiments and the significant differences among the means were evaluated by t-test using GraphPad Software). Statistically significant differences were express as follows: *p < 0.05, **p < 0.005, ***p < 0.0005 and ****p < 0.00005.

Computational methods. The ωB97X-D[46]/6-31+G(d,p)[47] combination was employed to optimize the geometries of stationary points. This functional has a track record of retrieving accurate geometries for systems with non-covalent interactions, such as hydrogen bonds[46,65]. To confirm that the optimized geometries were either energy minima or transition states, vibrational frequency calculations were carried out, generating vibrational information to calculate thermochemistry data using *GoodVibes*. Electronic energies were refined using single point energy corrections at the ωB97X-D/Def2-QZVPP[52] level. Furthermore, solvent effects were considered in all calculations using the integral equation formalism variant of the polarizable continuum model (IEF-PCM) with the SMD solvation model (solvent = water)[59].

Gaussian 16[42] was used to run all the density functional theory (DFT) calculations. *AQME*[43] was employed to i) generate conformers (program = RDKit)[44], ii) identify and correct errors from geometry optimization and frequency DFT calculations, iii) remove duplicates, and iv) generate input files for single-point corrections in an automated manner (the command lines and input CSV file used are included in the ESI). Molecular representations were created using *PyMOL*[66] with the display settings developed by Dr. Robert S. Paton from Colorado State University, which are openly accessible[67].

The calculated vibrational entropies were corrected using quasi-harmonic (QHA) corrections, with a frequency cut-off value of 100.0 cm^{-1}, as proposed by Grimme[68]. This correction was performed using the *GoodVibes*[60] program at a temperature of 310.15 K (37 °C). In addition, a correction for

the change in standard state from gas phase at 1 atm to a 1 M solution was introduced using the "-c 1" option in *GoodVibes*. The single point energies from ωB97X-D/Def2-QZVPP were corrected using the G corrections computed with ωB97X-D/6-31+G(d,p) to obtain the final G values. This correction was performed using the "--spc SUFFIX" option in *GoodVibes*. All the conformers were considered to calculate the reported Boltzmann-weighted G values of the different reaction steps using the "--pes FILENAME.yaml" option in *GoodVibes*. All these thermochemical values were tabulated in a separate file of the ESI. Automating the generation of G profiles helped us avoid potential errors resulting from manual manipulation of the data.

References – Chapter 4

1. Sousa-Castillo, A.; Mariño-López, A.; Puértolas, B.; Correa-Duarte, M. A., Nanostructured Heterogeneous Catalysts for Bioorthogonal Reactions. *Angewandte Chemie International Edition* **2023,** *62* (10), e202215427.

2. Pérez-López, A. M.; Rubio-Ruiz, B.; Sebastián, V.; Hamilton, L.; Adam, C.; Bray, T. L.; Irusta, S.; Brennan, P. M.; Lloyd-Jones, G. C.; Sieger, D.; Santamaría, J.; Unciti-Broceta, A., Gold-Triggered Uncaging Chemistry in Living Systems. *Angewandte Chemie International Edition* **2017,** *56* (41), 12548-12552.

3. Clavadetscher, J.; Hoffmann, S.; Lilienkampf, A.; Mackay, L.; Yusop, R. M.; Rider, S. A.; Mullins, J. J.; Bradley, M., Copper Catalysis in Living Systems and In Situ Drug Synthesis. **2016,** *55* (50), 15662-15666.

4. Chen, Z.; Li, H.; Bian, Y.; Wang, Z.; Chen, G.; Zhang, X.; Miao, Y.; Wen, D.; Wang, J.; Wan, G.; Zeng, Y.; Abdou, P.; Fang, J.; Li, S.; Sun, C.-J.; Gu, Z., Bioorthogonal catalytic patch. *Nature Nanotechnology* **2021,** *16* (8), 933-941.

5. Liang, T.; Chen, Z.; Li, H.; Gu, Z., Bioorthogonal catalysis for biomedical applications. *Trends in Chemistry* **2022,** *4* (2), 157-168.

6. Huo, M.; Wang, L.; Wang, Y.; Chen, Y.; Shi, J., Nanocatalytic Tumor Therapy by Single-Atom Catalysts. *ACS Nano* **2019,** *13* (2), 2643-2653.

7. Yang, B.; Chen, Y.; Shi, J., Nanocatalytic Medicine. *Advanced Materials* **2019,** *31* (39), 1901778.

8. Liu, P.; Huo, M.; Shi, J., Nanocatalytic Medicine of Iron-Based Nanocatalysts. **2021,** *3* (2), 2445-2463.

9. Lin, L.-S.; Song, J.; Song, L.; Ke, K.; Liu, Y.; Zhou, Z.; Shen, Z.; Li, J.; Yang, Z.; Tang, W.; Niu, G.; Yang, H.-H.; Chen, X., Simultaneous Fenton-like Ion Delivery and Glutathione Depletion by MnO2-Based Nanoagent to Enhance Chemodynamic Therapy. *Angewandte Chemie International Edition* **2018,** *57* (18), 4902-4906.

10. Ma, B.; Wang, S.; Liu, F.; Zhang, S.; Duan, J.; Li, Z.; Kong, Y.; Sang, Y.; Liu, H.; Bu, W.; Li, L., Self-Assembled Copper–Amino Acid Nanoparticles for in Situ Glutathione "AND" H2O2 Sequentially Triggered Chemodynamic Therapy. *Journal of the American Chemical Society* **2019,** *141* (2), 849-857.

11. Meng, X.; Li, D.; Chen, L.; He, H.; Wang, Q.; Hong, C.; He, J.; Gao, X.; Yang, Y.; Jiang, B.; Nie, G.; Yan, X.; Gao, L.; Fan, K., High-Performance Self-Cascade Pyrite Nanozymes for Apoptosis–Ferroptosis Synergistic Tumor Therapy. *ACS Nano* **2021,** *15* (3), 5735-5751.

12. Wang, D.; Wu, H.; Wang, C.; Gu, L.; Chen, H.; Jana, D.; Feng, L.; Liu, J.; Wang, X.; Xu, P.; Guo, Z.; Chen, Q.; Zhao, Y., Self-Assembled Single-Site Nanozyme for Tumor-Specific Amplified Cascade Enzymatic Therapy. *Angewandte Chemie International Edition* **2021,** *60* (6), 3001-3007.

13. Xiong, Y.; Xiao, C.; Li, Z.; Yang, X., Engineering nanomedicine for glutathione depletion-augmented cancer therapy. *Chemical Society Reviews* **2021,** *50* (10), 6013-6041.

14. Yang, B.; Chen, Y.; Shi, J., Reactive Oxygen Species (ROS)-Based Nanomedicine. *Chemical Reviews* **2019,** *119* (8), 4881-4985.

15. Tang, Z.; Zhao, P.; Wang, H.; Liu, Y.; Bu, W., Biomedicine Meets Fenton Chemistry. *Chemical Reviews* **2021,** *121* (4), 1981-2019.

16. Szatrowski, T. P.; Nathan, C. F. J. C. r., Production of large amounts of hydrogen peroxide by human tumor cells. **1991,** *51* (3), 794-798.

17. Wang, C.; Yang, J.; Dong, C.; Shi, S., Glucose Oxidase-Related Cancer Therapies. *Advanced Therapeutics* **2020,** *3* (10), 2000110.

18. Hayes, J. D.; Dinkova-Kostova, A. T.; Tew, K. D., Oxidative Stress in Cancer. *Cancer cell* **2020,** *38* (2), 167-197.

19. Liberti, M. V.; Locasale, J. W., The Warburg Effect: How Does it Benefit Cancer Cells? *Trends in biochemical sciences* **2016,** *41* (3), 211-218.

20. Wu, C.; Liu, Z.; Chen, Z.; Xu, D.; Chen, L.; Lin, H.; Shi, J., A nonferrous ferroptosis-like strategy for antioxidant inhibition-synergized nanocatalytic tumor therapeutics. *Science advances* **2021,** *7* (39), eabj8833.

21. Chen, S.; Yang, J.; Liang, Z.; Li, Z.; Xiong, W.; Fan, Q.; Shen, Z.; Liu, J.; Xu, Y., Synergistic Functional Nanomedicine Enhances Ferroptosis Therapy for Breast Tumors by a Blocking Defensive Redox System. *ACS Applied Materials & Interfaces* **2023,** *15* (2), 2705-2713.

22. Sun, Y.; Zhou, Z.; Yang, S.; Yang, H., Modulating hypoxia inducible factor-1 by nanomaterials for effective cancer therapy. *WIREs Nanomedicine and Nanobiotechnology* **2022,** *14* (1), e1766.

23. Mayer, R. J.; Kaur, H.; Rauscher, S. A.; Moran, J., Mechanistic Insight into Metal Ion-Catalyzed Transamination. *Journal of the American Chemical Society* **2021,** *143* (45), 19099-19111.

24. Dherbassy, Q.; Mayer, R. J.; Muchowska, K. B.; Moran, J., Metal-Pyridoxal Cooperativity in Nonenzymatic Transamination. *Journal of the American Chemical Society* **2023**.

25. Bonet-Aleta, J.; Encinas-Gimenez, M.; Urriolabeitia, E.; Martin-Duque, P.; Hueso, J. L.; Santamaria, J., Unveiling the interplay between homogeneous and heterogeneous catalytic mechanisms in copper–iron nanoparticles working under chemically relevant tumour conditions. *Chemical Science* **2022,** *13* (28), 8307-8320.

26. Vander Heiden, M. G.; Cantley, L. C.; Thompson, C. B., Understanding the Warburg effect: the metabolic requirements of cell proliferation. *Science (New York, N.Y.)* **2009,** *324* (5930), 1029-33.

27. Butler, M.; van der Meer, L. T.; van Leeuwen, F. N., Amino Acid Depletion Therapies: Starving Cancer Cells to Death. *Trends in endocrinology and metabolism: TEM* **2021,** *32* (6), 367-381.

28. DeBerardinis, R. J.; Chandel, N. S., Fundamentals of cancer metabolism. **2016,** *2* (5), e1600200.

29. Fagan, R. L.; Palfey, B. A., 7.03 - Flavin-Dependent Enzymes. In *Comprehensive Natural Products II*, Liu, H.-W.; Mander, L., Eds. Elsevier: Oxford, 2010; pp 37-113.

30. Ohgami, R. S.; Campagna, D. R.; McDonald, A.; Fleming, M. D., The Steap proteins are metalloreductases. *Blood* **2006,** *108* (4), 1388-94.

31. Chen, L.; Min, J.; Wang, F., Copper homeostasis and cuproptosis in health and disease. *Signal Transduction and Targeted Therapy* **2022,** *7* (1), 378.

32. Bonet-Aleta, J.; Sancho-Albero, M.; Calzada-Funes, J.; Irusta, S.; Martin-Duque, P.; Hueso, J. L.; Santamaria, J., Glutathione-Triggered catalytic response of Copper-Iron mixed oxide Nanoparticles. Leveraging tumor microenvironment conditions for chemodynamic therapy. *Journal of Colloid and Interface Science* **2022,** *617*, 704-717.

33. Wang, Z.; Li, N.; Zhao, J.; White, J. C.; Qu, P.; Xing, B., CuO Nanoparticle Interaction with Human Epithelial Cells: Cellular Uptake, Location, Export, and Genotoxicity. *Chemical Research in Toxicology* **2012,** *25* (7), 1512-1521.

34. Rennick, J. J.; Johnston, A. P. R.; Parton, R. G., Key principles and methods for studying the endocytosis of biological and nanoparticle therapeutics. *Nature Nanotechnology* **2021,** *16* (3), 266-276.

35. Bonet-Aleta, J.; Sancho-Albero, M.; Calzada-Funes, J.; Irusta, S.; Martin-Duque, P.; Hueso, J. L.; Santamaria, J., Glutathione-Triggered catalytic response of Copper-Iron mixed oxide Nanoparticles. Leveraging tumor microenvironment conditions for chemodynamic therapy. *Journal of colloid and interface science* **2022,** *617*, 704-717.

36. Elia, I.; Rossi, M.; Stegen, S.; Broekaert, D.; Doglioni, G.; van Gorsel, M.; Boon, R.; Escalona-Noguero, C.; Torrekens, S.; Verfaillie, C.; Verbeken, E.; Carmeliet, G.; Fendt, S.-M., Breast cancer cells rely on environmental pyruvate to shape the metastatic niche. *Nature* **2019,** *568* (7750), 117-121.

37. Yoo, H. C.; Yu, Y. C.; Sung, Y.; Han, J. M., Glutamine reliance in cell metabolism. *Experimental & Molecular Medicine* **2020,** *52* (9), 1496-1516.

38. Höckel, M.; Vaupel, P., Tumor Hypoxia: Definitions and Current Clinical, Biologic, and Molecular Aspects. *JNCI: Journal of the National Cancer Institute* **2001,** *93* (4), 266-276.

39. Ngamchuea, K.; Batchelor-McAuley, C.; Compton, R. G., The Copper(II)-Catalyzed Oxidation of Glutathione. *Chemistry – A European Journal* **2016,** *22* (44), 15937-15944.

40. Krebs, H. A., The effect of inorganic salts on the ketone decomposition of oxaloacetic acid. *Biochemical Journal* **1942,** *36* (3-4), 303-305.

41. Bansal, A.; Simon, M. C., Glutathione metabolism in cancer progression and treatment resistance. *The Journal of cell biology* **2018,** *217* (7), 2291-2298.

42. Frisch, M. J.; Trucks, G. W.; Schlegel, H. B.; Scuseria, G. E.; Robb, M. A.; Cheeseman, J. R.; Scalmani, G.; Barone, V.; Petersson, G. A.; Nakatsuji, H.; Li, X.; Caricato, M.; Marenich, A. V.; Bloino, J.; Janesko, B. G.; Gomperts, R.; Mennucci, B.; Hratchian, H. P.; Ortiz, J. V.; Izmaylov, A. F.; Sonnenberg, J. L.; Williams; Ding, F.; Lipparini, F.; Egidi, F.; Goings, J.; Peng, B.; Petrone, A.; Henderson, T.; Ranasinghe, D.; Zakrzewski, V. G.; Gao, J.; Rega, N.; Zheng, G.; Liang, W.; Hada, M.; Ehara, M.; Toyota, K.; Fukuda, R.; Hasegawa, J.; Ishida, M.; Nakajima, T.; Honda, Y.; Kitao, O.; Nakai, H.; Vreven, T.; Throssell, K.; Montgomery Jr., J. A.; Peralta, J. E.; Ogliaro, F.; Bearpark, M. J.; Heyd, J. J.; Brothers, E. N.; Kudin, K. N.; Staroverov, V. N.; Keith, T. A.; Kobayashi, R.; Normand, J.; Raghavachari, K.; Rendell, A. P.; Burant, J. C.; Iyengar, S. S.; Tomasi, J.; Cossi, M.; Millam, J. M.; Klene, M.; Adamo, C.; Cammi, R.; Ochterski, J. W.; Martin, R. L.; Morokuma, K.; Farkas, O.; Foresman, J. B.; Fox, D. J. *Gaussian 16 Rev. C.01*, Wallingford, CT, 2016.

43. Alegre-Requena, J. V.; Shree, S. S. V.; Perez-Soto, R.; Alturaifi, T. M.; Paton, R. S., AQME: Automated quantum mechanical environments for researchers and educators. *Wires Comput Mol Sci* **2023**, e1663.

44. Landrum, G. Rdkit: Open-source cheminformatics software.

45. Becke, A. D., Density-functional thermochemistry. V. Systematic optimization of exchange-correlation functionals. *The Journal of Chemical Physics* **1997,** *107* (20), 8554-8560.

46. Chai, J.-D.; Head-Gordon, M., Long-range corrected hybrid density functionals with damped atom–

atom dispersion corrections. *Physical Chemistry Chemical Physics* **2008,** *10* (44), 6615-6620.

47. Hehre, W. J.; Ditchfield, R.; Pople, J. A., Self—Consistent Molecular Orbital Methods. XII. Further Extensions of Gaussian—Type Basis Sets for Use in Molecular Orbital Studies of Organic Molecules. *The Journal of Chemical Physics* **2003,** *56* (5), 2257-2261.

48. Hariharan, P. C.; Pople, J. A., The influence of polarization functions on molecular orbital hydrogenation energies. *Theoretica chimica acta* **1973,** *28* (3), 213-222.

49. Krishnan, R.; Binkley, J. S.; Seeger, R.; Pople, J. A., Self-consistent molecular orbital methods. XX. A basis set for correlated wave functions. *The Journal of Chemical Physics* **2008,** *72* (1), 650-654.

50. McLean, A. D.; Chandler, G. S., Contracted Gaussian basis sets for molecular calculations. I. Second row atoms, Z=11–18. *The Journal of Chemical Physics* **2008,** *72* (10), 5639-5648.

51. Francl, M. M.; Pietro, W. J.; Hehre, W. J.; Binkley, J. S.; Gordon, M. S.; DeFrees, D. J.; Pople, J. A., Self-consistent molecular orbital methods. XXIII. A polarization-type basis set for second-row elements. *The Journal of Chemical Physics* **1982,** *77* (7), 3654-3665.

52. Weigend, F.; Ahlrichs, R., Balanced basis sets of split valence, triple zeta valence and quadruple zeta valence quality for H to Rn: Design and assessment of accuracy. *Physical Chemistry Chemical Physics* **2005,** *7* (18), 3297-3305.

53. Weigend, F., Accurate Coulomb-fitting basis sets for H to Rn. *Physical Chemistry Chemical Physics* **2006,** *8* (9), 1057-1065.

54. Cancès, E.; Mennucci, B.; Tomasi, J., A new integral equation formalism for the polarizable continuum model: Theoretical background and applications to isotropic and anisotropic dielectrics. *The Journal of Chemical Physics* **1997,** *107* (8), 3032-3041.

55. Mennucci, B.; Cancès, E.; Tomasi, J., Evaluation of Solvent Effects in Isotropic and Anisotropic Dielectrics and in Ionic Solutions with a Unified Integral Equation Method: Theoretical Bases, Computational Implementation, and Numerical Applications. *The Journal of Physical Chemistry B* **1997,** *101* (49), 10506-10517.

56. Mennucci, B.; Tomasi, J., Continuum solvation models: A new approach to the problem of solute's charge distribution and cavity boundaries. *The Journal of Chemical Physics* **1997,** *106* (12), 5151-5158.

57. Tomasi, J.; Mennucci, B.; Cancès, E., The IEF version of the PCM solvation method: an overview of a new method addressed to study molecular solutes at the QM ab initio level. *Journal of Molecular Structure: THEOCHEM* **1999,** *464* (1), 211-226.

58. Scalmani, G.; Frisch, M. J., Continuous surface charge polarizable continuum models of solvation. I. General formalism. *The Journal of Chemical Physics* **2010,** *132* (11).

59. Marenich, A. V.; Cramer, C. J.; Truhlar, D. G., Universal Solvation Model Based on Solute Electron Density and on a Continuum Model of the Solvent Defined by the Bulk Dielectric Constant and Atomic Surface Tensions. *The Journal of Physical Chemistry B* **2009,** *113* (18), 6378-6396.

60. Luchini, G.; Alegre-Requena, J.; Funes-Ardoiz, I.; Paton, R. S. J. F., GoodVibes: automated thermochemistry for heterogeneous computational chemistry data. *F1000Research* **2020**, *9*, 291.

61. DeBerardinis, R. J.; Mancuso, A.; Daikhin, E.; Nissim, I.; Yudkoff, M.; Wehrli, S.; Thompson, C. B., Beyond aerobic glycolysis: Transformed cells can engage in glutamine metabolism that exceeds the requirement for protein and nucleotide synthesis. **2007,** *104* (49), 19345-19350.

62. Nelson, D. L.; Lehninger, A. L.; Cox, M. M., *Lehninger Principles of Biochemistry*. W. H. Freeman: 2008.

63. Tardito, S.; Oudin, A.; Ahmed, S. U.; Fack, F.; Keunen, O.; Zheng, L.; Miletic, H.; Sakariassen, P. Ø.; Weinstock, A.; Wagner, A.; Lindsay, S. L.; Hock, A. K.; Barnett, S. C.; Ruppin, E.; Mørkve, S. H.; Lund-Johansen, M.; Chalmers, A. J.; Bjerkvig, R.; Niclou, S. P.; Gottlieb, E., Glutamine synthetase activity fuels nucleotide biosynthesis and supports growth of glutamine-restricted glioblastoma. *Nature Cell Biology* **2015,** *17* (12), 1556-1568.

64. Altman, B. J.; Stine, Z. E.; Dang, C. V., From Krebs to clinic: glutamine metabolism to cancer therapy. *Nature Reviews Cancer* **2016,** *16* (10), 619-634.

65. Goerigk, L.; Grimme, S., A thorough benchmark of density functional methods for general main group thermochemistry, kinetics, and noncovalent interactions. Phys. *Chem. Chem. Phys*. **2011**, *13*, 6670–6688.

66. The PyMOL Molecular Graphics System, version 2.0.7, Schrödinger, LLC.

67. https://gist.github.com/bobbypaton (accessed 09 July 2021).

68. Grimme, S., Supramolecular Binding Thermodynamics by Dispersion-Corrected Density Functional Theory. *Chem. Eur. J*. **2012**, *18*, 9955–9964

Supplementary information – Chapter 4

Adapted from:

Cu-releasing nanoparticles induce the catalytic transamination of amino acids and GSSG under tumor microenvironment conditions

Javier Bonet-Aleta[1,2,3,4], Juan Vicente Alegre-Requena[5], Javier Martin-Martin[1,6], Miguel Encinas-Gimenez[1,2,3,4], Ana Martín-Pardillos[1,2,3,4], Jose L. Hueso[1,2,3,4,*], Jesus Santamaria[1,2,3,4,*]

[1] Instituto de Nanociencia y Materiales de Aragon (INMA) CSIC-Universidad de Zaragoza, Campus Rio Ebro, Edificio I+D, C/ Poeta Mariano Esquillor, s/n, 50018, Zaragoza, (Spain).

[2] Department of Chemical and Environmental Engineering, University of Zaragoza, Campus Rio Ebro, C/María de Luna, 3, 50018 Zaragoza (Spain).

[3] Networking Res. Center in Biomaterials, Bioengineering and Nanomedicine (CIBER-BBN), Instituto de Salud Carlos III; 28029 Madrid (Spain)

[4] Instituto de Investigación Sanitaria (IIS) de Aragón, Avenida San Juan Bosco, 13, 50009 Zaragoza, Spain.

[5] Departamento de Química Inorgánica, Instituto de Síntesis Química y Catálisis Homogénea (ISQCH) CSIC-Universidad de Zaragoza, C/ Pedro Cerbuna 12, 50009 Zaragoza, Spain.

[6] Department of Organic Chemistry, University of Zaragoza, Zaragoza (Spain).

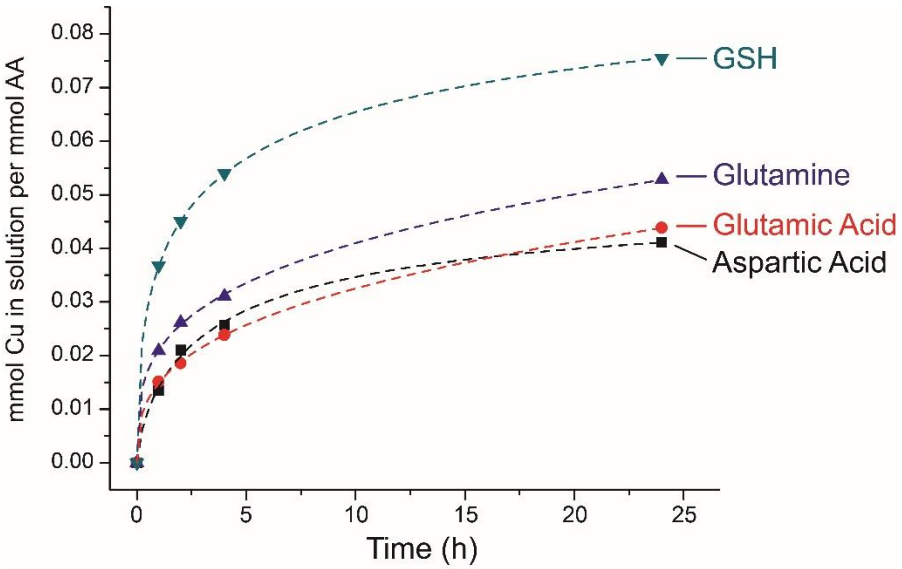

Figure S1. *Evolution of copper leached from $CuFe_2O_4$ nanoparticles in the presence of different biomolecules evaluated in this work for the transamination reaction including GSH, glutamine, glutamic acid and aspartic acid, normalized per mmol of GSH/AA. Reaction conditions: $[AA]_0$ = 20 mM, $[GSH]_0$ = 5 mM, T = 37ºC, pH = 7.4 (buffered with TRIS 0.01 M).*

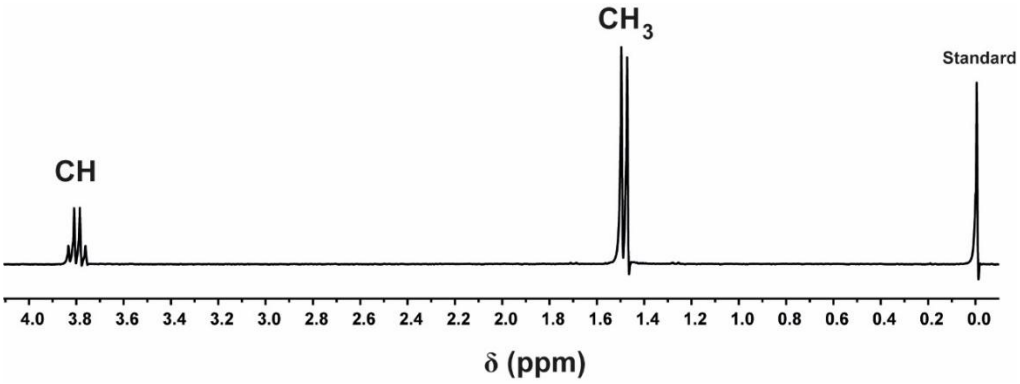

Figure S2. *^{1}H-NMR spectra of commercial Alanine at pH = 7.4.*

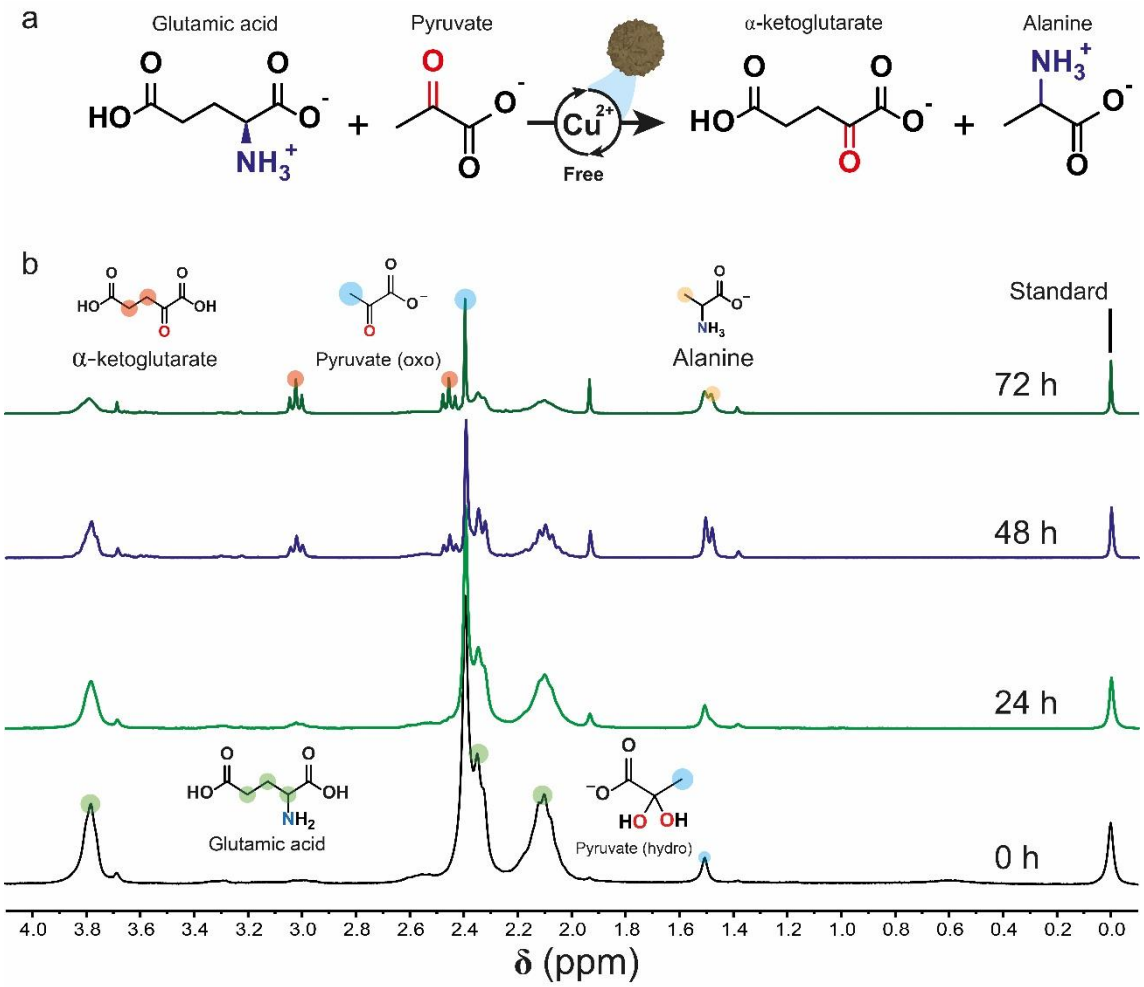

Figure S3. *(**a**) Transamination reaction between glutamic acid and pyruvate catalyzed by Cu^{2+} released from nanoparticles. (**b**) ^{1}H-NMR analysis of glutamic acid / pyruvate transamination catalyzed by CuFe nanoparticles reveals the formation of alanine with time. Reaction conditions: [Cu] = 6 mM, [Pyruvate] = 30 mM, [Glutamic Acid] = 45 mM, [GSH] = 5 mM, pH = 7.4 (Na_2HPO_4/NaH_2PO_4 1M), T = 37ºC.*

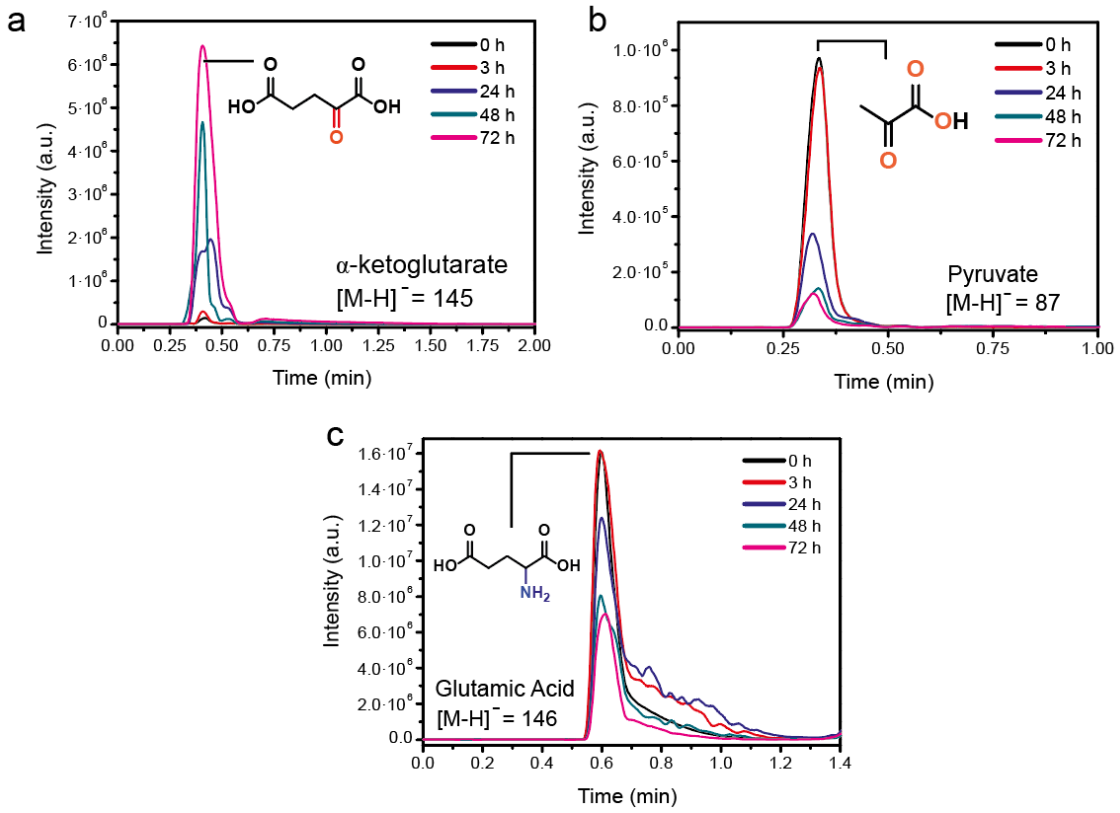

Figure S4. *UPLC-MS chromatograms analysis of the Glutamic Acid/Pyruvate transamination catalyzed by Cu^{2+} released from $CuFe_2O_4$ nanoparticles UPLC-MS chromatograms of (**a**) α-ketoglutarate, (**b**) pyruvate and (**c**) glutamic acid show a clear increase in the peak intensity of α-ketoglutarate and a decrease in the case of pyruvate and glutamic acid. Reaction conditions: [Cu] = 6 mM, [Pyruvate] = 30 mM, [Glutamic Acid] = 45 mM, [GSH] = 5 mM, pH = 7.4 (Na_2HPO_4/NaH_2PO_4 1M), T = 37 ºC.*

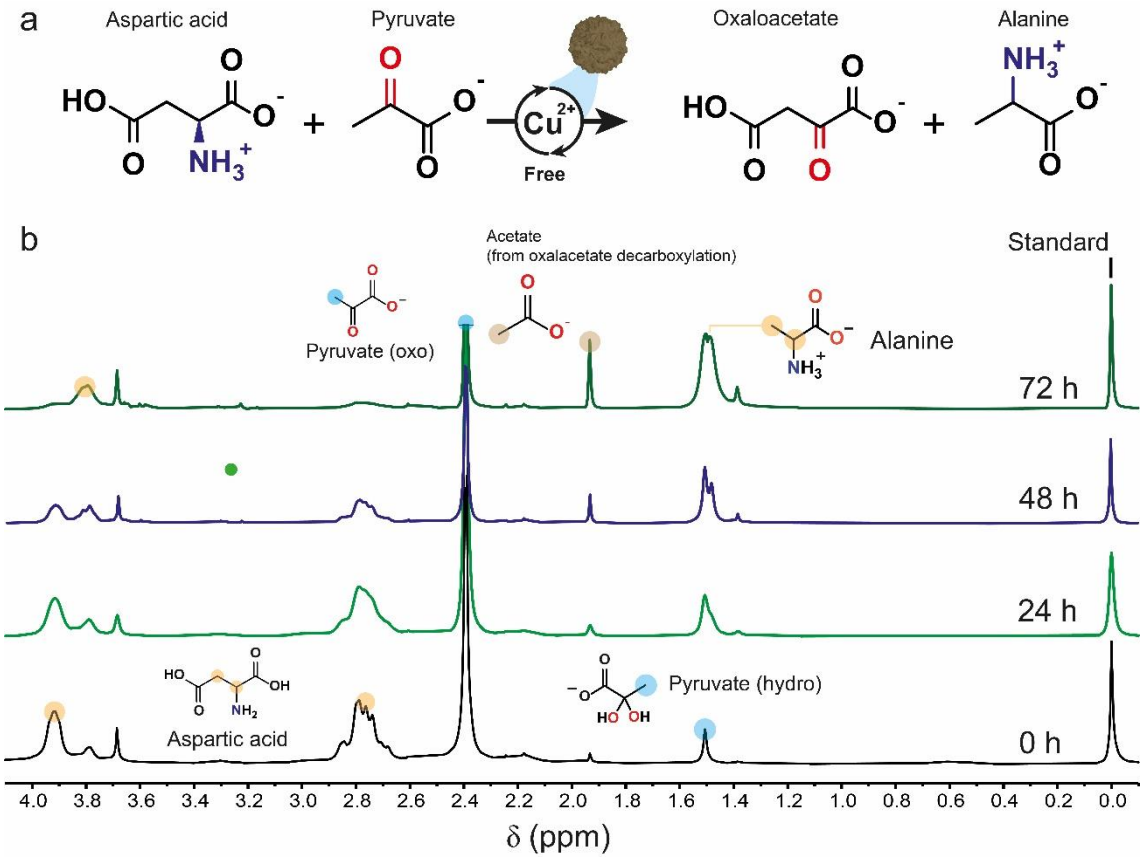

Figure S5. *(**a**) Transamination reaction between aspartic acid and pyruvate catalyzed by Cu^{2+} released from nanoparticles. (**b**). ^{1}H-NMR analysis of aspartic acid / pyruvate transamination catalyzed by CuFe nanoparticles reveals the formation of alanine with time. Reaction conditions: [Cu] = 6 mM, [Pyruvate] = 30 mM, [Aspartic Acid] = 45 mM, [GSH] = 5 mM, pH = 7.4 (Na_2HPO_4/NaH_2PO_4 1M), T = 37ºC.*

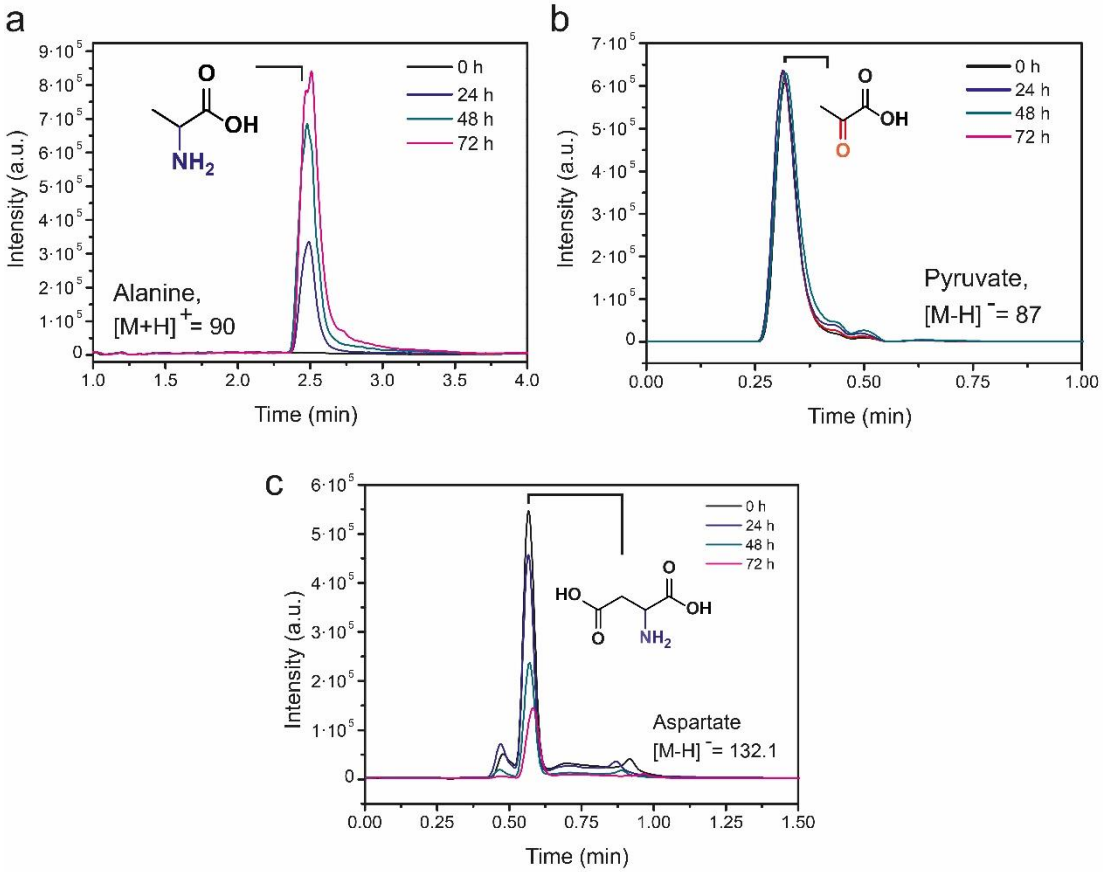

Figure S6. *UPLC-MS chromatograms analysis of the aspartic acid / pyruvate transamination catalyzed by Cu^{2+} derived from $CuFe_2O_4$ nanoparticles. (a) UPLC-MS chromatograms of Alanine, (b) Pyruvate and (c) Aspartate. Results show an increase in the peak intensity of alanine and a decrease in aspartic acid with time. In this reaction, we were not able to detect the corresponding α-ketoacid likely because it can undergo decarboxylation to pyruvate in the presence of Cu^{2+} [1]. Also, we suggest this may be the reason of not finding a pyruvate decay. Reaction conditions: [Cu] = 6 mM, [Pyruvate] = 30 mM, [Aspartic Acid] = 45 mM, [GSH] = 5 mM, pH = 7.4 (Na_2HPO_4/NaH_2PO_4 1M), T = 37ºC.*

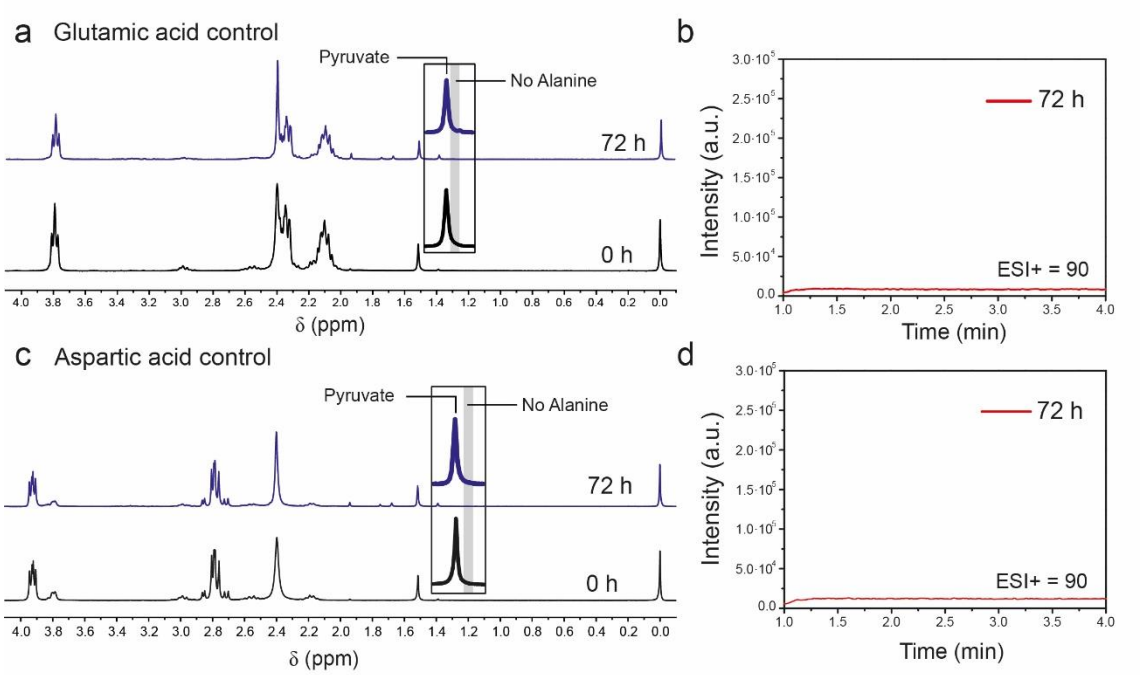

Figure S7. *Control experiment followed by (**a**) ^{1}H-NMR and (**b**) UPLC-MS analysis of the glutamic acid / pyruvate reaction in the absence of the catalyst revealed no alanine formation. (**c**) ^{1}H-NMR and (**d**) UPLC-MS analysis of the aspartic acid / pyruvate reaction in the absence of the catalyst revealed no alanine formation. Reaction conditions: [Cu] = 0 mM, [Pyruvate] = 30 mM, [Amino Acid] = 45 mM, [GSH] = 5 mM, pH = 7.4 (Na_2HPO_4/NaH_2PO_4 1M), T = 37ºC.*

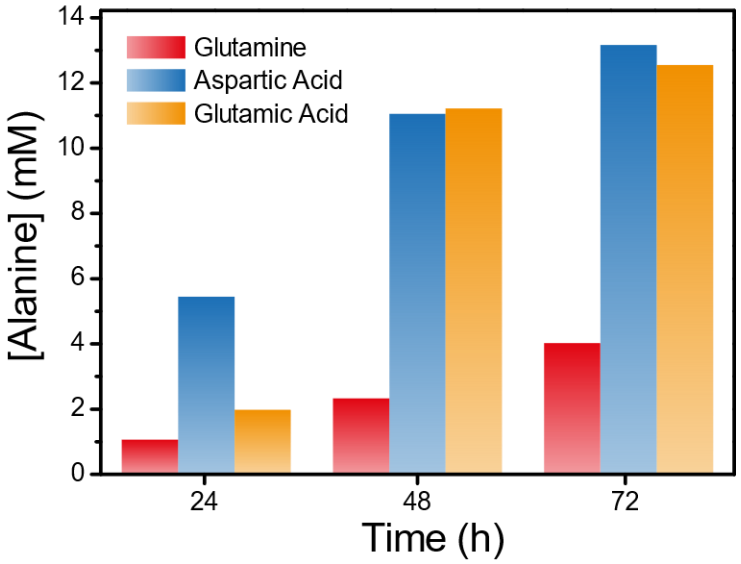

Figure S8. *Alanine production at different times using glutamine (red), aspartic acid (blue) and glutamic acid (orange) quantified by ^{1}H NMR. Reaction conditions [Cu] = 6 mM, [Pyruvate] = 30 mM, [Amino Acid] = 45 mM, [GSH] = 5 mM, pH = 7.4 (Na_2HPO_4/NaH_2PO_4 1M), T = 37ºC.*

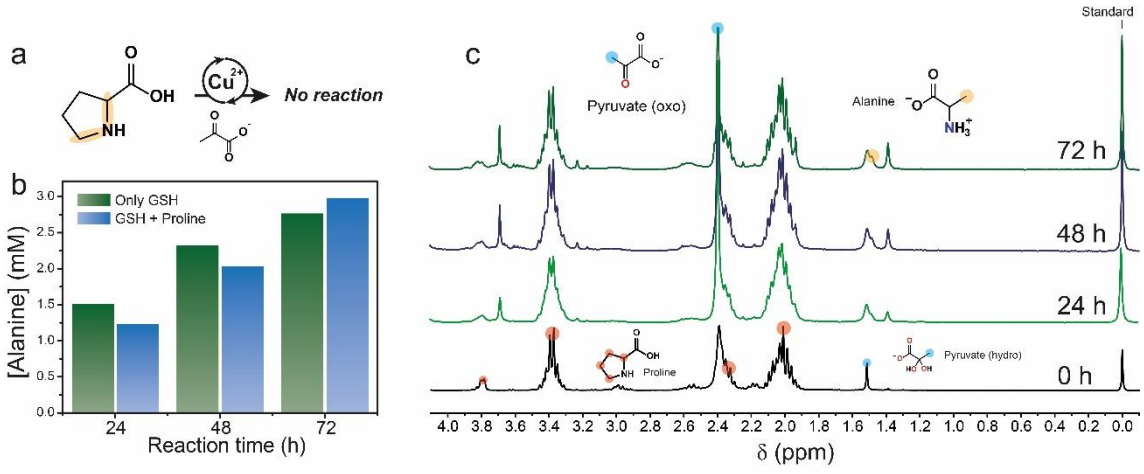

Figure S9. *Attempt to perform the transamination reaction with pyruvate using proline as amino donor. (a) Proline is the only proteinogenic amino acid that contains a secondary amine. (b) The presence of pyruvate as keto-group source and Cu^{2+} as catalyst did not produce any significant increase in alanine concentration in comparison to control only with GSH. This indicates that only the free -NH_3^+ bonded to α-C from glutamic acid residue is a suitable substrate for transamination reaction. (c) ^{1}H-NMR spectra of reaction did not show a clear increase in alanine signal (CH_3, 1.48 ppm) rather than the generated through GSH-transamination. Reaction conditions [Cu] = 6 mM, [Pyruvate] = 30 mM, [Amino Acid] = 45 mM, [GSH] = 5 mM, pH = 7.4 (Na_2HPO_4/NaH_2PO_4 1M), T = 37ºC.*

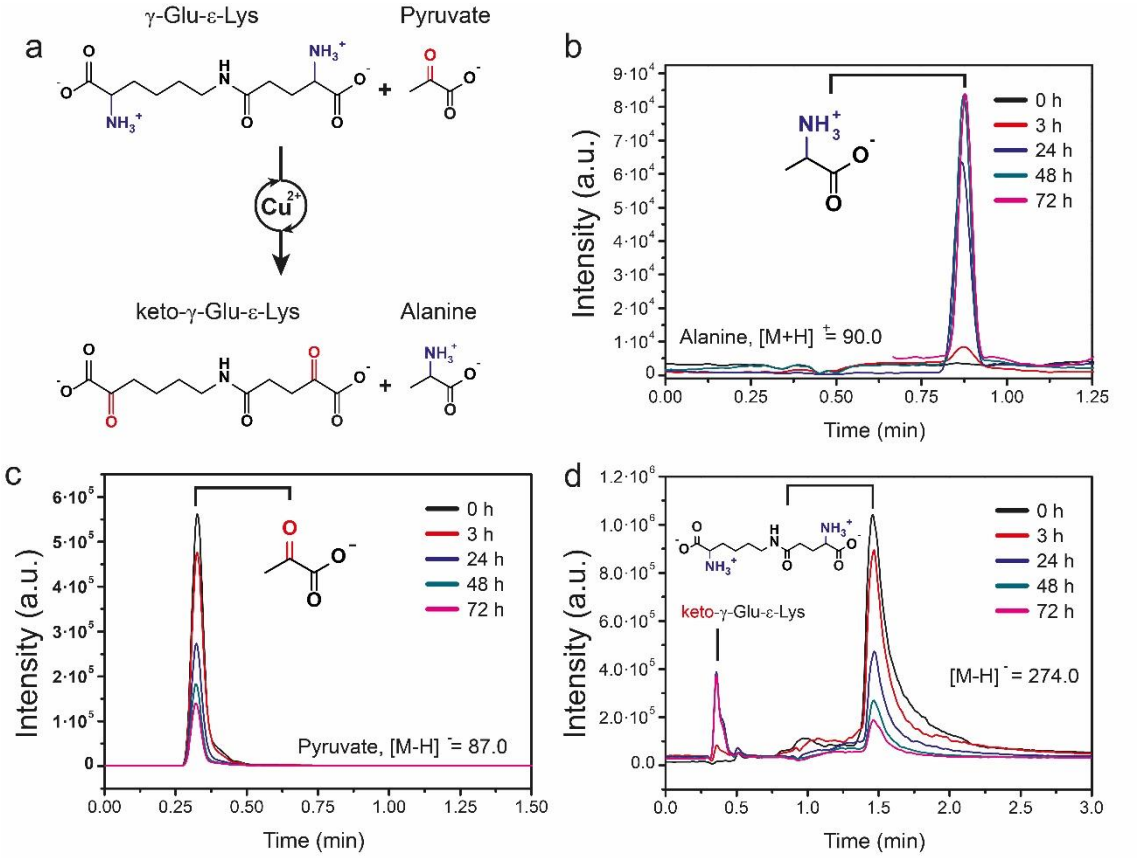

Figure S10. *(a) Transamination reaction using a dipeptide (i.e. γ-Glu-ε-Lys) as substrate. (b-d) UPLC-MS analysis of the reaction at different times for (b) Alanine, (c) Pyruvate and (d) γ-Glu-ε-Lys revealed the formation of alanine and keto- γ-Glu-ε-Lys whereas pyruvate and γ-Glu-ε-Lys were consumed. Reaction conditions: [Cu] = 2 mM, [Pyruvate] = 7.5 mM, [Amino Acid] = 11.25 mM, [GSH] = 5 mM, pH = 7.4 (Na_2HPO_4/NaH_2PO_4 1M), T = 37ºC. Concentration of Aminoacid was reduced due to its lower solubility in aqueous solvents.*

References

1. Mayer, R. J.; Kaur, H.; Rauscher, S. A.; Moran, J., Mechanistic Insight into Metal Ion-Catalyzed Transamination. *Journal of the American Chemical Society* **2021,** *143* (45), 19099-19111.

Chapter 5 |

Tracking copper fate within cancer cells

Summary – Chapter 5

A central part of this thesis is the investigation of the catalytic activity exhibited by CuFe-based nanoparticles both within and outside of cells. A prominent challenge that arises in this line of research is the investigation of the *in situ* transformation of these nanoparticles in cells. We find this crucial as it holds the potential to unravel the cellular responses subsequent to nanoparticle internalization, thereby revealing underlying vulnerabilities within the cell.

Traditionally, two commonly employed techniques have been utilized to address this challenge. First, elemental analysis of the cells enables quantification of how nanoparticle treatments impact the overall levels of metals. However, this method cannot distinguish between leached copper and the copper species that remains encapsulated within the nanoparticles. Secondly, transmission electron microscopy or confocal microscopy can be used to follow single nanoparticle or nanoparticle aggregates through their reflective properties, respectively, within cells. Nevertheless, these techniques are limited to visualizing solid structures, as illustrated in **Figure Summary-1**, and not individual clusters or ionic species. Furthermore, it is important to note that released copper can exist in different oxidation states, namely Cu(I) or Cu(II), and neither of these techniques is capable of differentiating between these oxidation states, further complicating the comprehensive characterization of the in situ transformation of CuFe nanoparticles and their biological interactions. To address this challenge, we initiated a collaboration with Professor Christopher J. Chang, from the University of California in Berkeley. His research group has made groundbreaking contributions in the development of activity-based probes. These probes have been specifically designed to exploit the specific reactivity between the analyte and the probe, enabling highly accurate *in vitro* sensing applications.

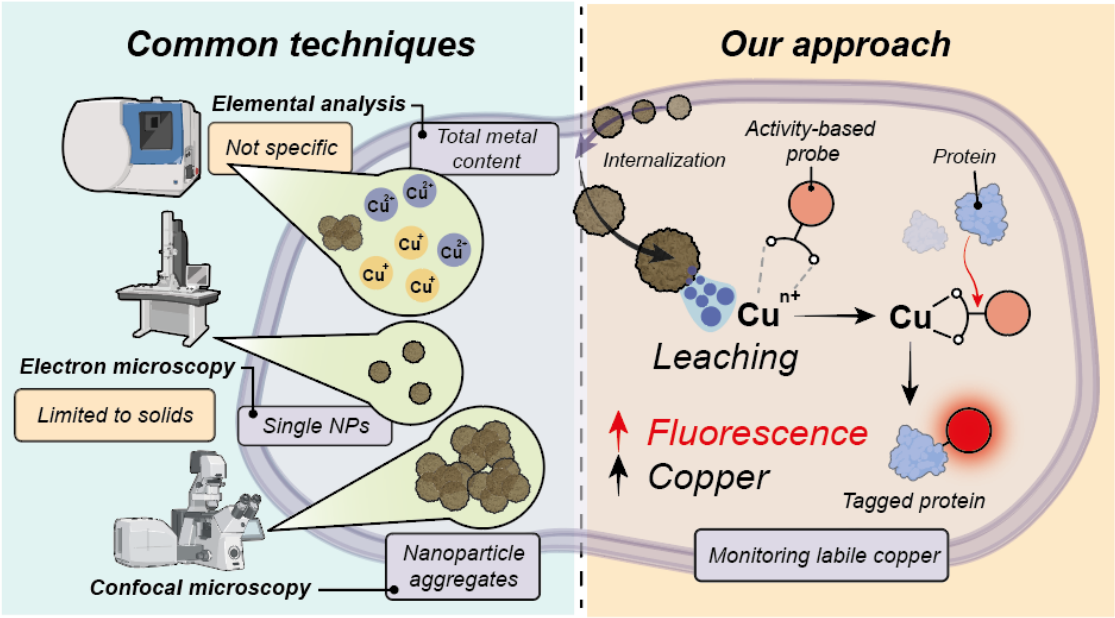

Figure Summary-1. *An activity-based approach towards monitoring labile copper species derived from nanoparticles in living systems. Common techniques to study nanoparticles in cells include elemental analysis, confocal microscopy or transmission electron microscopy.*

In the context of our research, we synthesized two variants of the probe (**Figure Summary-2**). The first variant, **CD644**, exhibits the capability to recognize and measure total labile copper, regardless of its oxidation state. This broad-spectrum probe provides a comprehensive view of the labile copper pool within the cellular environment. The second variant, **CD649.2**, has been specifically designed to target and measure Cu(II). By tailoring the chemistry of the coordination site, the selectivity for Cu(II) detection is improved, enabling the precise location of this particular copper oxidation state within cells. This ability to differentiate between these oxidation states adds a new dimension to our research, as it allows us to precisely characterize and monitor the specific forms of released copper within the cellular environment. Within a cell, two distinct forms of copper can exist: (i) tightly-bond copper, which is firmly bond to proteins, and (ii) labile copper, which is weakly bond to biomolecules or exists in a free state. Building upon this knowledge, we hypothesized that if copper from our nanoparticles was indeed being released within the cell, it would elevate the levels of labile copper.

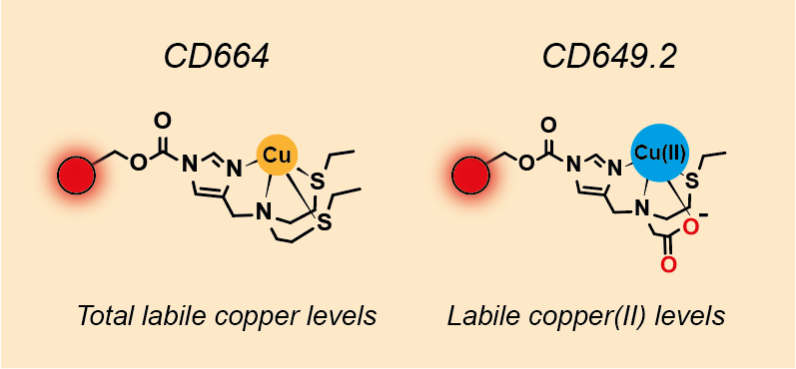

Figure Summary-2. *Chemical structure of coordination sites of **CD664** and **CD649.2**.*

To our surprise, upon treating A549 lung cancer cells with CuFe nanoparticles, we observed a surprising reduction in the total labile copper levels instead of an increase. However, a striking elevation in Cu(II) levels was detected. These unexpected findings led us to postulate that the cells were mounting a response to counterbalance the sudden surge in the labile copper pool, employing various mechanisms to restore Cu homeostasis.

By selectively inhibiting specific pathways and by specifically targeting certain coordination complexes, we unraveled the intricate control mechanisms employed by the cells to regulate the copper derived from the nanoparticles. Thus, we discovered that cells rely on intracellular glutathione (GSH) as a pivotal player in copper homeostasis. In addition to its well-known antioxidant role, GSH robustly coordinates with copper, forming the $Cu(SG)_2$ complex previously investigated in Chapter 3. This coordination serves as a critical means for the cells to sequester and neutralize excess copper generated from the nanoparticles. Furthermore, we explored the involvement of the NRF2 pathway, a cellular signaling cascade implicated in antioxidant responses. Activation of the NRF2 pathway leads to the synthesis of several antioxidant molecules possessing metal-binding properties. Our investigations revealed that cells employ this pathway to exert control over the copper derived from the nanoparticles. We delved into the impact of CuFe nanoparticle treatment on two copper-related proteins: CTR1, a copper importer, and ATP7B, a copper exporter. Intriguingly, we observed a decrease in ATP7B expression, coupled with an increase in CTR1 expression. This observation suggests that cells prioritize the export of labile

copper via CTR1 in an effort to remove as much copper as possible before it reaches cytotoxic levels.

Understanding of these intricate cellular mechanisms sheds light on the remarkable adaptive responses employed by cells to mitigate the cytotoxic effects of labile copper originating from CuFe nanoparticles. Unraveling these regulatory pathways increases our understanding of cellular copper homeostasis and may help to identify potential therapeutic targets for interventions aimed at modulating copper-related processes in cancer cells.

Adapted from:

An Activity-Based Sensing Approach to Monitor Nanomaterial-Promoted Changes in Labile Metal Pools in Living Systems

Javier Bonet-Aleta[1,2,3,4], Aidan T. Pezacki[5], Miku Oi[5], Jose L. Hueso[1,2,3,4], Jesus Santamaria[1,2,3,4], Christopher J. Chang[5,6,7,8*]*

[1] Instituto de Nanociencia y Materiales de Aragon (INMA) CSIC-Universidad de Zaragoza, Campus Rio Ebro, Edificio I+D, C/ Poeta Mariano Esquillor, s/n, 50018, Zaragoza, Spain

[2] Networking Res. Center in Biomaterials, Bioengineering and Nanomedicine (CIBER-BBN), Instituto de Salud Carlos III, 28029 Madrid, Spain

[3] Department of Chemical and Environmental Engineering, University of Zaragoza, Campus Rio Ebro, C/María de Luna, 3, 50018 Zaragoza, Spain

[4] Instituto de Investigación Sanitaria (IIS) de Aragón, Avenida San Juan Bosco, 13, 50009 Zaragoza, Spain

[5] Department of Chemistry, University of California, Berkeley, CA, 94720, United States

[6] Department of Molecular and Cell Biology, University of California, Berkeley, CA, 94720, United States

[7] Helen Wills Neuroscience Institute, University of California, Berkeley, CA, 94720, United States

[8] Chemical Sciences Division, Lawrence Berkeley National Laboratory, Berkeley, CA, 94720, United States

Graphical abstract

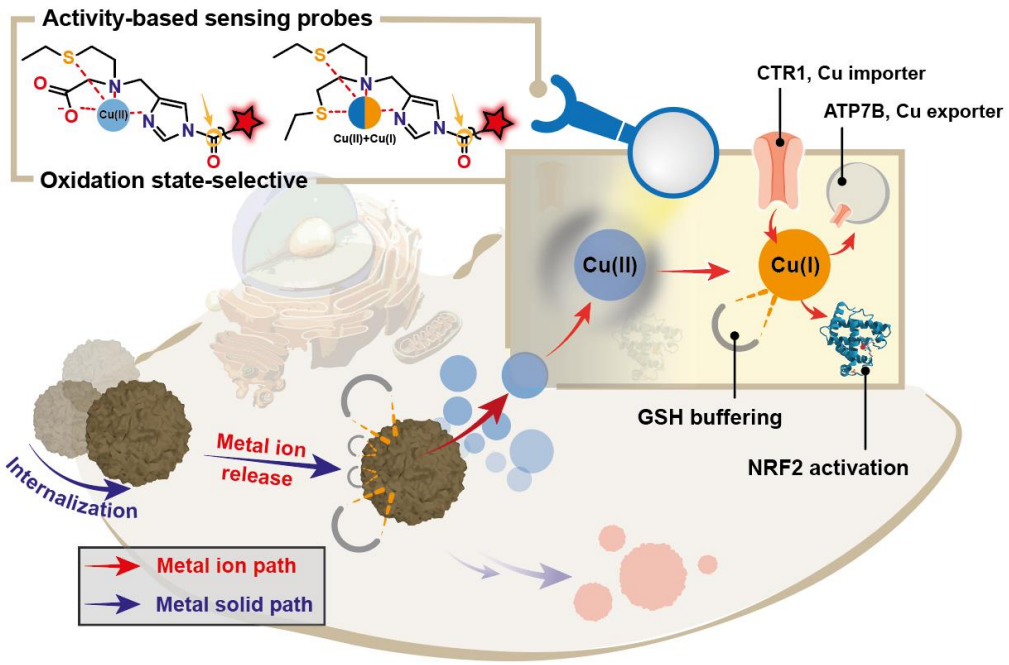

Abstract

Metal-based nanoparticles are a promising class of materials for diagnosis and treatment of cancer and other diseases. However, mechanisms of action of these nanomedicines remain insufficiently understood due in large part to our limited understanding of the dynamic equilibria between solid metal nanoparticles and labile metal ions generated from these nanoparticles within complex biological milieus. Here we apply activity-based sensing to directly identify and investigate the fate of labile copper pools with metal and oxidation state-specificity generated by anticancer copper nanomedicines. We found that treatment of cells with copper-releasing $CuFe_2O_4$ and $Cu_2Fe(CN)_6$ nanoparticles alter labile Cu(I)/Cu(II) ratios through an increase in labile Cu(II), while overall labile copper levels decrease. Labile copper release triggers compensatory responses in two major antioxidant pathways, glutathione (GSH) and nuclear factor erythroid 2–related factor 2 (NRF2), as well as in metal homeostasis to limit copper availability via synergistic upregulation of copper export (ATP7B) and downregulation of copper import (CTR1) proteins. These findings establish the value of activity-based sensing as a generalizable approach for labile metal imaging to help decipher molecular mechanisms of bioactive metal nanoparticles and guide the development of more effective nanomedicine diagnostics and therapies to target metal-dependent disease vulnerabilities.

Introduction – Chapter 5

Nanoparticle materials offer a wealth of new opportunities in diagnosis and treatment of disease. In this context, catalytic metal-based nanoparticles show promise in cancer nanomedicine owing to their capacity to leverage unique chemical conditions within the tumor microenvironment (TME) to perform localized therapy without the need for external stimuli such as light, X-rays, or ultrasound.[1] In particular, nanoparticles are delivered with the aim of catalyzing cytotoxic chemical reactions using differential features of the TME.[2] These reaction pathways include an increased production of reactive oxygen species (ROS) in response to the higher metabolic needs associated with tumorigenesis and metastasis, along with overexpression of antioxidant-associated elements as a compensatory mechanism to maintain a suitable intracellular redox balance.[3, 4, 5, 6] Glutathione (GSH) is of particular interest as an antioxidant whose biosynthesis and

reduction have been shown to be upregulated upon oncogenic mutations.[7] Nanoparticles composed of biologically relevant metal nutrients, including copper,[8-10] iron,[11, 12] manganese,[13, 14] or molybdenum,[15-17] as well as noble-metals[18] or hybrids,[19] have been successfully employed to exploit the TME through their ability to simultaneously produce ROS and oxidize GSH to its disulfide form (GSSG). Studies on intracellular metal nanoparticle trafficking, including internalization/excretion mechanisms and effects on internal organelles, are prevalent in the literature.[20-23] In contrast, the fate of leached labile metal ion species derived from these nanoparticles and the corresponding cellular responses have received much less attention. Indeed, since metal ion nutrients are under strict regulation by cells, a better fundamental understanding of how metal nanoparticle treatments can influence metal homeostatic equilibria can create new therapeutic and diagnostic opportunities for nanomedicine.

Against this backdrop, copper (Cu) has emerged as a key component in a multitude of nanomedicines.[1, 8, 9, 24-27] This metal has potent intrinsic catalytic activity that can be exploited for diagnostic and/or therapeutic purposes. On the other hand, it is also an essential nutrient for life,[28] acting as a static metabolic cofactor to regulate the enzymatic activity at protein active sites[29-33] or as a transition metal signaling agent in labile forms that are loosely-bound to small-molecule and protein ligands with freedom to move and exchange along different cellular locations and regulate protein function beyond active sites by metalloallostery.[34-38] Labile copper acts as a signaling agent in regulating a diverse array of biological processes, including neuronal activity and neuroinflammation,[39-42] lipid metabolism and lipolysis,[43] and kinase signaling.[44-48] However, dysregulation of biological copper homeostasis with aberrant elevations in this metal nutrient can lead to the production of harmful ROS through the Fenton reaction,[49] in addition to triggering a newly-identified form of copper-dependent cell death, termed cuproptosis,[50] and thus it is strictly regulated by the cell.[51, 52] Moreover, copper deficiency is as harmful as copper excess, this metal nutrient plays a key role in cell health and survival pathways, through a novel copper-dependent form of cell proliferation termed cuproplasia.[53] Thus, both the selective supplementation or sequestration of this metal nutrient in the TME could form the basis for development of novel nanomedicines.

Recent reports show how nanostructured catalysts containing copper are susceptible to copper dissolution *in vitro*, particularly in the presence of GSH,[54-56] but to the best of our knowledge, the application of direct labile metal imaging to uncover regulatory mechanisms that govern the adaptation of cells to this sudden influx of metal remain limited. In this context, our laboratory has advanced the concept of activity-based sensing, which employs chemical reactivity between probe and analyte rather than molecular recognition to achieve high selectivity for molecular imaging in biological systems.[57-59] We posited that activity-based sensing could be applied to study labile copper released upon internalization and metal leaching of copper-based nanoparticles and subsequent cellular responses (**Figure 1**). In particular, we sought to apply a tandem activity-based sensing and labeling strategy recently developed by our laboratory which covalently anchors copper-selective fluorescent probes upon analyte detection to preserve spatial information on localized copper hotspots and avoid probe diffusion within and/or out of the cell, coined as the copper-directed acyl imidazole (CDAI or CD) approach.[42, 60] CD probes chelate labile copper, which then subsequently activates a proximal acyl imidazole electrophile by using the metal Lewis acid to withdraw electron density from the acyl group, making it susceptible to irreversible addition onto nucleophilic residues found in proteins and other biologically relevant macromolecules. This tandem activity-based sensing/labeling strategy can provide insight not only on the spatial localization of leached labile copper pools but also do so in an oxidation state-specific manner, as CD probes have been developed for the detection of labile Cu(I) and Cu(II) pools simultaneously[42] and for the oxidation state-specific detection of labile Cu(II).[60]

In this work, we employed two representative types of copper-containing nanoparticles that have been proposed as catalytic vectors in cancer therapy,[54, 61] $CuFe_2O_4$[3, 54] and $Cu_2Fe(CN)_6$,[61] both of which contain leachable copper and are thus inherently toxic to cancer cells. Using activity-based sensing, we monitored their effects on labile copper status in cancer cells using two CD probes, one that is responsive to both Cu(I) and Cu(II) (**CD664**) and one that is responsive only to Cu(II) (**CD649.2**[60]). We observed that these nanoparticles significantly alter labile Cu(I)/Cu(II) homeostasis in a A549 lung cancer cell model with decreases in overall labile copper levels but increases in labile Cu(II) pools, which in turn affect metabolic pathways responsible for controlling glutathione (GSH) biosynthesis, Nuclear Factor-erythroid factor 2-related factor 2 (NRF2), and

copper import/export trafficking pathways. Taken together, the results obtained provide valuable information into foundational biochemical mechanisms of action for catalytic metal nanoparticle therapeutics. More generally, this work also establishes the utility of activity-based sensing as a molecular imaging platform to inform the rational design of metal-based nanomedicines in the diagnosis and treatment of cancer and a broader array of diseases.

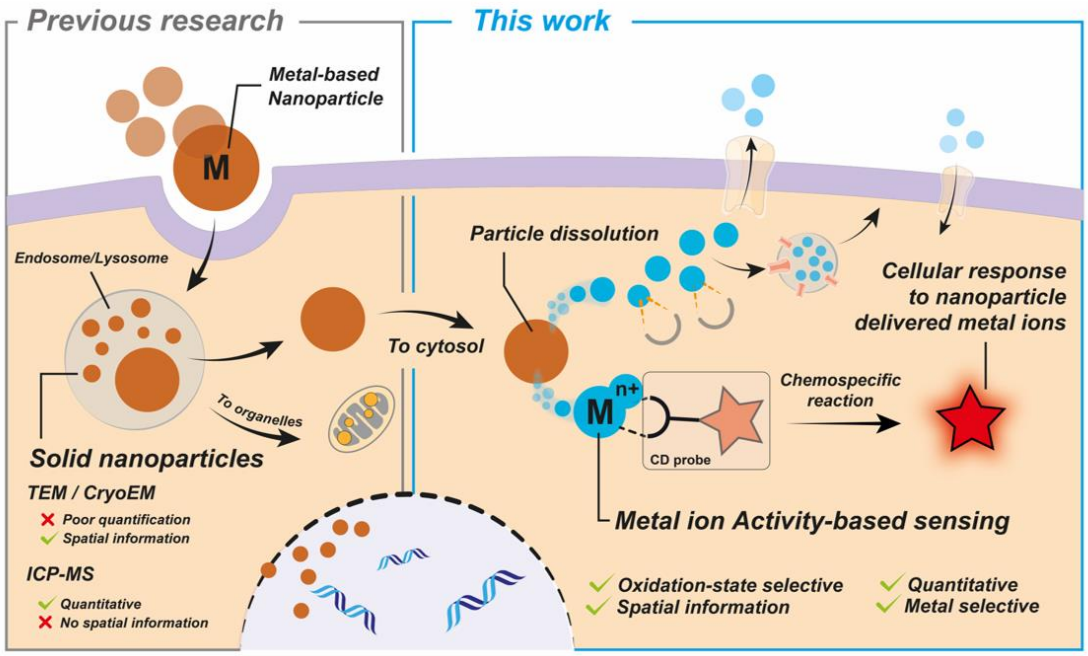

Figure 1. *Copper leaches from catalytic anticancer nanoparticle therapeutics and activates cellular pathways designed to control the concentrations and bioavailability of labile copper ions, providing a distinct route from the traditional mode of action followed by solid metal nanoparticles. Activity-based sensing probes for direct labile metal imaging with element and oxidation state-specificity, when used in conjunction with inhibitors or promoters of specific biochemical pathways, can reveal fundamental cellular responses to treatment with copper-based nanomedicines and mechanisms of action.*

Results and discussion – Chapter 5

Synthesis and Characterization of Therapeutic Copper Nanoparticles. We used $CuFe_2O_4$ and $Cu_2Fe(CN)_6$ as representative examples of therapeutic copper-based nanoparticles,[3, 54, 61, 62] both of which have been previously reported to undergo copper leaching during catalysis[54, 63] and boast distinct copper coordination geometries. In the case of $CuFe_2O_4$, copper occupies tetrahedral sites surrounded by oxygen atoms (**Figure 2a**)[64] whereas copper occupies octahedral sites coordinated

to nitrogen atoms in $Cu_2Fe(CN)_6$ (**Figure 2b**).[65] Oxide particles were synthesized via a hydrothermal method following our previous works.[54] $Cu_2Fe(CN)_6$ nanoparticles were synthesized via self-assembly mixing of Cu(II) with $Fe(CN)_6^{3-}$ ions in the presence of citric acid to modulate the particle size[61] (see Experimental Information for further details). Representative transmission electron microscopy (TEM) images of both nanoparticles are shown in **Figure 2a** and **Figure 2b**, respectively**.** $CuFe_2O_4$ particles display a spherical morphology with an average diameter of 9.5 ± 1.0 nm (**Figure S1**), whereas $Cu_2Fe(CN)_6$ particles possess a cubic morphology with an average diameter of 80.0 ± 14.1 nm (**Figure S1**). XRD patterns of $Cu_2Fe(CN)_6$ confirmed the crystallinity of the sample with the coordination environment of Cu-N_6 and Fe-C_6 fitting well within the standard (JCPDS#02-0381) (**Figure S2**), while corresponding XRD pattern of $CuFe_2O_4$ matched with our previous works.[66] To validate that these nanoparticles undergo copper leaching, we performed elemental analysis on nanoparticle solutions after treatment with 5 mM GSH, which is abundant in the TME[3] and known to cause dissolution of copper-based nanoparticles.[54] $CuFe_2O_4$ nanoparticles have a considerably smaller size, and therefore a larger external area per unit volume. However, both the copper leaching rate and total amount of copper released in a 24 h period were decreased when compared to $Cu_2Fe(CN)_6$ (**Figure S3**). We suggest that the presence of vacancies typically present in Prussian Blue Analogues[67] as $Cu_2Fe(CN)_6$ together with the Jahn-Teller distortion induced by the Cu^{2+} in the nanostructure[68] (**Figure S4**) may be responsible for the greater extent of copper dissolution displayed by the $Cu_2Fe(CN)_6$ nanoparticles. Based on these *in vitro* assays, we reasoned that intracellular copper ion release takes place with a higher propensity for $Cu_2Fe(CN)_6$ nanoparticles. Both nanoparticles possess catalytic activity towards GSH depletion and are thus interesting candidates for catalytic nanomedicine therapy. In our previous work,[54] $CuFe_2O_4$ nanoparticles showed a GSH depletion rate of 0.048 μmol GSH·min^{-1}·mg Cu^{-1} whereas $Cu_2Fe(CN)_6$ reached the value of 0.38 μmol GSH·min^{-1}·mg Cu^{-1} under physiological conditions (**Figure S5**). The higher GSH depletion rate relates to the faster copper release rate of $Cu_2Fe(CN)_6$ nanoparticles relative to the $CuFe_2O_4$ congeners.[54]

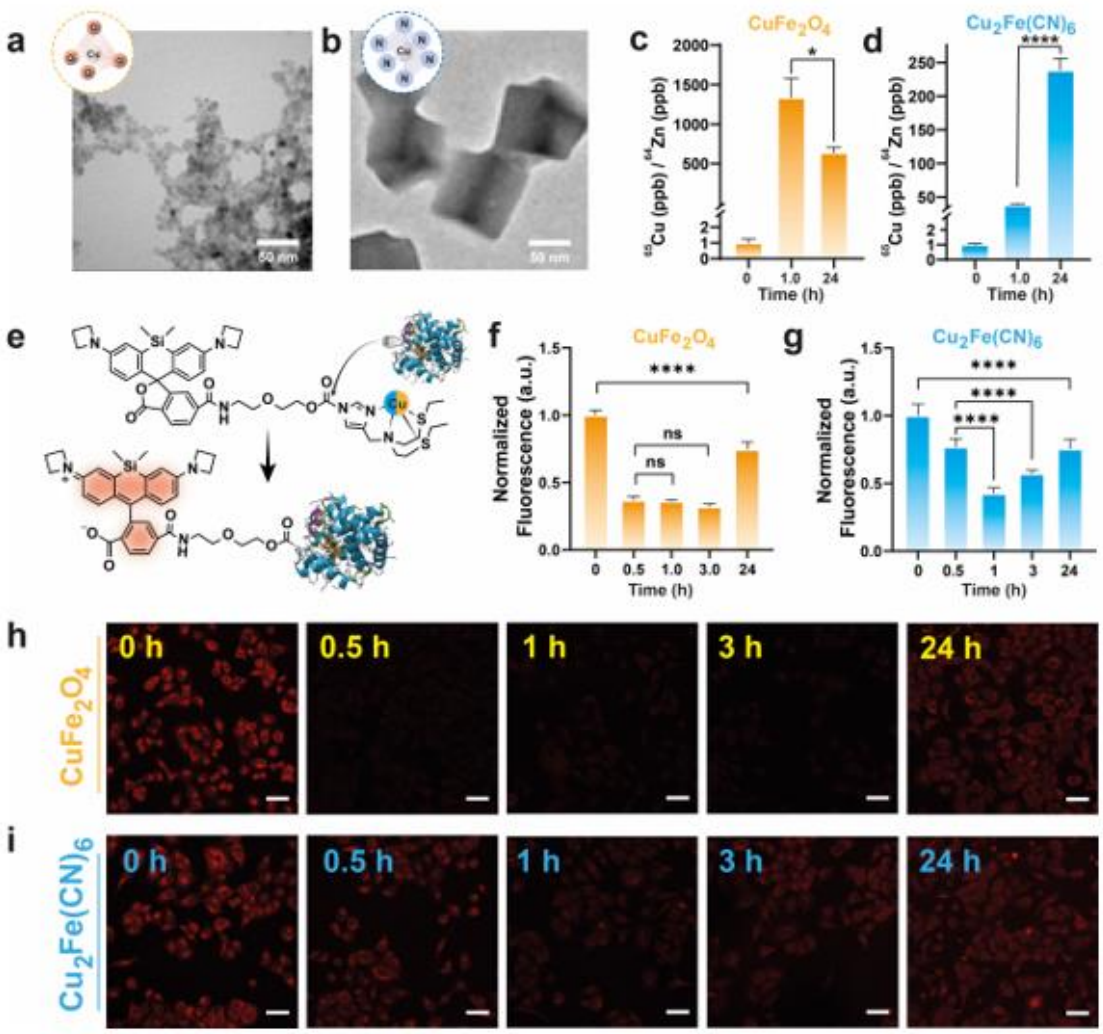

Figure 2. *Copper coordination and TEM images of (a) $CuFe_2O_4$ and (b) $Cu_2Fe(CN)_6$ nanoparticles employed in this study. Inset: (a) $CuFe_2O_4$ and (b) $Cu_2Fe(CN)_6$ single nanoparticle at an enhanced resolution. Inset scale bar: 20 and 200 nm, respectively. ICP-MS analysis of A549 cells treated with (c) $CuFe_2O_4$ and (d) $Cu_2Fe(CN)_6$ nanoparticles for 1 h or 24 h reveals an increase in total copper levels upon nanoparticle treatment. Total cellular ^{63}Cu levels were normalized to total ^{64}Zn levels. Error bars denote S.E.M (n = 6). (e) Mechanism of action for the activity-based sensing probe* **CD664**[42, 60] *to measure intracellular levels of labile copper. Binding of Cu(I) and/or Cu(II) Lewis acids to the N_2S_2 coordination pocket activates the pendant acyl imidazole electrophile for attack from nucleophilic residues from nearby proteins, anchoring the probe to site of elevated labile copper. Quantification of* **CD664** *fluorescence signal of A549 cells at different nanoparticle incubation times using (f) 6.25 μg $Cu{\cdot}mL^{-1}$ $CuFe_2O_4$ and (g) 3.125 μg $Cu{\cdot}mL^{-1}$ $Cu_2Fe(CN)_6$. (h-i) Confocal fluorescence images of* **CD664** *in A549 cells treated with (h) $CuFe_2O_4$ and (i) $Cu_2Fe(CN)_6$. Early incubation times show a*

significant decrease in ***CD664*** *fluorescence as the cells appear to enter into a copper regulatory state where the metal nutrient is more tightly controlled and is less bioavailable within the cells. Fluorescence intensity of* ***CD664*** *was determined from experiments with* λ_{ex} *= 633 nm. Scale bar = 50 µm. *P < 0.05, **P < 0.01, ***P < 0.001, and ****P < 0.0001; ns, not statistically significant. Error bars denote S.E.M (n = 8).*

Copper-Based Nanoparticle Treatment Decreases Overall Labile Copper Levels But Increases Labile Cu(II) Levels. We chose A549 cells as a model lung cancer cell line to study biochemical mechanisms of cellular responses to copper-based nanoparticle treatment and labile copper ion leaching. Previous reports suggest that A549 cells are resistant to treatment with elesclomol, a mitochondrial-targeted copper ionophore,[50] and CuO nanoparticles,[69] thus we hypothesized that these cells would display a fast and effective response against copper leaching. As a starting point, we studied the toxicity of the nanoparticles in A549 cells to determine a sub-cytotoxic dose to administer for further experiments (**Figure S6**). As expected, $Cu_2Fe(CN)_6$ was more toxic (CC_{50} = 5.65 µg Cu·mL^{-1}) than $CuFe_2O_4$ (CC_{50} = 21.6 µg Cu·mL^{-1}), given the faster copper release for the former. At this point, we fixed the [Cu] dose in subsequent experiments at 6.25 and 3.125 µg Cu·mL^{-1} for $CuFe_2O_4$ and $Cu_2Fe(CN)_6$, respectively. We then quantified total internalized copper in A549 cells upon nanoparticle treatment using inductively coupled plasma mass spectrometry (ICP-MS) analysis (**Figure 2c-d**). Total copper levels in cells were significantly increased after 1 h, particularly in the case of $CuFe_2O_4$ nanoparticles, as their smaller size likely results in a higher degree of internalization.[70] After 24 h of nanoparticle treatment, total copper levels decreased for cells exposed to $CuFe_2O_4$ nanoparticles (**Figure 2c**), whereas total copper levels continued to increase for $Cu_2Fe(CN)_6$ nanoparticles (**Figure 2d**). While these data provide us with information on total copper status, it does not provide information on the bioavailability of the leached copper. Thus, we hypothesized that application of our recently developed tandem activity-based sensing and labeling probes could provide an effective means of measuring relative levels of labile Cu(I) and Cu(II) pools rather than total copper. This reasoning is supported by previous work from our laboratory using fluorescent copper sensors to identify intracellular accumulation of labile Cu(I) in response to contact killing of bacteria[71] and yeast[72] with antimicrobial copper surfaces. To meet this goal, activity-based sensing probes have been

previously applied to successfully study changes in labile copper pools in these A549 cell models.[60] To investigate labile copper status upon nanoparticle treatment, we designed and synthesized the new activity-based sensing probe **CD664** that bears a robust azetidine-based silicon rhodamine fluorophore scaffold.[73] **CD664** is highly selective for labile copper over other biologically relevant metal ions but lacks oxidation state-specificity for Cu(I) vs Cu(II), and thus it can act as a tool for measuring total labile copper levels rather than a single oxidation state. The probe chelates labile copper via a favorable N_2S_2 ligand donor set (**Figure 2e**). **CD664** was synthesized following a similar methodology as previously published[42] (see Experimental Information for further details). We investigated whether **CD664** was capable of monitoring leached copper ions from both nanoparticles using A549 cell lysates to simulate labeling of the whole cellular proteome. Nanoparticles were preincubated with excess GSH for 24 h to ensure that majority of the leachable copper was released from the nanoparticles. Subsequently, this mixture was added to A549 cell lysate followed by **CD664**, and protein labelling was analyzed via sodium dodecyl sulfate–polyacrylamide gel electrophoresis (SDS-PAGE). In-gel fluorescence analysis revealed a dose-dependent increase in fluorescence for increasing concentration of either species of leached nanoparticle (**Figure S7**). These results validate **CD664** as a fluorescent probe capable of analyzing labile copper derived from a nanoparticle. Fluorescence signals obtained using $Cu_2Fe(CN)_6$ nanoparticles were higher, in agreement with a greater extent of labile copper release (**Figure S3**). Interestingly, although both types of nanoparticles raised total amounts of intracellular copper and increased *in vitro* **CD664** fluorescence, activity-based imaging with **CD664** in live A549 cells shows that the labile copper pool rapidly decreases after treatment with either catalytic nanoparticle (**Figure 2f-i,** bright field images are found in **Figure S8** and **S9**).

Quantification of **CD664** fluorescence signals revealed a fast and significant decrease in labile copper levels upon $CuFe_2O_4$ treatment, in comparison to a more gradual depletion of labile copper pools for $Cu_2Fe(CN)_6$ (**Figure 2f-g**). Additionally, these effects are dose-dependent, as the **CD664** fluorescence signal decreased more rapidly for treatment with $CuFe_2O_4$ at higher concentrations, while the addition of lower amounts of $CuFe_2O_4$ resulted in a more modest relative decrease in **CD664** fluorescence signal (**Figure S10** and **Figure S11**). Overall, the pattern of observed overall decreases in labile copper as directly imaged by **CD664** suggests that the cell activates machinery

to sequester and/or regulate labile copper pools triggered by the presence of leached copper ions derived from nanoparticle treatment. It is interesting to note that when these results are compared against analogous experiments with $CuCl_2$ as a soluble copper source, previously explored using activity-based sensing probes,[42, 58, 60] the opposite result was obtained, namely that such treatments led to an increase and expansion of the labile copper pool.

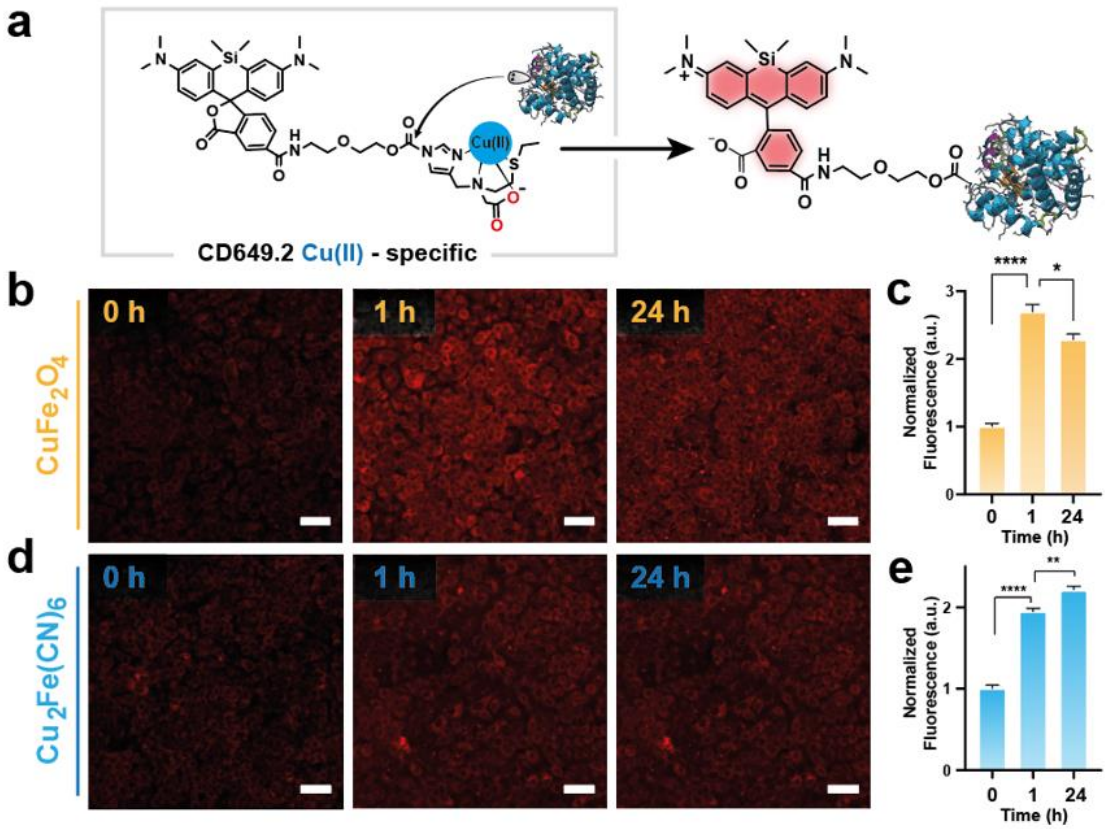

Figure 3. *The Cu(II)-specific probe* ***CD649.2*** *with both copper- and oxidation state-specificity reveals an increase in labile Cu(II) pools in A549 cells following internalization of copper-based nanoparticles. (a) Mechanism of action for activity-based sensing of Cu(II) with the* ***CD649.2*** *probe. Introducing a harder carboxylate Lewis base at the coordination site switches the selectivity of the probe to Cu(II)[60] while not compromising its capabilities to undergo nucleophilic conjugation with proteins in the same manner as* ***CD664****. (b-c) Confocal* ***CD649.2*** *fluorescence images and quantification of A549 cells treated with 6.25 μg Cu·mL^{-1} $CuFe_2O_4$ nanoparticles at different incubation times. Fluorescence quantification reveals a significant increase in labile Cu(II) after 1 and 24 h in comparison to control. (d-e) Confocal* ***CD649.2*** *fluorescence images and quantification of A549 cells treated with 3.125 μg Cu·mL^{-1} $Cu_2Fe(CN)_6$ nanoparticles at different incubation times. Fluorescence quantification reveals*

a time-dependent increase in labile Cu(II). Fluorescence intensity of ***CD649.2*** *was determined from experiments with* λ_{ex} *= 633 nm. Scale bar = 50 µm. *P < 0.05, **P < 0.01, ***P < 0.001, and ****P < 0.0001; ns, not statistically significant. Error bars denote S.E.M (n = 8).*

Under native nutrient sensing conditions, copper ions are typically internalized into the cell through the high-affinity Cu(I)-selective copper ion channel/transporter CTR1,[74] where STEAP metalloreductases are required for internalization,[75] which allows for the precise control of copper uptake for a suitable metal homeostasis. DMT1 provides a complementary pathway for Cu(II) uptake.[60] In contrast, nanoparticle internalization typically occurs via endosome and eventual lysosome formation,[3, 76, 77] which results in a high degree of metal internalization and, simultaneously, a lack of oxidation state-specific regulation for the absorbed copper pool. We posit that this rapid accumulation of copper upon nanoparticle treatment may elicit responses by the cell to counteract the disruption of its tightly regulated metal homeostasis. Indeed, while **CD664** provides information on overall levels of labile copper, it does not discriminate against Cu(I) vs Cu(II). To confirm that the nanoparticles release Cu(I) in the presence of intracellular concentrations of GSH, we applied **FCP-1**, previously reported to successfully monitor fluxes in intracellular labile Cu(I).[58] This probe contains three components: a red-emitting rhodamine (F_{576}) unit connected to a green-emitting (F_{526}) fluorescein moiety via a Tris(2-pyridylmethyl)amine (TPA) group; the TPA trigger is susceptible to Cu(I)-induced C-O oxidative bond cleavage (**Figure S12a**), providing an activity-based sensing approach to visualizing liable Cu(I) pools.[58, 78] In the absence of Cu(I), the rhodamine group quenches the green emission from fluorescein via Förster Resonance Energy Transfer (FRET), leading to rhodamine-dominated red-shifted fluorescence, but in the presence of Cu(I), the bond between TPA and fluorescein is cleaved, disabling FRET (**Figure S12a**) and resulting in green fluorescein emission.[58] Therefore, the generation of Cu(I) species is related to an increase in the F_{526}/F_{576} ratio (**Figure S12b**). After incubation of either $CuFe_2O_4$ and $Cu_2Fe(CN)_6$ nanoparticles with GSH to induce leaching and subsequent incubation with **FCP-1,** a rapid increase in the F_{526}/F_{576} ratio is observed, indicating a specific generation of Cu(I) during the leaching process (**Figure S12c**). Owing to the high intracellular GSH levels, Cu(I) is considered the predominant form of intracellular labile copper. However recent work from our

laboratory has also identified the existence of a labile Cu(II) pool and suggests that a heightened oxidative environment, such as driven by oncogenes, can promote expansion of this pool.[60] Given the dynamic equilibrium that exists between these two forms of labile copper, we sought to study how internalization of copper-releasing particles affects labile copper pools in an oxidation state-specific manner. To this end, we selected the CD649.2 probe[60], an activity-based sensor which replaces an ethylthioether ligand with a carboxylate group, which introduces a harder Lewis base into the coordination site of the first-generation CD649 probe. This substitution enhances the selectivity towards the harder Cu(II) Lewis acid over softer Cu(I) (Figure 3a).[60] Analogous to **CD664**, we validated the ability of **CD649.2** to label proteins in the presence of leached Cu(II) with A549 cell lysates. Both nanoparticles produced an increase in **CD649.2** fluorescence in the presence of A549 cell lysate, thereby confirming the capability of this probe to selectively track Cu(II) species generated from leached nanoparticles (**Figure S13**). We found a larger fluorescence turn-on response in the case of $CuFe_2O_4$ nanoparticles, indicating a larger generation of Cu(II) from these particles. Confocal imaging experiments with **CD649.2** in live A549 cells reveal the generation of intracellular labile Cu(II) pools using both nanoparticles (**Figure 3b-e** and **Figure S14, S15**). We found a higher **CD649.2** fluorescence signal in the case of $CuFe_2O_4$ nanoparticles, in agreement with protein labeling experiments (**Figure S13**). Treatment with $CuFe_2O_4$ provokes an abrupt elevation of labile Cu(II) after 1 h of incubation, which slightly decreases after 24 h (**Figure 3b-c**). This observation is in agreement with total copper decreasing at 24 h, as detected by ICP-MS (**Figure 2c**). On the other hand, cells treated with $Cu_2Fe(CN)_6$ nanoparticles display a continuous increase in **CD649.2** signal after 1 and 24 h of incubation (**Figure 3d-e**), again tracking with the total copper increases measured by ICP-MS (**Figure 2d**).

The collective results suggest that upon internalization, both nanoparticles leach copper, which is distributed in the form of labile Cu(II). To the best of our knowledge, activity-based sensing offers the first example of a method to directly monitor the redox status of labile metal ions leached from nanoparticles in a biological setting. Interestingly, the results suggest that internalization of copper-based nanoparticles reduce overall levels of labile copper in cells even though total copper levels increase. Moreover, upon further investigation, we find a relative elevation in labile Cu(II) with a shift in labile Cu(I)/Cu(II) ratios. Indeed, we observed distinct evolution patterns in total, overall

labile, and oxidation state-specific labile copper pools depending on the nanoparticle used, in line with varying cellular responses to differences in nanoparticle internalization and labile copper ion leaching rates.

GSH and NRF2 Pathways Play Central Roles in Regulating Labile Copper Ion Pools Generated From Nanoparticle Treatment in Cells. Although treatment with copper nanoparticles induced an increase in labile Cu(II) pools, the overall labile copper content in cells was significantly decreased almost immediately upon nanoparticle incubation (**Figure 2f-i**). These observations indicate that a cellular response is occurring to counter this sudden metal imbalance. Given the established link between copper and cellular redox status,[58, 60] we first sought to test whether this sudden imbalance in elevated labile Cu(II) would lead to a heightened production of ROS. Indeed, Cu(II) has been widely explored in nanocatalytic therapy for its ability to deplete intracellular antioxidant reservoirs.[4] Along these lines, both $CuFe_2O_4$ and $Cu_2Fe(CN)_6$ treatment induced a significant increase in the green fluorescence signal of CellROX, a broad-spectrum fluorescent ROS probe in comparison to non-treated cells (**Figure S16**), confirming that nanoparticle incubation increases ROS in A549 cells. The released Cu(I) can also reduce endogenous H_2O_2, forming hydroxide and the highly oxidative hydroxyl radical species via Fenton-like chemistry.[9] In addition, the residual fraction of solid nanoparticle after labile copper leaching, mainly composed of FeO_x and $Fe(CN)_6$ units respectively, remained internalized in A549 cells as treatment with either nanoparticle increased total iron content, as shown by ICP-MS analysis (**Figure S17)**. These species may also contribute to the generation of ROS due to their widely-known Peroxidase-like activity[79, 80] (i.e. oxidation of organic substrates using H_2O_2), which are especially active in mildly-acidic intracellular environments such as lysosomes.[81]

In this context, cells typically increase their levels of the antioxidant buffering molecule glutathione (GSH) in response to an increase in oxidative stress, with previous reports indicating upregulation of GSH biosynthesis and regeneration in cancer models (**Figure 4a**).[7] Moreover, GSH is also involved in controlling the bioavailability of labile copper through a variety of mechanisms, including interactions with metallochaperones and metal-buffering proteins such as metallothionein.[58]

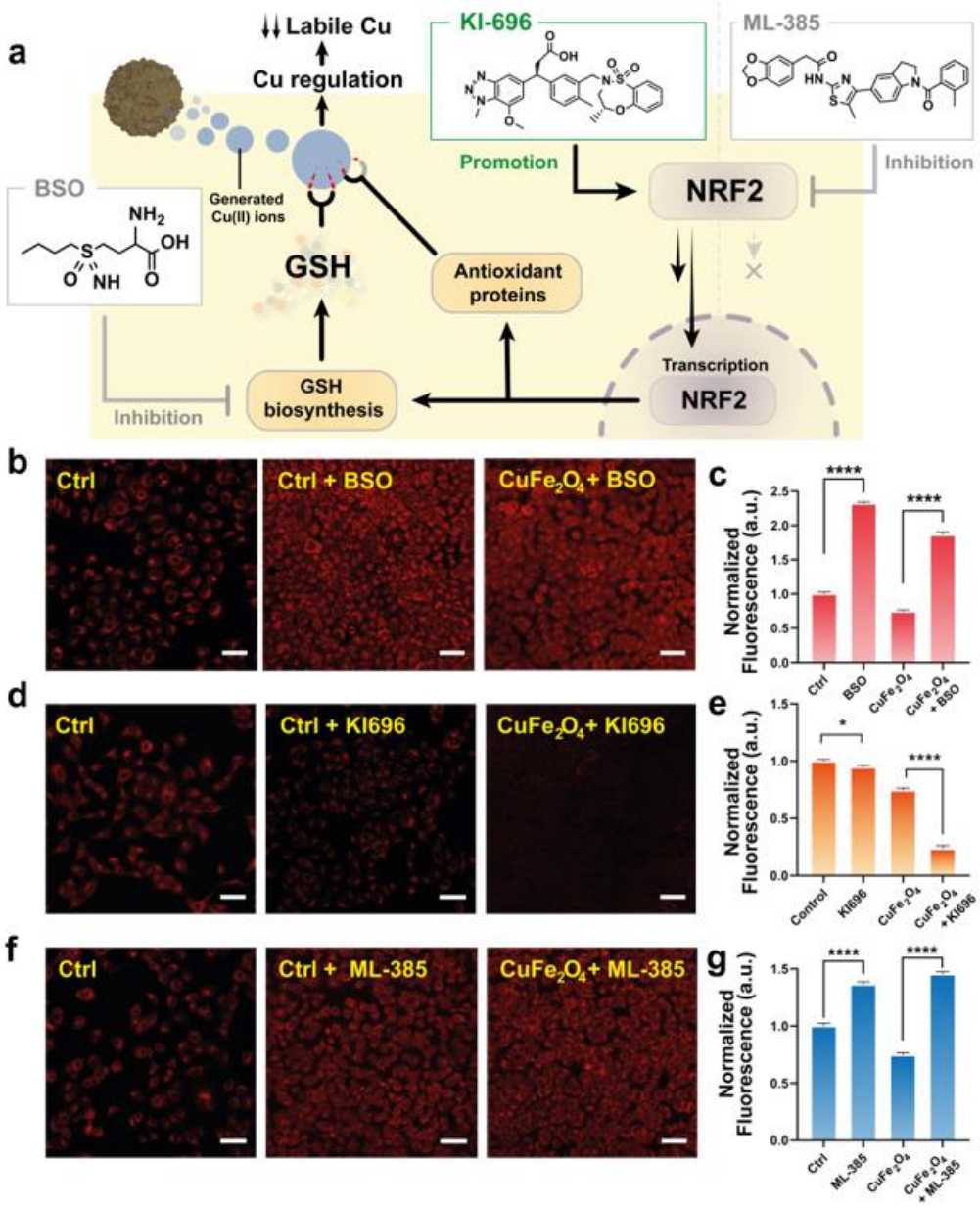

Figure 4. *Pharmacological modulation of GSH biosynthesis and NRF2 activation pathways regulate maintenance of labile copper pools in cells acquired from nanoparticle internalization. (a) Interplay between GSH and NRF2 pathways and labile copper ions generated from nanoparticle dissolution together with inhibitors and promoters employed in the study. GSH and NRF2 pathways can modulate overall labile copper levels through a variety of potential mechanisms. BSO blocks GSH biosynthesis[83] thereby reducing copper buffering and sequestration. KI696[86] and ML-385[87] promote or inhibit the antioxidant response element NRF2, decreasing or increasing overall labile copper*

levels, respectively. Labile copper imaging with the activity-based sensor ***CD664*** *in conjunction with these pharmacological treatments provides insights into how these biochemical pathways regulate labile copper ion pools released by nanoparticles. (b-c) Confocal* ***CD664*** *fluorescence images and quantification of A549 cells treated with 0.5 mM BSO and 6.25 µg Cu·mL^{-1} of $CuFe_2O_4$ for 24 h. Inhibition of GSH biosynthesis with BSO promotes the accumulation of intracellular labile copper pools. (d-e) Confocal* ***CD664*** *fluorescence images and quantification of A549 cells treated with 1 µM KI696 and 6.25 µg Cu·mL^{-1} of $CuFe_2O_4$ for 24 h. Activation of the NRF2 pathway leads to a decrease in intracellular labile copper pools, as measured by* ***CD664****, likely due to upregulation in the expression of copper-sequestering proteins.[88] (f-g) Confocal fluorescence images and quantification of A549 cells treated with 10 µM ML-385[86] and 6.25 µg Cu·mL^{-1} of $CuFe_2O_4$ for 24 h. Inhibition of the NRF2 pathway prevents the upregulation of metal-buffering proteins in A549 cells, favoring an accumulation of labile copper after internalization of $CuFe_2O_4$ nanoparticles. Fluorescence intensity of* ***CD664*** *was determined from experiments with λ_{ex} = 633 nm. Scale bar = 50 µm. *P < 0.05, **P < 0.01, ***P < 0.001, and ****P < 0.0001; ns, not statistically significant. Error bars denote S.E.M (n = 8).*

GSH also has the potential to chelate copper directly, given its tight complex formation constant with Cu(I) ($\log K_f$'=26.6) measured *in vitro*,[54, 82] but the direct evidence for physiological roles of cellular copper-GSH complexes remains elusive. We therefore explored whether GSH was involved in sequestering copper ions released from nanoparticles using buthionine sulfoximine (BSO), an inhibitor for the γ-glutamylcysteine synthetase (GCS) enzyme involved in the first step of GSH biosynthesis.[83] We hypothesized that if GSH could buffer labile copper pools, then depleting GSH levels would lead to an increase in overall labile copper levels upon nanoparticle treatment. To rule out the possibility that BSO can directly bind copper and itself lead to fluorescent changes under these experimental conditions, we investigated whether **CD664, CD649.2 (Figure S18)** or **FCP-1 (Figure S19)** were capable of monitoring the produced labile copper species after nanoparticle leaching in the presence or absence of BSO. We used A549 cell lysate to simulate labeling of the whole cellular proteome. Indeed, the fluorescence signals of **CD664**, **CD649.2** or **FCP-1** in this *in vitro* system containing $CuFe_2O_4$, $Cu_2Fe(CN)_6$ or $CuSO_4$ in the presence of 0.5 mM BSO were similar to treatments with the nanoparticles or $CuSO_4$ alone

(**Figure S18** and **S19**), indicating that BSO was not binding labile Cu(I) and Cu(II). After the treatment with BSO, the overall basal levels of labile copper in live A549 cells increased (**Figure 4b**), consistent with the role of GSH as a labile copper buffer in the cytosol[84, 85] and in agreement with previous studies in HeLa cells.[58] Upon 24 h of incubation with 0.5 mM BSO and either $CuFe_2O_4$ (**Figure 4b-c**, bright field images are shown in **Figure S20**) or $Cu_2Fe(CN)_6$ nanoparticles (**Figure S21**), we found significant increases in overall labile copper levels.

While these imaging results are in agreement with previous studies from our laboratory that link labile copper bioavailability with total GSH levels,[58] we found that labile copper levels in cells treated with BSO alone were still higher than in cells treated with BSO in conjunction with nanoparticles, suggesting additional pathways may be involved in regulating the nanoparticle-based copper influx. We speculated that the transcription factor Nuclear Factor-erythroid factor 2-related factor 2 (NRF2) might be responsible, as it is activated upon disruption of GSH pools[89] and its activation leads to the upregulation of antioxidants and metal-buffering agents, including GSH[90] (**Figure 4a**). Cytosolic NRF2 levels are regulated by its interaction with the Kelch like-ECH-associated protein 1 (KEAP1)/Cullin3 system through ubiquitination.[91] When the interplay between KEAP1/Cullin3 and NRF2 is blocked, the entrance of NRF2 into the nuclei is favored, and consequently an upregulation in antioxidant and metal-buffering agents occurs which should directly affect labile copper levels in the cell.

To evaluate the interplay between labile copper pools and NRF2 status, we treated A549 cells with 1 μM of KI696, a potent and selective inhibitor of the KEAP1/NRF2 interaction. Analogous to control experiments with BSO, we demonstrated that KI696 also does not interfere with the copper responses of the activity-based sensing probes, as **CD664**, **CD649.2** and **FCP-1** fluorescence signals in the presence of KI696 and nanoparticles were similar to signals measured with nanoparticle treatments alone (**Figure S18** and **S19**). KI696 acts effectively as a NRF2 promoter,[87] and we measured the effects of this pharmacological treatment on labile copper pools using **CD664** imaging. As expected, in the absence of nanoparticle treatment, activation of the NRF2 pathway led to a decrease in overall basal labile copper levels (**Figure 4d-e** and **Figure S20**). However, co-treatment with $CuFe_2O_4$ nanoparticles and KI696 provoked a significant decay in total

labile copper levels that was significantly larger than treatment with $CuFe_2O_4$ or KI696 alone, indicating that the NRF2 pathway plays a significant role in the cellular response to copper exposure upon nanoparticle treatment (**Figure 4d-e** and **Figure S20**). Correspondingly, we hypothesized that inhibition of the NRF2 pathway would block the upregulation of metal-buffering proteins and lead to an increase in labile copper pools. Indeed, we observed that upon incubation with 10 µM ML-385, a potent NRF2 inhibitor[86] without copper-binding capabilities (**Figure S18** and **S19**), that **CD664** imaging shows an increase in overall basal labile copper levels, which was even higher in the presence of $CuFe_2O_4$ nanoparticles (**Figure 4f-g** and **Figure S20**). Analogous results were obtained using $Cu_2Fe(CN)_6$ nanoparticles (**Figure S21**). These data provide further support that the NRF2 pathway as a key regulator of labile copper ion pools generated from nanoparticle leaching. Taken together, the results suggest that upon internalization of copper-containing nanoparticles and subsequent labile copper ion release, cells respond by promoting the NRF2 pathway to limit the bioavailability of labile copper.

Cells Respond to Internalization of Copper-Based Nanoparticles to Limit Copper Exposure via Upregulating the Copper Exporter ATP7B and Downregulating the Copper Importer CTR1. The fate of copper in cells is driven by dynamic and coordinated responses by copper storage, copper metallochaperone, and copper import/export and related transport proteins.[92] In this context, we tested the hypothesis that another possible explanation for the observed decrease in **CD664** signal, indicating a loss of intracellular labile copper, could be attributed to changes in the expression of proteins that are involved in Cu import/export. In this context, ATP7B is a copper-dependent ATPase protein present in the membrane of the trans-Golgi network and is responsible for the metalation of proteins under basal levels of copper; however, upon exposure to elevated levels of copper, ATP7B is trafficked towards the cell surface and towards lysosomal compartments[93] as a primary pathway for copper efflux.[53 94] Given that nanoparticles are internalized via the endosomal-lysosomal pathway, we sought to quantify the protein expression of ATP7B in A549 cells upon exposure to $CuFe_2O_4$ or $Cu_2Fe(CN)_6$. Interestingly, Western Blot analysis (**Figure 5a-b**) revealed a significant increase in ATP7B expression after 1 h of treatment with $CuFe_2O_4$ whereas expression did not change for $Cu_2Fe(CN)_6$ in the same early time frame (**Figure 5c**).

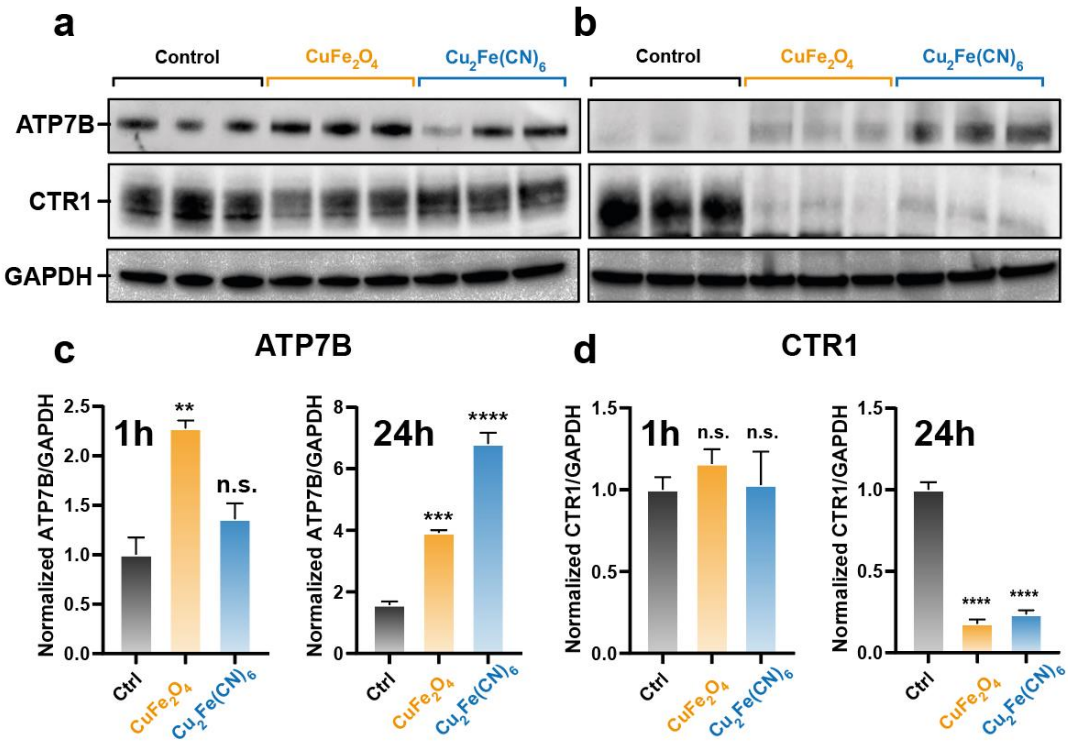

Figure 5. *Copper-based nanoparticle internalization promotes the upregulation of cellular copper ion efflux and the downregulation of copper ion influx machinery. Western Blot analysis of ATP7B, CTR1, and Glyceraldehyde 3-phosphate dehydrogenase (GAPDH) proteins in A549 cells treated with 6.25 μg Cu·mL^{-1} $CuFe_2O_4$, 3.125 μg Cu·mL^{-1} $Cu_2Fe(CN)_6$, or vehicle control for (a) 1 h or (b) 24 h. Quantified ATP7B (c) and CTR1 (d) expression after incubation with $CuFe_2O_4$ or $Cu_2Fe(CN)_6$ for 1 h or 24h. After nanoparticle internalization, A549 cells rapidly increase the expression of the copper ion exporter ATP7B to remove excess copper generated from nanoparticle dissolution. In addition, expression of the CTR1 copper ion importer is downregulated after 24 h of incubation to avoid the internalization of additional labile copper ions. Error bars denote S.E.M (n = 3).*

We attribute this discrepancy to the slower internalization of $Cu_2Fe(CN)_6$ nanoparticles (see **Figure 2d**) and consequently, a more delayed cellular response. Indeed, ATP7B expression increased for both particles after a 24 h of treatment (**Figure 5c**), consistent with a compensatory cellular response to elevations the labile Cu(II) pools generated from nanoparticle internalization and leaching over these longer time scales (**Figure 3**).[95] We note that these finding complement work by Lu and colleagues,[56] who also detected a transient increase in ATP7B levels in hepatocyte cells treated with CuS nanoparticles, but its expression decayed after 1 h of treatment. These findings

suggest a positive correlation between nanoparticle copper ion leaching rate and ATP7B expression. In addition, we also monitored the expression levels of high affinity copper uptake protein 1 (CTR1), the principal importer of extracellular Cu.[96] While incubation with either $CuFe_2O_4$ or $Cu_2Fe(CN)_6$ did not produce significant changes to CTR1 expression in A549 cells within 1 h, a significant downregulation of this copper importer protein was observed after 24 h of treatment for both particles (**Figure 5d**). In addition to its role as a copper nutrient importer, CTR1 can also act as a promoter of angiogenesis through activation of Vascular Endothelial Growth Factor receptor type 2 (VEGFR2).[97] Along these lines, CTR1 downregulation using copper-containing nanoparticles could also contribute to a reduced nutrient flux towards the TME.[98] These data reveal additional cellular response pathways towards copper-containing nanoparticle internalization, where the cell limits its copper exposure by upregulation of the ATP7B exporter to promote removal of excess labile copper ions generated after particle dissolution and the downregulation of CTR1 importer to decrease further copper ion uptake.

Conclusions – Chapter 5

We have established the utility of activity-based sensing as a method for applications in nanomedicine, where we have studied the biochemical mechanisms of redox and metal homeostasis in cells in response to treatment with anticancer metal-containing nanoparticle therapeutics. Using a pair of activity-based sensing probes that respond to either labile Cu(I) and Cu(II) (**CD664**) or Cu(II) alone (**CD649.2**), we have studied the effects of therapeutic copper-leaching nanoparticles on labile copper levels and compensatory cellular responses in a lung cancer A549 cell model. Interestingly, although we observed that copper-containing nanomedicines increase the total copper content in cells as measured by ICP-MS (**Figure 2c-d**), internalization of copper-based nanoparticles results in a decrease in the overall levels of bioavailable labile copper pools (**Figure 2f-i**). This decrease in overall labile copper is accompanied by a shift in relative labile Cu(I)/Cu(II) ratios, as activity-based sensing using the oxidation state-selective probe **CD649.2** revealed an accumulation of labile Cu(II) (**Figure 3**). In response to the increases in total copper and oxidized labile Cu(II), the cell triggers the activation

of two distinct antioxidant pathways in response to oxidative stress, the elevation in bioavailability of the redox buffering molecule GSH and the activation of the redox-responsive transcription factor NRF2 (**Figure 5**). Moreover, the cell also responds to copper nanoparticle treatment via changes in metal homeostasis machinery, and minimizes copper exposure by upregulation of copper ion export via ATP7B and downregulation of copper ion import by CTR1 (**Figure 6a, b**). Overall, this work provides insights into foundational biochemical mechanisms of how metal nanoparticles influence metal homeostasis in living biological systems and compensatory cellular responses, particularly in the partitioning of total and labile metal ion pools and in the redox balance of metal oxidation states. Furthermore, our results establish that the activity-based sensing methodology can identify key factors to inform the future design of more effective nanoparticle-based platforms for nanomedicine. In the context of nanomedicine therapeutics for cancer, such strategies could involve combinatorial treatments of copper-leaching nanoparticles with relevant inhibitors to boost their efficiency towards selective killing of tumor cells versus healthy tissue. The growing connections between copper and cancer,[53] particularly in the discovery and emergence of novel pathways for copper-dependent cell proliferation (cuproplasia) and copper-dependent cell death (cuproptosis), presage a wealth of opportunities for nanomedicine to diagnose and treat metal-dependent disease vulnerabilities.

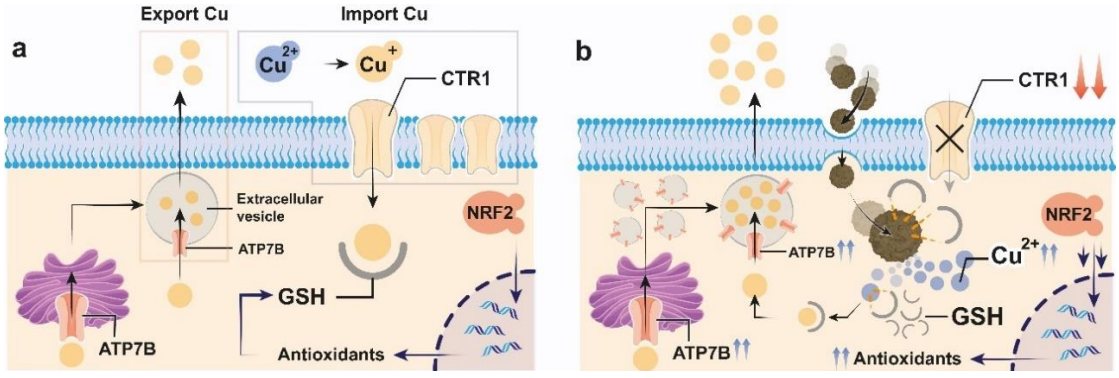

Figure 6. *Schematic depiction of a model showing the effects of copper-based nanoparticles on copper homeostasis and compensatory biochemical responses in cells. (a) A basal, physiological scenario where copper and intracellular redox status are under normal and regulated homeostatic control. (b) A high-copper perturbation scenario following nanoparticle internalization and copper ion leaching where a significant pool of labile Cu(II) is generated. To overcome this acute or chronic aberrant exposure to excess of this metal nutrient and accompanying oxidative stress, cells*

sequester excess copper via GSH and NRF2 antioxidant pathways, with concomitant upregulation of the copper ion export protein ATP7B to promote copper efflux and downregulation of the copper ion import protein CTR1 to block copper influx.

Experimental section – Chapter 5

Chemicals and Materials. Reagents were purchased from commercial sources and used without further purification unless otherwise noted. Janelia Fluor® 646, free acid was purchased from Tocris biotechne. Phosphate Buffer Saline (PBS without Ca and Mg, Corning), Dulbecco's Modified Eagle's Medium (DMEM, (GlutaMax)), Hanks' Balanced Salt Solution (HBSS + $CaCl_2$, + $MgCl_2$, Gibco), Cell Counting Kit-8 (CCK-8, Dojindo), CellROX-Green reagent (InvitroGen) were purchased from Thermo Fisher Scientific.

Instruments. Transmission electron microscopy (TEM) was performed using a FEI TECNAI T20 microscope operated at 200 keV. Confocal fluorescence imaging was performed with a Zeiss laser scanning microscope LSM880 with a 20x dry objective lens using Zen 2015 software (Carl Zeiss, Zen 2.3 black). X-ray diffraction (XRD) patterns were obtained in a PANalytical Empyrean equipment in Bragg-Brentano configuration using CuKa radiation and equipped with a PIXcel1D detector. Metal release from nanoparticles was measured using a 4100 Agilent MP-AES. Metarel content in cells was determined by measuring ^{63}Cu and ^{64}Zn using a Thermo Fisher iCAP-Qc ICP-MS in KED mode. Aristar BDH Ultra Concentrated nitric acid to dissolve samples was purchased from VWR. X-ray photoelectron spectroscopy (XPS) was performed with an Axis Supra spectrometer (Kratos Tech). The samples were mounted on a sample rod placed in the pretreatment chamber of the spectrometer and then evacuated at room temperature. The sample was excited by a monochromatized Al Ka source at 1486.6 eV and subsequently run at 8 kV and 15 mA. A survey spectrum was measured at 160 eV of pass energy, and for the individual peak regions, spectra were recorded with a pass energy of 20 eV. Analysis of the Cu2p peak was performed with the CasaXPS software using a weighted sum of Lorentzian and Gaussian component.

Synthesis of $CuFe_2O_4$. Copper-Iron oxide was synthesized following previous works[54] without further modification.

Synthesis of $Cu_2Fe(CN)_6$. $Cu_2Fe(CN)_6$ nanoparticle synthesis was adapted from the literature,[61] modifying the protocol to introduce Fe^{III} instead of Fe^{II}. 300 mg of Citric Acid tribasic (Sigma Aldrich, 99.0 %) and 36.8 mg of $K_3Fe(CN)_6$ were dissolved in 20 mL of distilled water. 10 mL of a 3.5 $mg \cdot mL^{-1}$ solution of $CuSO_4 \cdot 5H_2O$ was added dropwise to the previous solution. The mixture was left to stir overnight at room temperature. Final product was collected by centrifugation (two cycles of 10 000 rpm, 10 minutes) and stored at 4 ºC for further use.

In Vitro Measurements of Copper Release from Nanoparticles. To a 5 mM GSH solution (pH = 7.4, buffered with HCO_3^-/CO_2), $Cu_2Fe(CN)_6$ nanoparticles were added until a final [Cu] = 0.1 $mg \cdot mL^{-1}$ was reached. 1 mL of solution was sampled and centrifuged at 13 300 rpm for 10 minutes. Supernatant was analyzed using MP-AES. to quantify the released Cu.

GSH Oxidation Catalyzed by $Cu_2Fe(CN)_6$. To a 0.1 M PBS solution, GSH and $Cu_2Fe(CN)_6$ catalyst were added to a final concentration of 4 mM and 0.01 mg $Cu \cdot mL^{-1}$, respectively. Temperature was fixed at 37 ºC. Samples were analyzed by UPLC-PDA following methodology from previous works[54] without further modification.

Cell Viability Assays. All cells used in this research were maintained by the UC Berkeley Tissue Culture Facility. A549 cells were seeded at 75 % confluency in a 96-well cell plate. $CuFe_2O_4$ and $Cu_2Fe(CN)_6$ nanoparticles from stock solution in PBS were added to DMEM to achieve a final concentration ranging from 0.00625 to 0.10 $mg \cdot mL^{-1}$. Prior to the addition of the solution, nanoparticles were sonicated for 20 minutes. After 24 hours, cells were washed with PBS (1x) and 100 µL of 10% v/v CCK-8 in DMEM solution was added to the well. Cells were then incubated at 37 ºC in a 5% CO_2 incubator for 3 hours. Finally, the absorbance at 450 nm was measured using a plate reader. Viability is presented as a percentage of control (n = 3 ± S.E.M).

***ICP-MS Analysis*.** A549 cells were seeded in Falcon® 6-well clear plates (Ref. 353046) at 75% confluency. $CuFe_2O_4$ and $Cu_2Fe(CN)_6$ nanoparticles resuspended in DMEM were added to a final concentration of 6.25 µg $Cu \cdot mL^{-1}$ and 3.15 µg $Cu \cdot mL^{-1}$, respectively, and incubated for 1 and 24

hours. Then, wells were washed with ice-cold PBS (1x) three times. Finally, 350 µL of concentrated nitric acid was added to the plate and incubated for 48 h at room temperature. Before analysis, 20 ppb of Ga was added to each sample as an internal standard. Results are expressed as an average ratio of [Cu]/[Zn] ± S.E.M (n = 6). Intracellular Zn concentration was used to normalize total cell number.

Synthesis of CD664. The complete synthetic route is shown in **Figure S22.** Methods are adapted from previous works.[42, 60]

Synthesis of Compound 1. Sodium ethanethioate (727 mg, 8.65 mmol) and NaOH (188 mg, 4.71 mmol) were dissolved in 2 mL of MeOH through sonication and vigorous stirring for 30 minutes. Bis(2-chloroethyl)amine hydrochloride (701 mg, 3.93 mmol) was dissolved in 2.5 mL of MeOH and was slowly added to the previous solution. The mixture was stirred at room temperature overnight. MeOH was then removed under reduced pressure. The obtained slurry was extracted with hexane three times. The solution was filtered through a short plug of basic alumina and the filter was washed with DCM and ethyl acetate. Solvent was removed under reduced pressure and product was dried under high vacuum. ^{1}H NMR ($CDCl_3$, 400 MHz): δ 2.85 (t, *J* = 8 Hz, 4H, $NHCH_2$), 2.71 (t, *J* = 8 Hz, 4H, SCH_2), 2.55 (q, *J* = 8 Hz, 4H, SCH_2), 1.76 (s, broad, 1H, NH), 1.27 (t, *J* = 8 Hz, 6H, CH_3) (**Figure S23**).

Synthesis of Compound 2. 4-Imidazole aldehyde (260 mg, 2.71 mmol) was dissolved in 1.40 mL of MeOH. Compound **1** (525 mg, 2.71 mmol) was dissolved in 7.2 mL of MeOH: Acetic acid mixture (10:1) and was slowly added to the previous solution. $NaBH_3CN$ (275 mg, 4.38 mmol) in 2 mL of MeOH was then added dropwise and stirred at room temperature overnight. N_2 was added to the solution and sealed with a septum. Reaction was quenched with 4-5 drops of HCl. Then, solvent was removed at high vacuum, extracted with DCM and dried with Na_2SO_4. Final product was purified with an alumina column (DCM: MeOH = 100:0 to 95:5). ^{1}H NMR ($CDCl_3$, 400 MHz): δ 7.70 (s, 1H, NCHN), 7.00 (s, 1H, CHN), 3.70 (s, 2H, NCH_2), 2.85 (t, *J* = 8 Hz, 4H, $NHCH_2$), 2.71 (t, *J* = 8 Hz, 4H, SCH_2), 2.55 (q, *J* = 8 Hz, 4H, SCH_2), 1.27 (t, *J* = 8 Hz, 6H, CH_3) (**Figure S24**).

***Synthesis of Compound 3*.** A solution of *N*-(*tert*-butoxycarbonyl)-2-(2-aminoethoxy)ethanol (1.00 g, 4.74 mmol), *N,N'*-disuccinimidyl carbonate (2.50 g, 9.75 mmol), and triethylamine (0.98 g, 9.75

mmol) in CH_3CN (35 mL) was stirred for 2 hours at 40 °C. After removal of the solvent by evaporation, the residue was dissolved in EtOAc. The organic layer was washed with sat. $NaHCO_3$ and dried over Na_2SO_4 followed by concentration *in vacuo*. The residue was purified by flash column chromatography on silica gel (EtOAc: Hexane = 50:50 to 75:25). ^{1}H NMR (400 MHz, $CDCl_3$) δ 4.47 (t, *J* = 4.8 Hz, 2H), 3.74 (t, *J* = 4.8 Hz, 2H), 3.56 (t, *J* = 4.8 Hz, 2H), 3.33 (m, 2H), 2.85 (s, 4H), 1.45 (s, 9H) (**Figure S25**).

Synthesis of Compound 4. A solution of compound **2** (315 mg, 1.15 mmol), **3** (329 mg, 0.95 mmol), and pyridine (223 µL, 2.81 mmol) in dry DMF (7.5 mL) was stirred at room temperature for 12 hours under an N_2 atmosphere. The reaction was subsequently diluted with EtOAc, washed with water (×2) and brine, and then dried over Na_2SO_4, filtered, and evaporated. The crude residue was purified by column chromatography on silica gel (50–75% EtOAc/hexane, linear gradient) to yield the product (286.15 mg, 0.58 mmol, 61%) as a colorless oil. ^{1}H NMR ($CDCl_3$, 400 MHz) δ 8.09 (d, *J* = 1.3 Hz, 1H), 7.35 (d, *J* = 1.3 Hz, 1H), 4.86 (s, 1H), 4.54 (t, *J* = 4 Hz, 2H), 3.79 (t, *J* = 4 Hz, 2H), 3.68 (s, 2H), 3.57 (t, *J* = 5.4 Hz, 2H), 3.33 (t, *J* = 5.4 Hz, 2H), 2.80–2.72 (m, 4H), 2.71–2.63 (m, 4H), 2.55 (q, *J* = 7.4 Hz, 4H), 1.44 (s, 9H), 1.25 (t, *J* = 7.4 Hz, 6H). (**Figure S26**).

Synthesis of CD664. Compound **4** (12.4 mg, 24.6 µmol, 1.5 eq.) was dissolved in 5:1 DCM: TFA (1.20 mL: 0.25 mL) and stirred at room temperature for 30 minutes. Solvent was removed via rotary evaporation and residual TFA was removed by azeotroping 3 times with toluene (1.20 mL each time) and left under high vacuum for 30 minutes. Deprotected compound **4**, Janelia Fluor® 664, free acid (10.0 mg, 16.3 µmol), and DIPEA (22.0 µL, 131 µmol, 8.0 eq.) were then dissolved in dry DMF (1 mL). BOP (8.7 mg, 19.7 µmol, 1.2 eq.) was then added and the reaction was stirred at room temperature for 20 minutes. The product was then purified via prep-HPLC (conditions: 20% → 70% CH_3CN in H_2O with 10 mM NH_4OAc pH = 5 over 40 minutes and hold at 70% for another 40 minutes, 8 mL/min flow rate). HPLC fractions were combined and lyophilized to obtain a light blue powder (8.8 mg, 62%). UV-vis and MS spectra of the purified compound are shown in **Figure S27.** ^{1}H NMR (600 MHz, DMSO-d_6) δ 8.77 (t, *J* = 5.7 Hz, 1H), 8.14 (d, *J* = 1.3 Hz, 1H), 8.12 (d, *J* = 1.3 Hz, 1H), 8.03 (dd, *J* = 8.0, 1.3 Hz, 1H), 7.97 (d, *J* = 8.0 Hz, 1H), 7.65 (d, *J* = 1.3 Hz, 1H),

7.40 (d, *J* = 1.3 Hz, 1H), 6.70 (d, *J* = 2.6 Hz, 2H), 6.60 (d, *J* = 8.7 Hz, 2H), 6.30 (dd, *J* = 8.7, 2.6 Hz, 2H), 4.44 (t, *J* = 4.6 Hz, 2H), 3.81 (t, *J* = 7.3 Hz, 8H), 3.73 (t, *J* = 4.6 Hz, 2H), 3.57 – 3.55 (m, 4H), 3.39 (td, *J* = 11.5, 5.7 Hz, 2H), 2.63 – 2.55 (m, 8H), 2.47 (q, *J* = 7.3 Hz, 4H), 2.23 – 2.25 (m, 4H), 1.13 (t, *J* = 7.3 Hz, 6H), 0.59 (s, 3H), 0.48 (s, 3H). (**Figure S26**). ^{13}C NMR (600 MHz, DMSO-d_6) δ 169.2, 165.0, 154.6, 150.8, 148.2, 140.5, 139.8, 136.7, 135.7, 131.3, 128.1, 127.4, 125.4, 122.8, 115.4, 115.1, 112.6, 91.2, 68.5, 67.5, 67.0, 53.3, 51.9, 49.6, 28.6, 25.1, 16.3, 14.8, 0.0, -1.4. (**Figure S29**). HR-MS (ESI) *m/z* calculated for $[M+H]^+$ 883.370, found 883.371 (**Figure S30**).

Synthesis of CD649.2. The **CD649.2** dye was synthesized following previous works[60] without further modification.

In vitro Protein Labelling. To prepare cell lysate, A549 cells were seeded in Falcon® 6-well clear plates (Ref. 353046) at 75% confluency. Cells were washed using cold PBS (1x) twice. Cells were then collected using a cell scraper, and centrifuged at 6,000 rpm for 20 minutes at 4 ºC. Supernatant was discarded and cell pellets were lysed with 150 µL of RIPA buffer (Thermo Scientific, 89900) with an added protease inhibitor cocktail (Roche, 05892953001) for 30 minutes. The protein concentrations were quantified by Pierce BCA assay (Thermo Scientific, 23250). To release all possible copper from either $CuFe_2O_4$ or $Cu_2Fe(CN)_6$, each nanoparticle (50 µg/mL) was incubated with 10 mM GSH in PBS (pH = 7.4, titrated with 1 M NaOH) for 24 h at 37 ºC . Then, 2.40 µL of A549 cell lysate (5.2 mg·mL^{-1}) was pre-incubated with various concentrations of the CuFe + GSH mixture for 5 minutes at room temperature (diluted with PBS to a final volume of 24.5 µL). Finally, 0.5 µL of **CD664** or **CD649.2** (0.5 mM) was added to the previous solution and left to incubate for 1 h. The solution mixture was mixed with NuPAGE® LDS Sample Buffer (4X) and heated at 95 ºC for 5 minutes, followed by separation on Novex tris-glycine gels (Invitrogen) and scanned by ChemiDoc MP (Bio-Rad Laboratories, Inc) for measuring in-gel fluorescence. The fluorescence was measured by 695/55 nm band pass filter with excitation using red epi-illumination. The total protein level on the gel was then assayed by Coomassie Brilliant Blue R-250 (Biorad; 1610400) according to the manufacturer's protocol and scanned by ChemiDoc MP. The integrated intensities were analyzed by ImageLab.

Detection of Cu^+ generation using FCP-1. A solution containing 10 mM GSH and 50 μg·mL^{-1} of $CuFe_2O_4$ or $Cu_2Fe(CN)_6$ was incubated in PBS (pH = 7.4, titrated with 1 M NaOH) for 24 h at 37 ºC to induce the release of copper. Leached nanoparticles were then diluted into PBS with 40 vol % PEG-400 to a final concentration of 10 or 1 μg·mL^{-1} (final volume 999 μL). 1 μL of **FCP-1** (5 mM) was then added to the solution and incubated for 1, 15, and 30 minutes, respectively. Finally, the fluorescence spectra of the solution were acquired using an excitation wavelength (λ_{exc} = 458 nm).

***Confocal Fluorescence Imaging*.** A549 cells were seeded at 75% confluency in a poly L-lysine coated 8-well chamber slide (Nunc Lab-Tek). $CuFe_2O_4$ and $Cu_2Fe(CN)_6$ nanoparticles resuspended in DMEM were added to a final concentration of 6.25 μg Cu·mL^{-1} and 3.15 μg Cu·mL^{-1}, respectively, and incubated for various times. Wells were then washed with HBSS once, and **CD664** was added to a final concentration of 1 μM (0.6% of DMSO). Cells were incubated for 15 minutes at 37 ºC in a 5% CO_2 incubator prior to imaging. **CD664** was excited with a 633 nm laser, and the emissions were collected using a META detector between 650 and 750 nm. For **CD649.2**, cells were treated in the same way, however staining with **CD649.2** was performed for 1 hour and cells were then washed once with HBSS prior to imaging. All results are expressed considering average signal of control = 1 ± S.E.M (n = 8).

Detection of Labile Copper in the Presence of BSO, KI696, and ML-385. We evaluated whether the labile copper detection properties of **CD664**, **CD649.2,** or **FCP-1** were affected by the presence of BSO, KI696 or ML-385. Cell lysates were prepared by seeding A549 cells in Falcon® 6-well clear plates (Ref. 353046) at 75% confluency. Cells were washed using cold PBS (1x) twice. Cells were then collected using a cell scraper, and centrifuged at 6,000 rpm for 20 minutes at 4 ºC. Supernatant was discarded and cell pellets were lysed with 150 μL of RIPA buffer (Thermo Scientific, 89900) with an added protease inhibitor cocktail (Roche, 05892953001) for 30 minutes. The protein concentrations were quantified by Pierce BCA assay (Thermo Scientific, 23250). To release all possible copper from either $CuFe_2O_4$ or $Cu_2Fe(CN)_6$, each nanoparticle (10 μg/mL) was incubated with 10 mM GSH in PBS (pH = 7.4, titrated with 1 M NaOH) and 0.5 mM BSO, 1 μM KI696 or 10 μM ML-385 for 24 h at 37 ºC. Then, 3.23 μL of A549 cell lysate (3.87 mg·mL^{-1}) was pre-incubated with the previous solutions for 5 minutes at room temperature (diluted with PBS to

a final volume of 24.5 µL). Finally, 0.5 µL of **CD664** or **CD649.2** (0.5 mM) was added to the previous solution and left to incubate for 1 h. The solution mixture was mixed with NuPAGE® LDS Sample Buffer (4X) and heated at 95 °C for 5 minutes, followed by separation on Novex tris-glycine gels (Invitrogen) and scanned by ChemiDoc MP (Bio-Rad Laboratories, Inc) for measuring in-gel fluorescence. The fluorescence was measured by 695/55 nm band pass filter with excitation using red epi-illumination. The total protein level on the gel was assayed by silver staining (ThermoFisher Scientific; 24612) according to the manufacturer's protocol and scanned by ChemiDoc MP. The integrated intensities were analyzed by ImageLab.

In the case of Cu^{+}, a solution containing 10 mM GSH and 1 µg·mL^{-1} of $CuFe_2O_4$ or $Cu_2Fe(CN)_6$ was incubated in PBS (pH = 7.4, titrated with 1 M NaOH), to induce the release of copper, and 0.5 mM BSO, 1 µM KI696 or 10 µM ML-385 for 24 h at 37 °C.. Leached nanoparticles were then diluted into PBS with 40 vol % PEG-400 to a final concentration of 10 or 1 µg·mL^{-1} (final volume 999 µL). 1 µL of **FCP-1** (5 mM) was then added to the solution and incubated 30 minutes, respectively. Finally, the fluorescence spectra of the solution were acquired using an excitation wavelength (λ_{exc} = 458 nm).

***Image Analysis and Quantification*.** Nanoparticle diameter and confocal microscopy images of A549 cells were quantified using Image J software. Fluorescence intensity both of **CD664** and **CD649.2** was measured from two independent wells from a total of 8 pictures taken at x20 augments. For quantification, the area of stained cells was selected by fixing the appropriate threshold for each image with a Gaussian blur filter (sigma = 1). The "Create Mask" function followed by the "Create Selection" function were then used to create a selection from this threshold to finally quantify signal. Mean intensity of control samples was employed to perform the final statistic analysis using Prism7 (GraphPad).

Reactive Oxygen Species (ROS) Imaging. A549 cells were seeded at 60% of confluency in a poly L-lysine coated 8-well chamber slide (Nunc Lab-Tek). $CuFe_2O_4$ and $Cu_2Fe(CN)_6$ nanoparticles resuspended in DMEM were added to a final concentration of 6.25 µg Cu·mL^{-1} and 3.15 µg Cu·mL^{-1}, respectively, and incubated for 1 hour or 24 hours. Wells were washed with HBSS once, and then CellRox reagent was added to a final concentration of 5 µM (1% DMSO). Cells were incubated

for 30 minutes at 37 ºC in a 5% CO_2 incubator. Wells were then washed with HBSS twice, and fixed with paraformaldehyde (3.7%) for 15 minutes at 37 ºC prior to imaging. CellROX was excited with 485 nm with an Ar laser, and the emissions were collected using a META detector between 500 and 540 nm. Results are normalized to control fluorescence = 1 ± S.E.M (n = 8).

Western Blot Analysis. A549 cells were treated with $CuFe_2O_4$ and $Cu_2Fe(CN)_6$ with a final concentration of 6.25 μg $Cu{\cdot}mL^{-1}$ and 3.15 μg $Cu{\cdot}mL^{-1}$, respectively, and incubated for 1 hour or 24 hours. Cells were washed using cold PBS (1x) twice. Finally, cells were collected using a cell scraper, and centrifuged at 6,000 rpm for 20 minutes at 4 ºC. Supernatant was discarded and cell pellets were lysed with 150 μL of RIPA buffer (Thermo Scientific, 89900) with an added protease inhibitor cocktail (Roche, 05892953001) for 30 minutes. The protein concentrations were quantified by Pierce BCA assay (Thermo Scientific, 23250). GAPDH antibody was purchased from Cell Signaling Technologies (Asp175, no. 9661) and used with a dilution 1:3000. ATP7B antibody was purchased from Novus Biological (NB100-360) and used with a dilution of 1:1000. CTR1 antibody was purchased from Novus Biological (NBP2-36573) and used with a dilution of 1:500. Results are normalized by GAPDH expression (n = 3).

Statistical Analysis*.* All the results are expressed as mean ± SEM. Statistical analysis of the biological experiments and the significant differences among the means were evaluated by two-way analysis of variance (ANOVA) for multiple comparisons by Dunnett's multiple comparisons test using GraphPad Software). Statistically significant differences were express as follows: *$p < 0.05$, **$p < 0.005$, ***$p < 0.0005$ and ****$p < 0.00005$.

References – Chapter 5

1. Wang, X.; Zhong, X.; Liu, Z.; Cheng, L., Recent progress of chemodynamic therapy-induced combination cancer therapy. Nano Today 2020, 35, 100946.

2. Chen, J.; Zhu, Y.; Wu, C.; Shi, J., Nanoplatform-based cascade engineering for cancer therapy. Chemical Society Reviews 2020, 49 (24), 9057-9094.

3. Bonet-Aleta, J.; Sancho-Albero, M.; Calzada-Funes, J.; Irusta, S.; Martin-Duque, P.; Hueso, J. L.; Santamaria, J., Glutathione-Triggered catalytic response of Copper-Iron mixed oxide Nanoparticles. Leveraging tumor microenvironment conditions for chemodynamic therapy. Journal of Colloid and Interface Science 2022, 617, 704-717.

4. Ding, Y.; Dai, Y.; Wu, M.; Li, L., Glutathione-mediated nanomedicines for cancer diagnosis and therapy. Chemical Engineering Journal 2021, 426, 128880.

5. López-Lázaro, M., Dual role of hydrogen peroxide in cancer: Possible relevance to cancer chemoprevention and therapy. Cancer Letters 2007, 252 (1), 1-8.

6. Burdon, R. H., Superoxide and hydrogen peroxide in relation to mammalian cell proliferation. Free Radical Biology and Medicine 1995, 18 (4), 775-794.

7. Harris, Isaac S.; Treloar, Aislinn E.; Inoue, S.; Sasaki, M.; Gorrini, C.; Lee, Kim C.; Yung, Ka Y.; Brenner, D.; Knobbe-Thomsen, Christiane B.; Cox, Maureen A.; Elia, A.; Berger, T.; Cescon, David W.; Adeoye, A.; Brüstle, A.; Molyneux, Sam D.; Mason, Jacqueline M.; Li, Wanda Y.; Yamamoto, K.; Wakeham, A.; Berman, Hal K.; Khokha, R.; Done, Susan J.; Kavanagh, Terrance J.; Lam, C.-W.; Mak, Tak W., Glutathione and Thioredoxin Antioxidant Pathways Synergize to Drive Cancer Initiation and Progression. Cancer Cell 2015, 27 (2), 211-222.

8. Lin, L.-S.; Huang, T.; Song, J.; Ou, X.-Y.; Wang, Z.; Deng, H.; Tian, R.; Liu, Y.; Wang, J.-F.; Liu, Y.; Yu, G.; Zhou, Z.; Wang, S.; Niu, G.; Yang, H.-H.; Chen, X., Synthesis of Copper Peroxide Nanodots for H2O2 Self-Supplying Chemodynamic Therapy. Journal of the American Chemical Society 2019, 141 (25), 9937-9945.

9. Ma, B.; Wang, S.; Liu, F.; Zhang, S.; Duan, J.; Li, Z.; Kong, Y.; Sang, Y.; Liu, H.; Bu, W.; Li, L., Self-Assembled Copper–Amino Acid Nanoparticles for in Situ Glutathione "AND" H_2O_2 Sequentially Triggered Chemodynamic Therapy. Journal of the American Chemical Society 2019, 141 (2), 849-857.

10. Lu, X.; Gao, S.; Lin, H.; Yu, L.; Han, Y.; Zhu, P.; Bao, W.; Yao, H.; Chen, Y.; Shi, J., Bioinspired Copper Single-Atom Catalysts for Tumor Parallel Catalytic Therapy. Advanced Materials 2020, 32 (36), 2002246.

11. Huo, M.; Wang, L.; Chen, Y.; Shi, J., Tumor-selective catalytic nanomedicine by nanocatalyst delivery. Nature Communications 2017, 8 (1), 357.

12. Yang, B.; Yao, H.; Tian, H.; Yu, Z.; Guo, Y.; Wang, Y.; Yang, J.; Chen, C.; Shi, J., Intratumoral synthesis of nano-metalchelate for tumor catalytic therapy by ligand field-enhanced coordination. Nature Communications 2021, 12 (1), 3393.

13. Lin, L.-S.; Song, J.; Song, L.; Ke, K.; Liu, Y.; Zhou, Z.; Shen, Z.; Li, J.; Yang, Z.; Tang, W.; Niu, G.; Yang, H.-H.; Chen, X., Simultaneous Fenton-like Ion Delivery and Glutathione Depletion by MnO_2-Based Nanoagent to Enhance Chemodynamic Therapy. Angewandte Chemie International Edition 2018, 57 (18), 4902-4906.

14. Wu, F.; Du, Y.; Yang, J.; Shao, B.; Mi, Z.; Yao, Y.; Cui, Y.; He, F.; Zhang, Y.; Yang, P., Peroxidase-like Active Nanomedicine with Dual Glutathione Depletion Property to Restore Oxaliplatin Chemosensitivity and Promote Programmed Cell Death. ACS Nano 2022, 16 (3), 3647-3663.

15. Yang, B.; Chen, Y.; Shi, J., Nanocatalytic Medicine. Advanced materials, 2019, 31 (39), e1901778.

16. Tang, Z.; Zhao, P.; Wang, H.; Liu, Y.; Bu, W., Biomedicine Meets Fenton Chemistry. Chemical Reviews 2021, 121 (4), 1981-2019.

17. Koo, S.; Park, O. K.; Kim, J.; Han, S. I.; Yoo, T. Y.; Lee, N.; Kim, Y. G.; Kim, H.; Lim, C.; Bae, J.-S.; Yoo, J.; Kim, D.; Choi, S. H.; Hyeon, T., Enhanced Chemodynamic Therapy by Cu–Fe Peroxide Nanoparticles: Tumor Microenvironment-Mediated Synergistic Fenton Reaction. ACS Nano 2022, 16 (2), 2535-2545.

18. Garcia-Peiro, J. I.; Bonet-Aleta, J.; Santamaria, J.; Hueso, J. L., Platinum nanoplatforms: classic catalysts claiming a prominent role in cancer therapy. Chemical Society Reviews 2022, 51 (17), 7662-7681.

19. Gao, S.; Lin, H.; Zhang, H.; Yao, H.; Chen, Y.; Shi, J., Nanocatalytic Tumor Therapy by Biomimetic Dual Inorganic Nanozyme-Catalyzed Cascade Reaction. Advanced Science 2019, 6 (3), 1801733.

20. Zhao, P.; Li, H.; Bu, W., A Forward Vision for Chemodynamic Therapy: Issues and Opportunities. Angewandte Chemie International Edition 2023, 62 (7), e202210415.

21. Francia, V.; Reker-Smit, C.; Salvati, A., Mechanisms of Uptake and Membrane Curvature

Generation for the Internalization of Silica Nanoparticles by Cells. Nano Letters 2022, 22 (7), 3118-3124.

22. Donahue, N. D.; Acar, H.; Wilhelm, S., Concepts of nanoparticle cellular uptake, intracellular trafficking, and kinetics in nanomedicine. Advanced Drug Delivery Reviews 2019, 143, 68-96.

23. Soenen, S. J.; Parak, W. J.; Rejman, J.; Manshian, B., (Intra)Cellular Stability of Inorganic Nanoparticles: Effects on Cytotoxicity, Particle Functionality, and Biomedical Applications. Chemical Reviews 2015, 115 (5), 2109-2135.

24. Liu, J.; Yuan, Y.; Cheng, Y.; Fu, D.; Chen, Z.; Wang, Y.; Zhang, L.; Yao, C.; Shi, L.; Li, M.; Zhou, C.; Zou, M.; Wang, G.; Wang, L.; Wang, Z., Copper-Based Metal–Organic Framework Overcomes Cancer Chemoresistance through Systemically Disrupting Dynamically Balanced Cellular Redox Homeostasis. Journal of the American Chemical Society 2022, 144 (11), 4799-4809.

25. Zhou, M.; Tian, M.; Li, C., Copper-Based Nanomaterials for Cancer Imaging and Therapy. Bioconjugate Chemistry 2016, 27 (5), 1188-1199.

26. Aishajiang, R.; Liu, Z.; Wang, T.; Zhou, L.; Yu, D., Recent Advances in Cancer Therapeutic Copper-Based Nanomaterials for Antitumor Therapy. 2023, 28 (5), 2303.

27. Zhong, X.; Dai, X.; Wang, Y.; Wang, H.; Qian, H.; Wang, X., Copper-based nanomaterials for cancer theranostics. WIREs Nanomedicine and Nanobiotechnology 2022, 14 (4), e1797.

28. Lippard, S. J.; Berg, J. M.; Klatt, G., Principles of Bioinorganic Chemistry. University Science Books: 1994.

29. Lancaster, K. M.; DeBeer George, S.; Yokoyama, K.; Richards, J. H.; Gray, H. B., Type-zero copper proteins. Nature chemistry 2009, 1 (9), 711-5.

30. Solomon, E. I.; Heppner, D. E.; Johnston, E. M.; Ginsbach, J. W.; Cirera, J.; Qayyum, M.; Kieber-Emmons, M. T.; Kjaergaard, C. H.; Hadt, R. G.; Tian, L., Copper Active Sites in Biology. Chemical Reviews 2014, 114 (7), 3659-3853.

31. Guengerich, F. P., Introduction to Metals in Biology 2018: Copper homeostasis and utilization in redox enzymes. Journal of Biological Chemistry 2018, 293 (13), 4603-4605.

32. Gaggelli, E.; Kozlowski, H.; Valensin, D.; Valensin, G., Copper homeostasis and neurodegenerative disorders (Alzheimer's, prion, and Parkinson's diseases and amyotrophic lateral sclerosis). Chemical Reviews 2006, 106 (6), 1995-2044.

33. Adam, S. M.; Wijeratne, G. B.; Rogler, P. J.; Diaz, D. E.; Quist, D. A.; Liu, J. J.; Karlin, K. D., Synthetic Fe/Cu Complexes: Toward Understanding Heme-Copper Oxidase Structure and Function. Chemical Reviews 2018, 118 (22), 10840-11022.

34. Chang, C. J., Searching for harmony in transition-metal signaling. Nature Chemical Biology 2015, 11 (10), 744-747.

35. Chang, C. J., Bioinorganic Life and Neural Activity: Toward a Chemistry of Consciousness? Accounts of Chemical Research 2017, 50 (3), 535-538.

36. Ackerman, C. M.; Chang, C. J., Copper signaling in the brain and beyond. The Journal of biological chemistry 2018, 293 (13), 4628-4635.

37. Tsang, T.; Davis, C. I.; Brady, D. C., Copper biology. Current biology : CB 2021, 31 (9), R421-r427.

38. Pham, V. N.; Chang, C. J., Metalloallostery and Transition Metal Signaling: Bioinorganic Copper Chemistry Beyond Active Sites. Angewandte Chemie International Edition 2023, 62 (11), e202213644.

39. Dodani, S. C.; Domaille, D. W.; Nam, C. I.; Miller, E. W.; Finney, L. A.; Vogt, S.; Chang, C. J., Calcium-dependent copper redistributions in neuronal cells revealed by a fluorescent copper sensor and X-ray fluorescence microscopy. Proceedings of the National Academy of Sciences of the United States of America 2011, 108 (15), 5980-5.

40. Dodani, S. C.; Firl, A.; Chan, J.; Nam, C. I.; Aron, A. T.; Onak, C. S.; Ramos-Torres, K. M.; Paek, J.; Webster, C. M.; Feller, M. B.; Chang, C. J., Copper is an endogenous modulator of neural circuit spontaneous activity. Proceedings of the National Academy of Sciences of the United States of America 2014, 111 (46), 16280-5.

41. Xiao, T.; Ackerman, C. M.; Carroll, E. C.; Jia, S.; Hoagland, A.; Chan, J.; Thai, B.; Liu, C. S.; Isacoff, E. Y.; Chang, C. J., Copper regulates rest-activity cycles through the locus coeruleus-norepinephrine system. Nat Chem Biol 2018, 14 (7), 655-663.

42. Lee, S.; Chung, C. Y.-S.; Liu, P.; Craciun, L.; Nishikawa, Y.; Bruemmer, K. J.; Hamachi, I.; Saijo, K.; Miller, E. W.; Chang, C. J., Activity-Based Sensing with a Metal-Directed Acyl Imidazole Strategy Reveals Cell Type-Dependent Pools of Labile Brain Copper. Journal of the American Chemical Society 2020, 142 (35), 14993-15003.

43. Krishnamoorthy, L.; Cotruvo, J. A.; Chan, J.; Kaluarachchi, H.; Muchenditsi, A.; Pendyala, V. S.; Jia, S.; Aron, A. T.; Ackerman, C. M.; Wal, M. N. V.; Guan, T.; Smaga, L. P.; Farhi, S. L.; New, E. J.; Lutsenko, S.; Chang, C. J., Copper regulates cyclic-AMP-dependent lipolysis. Nature Chemical Biology 2016, 12 (8), 586-592.

44. Brady, D. C.; Crowe, M. S.; Turski, M. L.; Hobbs, G. A.; Yao, X.; Chaikuad, A.; Knapp, S.; Xiao, K.; Campbell, S. L.; Thiele, D. J.; Counter, C. M., Copper is required for oncogenic BRAF signalling and tumorigenesis. Nature 2014, 509 (7501), 492-496.

45. Tsang, T.; Posimo, J. M.; Gudiel, A. A.; Cicchini, M.; Feldser, D. M.; Brady, D. C., Copper is an essential regulator of the autophagic kinases ULK1/2 to drive lung adenocarcinoma. Nature Cell Biology 2020, 22 (4), 412-424.

46. Guo, J.; Cheng, J.; Zheng, N.; Zhang, X.; Dai, X.; Zhang, L.; Hu, C.; Wu, X.; Jiang, Q.; Wu, D.; Okada, H.; Pandolfi, P. P.; Wei, W., Copper Promotes Tumorigenesis by Activating the PDK1-AKT Oncogenic Pathway in a Copper Transporter 1 Dependent Manner. Advanced Science 2021, 8 (18), 2004303.

47. Chojnowski, J. E.; Li, R.; Tsang, T.; Alfaran, F. H.; Dick, A.; Cocklin, S.; Brady, D. C.; Strochlic, T. I., Copper Modulates the Catalytic Activity of Protein Kinase CK2. Front Mol Biosci 2022, 9, 878652.

48. Turski, M. L.; Brady, D. C.; Kim, H. J.; Kim, B.-E.; Nose, Y.; Counter, C. M.; Winge, D. R.; Thiele, D. J., A Novel Role for Copper in Ras/Mitogen-Activated Protein Kinase Signaling. Molecular and Cellular Biology 2012, 32 (7), 1284-1295.

49. Que, E. L.; Domaille, D. W.; Chang, C. J., Metals in Neurobiology: Probing Their Chemistry and Biology with Molecular Imaging. Chemical Reviews 2008, 108 (5), 1517-1549.

50. Tsvetkov, P.; Coy, S.; Petrova, B.; Dreishpoon, M.; Verma, A.; Abdusamad, M.; Rossen, J.; Joesch-Cohen, L.; Humeidi, R.; Spangler, R. D.; Eaton, J. K.; Frenkel, E.; Kocak, M.; Corsello, S. M.; Lutsenko, S.; Kanarek, N.; Santagata, S.; Golub, T. R., Copper induces cell death by targeting lipoylated TCA cycle proteins. Science (New York, N.Y.) 2022, 375 (6586), 1254-1261.

51. Ackerman, C. M.; Lee, S.; Chang, C. J., Analytical Methods for Imaging Metals in Biology: From Transition Metal Metabolism to Transition Metal Signaling. Analytical Chemistry 2017, 89 (1), 22-41.

52. Hare, D. J.; New, E. J.; de Jonge, M. D.; McColl, G., Imaging metals in biology: balancing sensitivity, selectivity and spatial resolution. Chemical Society Reviews 2015, 44 (17), 5941-5958.

53. Ge, E. J.; Bush, A. I.; Casini, A.; Cobine, P. A.; Cross, J. R.; DeNicola, G. M.; Dou, Q. P.; Franz, K. J.; Gohil, V. M.; Gupta, S.; Kaler, S. G.; Lutsenko, S.; Mittal, V.; Petris, M. J.; Polishchuk, R.; Ralle, M.; Schilsky, M. L.; Tonks, N. K.; Vahdat, L. T.; Van Aelst, L.; Xi, D.; Yuan, P.; Brady, D. C.; Chang, C. J., Connecting copper and cancer: from transition metal signalling to metalloplasia. Nature Reviews Cancer 2022, 22 (2), 102-113.

54. Bonet-Aleta, J.; Encinas-Gimenez, M.; Urriolabeitia, E.; Martin-Duque, P.; Hueso, J. L.; Santamaria, J., Unveiling the interplay between homogeneous and heterogeneous catalytic mechanisms in copper–iron nanoparticles working under chemically relevant tumour conditions. Chemical Science 2022, 13 (28), 8307-8320.

55. Liu, C.; Wang, D.; Zhang, S.; Cheng, Y.; Yang, F.; Xing, Y.; Xu, T.; Dong, H.; Zhang, X., Biodegradable Biomimic Copper/Manganese Silicate Nanospheres for Chemodynamic/Photodynamic Synergistic Therapy with Simultaneous Glutathione Depletion and Hypoxia Relief. ACS Nano 2019, 13 (4), 4267-4277.

56. Wang, X.; Guo, L.; Zhang, S.; Chen, Y.; Chen, Y.-T.; Zheng, B.; Sun, J.; Qian, Y.; Chen, Y.; Yan, B.; Lu, W., Copper Sulfide Facilitates Hepatobiliary Clearance of Gold Nanoparticles through the Copper-Transporting ATPase ATP7B. ACS Nano 2019, 13 (5), 5720-5730.

57. Chan, J.; Dodani, S. C.; Chang, C. J., Reaction-based small-molecule fluorescent probes for chemoselective bioimaging. Nature chemistry 2012, 4 (12), 973-84.

58. Chung, C. Y.-S.; Posimo, J. M.; Lee, S.; Tsang, T.; Davis, J. M.; Brady, D. C.; Chang, C. J., Activity-based ratiometric FRET probe reveals oncogene-driven changes in labile copper pools induced by altered glutathione metabolism. Proceedings of the National Academy of Sciences 2019, 116 (37), 18285-18294.

59. Bruemmer, K. J.; Crossley, S. W. M.; Chang, C. J., Activity-Based Sensing: A Synthetic Methods Approach for Selective Molecular Imaging and Beyond. Angewandte Chemie International Edition 2020, 59 (33), 13734-13762.

60. Pezacki, A. T.; Matier, C. D.; Gu, X.; Kummelstedt, E.; Bond, S. E.; Torrente, L.; Jordan-Sciutto, K. L.; DeNicola, G. M.; Su, T. A.; Brady, D. C.; Chang, C. J., Oxidation state-specific fluorescent copper sensors reveal oncogene-driven redox changes that regulate labile copper(II) pools. Proceedings of the National Academy of Sciences 2022, 119 (43), e2202736119.

61. Wang, D.; Wu, H.; Wang, C.; Gu, L.; Chen, H.; Jana, D.; Feng, L.; Liu, J.; Wang, X.; Xu, P.; Guo, Z.; Chen, Q.; Zhao, Y., Self-Assembled Single-Site Nanozyme for Tumor-Specific Amplified Cascade Enzymatic Therapy. Angewandte Chemie International Edition 2021, 60 (6), 3001-3007.

62. Liu, Y.; Zhen, W.; Jin, L.; Zhang, S.; Sun, G.; Zhang, T.; Xu, X.; Song, S.; Wang, Y.; Liu, J.; Zhang, H., All-in-One Theranostic Nanoagent with Enhanced Reactive Oxygen Species Generation and Modulating Tumor Microenvironment Ability for Effective Tumor Eradication. ACS Nano 2018, 12 (5), 4886-4893.

63. Shi, L.; Newcomer, E.; Son, M.; Pothanamkandathil, V.; Gorski, C. A.; Galal, A.; Logan, B. E., Metal-Ion Depletion Impacts the Stability and Performance of Battery Electrode Deionization over Multiple Cycles. Environmental Science & Technology 2021, 55 (8), 5412-5421.

64. Xing, Z.; Ju, Z.; Yang, J.; Xu, H.; Qian, Y., One-step solid state reaction to selectively fabricate cubic and tetragonal $CuFe_2O_4$ anode material for high power lithium ion batteries. Electrochimica Acta 2013, 102, 51-57.

65. Wessells, C. D.; Huggins, R. A.; Cui, Y., Copper hexacyanoferrate battery electrodes with long cycle life and high power. Nature Communications 2011, 2 (1), 550.

66. Bonet-Aleta, J.; Hueso, J. L.; Sanchez-Uriel, L.; Encinas-Gimenez, M.; Irusta, S.; Martin-Duque, P.; Martinez, G.; Santamaria, J., Synergistic assembly of gold and copper-iron oxide nanocatalysts to promote the simultaneous depletion of glucose and glutathione. Materials Today Chemistry 2023, 29, 101404.

67. Boström, H. L. B.; Collings, I. E.; Daisenberger, D.; Ridley, C. J.; Funnell, N. P.; Cairns, A. B., Probing the Influence of Defects, Hydration, and Composition on Prussian Blue Analogues with Pressure. Journal of the American Chemical Society 2021, 143 (9), 3544-3554.

68. Matsuda, T.; Kim, J.; Moritomo, Y., Control of the alkali cation alignment in Prussian blue framework. Dalton Transactions 2012, 41 (25), 7620-7623.

69. Wang, X.; Wang, W.-X., Cell-Type-Dependent Dissolution of CuO Nanoparticles and Efflux of Cu Ions following Cellular Internalization. Environmental Science & Technology 2022, 56 (17), 12404-12415.

70. Gratton, S. E. A.; Ropp, P. A.; Pohlhaus, P. D.; Luft, J. C.; Madden, V. J.; Napier, M. E.; DeSimone, J. M., The effect of particle design on cellular internalization pathways. Proceedings of the National Academy of Sciences 2008, 105 (33), 11613-11618.

71. Espirito Santo, C.; Lam, E. W.; Elowsky, C. G.; Quaranta, D.; Domaille, D. W.; Chang, C. J.; Grass, G., Bacterial killing by dry metallic copper surfaces. Appl Environ Microbiol 2011, 77 (3), 794-802.

72. Quaranta, D.; Krans, T.; Espirito Santo, C.; Elowsky, C. G.; Domaille, D. W.; Chang, C. J.; Grass, G., Mechanisms of contact-mediated killing of yeast cells on dry metallic copper surfaces. Appl Environ Microbiol 2011, 77 (2), 416-26.

73. Grimm, J. B.; Muthusamy, A. K.; Liang, Y.; Brown, T. A.; Lemon, W. C.; Patel, R.; Lu, R.; Macklin, J. J.; Keller, P. J.; Ji, N.; Lavis, L. D., A general method to fine-tune fluorophores for live-cell and in vivo imaging. Nature Methods 2017, 14 (10), 987-994.

74. Chen, L.; Min, J.; Wang, F., Copper homeostasis and cuproptosis in health and disease. Signal Transduction and Targeted Therapy 2022, 7 (1), 378.

75. Ohgami, R. S.; Campagna, D. R.; McDonald, A.; Fleming, M. D., The Steap proteins are metalloreductases. Blood 2006, 108 (4), 1388-94.

76. Wang, Z.; Li, N.; Zhao, J.; White, J. C.; Qu, P.; Xing, B., CuO Nanoparticle Interaction with Human Epithelial Cells: Cellular Uptake, Location, Export, and Genotoxicity. Chemical Research in Toxicology 2012, 25 (7), 1512-1521.

77. Rennick, J. J.; Johnston, A. P. R.; Parton, R. G., Key principles and methods for studying the endocytosis of biological and nanoparticle therapeutics. Nature Nanotechnology 2021, 16 (3), 266-276.

78. Taki, M.; Iyoshi, S.; Ojida, A.; Hamachi, I.; Yamamoto, Y., Development of highly sensitive fluorescent probes for detection of intracellular copper(I) in living systems. J Am Chem Soc 2010, 132 (17), 5938-9.

79. Gao, L.; Zhuang, J.; Nie, L.; Zhang, J.; Zhang, Y.; Gu, N.; Wang, T.; Feng, J.; Yang, D.; Perrett, S.; Yan, X., Intrinsic peroxidase-like activity of ferromagnetic nanoparticles. Nature Nanotechnology 2007, 2 (9), 577-583.

80. Chen, J.; Wang, Q.; Huang, L.; Zhang, H.; Rong, K.; Zhang, H.; Dong, S., Prussian blue with intrinsic heme-like structure as peroxidase mimic. Nano Research 2018, 11 (9), 4905-4913.

81. Fu, J.; Shao, Y.; Wang, L.; Zhu, Y., Lysosome-controlled efficient ROS overproduction against cancer cells with a high pH-responsive catalytic nanosystem. Nanoscale 2015, 7 (16), 7275-7283.

82. Walsh, M. J.; Ahner, B. A., Determination of stability constants of Cu(I), Cd(II) & Zn(II) complexes with thiols using fluorescent probes. Journal of inorganic biochemistry 2013, 128, 112-23.

83. Drew, R.; Miners, J. O., The effects of buthionine sulphoximine (BSO) on glutathione depletion and xenobiotic biotransformation. Biochemical pharmacology 1984, 33 (19), 2989-94.

84. Morgan, M. T.; Nguyen, L. A. H.; Hancock, H. L.; Fahrni, C. J., Glutathione limits aquacopper(I) to sub-femtomolar concentrations through cooperative assembly of a tetranuclear cluster. The Journal of biological chemistry 2017, 292 (52), 21558-21567.

85. Hatori, Y.; Clasen, S.; Hasan, N. M.; Barry, A. N.; Lutsenko, S., Functional partnership of the copper export machinery and glutathione balance in human cells. The Journal of biological chemistry 2012, 287 (32), 26678-87.

86. Singh, A.; Venkannagari, S.; Oh, K. H.; Zhang, Y. Q.; Rohde, J. M.; Liu, L.; Nimmagadda, S.; Sudini, K.; Brimacombe, K. R.; Gajghate, S.; Ma, J.; Wang, A.; Xu, X.; Shahane, S. A.; Xia, M.; Woo, J.; Mensah, G. A.; Wang, Z.; Ferrer, M.; Gabrielson, E.; Li, Z.; Rastinejad, F.; Shen, M.; Boxer, M. B.; Biswal, S., Small Molecule Inhibitor of NRF2 Selectively Intervenes Therapeutic Resistance in KEAP1-Deficient NSCLC Tumors. ACS chemical biology 2016, 11 (11), 3214-3225.

87. Davies, T. G.; Wixted, W. E.; Coyle, J. E.; Griffiths-Jones, C.; Hearn, K.; McMenamin, R.; Norton, D.; Rich, S. J.; Richardson, C.; Saxty, G.; Willems, H. M. G.; Woolford, A. J. A.; Cottom, J. E.; Kou, J.-P.; Yonchuk, J. G.; Feldser, H. G.; Sanchez, Y.; Foley, J. P.; Bolognese, B. J.; Logan, G.; Podolin, P. L.; Yan, H.; Callahan, J. F.; Heightman, T. D.; Kerns, J. K., Monoacidic Inhibitors of the Kelch-like ECH-Associated Protein 1: Nuclear Factor Erythroid 2-Related Factor 2 (KEAP1:NRF2) Protein–Protein Interaction with High Cell Potency Identified by Fragment-Based Discovery. Journal of Medicinal Chemistry 2016, 59 (8), 3991-4006.

88. MacLeod, A. K.; McMahon, M.; Plummer, S. M.; Higgins, L. G.; Penning, T. M.; Igarashi, K.; Hayes, J. D., Characterization of the cancer chemopreventive NRF2-dependent gene battery in human keratinocytes: demonstration that the KEAP1–NRF2 pathway, and not the BACH1–NRF2 pathway, controls cytoprotection against electrophiles as well as redox-cycling compounds. Carcinogenesis 2009, 30 (9), 1571-1580.

89. Cvetko, F.; Caldwell, S. T.; Higgins, M.; Suzuki, T.; Yamamoto, M.; Prag, H. A.; Hartley, R. C.; Dinkova-Kostova, A. T.; Murphy, M. P., Nrf2 is activated by disruption of mitochondrial thiol homeostasis but not by enhanced mitochondrial superoxide production. Journal of Biological Chemistry 2021, 296.

90. Harvey, C. J.; Thimmulappa, R. K.; Singh, A.; Blake, D. J.; Ling, G.; Wakabayashi, N.; Fujii, J.; Myers, A.; Biswal, S., Nrf2-regulated glutathione recycling independent of biosynthesis is critical for cell survival during oxidative stress. Free radical biology & medicine 2009, 46 (4), 443-53.

91. Itoh, K.; Wakabayashi, N.; Katoh, Y.; Ishii, T.; Igarashi, K.; Engel, J. D.; Yamamoto, M., Keap1 represses nuclear activation of antioxidant responsive elements by Nrf2 through binding to the amino-terminal Neh2 domain. Genes & development 1999, 13 (1), 76-86.

92. Banci, L.; Bertini, I.; Ciofi-Baffoni, S.; Kozyreva, T.; Zovo, K.; Palumaa, P., Affinity gradients drive copper to cellular destinations. Nature 2010, 465 (7298), 645-648.

93. Polishchuk, Elena V.; Concilli, M.; Iacobacci, S.; Chesi, G.; Pastore, N.; Piccolo, P.; Paladino, S.; Baldantoni, D.; van Ijzendoorn, Sven C. D.; Chan, J.; Chang, Christopher J.; Amoresano, A.; Pane, F.; Pucci, P.; Tarallo, A.; Parenti, G.; Brunetti-Pierri, N.; Settembre, C.; Ballabio, A.; Polishchuk, Roman S., Wilson Disease Protein ATP7B Utilizes Lysosomal Exocytosis to Maintain Copper Homeostasis. Developmental Cell 2014, 29 (6), 686-700.

94. Cater, M. A.; La Fontaine, S.; Shield, K.; Deal, Y.; Mercer, J. F. B., ATP7B Mediates Vesicular Sequestration of Copper: Insight Into Biliary Copper Excretion. Gastroenterology 2006, 130 (2), 493-506.

95. Lim, C. M.; Cater, M. A.; Mercer, J. F. B.; La Fontaine, S., Copper-dependent interaction of glutaredoxin with the N termini of the copper-ATPases (ATP7A and ATP7B) defective in Menkes and Wilson diseases. Biochemical and Biophysical Research Communications 2006, 348 (2), 428-436.

96. Kuo, Y. M.; Zhou, B.; Cosco, D.; Gitschier, J., The copper transporter CTR1 provides an essential function in mammalian embryonic development. Proceedings of the National Academy of Sciences of the United States of America 2001, 98 (12), 6836-41.

97. Das, A.; Ash, D.; Fouda, A. Y.; Sudhahar, V.; Kim, Y.-M.; Hou, Y.; Hudson, F. Z.; Stansfield, B. K.; Caldwell, R. B.; McMenamin, M.; Littlejohn, R.; Su, H.; Regan, M. R.; Merrill, B. J.; Poole, L. B.; Kaplan, J. H.; Fukai, T.; Ushio-Fukai, M., Cysteine oxidation of copper transporter CTR1 drives VEGFR2 signalling and angiogenesis. Nature Cell Biology 2022, 24 (1), 35-50.

98. Lugano, R.; Ramachandran, M.; Dimberg, A., Tumor angiogenesis: causes, consequences, challenges and opportunities. Cellular and Molecular Life Sciences 2020, 77 (9), 1745-1770.

Supplementary information – Chapter 5

Adapted from:

An Activity-Based Sensing Approach to Monitor Nanomaterial-Promoted Changes in Labile Metal Pools in Living Systems

Javier Bonet-Aleta[1,2,3,4], Aidan T. Pezacki[5], Miku Oi[5], Jose L. Hueso[1,2,3,4], Jesus Santamaria[1,2,3,4], Christopher J. Chang[5,6,7,8*]*

[1] Instituto de Nanociencia y Materiales de Aragon (INMA) CSIC-Universidad de Zaragoza, Campus Rio Ebro, Edificio I+D, C/ Poeta Mariano Esquillor, s/n, 50018, Zaragoza, Spain

[2] Networking Res. Center in Biomaterials, Bioengineering and Nanomedicine (CIBER-BBN), Instituto de Salud Carlos III, 28029 Madrid, Spain

[3] Department of Chemical and Environmental Engineering, University of Zaragoza, Campus Rio Ebro, C/María de Luna, 3, 50018 Zaragoza, Spain

[4] Instituto de Investigación Sanitaria (IIS) de Aragón, Avenida San Juan Bosco, 13, 50009 Zaragoza, Spain

[5] Department of Chemistry, University of California, Berkeley, CA, 94720, United States

[6] Department of Molecular and Cell Biology, University of California, Berkeley, CA, 94720, United States

[7] Helen Wills Neuroscience Institute, University of California, Berkeley, CA, 94720, United States

[8] Chemical Sciences Division, Lawrence Berkeley National Laboratory, Berkeley, CA, 94720, United States

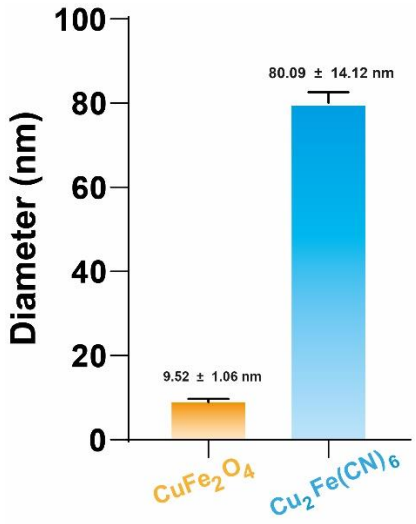

Figure S1. *Analysis of particle size of $CuFe_2O_4$ and $Cu_2Fe(CN)_6$ nanoparticles (n = 30) measured using Image J software. Error bars denote S.E.M (n = 30).*

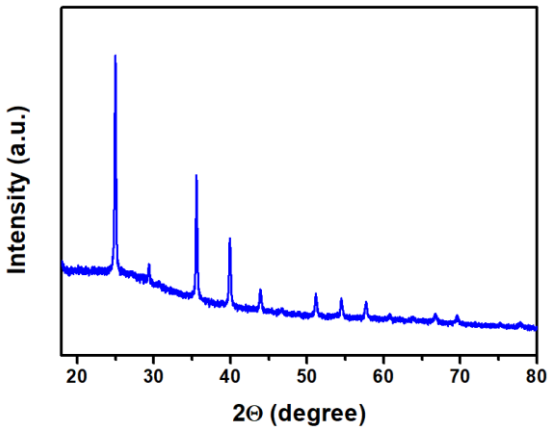

Figure S2. *XRD pattern of $Cu_2Fe(CN)_6$ nanoparticles.*

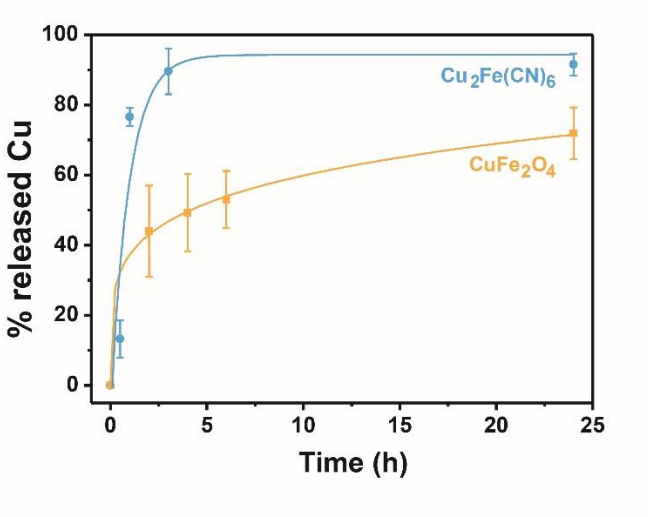

Figure S3. *Evolution of released Cu from different Cu-containing nanoparticles after exposure to 5 mM GSH solution (pH = 7.4, buffered with HCO_3^-/CO_2, T = 37ºC) analyzed by MP-AES (n = 3). $Cu_2Fe(CN)_6$ were more susceptible to release copper in the presence of the abundant cytosolic molecule GSH. Results from $CuFe_2O_4$ were obtained from our previous work[1] and shown together with $Cu_2Fe(CN)_6$ for a better comparison. Error bars denote S.D. (n =3).*

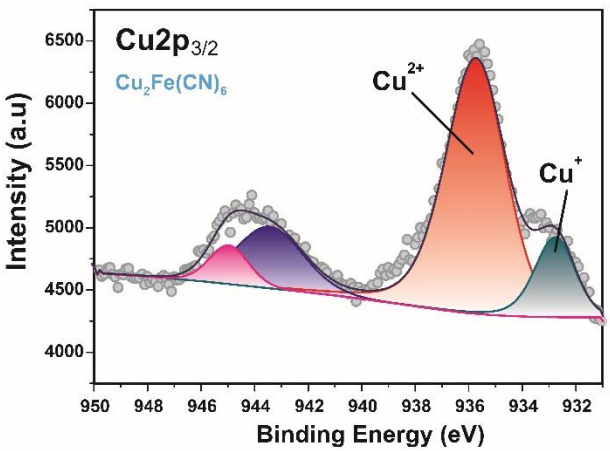

Figure S4. *X-ray photoemission spectra of $Cu2p_{3/2}$ region. The peak centered at 935.5 eV demonstrates the dominant presence of copper (II) within the $Cu_2Fe(CN)_6$ nanostructure.*

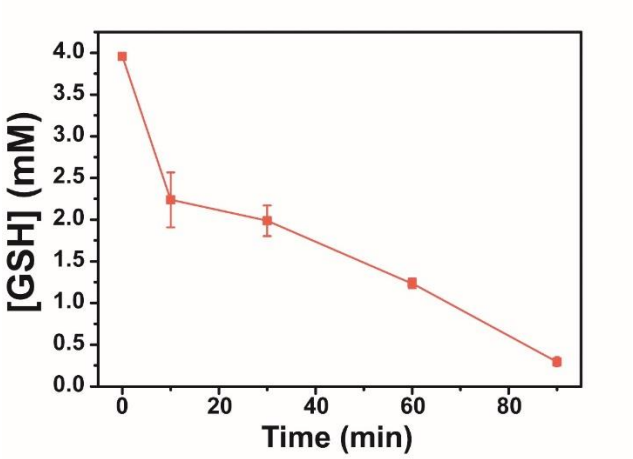

Figure S5. *Evolution of GSH concentrations in a solution containing $Cu_2Fe(CN)_6$ nanoparticles. Reaction conditions: $[GSH]_0$ = 4 mM, [Cu] = 0.01 mg·mL^{-1}, Temperature = 37 ºC, pH = 7.4 (adjusted with PBS 1x buffer). Error bars denote S.D. (n =3).*

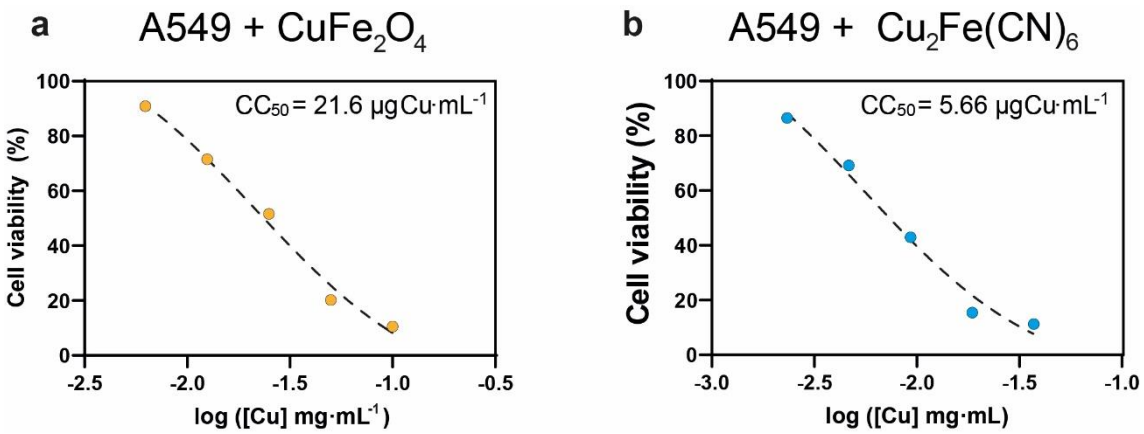

Figure S6. *Cytotoxicity of (a) $CuFe_2O_4$ and (b) $Cu_2Fe(CN)_6$ nanoparticles in A549 cells after 24 hours of incubation. Error bars denote S.E.M (n = 3).*

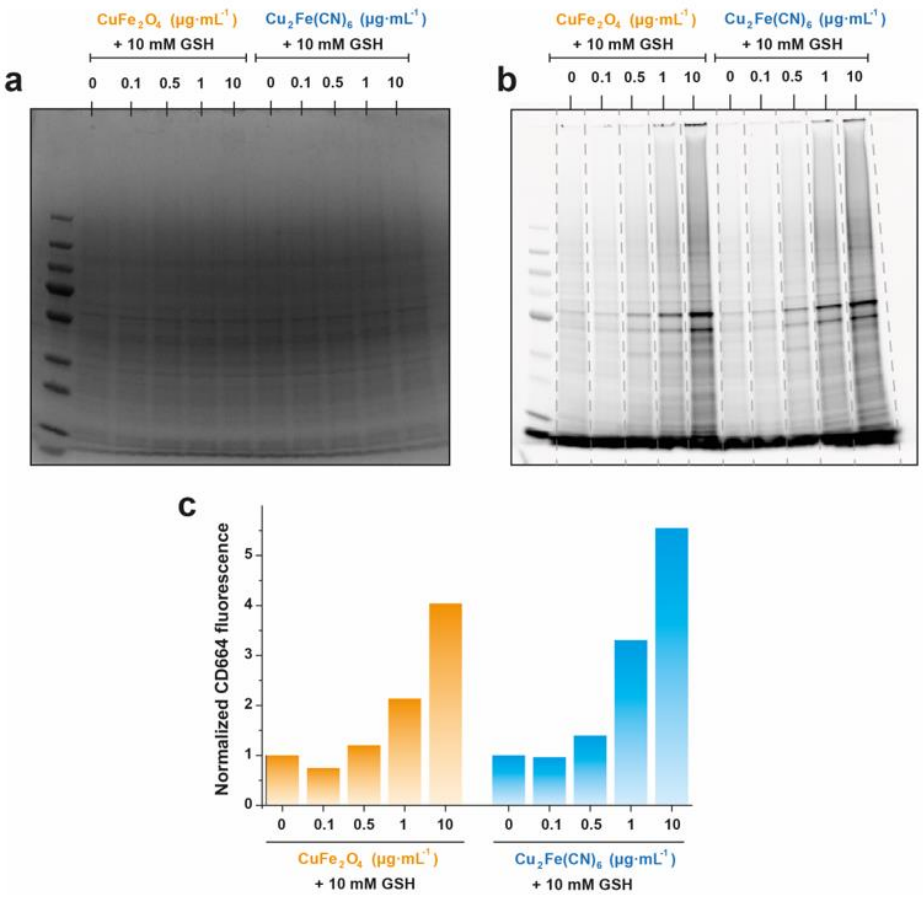

Figure S7. *(a) Coomassie staining (b) In-gel fluorescence and (c) fluorescence quantification of* ***CD664*** *incubated with a mixture of leached $CuFe_2O_4$ or $Cu_2Fe(CN)_6$ nanoparticles and A549 cell lysates.* ***CD664*** *fluorescence increases in a dose-dependent manner in response to the leached copper. 50 μg·mL^{-1} copper-containing nanoparticles were mixed with 10 mM GSH at in PBS (pH = 7.4 titrated with 1.0 M NaOH) for 24 h at 37 °C to ensure majority of the copper was released. Then, various concentrations of leached nanoparticles were added to A549 cell lysate and incubated for 5 minutes. Finally, 10 μM of* ***CD664*** *probe was added and incubated for 1 h at room temperature. In-gel fluorescence for sodium dodecyl-sulfate-poyacrylamide gel electrophoresis was performed and imaged using ChemiDoc™. Signal intensity was analyzed using Image Lab software and normalized to vehicle control (i.e. no addition of copper-based nanoparticle).*

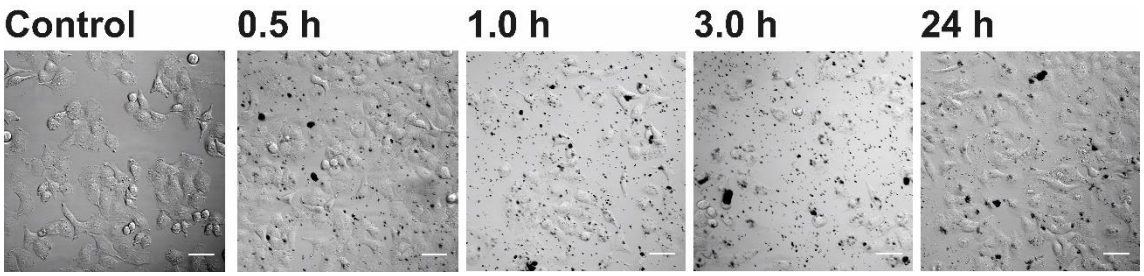

Figure S8. *Brightfield images of A549 cells treated with $CuFe_2O_4$ nanoparticles ([Cu] = 6.25 µg·mL^{-1}) at different incubation times for imaging with* ***CD664****. Scale bar = 50 µm.*

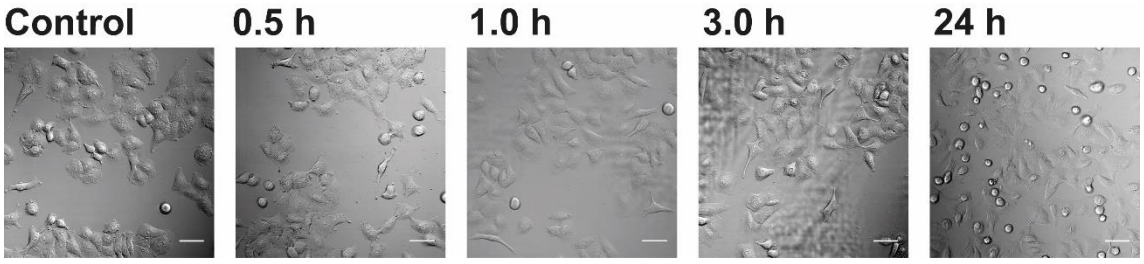

Figure S9. *Brightfield images of A549 cells treated with $Cu_2Fe(CN)_6$ nanoparticles ([Cu] = 3.12 µg·mL^{-1}) at different incubation times for imaging with* ***CD664****. Scale bar = 50 µm.*

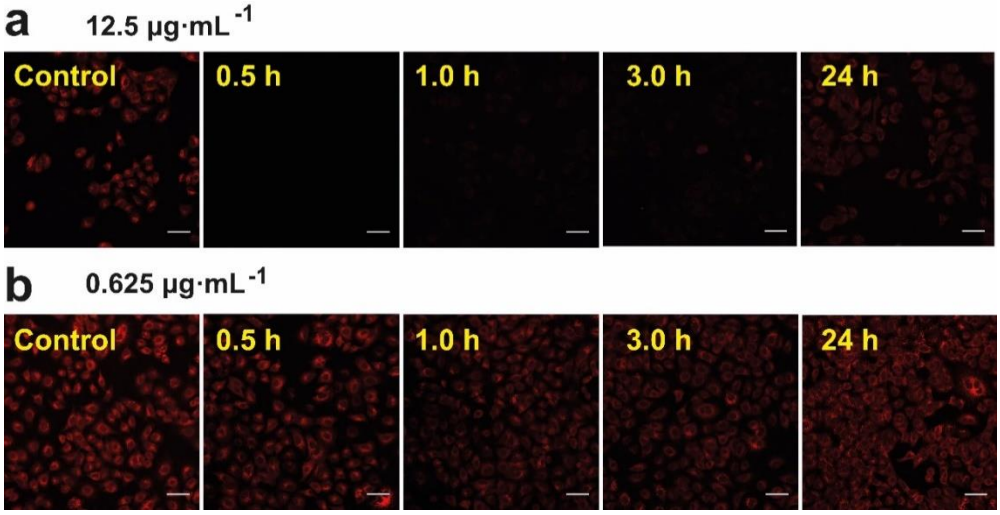

Figure S10. *Representative confocal microscopy images of A549 cells treated with varying concentrations of nanoparticles. A549 cells were incubated at different times with $CuFe_2O_4$ at (a) 12.5 µg·mL^{-1} and (b) 0.625 µg·mL^{-1} followed by staining with 1 µM* ***CD664*** *for 15 min. Intensity in* ***CD664*** *signal inversely depends on the concentration of copper-containing nanoparticles added to the cell culture. Fluorescence intensity of* ***CD664*** *was determined from experiments with λ_{ex} = 633 nm. Scale bar = 50 µm.*

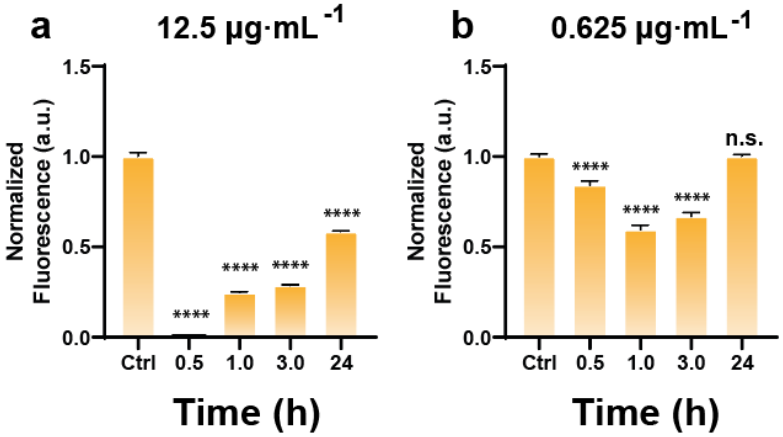

Figure S11. *Fluorescence quantification of* ***CD664*** *in A549 cells incubated with (a) 12.5 µg·mL^{-1} and (b) 0.625 µg·mL^{-1} of $CuFe_2O_4$ nanoparticles. The observed decrease in fluorescence signal is correlated to treatment with higher nanoparticle concentrations, suggesting a more intense regulation of labile copper pool by the cell. *P < 0.05, **P < 0.01, ***P < 0.001, and ****P < 0.0001; ns, not statistically significant. Error bars denote S.E.M (n = 8).*

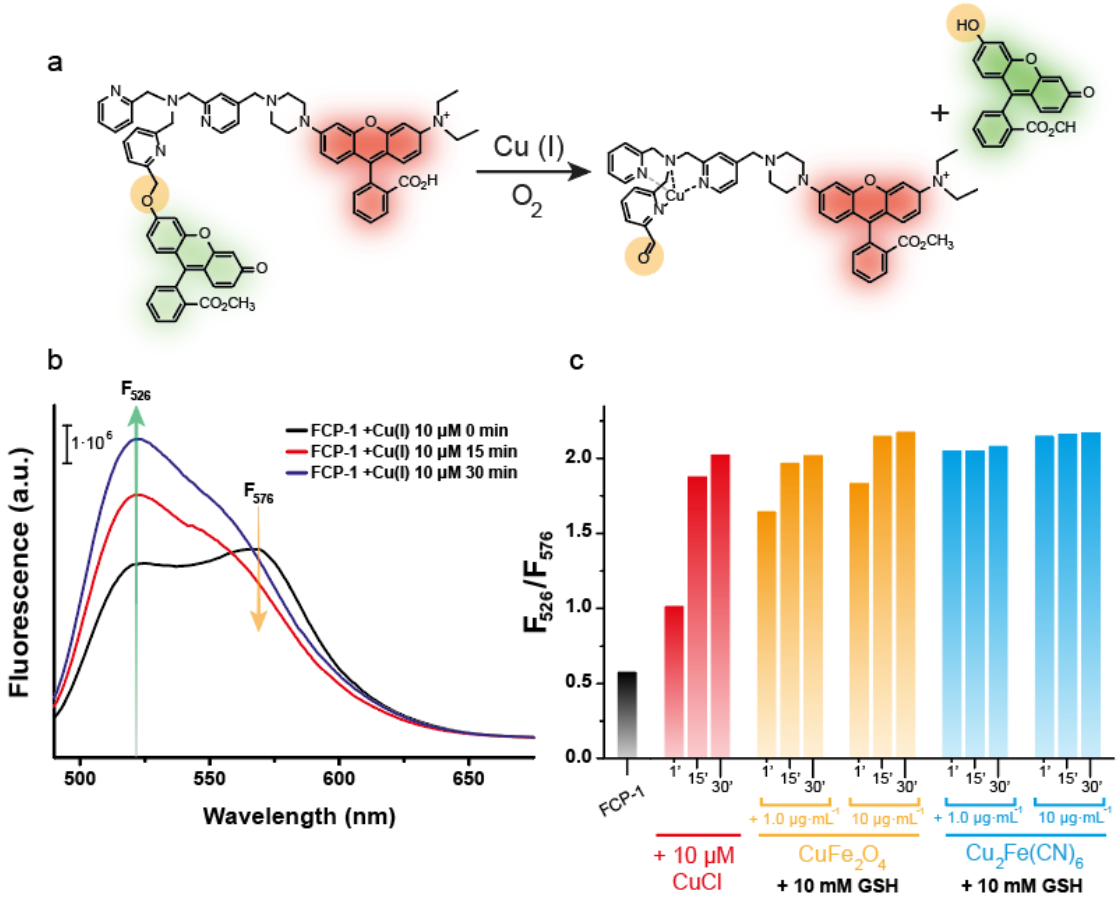

Figure S12. *Detection of labile Cu(I) release using the Cu(I)-selective activity-based probe* ***FCP-1****. (a) Mechanism of Cu(I) detection and quantification for* ***FCP-1****. (b) The oxidative Cu(I)/O_2 system can specifically break the highlighted C-O bond which is directly related to an increase in F_{526}/F_{576} ratio. (c) After addition of 5 µM of* ***FCP-1*** *to the supernatant containing released copper and GSH the increase of the $F_{526/576}$ ratio is readily observable, as a result of the leaching of Cu(I) species from nanoparticles.*

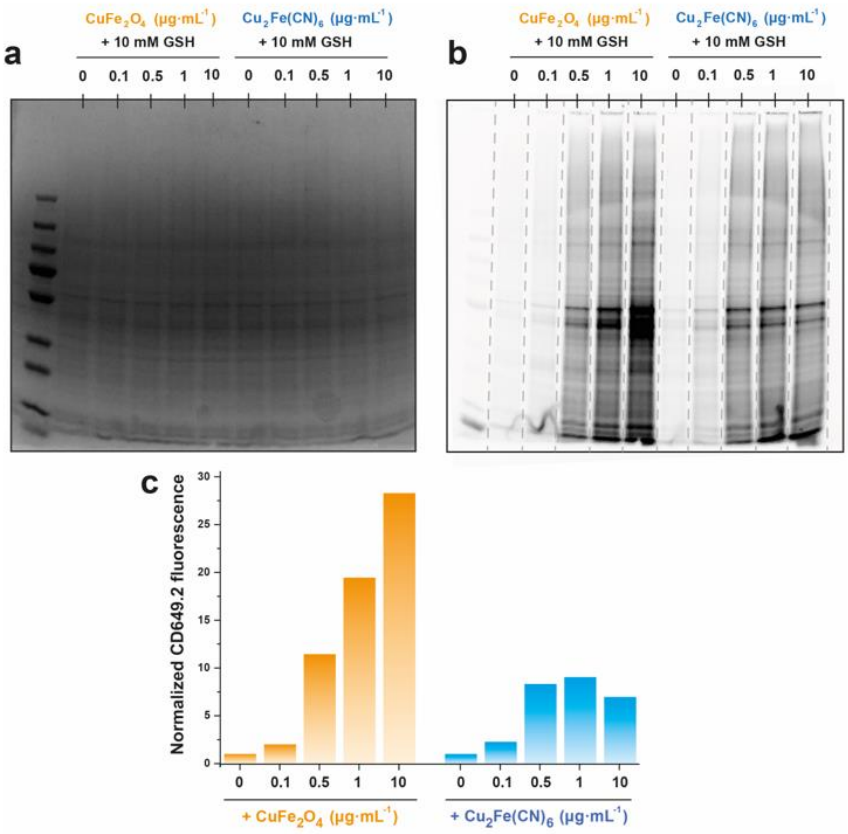

Figure S13. *(a) Coomassie staining, (b) In-gel fluorescence and (c) fluorescence quantification of* ***CD649.2*** *incubated with a mixture of leached $CuFe_2O_4$ or $Cu_2Fe(CN)_6$ nanoparticles and A549 cell lysates.* ***CD649.2*** *fluorescence increases in a dose-dependent manner in response to the leached copper. 50 μg·mL^{-1} copper-containing nanoparticles were mixed with 10 mM GSH in PBS (pH = 7.4 titrated with 1.0 M NaOH) for 24 h at 37 °C to ensure majority of the copper was released. Then, various concentrations of leached nanoparticles were added to A549 cell lysate and incubated for 5 minutes. Finally, 10 μM of* ***CD649.2*** *probe was added and incubated for 1 h at room temperature. In-gel fluorescence for sodium dodecyl-sulfate-poyacrylamide gel electrophoresis was performed and imaged using ChemiDoc™. Signal intensity was analyzed using Image Lab software and normalized to vehicle control (i.e. no addition of copper-based nanoparticle).*

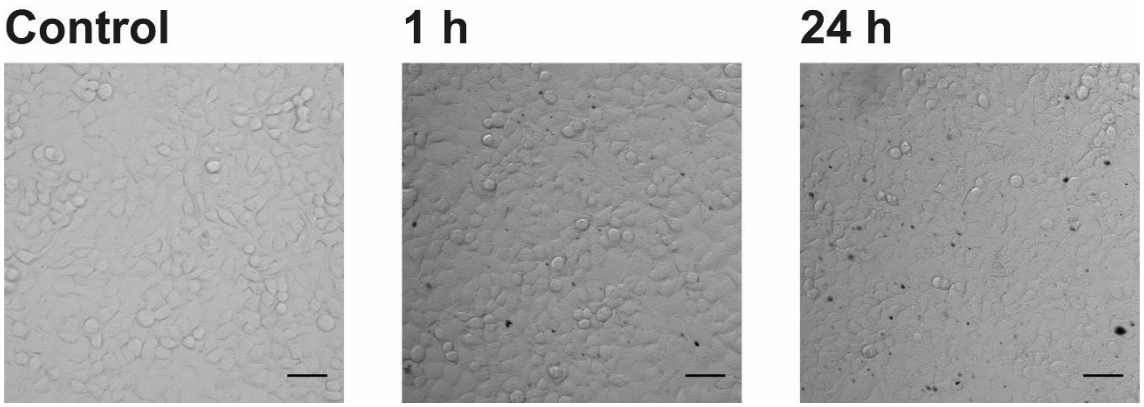

Figure S14. *Brightfield images of A549 cells treated with $CuFe_2O_4$ nanoparticles ([Cu] = 6.25 μg·mL^{-1}) at different incubation times for imaging with* ***CD649.2****. Scale bar = 50 μm.*

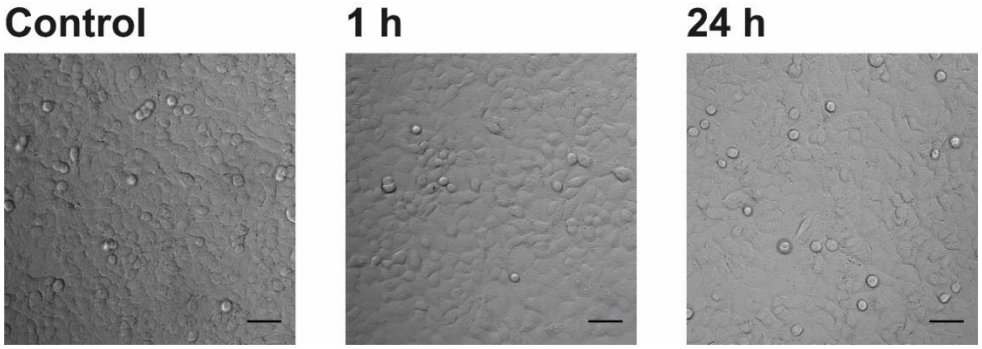

Figure S15. *Brightfield images of A549 cells treated with $CuFe_2O_4$ nanoparticles ([Cu] = 3.12 µg·mL^{-1}) at different incubation times for imaging with* ***CD649.2****. Scale bar = 50 µm*

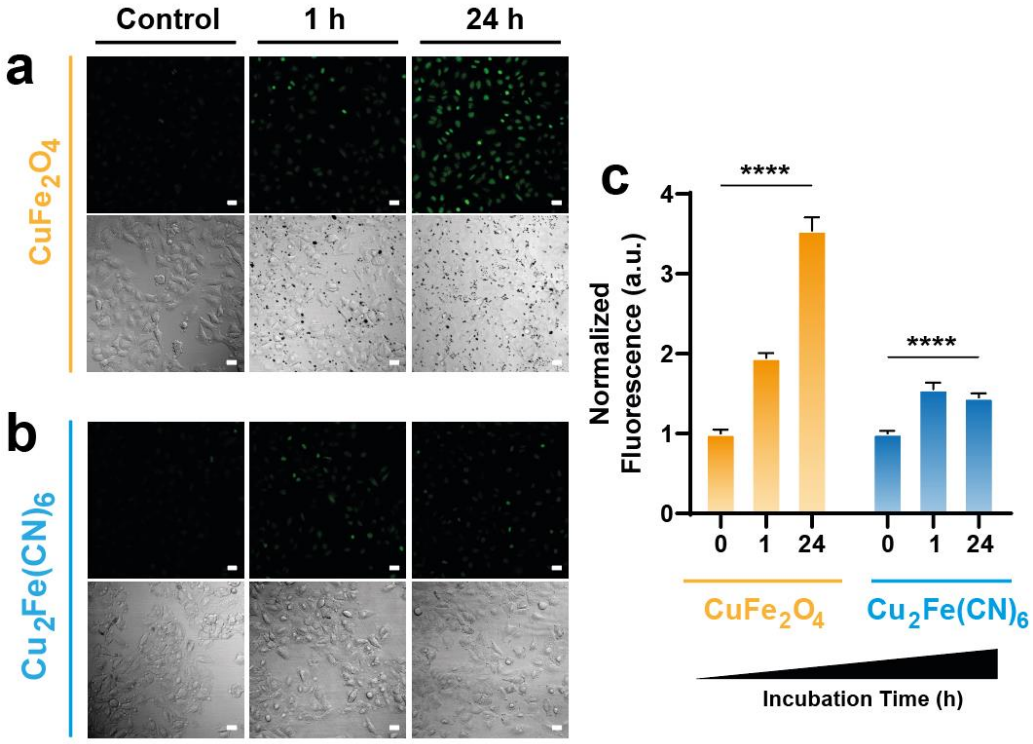

Figure S16. *Monitoring levels of reactive oxygen species (ROS) in A549 cells treated with (a) $CuFe_2O_4$ and $Cu_2Fe(CN)_6$ nanoparticles at different times. (c) Quantification of fluorescence signals shows a steep increase in ROS production for $CuFe_2O_4$ treatment while a more gradual rise was observed for $Cu_2Fe(CN)_6$ exposure. Fluorescence intensity of CellROX was determined from experiments with λ_{ex} = 485 nm. Scale bar = 50 µm. *P < 0.05, **P < 0.01, ***P < 0.001, and ****P < 0.0001; ns, not statistically significant. Error bars denote S.E.M (n = 8).*

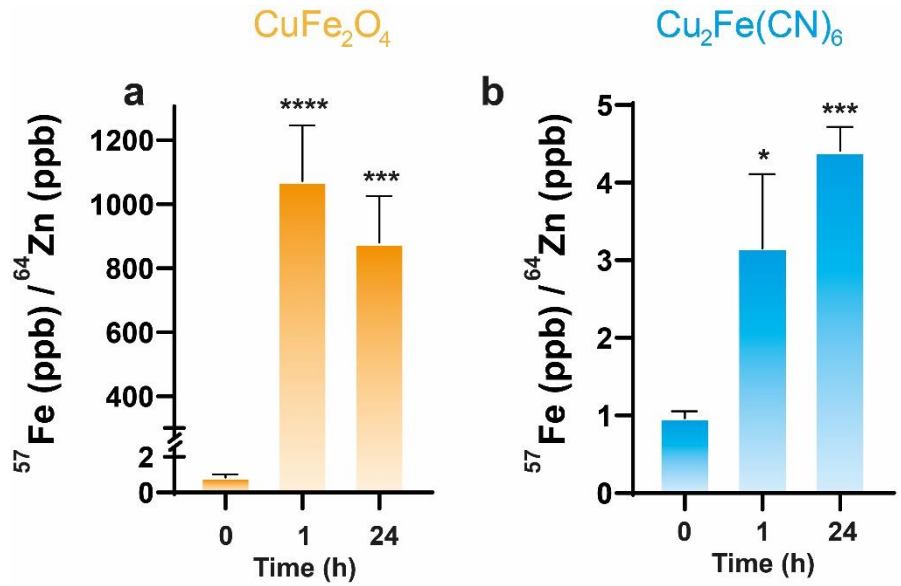

Figure S17. *ICP-MS analysis of A549 cells treated with (a) $CuFe_2O_4$ and (b) $Cu_2Fe(CN)_6$ nanoparticles for 1 h or 24 h reveals an increase in total iron levels upon nanoparticle treatment. Total cellular ^{57}Fe levels were normalized to total ^{64}Zn levels. Error bars denote S.E.M (n = 6). *P < 0.05, **P < 0.01, ***P < 0.001, and ****P < 0.0001; ns, not statistically significant.*

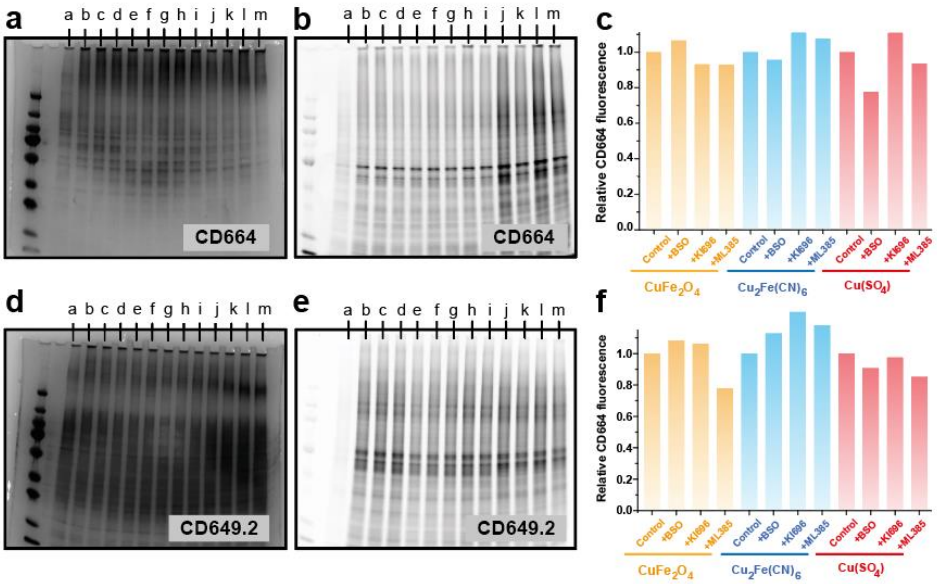

Figure S18. *(a) Silver staining, (b) In-gel fluorescence and (c) fluorescence quantification of* ***CD664*** *incubated with leached $CuFe_2O_4$ / $Cu_2Fe(CN)_6$ nanoparticles or $CuSO_4$ in the presence of 0.5 mM BSO, 1 μM KI696 or 10 μM ML-385 and A549 cell lysates. (d) Silver staining, (e) In-gel fluorescence and (f) fluorescence quantification of* ***CD649.2*** *incubated with leached $CuFe_2O_4$ / $Cu_2Fe(CN)_6$ nanoparticles or $CuSO_4$ in the presence of 0.5 mM BSO, 1 μM KI696 or 10 μM ML-385 and A549 cell lysates. 10 $\mu g \cdot mL^{-1}$ copper-containing nanoparticles were mixed with 10 mM GSH in PBS to ensure majority of the copper was released. (pH = 7.4 titrated with 1.0 M NaOH) and the corresponding drug (BSO, KI695 or ML-386) for 24 h at 37 °C. In-gel fluorescence for sodium dodecyl-sulfate-poyacrylamide gel electrophoresis was performed and imaged using ChemiDoc™. Signal intensity was analyzed using Image Lab software and normalized to nanoparticle control (i.e. no addition of drug). Experiment code: (a) Control, (b) 10 $\mu g \cdot mL^{-1}$ $CuFe_2O_4$ (c) 10 $\mu g \cdot mL^{-1}$ $CuFe_2O_4$ + 0.5 mM BSO, (d) 10 $\mu g \cdot mL^{-1}$ $CuFe_2O_4$ + 1 μM KI696, (e) 10 $\mu g \cdot mL^{-1}$ $CuFe_2O_4$ + 10 μM ML-385, (f) 10 $\mu g \cdot mL^{-1}$ $Cu_2Fe(CN)_6$ (g) 10 $\mu g \cdot mL^{-1}$ $Cu_2Fe(CN)_6$ + 0.5 mM BSO, (h) 10 $\mu g \cdot mL^{-1}$ $Cu_2Fe(CN)_6$ + 1 μM KI696, (i) 10 $\mu g \cdot mL^{-1}$ $Cu_2Fe(CN)_6$ + 10 μM ML-385, (j) 50 μM $CuSO_4$ (k) 50 μM $CuSO_4$ + 0.5 mM BSO, (l) 50 μM $CuSO_4$ + 1 μM KI696, (m) 50 μM $CuSO_4$ + 10 μM ML-385.*

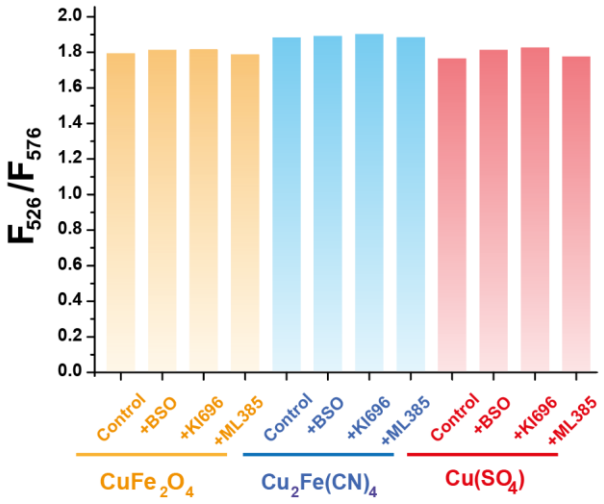

Figure S19. *Quantification of F_{526}/F_{576} fluorescence ratio of* ***FCP-1*** *in different solutions containing leached nanoparticles with 0.5 mM BSO, 1 μM KI696 or 10 μM ML-385. μg·mL^{-1} copper-containing nanoparticles (or 10 μM $CuSO_4$) were mixed with 10 mM GSH in PBS to ensure majority of the copper was released. (pH = 7.4 titrated with 1.0 M NaOH) and the corresponding drug (BSO, KI695 or ML-386) for 24 h at 37 °C.*

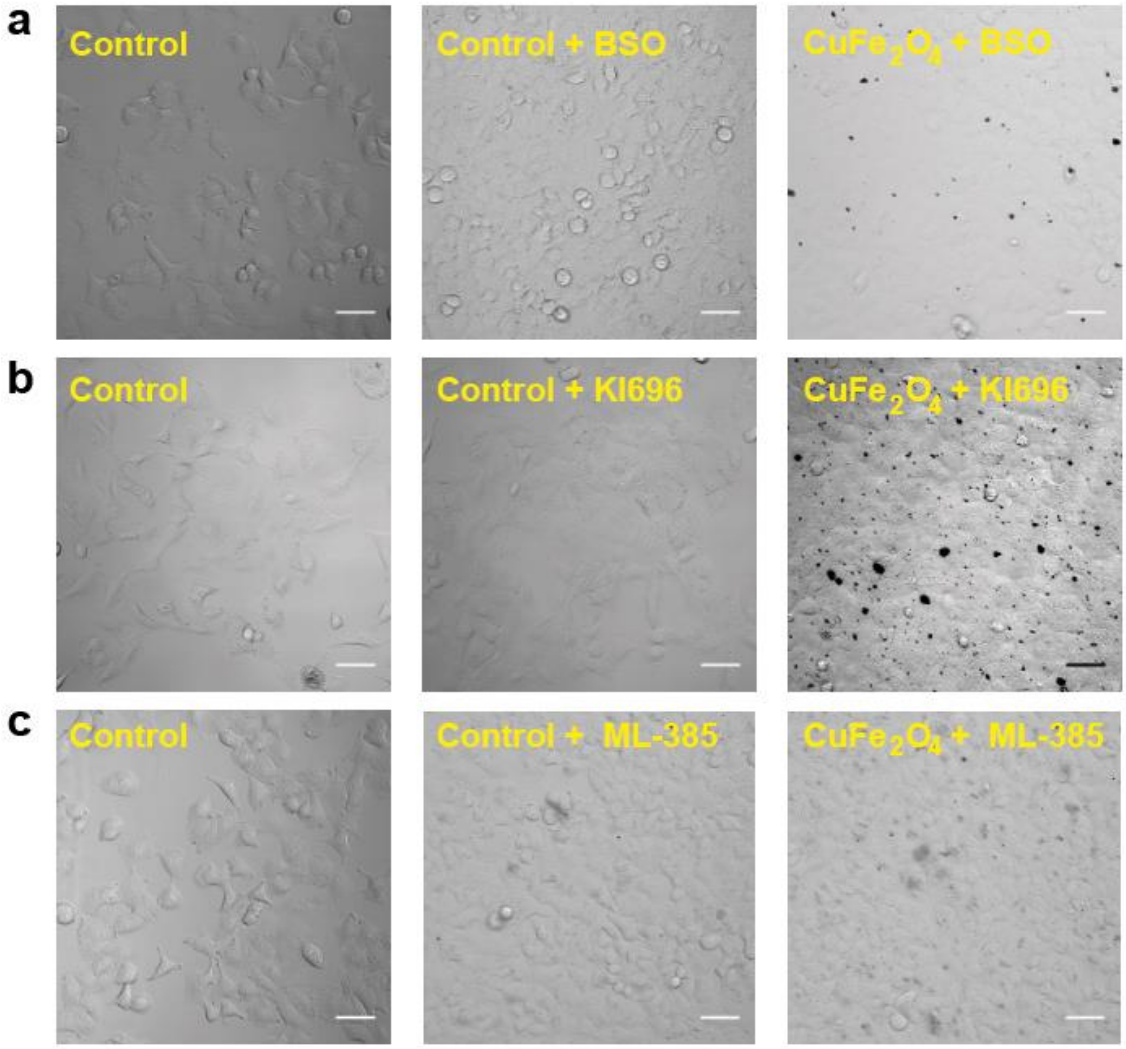

Figure S20. *Corresponding Brightfield images of A549 cells treated with $CuFe_2O_4$ nanoparticles and (a) 0.5 mM BSO, (b) 1 μM KI696 and (c) 10 μM of ML-385 for imaging with* ***CD664****. Black dots correspond to aggregated $CuFe_2O_4$ nanoparticles. Scale bar = 50 μm.*

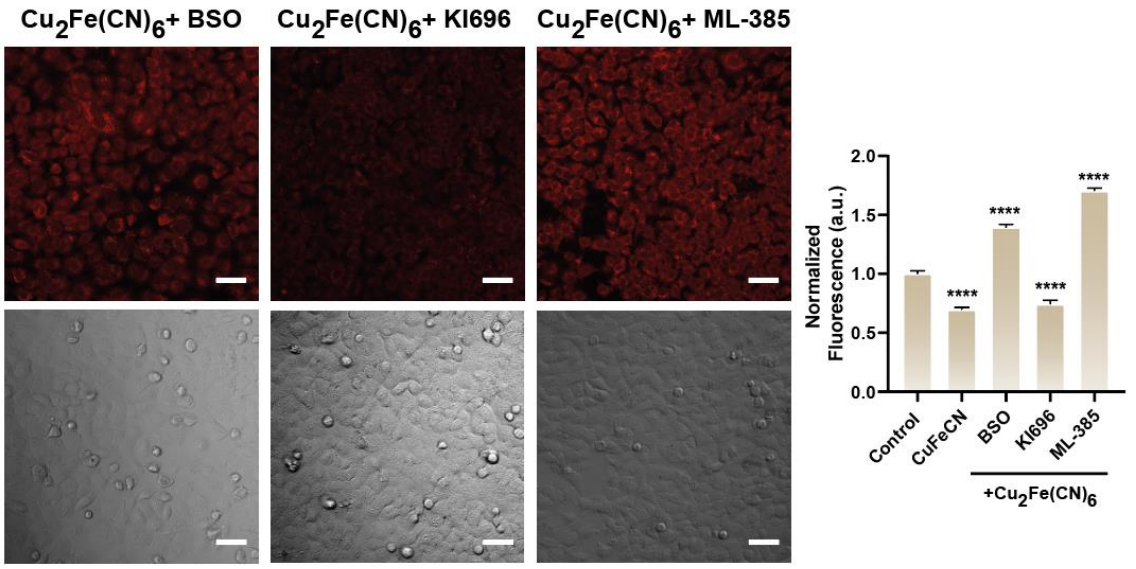

Figure S21. *Fluorescence and brightfield images of A549 cells incubated with $Cu_2Fe(CN)_6$ nanoparticles and BSO, KI696, and ML385 respectively. Fluorescence quantification reveals that the combination of nanoparticles with BSO or ML-385 affects copper homeostasis upon $Cu_2Fe(CN)_6$ treatment, while KI696 had no influence in comparison to $Cu_2Fe(CN)_6$ control. Fluorescence intensity of **CD664** was determined from experiments with λ_{ex} = 633 nm. Scale bar = 50 µm. *P < 0.05, **P < 0.01, ***P < 0.001, and ****P < 0.0001; ns, not statistically significant. Error bars denote S.E.M (n = 8).*

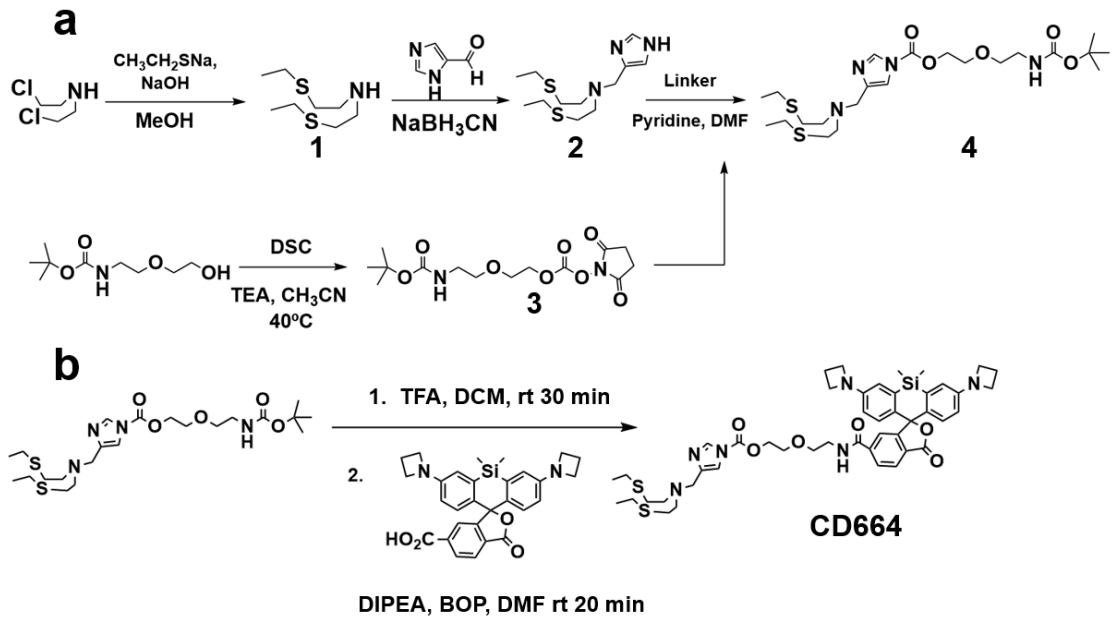

Figure S22. *Synthetic route to the activity-based sensing copper probe **CD664**.*

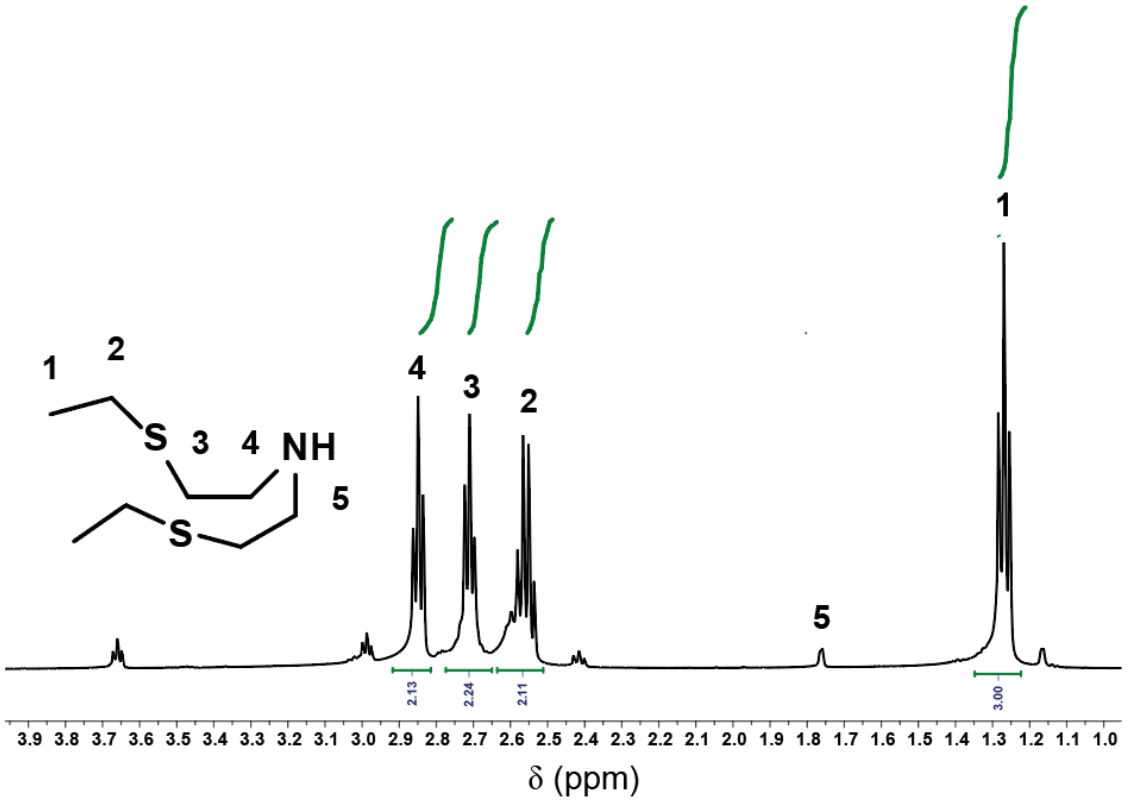

Figure S23. *^{1}H NMR spectrum of compound **1**.*

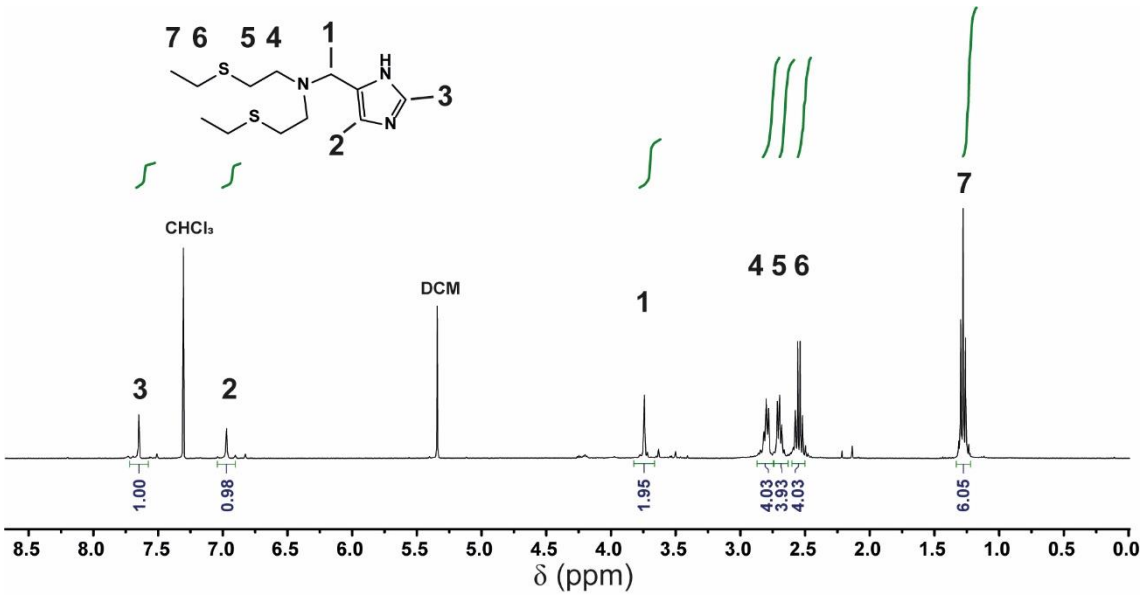

Figure S24. *^{1}H NMR spectrum of compound **2**.*

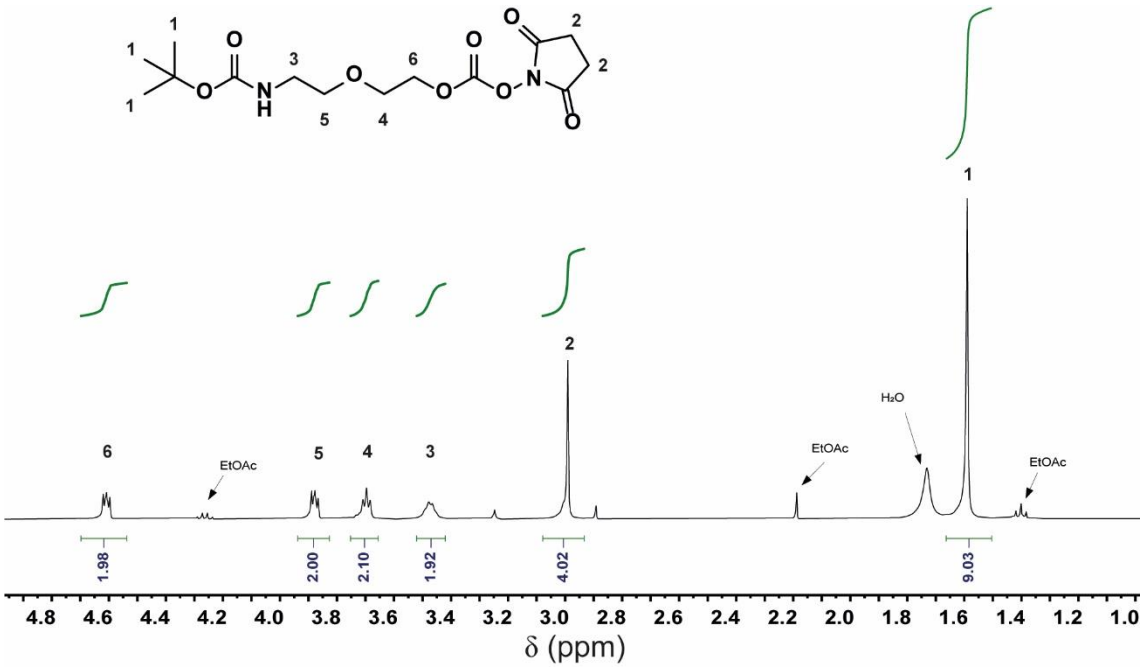

Figure S25. *[1]H NMR spectrum of compound **3**.*

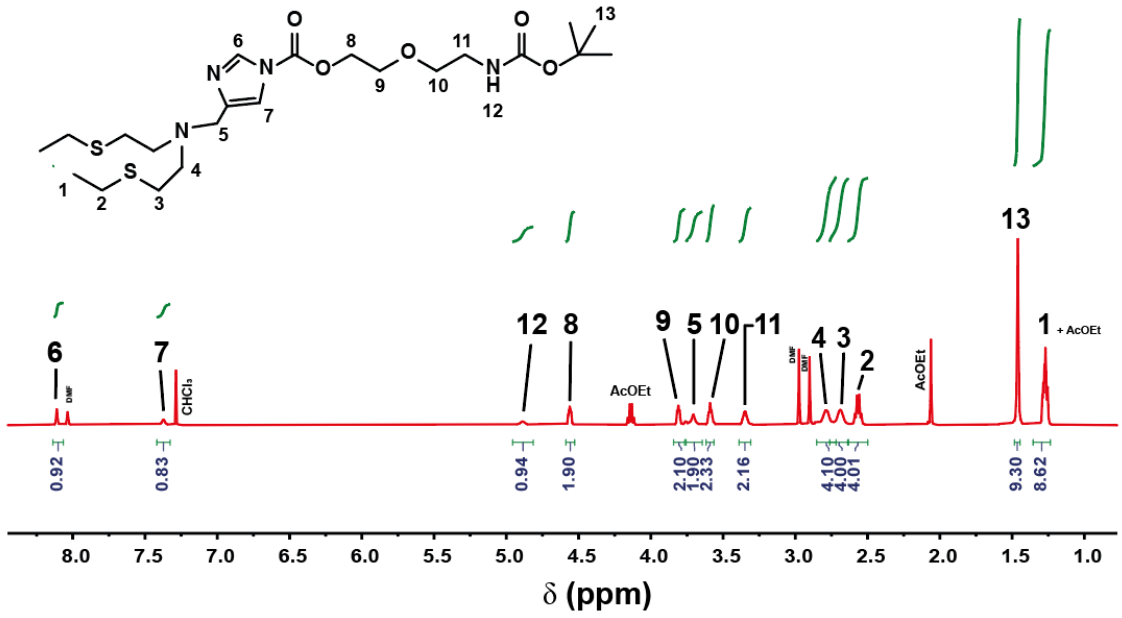

Figure S26. *[1]H-NMR spectrum of compound **4**.*

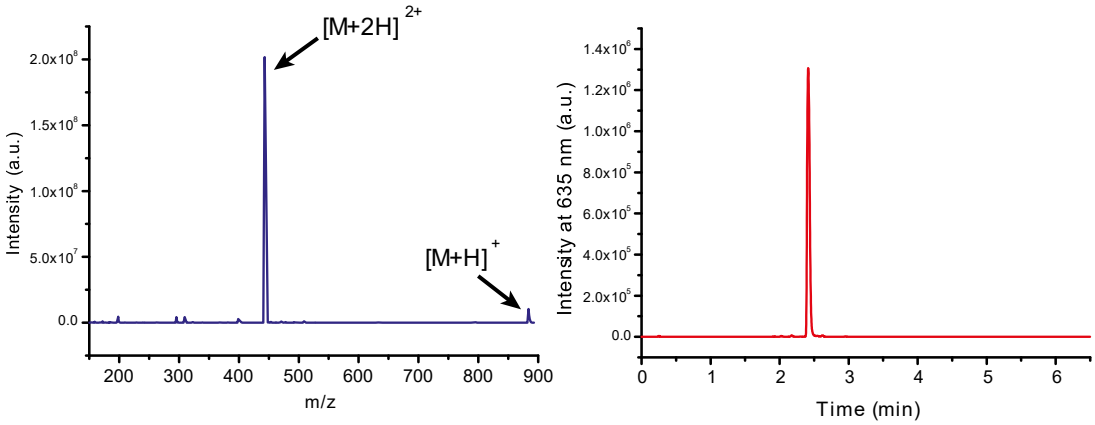

Figure S27. *MS spectrum (left) and HPLC-UV/vis absorbance trace at 635 nm (right) of* ***CD664****.*

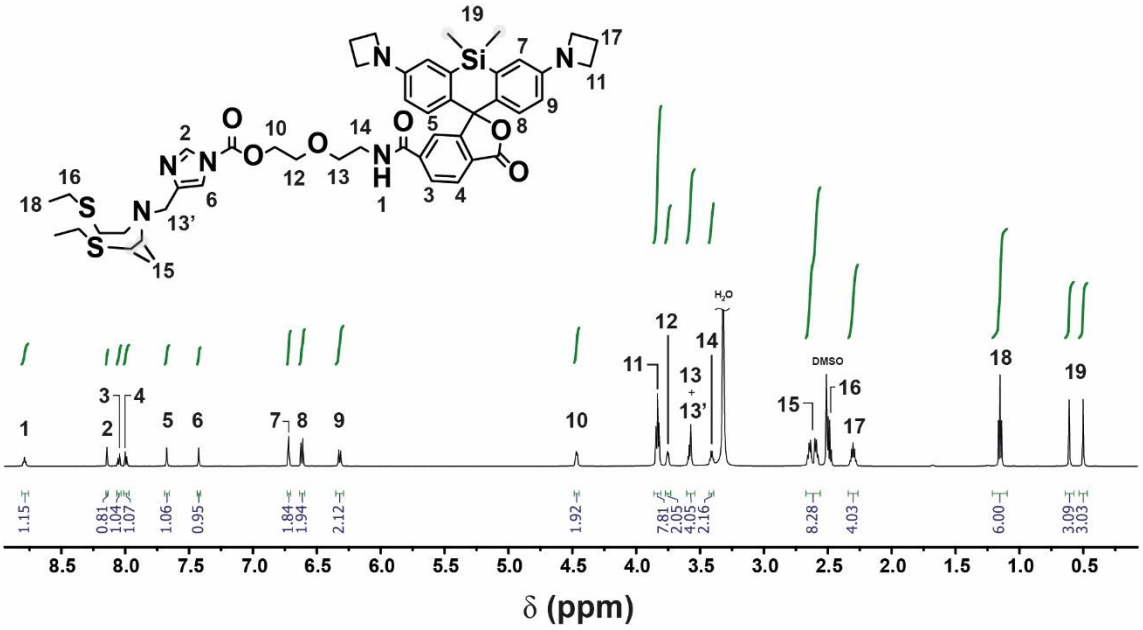

Figure S28. *[1]H-NMR spectrum of compound* ***CD664.***

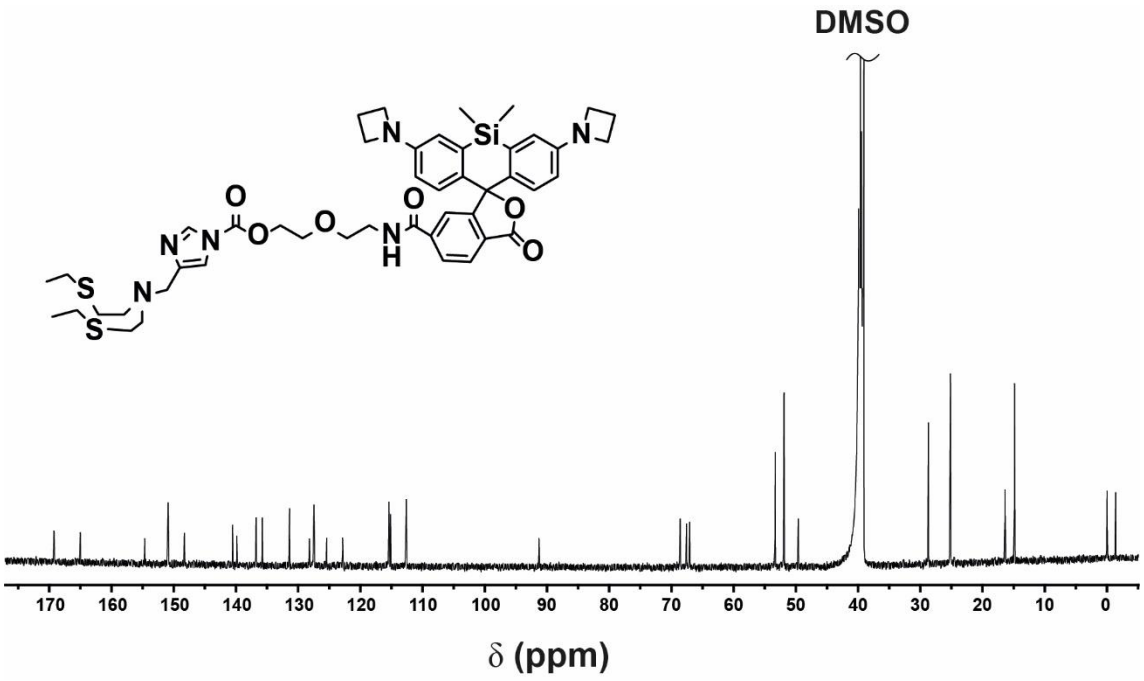

Figure S29. *^{13}C-NMR spectrum of compound **CD664**.*

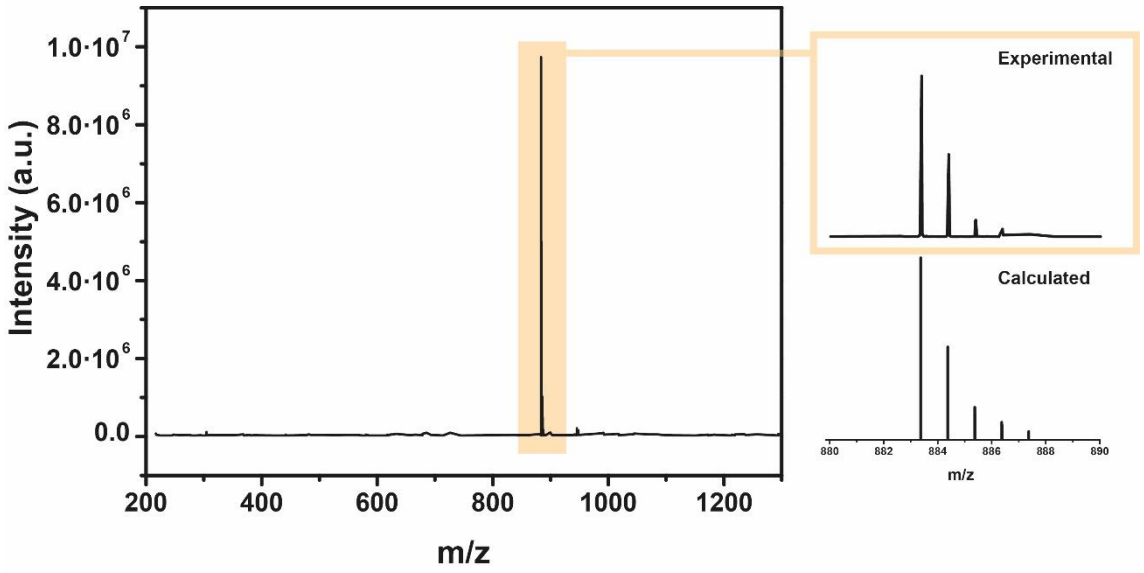

Figure S30. *HR-MS of **CD664**.*

References – Supplementary information Chapter 5

1. Bonet-Aleta, J.; Encinas-Gimenez, M.; Urriolabeitia, E.; Martin-Duque, P.; Hueso, J. L.; Santamaria, J., Unveiling the interplay between homogeneous and heterogeneous catalytic mechanisms in copper–iron nanoparticles working under chemically relevant tumour conditions. *Chemical Science* **2022,** *13* (28), 8307-8320.

Chapter 6 |

Copper depletion for cancer therapy

Summary – Chapter 6

Throughout this Ph.D. thesis, our primary focus has been on utilizing transition metal nanoparticles as catalysts to induce specific chemical reactions within cells. By increasing the levels of metals, particularly copper and iron, we have successfully triggered a series of detrimental chemical reactions that disrupt the redox or amino acid homeostasis of cancer cells. These reactions include depleting intracellular glutathione (GSH) and generating reactive oxygen species (ROS), as well as modulating the amino acid/GSSG pool through transamination reactions (**Figure Summary-1a**). However, an alternative approach that has not been explored in this Ph.D. thesis involves reducing the intracellular levels of transition metal ions rather than increasing them. Transition metal ions serve as crucial cofactors for various enzymes and proteins involved in essential biological reactions including ROS detoxification, catalyzed by *superoxide dismutase 1* (SOD-1), or ATP production, where *cytochrome c oxidase* is involved. Therefore, we hypothesize that reducing the availability of these ions within cells could lead to the malfunctioning of these processes, potentially offering a novel therapeutic strategy.

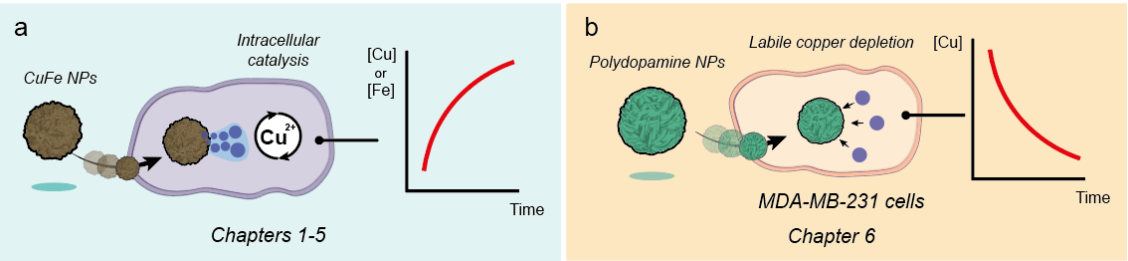

Figure Summary-1. *Dual strategies for cancer therapy explored in this Ph.D. thesis. (a) Use of transition metal nanoparticles to rise intracellular metal species and induce detrimental catalytic reactions to target cancer cells, or (b) polymer-based nanoparticles with metal-binding capabilities to deplete essential metal cofactors and disrupt specific metabolic processes.*

In particular, chelating intracellular copper has shown significant efficacy against triple-negative breast cancer (TNBC) cells, as these cells exhibit a distinct dependence on copper. By targeting and reducing intracellular copper levels using molecular chelators, promising outcomes have

been achieved in combating TNBC. We found valuable the exploration of this approach as it could further provide valuable insights and potential therapeutic avenues for the treatment of copper-dependent cancers.

This project is also linked to the collaboration with Prof. Christopher J. Chang from the University of California, Berkeley that was mentioned in the previous chapter. In order to deplete intracellular labile copper, we employed polydopamine nanoparticles (PDA NPs), which have previously been used for metal decontamination purposes due to their affinity for transition metal cations. In particular, we have used PDA nanoparticles with a size of 120 nm, prepared according to a procedure developed by the group of Prof. Eva del Valle at the University of Salamanca, with who there is also an ongoing collaboration. Remarkably, these particles exhibited significant toxicity specifically against the MDA-MB-231 cell line (**Figure Summary-1b**), a type of triple-negative breast cancer (TNBC) cell line, while showing no harmful effects on MCF-10 cells, which are healthy breast cells. Using the activity-based probe **FCP-1**, developed by Chang's group in 2019, we demonstrated a specific reduction in labile copper levels in MDA-MB-231 cells after treatment with PDA nanoparticles. STEM-EDS analysis of a single MDA-MB-231 cell treated with PDA nanoparticles revealed the presence of copper adsorbed onto the surface of the internalized PDA nanoparticles, allowing to conclude that PDA nanoparticles can deplete labile copper thanks to the presence of chelating groups on the nanoparticle surface.

In order to elucidate the mechanism of cell death, we continued investigating into the effects of PDA nanoparticles on the redox homeostasis and metabolism of MDA-MB-231 cells. Our findings revealed that PDA nanoparticles induced an elevation in reactive oxygen species (ROS) levels, which could be a potential source of toxicity. We established a connection between this phenomenon and the reduction in activity of the SOD-1 enzyme, which requires copper as a cofactor. This strongly suggests that PDA nanoparticles induce cell apoptosis by disturbing the redox homeostasis and metabolism of MDA-MB-231 cells. Furthermore, to provide proof of concept for the therapeutic potential of PDA nanoparticles, we conducted an in vivo experiment with promising results. Following the administration of three doses of 10 mg PDA/kg, we observed a relative reduction in tumor size (V/V_0) of approximately 1.65 fold. By harnessing the chelating

capabilities of the nanoplatform, we have shown that targeted disruption of metal homeostasis can have detrimental effects on cancer cells. This expands the scope of nanoparticle-based cancer therapy beyond catalytic approaches, emphasizing the importance of using the control of transition metal concentrations as a therapeutic strategy.

Adapted from:

Labile copper chelation using Polydopamine nanoparticles stops MDA-MB-231 tumor growth in mice through altering metabolism and redox homeostasis.

Javier Bonet-Aleta[1,2,3], Miguel Encinas-Giménez[1,2,3], Miku Oi[4], Aidan T. Pezacki[4], Victor Sebastian[1,2,3], Ana Martin Pardillos[1,2,3], Pilar Martin-Duque[2,5,6], Jose L. Hueso[1,2,3], Jesus Santamaria[1,2,3], Christopher J. Chang[4,7,8*].*

[1] Instituto de Nanociencia y Materiales de Aragon (INMA) CSIC-Universidad de Zaragoza, Campus Rio Ebro, Edificio I+D, C/ Poeta Mariano Esquillor, s/n, 50018, Zaragoza, (Spain).

[2] Networking Res. Center in Biomaterials, Bioengineering and Nanomedicine (CIBER-BBN), Instituto de Salud Carlos III; 28029 Madrid (Spain)

[3] Department of Chemical and Environmental Engineering, University of Zaragoza, Campus Rio Ebro, C/María de Luna, 3, 50018 Zaragoza (Spain).

[4] Department of Chemistry, University of California, Berkeley, CA, 94720

[5] Instituto de Investigación Sanitaria (IIS) de Aragón, Avenida San Juan Bosco, 13, 50009 Zaragoza, Spain.

[6] Departamento de Cirugía, Facultad de Medicina, Universidad de Zaragoza, 50009, Zaragoza, Spain

[7] Department of Molecular and Cell Biology, University of California, Berkeley, CA, 94720

[8] Helen Willis Neuroscience Institute, University of California, Berkeley, CA, 94720

Graphical abstract

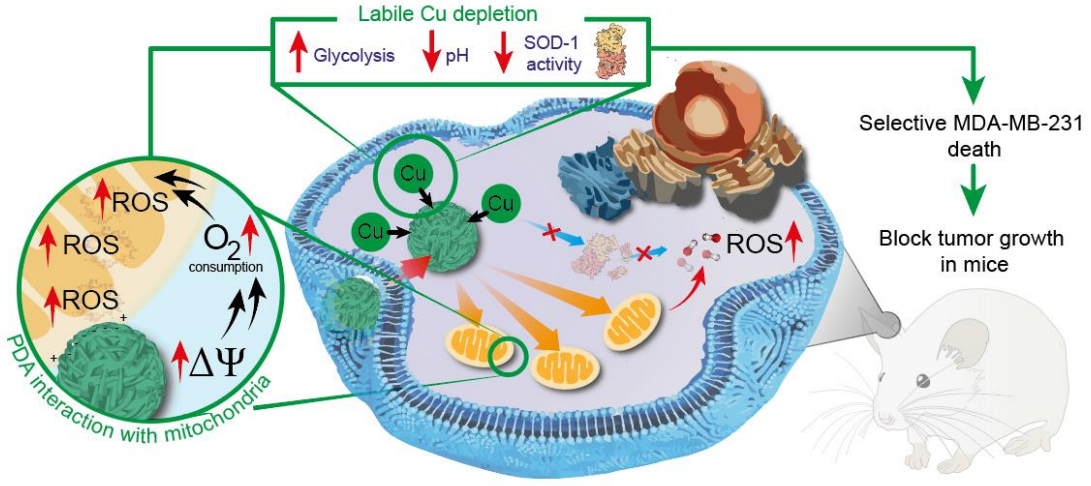

Abstract

Copper plays a critical role as a metal cofactor for enzymes involved in cell proliferation and metabolism, making it an attractive target for cancer therapy. In this study, we investigated the efficacy of polydopamine nanoparticles (PDA NPs), classically applied in metal removal from water, as a therapeutic strategy for depleting intracellular labile copper in a triple negative breast cancer cells through their metal-chelating groups present on PDA surface. By using the activity-based sensing probe FCP-1, we could track the PDA induced copper depletion and link to the selective MDA-MB-231 cell death.. Further mechanistic investigations revealed that PDA NPs increased reactive oxygen species (ROS) levels, potentially through the inactivation of superoxide dismutase 1, an enzyme requiring copper. Additionally, PDA NPs were found to interact with the mitochondrial membrane, resulting in an increase in mitochondrial membrane potential, which may contribute to enhanced ROS production. We employed an in vivo tumor model to validate the therapeutic efficacy of PDA NPs. Remarkably, in the absence of any additional treatment, the presence of PDA NPs alone led to a significant reduction in tumor volume by a factor of 1.66 after 25 days of tumor administration. Our findings highlight the potential of PDA NPs as a promising therapeutic approach for selectively target triple negative breast cancer cells by modulating copper levels and inducing oxidative stress, PDA NPs demonstrate an effective strategy to inhibit tumor growth.

Introduction – Chapter 6

Copper is subjected to a delicate balance in living systems. Its presence must be guaranteed as cofactor or metallosteric agent in proteins to sustain key biological processes, yet a copper excess is associated with potential oxidative stress and cytotoxicity[1, 2]. Indeed, an impairment in intracellular copper levels is associated with several tissue abnormalities and diseases[3]. Several studies link the augment of copper levels in different cancers including breast[4, 5], lung[6] or prostate[7] with their growth and proliferation, grouped in a new concept termed *cuproplasia*[8]. For instance, copper plays a pivotal role in energy metabolism as cofactor of *cytochrome c oxidase*, an enzyme present in the mitochondria membrane involved in ATP biosynthesis. It has been proved that

removing mitochondrial copper is an effective strategy against cancer, in accordance with the higher energetic demand cancer cells have to meet to keep with their accelerated expansion[9, 10].

Removal of copper for cancer therapy is not only interesting from the energetic perspective, since disruption of copper homeostasis is also involved in changes in glycolysis[11, 12], metastatic expansion through ATOX-ATP7A-LOX pathway[13] or blood vessel formation[14]. In addition to the classic visualization as static cofactor, copper can also act as signaling or regulation agent through its dynamic binding to non-catalytic sites in proteins[15], known as labile copper. Recent studies highlight the role of labile copper in the regulation of proteins involved in cell growth and proliferation as Mitogen-activated protein kinase kinase 1 (MEK1/2) or Extracellular signal-regulated kinase 1 (ERK1/2)[16] . Therefore, regulating intracellular copper levels represents an appealing and promising alternative for cancer treatment.

This strategy has shown promising results against Triple Negative Breast Cancer (TNBC)[9, 10, 17], reaching Phase II clinical trials using a copper chelator such as tetrathiomolybdate[18]. TNBC cells are characterized by the lack of expression in three receptors: estrogen (ER-), progesterone (PR-) and epidermal growth factor (HER2-)[19]. This type of tumors is also characterized by its aggressiveness and poor therapeutic outcome, which is a problem considering that about 10-15% of all breast cancers are associated to TNBC[19]. Regarding copper levels, TNBC cells also exhibit an upregulation for mitochondrial copper chaperone and cochaperone proteins (COX17 and SCO2)[20, 21] thereby suggesting an increased copper trafficking to the mitochondria in comparison to healthy cells. Although copper chelation has been proved to be an effective weapon against TNBC, this is not an explored horizon with therapeutic nanoparticles[22]. To the best of our knowledge, only Cui et al.[9] have followed this strategy using nanoparticles loaded with an effective copper chelator. In view of the limited number of FDA-approved medicines for TNBC[23], we found a lack of nanostructures with the capability of sequestration of copper applied for a selective TNBC therapy.

Given its application as metal-removal agent[24, 25], we envisioned polydopamine (PDA) nanoparticles as potential candidates to remove copper from TNBC cancer cells. In addition PDA coatings has been proved to display low affinity for abundant metals in cell as Na^+, K^+, Ca^{2+} or Mg^{2+}

[25] which represents an additional advantage to gain selectivity towards cellular copper[24, 26]. Typically, cancer-related research using PDA focuses on its use to tailor a metal-based nanostructure to maximize the photothermal response of the hybrid platform or load anticancer medicines as doxorubicin or paclitaxel either to perform chemotherapy[27]. Therefore the therapeutic performance of PDA typically relies on remote stimuli as light or drugs release efficacy. In this work, we have explored a novel strategy in cancer therapy based on the sequestration of intracellular labile copper and its influence to kill TNBC cells. together with its consequences (**Figure 1a**). We have demonstrated that the viability of MDA-MB-231 cells is strongly compromised by the presence of low concentrations of PDA nanoparticles because of the sequestration of copper, but not related to other relevant biological transition metals as iron or zinc. The use of the activity-based probe, FCP-1[28], allowed us to confirm and quantify labile copper levels depletion in the presence of PDA NPs in cancer cells. In contrast, this phenomena was less relevant for healthy cells (i.e. MCF-10A). Furthermore, we have also evaluated the influence of the PDA NPs beyond the regulation of the cell metabolism. The presence of PDA NPs affected the activity of the copper-dependent enzyme superoxide dismutase-1 (SOD-1). Hence, the adhesive properties of PDA[29] likely promoted a closer interaction with mitochondria, affecting to their membrane potential ($\Delta\Psi$) and triggering an overproduction and enhanced generation of Reactive Oxygen Species (ROS). All these features converged in stopping the tumor growth in xenograft-bearing mice after administration of low doses of PDA. In our opinion, the present study will pave the way towards leveraging the TNBC weakness to copper depletion by different nanomaterials for a more efficient, selective and safer cancer therapy.

Results and discussion – Chapter 6

Synthesis of PDA nanoparticles. The synthesis of the PDA nanoparticles was conducted via polymerization of dopamine hydrochloride in a water/isopropyl alcohol mixture in basic media[30] (see further details in Experimental information). TEM images and further dynamic light scattering analysis revealed the formation of well-dispersed particles with an homogeneous size distribution around 120 nm (**Figures 1b-c**).

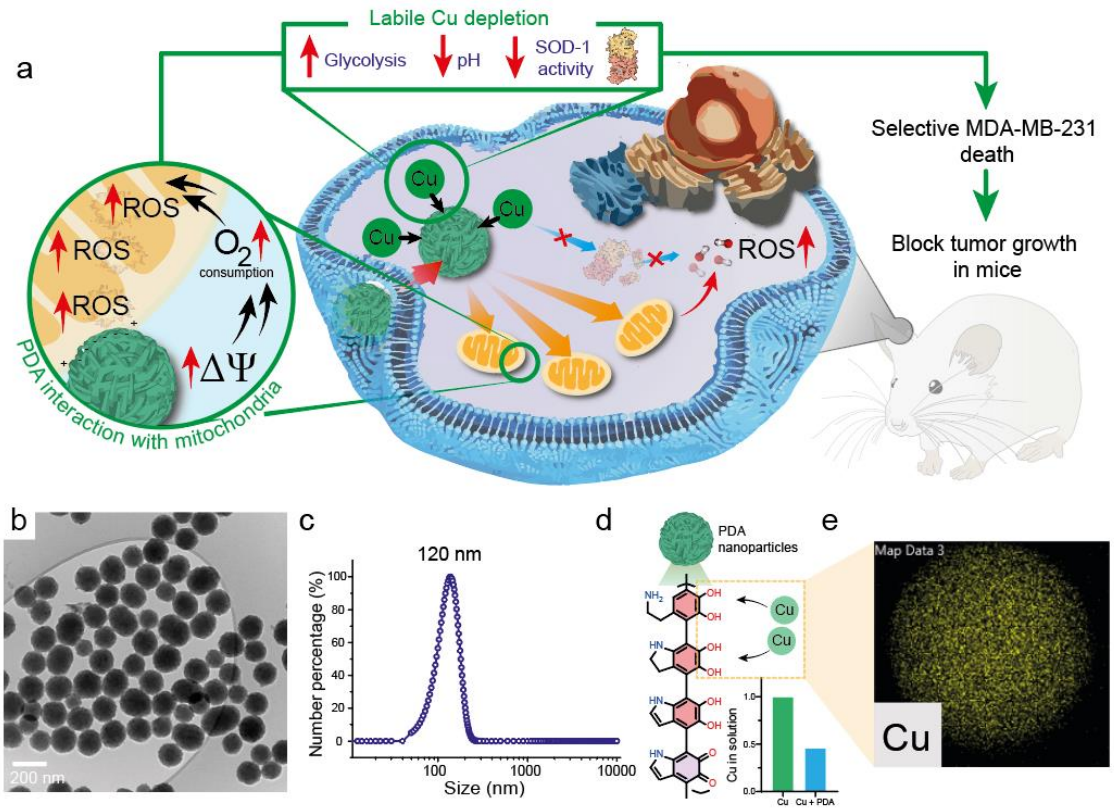

Figure 1. *PDA nanoparticles for novel anticancer strategies based on metal depletion* ***(a)*** *PDA nanoparticles can disrupt the labile copper equilibrium in MDA-MB-231 cells. The labile copper depletion possess important implications not only in metabolism, but also in the activity of the key detoxifying enzyme SOD-1. After internalization, negatively-charged PDA can interact with the positively-charged membrane of mitochondria, affecting to the membrane potential (ΔΨ) and thereby to their metabolic activity. The combination of all these features is responsible of a selective MDA-MB-231 death and achieves to stop the tumor growth in mice;* ***(b)*** *TEM image of PDA nanoparticles;* ***(c)*** *Hydrodynamic size of PDA nanoparticles;* ***(d)*** *Chemical structure of PDA nanoparticles contains amino and catechol groups with affinity to* Cu^{2+} *to reduce its levels in solution. (Conditions: [PDA] = 0.1 mg·mL*$^{-1}$*, [Cu] = 0.1 mg·mL*$^{-1}$*, pH = 7.4 buffered with TRIS 0.1 M);* ***(e)*** *EDS mapping analysis of copper in a single PDA particle after exposition to a solution containing Cu reveals its homogeneous absorption all over the PDA surface.*

Although the precise chemical structure is still on debate[31, 32], PDA possess different subunits within its chemical structure, mainly composed of catechol groups which exhibit a high affinity by transition metal ions including copper[24, 26] (***Figure 1d***). This was corroborated by adding 0.1

$mg \cdot mL^{-1}$ of PDA to a 0.1 $mg \cdot mL^{-1}$ Cu solution, more than 50% of the initial Cu amount was absorbed onto PDA surface (***Figure 1d***) which was further confirmed by STEM-EDS (**Figure 1e**).

PDA nanoparticles promote MDA-MB-231 cell death through labile copper depletion. After evaluating the capacity of PDA NPs to sequester copper ions, we decided to evaluate their toxicity for different breast cell lines, including TNBC (MDA-MB-231 and MDA-MB-468), MCF-7 as another non-TNBC cancer line, and healthy MCF-10A cells (**Figure S1**). The addition of low levels of PDA NPs decreased cell viability very critically in MDA-MB-231, in contrast, MCF-10A cells remained alive under equivalent doses of PDA (**Figure 2a**). We attributed this effect to the role of PDA as copper-sequestration agent affecting the cell viability in MDA-MB-231 cells. Indeed, supplementation of cell media with $CuCl_2$ augmented cell viability in presence of PDA (**Figure 2b**), but no effect was detected after the addition of other biological metals such as Fe or Zn (**Figure S2**), indicating the close relation of copper and cell viability of MDA-MB-231. The labile copper pool is defined as the copper not tightly bonded to proteins, and is subjected to a fast intracellular-extracellular transport[15]. Activity-based probes are metal-selective molecules designed to selectively react with the labile copper available and yield a fluorescent product[33].

FCP-1 is an interesting activity-based probe due to its self-calibration properties[28] to quantify the labile copper in MDA-MB-231 and MCF-10 cells after treatment with PDA. FCP-1 contains three main active units: a green-emitting (F_{526}) fluorescein moiety connected to a red-emitting rhodamine (F_{576}) through a Tris(2-pyridylmethyl)amine (TPA) which acts as pocket for labile Cu(I) (**Figure 2c**). When they are part of the same molecule rhodamine quench fluorescein fluorescence through Förster Resonance Energy Transfer (FRET) phenomena, but in the presence of the oxidative couple Cu(I)/O_2 the C-O bond between fluorescein and TPA is broken,[28] disabling FRET phenomena. Thus, sequestration of labile Cu can be directly related to a decay in green fluorescence from the fluorescein moiety (F_{526}) and thereby a decrease in the F_{526}/F_{576} ratio.[28] (**Figure 2d-f**).

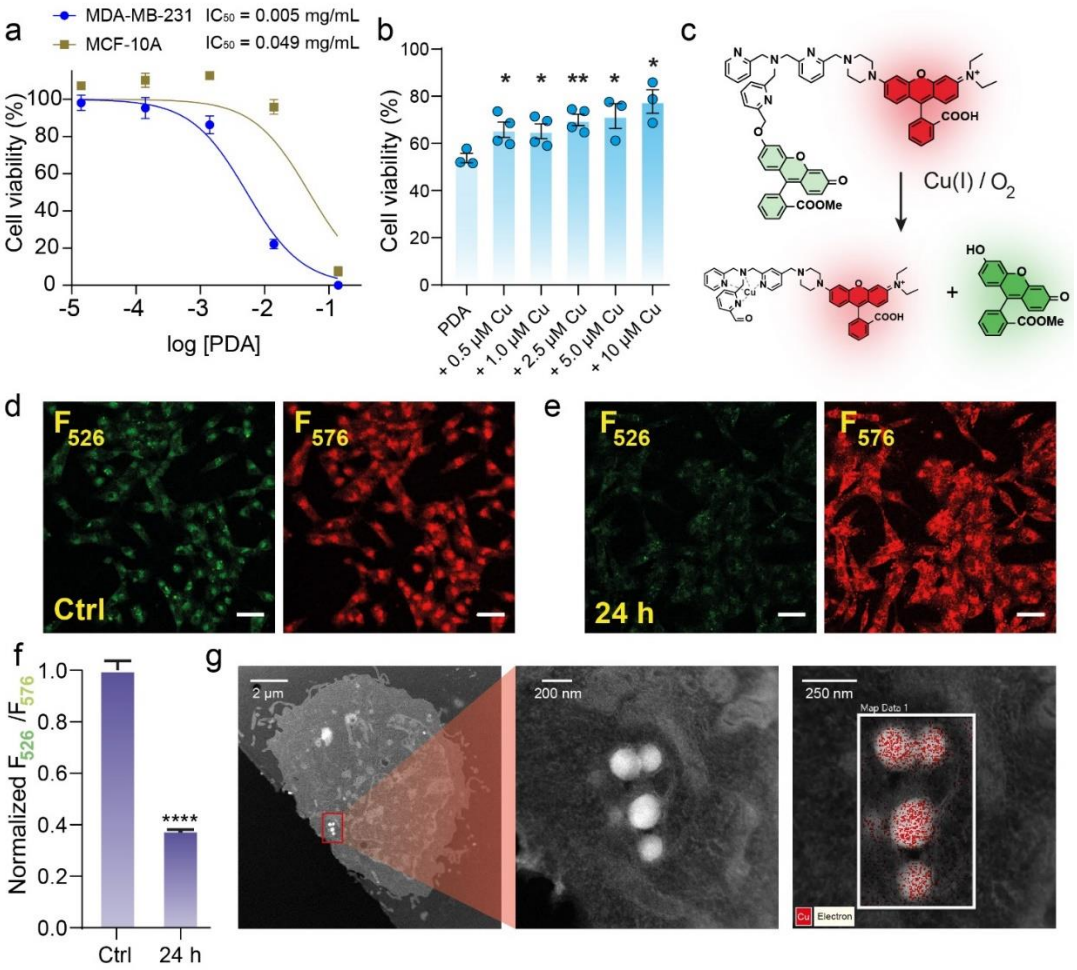

Figure 2. *Cytotoxicity of PDA nanoparticles towards MDA-MB-231 cells is correlated with the sequestration of labile copper. (a) Comparison of the cell viability of MDA-MB-231 and MCF-10A cell lines in the presence of different concentration of PDA NPs. (b) Cell viability of MDA-MB-231 treated with $5{\cdot}10^{-3}$ mg·mL^{-1} of PDA NPs with/without an external copper supplementation (c) Mechanism of detection and quantification of labile Cu(I) using FCP-1 probe. Under an oxidative environment caused by the presence of labile Cu(I) and O_2, the breakage of C-O bond which binds both fluorescent subunits is favored. This cancels FRET phenomena and is related with changes in the fluorescence spectra of the solution, which allows the detection and quantification of labile copper. (d-e) Confocal microscopy images of (d) control and (e) treated MDA-MB-231 cells treated with $1.40{\cdot}10^{-3}$ mg·mL^{-1} of PDA NPs for 24 h. Fluorescence emitted at 526 nm (F_{526}) by the fluorescein unit is acquired using the green channel, while the fluorescence emitted at 576 nm (F_{576}) by the rhodamine group is captured using the orange channel. (f) Quantification of the F_{526}/F_{576} ratio fluorescence in MDA-MB-231 and MCF-10 A cells treated with $1.40{\cdot}10^{-3}$ mg·mL^{-1} of PDA NPs for 24 h. (g) STEM-*

*EDS-HAADF images of treated MDA-MB-231 cells revealed the colocalization of copper onto the surface of PDA nanoparticles after 24 h of incubation with a concentration of $1.14 \cdot 10^{-3}$ mg·mL^{-1}. Fluorescence intensity of FCP-1 was determined from experiments with λ_{ex} = 458 nm. Scale bar = 50 μm. *P < 0.05, **P < 0.01, ***P < 0.001, and ****P < 0.0001; ns, not statistically significant. Error bars denote S.E.M (n = 8).*

After 24 h of incubation with PDA nanoparticles, we could detect a drop of 65% in F_{526}/F_{576} ratio in MDA-MB-231 cells (**Figure 2d-f** and **Figure S3**). In contrast, just a 20% was observed for MCF-10A cells (**Figure S4** and **Figure S5**).The total copper levels for both MDA-MB-231 and MCF-10A remained unvaried thereby suggesting that copper was sequestered intracellularly but not released by the NPs (**Figure S6**). TEM and STEM-HAADF-EDX microscopies further confirmed not only MDA-MB-231 cells successfully internalize PDA nanoparticles within their cytosol (**Figure S7**), but also they absorb the labile copper ions onto their surface (**Figure 2g and Figure S8**), in agreement with the previously observed drop in FCP-1 fluorescence. In addition, the copper signal was barely negligible outside the surface of the PDA nanoparticle (**Figure S9**). All this information suggest that the sequestration of an important part of the intracellular labile copper by PDA NPs, and its correlation with a selective decrease in MDA-MB-231 viability.

PDA treatment fosters disruption of redox homeostasis and metabolism in MDA-MB-231. Given the huge cytotoxicity of PDA nanoparticles towards MDA-MB-231 cells, we investigated the mechanism behind of the cell death. Firstly, we explored the influence of PDA treatment in redox homeostasis by analyzing the intracellular ROS generation using CellROX™ as a common fluorescent probe. We could detect a time-dependent increase in ROS levels after the treatment of MDA-MB-231 cells with $5 \cdot 10^{-2}$ mg·mL^{-1} of PDA NPs (**Figure 3a,b**). In addition, we could also detect a downregulation in α-tubulin expression after the treatment of MDA-MB-231 cells with PDA (**Figure S10**), which has been previously attributed to ROS generation [34, 35]. PDA-induced generation of ROS was unexpected, since several reports endorse PDA nanoparticles with antioxidant activity in different cells lines, including human gingival epithelial cell [36] or fibroblasts[37]. Indeed, the treatment of MCF-10A cells with an analogous dose of PDA yielded a ROS scavenging effect (**Figure S11**). At this point we focused on stablishing a correlation between the decrease in

labile copper induced by PDA and ROS generation. This might be counterintuitive since a raise in labile copper levels is typically related to oxidative stress.[8] Yet, another possibility may imply that cells are not being able to remove already existing ROS. Copper is a crucial cofactor of the enzyme SOD-1, one of the most common antioxidant enzymes present in the cytosol of eukaryotic cells[38]. Although the expression of SOD-1 did not change after PDA treatment of MDA-MB-231 cells (**Figure 3c, Figure S12**), its intrinsic activity was decreased by a factor of almost three (**Figure 3d**). Similar results were obtained by Cui et al.[9] after treating MDA-MB-231 cells using a copper-selective chelator. We hypothesize that the copper scarcity scenario induced by the internalization of PDA NPs in MDA-MB-231 cells (**Figure 2f**) may block the delivery of copper to SOD-1 enzyme through copper chaperone for superoxide dismutase (CCS) enzyme[38] and as consequence, the produced ROS can not be removed.

We then decided to study the mitochondrial respiration, as one of the major source of ROS in cell[39], to check potential changes triggered by the presence of PDA nanoparticles. Measurement of the Oxygen Consumption Rate (OCR) by Seahorse indicated a significant raise in the basal OCR after the treatment of MDA-MB-231 cells with PDA nanoparticles (**Figure 3e**). Moreover, the addition of the mitochondrial membrane uncoupling drug FCCP during the experiment revealed large differences in the maximum respiration between treated and control MDA-MB-231 cells (**Figure 3e**). In contrast, no significant effects could be detected for the corresponding treatment in MCF-10A cells (**Figure S13**). This fact suggests that the treatment with PDA NPs may be affecting to the mitochondrial membrane potential (Δψ) of MDA-MB-231 cells. The hyperpolarization of the mitochondria can also be related to the increasement in ROS production[40], and would be in agreement with the results displayed in **Figure 3a,b**. By using the fluorescent dye JC-1, we analyzed the Δψ of mitochondria from treated MDA-MB-231 cells (**Figure 3f**). JC-1 dye mechanism of action is based on its aggregation forming dimers with red emission within mitochondria with a high Δψ, whereas a decrease in Δψ favors its monomeric state with green emission[41]. According to the OCR results, the addition of PDA resulted in a higher red fluorescence of JC-1, thereby indicating that PDA was inducing MDA-MB-231 cells to a larger Δψ (**Figure 3f**).

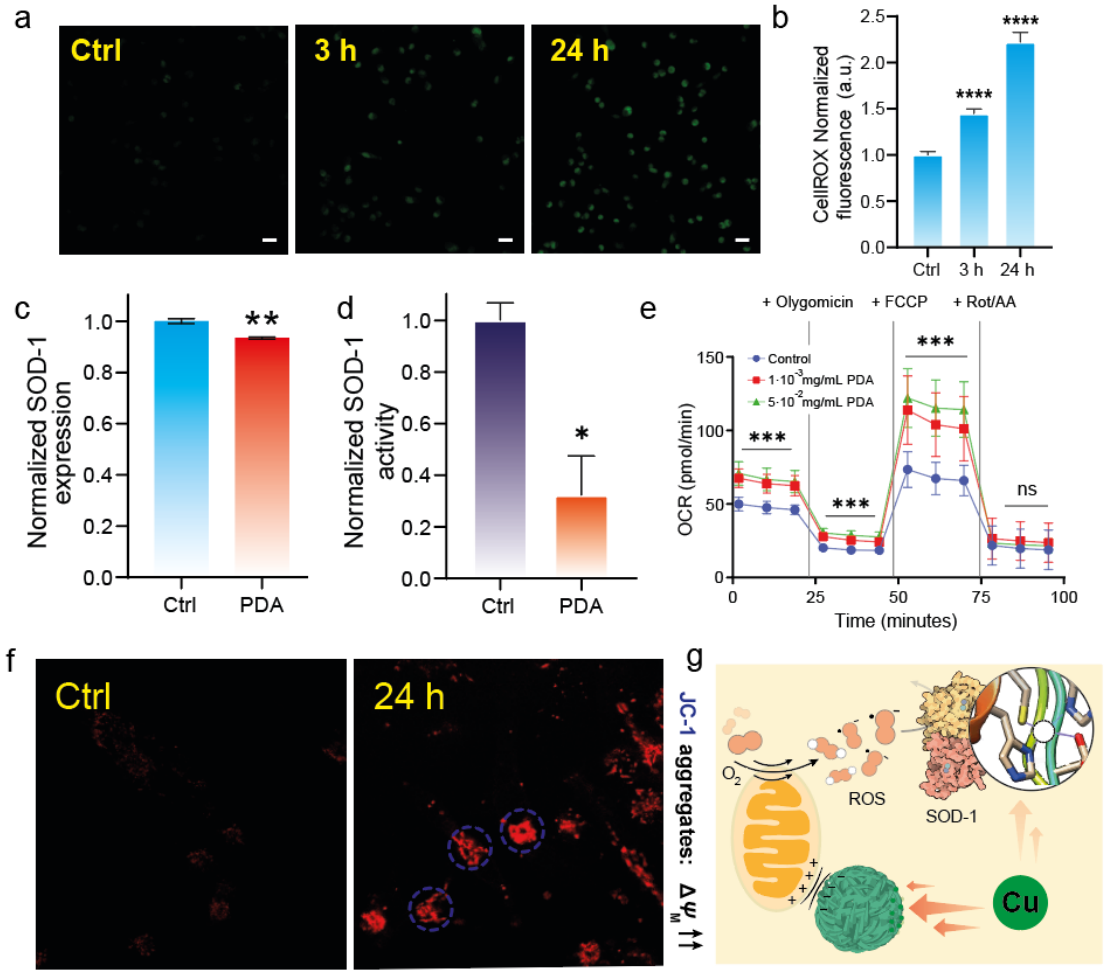

Figure 3. *Disruption of redox homeostasis and metabolism driven by PDA in MDA-MB-231 cells. (a-b) Confocal microscopy analysis of ROS in MDA-MB-231 cells treated with $5{\cdot}10^{-2}$ mg·mL^{-1} using fluorescent probe CellRox at different incubation times. Fluorescence intensity of CellRox probe was determined from experiments with λ_{ex} = 485 nm. Scale bar = 50 µm. Results are normalized to control fluorescence = 1. Error bars denote S.E.M (n=8). (c) Quantification of SOD-1 expression by Western-Blot in MDA-MB-231 cells treated with $5{\cdot}10^{-3}$ mg·mL^{-1} of PDA for 24 h, using glyceraldehyde 3-phosphate dehydrogenase as control protein. Error bars denote S.E.M (n = 3). (d) Determination of SOD-1 protein activity in MDA-MB-231 cells after the treatment with $5{\cdot}10^{-3}$ mg·mL^{-1} of PDA for 24 h. Error bars denote S.E.M (n = 3). (e) OCR analysis of MDA-MB-231 cells treated with different concentrations of PDA for 24 h. The measurement was performed by Seahorse analyzer, by adding 1 µM of oligomicin after 28 minutes, FCCP (1 µM) after 54 minutes and a 1:1 mixture of rotenone A/antimicin (0.5 µM) after 80 minutes. Error bars denotes S.E.M (n = 9). (f) Confocal microscopy analysis of mitochondrial membrane potential (ΔΨ) using JC-1 fluorescent probe after the treatment*

*of MDA-MB-231 cells incubated with 1.10·10^{-3} mg·mL^{-1} of PDA for 24 h. The increase in red fluorescence by JC-1 indicates a major state of aggregation within the mitochondrial membrane due to its larger membrane potential. JC-1 aggregates were excited with 535 nm with an Ar laser. Scale bar = 50 µm (g) Schematic summary of the influence of PDA in redox homeostasis and metabolism in MDA-MB-231 cells. PDA promotes the depletion of labile copper, one of the metal cofactors of SOD-1, thus blocking its activity towards ROS detoxification. On the other hand, PDA treatment disrupts mitochondrial ΔΨ which can be correlated to a increase in OCR and a subsequent ROS by-production. *P < 0.05, **P < 0.01, ***P < 0.001, and ****P < 0.0001; ns, not statistically significant. Error bars denote S.E.M (n = 8).*

Additionally, we investigated the effects of PDA treatment on the metabolism of MDA-MB-231 and MCF-10A cells, respectively. By analyzing the extracellular acidification rate (ECAR) it is possible to determine the source of the produced ATP and determine potential changes induced by PDA NPs. In the case of MDA-MB-231 cells, the basal levels of ECAR were significantly higher than control experiment (**Figure S14**) in contrast to the absence of effect for MCF-10A cells (**Figure S15**). These results were indicative of change towards a more glycolytic metabolism under the presence of PDA nanoparticles in MDA-MB-231 cells. A similar trend was reported by Ishida et al.[11] in different cancer cells including BxPC3, SUIT2, MDA-MB-157 and SKOV3. They quantified both an important increase in lactate levels and upregulation of AMP-activated protein kinase (AMPK) under copper chelation conditions, indicating an enhanced glycolytic pathway[11] which indeed was analogous to ours with PDA NPs. To quantify the ATP production rate and its specific source, we measured both OCR and ECAR in PDA-treated cells under the addition of specific mitochondrial units inhibitors. Changes in pH can be directly related to the lactate, and glycolytic produced ATP (glycoATP), generated in the glycolysis pathway. In the case of mitochondrial-ATP (mitoATP), it can be determined through OCR measurement as O_2 is required for the biosynthesis of ATP in mitochondria. By adding oligomycin to inhibit ATP synthase, and rotenone/antimycin A to inhibit complex I and IV of mitochondria, respectively, it was possible to finally differentiate the sources of produced ATP (**Figure S16**). We could quantify a 1.5-fold increase in production of ATP via glycolysis, while the production of mitochondrial ATP was slightly decreased (**Figure S17**). This finding is in agreement with Ramchandani et al.[10] work, where the treatment of TNBC using

tetrathiomolybdate to reprogram cell metabolism towards the upregulation of glycolysis via AMPK activation, inducing a lower mitoATP/glycoATP ratio.

Taking into account all the data, we posit that PDA nanoparticles can induce MDA-MB-231 cells into an oxidative-stress situation by the simultaneous generation of ROS via increasing Δψ, and through depletion of labile copper and the subsequent loss of activity of the antioxidant enzyme, SOD-1 (**Figure 3g**). Additionally, depletion of copper has an effect on the source of ATP production in MDA-MB-231, which changes towards glycolysis after PDA treatment. Both the impossibility of detoxifying mitochondrial ROS and its enhanced generation led to the cell to apoptosis, as we could observe due to an increase in cell viability after the addition of 10 μM of the apoptosis rescuer Z-VAD-FMK (**Figure S18**).

Therapeutic efficacy of PDA and metal analysis i*n vivo*. Encouraged by the remarkable cytotoxicity of PDA nanoparticles towards MDA-MB-231 cells and their low toxicity towards MCF-10A cells, we proceeded to investigate the antitumoral effectiveness of PDA nanoparticles *in vivo*. We assessed the therapeutic effect with a MDA-MB-231 breast cancer model in nude mice. In the treatment group, mice with MDA-MB-231 tumors received intratumoral injections of PDA nanoparticles at a dose of 10 $mg \cdot kg^{-1}$ on days 6, 11, and 14 after tumor inoculation (n=9) (**Figure 4a**). PDA treatment was initiated when the tumor volume reached approximately 200 mm^3. Notably, PDA treatment significantly impeded tumor progression and growth 21 days after tumor inoculation. Tumors in the control group exhibited a considerable increase in size, reaching 729 ± 125 mm^3 (n=8, ± indicates S.E.M), whereas the treated group demonstrated a restrained growth (397±68 mm^3, n=9, ± indicates S.E.M), underscoring the potential therapeutic efficacy of PDA nanoparticles (**Figure 4b**). Importantly, the treatment did not result in significant weight loss among the mice (**Figure 4c**). Furthermore, we conducted an analysis of the total content of biologically relevant metals (Zn, Fe, and Cu) in various organs, including the tumor, heart, brain, muscle, spleen, kidney, pancreas, lung, and liver. This analysis aimed to confirm that treatment with PDA nanoparticles did not significantly alter the metal levels in these organs, thus reinforcing the safety of the treatment.

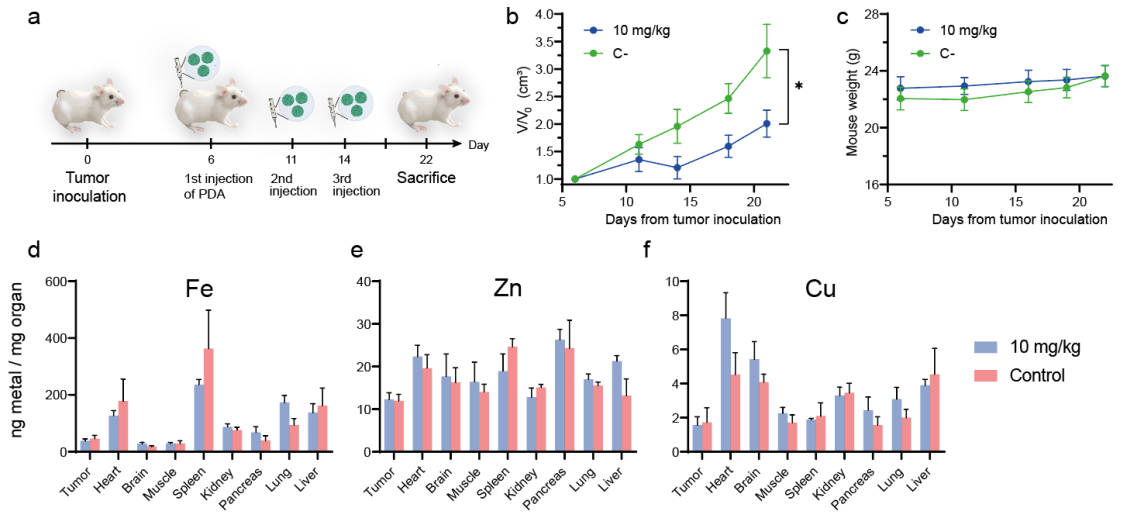

Figure 4. *In vivo therapeutic efficacy of PDA nanoparticles in MDA-MB-231 model. (a) Treatment strategy for therapeutic efficacy of PDA NPs study in MDA-MB-231 tumor-bearing mice. The treated group comprised 9 mice that received 3 doses of 10 mg·kg^{-1} PDA NPs on days 6, 11, and 14 after tumor inoculation.. (b) Relative tumor volume (V/V_0) evolution with time in control and treated groups. Error bars denote S.E.M (n = 8 for control group and n=9 for treated group). (c) Monitoring of mouse weight throughout the experiment in control and treated groups. Error bars denote S.E.M (n = 8 for control group and n=9 for treated group). Analysis of (d) iron (e) zinc and (f) copper in different organs (expressed as ng metal/mg organ) in control and treated groups. Error bars denote S.E.M (n = 3). No statistically significant differences were found *P < 0.05, **P < 0.01, ***P < 0.001, and ****P < 0.0001; ns, not statistically significant.*

Conclusions – Chapter 6

This study demonstrates the promising therapeutic potential of polydopamine nanoparticles (PDA NPs) as an effective strategy for targeting triple negative breast cancer cells through the modulation of copper levels and induction of oxidative stress. We could track the specific depletion of labile copper levels, using the activity-based probe FCP-1, induced by the treatment with PDA NPs in MDA-MB-231 cells. The metal-chelating groups present on the surface of PDA NPs could effectively absorb labile copper present in MDA-MB-231 cells which was linked to their selective cell death. Mechanistic investigations revealed that PDA NPs increased reactive oxygen species (ROS) levels, potentially through the inactivation of superoxide dismutase 1, an enzyme that relies

on copper. Additionally, PDA NPs interacted with the mitochondrial membrane, resulting in an increase in mitochondrial membrane potential, which likely contributed to enhanced ROS production. These findings highlight the ability of PDA NPs to disrupt redox homeostasis and trigger oxidative stress-mediated cell death in triple negative breast cancer cells to induce them into apoptosis.

Furthermore, the in vivo tumor model validated the therapeutic efficacy of PDA NPs. Remarkably, the administration of PDA NPs alone led to a significant reduction in tumor volume by a factor of 1.66 after 25 days of tumor administration, without the need for additional treatments. This underscores the potential of PDA NPs as a standalone therapeutic approach for inhibiting tumor growth in triple negative breast cancer. Overall, this study provides valuable insights into the therapeutic mechanism of PDA NPs in selectively targeting cancer cells by modulating copper levels and inducing oxidative stress. The findings suggest that PDA NPs hold great promise as an innovative and effective strategy for the treatment of triple negative breast cancer and warrant further exploration and development as a potential therapeutic intervention.

Experimental section – Chapter 6

Chemicals and Materials. Dopamine hydrochloride (DA·HCl, Sigma-Aldrich), $CuCl_2$ (>99.0%, Sigma-Aldrich), $FeSO_4$ (98%, Alpha Aesar), $ZnCl_2$ (≥ 98.0 %Sigma-Aldrich), 2-isopropanol, (2-PrOH, >90%, VWR), NH_4OH (J.T. Baker, 14.8 M in water), Phosphate Buffer Saline (PBS without Ca and Mg, Corning), Dulbecco's Modified Eagle's Medium (DMEM, (GlutaMax)), Hanks' Balanced Salt Solution (HBSS + $CaCl_2$, + $MgCl_2$, Gibco), Cell Counting Kit-8 (CCK-8, Dojindo), CellROX-Green reagent (InvitroGen), JC-1 (Thermofisher Scientific), Agilent Seahorse XF Calibrant (pH = 7.4), Seahorse XF Base medium without phenol red, Seahorse XF 1.0 M glucose solution, Seahorse XF 100 mM pyruvate solution, Seahorse XF 200 mM glutamine solution, Cell MitoStress and ATP-rate cell kits were purchased from Agilent Technologies.

Instruments. Confocal fluorescence imaging was performed with a Zeiss laser scanning microscope LSM880 with a 20x dry objective lens using Zen 2015 software (Carl Zeiss, Zen 2.3

black). Metal content in cells was determined by measuring ^{63}Cu and ^{64}Zn using a Thermo Fisher iCAP-Qc ICP-MS in KED mode. Aristar BDH Ultra Concentrated nitric acid to dissolve samples was purchased from VWR. In vitro OCR and ECAR measurements were performed using Seahorse XF96 Analyzer. Superoxide Dismutase activity test was purchased from Sigma Aldrich.

***Polydopamine nanoparticles (PDA) synthesis*.** Firstly, to a round-bottom flask 42.5 mL of 2-PrOH, 90 mL of mili-Q water and 3.75 mL of NH_4OH were added, and the solution was left to stir for 30 minutes. Then. 500 mg of DA·HCl were dissolved in 10 mL of mili-Q water were added dropwisely. Mixture was stirred overnight at room temperature. Product was isolated by centrifugation (10 000 rpm, 10 minutes, two cycles). Final product was resuspended in PBS and maintained at room temperature for further use.

Cell viability experiments. All cells used in this research were maintained by the UC Berkeley Tissue Culture Facility. MDA-MB-231, MDA-MB-438 and MCF-7 were seeded in 75 % of confluency in 96-well cell plates. In the case of MCF-10A, $1{\cdot}10^5$ cells were seeded. PDA nanoparticles from stock solution in PBS were added to DMEM to achieve a final concentration ranging from $1.40{\cdot}10^{-5}$ to $1.40{\cdot}10^{-1}$ mg·mL^{-1}. Prior to the addition, PDA nanoparticle stock solution was sonicated for 20 minutes. After 24 hours, wells were washed with PBS (1x) and 100 µL of 10% v/v CCK-8 in DMEM solution were added to the well. Cell plate was incubated for 37 ºC in a 5% CO_2 incubator for 3 h (in the case of MDA-MB-231, MDA-MB-468 and MCF-7 cells) or 3.5 h (in the case of MCF-10A cells). Finally, the absorbance at 450 nm was measured using a plate reader. Viability is presented as percentage of control (n = 3 ± SEM). For **Recovery experiments** using Cu, Fe and Zn, cells were seeded in the same conditions as in the cell viability experiment. Stock solutions of $CuCl_2$, $FeSO_4$ and $ZnCl_2$ were prepared dissolving the metal salts in H_2O to a final concentration of 0.70 mM, and then subsequently dissolved in DMEM to a final concentration of 35 µM. PDA was added to a final concentration of $5.0{\cdot}10^{-3}$ mg·mL^{-1} and incubated for 24 hours. Cell viability was measured following the same protocol mentioned before. Absorbance at 450 nm was measured using BioTek Synergy MX Microplate Reader. For apoptosis experiment, apoptosis inhibitor Z-VAD-FMK was co-incubated with PDA particles in 10 µM and $1.14{\cdot}10^{-3}$ mg·mL^{-1} for 24 h. Cell viability was measured using the same protocol mentioned before.

Intracellular Labile Cu analysis using FCP-1. FCP-1 was synthesized following previous reports [ADD REF]. MDA-MB-231 and MCF-10A cells were seeded in 60% of confluency in a Chamber slide 8-well. PDA nanoparticles resuspended in DMEM were added to a final concentration of $1.40 \cdot 10^{-3}$ mg·mL^{-1} and incubated for 24 h. Wells were washed with HBSS once, and then FCP-1 was added to a final concentration of 1 μM (0.6% of DMSO). Cells were incubated for 30 minutes at 37 ºC in a 5% CO_2 incubator prior to imaging. FCP-1 was excited with 458 nm with an Ar laser, and the emissions were collected using a META detector between 465 and 541 nm (F_{525}), and between 559 and 710 nm (F_{575}). Results are expressed considering average F_{525}/F_{575} of control = 1 ± S.E.M (n = 8).

ICP-MS analysis of MDA-MB-231 and MCF-10A cells. MDA-MB-231 or MCF-10A cells were seeded in 6-well plates in 75% confluency. PDA nanoparticles resuspended in DMEM were added to a final concentration of $1.40 \cdot 10^{-3}$ mg·mL^{-1} and incubated for 3 and 24 h. Then, wells were washed with ice-cold PBS (1x) three times. Finally, 350 μL of concentrated nitric acid were added to the plate and incubated for 48 h at room temperature. Before analysis, 20 ppb of Ga was added to each sample as internal standard. Results are expressed considering average Cu/Zn of control = 1 ± S.E.M (n = 6).

OCR and ECAR measurements. Firstly, $5 \cdot 10^4$ cells from MDA-MB-231 or MCF-10A cell line were seeded in Agilent Seahorse XF96 Cell Culture microplates. PDA nanoparticles were added to a final concentration of $1 \cdot 10^{-3}$ or $5 \cdot 10^{-2}$ mg·mL^{-1} and incubated with cells for 24 hours. For mitochondrial stress assay, cells were washed two times using freshly prepared Seahorse XF DMEM medium (10 mM glucose, 1 mM pyruvate and 2 mM glutamine) and incubated with this medium for 1 h at 37ºC in a non-CO_2 incubator. OCR and ECAR were measured at basal conditions and after the sequential addition of oligomycin (1 μM, added after 28 minutes), FCCP (1 μM, added after 54 minutes) and Rotenone/Antimycin A (0.5 μM, added after 80 minutes) (n = 9 per condition for OCR and ECAR for each cell line). For ATP-rate assay, cells were washed once with Seahorse XF DMEM medium (same composition as mitochondrial-stress assay) and incubated for 1 h at 37ºC in a non-CO_2 incubator. Before measurement, cells were washed once using Seahorse XF DMEM medium. OCR and ECAR were measured at basal conditions and after the sequential

addition of oligomycin (1 μM, added after 28 minutes) and Rotenone/Antimycin A (0.5 μM, added after 54 minutes) (n = 9 per condition for OCR and ECAR for each cell line).

***Reactive Oxygen Species (ROS) analysis using CellROX*.** MDA-MB-231 and MCF-10A cells were seeded in 60% of confluency in a Chamber slide 8-well. PDA nanoparticles resuspended in DMEM were added to a final concentration of $5{\cdot}10^{-2}$ mg·mL^{-1} and incubated for 24 h. Wells were washed with HBSS once, and then CellRox reagent was added to a final concentration of 5 μM (1% DMSO). Cells were incubated for 30 minutes at 37 ºC in a 5% CO_2 incubator. Then, wells were washed using HBSS twice, and fixed with paraformaldehyde (3.7%) for 15 minutes at 37ºC prior to imaging. CellROX was excited with 485 nm with an Ar laser, and the emissions were collected using a META detector between 500 and 540 nm. Results are normalized to control fluorescence = 1 ± S.E.M (n = 8).

***In vitro mitochondrial membrane potential using JC-1*.** MDA-MB-231 and MCF-10A cells were seeded in 60% of confluency in a Chamber slide 8-well. PDA nanoparticles resuspended in DMEM were added to a final concentration of $1.10{\cdot}10^{-3}$ mg·mL^{-1} and incubated for 24 h. Wells were washed with HBSS once, and then JC-1 reagent was added to a final concentration of 10 μg·mL^{-1} (1% DMSO). Cells were incubated for 10 minutes at 37 ºC in a 5% CO_2 incubator. Then, wells were washed using HBSS once prior to imaging . JC-1 aggregates were excited with 535 nm with an Ar laser, and the emissions were collected using a META detector between 570 and 620 nm.

Western blot analysis. MDA-MB-231 Cells were treated with $5.{\cdot}10^{-3}$ mg·mL-1 PDA nanoparticles for 24 h. Cells were washed using cold PBS (1x) twice. Finally, cells were collected using a cell scratch, and centrifuged at 6 000 rpm, 20 minutes at 4ºC. Supernactant was discarded and cell pellets were stored at -80ºC. 150 μL of RIPA buffer (Thermo, cat. no. 89900) was added to cell pellets and incubated for 30'. The protein concentrations were quantified by Pierce BCA assay (Thermo Scientific, 23250). GAPDH antibody was purchased from Cell Signaling Technologies (Asp175, no. 9661) and used with a dilution 1:3000. SOD1 antibody was purchased from Santa Cruz Biotechnologies (sc-101523) and used with a dilution of 1:250. α-tubulin antibody was purchased from Cell Signaling Technology (3873S) and used with a dilution 1:1000. Results are normalized by GAPDH expression (n = 3).

SOD-1 activity analysis. MDA-MB-231 cells were seeded in 6-well plates in 75% confluency. PDA nanoparticles dissolved in DMEM were added to the well in a concentration of $5 \cdot 10^{-3}$ mg·mL^{-1} and incubated for 24 h. Then, cell were trypsinized and centrifuged at 250 g for 10' at 4ºC and them with ice-cold PBS with the same conditions. Cells were sonicated and finally centrifuged at 1500 g for 10' at 4ºC. Supernactant was diluted 1:4 and analyzed using SOD-1 activity test.

In vivo therapeutic efficacy of PDA. The study procedures described herein were conducted in accordance with the necessary project licenses, namely [Project License 1] and [Project License 2]. These licenses were obtained after receiving approval from the Ethic Committee for Animal Experiments at the University of Zaragoza. The experiments took place within the animal facility situated at the Centro de Investigación Biomédica de Aragón (CIBA) in Zaragoza. Throughout the entire process, strict adherence was maintained to the guidelines set forth by the European Union Directive (2010/63/EU) and the Spanish Legislation (RD53/2013). For the experimental procedures, female Hsd:Athymic Nude-Fox1nu mice (Envigo) aged between 6 to 10 weeks were specifically selected. Upon arrival at the animal facilities, these mice underwent a one-week quarantine period before the initiation of any procedures. During the course of the study, the mice were provided with ad libitum access to food and water and were subjected to a 12-hour light-dark cycle under sterile conditions.

In this in vivo assay, a total of 10 mice were utilized. Xenograft tumors were generated from $5 \cdot 10^6$ MDA-MB-231 cells suspended in 200 µL of PBS. The tumors were allowed to grow until reaching an approximate volume of 0.15 cm^3. Subsequently, the mice were divided into two groups: a control group receiving PBS injections, and a treatment group receiving intratumoral injections of 10 mg·kg^{-1} of PDA. The corresponding solutions were administered to the mice every four days throughout the duration of the study. During this period, the mice were regularly weighed, and the size of the tumors was measured every other day to monitor their growth. After two weeks of treatment initiation, the mice were humanely euthanized using a CO_2 chamber. Following euthanasia, several major organs were collected for further analysis.

Metal analysis of organs by MP-AES. The collected organs were carefully processed to assess the copper, iron or zinc content in each of them. Firstly, the major organs were weighed, and then they were placed into 15 mL centrifuge tubes. In each tube, 2 mL of Aqua Regia was added for digestion purposes. However, considering their larger size, the livers were placed in 50 mL centrifuge tubes and treated with 5 mL of Aqua Regia. After complete digestion, the mass of copper and iron in each organ was determined using Agilent 4100 MP-AES analysis. To ensure accurate measurements, the obtained values were then normalized by considering both the total volume of the solution and the weight of the respective organ. By employing this approach, we were able to evaluate the copper and iron levels present in the collected organs accurately and reliably.

Statistical Analysis. All the results are expressed as mean ± SEM. Statistical analysis of the biological experiments and the significant differences among the means were evaluated by two-way analysis of variance (ANOVA) for multiple comparisons by Dunnett's multiple comparisons test using GraphPad Software). Statistically significant differences were express as follows: *$p < 0.05$, **$p < 0.005$, ***$p < 0.0005$ and ****$p < 0.00005$.

References – Chapter 6

1. Solomon, E. I.; Sundaram, U. M.; Machonkin, T. E., Multicopper Oxidases and Oxygenases. Chemical Reviews 1996, 96 (7), 2563-2606.

2. Que, E. L.; Domaille, D. W.; Chang, C. J., Metals in Neurobiology: Probing Their Chemistry and Biology with Molecular Imaging. Chemical Reviews 2008, 108 (5), 1517-1549.

3. Adelstein, S.; Vallee, B. J. N. E. J. o. M., Copper metabolism in man. 1961, 265 (18), 892-897.

4. Kuo, H. W.; Chen, S. F.; Wu, C. C.; Chen, D. R.; Lee, J. H. J. B. t. e. r., Serum and tissue trace elements in patients with breast cancer in Taiwan. 2002, 89, 1-11.

5. Pavithra, V.; Sathisha, T.; Kasturi, K.; Mallika, D. S.; Amos, S. J.; Ragunatha, S. J. J. o. c.; JCDR, d. r., Serum levels of metal ions in female patients with breast cancer. 2015, 9 (1), BC25.

6. Jin, Y.; Zhang, C.; Xu, H.; Xue, S.; Wang, Y.; Hou, Y.; Kong, Y.; Xu, Y. J. C. E., Combined effects of serum trace metals and polymorphisms of CYP1A1 or GSTM1 on non-small cell lung cancer: A hospital based case–control study in China. 2011, 35 (2), 182-187.

7. Saleh, S. A.; Adly, H. M.; Abdelkhaliq, A. A.; Nassir, A. M. J. C. u., Serum levels of selenium, zinc, copper, manganese, and iron in prostate cancer patients. 2020, 14 (1), 44-49.

8. Ge, E. J.; Bush, A. I.; Casini, A.; Cobine, P. A.; Cross, J. R.; DeNicola, G. M.; Dou, Q. P.; Franz, K. J.; Gohil, V. M.; Gupta, S.; Kaler, S. G.; Lutsenko, S.; Mittal, V.; Petris, M. J.; Polishchuk, R.; Ralle, M.; Schilsky, M. L.; Tonks, N. K.; Vahdat, L. T.; Van Aelst, L.; Xi, D.; Yuan, P.; Brady, D. C.; Chang, C. J., Connecting copper and cancer: from transition metal signalling to metalloplasia. Nature Reviews Cancer 2022, 22 (2), 102-113.

9. Cui, L.; Gouw, A. M.; LaGory, E. L.; Guo, S.; Attarwala, N.; Tang, Y.; Qi, J.; Chen, Y.-S.; Gao, Z.; Casey, K. M.; Bazhin, A. A.; Chen, M.; Hu, L.; Xie, J.; Fang, M.; Zhang, C.; Zhu, Q.; Wang, Z.; Giaccia, A. J.; Gambhir, S. S.; Zhu, W.; Felsher, D. W.; Pegram, M. D.; Goun, E. A.; Le, A.; Rao, J., Mitochondrial copper depletion suppresses triple-negative breast cancer in mice. Nature Biotechnology 2021, 39 (3), 357-367.

10. Ramchandani, D.; Berisa, M.; Tavarez, D. A.; Li, Z.; Miele, M.; Bai, Y.; Lee, S. B.; Ban, Y.; Dephoure, N.; Hendrickson, R. C.; Cloonan, S. M.; Gao, D.; Cross, J. R.; Vahdat, L. T.; Mittal, V., Copper depletion modulates mitochondrial oxidative phosphorylation to impair triple negative breast cancer metastasis. Nature Communications 2021, 12 (1), 7311.

11. Ishida, S.; Andreux, P.; Poitry-Yamate, C.; Auwerx, J.; Hanahan, D., Bioavailable copper modulates oxidative phosphorylation and growth of tumors. 2013, 110 (48), 19507-19512.

12. Viale, A.; Corti, D.; Draetta, G. F. J. C. r., Tumors and Mitochondrial Respiration: A Neglected ConnectionMitochondrial Role in Tumor Progression. 2015, 75 (18), 3687-3691.

13. Erler, J. T.; Bennewith, K. L.; Nicolau, M.; Dornhöfer, N.; Kong, C.; Le, Q.-T.; Chi, J.-T. A.; Jeffrey, S. S.; Giaccia, A. J. J. N., Lysyl oxidase is essential for hypoxia-induced metastasis. 2006, 440 (7088), 1222-1226.

14. Habeck, M., Copper and angiogenesis—a new piece to the puzzle. The Lancet Oncology 2002, 3 (11), 650.

15. Pham, V. N.; Chang, C. J., Metalloallostery and Transition Metal Signaling: Bioinorganic Copper Chemistry Beyond Active Sites. Angewandte Chemie International Edition 2023, 62 (11), e202213644.

16. Turski, M. L.; Brady, D. C.; Kim, H. J.; Kim, B.-E.; Nose, Y.; Counter, C. M.; Winge, D. R.; Thiele, D. J. J. M.; biology, c., A novel role for copper in Ras/mitogen-activated protein kinase signaling. 2012, 32 (7), 1284-1295.

17. Liu, Y. L.; Bager, C. L.; Willumsen, N.; Ramchandani, D.; Kornhauser, N.; Ling, L.; Cobham, M.; Andreopoulou, E.; Cigler, T.; Moore, A.; LaPolla, D.; Fitzpatrick, V.; Ward, M.; Warren, J. D.; Fischbach, C.; Mittal, V.; Vahdat, L. T., Tetrathiomolybdate (TM)-associated copper depletion influences collagen remodeling and immune response in the pre-metastatic niche of breast cancer. npj Breast Cancer 2021, 7 (1), 108.

18. Chan, N.; Willis, A.; Kornhauser, N.; Ward, M. M.; Lee, S. B.; Nackos, E.; Seo, B. R.; Chuang, E.; Cigler, T.; Moore, A.; Donovan, D.; Vallee Cobham, M.; Fitzpatrick, V.; Schneider, S.; Wiener, A.; Guillaume-Abraham, J.; Aljom, E.; Zelkowitz, R.; Warren, J. D.; Lane, M. E.; Fischbach, C.; Mittal, V.; Vahdat, L., Influencing the Tumor Microenvironment: A Phase II Study of Copper Depletion Using Tetrathiomolybdate in Patients with Breast Cancer at High Risk for Recurrence and in Preclinical Models of Lung Metastases. Clinical Cancer Research 2017, 23 (3), 666-676.

19. Chavez, K. J.; Garimella, S. V.; Lipkowitz, S., Triple negative breast cancer cell lines: one tool in the search for better treatment of triple negative breast cancer. Breast disease 2010, 32 (1-2), 35-48.

20. Nagaraja, G. M.; Othman, M.; Fox, B. P.; Alsaber, R.; Pellegrino, C. M.; Zeng, Y.; Khanna, R.; Tamburini, P.; Swaroop, A.; Kandpal, R. P., Gene expression signatures and biomarkers of noninvasive and invasive breast cancer cells: comprehensive profiles by representational difference analysis,

microarrays and proteomics. Oncogene 2006, 25 (16), 2328-38.

21. Blockhuys, S.; Celauro, E.; Hildesjö, C.; Feizi, A.; Stål, O.; Fierro-González, J. C.; Wittung-Stafshede, P., Defining the human copper proteome and analysis of its expression variation in cancers. Metallomics : integrated biometal science 2017, 9 (2), 112-123.

22. Thakur, V.; Kutty, R. V., Recent advances in nanotheranostics for triple negative breast cancer treatment. Journal of Experimental & Clinical Cancer Research 2019, 38 (1), 430.

23. Malhotra, M. K.; Emens, L. A., The evolving management of metastatic triple negative breast cancer. Seminars in oncology 2020, 47 (4), 229-237.

24. Yu, Y.; Shapter, J. G.; Popelka-Filcoff, R.; Bennett, J. W.; Ellis, A. V., Copper removal using bio-inspired polydopamine coated natural zeolites. Journal of Hazardous Materials 2014, 273, 174-182.

25. Sun, D. T.; Peng, L.; Reeder, W. S.; Moosavi, S. M.; Tiana, D.; Britt, D. K.; Oveisi, E.; Queen, W. L., Rapid, Selective Heavy Metal Removal from Water by a Metal–Organic Framework/Polydopamine Composite. ACS Central Science 2018, 4 (3), 349-356.

26. Xing, J.; Wang, Q.; He, T.; Zhou, Z.; Chen, D.; Yi, X.; Wang, Z.; Wang, R.; Tan, G.; Yu, P.; Ning, C., Polydopamine-Assisted Immobilization of Copper Ions onto Hemodialysis Membranes for Antimicrobial. ACS Applied Bio Materials 2018, 1 (5), 1236-1243.

27. Mrówczyński, R., Polydopamine-Based Multifunctional (Nano)materials for Cancer Therapy. ACS Applied Materials & Interfaces 2018, 10 (9), 7541-7561.

28. Chung, C. Y.-S.; Posimo, J. M.; Lee, S.; Tsang, T.; Davis, J. M.; Brady, D. C.; Chang, C. J., Activity-based ratiometric FRET probe reveals oncogene-driven changes in labile copper pools induced by altered glutathione metabolism. 2019, 116 (37), 18285-18294.

29. Lee, H.; Dellatore, S. M.; Miller, W. M.; Messersmith, P. B., Mussel-inspired surface chemistry for multifunctional coatings. Science (New York, N.Y.) 2007, 318 (5849), 426-30.

30. Nieto, C.; Marcelo, G.; Vega, M.; Martín del Valle, E. M., Antineoplastic behavior of polydopamine nanoparticles prepared in different water/alcohol media. Colloids and Surfaces B: Biointerfaces 2021, 199, 111506.

31. Dreyer, D. R.; Miller, D. J.; Freeman, B. D.; Paul, D. R.; Bielawski, C. W., Elucidating the structure of poly(dopamine). Langmuir 2012, 28 (15), 6428-35.

32. Liebscher, J.; Mrówczyński, R.; Scheidt, H. A.; Filip, C.; Hădade, N. D.; Turcu, R.; Bende, A.; Beck, S., Structure of Polydopamine: A Never-Ending Story? Langmuir 2013, 29 (33), 10539-10548.

33. Bruemmer, K. J.; Crossley, S. W. M.; Chang, C. J., Activity-Based Sensing: A Synthetic Methods Approach for Selective Molecular Imaging and Beyond. Angewandte Chemie International Edition 2020, 59 (33), 13734-13762.

34. Goldblum, R. R.; McClellan, M.; White, K.; Gonzalez, S. J.; Thompson, B. R.; Vang, H. X.; Cohen, H.; Higgins, L.; Markowski, T. W.; Yang, T. Y.; Metzger, J. M.; Gardner, M. K., Oxidative stress pathogenically remodels the cardiac myocyte cytoskeleton via structural alterations to the microtubule lattice. Developmental cell 2021, 56 (15), 2252-2266.e6.

35. Mackeh, R.; Lorin, S.; Ratier, A.; Mejdoubi-Charef, N.; Baillet, A.; Bruneel, A.; Hamaï, A.; Codogno, P.; Poüs, C.; Perdiz, D., Reactive oxygen species, AMP-activated protein kinase, and the transcription cofactor p300 regulate α-tubulin acetyltransferase-1 (αTAT-1/MEC-17)-dependent microtubule hyperacetylation during cell stress. The Journal of biological chemistry 2014, 289 (17), 11816-11828.

36. Bao, X.; Zhao, J.; Sun, J.; Hu, M.; Yang, X., Polydopamine Nanoparticles as Efficient Scavengers for Reactive Oxygen Species in Periodontal Disease. ACS Nano 2018, 12 (9), 8882-8892.

37. Battaglini, M.; Carmignani, A.; Martinelli, C.; Colica, J.; Marino, A.; Doccini, S.; Mollo, V.; Santoro, F.; Bartolucci, M.; Petretto, A.; Santorelli, F. M.; Ciofani, G., In vitro study of polydopamine nanoparticles as protective antioxidant agents in fibroblasts derived from ARSACS patients. Biomaterials Science 2022, 10 (14), 3770-3792.

38. Wong, P. C.; Waggoner, D.; Subramaniam, J. R.; Tessarollo, L.; Bartnikas, T. B.; Culotta, V. C.; Price, D. L.; Rothstein, J.; Gitlin, J. D., Copper chaperone for superoxide dismutase is essential to activate mammalian Cu/Zn superoxide dismutase. 2000, 97 (6), 2886-2891.

39. Snezhkina, A. V.; Kudryavtseva, A. V.; Kardymon, O. L.; Savvateeva, M. V.; Melnikova, N. V.; Krasnov, G. S.; Dmitriev, A. A., ROS Generation and Antioxidant Defense Systems in Normal and Malignant Cells. Oxidative medicine and cellular longevity 2019, 2019, 6175804.

40. Yu, T.; Robotham, J. L.; Yoon, Y., Increased production of reactive oxygen species in hyperglycemic conditions requires dynamic change of mitochondrial morphology. Proceedings of the National Academy of Sciences of the United States of America 2006, 103 (8), 2653-8.

41. Sivandzade, F.; Bhalerao, A.; Cucullo, L., Analysis of the Mitochondrial Membrane Potential Using the Cationic JC-1 Dye as a Sensitive Fluorescent Probe. Bio-protocol 2019, 9 (1).

Supplementary information – Chapter 6

Adapted from:

Labile copper chelation using Polydopamine nanoparticles stops MDA-MB-231 tumor growth in mice through altering metabolism and redox homeostasis.

Javier Bonet-Aleta[1,2,3], Miguel Encinas-Giménez[1,2,3], Miku Oi[4], Aidan T. Pezacki[4], Victor Sebastian[1,2,3], Ana Martin Pardillos[,1,2,3], Pilar Martin-Duque[2,5,6], Jose L. Hueso[1,2,3], Jesus Santamaria[1,2,3], Christopher J. Chang[4,7,8*].*

[1] Instituto de Nanociencia y Materiales de Aragon (INMA) CSIC-Universidad de Zaragoza, Campus Rio Ebro, Edificio I+D, C/ Poeta Mariano Esquillor, s/n, 50018, Zaragoza, (Spain).

[2] Networking Res. Center in Biomaterials, Bioengineering and Nanomedicine (CIBER-BBN), Instituto de Salud Carlos III; 28029 Madrid (Spain)

[3] Department of Chemical and Environmental Engineering, University of Zaragoza, Campus Rio Ebro, C/María de Luna, 3, 50018 Zaragoza (Spain).

[4] Department of Chemistry, University of California, Berkeley, CA, 94720

[5] Instituto de Investigación Sanitaria (IIS) de Aragón, Avenida San Juan Bosco, 13, 50009 Zaragoza, Spain.

[6] Departamento de Cirugía, Facultad de Medicina, Universidad de Zaragoza, 50009, Zaragoza, Spain

[7] Department of Molecular and Cell Biology, University of California, Berkeley, CA, 94720

[8] Helen Willis Neuroscience Institute, University of California, Berkeley, CA, 94720

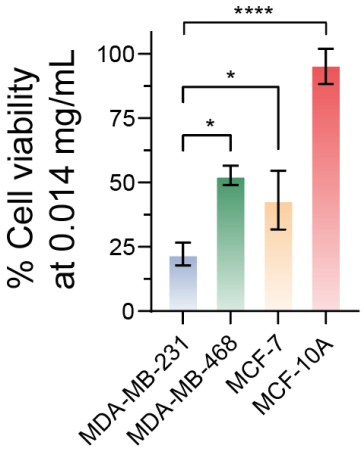

Supplementary Figure 1. *Cell viability of different cell lines after 24 h of incubation with 0.014 mg·mL^{-1} of PDA. Results revealed breast cancer cells (MDA-MB-231, MDA-MB-468 and MCF-7) viability is reduced in comparison to healthy cells (MCF-10A) after treatment with PDA particles. Results are expressed as Mean ± S.E.M, n =3 biological independent experiments. *P < 0.05, **P < 0.01, ***P < 0.001, and ****P < 0.0001; ns, not statistically significant.*

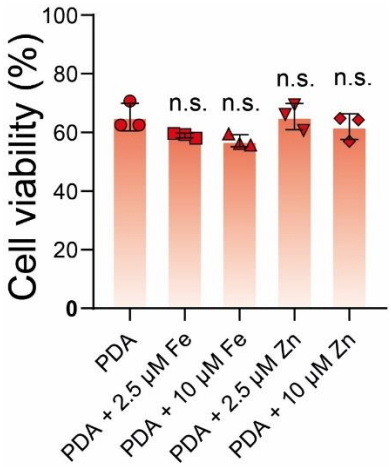

Supplementary Figure 2. *Cell viability of MDA-MB-231 treated with 5·10^{-3} mg·mL^{-1} of PDA NPs with an external supplementation of zinc and iron. Results are expressed as Mean ± S.E.M, n =3 biological independent experiments. *P < 0.05, **P < 0.01, ***P < 0.001, and ****P < 0.0001; ns, not statistically significant.*

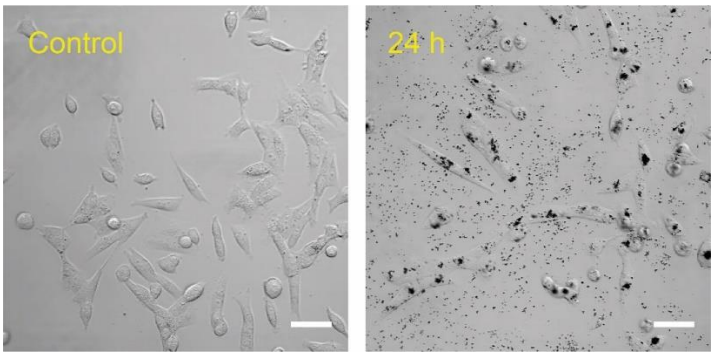

Supplementary Figure 3. *Bright field images of control (left) and treated (right) MDA-MB-231 cells with $1.14 \cdot 10^{-3}$ mg·mL^{-1} after 24 h.*

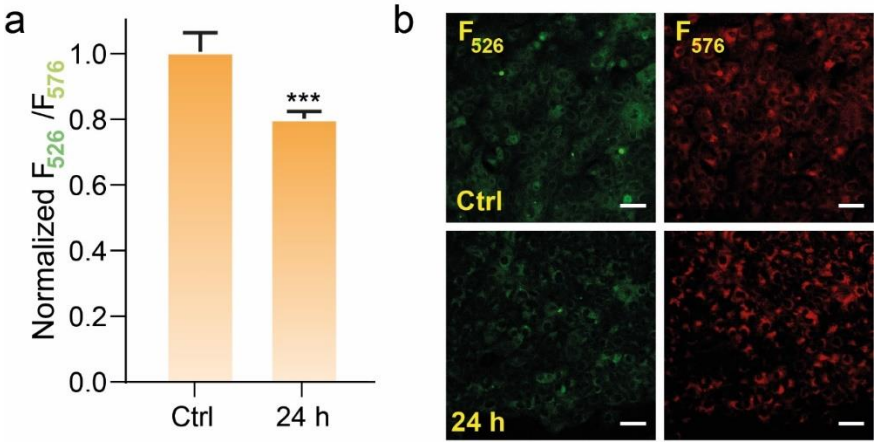

Supplementary Figure 4. *(a) Quantification of F526/F576 ratio and (b) confocal microscopy images of control and treated MCF-10A cells treated with $1.40 \cdot 10^{-3}$ mg·mL^{-1} of PDA NPs for 24 h.*

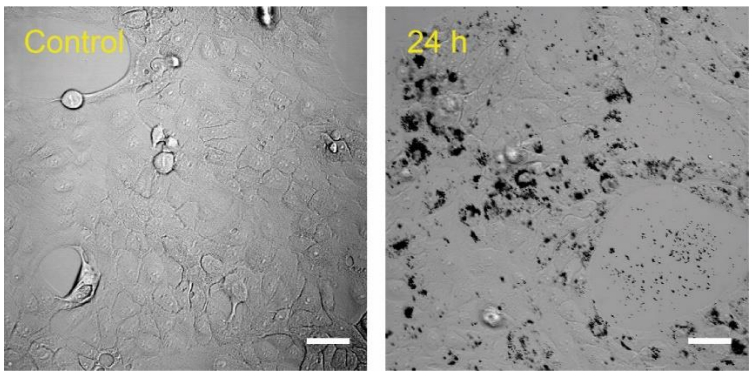

Supplementary Figure 5. *Bright field images of control (left) and treated (right) MCF-10A cells with $1.14 \cdot 10^{-3}$ mg·mL^{-1} after 24 h.*

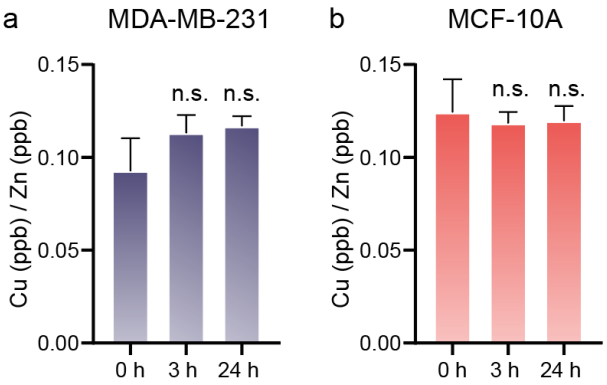

Supplementary Figure 6. *ICP-MS analysis of intracellular copper levels in (a) MDA-MB-231 and (b) MCF-10A cells after the treatment with $1.40 \cdot 10^{-3}$ mg·mL^{-1} for 3 h and 24 h. Results are expressed as $^{63}Cu/^{64}Zn$ to normalized by number of cells based on the cellular ^{64}Zn content. Error bars denote S.E.M, n=6 biological independent experiments. *P < 0.05, **P < 0.01, ***P < 0.001, and ****P < 0.0001; ns, not statistically significant.*

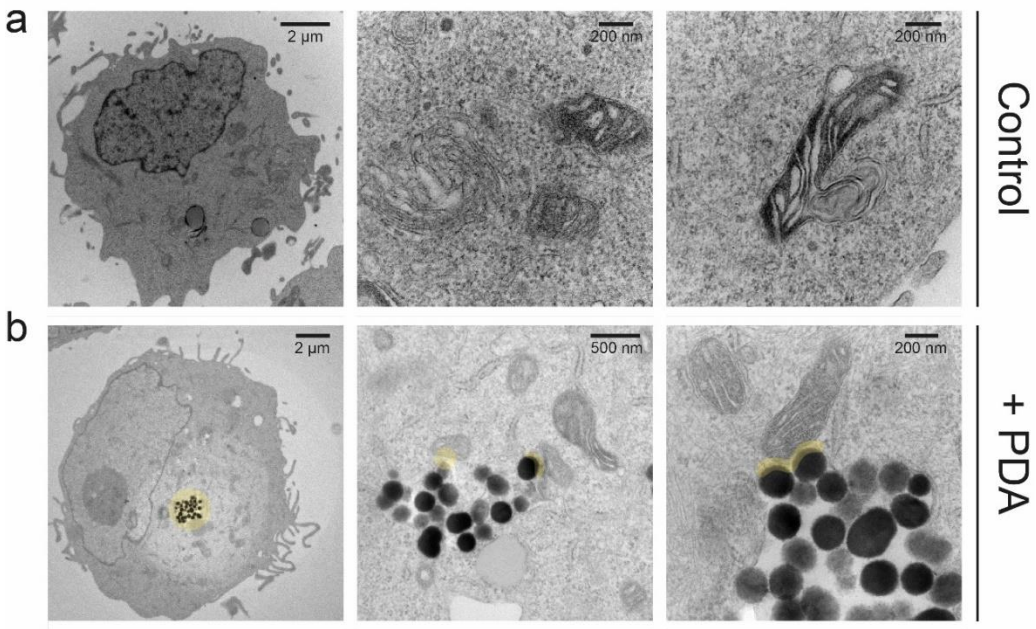

Supplementary Figure 7. *Representative transmission electron microscopy images of (a) control MDA-MB-231 cells and (b) treated MDA-MB-231 cells with $1.4 \cdot 10^{-3}$ mg·mL^{-1} of PDA for 24 h.*

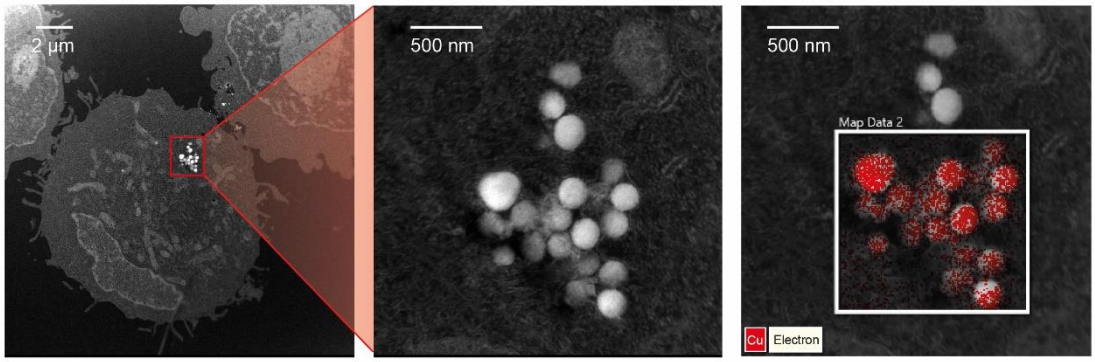

Supplementary Figure 8. *STEM-EDS-HAADF images of treated MDA-MB-231 cells revealed the colocalization of copper onto the surface of PDA nanoparticles after 24 h of incubation with a concentration of 1.14·10^{-3} mg·mL^{-1}.*

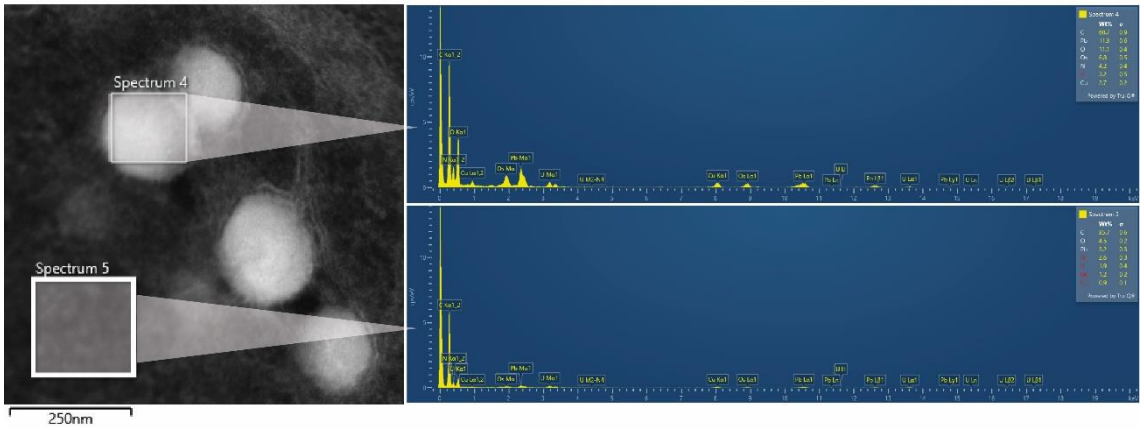

Supplementary Figure 9. *EDS spectra of the surface of a single internalized PDA nanoparticle revealed a 2.7 % of copper, while the background signal posses a residual amount of copper.*

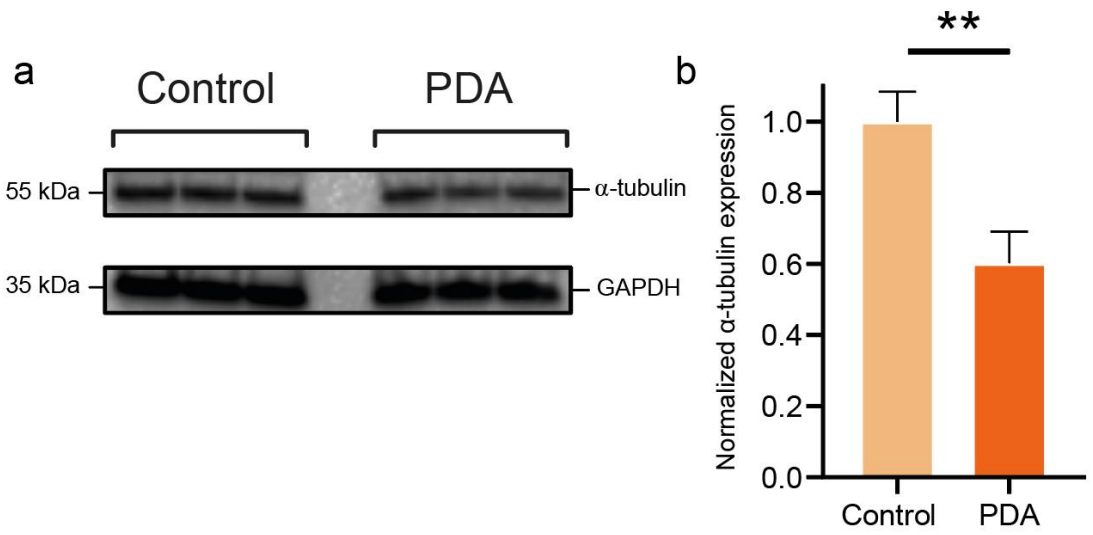

Supplementary Figure 10. *(a) Western-Blot analysis and (b) quantification of α-tubulin and Glyceraldehyde 3-phosphate dehydrogenase (GAPDH) proteins in MDA-MB-231 cells treated $5.0 \cdot 10^{-3}$ mg/mL of PDA for 24 h. *P < 0.05, **P < 0.01, ***P < 0.001, and ****P < 0.0001; ns, not statistically significant. Error bars denote S.E.M (n = 3).*

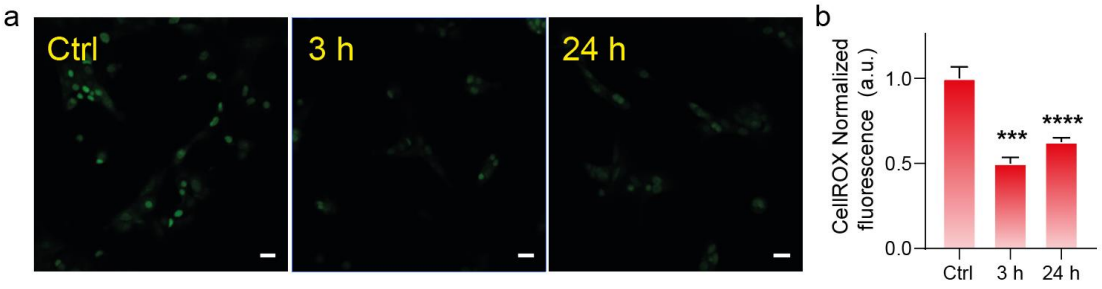

Supplementary Figure 11. *(a) Confocal microscopy analysis and (b) quantification of ROS present in MCF-10A cell using CellROX™ fluorescent probe after the treatment with $5.0 \cdot 10^{-2}$ mg·mL^{-1} of PDA revealed its role quenching intracellular ROS. λ_{ex} = 485 nm. Scale bar = 50 μm. Error bars denote S.E.M, n=8 biological independent experiments. *P < 0.05, **P < 0.01, ***P < 0.001, and ****P < 0.0001; ns, not statistically significant.*

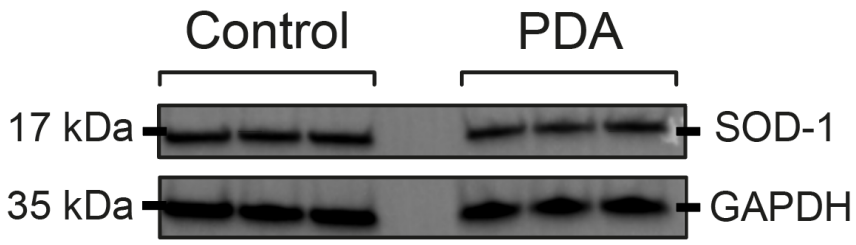

Supplementary Figure 12. *Western-Blot analysis of SOD-1 and GAPDH proteins in MDA-MB-231 cells treated with $5.0 \cdot 10^{-3}$ mg/mL of PDA for 24 h.*

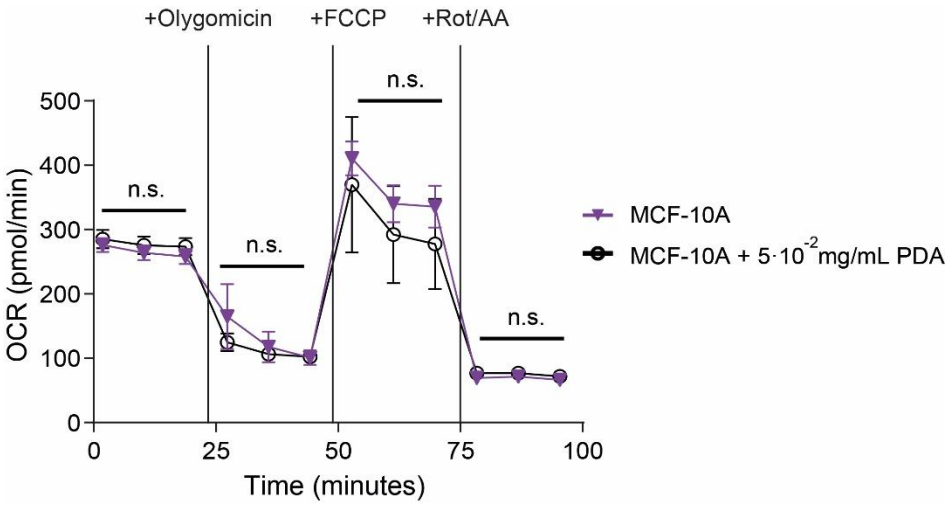

Supplementary Figure 13. *OCR analysis in MCF-10A after the treatment with PDA for 24 h. The measurement was performed by Seahorse analyzer, by adding 1 μM of oligomicin after 28 minutes, FCCP (1 μM) after 54 minutes and a 1:1 mixture of rotenone A/antimicin (0.5 μM) after 80 minutes. *P < 0.05, **P < 0.01, ***P < 0.001, and ****P < 0.0001; ns, not statistically significant. Error bars denotes S.E.M (n = 9 per condition).*

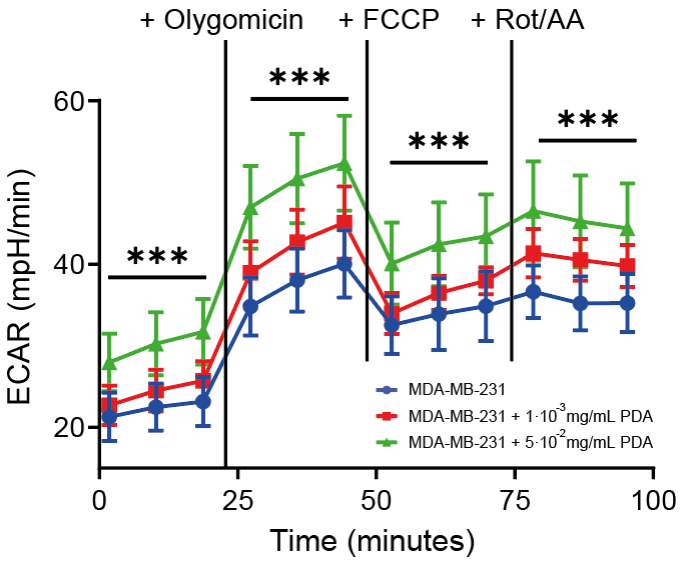

Supplementary Figure 14. *Extracellular acidification rate (ECAR) analysis of MDA-MB-231 cells treated with different concentrations of PDA nanoparticles for 24 h. The measurement was performed by Seahorse analyzer, by adding 1 μM of oligomicin after 28 minutes, FCCP (1 μM) after 54 minutes and a 1:1 mixture of rotenone A/antimicin (0.5 μM) after 80 minutes. Error bars denotes S.E.M (n = 9). *P < 0.05, **P < 0.01, ***P < 0.001, and ****P < 0.0001; ns, not statistically significant.*

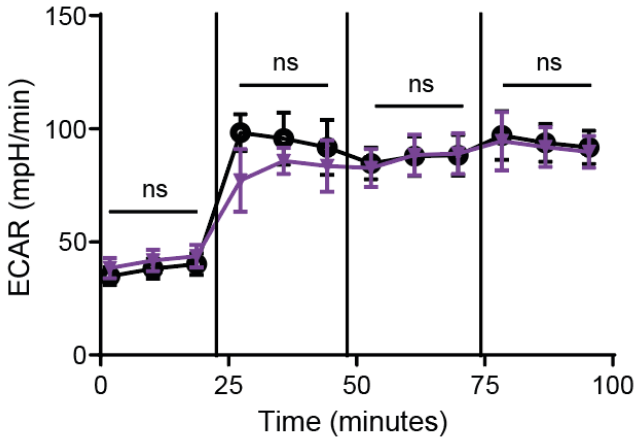

Supplementary Figure 15. *ECAR analysis of MCF-10A cells treated with $5{\cdot}10^{-2}$ mg·mL^{-1} of PDA nanoparticles for 24 h. The measurement was performed by Seahorse analyzer, by adding 1 μM of oligomicin after 28 minutes, FCCP (1 μM) after 54 minutes and a 1:1 mixture of rotenone A/antimicin (0.5 μM) after 80 minutes. Error bars denotes S.E.M (n = 9). *P < 0.05, **P < 0.01, ***P < 0.001, and ****P < 0.0001; ns, not statistically significant.*

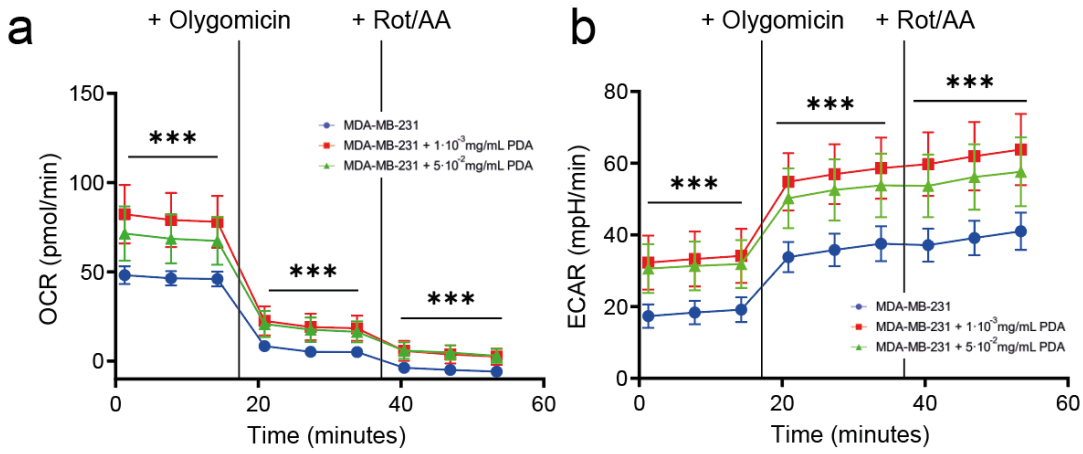

Supplementary Figure 16. *(a) OCR and (b) ECAR measurements of MDA-MB-231 cells treated with different doses of PDA for 24 h. The measurement was performed by Seahorse analyzer, by adding 1 μM of oligomicin after 18 minutes and a 1:1 mixture of rotenone A/antimicin (0.5 μM) after 38 minutes. Error bars denotes S.E.M (n = 9). *P < 0.05, **P < 0.01, ***P < 0.001, and ****P < 0.0001; ns, not statistically significant.*

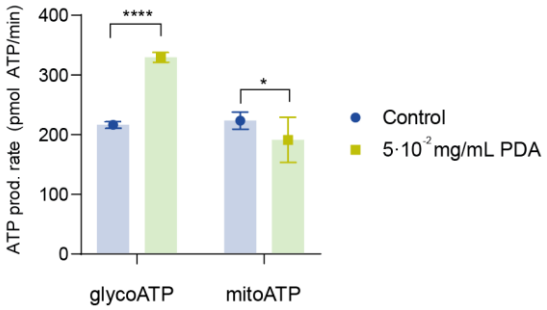

Supplementary Figure 17. *Quantification of ATP production rate classified by its source whether glycolytic route or oxidative phosphorylation at mitochondria in MDA-MB-231 treated with PDA for 24 h. Error bars denotes S.E.M (n = 9). *P < 0.05, **P < 0.01, ***P < 0.001, and ****P < 0.0001; ns, not statistically significant.*

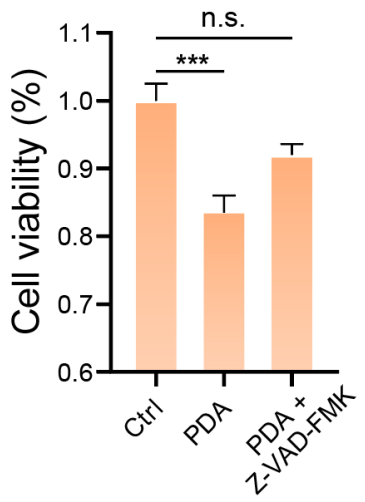

Supplementary Figure 18. *MDA-MB-231 viability after 24 h in the presence of $1.14 \cdot 10^{-3}$ mg·mL^{-1} of PDA or $1.14 \cdot 10^{-3}$ mg·mL^{-1} of PDA with 10 μM of Z-VAD-FMK, a well-known apoptosis inhibitor. *P < 0.05, **P < 0.01, ***P < 0.001, and ****P < 0.0001; ns, not statistically significant. Error bars denotes S.E.M (n = 3).*

Conclusions

The main conclusions from each chapter are listed below:

Chapter #1. Glutathione-Triggered catalytic response of Copper-Iron mixed oxide Nanoparticles. Leveraging tumor microenvironment conditions for chemodynamic therapy.

i) $CuFe_2O_4$ (CuFe) nanoparticles prepared in our laboratory exhibit remarkable catalytic properties in the presence of GSH and H_2O_2. Specifically, CuFe facilitates a reaction cascade leading to the oxidation of GSH into GSSG and the decomposition of H_2O_2 into •OH.

ii) This reactivity holds significant potential for the induction of apoptosis in cancer cells, as shown with the U251 cell line investigated in this study. Notably, the intracellular GSH levels of U251 cells are considerably higher than those of the healthy cells examined (hpMSC), making them particularly susceptible to CuFe-mediated apoptosis.

Chapter #2. Synergistic assembly of gold and copper-iron oxide nanocatalysts to promote the simultaneous depletion of glucose and glutathione.

i) A hybrid bifunctional catalyst can be assembled combining CuFe and Au nanoparticles in the same nanoplatform to achieve glucose oxidation (Au) and GSH oxidation (CuFe),

ii) The presence of CuFe effectively hinders deactivation of Au nanoparticles by GSH, as evidenced by a comparative analysis with Au nanoparticles attached to inert SiO_2 nanoparticles, that underwent rapid deactivation of Au towards glucose oxidation.

Chapter #3. Unveiling the interplay between homogeneous and heterogeneous catalytic mechanisms in copper–iron nanoparticles working under chemically relevant tumour conditions.

i) Heterogeneous catalysts can give rise to processes that extend beyond purely heterogeneous behavior. In particular a copper-iron-based nanocatalyst can generate a combination of homogeneous and heterogeneous processes under conditions relevant to the tumor microenvironment.

ii) The majority of the contributing reactions to GSH oxidation occur within a homogeneous cycle, catalyzed by released Cu species.

iii) The role of the remaining Fe-enriched nanoparticles consists on regenerating the required O_2 for the GSH oxidation using the by products (i.e. $\bullet O_2^-$ or H_2O_2) from this reaction.

iv) In catalytic scenarios where a solid releases ions with catalytic activity, homogeneous and heterogeneous processes are no longer isolated events. This must be considered in catalyst design that becomes more complex, as it must account for the influence of environmental species on catalyst stability. However, it also becomes more powerful, as leaching processes can be engineered to yield synergistic catalytic actions. In this context, catalyst design goes beyond merely favoring specific surface reactions; it now encompasses the catalyst role as a reservoir for the controlled, long-term release of active ions in response to stimuli from the chemical environment.

Chapter #4. Cu-releasing nanoparticles induce the catalytic transamination of amino acids and GSSG under tumor microenvironment conditions.

i) Copper cations released from CuFe nanoparticles are able to catalyze transamination reactions using glutamine, glutamic acid, and aspartic acid as amino acid substrates, and pyruvate as oxo-group donor, under conditions comparable to those in the tumor microenvironment, including hypoxia and GSH.

ii) GSSG, a crucial biomolecule within the TME responsible for maintaining redox homeostasis, can undergo transamination reactions akin to single amino acids.

iii) As consequence of these catalyzed transamination processes, the internalization of CuFe nanoparticles in U251-MG cells enhanced the consumption of glutamine while elevating intracellular alanine levels for up to 48 hours of incubation.

Chapter #5. An Activity-Based Sensing Approach to Monitor Nanomaterial-Promoted Changes in Labile Metal Pools in Living Systems.

i) Activity-based sensing as an effective method to monitorize the fate and location of suitable cations released from nanoparticles, in particular activity-based sensing probes were able specifically designed to detect labile Cu(I) and Cu(II) (**CD664**) or Cu(II) alone (**CD649.2**) inside living systems.

ii) While the total copper content in cells increased upon exposure to copper-containing nanomedicines, (i.e. $CuFe_2O_4$ or $Cu_2Fe(CN)_6$ nanoparticles), a simultaneous decrease in the overall levels of bioavailable labile copper pools was observed.

iii) In response to the altered copper dynamics, A549 cells initiated two distinct antioxidant pathways to counteract oxidative stress. First, the bioavailability of the redox buffering molecule GSH increased. Also, the redox-responsive transcription factor NRF2 was activated. Additionally, the cells exhibited adaptive changes in metal homeostasis machinery, limiting copper exposure by upregulating copper ion export via ATP7B and downregulating copper ion import via CTR1.

Chapter #6. Labile copper chelation using Polydopamine nanoparticles stops MDA-MB-231 tumor growth in mice through altering metabolism and redox homeostasis.

i) Polydopamine nanoparticles (PDA NPs) are effective for depleting intracellular labile copper in triple negative breast cancer cells. Copper, a critical metal cofactor for enzymes involved in cell proliferation and metabolism, was selectively targeted using the metal-chelating groups present on the surface of PDA NPs.

ii) Activity-based sensing probe FCP-1, allowed to track the depletion of labile copper induced by PDA NPs.

iii) PDA NPs increased reactive oxygen species (ROS) levels, likely by inactivating superoxide dismutase 1, an Cu-dependent enzyme.

iv) PDA NPs interacted with the mitochondrial membrane, leading to an increase in mitochondrial membrane potential and contributing to enhanced ROS production.

The general conclusions of this Ph.D. thesis are:

#1. Catalysis may be a valuable tool in cancer therapy. Apart from the strategies focused on deprotection chemistry, nanoparticles can catalyze specific harmful chemical reactions for cancer cells using characteristic the tumor microenvironment molecules.

#2. Heterogeneous catalysts can evolve. When a nanoparticle is internalized by a cell, certain chemical conditions that it faces can provoke a transformation that potentially will play a pivotal role on its therapeutic efficacy.

#3. Activity-based sensing enables the detection of nanomaterial-induced changes in cells, facilitating a more comprehensive understanding of the impact of nanoparticles on labile metal levels to unravel potential vulnerabilities of cancer cells.

Conclusiones

Las principales conclusiones de cada capítulo se enumeran a continuación:

Capítulo 1. Respuesta catalítica desencadenada por el glutatión de nanopartículas de óxido mixto de cobre-hierro. Aprovechamiento de las condiciones del microentorno tumoral para la terapia quimiodinámica.

i) Las nanopartículas $CuFe_2O_4$ (CuFe) preparadas en nuestro laboratorio exhiben propiedades catalíticas en presencia de GSH y H_2O_2. Específicamente, CuFe facilita una cascada de reacciones que conducen a la oxidación de GSH en GSSG y a la descomposición de H_2O_2 en •OH.

ii) Esta reactividad tiene un gran potencial para inducir apoptosis en células cancerosas, como se muestra en la línea celular U251 investigada en este estudio. Es importante destacar que los niveles intracelulares de GSH en las células U251 son considerablemente más altos que los de las células sanas examinadas (hpMSC), lo que las hace particularmente susceptibles a la apoptosis mediada por CuFe.

Capítulo 2. Ensamblaje sinérgico de nanocatalizadores de oro y óxido de cobre-hierro para promover la depleción simultánea de glucosa y glutatión.

i) Se puede ensamblar un catalizador bifuncional híbrido combinando nanopartículas de CuFe y Au en la misma nanoplataforma para lograr la oxidación de la glucosa (Au) y la oxidación de GSH (CuFe).

ii) La presencia de CuFe inhibe eficazmente la desactivación de las nanopartículas de Au por GSH, como se demuestra comparando la actividad con nanopartículas de Au unidas a nanopartículas inertes de SiO_2, que experimentaron una rápida desactivación de Au hacia la oxidación de glucosa.

Capítulo 3. Revelando la interacción entre mecanismos catalíticos homogéneos y heterogéneos en nanopartículas de cobre-hierro que funcionan en condiciones químicamente relevantes para el tumor.

i) Los catalizadores heterogéneos pueden dar lugar a procesos que van más allá de un comportamiento puramente heterogéneo. En particular, un nanocatalizador basado en cobre y hierro puede generar una combinación de procesos homogéneos y heterogéneos en condiciones relevantes para el microentorno tumoral.

ii) La mayoría de las reacciones que contribuyen a la oxidación de GSH ocurren dentro de un ciclo homogéneo, catalizado por especies de Cu liberadas.

iii) El papel de las nanopartículas enriquecidas con Fe restantes consiste en regenerar el O_2 requerido para la oxidación de GSH utilizando los subproductos (es decir, $\bullet O_2^-$ o H_2O_2) de esta reacción.

iv) En escenarios catalíticos en los que un sólido libera iones con actividad catalítica, los procesos homogéneos y heterogéneos ya no son eventos aislados. Esto debe tenerse en cuenta en el diseño de catalizadores, que se vuelve más complejo, ya que debe considerar la influencia de las especies ambientales en la estabilidad del catalizador. Sin embargo, también se vuelve más poderoso, ya que los procesos de lixiviación se pueden diseñar para producir acciones catalíticas sinérgicas. En este contexto, el diseño del catalizador va más allá de favorecer simplemente reacciones superficiales específicas; ahora abarca el papel del catalizador como un reservorio para la liberación controlada y a largo plazo de iones activos en respuesta a estímulos del entorno químico.

Capítulo 4. Las nanopartículas liberadoras de cobre inducen la transaminación catalítica de aminoácidos y GSSG en condiciones del microentorno tumoral.

i) Los cationes de cobre liberados de las nanopartículas de CuFe pueden catalizar reacciones de transaminación utilizando glutamina, ácido glutámico y ácido aspártico como sustratos de aminoácidos, y piruvato como donante de grupo oxo, en condiciones comparables a las del microentorno tumoral, incluida la hipoxia y GSH.

ii) GSSG, una biomolécula crucial dentro del microentorno tumoral responsable de mantener la homeostasis redox, puede someterse a reacciones de transaminación similares a los aminoácidos individuales.

iii) Como consecuencia de estos procesos de transaminación catalizada, la internalización de las nanopartículas de CuFe en las células U251-MG aumentó el consumo de glutamina al tiempo que elevaba los niveles de alanina intracelular durante hasta 48 horas de incubación.

Capítulo 5. La estrategia "Activity-based sensing" para monitorear cambios inducidos por nanomateriales en los niveles de metales lábiles en sistemas vivos.

i) La "Activity-based sesing" es un método efectivo para monitorear el destino y la ubicación de cationes adecuados liberados por nanopartículas, en particular, las sondas de detección basadas en la actividad fueron diseñadas específicamente para detectar cobre lábil Cu(I) y Cu(II) (**CD664**) o solo Cu(II) (**CD649.2**) dentro de sistemas vivos.

ii) Si bien el contenido total de cobre en las células aumentó después de la exposición a nanomedicamentos que contienen cobre (es decir, nanopartículas de $CuFe_2O_4$ o $Cu_2Fe(CN)_6$), se observó una disminución simultánea en los niveles generales de reservas de cobre lábil bioaccesibles.

iii) En respuesta a la dinámica alterada del cobre, las células A549 iniciaron dos vías antioxidantes distintas para contrarrestar el estrés oxidativo. En primer lugar, aumentó la bioaccesibilidad de la molécula tampón redox GSH. Además, se activó el factor de transcripción sensible al redox NRF2. Además, las células mostraron cambios adaptativos en la maquinaria de homeostasis del metal, limitando la exposición al cobre al aumentar la exportación de iones de cobre a través de ATP7B y disminuir la importación de iones de cobre a través de CTR1.

Capítulo 6. La quelación de cobre lábil mediante nanopartículas de polidopamina detiene el crecimiento de tumores MDA-MB-231 en ratones mediante la alteración del metabolismo y la homeostasis redox.

i) Las nanopartículas de polidopamina (PDA NPs) son efectivas para agotar el cobre lábil intracelular en células de cáncer de mama triple negativo. El cobre, un cofactor metálico crítico

para enzimas involucradas en la proliferación celular y el metabolismo, fue selectivamente dirigido utilizando los grupos quelantes de metales presentes en la superficie de las PDA NPs.

ii) La sonda de detección basada en la actividad FCP-1 permitió rastrear la disminución del cobre lábil inducida por las PDA NPs.

iii) Las PDA NPs aumentaron los niveles de especies reactivas de oxígeno (ROS), probablemente inactivando la superóxido dismutasa 1, una enzima dependiente de Cu.

iv) Las PDA NPs interactuaron con la membrana mitocondrial, lo que llevó a un aumento en el potencial de la membrana mitocondrial y contribuyó a una mayor producción de ROS.

Las conclusiones generales de esta tesis doctoral son:

#1. La catálisis puede ser una herramienta valiosa en la terapia del cáncer. Además de las estrategias enfocadas en la química de desprotección, las nanopartículas pueden catalizar reacciones químicas dañinas específicas para las células cancerosas utilizando moléculas características del microentorno tumoral.

#2. Los catalizadores heterogéneos pueden evolucionar. Cuando una nanopartícula es internalizada por una célula, ciertas condiciones químicas a las que se enfrenta pueden provocar una transformación que potencialmente desempeñará un papel fundamental en su eficacia terapéutica.

#3. La detección basada en la actividad permite detectar cambios inducidos por nanomateriales en las células, lo que facilita una comprensión más completa del impacto de las nanopartículas en los niveles de metales lábiles para descubrir posibles vulnerabilidades de las células cancerosas.